



Modélisation et simulation numérique d'écoulements compressibles

Virginie Daru

► To cite this version:

Virginie Daru. Modélisation et simulation numérique d'écoulements compressibles. Mécanique des fluides [physics.class-ph]. Sorbonne université, 2020. tel-04438209

HAL Id: tel-04438209

<https://universite-paris-saclay.hal.science/tel-04438209>

Submitted on 14 Feb 2024

HAL is a multi-disciplinary open access archive for the deposit and dissemination of scientific research documents, whether they are published or not. The documents may come from teaching and research institutions in France or abroad, or from public or private research centers.

L'archive ouverte pluridisciplinaire **HAL**, est destinée au dépôt et à la diffusion de documents scientifiques de niveau recherche, publiés ou non, émanant des établissements d'enseignement et de recherche français ou étrangers, des laboratoires publics ou privés.

SORBONNE UNIVERSITÉ
Laboratoire DynFluid
Laboratoire d’Informatique pour la Mécanique et les Sciences de
l’Ingénieur

Mémoire présenté pour obtenir
L’HABILITATION À DIRIGER DES RECHERCHES

par

Virginie DARU

Modélisation et simulation numérique d’écoulements compressibles

Soutenue le **23 juin 2020**,

devant le jury composé de :

Rapporteurs **Christophe Corre**

Professeur des Universités,
Ecole Centrale de Lyon & LMFA, Lyon
Directeur de Recherche,
CNRS & LAUM, Le Mans
Directeur de Recherche,
CNRS & IMFT, Toulouse

Joël Gilbert

Directeur de Recherche,

Jacques Magnaudet

Directeur de Recherche,

Examinateurs **Jean-Christophe Robinet**

Professeur des Universités,

Christian Tenaud

ENSAM & DynFluid, Paris

Régis Wunenburger

Directeur de Recherche,

CNRS & LIMSI, Orsay

Professeur des Universités,

Sorbonne Université & ∂’Alembert, Paris

Table des matières

I Préambule	5
II Résumé de carrière	9
III Activités de recherche	23
1 Introduction	25
2 Schémas numériques pour les écoulements compressibles avec chocs	27
2.1 Construction et étude des propriétés des schémas OSMP	27
2.2 Application des schémas OSMP au calcul d'écoulements compressibles.	35
3 Écoulements diphasiques	51
3.1 Jet d'eau à haute pression	51
3.2 Impact de gouttes	52
3.3 Tension de surface	55
3.4 Écoulements liquide-gaz dans l'approche faible Mach	58
4 Streaming acoustique	64
IV Perspectives	77
Bibliographie	82
Articles en annexe	91
P. Kuszla, V. Daru, " Numerical simulation of high-speed liquid jets ", Computational Mechanics, New trends and applications, S. Idelsohn, E. Oñate and E. Dvorkin (Eds.), CIMNE, ©Barcelona, Spain (1998)	91
V. Daru, C. Tenaud, " High order one-step monotonicity-preserving schemes for unsteady compressible flows calculations ", Journal of Computational Physics, 193, p. 563-594 (2004).	107
V. Daru, P. Le Quéré, M.-C. Duluc, O. Le Maître, " A numerical method for the simulation of low Mach number liquid-gas flows ", Journal of Computational Physics, 229(23), p. 8844-8867 (2010).	141
L. Monasse, V. Daru, C. Mariotti, S. Piperno, C. Tenaud, " A conservative coupling algorithm between a compressible flow and a rigid body using an Embedded Boundary method ", Journal of Computational Physics 231, p. 2977-2994 (2012).167	

I. Reyt, H. Bailliet, D. Baltean-Carlès, V. Daru, S. Moreau, J.-C. Valière, C. Weisman, "Fast acoustic streaming in standing waves : Generation of an additional outer streaming cell ", Journal of the Acoustical Society of America, 134 (3), p. 1791– 1801 (2013).	187
V. Daru, I. Reyt, H. Bailliet, C. Weisman, D. Baltean-Carlès, "Acoustic and stream- ing velocity components in a resonant waveguide at high acoustic levels ", Journal of the Acoustical Society of America, 141 (1), pp. 563-574, (2017).	201
D. Baltean-Carlès, V. Daru, C. Weisman, S. Tabakova, H. Bailliet, "An unexpected balance between outer Rayleigh streaming sources ", Journal of Fluid Mecha- nics 867, p. 985-1011 (2019).	217
V. Daru, C. Weisman, D. Baltean-Carlès, H. Bailliet, "Thermal effects on fast acous- tic streaming inside a resonator", Soumis au Journal of Fluid Mechanics, février 2020.	247

I | Préambule

Cette HDR est inhabituelle à plusieurs égards. D'abord, j'ai 61 ans, et à cet âge en général on commence à envisager sa retraite plutôt que de repasser devant un jury pour obtenir encore un diplôme, qui ne me sera sans doute pas d'une grande utilité pour la fin de ma carrière. Il me permettra quand même de demander l'éméritat si je le désire, puisque l'ENSAM permet aux Maîtres de Conférences HDR de le faire. En deuxième lieu, il s'agit d'un projet collectif, imaginé lors de l'une de ces fêtes dont le LIMSI a le secret. Diana Baltean-Carlès, Catherine Weisman et moi avons décidé de soutenir nos HDR conjointement, l'une après l'autre sur deux jours consécutifs (dans l'idéal nous aurions aimé le faire en une seule journée, mais c'était difficilement réalisable). Nous collaborons depuis une dizaine d'années maintenant sur le thème du streaming acoustique, et cette collaboration (productive) est un véritable plaisir, du fait que nous nous entendons extrêmement bien. Diana, première partante, puis Catherine, ont eu du mal à me décider, mais je ne pouvais pas leur faire faux-bond. Il faut dire aussi qu'au LIMSI il y a pas mal de temps maintenant que certains (n'est-ce pas Patrick Le Quéré, Christian Tenaud, Olivier Daube ?) m'exhortent à faire cet effort. Je dois à Patrick, qui m'y a accueillie en tant que directeur, de le remercier sous cette forme, tardive il est vrai. Christian est celui qui est à l'origine de ma démarche pour venir au LIMSI. Je lui avais promis de passer mon HDR à la parution de l'article [102], et je n'avais pas tenu ma promesse. Ce projet collectif a fait tomber mes résistances.

Le troisième élément étonnant (je l'évoque en troisième bien qu'il soit passé au premier plan depuis quelques semaines) de cette HDR est le contexte inédit dans lequel elle se déroule. Une pandémie mondiale, une grande partie de la population mondiale confinée, c'est du jamais vu quel que soit l'âge que l'on a. Ayant prévu de rédiger le manuscrit en mars et avril, je me suis vite retrouvée à écrire à la maison, sans savoir si cette soutenance pourrait avoir lieu, ce qui entame un peu la motivation. Catherine a pris l'initiative de nous proposer de nous retrouver toutes les trois tous les jours par visioconférence, et d'écrire ensemble en échangeant et en nous soutenant mutuellement devant nos écrans, ce que nous avons fait. Cette excellente initiative aura encore un peu plus soudé notre projet je crois. Malheureusement, le contexte de pandémie va sans doute rendre la réalisation de ce projet collectif très éloignée de la forme prévue initialement.

Enfin il y a une dernière circonstance surprenante, qui est le fait que le LIMSI vit sa dernière année sous ce nom et dans sa forme. En effet, et ce malgré le dernier rapport dithyrambique du HCERES sur le fonctionnement et la gouvernance du laboratoire, les tutelles ont décidé que les deux laboratoires LIMSI et LRI du plateau de Saclay devaient fusionner. Cela entraîne que la mécanique va devenir ultra-minoritaire dans le nouveau laboratoire, le départ probable de ce fait de beaucoup de mécaniciens, et la perte du nom historique du LIMSI. C'est un coup dur et je ne sais pas ce qu'il restera de la mécanique (ou s'il en restera) dans ce nouveau laboratoire l'année prochaine.

Malgré cette note un peu triste, notre équipe des "filles du vent" est solide et continuera à vivre et à explorer ce domaine si passionnant de la thermoacoustique, où il reste encore beaucoup de connaissances à acquérir. Rêvons un peu, cette technologie propre, une fois bien maîtrisée, pourra peut-être apporter sa pierre à la transition énergétique dont nous avons tant besoin pour préserver notre belle planète.

II | Résumé de carrière

Virginie Daru | Maître de Conférences CNU section 60

DynFluid-ENSA, PARIS & LIMSI-CNRS, Orsay

• ☎ 01 44 24 62 78 • ✉ Virginie.Daru@ensam.eu
Née le 03/03/1959 • Célibataire, deux enfants

Domaine de recherche

Mécanique des fluides, simulation numérique, méthodes numériques, écoulements compressibles, écoulements diphasiques, faible Mach, streaming acoustique.

Déroulement de carrière

ENSA

Maître de Conférences

Hors Classe en 2009, échelon exceptionnel en 2017.

Centre de Paris

décembre 1984 – présent

Société d'Etudes et de Recherches de l'ENSA

Ingénierie de recherche

Étude numérique de l'écoulement dans un moteur 2-temps (financement PSA).

Paris

décembre 1983 – novembre 1984

ONERA

Doctorante

Direction Alain Lerat, Bourse ONERA.

Châtillon

octobre 1981 – novembre 1983

Formation

Université Pierre et Marie Curie

Paris

Doctorat de 3ème cycle

1981 – 1983

"Contribution à l'étude d'un schéma numérique implicite pour résoudre les équations d'Euler". Direction : A. Lerat.

UPMC

Diplôme d'Études Approfondies (DEA)

1980 – 1981

Paris

UPMC

Maîtrise de Mathématiques et Applications Fondamentales

1979–1980

Paris

Université de Nice

Licence de Mathématiques

1978 – 1979

Nice

Université de Nice

DEUG A : Science et structure de la matière

1976 – 1978

Nice

Recherche

Activité de Recherche.....

Depuis 1984 : recherche au laboratoire DynFluid (laboratoire SINUMEF jusqu'en 2008).

2001-2003 : détachement à mi-temps au LIMSI à Orsay (91). Je continue depuis une collaboration étroite avec

le LIMSI, auquel je suis toujours affiliée.

Thèmes de recherche : méthodes numériques pour la simulation numérique des écoulements fortement compressibles avec ondes de choc. Écoulements diphasiques liquide-gaz dans l'approximation faible Mach. Streaming acoustique, linéaire et non linéaire à forte intensité acoustique.

Publications.....

- 20 articles dans des revues internationales de rang A à comité de lecture (+ 1 soumis)
- 1 article dans une revue nationale (C. R. Mécanique)
- 1 conférence internationale invitée
- 18 proceedings à comité de lecture parus dans un ouvrage
- 15 conférences internationales avec actes
- 19 conférences nationales
- 13 conférences internationales sans actes

Encadrement de thèses.....

J'ai co-encadré les 6 thèses suivantes :

1. Lourdes Carpintero Arias, thèse de Doctorat de l'ENSA, intitulée : "*Méthodes GMRES parallélisées pour le calcul d'écoulements compressibles par des schémas implicites centrés*", sous la direction de A. Lerat, soutenue le 23 juin 1998. Participation à l'encadrement : 90 %.
2. Patrick Kuszla, thèse de Doctorat de l'ENSA, intitulée : "*Simulation numérique d'écoulements multi-fluides compressibles. Application aux jets d'eau à haute vitesse*", sous la direction de A. Lerat, soutenue le 23 septembre 1999. Participation à l'encadrement : 90 %.
3. Sydney Tekam, thèse CIFRE de Doctorat de l'ENSA, intitulée : "*Modélisation et simulation numérique d'écoulements gazeux chargés de particules d'huile dans un circuit de décantation de moteur*", sous la direction de A. Lerat, soutenue le 30 juin 2006. Participation à l'encadrement : 60 %.
4. Thomas Juès, thèse CIFRE de Doctorat de l'ENSA, intitulée : "*Modélisation et simulation numérique d'écoulements gazeux chargés de particules d'huile dans un circuit de décantation*", sous la direction de A. Lerat, soutenue le 1er juillet 2010. Participation à l'encadrement : 60%.
5. Laurent Monasse, thèse de Doctorat de l'Université Paris-Est, intitulée : "*Couplage fluide-structure en écoulement compressible*", sous la direction de S. Piperno, soutenue le 10 octobre 2011. Participation à l'encadrement : 30 %.
6. Leslie Kaprielian, thèse CIFRE de Doctorat de l'ENSA. Sujet : "*Modélisation de la combustion par des modèles 0D/1D*", sous la direction de P. Cinnella, soutenue le 12 juin 2015. Participation à l'encadrement : 40 %.

Par ailleurs j'ai encadré de nombreux étudiants en DEA puis Master 2 de recherche depuis le début de ma carrière.

Encadrement de post-doctorats.....

1. Ida Reyt, pendant ses contrats ATER UPSud puis ENSAM de 2012 à 2014 (participation 40%).
2. Ida Reyt, 3 mois en 2016 sur un financement que j'ai obtenu en interne à l'ENSA.
3. Omar Hireche, 1 an en 2018-2019 sur financement ANR TACOT (participation 10 %).

Écoles thématiques du CNRS.....

1. École de Printemps de Mécanique des Fluides Numérique (organisation LIMSI), Roscoff, Juin 2005. Thème : Méthodes numériques de haute précision. Intervention avec 3 heures de cours. Rédaction d'un polycopié de 95 pages en collaboration avec C. Tenaud.
2. École de Printemps de Mécanique des Fluides Numérique (organisation LIMSI), Porquerolles, Juin 2015. Thème : Ecoulements multiphasiques et multiespèces. Intervention pour le cours inaugural de 3 heures. Rédaction d'un polycopié de 62 pages.

Collaborations internationales et nationales.....

- Sonia Tabakova, Université Technique de Sofia, antenne de Plovdiv, et Académie des Sciences, Bulgarie.
- Hélène Baillet, Institut Pprime, Poitiers.

- Au LIMSI : C. Tenaud, P. Le Quéré, M.-C. Duluc, D. Baltean-Carlès, C. Weisman.

Enseignement

Mon activité d'enseignement a été jusqu'en 2011, essentiellement effectuée dans le cadre de la troisième année de l'ENSA et majoritairement constituée par des charges d'encadrement de projets de fin d'études (PFE). Les sujets proposés chaque année en PFE étaient soit en relation avec une entreprise, soit internes, avec une orientation recherche pour les étudiants qui choisissaient de suivre l'option Master. Voici les titres de quelques uns des PFE/Master que j'ai encadrés dans les années 2000 :

- Simulation numérique d'un circuit de soufflage de bouteilles en plastique (collaboration avec la société ADS, 2005-2006). Etudiants : Guillaume Devingt, Thomas Baude.
- Etude de l'interaction entre une onde de choc et une couche limite laminaire (recherche interne DynFluid, 2005-2006, Master recherche). Etudiants : Arnould Julien, Jolly Guillaume.
- Simulation numérique de la propagation d'infrasons dans l'atmosphère et des ondes de gravité (collaboration CEA/DAM, 2007-2008, Master recherche). Etudiant : Jean-Philippe Majorcrys.
- Simulation numérique d'un procédé de bullage (collaboration avec Saint Gobain et le LIMSI, 2007-2008, Master recherche). Etudiant : Marc Lebrequer.
- Etude acoustique et vibrationnelle d'un convertisseur d'énergie thermoacoustique (collaboration avec l'IPNO et le LIMSI, 2007-2008). Etudiant : Benjamin Siohan.
- Etude du risque d'inflammation de l'hydrogène par les recombinateurs catalytiques dans les réacteurs à eau pressurisée (collaboration avec l'IRSN, 2008-2009). Etudiant : Ouassim Tighza.
- Calcul d'écoulements instationnaires dans des tuyères par des schémas de haute précision (recherche interne DynFluid, 2009-2010, Master recherche). Etudiant : Jean-François Cabré.
- Etude numérique du streaming acoustique dans une cavité rectangulaire utilisant un schéma d'ordre élevé optimisé (recherche interne LIMSI, 2009-2010, Master recherche). Etudiant : Gurunath Gandikota.

Ma charge d'enseignement est actuellement d'environ 220h eqTD, et maintenant constituée pour 80% en enseignement présentiel (cours magistraux, TD, TP), le reste en tutorat de stage, encadrement de projets et mission pédagogique. J'interviens dans les 5 cours suivants :

- Bases de la simulation numérique des écoulements compressibles (Master Recherche FISE de l'ENSA/UPMC, CM), 15h eqTD
- Méthodes numériques (cours de 3ème année de l'ENSA, CM+TD), 25h eqTD
- Ecoulements diphasiques (cours de 3ème année de l'ENSA, CM+TD), 21h eqTD
- Mathématiques (Formation Ingénieur en Apprentissage 1ère année, CM+TD), 92h eqTD
- TP numériques d'optimisation (ENSA 2ème année), 32h eqTD

Depuis 2006 je suis responsable de l'Unité d'Enseignement d'Expertise (UEE) de 3ème année de l'ENSA, dénommée SISYF (Simulation des Systèmes Fluides), qui représente un volume de 150 heures de cours et concerne une vingtaine d'étudiants.

Fonctions d'intérêt collectif

Responsabilités et mandats locaux ou régionaux

J'ai régulièrement participé aux instances de l'ENSA, que ce soit au niveau local ou national :

- Membre titulaire élue du Conseil Scientifique de l'ENSA de 1991 à 1995, de 1995 à 1999, de 2008 à 2012, suppléant élue de 2012 à 2017 (4 mandats).
- Membre suppléant élue du Conseil d'Administration de l'ENSA de 1998 à 2002 et de 2002 à 2006 (2 mandats)
- Membre titulaire élue du Conseil de Centre de l'ENSA de Paris de 1994 à 1998, suppléant de 1998 à 2002 et de 2002 à 2006 (3 mandats).
- Membre de la commission des marchés de l'ENSA Paris de 1998 à 2006.

J'ai plusieurs fois été élue dans les Commissions de Spécialistes de l'ENSA et de l'UPMC depuis les années 90 jusqu'à leur disparition :

- Membre titulaire élue de la Commission de Spécialistes de l'ENSA de 1994 à 1997 (2ème vice-président) et de 1997 à 2000, suppléant de 2001 à 2004 (3 mandats).

- Membre titulaire nommée de la Commission de Spécialistes de l'Université Paris 6 de 1992 à 1995, de 1998 à 2001 et de 2001 à 2004 (3 mandats).

Depuis je participe régulièrement à des comités de sélection (6 depuis 2012) :

- Membre extérieur du comité de sélection du poste MCF 0217 à l'INPT (Toulouse) en 2012.
- Membre extérieur du comité de sélection du poste MCF 0705 à l'Université Paris 6 en 2012.
- Membre extérieur du comité de sélection du poste MCF 1046 à l'Université de Rouen en 2014.
- Membre intérieur du comité de sélection du poste MCF 0319 à l'ENSAM en 2014.
- Membre extérieur du comité de sélection du poste MCF 4156 à l'INSA de Lyon en 2016.
- Membre extérieur du comité de sélection du poste MCF 0370 à Polytech Orléans en 2018.

Responsabilités et mandats nationaux

J'ai été élue dans des instances nationales (CNU, Comité National du CNRS), et nommée en 2018 dans un comité de sélection de l'ANR :

- Membre élue de la section 10 du Comité National du CNRS (2004-2008)
- Membre élue du CNU, section 60 (2011-2015)
- Membre nommée d'un comité de sélection (CES 05) de l'ANR pour l'Appel à Projets Générique 2018.

Jurys de thèse

J'ai été membre du jury des thèses suivantes :

- Rapporteur et membre du jury de thèse de Maria-Teresa Parra Santos en juin 1999 à l'Université de Valladolid (Espagne).
- Membre du jury de thèse de Jérémie Demange le 21 octobre 2014 au laboratoire Jean Kuntzmann à Grenoble (Université de Grenoble).
- Membre du jury d'HDR de Jeanne Malet (IRSN), le 16 juin 2016.
- Membre du jury de thèse de Nabil Djati le 22 juin 2017 à l'INSA de Lyon.
- Membre du jury de thèse de Pierre Pineau le 30 novembre 2018 à l'Ecole Centrale de Lyon.

Expertises

- Expertise pour l'ANRT d'une demande de bourse CIFRE (Renault/Prisme Orléans) en 2010.
- Expertise du projet collaboratif EcoBioClean pour le pôle de compétitivité AlsaceBiovalley (2013)
- Expertise de projets pour l'ANR en 2018 (AAPG 2018).

Activité éditoriale

Depuis 2010, j'ai effectué 27 expertises pour les revues suivantes :

- Journal of Computational Physics (2)
- Journal of Fluid Mechanics (1)
- Computers and Fluids (3)
- Physical Review E (2)
- AIAA Journal (2)
- Journal of Scientific Computing (1)
- Journal of the Acoustic Society of America (3)
- Wave Motion (1)
- International Journal of Heat and Mass Transfer (2)
- Journal of Applied Physics (1)
- Computational Mechanics (1)
- Journal of Micromechanics and Microengineering (4)
- Journal of Zhejiang University - SCIENCE A (1)
- Mathematics and Computers in Simulation (1)
- Ultrasonics (1)
- Physical Review Fluids (1)

Financements, contrats, projets

J'ai participé à plusieurs contrats de recherche avec des industriels, notamment avec les constructeurs automobiles (PSA, Renault) et le CEA. J'ai également participé à des contrats résultant des appels à projets ANR.

Contrats de gré à gré :

- " Développement d'un code de calcul tridimensionnel pour la simulation numérique du balayage des gaz dans un moteur 2-temps ". Contrat d'étude et de recherche avec la société PSA, Responsable scientifique, 1985 (durée 1 an).
- " Simulation numérique tridimensionnelle du balayage des gaz dans des moteurs deux temps ". Contrat d'étude et de recherche avec la société PSA, Responsable scientifique, 1988 (durée 1 an).
- " Analyse de configurations de moteur deux temps par simulation numérique 3D ", Contrat d'étude et de recherche avec la société PSA, Responsable scientifique, 1990 (durée 1 an).
- " Etude de schémas numériques pour l'hydrodynamique ", Contrat d'étude et de recherche avec le CEA, Responsable scientifique, 1998 (durée 1 an).
- " Modélisation et simulation numérique d'écoulements gazeux chargés de particules d'huile dans un circuit de décanteur de moteur ", Contrat annuel d'accompagnement à la thèse CIFRE de Sydney Tekam, RENAULT, 2002-2005 (rapport de contrat annuel).
- " Modélisation et simulation d'écoulements diphasiques à phases séparées dans un décanteur ", Contrat annuel d'accompagnement à la thèse CIFRE de Thomas Juès, RENAULT, 2006-2009 (rapport de contrat annuel).
- " Simulation numérique d'un circuit de soufflage de bouteilles en plastique ", Contrat d'études pour la société ADS (PME spécialisée dans la conception de machines de soufflage de bouteilles), Responsable scientifique, 2007 (durée 1 an).
- " Modélisation de la combustion par des modèles 0D/1D ", Contrat annuel d'accompagnement à la thèse CIFRE de Leslie Kaprielian, RENAULT, 2011-2015 (rapport de contrat annuel).

Contrats évalués suite à appel à projet :

- Participante à l'ANR SPICEX (Simulations numériques hautes Performances d'une Interaction onde de Choc/couche limite en Ecoulement eXterne), 2008-2011. Coordinateur Xavier Glaerfelt, laboratoire DynFluid ENSAM.
- Participante à l'ANR TACOT (Thermo-Acoustic Cooler for On road Transportation, Pompe à chaleur thermo-acoustique pour le transport terrestre), 2018-2021. Coordinatrice Hélène Bailliet, laboratoire Pprime Poitiers.
- Participante à l'ANR ASCA (Advanced numerical Simulation for CAvitation, Modélisation et simulation de la cavitation), 2019-2022. Coordinateur Éric Goncalvès, laboratoire Pprime Poitiers.

Liste des publications

Les noms soulignés sont ceux de mes étudiants.

• Articles soumis dans des revues de rang A à comité de lecture

1. Virginie Daru, Catherine Weisman, Diana Baltean-Carlès, Hélène Bailliet ,
Thermal effects on fast acoustic streaming inside a resonator, soumis à J. Fluid Mech.

• Articles dans des revues de rang A à comité de lecture

1. Omar Hireche, Islam Ramadan, Catherine Weisman, Hélène Bailliet, Yann Fraigneau, Diana Baltean-Carlès, Virginie Daru,
Experimental and numerical investigation of natural convection flows in two horizontal thermoacoustic cavities, Int. J. Heat Mass Transfer 149, 119195, 2020.
2. D. Baltean-Carlès, V. Daru, C. Weisman, S. Tabakova, H. Bailliet,
An unexpected balance between outer Rayleigh streaming sources, J. Fluid Mech. 867, 985-1011, 2019.
3. V. Daru, C. Weisman, D. Baltean-Carlès, I. Reyt, H. Bailliet,
Inertial effects on acoustic Rayleigh streaming flow : Transient and established regimes, Wave Motion, Volume 74, Pages 1-17 (2017).
4. Daru, V., Reyt, I., Bailliet, H., Weisman, C., Baltean-Carlès, D.,
Acoustic and streaming velocity components in a resonant waveguide at high acoustic levels, Journal of the Acoustical Society of America, 141 (1), pp. 563-574, (2017).
5. Tenaud, C., Podvin, B., Fraigneau, Y., Daru, V.,

On wall pressure fluctuations and their coupling with vortex dynamics in a separated–reattached turbulent flow over a blunt flat plate, International Journal of Heat and Fluid Flow, 61, pp. 730-748, (2016).

6. Puscas M.A., Monasse L., Ern A., Tenaud C., Mariotti C., Daru V.,
A time semi-implicit scheme for the energy-balanced coupling of a shocked fluid flow with a deformable structure. J. Comput. Phys., 296 :241–262 (2015).
7. Podvin, B., Fraigneau, Y., Tenaud, C., Daru, V.
Coherent structures in the boundary layer of a flat thick plate, Comptes Rendus - Mecanique, 342 (6-7), pp. 417-424 (2014).
8. Feuillebois, F., Tabakova, S., Radev, S., Daru, V.
Entrained film of ice-water slurry with impinging supercooled water droplets, Journal of Engineering Physics and Thermophysics, 87 (1), pp. 54-68 (2014) .
9. Ida Reyt, Hélène Bailliet, Diana Baltean-Carlès, Virginie Daru, Solène Moreau, Jean-Christophe Valière, and Catherine Weisman,
Fast acoustic streaming in standing waves : Generation of an additional outer streaming cell, Journal of the Acoustical Society of America, **134**(3) : 1791–1801 (2013).
10. Virginie Daru, Diana Baltean-Carlès, Catherine Weisman, Philippe Debesse, Gurunath Gandikota V. S.,
Two-dimensional numerical simulations of nonlinear acoustic streaming in standing waves, Wave Motion, **50** : 955–963 (2013).
11. L. Monasse, V. Daru, C. Mariotti, S. Piperno, C. Tenaud,
A conservative coupling algorithm between a compressible flow and a rigid body using an Embedded Boundary method, Journal of Computational Physics, **231** : 2977–2994 (2012).
12. S. Tabakova, F. Feuillebois, A. Mongruel, V. Daru and St. Radev,
First stages of drop impact on a dry surface : asymptotic model, ZAMP, **63** : 313–330 (2012).
13. V. Daru, P. Le Quéré, M.-C. Duluc, O. Le Maître,
A numerical method for the simulation of low Mach number liquid-gas flows, Journal of Computational Physics, **229**(23) : 8844–8867 (2010).
14. A. Mongruel, V. Daru, F. Feuillebois, S. Tabakova,
Early post-impact times dynamics of viscous drops onto a solid dry surface, Physics of Fluids, **21** : 032101(1-13) (2009).
15. V. Daru, C. Tenaud,
Numerical simulation of the viscous shock tube problem by using a high resolution monotonicity preserving scheme, Computers and Fluids, **38**(3) : 664–676 (2009).
16. M.-C. Duluc, O. Le Maître, V. Daru, P. Le Quéré,
Oscillations of a liquid inclusion inside a closed cavity filled up with gas and externally heated, Microfluidics and Nanofluidics, **6**(2) : 163–177 (2009).
17. V. Daru, X. Gaoerfelt,
Aeroacoustic computations using a high order shock-capturing scheme, AIAA Journal, **45**(10) : 2474–2486 (2007).
18. Seungwon Shin, S. I. Abdel-Khalik, Virginie Daru and Damir Juric,
Accurate representation of surface tension using the level contour reconstruction method, Journal of Computational Physics, **203** : 493–516 (2005).
19. V. Daru and C. Tenaud,
High order one-step monotonicity preserving schemes for unsteady flow calculations, Journal of Computational Physics, **193** : 563–594 (2004).
20. V. Daru and C. Tenaud,
Evaluation of TVD high resolution schemes for unsteady viscous shocked flows, Computers & Fluids **30**, 89–113 (2001).

21. V. Daru,
Book review : Level Set Methods and Fast Marching Methods by J.A. Sethian, Eur. J. Mech. B-Fluids **19**, 531–532, 2000.

• Article dans une revue nationale

1. V. Daru, M.-C. Duluc, O. Le Maître, D. Juric, P. Le Quéré,
Modélisation et simulation numérique du changement de phase liquide-vapeur en cavité , C. R. Mécanique, **334** : 25–33 (2006).

• Conférence internationale invitée.

1. V. Daru,
A numerical study of Rayleigh streaming at high acoustic level, Acoustofluidics 2018, August 29-31, 2018, Lille, France.

• Proceedings à comité de lecture parus dans un ouvrage

1. Virginie Daru, Diana Baltean-Carlès and Catherine Weisman,
Inertial Effects on Non Linear Acoustic Streaming, 20th International Symposium on Nonlinear Acoustics, June 29- July 3, 2015, Lyon, France. AIP Conference Proceedings 1685, 030003 (2015);
<https://doi.org/10.1063/1.4934386>
2. V. Daru, D. Baltean-Carlès, C. Weisman,
Numerical Simulation of non linear acoustic streaming in a standing wave resonator, 19th International Symposium on Nonlinear Acoustics, May 21-24, 2012, Tokyo, Japan. AIP Conference Proceedings 1474, 87 (2012);
<https://doi.org/10.1063/1.4749305>
3. C. Tenaud, Y. Fraigneau, V. Daru,
Numerical simulation of the turbulent detached flow around a thick flat plate, Sixth International Conference on Computational Fluid Dynamics, July 12-16 2010, St Petersburg, Russia. Edité chez Springer en 2010 : Computational Fluid Dynamics 2010, A. Kuzmin Ed.
4. L. Monasse, V. Daru, C. Mariotti, S. Piperno,
A conservative coupling method for fluid-structure interaction in the compressible case, Sixth International Conference on Computational Fluid Dynamics, July 12-16 2010, St Petersburg, Russia. Edité chez Springer en 2010 : Computational Fluid Dynamics 2010, A. Kuzmin Ed.
5. Berland J., Le Garrec T., Gloerfelt X., Daru V.,
Assessment of high-order algorithms for aeroacoustic computation of shock-containing flows, 5th International Conference on Computational Fluid Dynamics (ICCFD5), 7-11 Juillet 2008, Séoul (Corée). Actes parus dans : Computational Fluid Dynamics 2008, Choi, Haecheon ; Choi, H. G. ; Yoo, J. Y. (Eds.), Springer 2009, ISBN 978-3-642-01272-3. 411-416
6. V. Daru, C. Tenaud,
Numerical simulation of the shock wave / boundary layer interaction in a shock tube by using a high resolution monotonicity-preserving scheme, Computational Fluid Dynamics 2004, C. Groth, D.W. Zingg eds, Springer, 2006
7. S. Tekam, V. Daru, M. Demoulin,
Prediction of the efficiency of an automotive oil separator : comparison of numerical simulations with experiments, Diesel Particulate Systems, Engines and Components, and Performance Additives 2004, SAE International Special Publication 1898, 2004. Aussi SAE Technical Papers Series 2004-01-3019, 2004.
8. V. Daru and C. Tenaud,
High resolution Monotonicity-Preserving schemes for unsteady compressible flows, Computational Fluid Dynamics 2002, S. Armfield, P. Morgan and K. Srinivas eds, Springer, 2003.
9. V. Daru and C. Tenaud,
Application of TVD high resolution schemes to the viscous shock tube problem, Godunov Methods : Theory and applications, E.F. Toro ed., Kluwer Academic/Plenum Publishers, 2001.

10. P. Kuszla and V. Daru,
Multifluid computation of droplets impact, Sixteenth International Conference on Numerical Methods in Fluid Dynamics, Lecture Notes in Physics Vol.515, C.H. Bruneau ed., Springer, 1998.
11. V. Daru, G. Fernandez, C. Tenaud,
On CFD to investigate bifurcated shock wave pattern , Proceedings of the 21th International Symposium on Shock Waves, Panther Publishing and Printing, Australia, R. Boyce et al. Eds., p. 1091-1097, 1997.
12. L. Carpintero and V. Daru,
Implicit multiblock Euler computations using a preconditioned GMRES method , Parallel Computational Fluid Dynamics, North Holland, Elsevier, P. Schiano, A. Ecer, J. Periaux and N. Satofuka eds., p. 274-281, 1997.
13. V. Daru and J.P. Damion,
Influence of the curvature of the diaphragm on flow quality in shock tubes, Proceedings of the 20th International Symposium on Shock Waves, World Scientific, B. Sturtevant, J.E. Shepherd, H.G. Hornung eds, p.1527-1532, 1996.
14. V. Daru and J.P. Damion,
Analysis of the flow perturbation in a shock tube due to the curvature of the diaphragm , Shock Waves@Marseille, Proceedings of the 19th International Symposium on Shock Waves, Springer, R. Brun, L.Z. Dumitrescu eds., p. 451-456, 1995.
15. Daru V. and Lerat A.,
An implicit centered scheme which gives non-oscillatory steady shocks, Nonlinear hyperbolic problems, Lecture Notes in Mathematics, Vol. 1270, pp. 115-17, 1987.
16. Daru V. and Lerat A.,
Analysis of an implicit solver, Numerical methods for the Euler equations of fluid dynamics, Angrand et al. eds., Philadelphia : SIAM Publications (1985).
17. Lerat A., Sidès J., Daru V.,
Efficient computation of steady and unsteady transonic flows by an implicit solver, Advances in Computational Transonics, W.G. Habashi ed., London : Pineridge Press (1985).
18. Lerat A., Sidès J., Daru V.,
An implicit finite volume method for solving the Euler equations, Lecture Notes in Physics, Vol. 170, pp. 343-9 (1982).

• Conférences internationales avec actes

1. C. Tenaud, Y. Fraigneau, V. Daru,
Numerical simulation of the turbulent separation reattachment flow around a thick flat plate, 13th European Turbulence Conference, 12-15 september 2011, Warsaw, Poland.
2. J. Malet, T. Gelain, O. Desgrées du Lou, V. Daru,
Evaporation over sump surface in containment studies : code validation on TOSQAN tests, 14th International Topical Meeting on Nuclear Reactor Thermalhydraulics, NURETH-14, Toronto, Ontario, Canada, September 25-30, 2011.
3. V. Daru, M.-C. Duluc, D. Juric, P. Le Quéré,
A numerical model for the simulation of low Mach number liquid-gas flows, 6th International Symposium on Multiphase flows, Heat Mass Transfer and Energy conversion, Xi'an, Chine, 11-15 Juillet 2009
4. Daru V., Millet C., Majorcryk J.-P.,
Application of a high resolution monotonicity preserving scheme to wave propagation in the atmosphere, 18th International Shock Interaction Symposium (ISIS18), 15-18 Juillet 2008, Rouen (France).
5. V. Daru, M.-C. Duluc, O. Le Maître, P. Le Quéré,
Numerical simulation of low Mach number liquid-gas flows, 19th International Symposium on Transport Phenomena, Reykjavik, Islande, 17-21 Août 2008

6. S. Tabakova, S. Radev, F. Feuillebois, V. Daru, and A. Stoilova,
Numerical modeling the lateral jet dynamics for a viscous drop impinging on a dry surface. In CMAM-3, Minsk, Belarus, June 25 - 30, 2007.
7. M.-C. Duluc, I. Elayyadi, V. Daru, P. Le Quéré,
Numerical simulations of a liquid-vapour phase change problem in a closed cavity, 13th International Heat Transfer Conference IHTC13, August 13-18, 2006, Sydney, Australia.
8. V. Daru, X. Gloerfelt,
Aeroacoustic computations using a high-order shock-capturing scheme , 12th AIAA/CEAS Aeroacoustics Conference (27th AIAA Aeroacoustics Conference), 8-10 May 2006, Cambridge, Massachusetts. AIAA Paper 2006-2414.
9. V. Daru, M.-C. Duluc, D. Juric, P. Le Quéré,
A numerical model for the simulation of liquid-vapor phase change in an enclosure , 4th International Conference on Computational Heat and Mass Transfer, May 17-20, 2005, Paris-Cachan, France.
10. S. Tekam, M. Demoulin, V. Daru,
Prediction of the efficiency of an automotive oil strainer : comparison of experiments with numerical simulations, Industrial Simulation Conference 2004, Malaga, Espagne, Juin 2004. Publié par Eurosis-ETI (J. Marin and V. Koncar eds.).
11. J.-Ch. Robinet, V. Daru and Ch. Tenaud,
Two-dimensional laminar shock wave / boundary layer interaction. BAIL2004, Toulouse, Juillet 2004.
12. T. Parra, F. Castro, V. Daru,
Modelling of premixed flames using FCT and TVD algorithms, Eurotherm Seminar N. 70 "Physical and Mathematical Modelling of Fires in Enclosures and Fire Protection", Turin, Italy, October 2002.
13. P. Kuszla and V. Daru,
Numerical oscillations in Euler monofluid and multifluid computations, in 4th Seminar on Euler and Navier-Stokes Equations, Prague, République Tchèque, 23-25 Mai 2001, p.87-92, 2001.
14. P. Kuszla and V. Daru,
Numerical simulation of compressible liquid impact, AMIF-ESF Workshop Computing Methods for Two-phase Flows, Aussois, France, janvier 2000. Actes publiés sous la forme d'un CD-ROM.
15. P. Kuszla and V. Daru,
Numerical simulation of high speed liquid jets, 4th World Congress on Computational Mechanics, Buenos-Aires, Argentine, Juin 1998. Actes publiés sous la forme d'un CD-ROM (Computational Mechanics, S.R. Idelsohn et al eds., CIMNE-IACM).

• **Conférences nationales**

1. O. Hireche, C. Weisman, D. Baltean-Carlès, V. Daru, Y. Fraigneau,
Numerical study of the effects of natural convection in a thermoacoustic device, Congrès Français de Mécanique, Brest, Août 2019.
2. H. Bailliet, I. Reyt, V. Daru, D. Baltean Carlès et C. Weisman,
Transitoire et changement de régime des écoulements redressés de Rayleigh à forts niveaux : Etudes numérique et expérimentale, Congrès Français d'Acoustique, Le Mans, 11 au 15 avril 2016.
3. V. Daru, I. Reyt, D. Baltean-Carlès et C. Weisman,
Streaming non linéaire : rôle de la composante radiale acoustique, Congrès Français d'Acoustique, Le Mans, 11 au 15 avril 2016.
4. I. Reyt, H. Baillet, D. Baltean-Carlès, V. Daru, J.-C. Valière, C. Weisman,
Influence de la propagation non-linéaire et de l'inertie sur le vent acoustique, Congrès Français de Mécanique, 26-30 août 2013, Bordeaux. Actes publiés sous la forme d'une clé USB.
5. L. Kaprielian, M. Demoulin, P. Cinnella, V. Daru,
Modélisation quasi-dimensionnelle multizone de la phase de combustion dans un moteur à essence, 21ème Congrès Français de Mécanique, Bordeaux, 26 au 30 août 2013.

6. V. Daru, C. Tenaud,
Schémas de haute résolution à capture de choc basés sur une condition de préservation de la monotonie pour la prédiction d'écoulements visqueux compressibles, 41ème Congrès Français d'Analyse Numérique CANUM'12, 21-25 mai 2012, Superbesse, Puy de Dôme.
7. V. Daru, D. Baltean-Carlès, G. Gandikota V. S., C. Weisman,
Etude numérique du vent acoustique non linéaire dans un résonateur à ondes stationnaires, Congrès Français de Mécanique, 29 août-2 septembre 2011, Besançon. Actes publiés sous la forme d'une clé USB.
8. L. Monasse, V. Daru, C. Mariotti, S. Piperno, C. Tenaud,
Un algorithme de couplage conservatif pour l'interaction fluide-structure dans le cas compressible, Congrès Français de Mécanique, 29 août-2 septembre 2011, Besançon. Actes publiés sous la forme d'une clé USB.
9. C. Tenaud, Y. Fraigneau, V. Daru,
Simulation numérique du décollement et recollement turbulent autour d'une plaque plane épaisse., Congrès Français de Mécanique, 29 août-2 septembre 2011, Besançon. Actes publiés sous la forme d'une clé USB.
10. L. Monasse, V. Daru, C. Mariotti, S. Piperno,
Une méthode conservative de couplage entre Eléments Discrets et méthode Volumes Finis pour l'interaction fluide-structure, poster présenté au 40ème Congrès d'Analyse Numérique (CANUM 2010), Carcans-Maubuisson, 31 mai-4 juin 2010.
11. S. Bensmina, C. Tenaud, Y. Fraigneau, V. Daru,
Une méthode de frontières immergées pour la simulation d'écoulements visqueux compressibles, Congrès Français de Mécanique, 24-28 août 2009, Marseille. Actes publiés sous la forme d'un CD-ROM.
12. V. Daru, M.-C. Duluc, P. Le Quéré, D. Juric,
Simulation numérique d'écoulements liquide-gaz en approximation bas Mach , Congrès Français de Mécanique, 24-28 août 2009, Marseille. Actes publiés sous la forme d'un CD-ROM.
13. A. Mongruel, V. Daru, S. Tabakova, A. Stoilova, F. Feuillebois, S. Radev,
Impact de gouttes sur une surface solide et sèche : étude aux temps courts , Congrès Français de Mécanique, 27-31 août 2007, Grenoble. Actes publiés sous la forme d'un CD-ROM.
14. M.-C. Duluc, V. Daru, I. Elayyadi, P. Le Quéré,
Déplacement d'interfaces liquide-gaz sous l'effet d'un chauffage . Congrès Français de Thermique, les Embiez, 29 mai-1er juin 2007. Actes publiés sous la forme d'un CD-ROM.
15. V. Daru, Y. Fraigneau, C. Tenaud,
Comportement d'un schéma à capture de choc de haute précision en Simulation des Grandes Echelles , Congrès Français de Mécanique, 29 août-2 Septembre 2005, Troyes. Actes publiés sous la forme d'un CD-ROM.
16. V. Daru, M.-C. Duluc, O. Le Maître, D. Juric, P. Le Quéré,
Simulation numérique d'écoulements liquide-vapeur faiblement compressibles , Congrès Français de Mécanique, 29 août-2 Septembre 2005, Troyes. Actes publiés sous la forme d'un CD-ROM.
17. D. Juric, V. Daru, M.-C. Duluc,
Simulation d'écoulements liquide-gaz à l'intérieur d'une cavité chauffée . Congrès Français de Thermique, Presqu'île de Giens, 25-28 mai 2004. Actes publiés sous la forme d'un CD-ROM.
18. V. Daru, C. Tenaud,
Simulation numérique de l'interaction choc-couche limite en fond de tube à choc , Congrès Français de Mécanique, 1-5 Septembre 2003, Nice. Actes publiés sous la forme d'un CD-ROM.
19. V. Daru,
Simulation numérique du balayage des gaz dans le cylindre d'un moteur 2 temps., Congrès International " Calcul scientifique et automobile ", Versailles, France, Novembre 1990.

• Conférences internationales sans actes

1. D. Baltean Carlès, V. Daru, H. Bailliet, I. Reyt et C. Weisman,
Numerical and experimental investigation of the role of inertia on acoustic Rayleigh streaming in a standing waveguide, Acoustics'17, 173rd Meeting of the Acoustical Society of America and the 8th Forum Acusticum, June 25-29, 2017, Boston, USA.
2. V. Daru, D. Baltean Carlès, H. Bailliet, I. Reyt et C. Weisman,
Evolution of Rayleigh streaming flow velocity components in a resonant wave guide at high acoustic levels, Acoustics'17, 173rd Meeting of the Acoustical Society of America and the 8th Forum Acusticum, June 25-29, 2017, Boston, USA.
3. L. Monasse, V. Daru, C. Mariotti, S. Piperno,
Conservative coupling of an Immersed Boundary Method with a Discrete Element Method for fluid-structure interaction, 4th European Conference on Computational Mechanics (ECCM2010), 16-21 mai 2010, Paris, France
4. L. Monasse, V. Daru, C. Mariotti, S. Piperno,
A conservative Immersed Boundary Method for the interaction of compressible inviscid flows with elastic structures, 9th World Congress on Computational Mechanics (WCCM2010), 19-23 juillet 2010, Sydney, Australia
5. L. Monasse, V. Daru, C. Mariotti, S. Piperno,
An explicit, conservative Immersed Boundary Method for the interaction of a compressible flow with an elastic structure. EUROMECH 507 and ERCOFTAC " Immersed Boundary Methods ", 15-17 June 2009, Amsterdam, The Netherlands.
6. Christophe Millet, Virginie Daru
Nonlinear propagation of acoustic-gravity waves from explosive sources in the atmosphere, 61st Annual Meeting of the APS Division of Fluid Dynamics, November 23-25 2008, San Antonio, Texas, USA.
7. Damir Juric, Patrick Le Quéré, Virginie Daru, Marie-Christine Duluc
On the numerical simulation of two phase liquid-vapor phenomena. XXI ICTAM, 15-21 August 2004, Varsovie, Pologne
8. V. Daru, C. Tenaud,
Unsteady computations of compressible flow problems by using high order shock capturing schemes, European Fluid Mechanics Conference, 25-28 August 2003, Toulouse, France.
9. V. Daru & C. Tenaud,
High order one-step schemes for unsteady compressible flows calculations, EUROMECH Conference 446, 10-11 March 2003, Darmstadt, Germany.
10. L. Carpintero and V. Daru,
A parallel Euler solver based on a preconditioned GMRES method, Algorithms for Sparse Large Scale Linear Algebraic Systems : State of the Art and Applications in Science and Engineering (NATO), Las Palmas de Gran Canaria, Espagne, juin 1996.
11. V. Daru,
A new high-resolution scheme for hyperbolic systems, ICFD Conference, Oxford, Grande Bretagne, Avril 1995.
12. V. Daru,
Visualiser la mécanique des fluides numériques, Conference on Computational Methods in Fluid Mechanics applied to Aeronautics, Antibes, mai 1989
13. Candau P., V. Daru, A. Lerat,
Numerical simulation of gas motion in the cylinder of a two-stroke engine, First ICIAM Conference, Paris, France, Juillet 1987.

• **Cours rédigés d'écoles thématiques :**

1. V. Daru, C. Tenaud
"Approximations d'ordre élevé pour les écoulements compressibles avec discontinuités". Rédigé en

support du cours donné à la 9ème Ecole de Printemps de Mécanique des Fluides Numérique, Roscoff, 95 pages, juin 2005.

2. V. Daru

"Des écoulements compressibles aux écoulements faiblement dilatables". Rédigé en support du cours introductif donné à la 14ème Ecole de Printemps de Mécanique des Fluides Numérique, Porquerolles, 62 pages, juin 2015.

III | Activités de recherche

1 Introduction.

Les travaux présentés dans ce mémoire synthétisent mon activité de recherche depuis le début de ma carrière. Ils s'inscrivent dans le cadre général de la Mécanique des Fluides Numérique. Plus précisément, je me suis essentiellement intéressée à des écoulements compressibles, d'abord dans le cadre de l'aérodynamique pendant ma thèse et dans les années suivantes, puis par la suite dans des domaines variés de la mécanique des fluides. J'ai en particulier travaillé sur les méthodes numériques destinées à simuler ce type d'écoulements (en différences finies ou volumes finis exclusivement), et également sur des aspects de modélisation.

Après ma thèse, effectuée à l'Onera sous la direction d'Alain Lerat, j'ai commencé ma carrière au laboratoire SINUMEF de L'ENSAM. Le laboratoire venait d'être créé par Alain Lerat, et nous étions seulement deux enseignants chercheurs, entourés de quelques doctorants et stagiaires de fin d'étude de l'ENSAM ou de DEA. Le laboratoire est resté dans cette configuration pendant plusieurs années, avant qu'un nouveau Maître de Conférences ne soit recruté. Durant cette période j'ai continué à travailler sur des sujets dans la continuité de mes travaux de thèse, sans grande motivation il faut bien le dire, et avec un certain sentiment d'isolement. J'ai aussi été responsable de contrats de recherche avec le constructeur automobile PSA, sur la simulation d'écoulements dans des moteurs, et commencé une activité dans le domaine des écoulements diphasiques à travers l'encadrement de la thèse de Patrick Kuszla. À la fin des années 90, j'ai commencé à collaborer avec Christian Tenaud, à travers le co-encadrement d'étudiants en DEA qui effectuaient leur stage au LIMSI. Cette collaboration s'est ensuite développée sur le sujet du tube à choc visqueux, qui a abouti à notre premier article commun [16]. Voyant que je me sentais isolée au laboratoire SINUMEF, Christian m'a incitée à demander mon rattachement au LIMSI, au moins temporairement. J'ai donc contacté Patrick Le Quéré, qui venait de prendre la direction du LIMSI. À sa demande, j'ai rédigé un projet de recherche portant sur les schémas numériques de haute précision d'une part, et sur le diphasique d'autre part. Ma démarche a abouti à mon intégration au LIMSI en 2001. Je peux dire que cela a été le début d'une nouvelle vie pour moi. J'ai trouvé au LIMSI un magnifique environnement scientifique et humain, où régnait un très fort sentiment du collectif, et j'y ai noué de nombreuses collaborations dont on peut voir le reflet dans mes publications. J'ai longtemps travaillé avec Christian sur le thème des schémas numériques. Avec Damir Juric, Marie-Christine Duluc, Patrick Le Quéré, Olivier Le Maitre, nous avons eu bien des heures de discussions passionnées sur les écoulements liquide-gaz, la tension de surface ou le changement de phase. La période récente a vu la constitution de notre groupe des "filles du vent", Diana Baltean-Carlès, Catherine Weisman et moi, complété par Hélène Bailliet à Poitiers. C'est un groupe chaleureux et soudé, et nos discussions scientifiques autour des thèmes de recherche passionnantes que sont le streaming acoustique et la thermoacoustique sont extrêmement stimulantes.

À partir des années 2000, le laboratoire SINUMEF, qui a changé de nom en devenant DynFluid en 2008, s'est fortement développé. Cette évolution a énormément élargi le spectre des thèmes scientifiques qui y sont abordés, et de nombreuses collaborations internes et externes ont été nouées. DynFluid est aujourd'hui un laboratoire qui fournit à ses membres un cadre propice aux échanges scientifiques et un environnement humain agréable. Je partage maintenant mon temps entre les deux laboratoires, bien qu'en recherche je collabore essentiellement avec les chercheurs du LIMSI.

Je présenterai mes travaux en trois axes principaux. Le premier, qui concerne le développement de schémas numériques de haute précision pour le calcul des écoulements avec ondes de chocs, a fait l'objet de la première partie de mon activité de recherche. Ces schémas, développés à l'origine pour simuler des écoulements turbulents avec chocs, ont trouvé des applications dans d'autres domaines, comme par exemple la propagation acoustique. Cet axe comporte éga-

lement des applications des schémas développés à différents types d'écoulements, comme le tube à choc visqueux, la propagation d'ondes dans l'atmosphère ou encore l'interaction entre un écoulement compressible et une structure.

Le deuxième axe concerne la simulation d'écoulements diphasiques à phases séparées, comportant un liquide et un gaz. Dans le type d'écoulements que j'ai étudiés, la compressibilité du fluide concerne généralement la phase gazeuse, mais la phase liquide peut aussi être compressible dans certaines conditions de haute pression ou de vitesse élevée. Dans d'autres situations elle peut être utilisée uniquement à des fins de développement d'une méthode numérique efficace.

Enfin, le troisième axe concerne la thermoacoustique et plus particulièrement le streaming acoustique, je m'y intéresse depuis une dizaine d'années. Le streaming, ou vent acoustique, est un écoulement secondaire moyen qui apparaît (entre autres) dans les résonateurs ainsi que dans les stacks des machines thermoacoustiques. Il est dû à l'interaction entre un écoulement principal oscillant (l'onde acoustique) et la couche limite créée près des parois. C'est un problème très riche qui mêle acoustique, hydrodynamique et thermique.

2 Schémas numériques pour les écoulements compressibles avec chocs.

J'ai commencé mes travaux sur les schémas numériques pour les écoulements compressibles lors de ma thèse, qui portait sur l'étude et la mise en oeuvre d'un schéma aux différences finies implicite pour résoudre les équations d'Euler d'un gaz parfait. L'utilisation d'un schéma implicite permet généralement de s'affranchir de la condition de stabilité CFL caractéristique d'un schéma explicite ($CFL \leq 1$), au prix cependant d'un surcoût CPU par itération lié à l'inversion de l'opérateur implicite. Les applications visées se situaient dans le domaine de l'aviation civile commerciale, en aérodynamique transsonique. Ce schéma, développé à l'origine par Alain Lerat dans une approche "à la" Lax-Wendroff [48], était centré et précis à l'ordre 2 en temps et en espace, et faisait appel à une procédure ADI (Alternated Direction Implicit) pour simplifier (par factorisation) et accélérer la résolution de la phase implicite. Dans mes travaux de thèse j'ai effectué une étude approfondie de la stabilité de ce schéma, et étudié sa vitesse de convergence vers un état stationnaire. Ces résultats ont permis d'aboutir à une version optimisée du schéma, que j'ai mise en oeuvre sur des cas d'écoulements autour de profils d'aile classiques tels que le NACA0012 [54].

En collaboration avec Alain Lerat, j'ai ensuite continué à travailler quelques années sur ce schéma, en développant l'étude d'aspects tels que la stabilité des conditions aux limites associées, ou la structure des chocs obtenus dans le cas stationnaire. En effet le schéma étant centré d'ordre 2 et ne comportant pas de procédure particulière pour traiter les discontinuités, il était naturellement sujet au phénomène de Gibbs, conduisant à l'apparition d'oscillations numériques parasites au voisinage des discontinuités. Dans le cas stationnaire cependant, la solution numérique étant dépendante du pas de temps, l'utilisation d'un grand CFL pour les simulations s'est révélée avoir l'effet supplémentaire intéressant de diminuer voire supprimer ces oscillations [14, 15].

Les travaux sur ce schéma se sont poursuivis au Laboratoire SINUMEF jusqu'au milieu des années 1990, en collaboration avec Jacques Sidès à l'ONERA. Par la suite, les chercheurs de SINUMEF ont pris un virage, initié par Alain Lerat et Christophe Corre, vers les schémas RBC (pour Residual Based Compact) qui ont fait l'objet de nombreuses publications et développements [52, 53], et le schéma implicite à la Lax-Wendroff a été abandonné. Je cite ici un passage de l'HDR de Christophe Corre en 2004, qui explique les raisons de cet abandon : *"La possibilité de mettre en oeuvre le schéma de Lerat en utilisant des CFL nettement plus élevés a mis en évidence en premier lieu l'inconvénient d'une dépendance de la solution stationnaire vis-à-vis du pas de temps, avec notamment une dissipation numérique pouvant parfois devenir excessive lorsque le pas de temps est grand. De plus, une comparaison critique des performances du schéma de Lax-Wendroff implicite avec celles des schémas décentrés implicites qui s'imposaient de plus en plus comme approche standard au milieu des années 90, a conduit inmanquablement au constat du manque de robustesse effective de l'approche Lax-Wendroff".*

Je n'ai pas participé au développement du schéma RBC, mais plutôt choisi une autre voie à la fin des années 90. En collaboration avec Christian Tenaud au LIMSI, j'ai en effet commencé à travailler sur des schémas décentrés de haute précision, pour traiter les écoulements instationnaires avec chocs forts. Nous avons développé une famille de schémas décentrés appelée OSMP p , p étant l'ordre de précision du schéma.

2.1 Construction et étude des propriétés des schémas OSMP.

Ces travaux ont fait l'objet notamment des articles [17, 18]. L'article [17] figure en annexe de ce mémoire.

Le développement de schémas de haute précision pour traiter les écoulements compressibles avec discontinuités (ondes de choc ou discontinuités de contact) a fait l'objet de nombreux travaux de recherche depuis les années 1990, et reste encore d'actualité du fait qu'il n'y a pas de schéma universel. Une précision élevée est nécessaire pour simuler les écoulements turbulents (qui sont bien sûr le cas général en aérodynamique), lesquels comportent des petites structures tourbillonnaires qui doivent être correctement représentées. Par exemple, dans l'approche de Simulation des Grandes Echelles (SGE), il est communément admis que le schéma numérique doit avoir une dissipation numérique très faible afin de minimiser l'interaction avec le modèle de sous-maille utilisé.

La nécessité de répondre à la double contrainte de robustesse et d'une précision suffisante pour représenter les petites structures d'un écoulement, rend la tâche redoutable. En effet, le mécanisme (dit de "capture de choc") utilisé pour empêcher l'apparition d'oscillations numériques au voisinage des discontinuités repose sur l'ajout de dissipation numérique, ce qui est par essence contraire à l'objectif précédent de minimisation de la dissipation. Le mécanisme de capture de choc associé à un schéma d'ordre élevé doit donc être extrêmement ciblé et agir uniquement dans un très petit voisinage des discontinuités.

Les méthodes de capture de choc développées dans la littérature peuvent se classer en trois catégories. La première, la plus ancienne, remonte aux années 1950 et aux travaux de Von Neumann et Richtmyer [111]. Elle est basée sur l'ajout de viscosité dite artificielle d'ordre 2 au schéma, sous la forme d'un Laplacien à coefficients non linéaires. D'autres viscosités artificielles plus élaborées et combinant des dérivées d'ordre plus élevé ont été développées dans les années 1980 notamment par Jameson et al. [40, 41]. Cette méthode a trouvé un regain d'intérêt à la fin des années 2000, couplée à l'utilisation de senseurs sophistiqués, à travers des travaux comme ceux de de Bogey et al. [7] dans le domaine de l'aéroacoustique. Elle a comme atouts sa grande simplicité et son coût CPU très faible. Néanmoins il s'agit d'une méthode qui n'élimine pas totalement les oscillations parasites, et ne contrôle pas précisément la dissipation ajoutée au schéma.

La deuxième catégorie, qui date des années 1970-80, est issue des travaux de Van Leer et de Harten [106, 107, 108, 109, 110, 33, 34]. Elle comprend les schémas dits TVD ("Total Variation Diminishing", à Variation Totale Décroissante), construits, pour des schémas d'ordre 2, à partir de la notion de limiteur (de flux ou de pente). Le mécanisme consiste à dégrader localement le schéma à l'ordre 1, en construisant un indicateur de régularité de la solution et en pondérant un schéma d'ordre 1 et un schéma d'ordre 2 par une fonction (le limiteur) qui dépend de cet indicateur. On obtient ainsi des schémas non oscillants d'ordre 2 presque partout. Ils présentent cependant l'inconvénient majeur de ne pas faire la distinction entre une discontinuité et un extremum local. Ainsi, le limiteur est activé aux extrema, et le schéma est d'ordre 1 à ces endroits. Ceci ne permet pas la restitution correcte des petites structures d'un écoulement, qui sont très rapidement dissipées. Par ailleurs, les schémas TVD restaient limités à l'ordre 2 dans ces travaux.

Enfin une troisième catégorie de méthodes, initialement introduite par Harten et ses co-auteurs en 1987 [35, 95], utilise le principe d'un stencil variable pour construire le flux numérique du schéma. Sur chaque face de cellule, le stencil est choisi, parmi l'ensemble des stencils possibles pour un ordre de précision donné, de manière à minimiser un indicateur de régularité. On obtient de la sorte un flux numérique dit Essentiellement Non Oscillant (ENO). Contrairement à la notion de schéma TVD, le concept ENO n'interdit pas à la solution numérique d'être oscillante, mais autorise seulement des oscillations décroissant en $\mathcal{O}(\delta x^k)$, δx étant le pas d'espace et k l'ordre de précision du schéma. Les schémas WENO [56, 42, 96] sont construits à partir d'une pondération de tous les stencils candidats, et visent à augmenter l'ordre de précision du schéma sans élargir le stencil de reconstruction de la fonction. Ils permettent

effectivement d'obtenir des schémas d'ordre très élevé, au moins spatialement (l'ordre temporel est généralement limité à 3), pas ou très peu oscillants. Néanmoins ils sont coûteux en temps CPU, et se montrent souvent très dissipatifs au voisinage des discontinuités.

Mes travaux sur les schémas OSMP entrent dans la deuxième catégorie. La première étape concerne le développement d'un schéma d'ordre élevé. Deux approches peuvent être suivies pour cela : l'approche couplée espace-temps, dans laquelle les discrétisations temporelle et spatiale sont simultanées et du même ordre, et l'approche découpée qui considère séparément ces deux discrétisations. Les méthodes découplées sont généralement basées sur une intégration temporelle à pas fractionnaire, le plus souvent de type Runge-Kutta. A chaque sous-étape de l'intégration temporelle, on applique une discrétisation spatiale d'ordre élevé, équipée d'une technique de capture de choc, qui assure les propriétés de conservation et de comportement non oscillant. Du fait que le support spatial d'une reconstruction d'ordre élevé est relativement large, le support global de ce type de schéma est beaucoup plus large que celui d'un schéma couplé espace-temps pour le même ordre de précision, la discrétisation spatiale étant appliquée à chaque sous-étape de l'intégration temporelle. De plus, il n'est pas possible d'atteindre des ordres de précision très élevés en temps sans retrouver un comportement oscillatoire de la solution. Par exemple, en utilisant un schéma Runge-Kutta, à partir de l'ordre 6 il n'est plus possible d'assurer une propriété TVD. De plus les schémas d'ordre 4 et 5 nécessitent de résoudre un problème adjoint supplémentaire au cours des sous-étapes, ce qui augmente encore le coût du schéma global. Dans la pratique les discrétisations temporelles sont donc généralement limitées à l'ordre 3. Les méthodes couplées, elles, sont développées dans une approche 'à la' Lax-Wendroff, et utilisent un stencil minimum. Cette approche permet un meilleur contrôle de l'erreur de troncature globale, et d'obtenir plus facilement des conditions optimales pour la capture de chocs non oscillants.

Nous sommes donc partis de l'approche couplée espace-temps pour développer les schémas OSMP p . Le mécanisme de capture de choc choisi repose sur le concept TVD, amélioré par une procédure (dite Monotonicity Preserving -MP-, introduite par Suresh et al. [100] dans le cadre des schémas découpés) qui permet d'éviter l'écrétage des maxima caractéristique de cette approche. Je vais reprendre rapidement la construction de ces schémas dans ce qui suit.

La démarche que nous avons adoptée pour la construction du schéma d'ordre élevé non limité OS (One Step) consiste à travailler de manière incrémentale, en utilisant **l'équation équivalente** d'un schéma d'ordre p pour construire le schéma d'ordre $p + 1$. L'équation équivalente d'un schéma est l'équation qui est résolue à un ordre supérieur à celui du schéma. Il s'agit cependant d'une approche qui est difficilement extensible au cas des systèmes non linéaires, hormis à travers l'utilisation d'une procédure de type Cauchy-Kowalewski [35] qui est presque impraticable. Néanmoins l'extension effectuée en suivant une approche localement linéarisée donne, malgré un ordre formel de précision qui est ramené à 2, des résultats de très bonne qualité, qui se comparent avantageusement à des schémas d'ordre théorique plus élevé [17]. En effet, les schémas OS possèdent un niveau d'erreur particulièrement bas, ce qui les rend utilisables avec de bons résultats sur des maillages relativement grossiers. Et, en mécanique des fluides numérique, il est rare de pouvoir utiliser des maillages aussi fins qu'on le souhaiterait ! L'extension au cas multidimensionnel utilise une méthode de splitting de Strang [99]. Pour plus de détails on se reporterà à [17].

Dans ce qui suit, je décris seulement le développement de ces schémas dans le cas d'une équation de transport scalaire linéaire (équation $w_t + f(w)_x = 0$, $f(w) = aw$, $a \in \mathbb{R}$), pour un maillage régulier de pas δx et un pas de temps δt .

Etant donné un schéma d'ordre p , on construit son équation équivalente à l'ordre p en effectuant des développements de Taylor jusqu'à l'ordre $p + 1$, puis en remplaçant les dérivées tem-

porelles par des dérivées spatiales *en réutilisant l'équation elle même*. Prenons l'exemple du schéma décentré d'ordre 1 (cas $a > 0$; on note W_j^n la solution numérique au point $(j\delta x, n\delta t)$) :

$$\frac{W_j^{n+1} - W_j^n}{\delta t} + a \frac{W_j^n - W_{j-1}^n}{\delta x} = 0 \quad (1)$$

Effectuons des développements de Taylor autour du point $(x, t) = (j\delta x, n\delta t)$, il vient :

$$\frac{\partial w}{\partial t} + a \frac{\partial w}{\partial x} = -\frac{\delta t}{2} w_{tt} + \frac{\delta x}{2} a w_{xx} + \mathcal{O}(\delta t^2, \delta x^2) \quad (2)$$

de (2) on tire :

$$\begin{aligned} w_t &= -aw_x + \mathcal{O}(\delta t, \delta x) \\ w_{tt} &= -aw_{xt} + \mathcal{O}(\delta t, \delta x) = a^2 w_{xx} + \mathcal{O}(\delta t, \delta x) \end{aligned} \quad (3)$$

En remplaçant dans (2) on trouve l'équation équivalente à l'ordre 1 du schéma décentré :

$$\frac{\partial w}{\partial t} + a \frac{\partial w}{\partial x} = a \frac{\delta x}{2} (1 - \nu) w_{xx} \quad (4)$$

avec $\nu = a\delta t/\delta x$ le nombre CFL. Pour construire un schéma d'ordre 2, on peut alors corriger le terme d'erreur dans le membre de droite de (4) en soustrayant au schéma décentré ce terme discrétisé (par une formule centrée puisque c'est une dérivée paire), ce qui donne le schéma :

$$\frac{W_j^{n+1} - W_j^n}{\delta t} + a \frac{W_j^n - W_{j-1}^n}{\delta x} = -a \frac{\delta x}{2} (1 - \nu) \frac{W_{j+1}^n - 2W_j^n + W_{j-1}^n}{\delta x^2} \quad (5)$$

Le flux numérique du schéma correspondant, formulé sous forme conservative :

$$W_j^{n+1} = W_j^n - \frac{\delta t}{\delta x} (F_{j+1/2}^2 - F_{j-1/2}^2),$$

s'écrit :

$$F_{j+1/2}^2 = aW_j^n + \frac{1 - \nu}{2} a(W_{j+1}^n - W_j^n) \quad (6)$$

C'est le schéma d'ordre 2 de Lax-Wendroff.

Cette procédure peut être poursuivie pour construire des schémas d'ordre de plus en plus élevé. L'équation équivalente à l'ordre 2 du schéma de Lax-Wendroff s'écrit :

$$\frac{\partial w}{\partial t} + a \frac{\partial w}{\partial x} = -a \frac{\delta x^2}{6} (1 - \nu^2) w_{xxx} \quad (7)$$

On obtient le flux corrigé correspondant au schéma d'ordre 3, en discrétisant le terme d'erreur par une formule aux différences décentrée vers l'amont pour des raisons de stabilité :

$$F_{j+1/2}^3 = F_{j+1/2}^2 - \frac{1 - \nu}{2} \cdot \frac{1 + \nu}{3} a(W_{j+1}^n - 2W_j^n + W_{j-1}^n) \quad (8)$$

En procédant de cette manière, on peut établir une relation de récurrence pour $p \geq 1$, qui permet d'obtenir le flux numérique d'un schéma d'ordre $p + 1$ à partir de celui d'un schéma d'ordre p :

$$F_{j+1/2}^{p+1} = F_{j+1/2}^p + \alpha_{p+1} \cdot \sum_{l=0}^p (-1)^l \mathbf{C}_p^l W_{j+m-l} \quad (9)$$

avec $m = \lfloor (p + 1)/2 \rfloor$ et :

$$\alpha_l = \prod_{k=2}^l (-1)^k \frac{\lfloor k/2 \rfloor - (-1)^k \nu}{k} \quad (10)$$

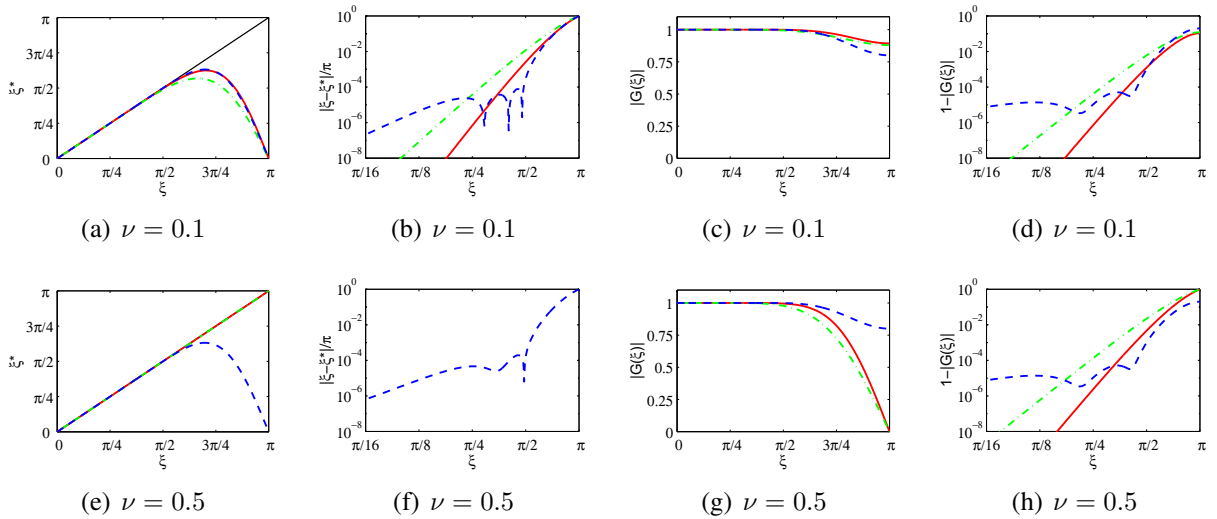


FIGURE 1 – De gauche à droite : nombre d’onde effectif, erreur dispersive, module du facteur d’amplification, erreur d’amplitude, en fonction du nombre d’onde réduit $\xi = k \delta x$ (k étant le nombre d’onde) : schémas OS11 (ligne pleine rouge), OS7 (tiret-point vert), et DRP (tiret bleu).

où la notation $\lfloor \cdot \rfloor$ désigne la division entière. Tous ces schémas sont stables sous la condition CFL habituelle ($0 \leq \nu \leq 1$), et possèdent la propriété de restituer la solution exacte si $\nu = 1$ (contrairement aux schémas semi discrets). Le stencil associé au schéma d’ordre p comprend $p + 1$ points pour les schémas d’ordre pair, $p + 2$ pour les schémas d’ordre impair. On peut interpréter ces schémas comme donnant une solution numérique W_j^{n+1} qui est une interpolation polynomiale d’ordre p , sur l’axe $t = t^n$, de la valeur exacte conservée le long de la droite caractéristique $x = at$ passant par le point (x_j, t^{n+1}) . Des schémas analogues ont été construits par Leonard [49] en suivant cette approche caractéristique.

Avant de passer à la description du mécanisme de capture de choc associé à ces schémas, je présente quelques résultats de l’analyse spectrale de leur erreur, comparée à celle des schémas DRP développés par Bogey et Bailly [6]. Il s’agit de schémas centrés d’ordre 4, découpés espace-temps et optimisés dans l’espace des nombres d’onde. L’avancement en temps est effectué en utilisant un schéma Runge-Kutta à 6 pas. Une procédure de filtrage d’ordre élevé permet de stabiliser le schéma aux grands nombres d’onde. Ces schémas, spécifiquement développés pour des applications en aéroacoustique, possèdent une erreur dispersive et dissipative très faible. Ils sont très bien adaptés à la simulation d’écoulements comportant des petites structures (acoustique, turbulence), mais sont peu robustes et deviennent très oscillants si des ondes de choc apparaissent. La figure 1 montre les résultats de l’analyse du facteur d’amplification des schémas OS7, OS11 et DRP. On constate que les schémas OS se comparent très bien au schéma DRP, avec un niveau de dispersion et de dissipation très faible pour les nombres d’onde réduits $\xi = k \delta x$ inférieurs à $\pi/2$ (4 points par longueur d’onde). Pour les nombres d’onde plus grands, le filtre associé au schéma DRP est générateur d’un niveau d’erreur dispersive supérieur au schéma OS11.

L’étape suivante pour obtenir un schéma TVD (donc non oscillant au voisinage des discontinuités) consiste à limiter le flux numérique du schéma en lui appliquant les contraintes de Harten [33]. Pour cela on écrit le flux du schéma d’ordre p quelconque sous la forme suivante, par analogie avec la forme utilisée par Harten dans le cas du schéma d’ordre 2 de Lax-Wendroff :

$$F_{j+1/2}^p = f_j^n + \phi_{j+1/2}^p \cdot \frac{1-\nu}{2}(f_{j+1}^n - f_j^n) \quad (11)$$

avec $f_j^n = f(W_j^n) = aW_j^n$ et

$$\phi_{j+1/2}^p = \frac{2}{1-\nu} \frac{F_{j+1/2}^p - f_j^n}{f_{j+1}^n - f_j^n} \quad (12)$$

À la différence de ce qui se passe pour un schéma d'ordre 2, la fonction $\phi_{j+1/2}^p$ va ici jouer un double rôle. Non modifiée, elle conserve le schéma d'ordre p . Mais elle peut également jouer le rôle d'un limiteur de flux, en lui appliquant les conditions établies par Harten dans le cas de l'ordre 2. Ces conditions s'écrivent :

$$\begin{cases} 0 \leq \phi_{j+1/2}^p \leq \frac{2}{1-\nu} \\ 0 \leq \phi_{j+1/2}^p \leq \frac{2r_{j+1/2}}{\nu} \end{cases} \quad (13)$$

$r_{j+1/2}$ représentant un indicateur de régularité de la solution numérique, défini par $r_{j+1/2} = (W_j^n - W_{j-1}^n)/(W_{j+1}^n - W_j^n)$. On peut alors définir un schéma TVD d'ordre p (OSTVD p) en définissant le flux du schéma limité comme :

$$F_{j+1/2}^{p,TVD} = f_j^n + \phi_{j+1/2}^{p,TVD} \cdot \frac{1-\nu}{2} (f_{j+1}^n - f_j^n) \quad (14)$$

avec :

$$\phi_{j+1/2}^{p,TVD} = \max(0, \min(\frac{2}{1-\nu}, \frac{2}{1-\nu} \frac{F_{j+1/2}^p - f_j^n}{f_{j+1}^n - f_j^n}, \frac{2r_{j+1/2}}{\nu})). \quad (15)$$

Cependant, comme à l'ordre 2, le défaut majeur d'un tel schéma reste le traitement à l'ordre 1 des extrema. Les conditions MP constituent un remède efficace à ce problème.

Les conditions MP telles que nous les avons développées dérivent du schéma préservant la monotonie introduit dans [100], dans une approche découpée espace-temps. Nous avons établi le lien entre l'approche TVD et les contraintes géométriques établies dans [100], permettant de considérer les contraintes MP comme un moyen de relaxer les contraintes TVD aux endroits nécessaires. De plus nous avons adapté leur formulation à l'approche couplée. Dans une première étape, on établit une interprétation géométrique des contraintes TVD. Pour cela, on écrit le flux du schéma d'ordre p comme :

$$F_{j+1/2}^p = f_j^n + \phi_{j+1/2}^p \frac{(1-\nu)}{2} (f_{j+1}^n - f_j^n) = f_j^n + \gamma^+ (f_{j+1}^n - f_j^n) \quad (16)$$

avec

$$\gamma^+ = \phi_{j+1/2} \frac{(1-\nu)}{2} \quad (17)$$

La première contrainte TVD, $0 \leq \phi_{j+1/2} \leq \frac{2}{1-\nu}$, équivaut à $0 \leq \gamma^+ \leq 1$, donc à dire que le flux numérique $F_{j+1/2}^p$ doit appartenir à l'intervalle $[f_j^n, f_{j+1}^n]$. Pour interpréter la seconde contrainte, on introduit d'abord le flux suivant :

$$f_j^{ul} = f_j^n + \frac{1-\nu}{\nu} (f_j^n - f_{j-1}^n) \quad (18)$$

et l'on réécrit $F_{j+1/2}^p$ comme :

$$F_{j+1/2}^p = f_j^n + \phi_{j+1/2} \frac{\nu}{2 r_{j+1/2}} (f_j^{ul} - f_j^n) = f_j^n + \gamma^- (f_j^{ul} - f_j^n) \quad (19)$$

avec

$$\gamma^- = \phi_{j+1/2} \frac{\nu}{2 r_{j+1/2}} \quad (20)$$

La seconde contrainte TVD, $0 \leq \phi_{j+1/2} \leq \frac{2r_{j+1/2}}{\nu}$, revient à dire que le coefficient γ^- doit prendre ses valeurs entre 0 and 1, *i.e.* le flux $F_{j+1/2}^p$ doit appartenir à l'intervalle $[f_j^n, f_j^{ul}]$. Finalement les conditions TVD reviennent à forcer le flux à appartenir à l'intersection des deux intervalles $[f_j^n, f_{j+1}^n]$ et $[f_j^n, f_j^{ul}]$. Cependant, aux extrema, l'intersection est réduite à un point, qui correspond au schéma d'ordre 1. En considérant qu'une discontinuité est une structure à profil monotone, le principe de la limitation MP est alors d'élargir ces intervalles seulement aux endroits où la solution n'est pas monotone (extrema), de sorte que la limitation TVD n'est pas activée et que le schéma reste à l'ordre p . Pour cela on définit de nouvelles valeurs de γ^\pm prenant en compte la courbure locale de la solution $d_{j\pm1/2}$:

$$\gamma^+ = \frac{1}{2}(1 - \frac{d_{j+1/2}}{f_{j+1}^n - f_j^n}) \quad (21)$$

$$\gamma^- = \frac{1}{2}(1 + \frac{d_{j-1/2}}{f_j^n - f_{j-1}^n}) \quad (22)$$

avec $d_{j+1/2} = \text{minmod}(d_j, d_{j+1})$ et $d_j = f_{j+1}^n - 2f_j^n + f_{j-1}^n$ (discrétisation au second ordre de la dérivée seconde de f).

Dans [17] on a montré que le schéma OSMP défini de cette manière possède la propriété d'être non oscillant pour tout profil monotone, tout en conservant une précision d'ordre élevé ailleurs. Les propriétés de convergence de la méthode sont illustrées par un résultat dans le cas scalaire linéaire pour une donnée initiale régulière ($w_0(x) = \sin^4(\pi x)$) (Table 1), qui fournit une comparaison du schéma OS7 avec ses versions limitées TVD et MP, et avec un schéma découpé [100] basé sur une discrétisation spatiale d'ordre 7 et un schéma temporel Runge-Kutta d'ordre 3. Ces résultats mettent en évidence l'intérêt de la méthode MP par rapport au TVD : dans un cas régulier comme celui-ci, l'application des contraintes MP laisse la solution numérique et donc l'ordre théorique des schémas inchangés, alors que la correction TVD dégrade fortement la précision. On peut également noter le bas niveau d'erreur associé au schéma OS7 (ou OSMP7) sur le maillage le plus grossier, comparé au schéma découpé. Le même pas de temps est utilisé pour tous les schémas, ce qui ne permet bien entendu pas de mettre en évidence l'ordre spatial du schéma semi-discret.

Le cas test suivant, toujours dans un cas d'advection scalaire linéaire, comporte des discontinuités, mettant en évidence le fonctionnement des limiteurs TVD et MP. La figure 2 compare les résultats obtenus après une période (les conditions aux limites sont périodiques) pour le schéma d'ordre 7 (OS7), sa version TVD (OSTVD7), et sa version MP (OSMP7). On constate que le schéma MP fait parfaitement son travail, en supprimant les oscillations du schéma de base comme le schéma TVD, mais en n'écrétant pas les maxima. De plus les discontinuités ne sont pas étalées comme ont tendance à le faire les schémas WENO par exemple. La figure 3 suivante montre les endroits où le limiteur TVD est activé, et l'on constate bien que le schéma OSMP supprime le mécanisme de limitation aux extrema. Il est intéressant de remarquer que le limiteur est activé uniquement dans les zones d'oscillations, et non dans la discontinuité elle-même. Notons aussi que ces schémas ne font intervenir aucun paramètre de réglage ad-hoc ou dépendant du type de problème considéré.

Je termine cette section avec un dernier cas test illustrant la capacité du schéma OSMP à advecter correctement, sur de longues distances, des petites structures discrétisées sur peu de points (par exemple des perturbations haute fréquence). On considère la propagation d'un paquet d'onde, discrétisé avec 6 points par longueur d'onde. La figure 4 présente les résultats obtenus pour les schémas OS11 et OSMP11, pour trois valeurs du CFL. On constate que le schéma OS11 donne une solution presque parfaite, quelque soit le CFL, et que le limiteur MP laisse la solution presque inchangée.

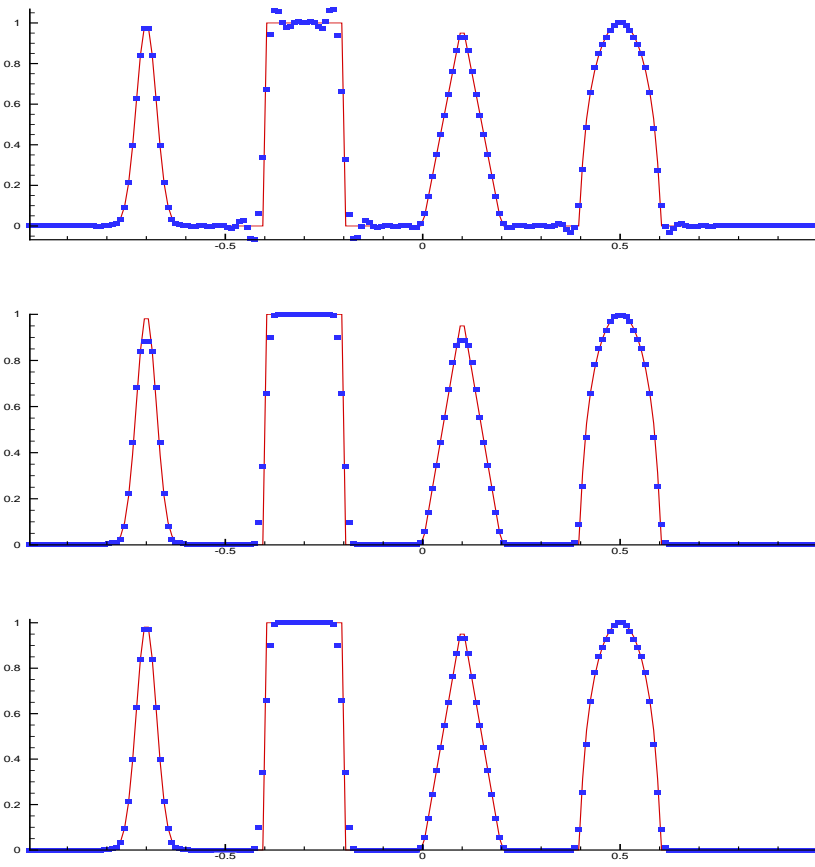


FIGURE 2 – Advection sur une période ($t = 2$). De haut en bas : schémas OS7, OSTVD7, OSMP7. Dans tous les cas $CFL=0.5$, maillage 200 points.

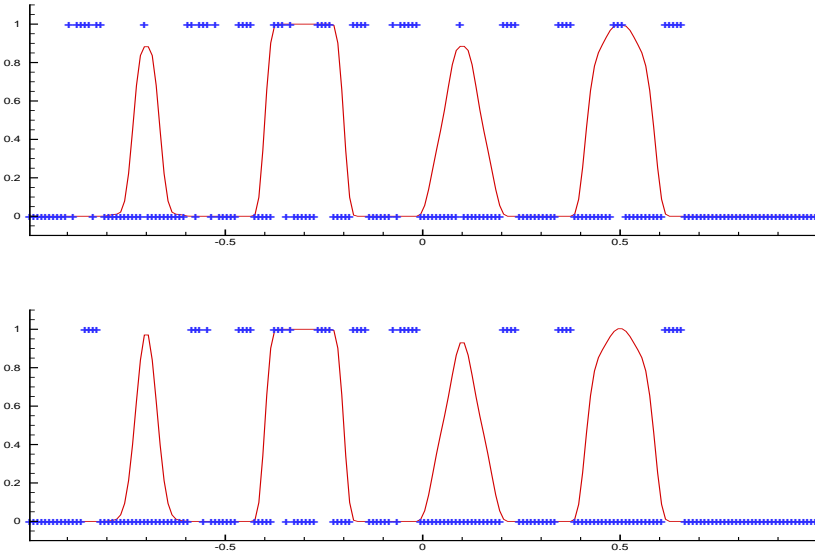


FIGURE 3 – Indicateur d’activation du limiteur TVD ($t = 2$). L’indicateur est à 1 lorsque le limiteur est activé, à 0 sinon (en rouge la solution numérique). De haut en bas : OSTVD7, OSMP7.

TABLE 1 – Advection de la condition initiale $u_0(x) = \sin^4(\pi x)$: erreur L_1 et ordre de précision pour les schémas couplé et RK3 à l’ordre 7 (1 période, CFL=0.5).

Méthode	Nombre de points	erreur L_1	ordre L_1
OS 7	20	$1.35976 \cdot 10^{-2}$	
OS MP 7	40	$1.52989 \cdot 10^{-4}$	6.47
	80	$1.25285 \cdot 10^{-6}$	6.93
	160	$1.00115 \cdot 10^{-8}$	6.97
	320	$7.86404 \cdot 10^{-11}$	6.99
RK3/7	20	$3.13055 \cdot 10^{-2}$	
RK3/7 MP	40	$2.78928 \cdot 10^{-3}$	3.49
	80	$3.28150 \cdot 10^{-4}$	3.09
	160	$4.10337 \cdot 10^{-5}$	3.00
	320	$5.12516 \cdot 10^{-6}$	3.00
OS TVD 7	20	$3.97304 \cdot 10^{-2}$	
	40	$7.98315 \cdot 10^{-3}$	2.31
	80	$1.46731 \cdot 10^{-3}$	2.44
	160	$2.57370 \cdot 10^{-4}$	2.51
	320	$4.24540 \cdot 10^{-5}$	2.60

L’article [17] est très cité (136 citations depuis sa parution). Il est intéressant de noter que ce schéma a diffusé vers d’autres domaine que l’aérodynamique. En effet il a semble-t-il été implémenté dans le code MITgcm, qui est le code du MIT qui traite de la circulation locale et globale dans les océans et l’atmosphère, et il est beaucoup cité dans ce domaine. Un exemple est donnée par la référence [9] qui concerne la "Modélisation de l’évolution à long terme des marées noires dans le pire des cas dans l’Arctique", un autre par [28], qui s’intéresse aux "Estimations globales du transfert d’énergie du vent à l’océan". Je dois dire que c’est une satisfaction d’apporter une (très) petite contribution aux études sur le changement climatique et la pollution dans le contexte actuel.

Soulignons pour terminer la polyvalence de ce schéma numérique. Je l’ai en effet utilisé pour simuler des écoulements très fortement compressibles (tube à choc, écoulement supersonique au dessus d’une cavité, explosion Misty picture, interaction fluide-structure), aussi bien que pour la simulation directe du streaming acoustique, pour lequel le nombre de Mach de l’écoulement principal est faible.

2.2 Application des schémas OSMP au calcul d’écoulements compressibles.

L’objectif de la construction des schémas OSMP était de mettre au point un outil très général, robuste et précis en toutes circonstances. Depuis leur mise au point en 2004, nous avons eu l’occasion d’appliquer ces schémas à des types d’écoulements très différents, avec de bons résultats. Leur coût CPU est assez élevé (essentiellement du fait du mécanisme de limitation), néanmoins ils se comparent de ce point de vue très avantageusement avec les schémas WENO : le schéma OSMP7 est six fois moins cher que le schéma RK3-WENO5. En revanche pour traiter des écoulements ne comportant que des chocs faibles, les schémas DRP équipés d’une viscosité

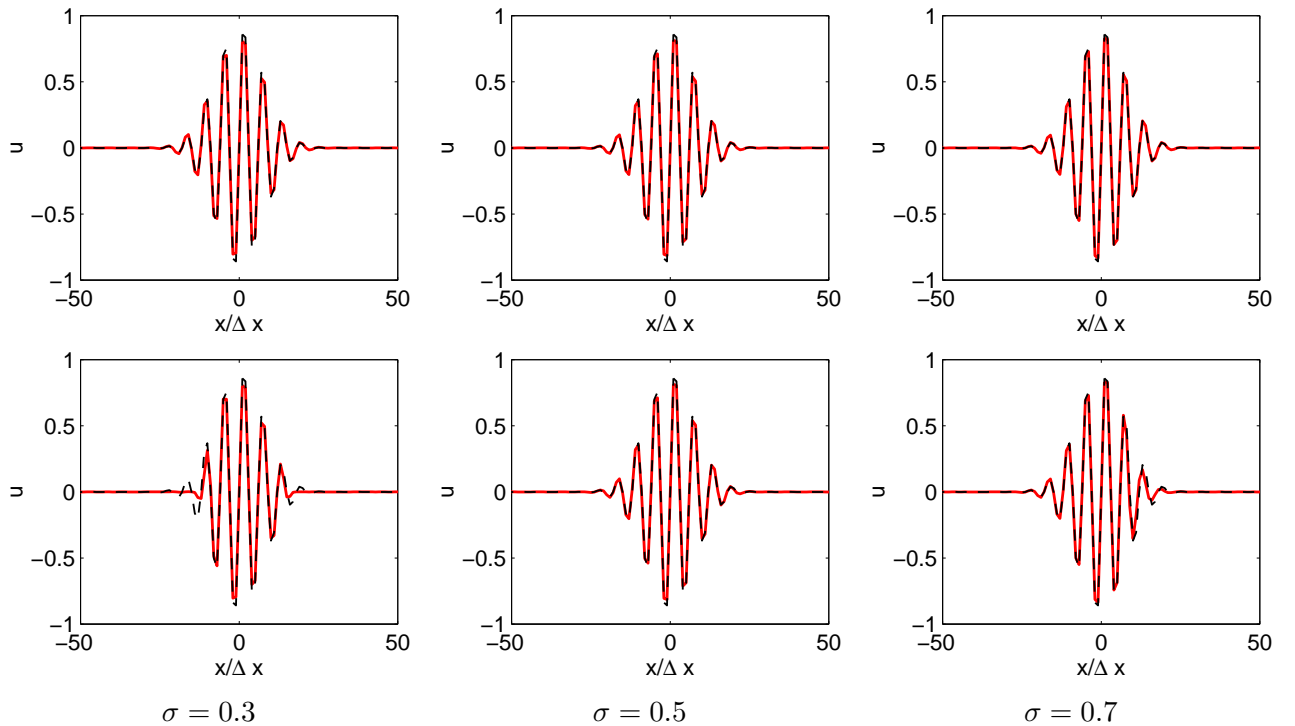


FIGURE 4 – Advection d’un paquet d’onde sur $200 \delta x$. En haut : schéma OS11, en bas : schéma OSMP11. Résultats avec $\nu = 0.3$ (gauche), $\nu = 0.5$ (milieu), et $\nu = 0.7$ (droite) pour 6 points par longueur d’onde. En rouge la solution numérique, en tirets noirs la solution analytique.

artificielle [7] sont nettement moins coûteux en termes de temps CPU.

Le schéma OSMP a été implémenté dans un code compressible 3D appelé CHORUS (Compressible High Order Unsteady Simulations), développé par Yann Fraigneau au LIMSI. Ce code a été déposé à l’Agence pour la Protection des Programmes en 2010 avec comme titulaires le CNRS et l’ENSA. CHORUS a par ailleurs été acquis par le CEA (Centre DAM Île de France) en 2010, pour des travaux en interaction fluide-structure (thèses de Laurent Monasse puis Adela Puscas).

Parmi les applications des schémas OSMP que nous avons traitées, je présenterai brièvement le cas du tube à choc visqueux, une étude de propagation atmosphérique, et quelques résultats de la thèse de Laurent Monasse sur l’interaction fluide-structure que j’ai co-encadrée. D’autres travaux en aéroacoustique (en collaboration avec Xavier Golerfelt du laboratoire DynFluid de l’ENSA [18]), sur l’interaction choc/couche limite (en collaboration avec Jean-Christophe Robinet du laboratoire DynFluid [87]), et sur la simulation aux grandes échelles (SGE) de l’écoulement turbulent autour d’une plaque plane épaisse (en collaboration avec Christian Tenuaud, Bérengère Podvin et Yann Fraigneau du LIMSI [102]) ont été menés.

Le tube à choc visqueux [16, 20].

Ce cas d’écoulement est représentatif des difficultés que les schémas OSMP ont vocation à traiter. En effet il comporte à la fois des interactions multiples d’ondes de choc de forte intensité et des structures régulières de petite échelle. Il s’agit d’un tube à choc fermé à ses extrémités, qui comporte initialement une chambre haute pression et une chambre basse pression séparées par une membrane. À la rupture de la membrane, un système d’ondes composé d’une détente, d’une discontinuité de contact et d’une onde de choc se développe. L’onde de choc, qui se propage dans la chambre basse pression, produit une couche limite le long de la paroi. Lorsque l’onde atteint le fond du tube, elle se réfléchit et entre en interaction avec la couche limite incidente,

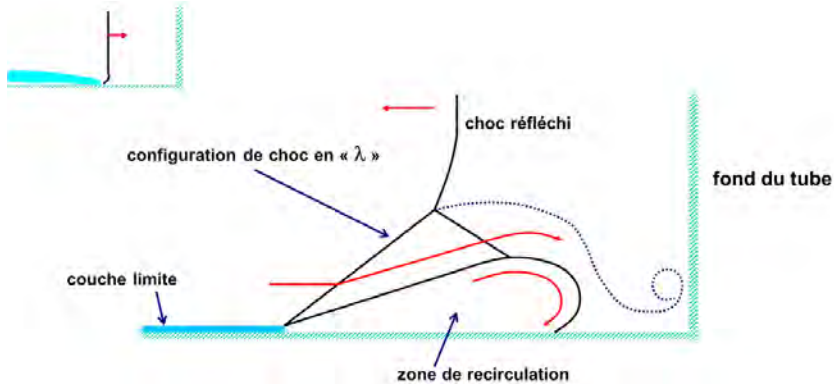


FIGURE 5 – Schéma de l’interaction choc/couche limite en fond de tube à choc. En haut à gauche, schéma de l’écoulement incident.

produisant dans certaines conditions un motif d’ondes de choc obliques "en lambda" et des structures tourbillonnaires (figure 5). C’est cette interaction à laquelle je me suis intéressée pendant plusieurs années, en collaboration avec Christian Tenaud. Il s’agit par ailleurs d’un problème qui intéresse de nombreuses applications. On peut par exemple citer le domaine de la distribution de gaz comprimé (c’est l’origine de la définition de ce cas test : l’entreprise Air Liquide avait rencontré des problèmes lors de la distribution d’air comprimé dans les hôpitaux, qu’elle soupçonnait être liés à ce type d’interaction), ou encore les installations expérimentales en aérodynamique à grande vitesse.

Nous avons abordé le problème dans le cas 2D plan (pour des raisons évidentes de coût de calcul), ce qui n’en fait pas un cas d’écoulement réaliste. Cependant il constitue un bon cas test pour l’évaluation des schémas numériques dans le cas instationnaire visqueux, et il est devenu un cas test de référence, en ayant été traité à notre suite par de nombreux auteurs (par exemple [98, 45], ..., [70], ...). Nous avons obtenu des solutions convergées pour plusieurs valeurs du nombre de Reynolds de l’écoulement, fournissant ainsi des solutions de référence qui sont utiles pour valider et comparer différents schémas numériques.

La configuration géométrique est très simple, un carré de côté 1, entouré de parois adiabatiques et rempli d’air. Le diaphragme est initialement situé au milieu du carré ($x = 0.5$). L’état initial, en quantités sans dimensions, est, à gauche du diaphragme : $\rho_L = 120$, $p_L = \rho_L/\gamma$, $u_L = v_L = 0$, et à droite : $\rho_R = 1.2$, $p_R = \rho_R/\gamma$, $u_R = v_R = 0$. Au temps initial le diaphragme est rompu. En fluide parfait, la solution (1D) est constituée d’une onde de choc et d’une discontinuité de contact se propageant vers la droite, et d’une onde de détente sonique se propageant vers la gauche. Ce régime d’ondes est représenté sur la figure 6, qui montre le diagramme $x - t$ de la masse volumique et de la vitesse. Le nombre de Mach du choc est égal à 2.37. La détente se réfléchit sur la paroi de gauche au temps sans dimension $t = 0.5$. Le choc incident est faible, et se réfléchit sur la paroi de droite au temps $t = 0.21$, puis interagit avec la discontinuité de contact. De multiples interactions se produisent ensuite, puis la discontinuité de contact reste stationnaire, proche de la paroi de droite. Par la suite le choc réfléchi commence à interagir avec la détente à $t = 0.4$, puis avec la détente réfléchie. Le temps total considéré est égal à 1.

Nous avons considéré 4 valeurs du nombre de Reynolds (basé sur la vitesse du son initiale) dans cette étude : 200, 500, 750 et 1000. Le scénario de l’interaction est décrit par la figure 7, qui représente la solution numérique à différents instants, pour $Re=200$ (seule la moitié inférieure du carré est représentée pour des raisons de symétrie). L’interaction entre le choc réfléchi et la couche limite incidente commence dans le coin en bas à droite, juste après la réflexion du choc sur la paroi de droite. A ce moment, la pression d’arrêt à l’intérieur de la couche limite est

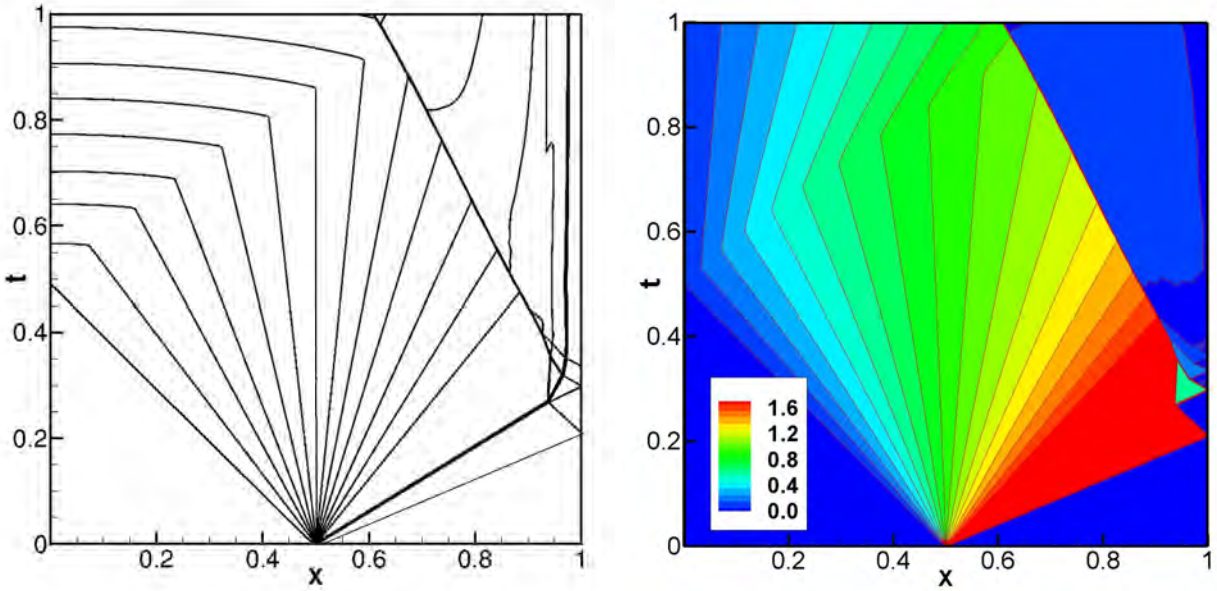


FIGURE 6 – Diagramme $x - t$ de la masse volumique (gauche), de la vitesse (droite).

plus faible que celle derrière le choc. Donc le fluide contenu dans la couche limite ne peut pas passer derrière l'onde de choc réfléchie, et une région d'écoulement séparée apparaît. Le fluide chauffé derrière le choc est dévié vers la paroi dans le coin en bas à droite, créant un jet pariétal à contrecourant, qui forme un bulbe de décollement enfermant du fluide chaud provenant de la zone à l'arrêt contre la paroi de droite. La déviation du fluide froid au dessus de la ligne de glissement (qui est une couche de mélange supersonique) délimitant le bulbe de fluide chaud induit alors un motif de choc dit en "lambda". Le jet à contrecourant impacte ensuite alternativement la paroi et la ligne de glissement, créant des tourbillons contre-rotatifs. Chaque tourbillon est constitué de trois couches : le fluide le plus chaud (choqué) est au centre du tourbillon, entouré de fluide plus froid de la couche limite, puis du fluide le plus froid venant de l'écoulement externe. Le jet a une grande énergie, et atteint des vitesses supersoniques à plusieurs endroits. Chaque impact du jet crée une zone de surpression, conduisant à la déformation de la ligne de glissement et à la génération d'ondes de choc secondaires.

Nous avons préalablement étudié la convergence de nos simulations, étape indispensable. Celles-ci ont toutes été réalisées en utilisant un maillage cartésien uniforme, constitué de mailles carrées. Comme attendu, des grilles plus fines ont été nécessaires pour atteindre la convergence aux plus grands nombres de Reynolds. Nos simulations nous ont montré que les grilles nécessaires à la convergence étaient de 1000×500 points pour $Re = 200$, 1500×750 points pour $Re = 500$, 2000×1000 points pour $Re = 750$ et 4000×2000 points pour $Re = 1000$. C'étaient donc de grosses simulations, qui ont été réalisées sur les machines vectorielles (à l'époque) de l'IDRIS. Nous avons ensuite analysé l'influence du nombre de Reynolds sur l'écoulement.

Les figures 8 et 9 montrent que lorsque Re augmente, du fait de la diminution des effets de la viscosité, la vitesse du jet pariétal augmente et donc aussi le nombre de réflexions alternées entre la paroi et la ligne de glissement pendant un temps fixé. Le nombre de tourbillons ainsi créés augmente aussi, comme on le voit sur la figure 8. Trois tourbillons sont créés dans le cas $Re = 200$ et six pour $Re = 1000$.

Le champ de gradient de masse volumique, illustré par une image stroboscopique numérique présentée Fig. 8 (gauche), montre très clairement le jet pariétal et la structure de l'écoulement à $t = 0.6$, au début de l'interaction. Le champ de température Fig. 8 (droite) donne des informations complémentaires sur l'écoulement, comme la répartition des zones chaudes et froides et le

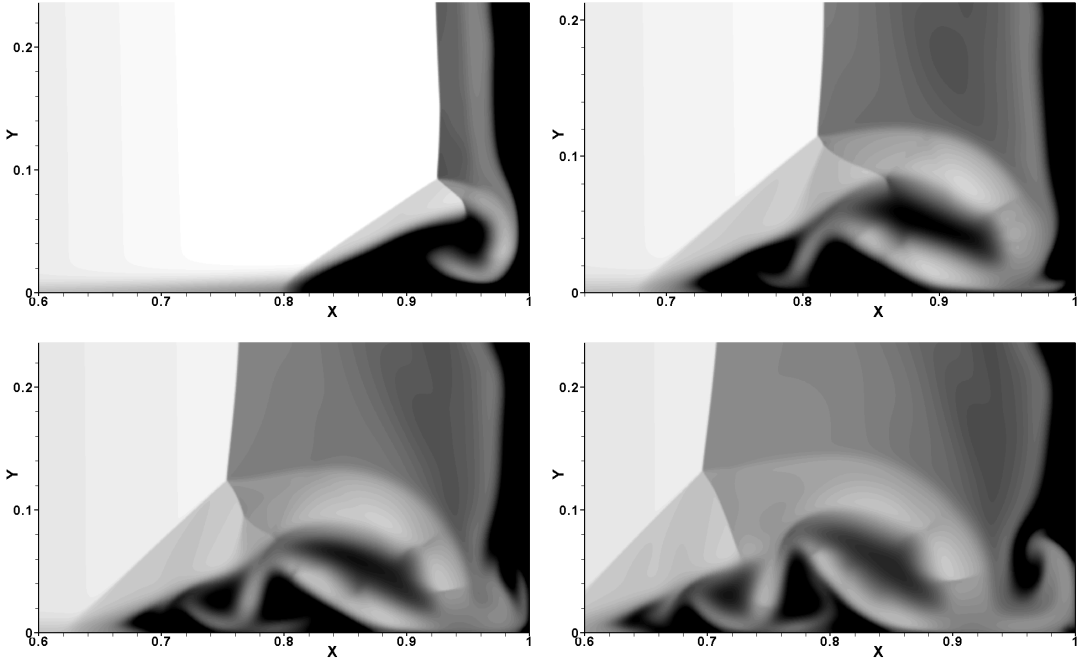


FIGURE 7 – Contours de la température obtenus sur la grille 1000×500 pour $t = 0.4$, $t = 0.6$, $t = 0.7$, $t = 0.8$ (de haut en bas et de gauche à droite); $Re = 200$. Fluide chaud en sombre, fluide froid en clair. 41 niveaux entre 0.4 et 1.2

flux provenant de la couche limite. À l'instant final $t = 1$, la figure 9 montre que l'organisation de l'écoulement dans le bulbe de décollement devient différente et beaucoup moins structurée lorsque le nombre de Reynolds augmente. Pour comprendre ce changement, on a représenté figure 10 les lignes de courant de l'écoulement, obtenues dans le référentiel du choc réfléchi, superposées au champ de vorticité, pour $Re = 200$ et $Re = 1000$. On voit que dans le cas $Re = 1000$, les tourbillons présents à l'intérieur du bulbe sont étirés par l'écoulement extérieur, jusqu'à la rupture (figure 10 (droite) pour $t = 0.9$). À la suite de cette rupture, un effet de "ressort" se produit qui vient comprimer les plus petits tourbillons qui s'agrègent. Cet effet n'est pas présent dans le cas $Re = 200$, pour lequel les tourbillons à l'intérieur du bulbe conservent une organisation ordonnée.

Propagation d'ondes dans l'atmosphère [19, 64].

Au cours d'une collaboration de quelques années avec le CEA (DAM), je me suis intéressée à un problème posé par Christophe Millet (CEA), relatif à la propagation d'ondes (infrasons et ondes de gravité inertielles) dans l'atmosphère. Au CEA, l'étude était motivée par la surveillance des essais nucléaires liée au traité d'interdiction complète de ces essais (ratifié par la France en 1998). Dans le but de veiller au respect de ce traité, un système de surveillance international a été mis en place avec 321 stations réparties tout autour du globe. Le CEA est responsable pour la France de la récupération et de l'interprétation des données de plusieurs stations. Dans ce but, des codes numériques sont utilisés pour recréer les conditions d'une propagation sur de très longues distances, et reproduire les phénomènes physiques mis en jeu lors de telles explosions. Notamment, une explosion de très forte intensité donne lieu à la propagation d'infrasons et d'ondes de gravité, qui peuvent servir de "signature" de l'explosion. Ces ondes sont néanmoins difficile à représenter numériquement. Il est ainsi impératif d'utiliser des schémas numériques de très bonne qualité et, comme il s'agit d'une explosion, qui soient aussi capables de traiter des discontinuités. Ce sujet a fait l'objet de deux Masters de Recherche

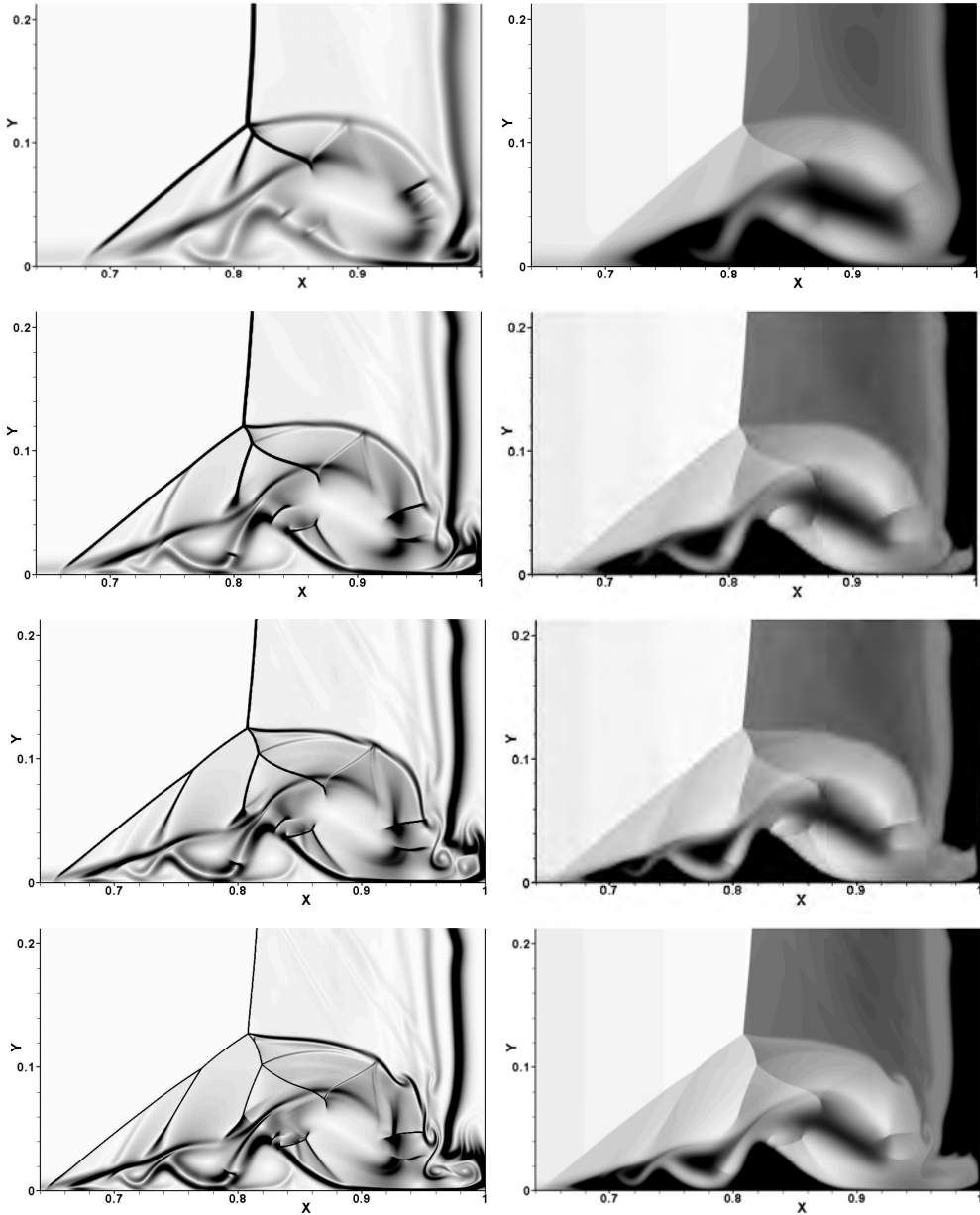


FIGURE 8 – Contours de $|\nabla \rho|$ (gauche) et T (droite, 41 niveaux entre 0.4 et 1.2) obtenus à $t = 0.6$ sur la grille la plus fine pour plusieurs nombres de Reynolds ; de haut en bas : $Re = 200$; $Re = 500$; $Re = 750$; $Re = 1000$.

successifs (Louis-Alfred Bordet et Vincent Elia en 2006-2007, et Jean-Philippe Majorcryk en 2007-2008).

Nous avons donc choisi le schéma OSMP7 pour simuler cet écoulement. Avant de réaliser un calcul en atmosphère réaliste, nous avons préalablement testé le schéma sur le benchmark dit d'Attenborough [3], pour lequel des solutions de référence existent. Pour ce cas test, le domaine est bidimensionnel et s'étend sur 4,5 km en hauteur et en largeur. Le sol est considéré comme une paroi solide et on ne prend pas la gravité en compte. L'état ambiant a un profil de vitesse du son augmentant linéairement en altitude, avec une pente de $0,1 \text{ s}^{-1}$, la pression et la masse volumique étant supposées constantes ($p_0 = 10^5 \text{ Pa}$, $\rho_0 = 1.19 \text{ kg/m}^3$). La source acoustique est une perturbation de pression sinusoïdale, de fréquence 10 Hz et d'amplitude 1000 Pa, imposée sur un disque de rayon 20 m centré à l'origine. On utilise un maillage cartésien uniforme de taille de maille $\delta x = 3 \text{ m}$, correspondant à peu près à 11 points par longueur d'onde. Les

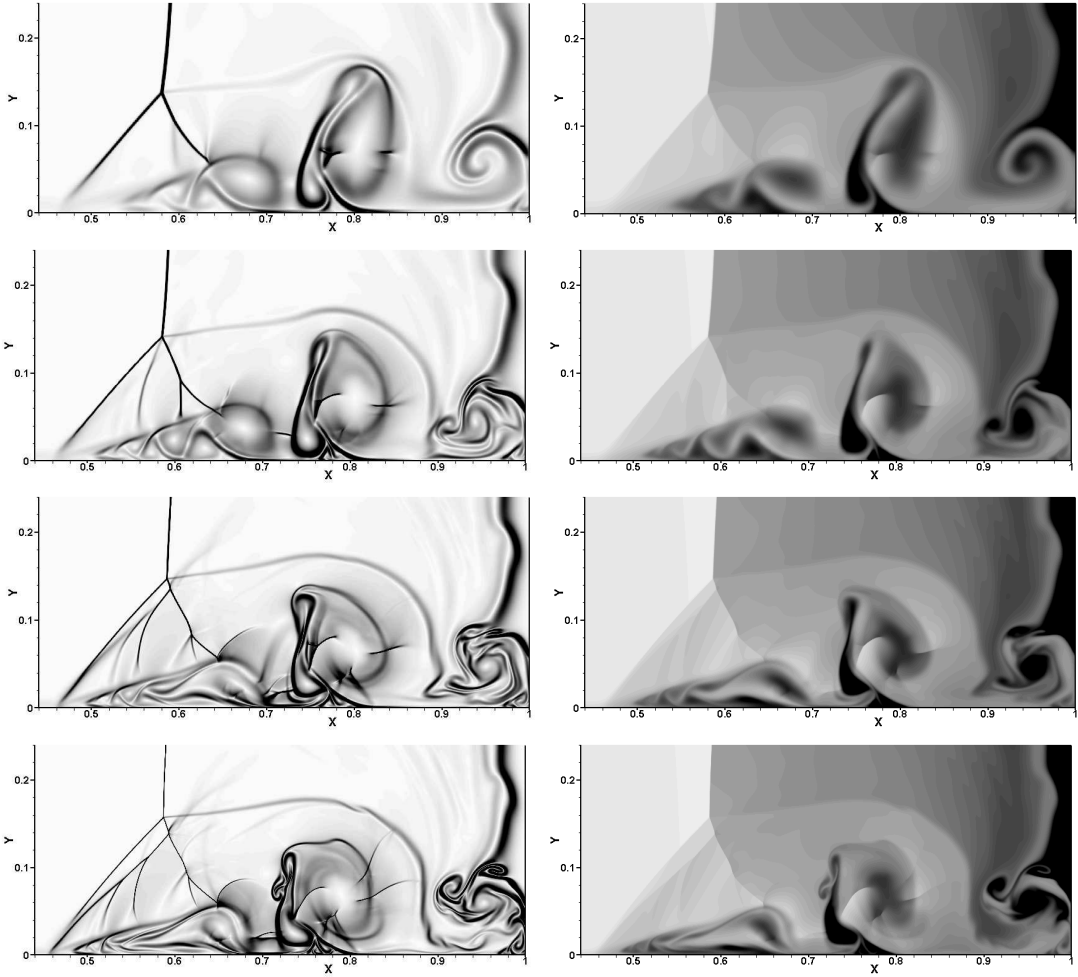


FIGURE 9 – Contours de $|\nabla \rho|$ (gauche) et T (droite, 41 niveaux entre 0.4 et 1.2) obtenus à $t = 1$ sur la grille la plus fine pour plusieurs nombres de Reynolds ; de haut en bas : $Re = 200$; $Re = 500$; $Re = 750$; $Re = 1000$.

résultats obtenus avec le schéma OSMP7 sont présentés sur la figure 11 au temps $t = 12$ s, montrant le champ de pression acoustique. La longueur d'onde augmentant avec l'altitude, du fait de l'augmentation de la vitesse du son, des interférences apparaissent près du sol à une certaine distance de la source (Fig. 11-a). Sur la figure 11-b est représenté le signal de pression le long du sol, obtenu avec le schéma OSMP7, et pour comparaison, sur la figure 11-c celui obtenu avec un schéma d'ordre 2 non limité (schéma de Mac Cormack). Le schéma d'ordre 2, même sans limiteur, est clairement beaucoup trop dissipatif et le signal a presque disparu après 2 km. Au contraire, le schéma OSMP7, bien qu'il soit équipé d'un limiteur, préserve très bien le signal, et se compare très bien avec la solution de référence.

Nous avons ensuite traité le cas dit de "Misty Picture". Cette expérience a été effectuée aux USA en mai 1987 [81]. C'est une explosion qui a fourni la puissance équivalente d'une bombe atomique de 8 kt. Des enregistrements microbarographiques ont été obtenus par le CEA en France, et par les Laboratoires Nationaux Sandia et Los Alamos aux USA. Le profil de température dans l'atmosphère est connu par sondages radio et fusées (Fig. 12-e). Dans une première approche, on ne prend pas en compte le vent et l'absorption acoustique. Le domaine simulé s'étend sur 180 km en altitude et 510 km le long du sol. La gravité est prise en compte, et les champs sont initialisés en utilisant le profil de température, la pression et la masse volumique étant obtenues à partir d'une équation de gaz parfait et de l'équilibre hydrostatique. Le profil de

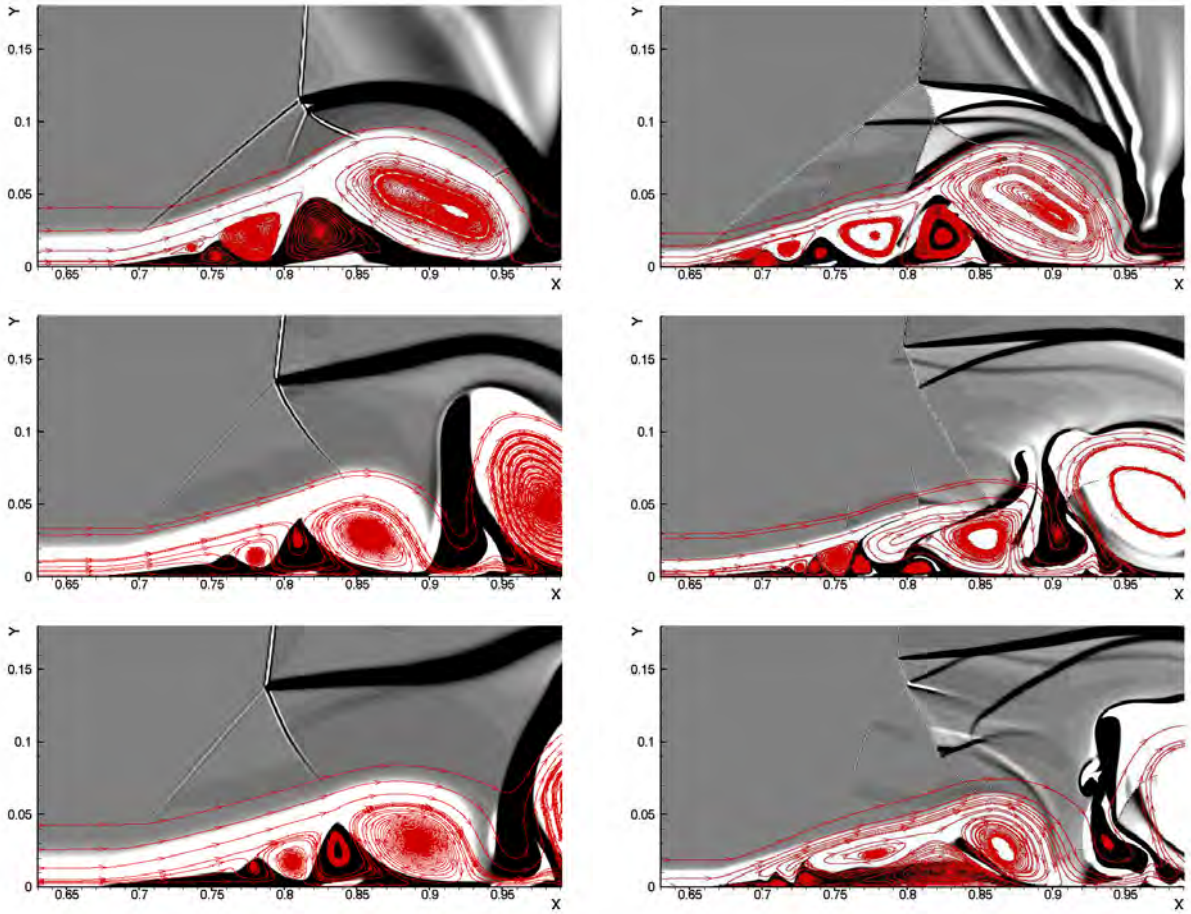


FIGURE 10 – Isocontours de la vorticité avec en surimpression les lignes de courant de l’écoulement dans le référentiel du choc réfléchi, pour, de haut en bas : $t = 0.6, 0.9$ et 1 . $Re = 200$ à gauche, $Re = 1000$ à droite.

masse volumique est représenté Fig. 12-f, montrant que de très faibles valeurs de 10^{-9} kg/m^3 sont atteintes en haute altitude (ce qui représente une difficulté numérique). L’explosion est simulée en ajoutant un terme source à l’équation d’énergie pendant un temps court.

Sur la figure 12 a-b-c-d sont montrés les isocontours de $|\nabla(p - p_0)|$ pour des temps successifs. La perturbation initiale est située à 60 km de la frontière gauche du domaine. Une onde de choc cylindrique se propage à partir de la source, suivie par une onde de détente (Fig. 12-a). Une réflexion parasite depuis la frontière gauche est visible sur la figure 12-b (ceci est dû au fait que les conditions de non réflexion ne sont pas bien adaptées pour les chocs). Ensuite on observe des réflexions multiples sur les différentes couches de l’atmosphère au cours de la propagation des ondes. Cela produit des phases différentes qui atteignent le sol à des temps différents, et qu’on identifie comme phases stratosphériques et thermosphériques. Plus tard on identifie des ondes de gravité internes qui sont produites dans le voisinage de l’explosion, et s’étendent jusqu’à environ 50 km d’altitude dans l’atmosphère. Les résultats se comparent bien, pour les temps d’arrivée des ondes acoustiques, avec les enregistrements expérimentaux, et des simulations précédentes basées sur une formulation perturbative et un schéma DRP de haute résolution [63]. Cependant dans les simulations [63] l’amplitude de la perturbation était plus faible que dans le cas de l’expérience, du fait du manque de robustesse des schémas DRP, et les ondes de gravité n’apparaissaient pas. L’utilisation du schéma OSMP7 s’est donc ici révélée adéquate, permettant à la fois de reproduire la propagation acoustique et les phénomènes de forte intensité.

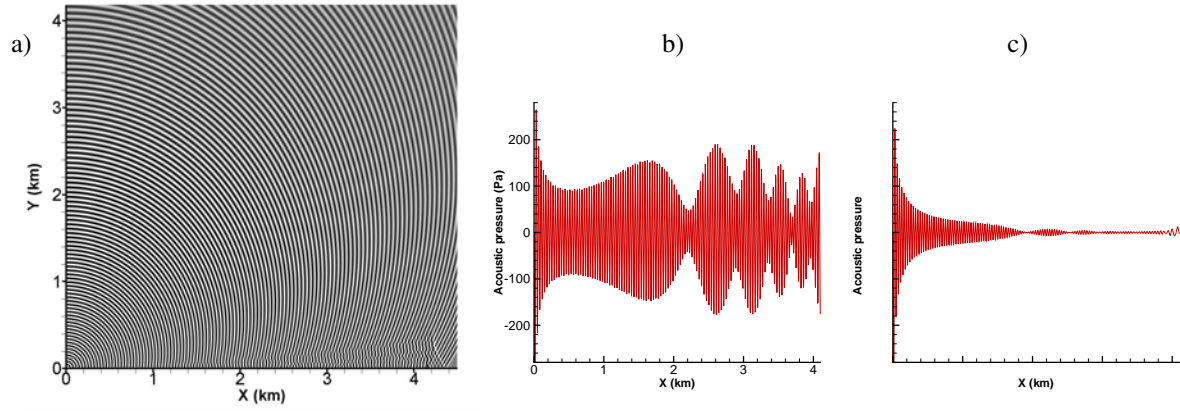


FIGURE 11 – Benchmark Attenborough : a) Contours de pression acoustique à $t = 12\text{ s}$, b) Signal de pression acoustique le long du sol, schéma OSMP7 , c) Signal de pression acoustique le long du sol, schéma d'ordre 2 non limité.

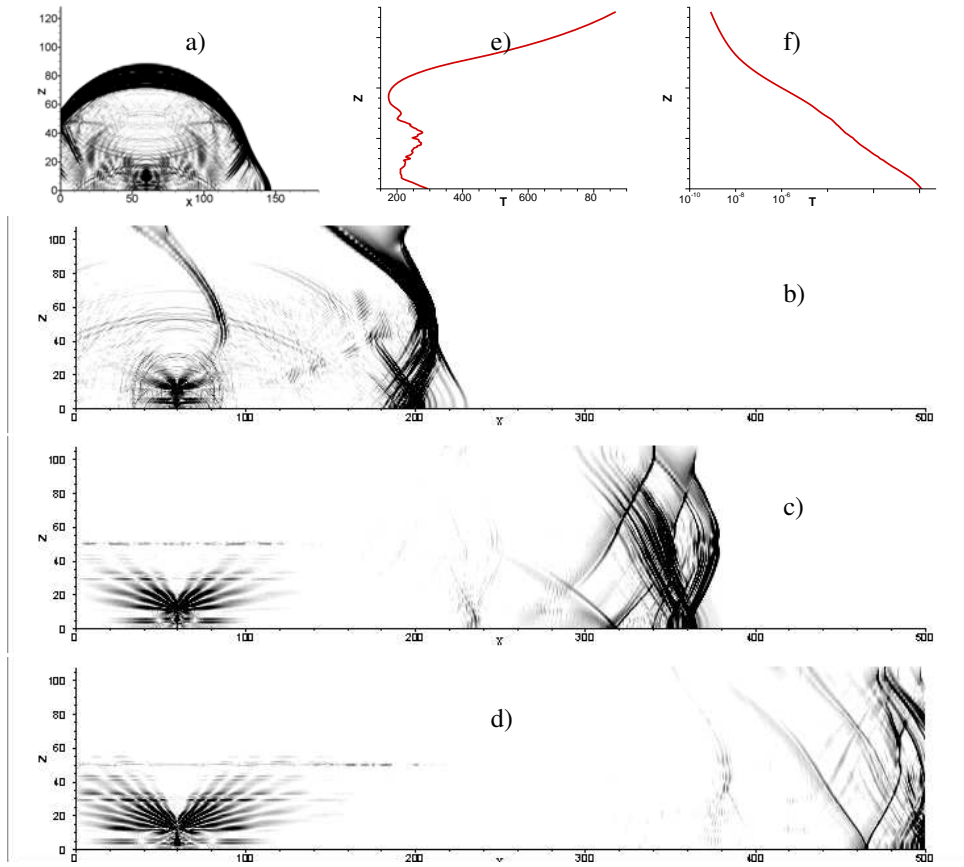


FIGURE 12 – Misty Picture : a), b), c), d) Isocontours du gradient de pression acoustique aux temps 250 s, 500 s, 1000 s, 1500 s. e) Profil de température dans l'atmosphère, f) Profil de masse volumique dans l'atmosphère.

Cette étude n'a pas été poursuivie par la suite dans notre équipe. Elle a donné lieu à des développements ultérieurs au LMFA à Lyon [58, 90].

Interaction fluide-structure (thèse de Laurent Monasse, soutenue en 2011, [65, 79]).

Toujours dans le cadre d'une collaboration avec le CEA, j'ai coencadré avec Serge Piperno (ENPC) la thèse de Laurent Monasse (financée par le CEA/DAM). Je présente ci-dessous quelques résultats de sa thèse.

L'objectif de cette thèse était d'étudier le couplage entre un fluide compressible et une structure déformable afin de simuler l'effet d'une onde de choc aérienne sur un bâtiment. Seul le cas bidimensionnel a été considéré. Une difficulté majeure du couplage tient au fait que le domaine de résolution du fluide varie en fonction du temps suivant le déplacement du solide avec, dans les cas qui nous intéressent, de grandes déformations de ce domaine et la possibilité de changements de topologie en raison de la rupture ou du contact. Trois principaux types d'approches sont envisageables pour traiter la déformation du domaine fluide : une approche multiphasique, une approche avec déformation de maillage ou une approche par domaine fictif. L'approche multiphasique (lagrangienne ou eulérienne) est limitée au cas où le solide et le fluide peuvent être décrits par les mêmes équations avec des paramètres physiques variables affectés à chaque phase et advectés au cours du mouvement de l'interface. Les approches avec déformation de maillage font apparaître des difficultés lorsque le déplacement de la structure est trop important : le domaine fluide doit alors être remaillé, ce qui peut entraîner des erreurs et des coûts de calculs accrus. C'est pour contourner la question du remaillage que les approches de domaine fictif ont été développées. Nous avons choisi cette dernière approche, dont le principe est de superposer un solide mobile sur un domaine fluide fixe, et d'imposer des conditions sur le domaine fluide fictif sous le solide afin d'assurer la non-pénétration du fluide à travers la frontière solide. Différentes méthodes ont été développées dans cette approche, dont les méthodes conservatives [68, 39], choisies ici, qui assurent une conservation exacte de la masse, de la quantité de mouvement et de l'énergie du système, propriété importante lorsqu'on considère un écoulement compressible comportant potentiellement des ondes de choc. Le principe de ces méthodes est le suivant : les flux numériques entre cellules fluides sont calculés sur toute la grille eulérienne fluide, sans prendre en compte la présence du solide, puis des corrections sont apportées à l'intégration des flux dans la formulation fluide afin d'assurer une conservation discrète exacte des quantités conservatives à la paroi solide. Cela amène une difficulté qui tient au fait que cette formulation fait intervenir des cellules coupées dont la surface est arbitrairement petite. Le pas de temps, proportionnel à la taille de la plus petite cellule du domaine pour des raisons de stabilité, risque alors de devenir infiniment petit. Une procédure supplémentaire doit donc être appliquée à ces petites cellules coupées pour que la simulation reste stable partout en utilisant un pas de temps basé sur la taille des cellules entières. Cette procédure consiste généralement à effectuer un mélange conservatif des petites cellules avec les cellules voisines [27, 39]. Par ailleurs, le schéma d'intégration en temps est un ingrédient important pour le couplage fluide-structure. Ici, une approche partitionnée globalement explicite a été choisie afin de limiter les coûts de calcul de l'algorithme de couplage. Les échanges fluide-structure étant entièrement localisés le long de l'interface, les propriétés de conservation et de consistance sont imposées à l'aide d'une résolution semi-implicite n'impliquant que les éléments fluide et solide à l'interface.

Un modèle de gaz parfait compressible non-visqueux, décrit par les équations d'Euler, est considéré pour le fluide. Les équations sont discrétisées en utilisant le schéma OSMP7. Pour la structure, on considère un solide indéformable ou déformable avec une loi de comportement élastique linéaire. Le solveur solide est basé sur une méthode d'Éléments Discrets, implémentée

dans un code appelé Mka3D au CEA [59]. Il peut prendre en compte l'élasticité aussi bien que la fracture et l'impact de solides.

Je renvoie le lecteur vers l'article [65], qui figure en annexe, pour la description précise de la méthode de couplage qui a été développée. Les résultats suivants ont été théoriquement prouvés sur cette méthode :

— *Conservation de la masse, de la quantité de mouvement et de l'énergie :*

S'il n'y a ni entrée ni sortie de fluide du domaine, la masse fluide est conservée. Pour des conditions aux limites périodiques, la quantité de mouvement est exactement répartie entre le fluide et le solide, et l'énergie reçue du solide est exactement compensée par le travail des forces de pression du fluide sur le solide.

— *Écoulement constant avec frontières mobiles :*

Pour le cas d'un solide rigide en mouvement de translation à vitesse constante immergé dans un fluide se déplaçant uniformément à la même vitesse, la vitesse uniforme du fluide et du solide est préservée par l'algorithme numérique de couplage.

— *Glissement libre le long d'une frontière rectiligne :*

Un écoulement uniforme parallèle à une paroi solide est préservé par l'algorithme de couplage. L'algorithme ne crée donc pas de couche limite artificielle au voisinage d'une paroi, même si elle n'est pas alignée avec le maillage.

L'article [65] présente plusieurs simulations numériques mettant en oeuvre la méthode développée, et leur comparaison avec les résultats d'autres auteurs. Plutôt que les résultats de [65], je vais plutôt ici présenter des résultats (non publiés) figurant dans la thèse de Laurent. Il s'agit de la comparaison que nous avons faite avec des expériences menées à l'IUSTI à Marseille dans l'équipe Écoulements Compressibles, Ondes de Choc et Interfaces, et publiées dans [8]. Le problème industriel à l'origine de l'expérience est le système de sécurité des moteurs d'avion. Dans un moteur à réaction, des ondes de choc peuvent apparaître qui menacent d'endommager le système mécanique et peuvent affecter les performances. Il est alors important de prévenir les augmentations de pression soudaines dans le compartiment du moteur. Pour cela, une valve de sécurité est utilisée pour permettre à l'air sous pression de s'écouler en partie hors du compartiment. Il s'agit donc de comprendre comment interagissent la valve et l'onde de choc incidente pour pouvoir prédire les éventuels dégâts causés à la structure de l'avion. Le dispositif expérimental est représenté figure 13. C'est un tube à choc de section carrée de 80 mm de côté, qui peut créer des chocs de nombre de Mach compris entre 1.1 et 5. Le tube est fermé d'un côté, et à l'autre extrémité se trouve une porte fixée par une charnière. La porte peut s'ouvrir librement en pivotant autour de l'axe horizontal de la charnière. L'ouverture de la porte est repérée par l'angle θ . La position initiale de la porte est en configuration fermée ($\theta = 0$), et elle est bloquée en rotation à $\theta = 90^\circ$. Quatre capteurs de pression (C_1 , C_7 , C_{10} et C_{12}) sont placés le long du tube, et trois à proximité de la porte (C_{bottom} , C_{top} et C_{side}), respectivement en bas, sur le côté et en haut du tube. Un capteur est positionné au centre de la porte (C_{door}).

Les simulations numériques sont faites en bidimensionnel. Le domaine à simuler est extrêmement long, avec des conditions aux limites d'écoulement libre dans une atmosphère ambiante. Afin de limiter le temps de calcul, le domaine de calcul est resserré autour du solide (figure 14). La grille de calcul fluide utilisée est assez grossière, de 528×24 cellules, soit une taille de cellule d'environ 8.33 mm.

Après la rupture contrôlée du diaphragme, une onde de choc (se dirigeant vers la porte) et une onde de détente sont engendrées. L'onde de détente se réfléchit contre le fond du tube, tandis que l'onde de choc se réfléchit contre la porte, sur laquelle elle exerce une poussée. L'ouverture de la porte permet à une partie de l'écoulement de se propager dans l'atmosphère environnante, tandis qu'une partie de l'onde incidente est réfléchie à l'intérieur du tube. Après une réflexion contre le fond du tube, l'onde de choc revient impacter la porte, qui s'est entre-

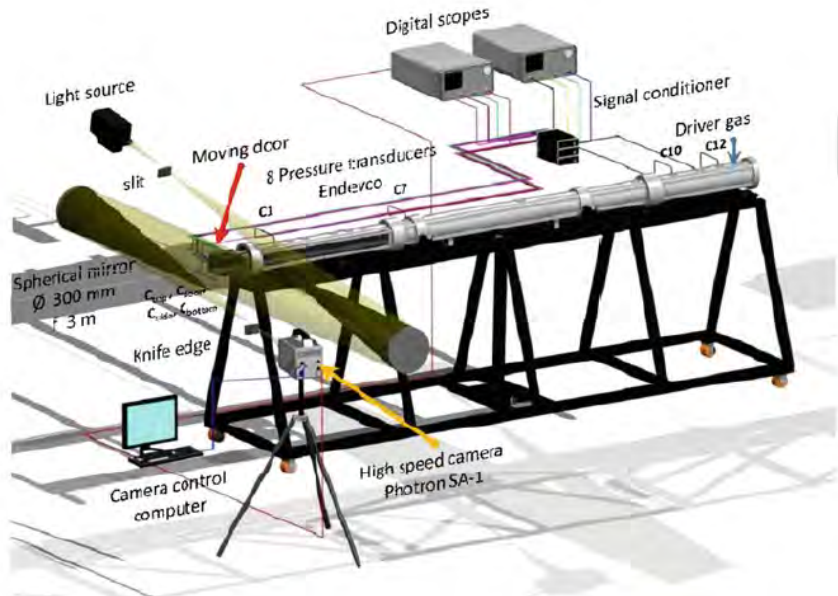


FIGURE 13 – Dispositif expérimental de l’IUSTI.

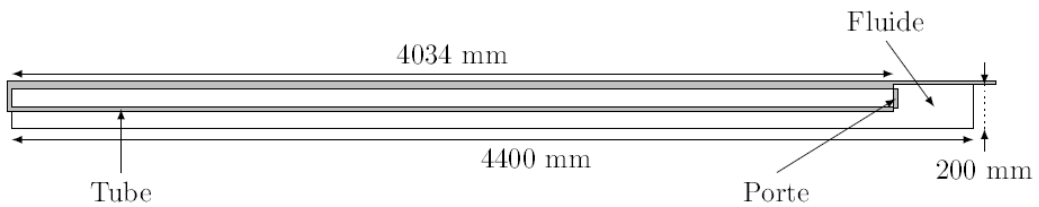


FIGURE 14 – Schéma du domaine de calcul numérique.

temps ouverte partiellement. L’onde de choc peut alors s’écouler hors du tube, avec de nouveau une réflexion partielle plus faible à l’intérieur du tube. Finalement, la porte, sous l’effet de son inertie, s’ouvre en totalité. Des isocontours de pression obtenus par la simulation numérique à des temps successifs sont présentés sur la figure 15. Les photographies de stroboscopie expérimentales correspondantes sont reprises de [8] sur la figure 16. Les résultats numériques obtenus se comparent bien qualitativement aux résultats expérimentaux.

Sur la figure 17 sont comparées les pressions expérimentales et numériques obtenues aux capteurs C_0 , C_7 , C_1 et C_{door} , pour un nombre de Mach du choc M égal à 1.1 et une porte en aluminium. Les temps d’arrivée et les amplitudes des ondes sont très proches dans les deux cas, montrant que la simulation numérique est en très bonne adéquation avec les expériences. L’angle d’ouverture de la porte en fonction du temps pour les cas $M = 1.1$ et $M = 1.25$ est représenté sur la figure 18. Les courbes d’évolution sont similaires à l’expérience, avec une première phase d’accélération de la porte sous l’effet des forces de pression, puis une deuxième phase où la porte s’ouvre à vitesse constante, sous l’effet de l’inertie. Les temps d’ouverture simulés pour les cas $M = 1.1$ et $M = 1.25$ sont respectivement de 37.6 ms et 14.4 ms, ce qui est remarquablement proche des temps mesurés expérimentalement de 37.5 ms et 13.8 ms. La dynamique de la porte est ainsi très bien reproduite numériquement en dépit des simplifications physiques effectuées et du maillage relativement grossier utilisé.

D’autres comparaisons avec ces expériences ont été faites pour une porte en acier, qui a une

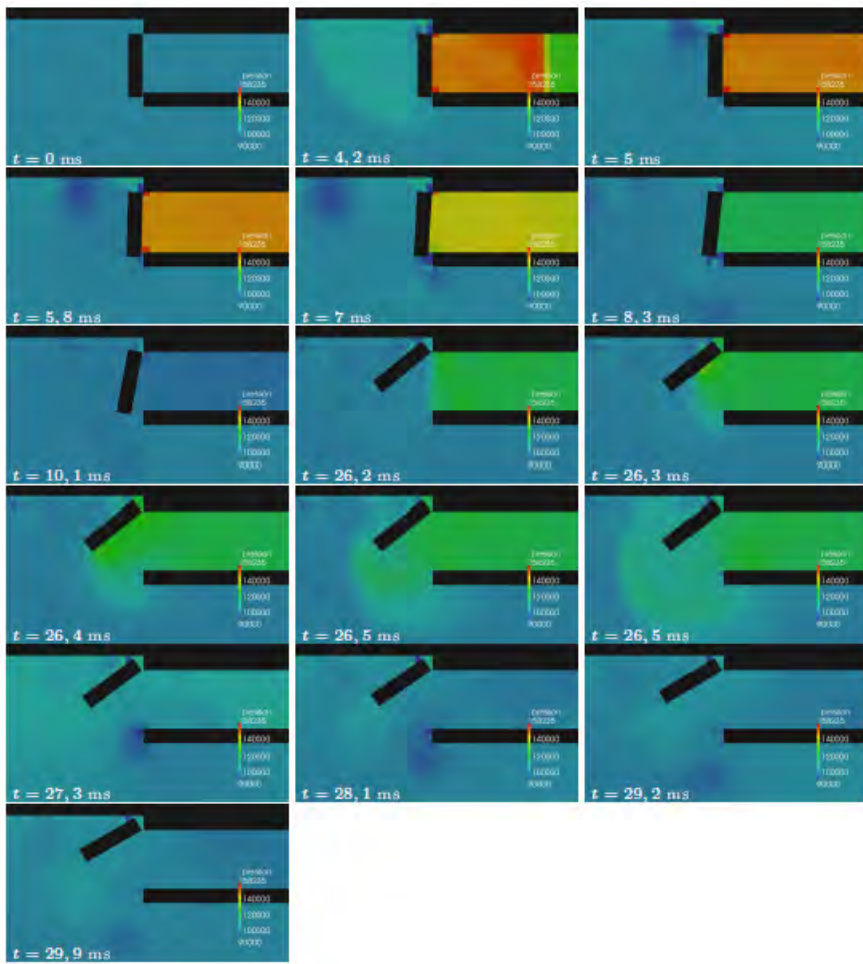


FIGURE 15 – Isocontours de pression simulés autour de la porte à des instants successifs.



FIGURE 16 – Photographies de stroboscopie expérimentale à des instants successifs (reprises de [8]).

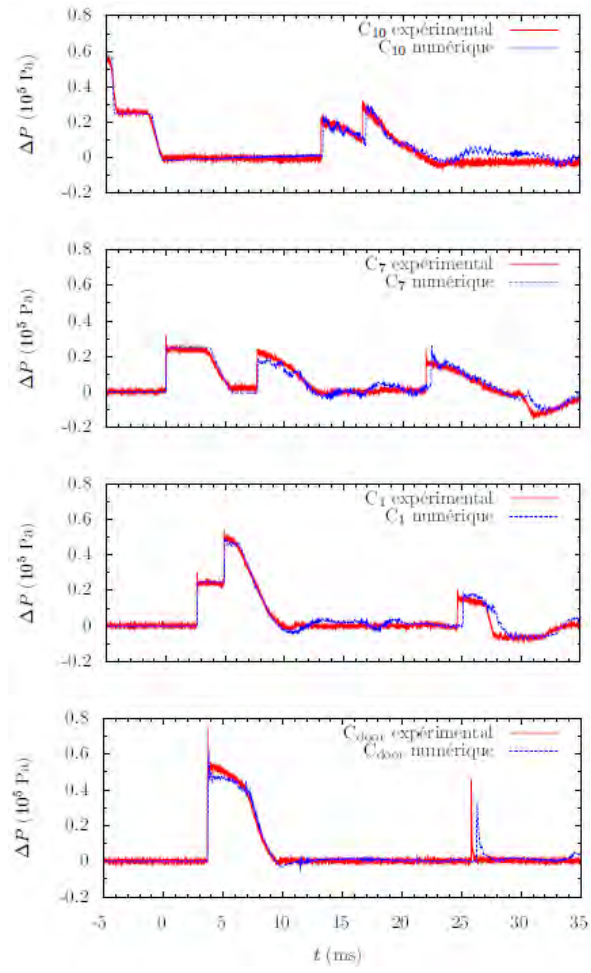


FIGURE 17 – Comparaison des pressions expérimentales et numériques aux capteurs C_{10} , C_7 , C_1 et C_{door} pour l’interaction entre un choc à $M = 1.1$ et une porte en aluminium.

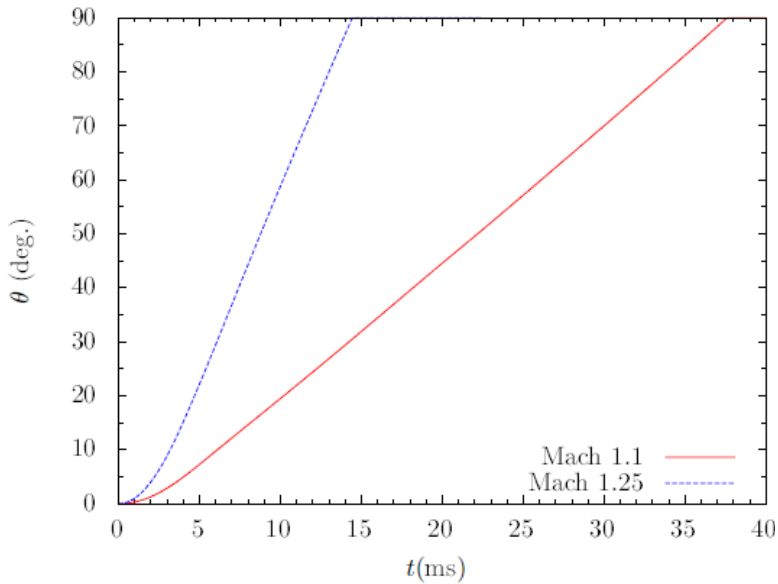


FIGURE 18 – Angle d’ouverture de la porte en fonction du temps pour deux valeurs de M .

plus grande inertie que la porte en aluminium, afin d'évaluer l'influence de la masse de la porte sur les temps d'ouverture. Là encore, les résultats ont été très concluants.

Finalement, les comparaisons quantitatives avec les données expérimentales donnent confiance en la validité de la méthode numérique. En particulier, l'obtention d'un temps d'ouverture de la porte en bonne adéquation avec les résultats expérimentaux est un signe de la bonne conservation de l'énergie par la méthode de couplage et de relations de transmission correctes entre les deux milieux.

Ce travail a été poursuivi par la thèse d'Adela Puscas (toujours financée par le CEA), qui a étendu au cas tridimensionnel la méthode développée par Laurent. Je n'ai pas co-encadré cette thèse mais j'ai participé à son suivi. Elle a donné lieu à la publication [79].

3 Écoulements diphasiques.

Mes travaux dans ce domaine concernent essentiellement les écoulements diphasiques à phases séparées (liquide-gaz). J'ai également eu une activité sur les écoulements diphasiques à phase dispersée, par des méthodes de suivi lagrangien de particules, en co-encadrant la thèse CIFRE de Sydney Tekam, puis celle de Thomas Juès, sur la simulation numérique d'écoulements gazeux chargés de particules d'huile dans un circuit de décantation de moteur, en collaboration avec Renault [101].

J'ai commencé mes travaux sur ce thème à la fin des années 90, avec la thèse de Patrick Kuszla à l'ENSAM, que j'ai co-encadrée. L'application visée concernait les jets d'eau à haute pression et grande vitesse. A mon arrivée au LIMSI en 2001, j'ai ensuite commencé à collaborer avec Marie-Christine Duluc, Damir Juric, Patrick Le Quéré et Olivier Le Maitre sur la simulation numérique des écoulements diphasiques liquide-gaz, pour des écoulements à faible vitesse (incompressibles ou dilatables). Avec Damir Juric, nous nous sommes intéressés à un problème purement numérique, celui des "courants parasites" observés dans le voisinage des interfaces. Avec Marie-Christine Duluc, Patrick Le Quéré et Olivier Le Maitre, nous avons travaillé sur le problème de la prise en compte de la compressibilité du gaz dans une approche dite "faible Mach".

Enfin j'ai collaboré dans les années 2000 avec Anne Mongruel et François Feuillebois (laboratoire PMMH de l'ESPCI), et Sonia Tabakova (Académie des Sciences Bulgare) sur le problème de l'impact de goutte sur une paroi solide et sèche.

Dans tous ces travaux, le modèle retenu pour traiter des écoulements comportant des interfaces séparant des fluides non miscibles est un modèle Eulérien basé sur une formulation dite "single-field". Ces modèles ont prouvé leur efficacité dans les configurations où l'interface est très fortement déformée [43, 10]. Pour décrire l'interface, il existe plusieurs types de méthodes, parmi lesquelles les plus classiquement utilisées sont les méthodes VOF [38], les méthodes dites de "front-tracking" [104] et les méthodes "Level Set" [93]. Une autre méthode plus immédiate consiste à simplement représenter l'interface comme une discontinuité, et utiliser une méthode numérique non oscillante (de type "capture de choc") pour la propager dans l'écoulement (comme on le fait pour simuler des écoulements avec chocs) [91]. Chaque méthode a ses avantages et ses inconvénients, et le choix d'une méthode dépend aussi bien des particularités de l'écoulement que des habitudes et de l'environnement de chacun.

Ayant de mon côté une longue histoire avec les méthodes de capture de choc, et Damir Juric ayant apporté ses compétences sur la méthode de front-tracking en arrivant au LIMSI au milieu des années 2000, ce sont ces deux méthodes que j'ai utilisées dans mes travaux.

3.1 Jet d'eau à haute pression.

La thèse de Patrick Kuszla portait sur le développement d'une méthode numérique destinée à simuler numériquement des jets d'eau à haute pression. Ces types de jets, qui permettent par exemple de décapier ou découper des matériaux, trouvent des applications dans bien des domaines de l'industrie. Ils fonctionnent à très haute pression, entre 500 et 1000 bars, voire plus. Les jets d'eau industriels produisent facilement des vitesses de jet de 500 m/s et plus, correspondant à un nombre de Mach dans l'eau de l'ordre de 0.3 ou plus. Si de plus on veut modéliser l'impact du jet sur une surface, il faut se placer en régime compressible. Nous avons donc considéré un modèle diphasique eau-air non visqueux, dans lequel les deux phases sont (fortement) compressibles. La loi d'état utilisée pour l'eau était une loi de type "gaz raide" (stiffened gas), l'air étant considéré comme un gaz parfait. Le suivi d'interface était assuré par une méthode de capture de choc (schéma de type TVD). Des simulations d'impact de goutte ou

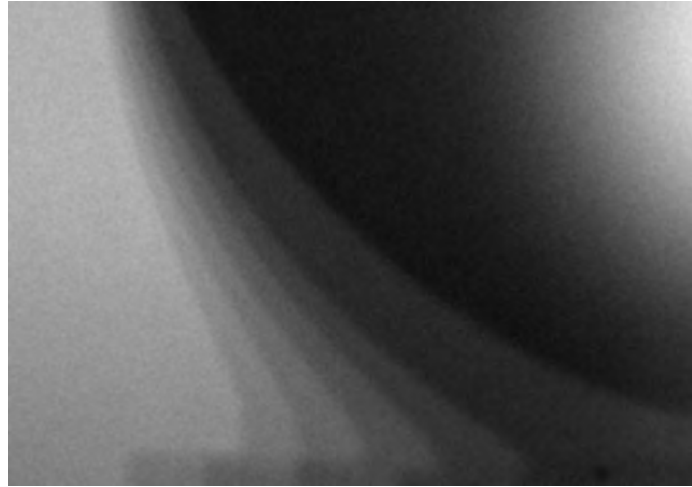


FIGURE 19 – Photos superposées des premiers instants de l’impact d’une goutte sur une paroi. Zoom sur la ligne triple et le jet pariétal.

de jets d’eau à haute vitesse ont été effectuées, et présentées dans plusieurs conférences [46, 47]. L’article [47] figure à la fin du mémoire.

3.2 Impact de gouttes.

On s’intéresse ici à la dynamique de l’impact de gouttes sur une paroi solide et sèche aux temps courts, et particulièrement à l’influence des effets visqueux qui jouent un grand rôle dans cette dynamique. L’impact de gouttes sur une paroi se retrouve dans un grand nombre de domaines d’application : givrage des avions par des gouttes sous-refroidies, imprimantes à jet d’encre, diffusion des pesticides, refroidissement par spray, injection de carburant, etc. D’un point de vue fondamental, la compréhension de l’étalement aux temps courts est importante pour l’étude des instabilités hydrodynamiques de la lamelle menant au “splashing” (éclatement).

On considère des gouttes composées d’un liquide de viscosité cinématique ν , de diamètre D de l’ordre de 3 mm, tombant verticalement dans l’air avant d’impacter une paroi à une vitesse U de l’ordre de 1 m/s. La durée totale du processus est de quelques millisecondes. On se place dans le régime dit de dépôt, pour lequel il n’y a pas d’éclatement (“splashing”). Dans les conditions d’impact considérées, on a $O(10) \leq Re \leq O(10^4)$ et $O(10^2) \leq We \leq O(10^3)$, où $Re = UD/\nu$ est le nombre de Reynolds et $We = \rho U^2 D / \sigma$ le nombre de Weber (ρ étant la masse volumique du liquide et σ la tension de surface entre le liquide et l’air). Dans ce régime, les premiers instants de l’impact (à partir de 10^{-5} s) se traduisent par l’apparition d’une fine lamelle de liquide à la base de la goutte, se propageant radialement le long de la paroi à une vitesse plus grande que la vitesse d’impact (figure 19). Ces premiers instants avaient été très peu étudiés au moment de cette étude, du fait des très petites échelles spatiales et temporelles impliquées (10^{-5} s et 10^{-5} m) [113]. L’évolution de la surface de contact aux premiers instants était souvent décrite comme de nature “cinématique” [86], à partir de considérations géométriques simples, et donc indépendante du nombre de Reynolds. Ici nous nous sommes spécifiquement intéressés aux effets visqueux.

Le problème a été traité expérimentalement et numériquement. Les expériences ont été menées par Anne Mongruel au PMMH, et j’ai effectué les simulations numériques. L’étude était donc focalisée sur la naissance et le développement de cette lamelle dans les premiers instants après l’impact ($t \ll \tau$, où $\tau = D/U$ représente le temps nécessaire à une goutte de diamètre D pour traverser un plan fixe à la vitesse U), notamment sur l’évolution temporelle de son

épaisseur, de son rayon et de sa vitesse, en fonction de la vitesse d'impact et de la viscosité cinématique du liquide. Une caméra rapide restituant 20,000 images/s était utilisée dans les expériences, et le liquide était composé d'eau et de différents mélanges d'eau et de glycérine, permettant de faire varier la viscosité de $\nu = 10^{-6}$ à $92 \times 10^{-6} \text{ m}^2/\text{s}$. Pour la simulation numérique, bien que l'écoulement soit essentiellement incompressible (les effets de compressibilité sont limités à un temps très court après l'impact), j'ai choisi une approche compressible (très similaire aux méthodes de compressibilité artificielle développées par Chorin [13]) permettant d'éviter d'avoir à résoudre un problème de Poisson. J'ai donc adapté un code compressible isentropique à ce cas (en géométrie axisymétrique), avec un suivi d'interface liquide-air assuré par une méthode de capture de choc (qui évite le problème classique de l'incompatibilité du déplacement de l'interface à la paroi avec la condition de non glissement). Un splitting des opérateurs de convection et de diffusion visqueuse était implémenté afin de minimiser l'étalement de l'interface dû à la dissipation numérique du schéma. La tension de surface n'était pas prise en compte du fait que, dans le régime considéré, la dynamique de la ligne de contact est essentiellement gouvernée par l'écoulement qui l'entoure [97].

Une comparaison entre les résultats expérimentaux et numériques, pour trois cas avec $82 \leq Re \leq 8391$, est montrée figure 20. On constate une bonne adéquation entre les résultats expérimentaux et numériques. Malgré les effets de diffusion numérique, l'interface numérique est localisée avec une précision comparable à l'expérimentation. L'extrémité de l'interface est plus arrondie dans le cas expérimental, du fait des effets de tension de surface qui sont forts à cet endroit où le rayon de courbure local est très petit. L'épaisseur et la vitesse de la lamelle liquide dépendent très clairement de Re .

Les vitesses instantanées au voisinage de la lamelle sont représentées sur la figure 21 peu de temps après l'impact, pour deux valeurs de Re . Le champ dans le liquide est analogue à celui observé lors de la vidange d'un récipient à travers un trou dans la paroi. Quand Re augmente, le champ de vitesse change peu, excepté près de la paroi où les effets visqueux diffusent le profil de vitesse dans le liquide. Ceci a pour conséquence d'accroître l'épaisseur du jet pariétal et, par conservation de la masse, de diminuer sa vitesse.

Pour comprendre le mécanisme de formation de la lamelle, il est intéressant de regarder les trajectoires des particules fluides situées sur la frontière de la goutte. Ces trajectoires sont représentées figure 22 (gauche) pour deux valeurs du nombre de Reynolds. Pour la plus grande valeur, $Re = 1500$, les particules fluides situées près du point d'impact sont les plus rapides et acquièrent une vitesse radiale qui leur permet de "s'échapper" de la zone couverte par le diamètre de la goutte avant que celle-ci soit recouverte. Au contraire, dans le cas $Re = 30$ la vitesse acquise par les particules situées près du point d'impact est insuffisante et elles sont ensuite recouvertes par le fluide initialement situé plus loin de la paroi. La déformation résultante de l'interface est représentée sur la figure 22 (droite). Dans le cas $Re = 1500$, une lamelle est formée, tandis que dans le cas $Re = 30$ la déformation de l'interface se traduit simplement par une sphère tronquée légèrement déformée.

Une analyse d'échelle simple, basée sur les échelles hydrodynamiques et négligeant les effets de tension de surface, a été menée pour prédire l'évolution temporelle de plusieurs points caractéristiques sur l'interface, notamment le point A caractérisant la position radiale extrême de la lamelle et le point K de courbure maximum au raccord entre la goutte et la lamelle. Deux régimes successifs sont identifiés, le régime visqueux et le régime inertiel. On montre que la transition entre les deux régimes se produit à un temps caractéristique τ/Re . Ce temps est très petit (de l'ordre de 10^{-6}s), mais donne un ordre de grandeur pour le temps d'apparition de la lamelle. De plus, la lamelle est éjectée en héritant des propriétés acquises dans le régime visqueux, gouvernées par le nombre de Reynolds, et ceci fournit les échelles initiales de temps τ/Re , et de longueur D/\sqrt{Re} . La figure 23 montre la position radiale adimensionnée du

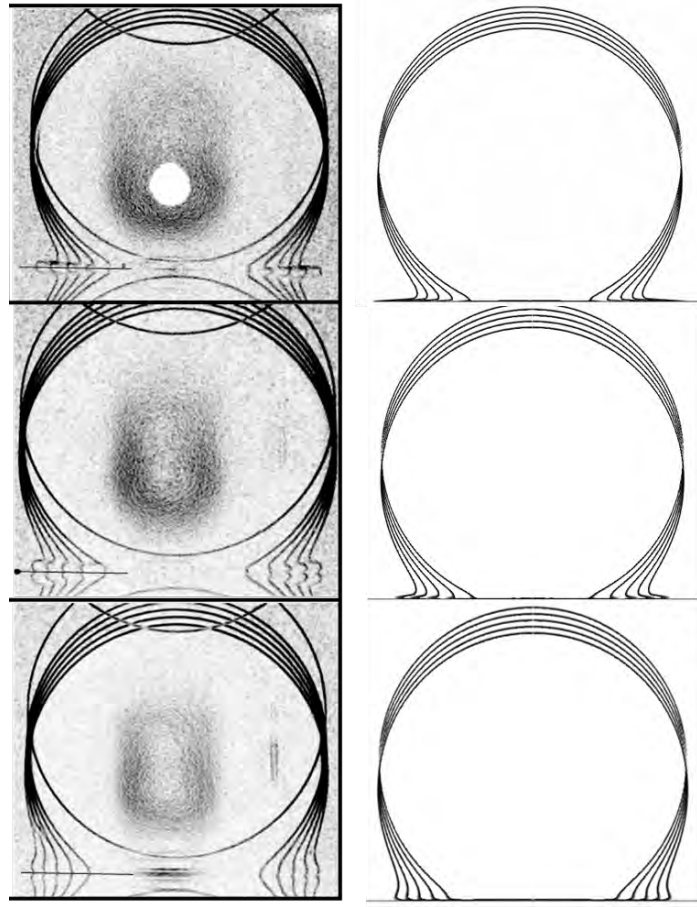


FIGURE 20 – Images superposées des premiers instants de l’impact d’une goutte sur une paroi. A gauche : expériences (contours de l’interface extraits) , à droite : simulations numériques (isocontours du gradient de masse volumique). Intervalle entre les images 50 microsecondes, première image à 78 μ s. En haut : eau ($\nu = 10^{-6}$ m 2 /s, $D = 4.85$ mm, $U = 1.73$ m/s, $Re = 8391$, $We = 194$). Au milieu : mélange eau-glycérine ($\nu = 10.5 \times 10^{-6}$ m 2 /s, $D = 4.44$ mm, $U = 1.76$ m/s, $Re = 744$, $We = 244$). En bas : mélange eau-glycérine ($\nu = 92.8 \times 10^{-6}$ m 2 /s, $D = 4.25$ mm, $U = 1.78$ m/s, $Re = 82$, $We = 262$).

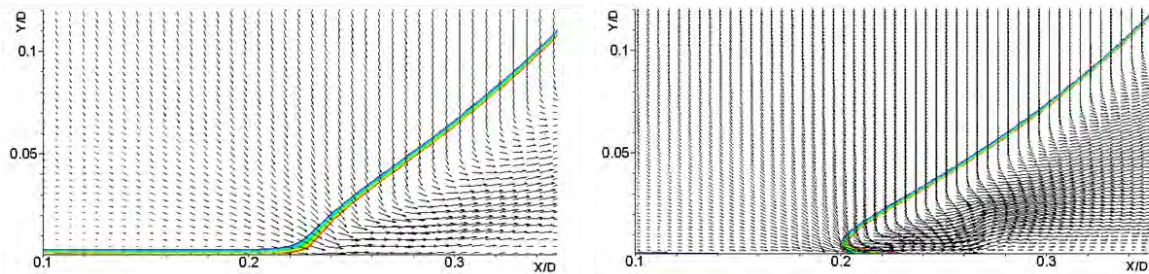


FIGURE 21 – Champ de vitesse superposé au contour de l’interface à 80 ms après l’impact (zoom autour de la ligne triple). À gauche : mélange eau-glycérine ($\nu = 92.8 \times 10^{-6}$ m 2 /s, $D = 4.25$ mm, $U = 1.78$ m/s, $Re = 82$, $We = 262$). À droite : eau ($\nu = 10^{-6}$ m 2 /s, $D = 4.85$ mm, $U = 1.73$ m/s, $Re = 8391$, $We = 194$).

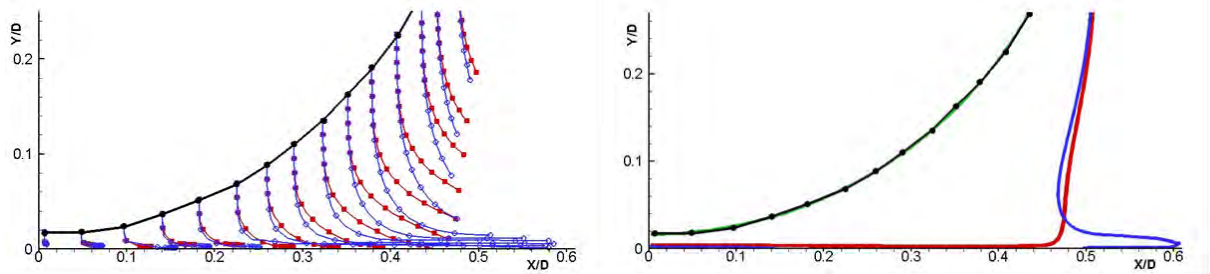


FIGURE 22 – À gauche : trajectoires des particules fluides initialement situées sur la frontière non déformée de la goutte pour $Re = 1500$ (cercles bleus) et $Re = 30$ (carrés rouges). Temps d'intégration $120 \mu\text{s}$, les différentes positions sont montrées toutes les $10 \mu\text{s}$. À droite : Déformation résultante de l'interface après $120 \mu\text{s}$: $Re = 1500$ (bleu), $Re = 30$ (rouge).

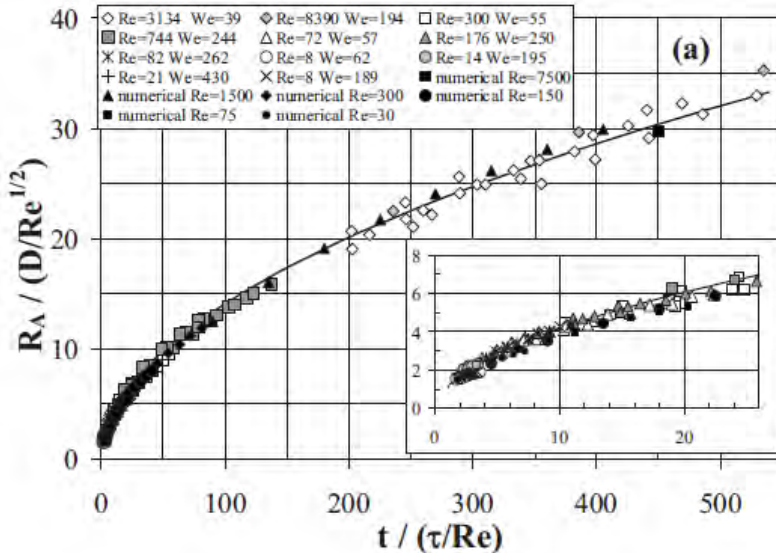


FIGURE 23 – Evolution de la position radiale de l'extrémité de la lamelle (point A). Expériences : symboles vides et gris ; simulations numériques : symboles noirs pleins.

point A, $r_A/(D/\sqrt{Re})$, en fonction du temps sans dimension $t/(\tau/Re)$, obtenue pour les différentes expériences et simulations numériques. Tous les résultats suivent une même courbe, avec une précision meilleure que la précision expérimentale, ce qui valide notre nouvelle analyse d'échelle dépendant du nombre de Reynolds, et montre aussi la bonne qualité des simulations numériques.

Ce travail a été publié dans [67].

3.3 Tension de surface.

Avec Damir Juric au LIMSI (et en collaboration également avec Seungwon Shin de Georgia Tech, Atlanta), nous nous sommes intéressés au milieu des années 2000 à un problème purement numérique, celui des "courants parasites", souvent observés dans les approches eulériennes sur grille fixe au voisinage des interfaces. Ces courants parasites peuvent apparaître lorsque la tension de surface est forte ou la viscosité du fluide faible, le paramètre caractéristique étant le nombre de Laplace $La = \sigma\rho L/\mu^2$ (L étant une longueur de référence, μ la viscosité dynamique du fluide et σ la tension de surface). Pour de grandes valeurs de La , ils peuvent contaminer la so-

lution et créer des oscillations numériques conduisant à la destruction de l'interface. Il ne s'agit donc pas seulement d'imprécision numérique mais aussi d'une limitation réelle des méthodes de suivi d'interface. Un cas simple très représentatif de ce problème est celui d'une goutte (ou une bulle) au repos, pour laquelle la loi de Laplace $\Delta p = \sigma\kappa$ doit être vérifiée, Δp étant la différence de pression entre l'intérieur et l'extérieur de la goutte, et κ la courbure locale de l'interface (constante dans le cas d'une goutte sphérique). Beaucoup d'approches numériques ne respectent pas correctement cette loi au niveau discret, ce qui constitue l'origine de ces courants parasites indésirables (voir une illustration figure 24).

Pour réduire ces courants parasites à des niveaux acceptables (il est difficile de les supprimer complètement), deux ingrédients de la méthode numérique sont fondamentaux : un calcul précis de la courbure locale de l'interface, et le respect au niveau discret de la loi de Laplace. On se place ici dans le cadre d'un modèle à un fluide pour décrire un écoulement diphasique, c'est à dire que l'interface est représentée par une fonction de Heaviside $H(x, y, z, t)$ qui permet de représenter les paramètres physiques du fluide composite, par exemple la masse volumique $\rho = \rho_l + H(\rho_g - \rho_l)$ (où ρ_l est la masse volumique du liquide et ρ_g celle du gaz), etc. L'équation de quantité de mouvement gouvernant l'écoulement s'écrit (on néglige ici la gravité) :

$$\rho \left(\frac{\partial \mathbf{v}}{\partial t} + \mathbf{v} \cdot \nabla \mathbf{v} \right) = -\nabla p + \nabla \cdot \boldsymbol{\tau} + \mathbf{F}$$

avec \mathbf{v} la vitesse, p la pression, $\boldsymbol{\tau}$ le tenseur des contraintes visqueuses, et \mathbf{F} la force due à la tension de surface. Ce terme s'écrit $\mathbf{F} = \sigma\kappa\mathbf{n}\delta$, où \mathbf{n} est la normale unitaire à l'interface, et δ est une fonction de Dirac localisée sur l'interface. Pour une goutte (ou une bulle) en équilibre, κ est constant, la vitesse est nulle et l'équation de quantité de mouvement devient

$$\nabla p = \mathbf{F} = \sigma\kappa\mathbf{n}\delta, \quad (23)$$

où σ est supposé constant. Une première nécessité pour reproduire correctement (23) au niveau discret est de calculer le rayon de courbure avec précision. Par ailleurs, il faut calculer le terme $\mathbf{n}\delta$. Supposons que \mathbf{F} puisse se décomposer en une partie rotationnelle et une partie irrotationnelle, soit :

$$\mathbf{F} = \mathbf{F}_{rot} + \nabla\phi.$$

À l'équilibre, pour une goutte statique, on doit avoir $\nabla p = \mathbf{F}$, et donc $0 = \nabla \times \nabla p = \nabla \times \mathbf{F}_{rot}$. Si \mathbf{F} comporte une partie rotationnelle, on voit donc qu'elle sera à l'origine d'un écoulement, qui produit les courants parasites. Il faut donc que \mathbf{F} soit irrotationnelle, et pour cela qu'elle dérive d'un potentiel. Cela avait déjà été remarqué dans [82] dans le cadre d'une méthode VOF. Beaucoup de méthodes précédemment développées ne respectaient pas cette contrainte. En remarquant que $\mathbf{n}\delta = \nabla H$, une méthode respectant (23) au niveau discret peut être obtenue, *sous réserve que la discréétisation numérique du gradient de pression et celle de ∇H soient les mêmes*. En effet, si dans l'équation $\nabla p = \sigma\kappa\nabla H$ les gradients de p et H ne sont pas discrétisés de la même manière, l'équilibre discret est à nouveau rompu. Cette contrainte correspond à ce que Stéphane Popinet appelle une méthode "well-balanced" dans sa récente revue des modèles numériques de tension de surface [78].

Nous avons travaillé sur ce problème, pour des écoulements incompressibles, dans le cadre d'une méthode de "front-tracking" pour le suivi de l'interface [105, 104]. Dans cette méthode, l'interface est représentée et advectée de façon lagrangienne, tandis que l'écoulement est calculé sur une grille eulérienne. À chaque pas de temps, des informations doivent être échangées entre la grille lagrangienne mobile et la grille eulérienne fixe, ce qui est effectué en utilisant la méthode de frontières immergées de Peskin [73]. Dans la nouvelle méthode de représentation de la tension de surface que nous avons développée, le calcul de la courbure de l'interface est

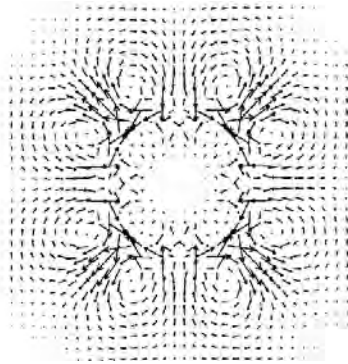


FIGURE 24 – Courants parasites observés autour d'une bulle stationnaire. Figure reproduite de [77]

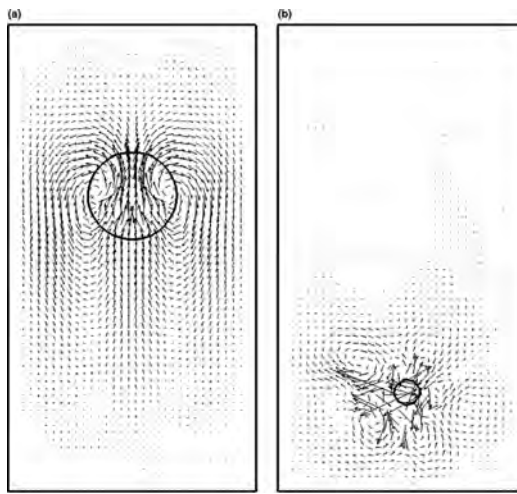


FIGURE 25 – Champ de vitesse pour le cas de l'ascension d'une bulle d'air dans de l'eau en 2D. a) nouvelle formulation de la tension de surface [94]; b) ancienne formulation.

effectué d'abord sur la grille lagrangienne, puis projeté sur la grille eulérienne de manière à respecter la propriété "well-balanced". Les résultats obtenus, publiés dans [94], montrent une spectaculaire diminution des courants parasites avec la nouvelle méthode. À titre d'illustration, la figure 25 montre la comparaison entre l'ancienne et la nouvelle méthode pour la simulation numérique du problème de l'ascension d'une bulle d'air dans de l'eau (à pression standard). Le rapport de masses volumiques et le nombre de Laplace sont ici élevés, ce qui en fait un test très difficile. Les courants parasites ne sont pas visibles avec la nouvelle méthode (à gauche). Au contraire, ils sont si importants en utilisant l'ancienne méthode (à droite) qu'ils mènent à la destruction de l'interface et à une perte de masse inacceptable.

Ce thème des modèles numériques de tension de surface continue à faire l'objet de recherches, malgré les améliorations très importantes obtenues dans les 20 dernières années [78]. On peut considérer que l'équilibre numérique entre le gradient de pression et les forces capillaires est maintenant acquis dans toutes les méthodes de suivi d'interface. Cependant, l'effet combiné de la tension de surface et de l'advection de l'interface peut réintroduire des courants parasites, comme récemment étudié dans [1]. De plus, les formulations dites volumiques (quasi universellement utilisées) du type de celle que nous avons étudiée, basées sur une approximation numérique de la fonction de Dirac caractérisant l'interface, ne permettent pas la conservation stricte de la quantité de mouvement, du fait que le terme de tension de surface n'est pas exprimé

de façon conservative. Une voie de recherche intéressante, très récemment explorée [2] dans le cadre d'une méthode level-set, est d'utiliser plutôt une formulation dite intégrale de la tension de surface, sans passer par un opérateur approché de projection de l'interface sur la grille eulérienne. Dans cette formulation, si l'on considère un volume élémentaire Ω dont la frontière extérieure est intersectée par une courbe en deux points A et B , on utilise la propriété :

$$\int_{\Omega} \mathbf{F} d\Omega = \oint_A^B \sigma dt = \sigma_B \mathbf{t}_B - \sigma_A \mathbf{t}_A$$

Le calcul de la force capillaire sur Ω ne nécessite donc que le calcul des vecteurs tangents à la courbe en A et en B \mathbf{t}_A et \mathbf{t}_B . Cette formulation est très naturelle et assure la conservation exacte de la quantité de mouvement. En conséquence, elle assure intrinsèquement la propriété que la force résultante exercée sur le fluide par une interface fermée est nulle. Elle inclut aussi naturellement les contraintes tangentielles dues à une tension de surface variable (effet Marangoni). C'est une voie que j'avais un peu explorée au milieu des années 2000, dans le cadre de méthodes de suivi d'interface de type capture de choc, avec de premiers résultats intéressants. Ce sujet faisait l'objet de la thèse de Adelina Stoilova, doctorante bulgare financée par l'Université Technique de Sofia en Bulgarie, dirigée par Sonia Tabakova avec laquelle je collabore depuis 1998. J'ai participé à l'encadrement de Adelina, et elle est venue passer deux séjours de plusieurs mois à Paris en 2005 et 2006. Malheureusement elle a interrompu sa thèse avant la fin, et ce travail n'a pas été poursuivi. Je continue à penser cependant que c'est une voie extrêmement prometteuse.

3.4 Écoulements liquide-gaz dans l'approche faible Mach.

La motivation à l'origine de ce travail était la simulation numérique de l'ébullition d'un liquide en environnement confiné. Lorsque l'environnement est ouvert, il est légitime d'envisager un modèle d'écoulement incompressible [44]. En environnement confiné, la pression thermodynamique dans la phase gazeuse doit être prise en compte, pour reproduire la courbe de saturation à l'équilibre liquide-vapeur. Par exemple, pour un cuiseur vapeur, c'est le fait que la pression moyenne dans le cuiseur devient supérieure à la pression atmosphérique qui permet au changement de phase liquide-vapeur de se produire à des températures bien supérieures à 100°C, augmentant le rendement de Carnot et réduisant le temps de cuisson. Pour modéliser ce type de situation, il faut donc prendre en compte les effets de compressibilité dans la vapeur. On se trouve donc ici confronté au problème de réunir dans une méthode numérique unique deux modèles d'écoulements différents, un modèle incompressible dans le liquide, et un modèle compressible dans la vapeur. La difficulté tient au fait que ces deux modèles d'écoulement sont de nature mathématique différente. En effet, la pression et la masse volumique sont fortement couplées en compressible, et complètement découplées en incompressible. En compressible l'équation de continuité est une équation de transport pour la masse volumique, alors qu'en incompressible elle devient une contrainte sur la divergence du champ de vitesse. La pression change fondamentalement de nature, de pression thermodynamique en compressible elle devient multiplicateur de Lagrange en incompressible (pression "hydrodynamique"). De plus, les méthodes numériques explicites basées sur le modèle compressible deviennent totalement inefficaces à la limite $M \rightarrow 0$ (M étant le nombre de Mach), du fait de la contrainte de stabilité numérique qui impose au pas de temps discret d'être proportionnel à M . En effet, dans le cas incompressible la condition de stabilité s'écrit $\delta t \leq \frac{\delta x}{|\mathbf{v}|}$ (où δx est la taille de la plus petite cellule et \mathbf{v} est la vitesse maximum du fluide). En compressible la condition de stabilité s'écrit $\delta t \leq \frac{\delta x}{|\mathbf{v}|+c}$ (où c est la vitesse du son), soit $\delta t \lesssim M \cdot \frac{\delta x}{|\mathbf{v}|}$ si $|\mathbf{v}| \ll c$. C'est ce qui explique que depuis les débuts de la simulation numérique en mécanique des fluides, les méthodes numériques

pour le compressible et l'incompressible ont suivi des voies de développement différentes. La recherche d'une méthode numérique générale capable de traiter simultanément ces deux types d'écoulement a néanmoins débuté très tôt [32], et se poursuit encore aujourd'hui [26]. Ces méthodes sont généralement dénommées "all speed" ou "all Mach".

Ce type de méthode peut être envisagé pour traiter notre problème. Cependant, l'écoulement produit dans la vapeur est a priori un écoulement où la vitesse des particules de vapeur est très faible devant la vitesse du son dans la vapeur, soit $M \ll 1$. Cela induit que les effets de compressibilité sont essentiellement des effets de compression (ou détente) en volume, pour lesquels on peut considérer que la pression thermodynamique est uniforme en espace, et ne dépend que du temps. En effet, on ne s'intéresse pas ici au détail de la propagation des ondes acoustiques dans le gaz, seul nous intéressons leur effet cumulé (c'est à dire intégré sur un temps caractéristique "significatif") sur la pression thermodynamique et le champ de vitesse dans la vapeur. On s'est donc plutôt intéressé dans ce travail aux méthodes dites "faible Mach" pour représenter la phase gazeuse. Ces méthodes ont été spécifiquement développées pour ce type d'écoulement [29, 72, 50], et il a été montré sur des cas de convection naturelle qu'elles sont beaucoup plus efficaces que les méthodes basées sur un modèle complètement compressible [51, 74]. Notre approche consiste donc à raccorder un modèle purement incompressible dans la phase liquide, avec un modèle compressible faible Mach dans la phase gazeuse.

Le modèle incompressible s'écrit :

$$\left\{ \begin{array}{l} \nabla \cdot \mathbf{v} = 0 \\ \rho_l \left(\frac{\partial \mathbf{v}}{\partial t} + \mathbf{v} \cdot \nabla \mathbf{v} \right) = -\nabla p_l + \nabla \cdot \boldsymbol{\tau} + \rho \mathbf{g} \\ \frac{\partial T}{\partial t} + \mathbf{v} \cdot \nabla T = \frac{1}{\rho_l c_p} \nabla \cdot (k \nabla T) \end{array} \right. \quad (24)$$

où ρ_l est la masse volumique (constante) du liquide, p_l la pression hydrodynamique et T la température. Dans ce modèle, les problèmes dynamique et thermique sont découplés si la viscosité du fluide ne dépend pas de la température.

Pour un écoulement de gaz parfait, un modèle faible Mach est construit à partir des équations de Navier-Stokes compressibles, en effectuant un développement asymptotique en puissances de M de chaque variable, puis en prenant la limite du système pour $M \rightarrow 0$. Pour chaque variable, le terme d'ordre le plus faible reste dans les équations, excepté pour la pression p qui se décompose de la manière suivante : $p(\mathbf{x}, t) \simeq P(t) + p_2(\mathbf{x}, t)$, avec $p_2(\mathbf{x}, t) \propto M^2 P(t)$ et donc $p_2 \ll P$. Ici P est la pression thermodynamique, uniforme en espace, associée pour un gaz parfait à la loi d'état $P = r\rho T$ (r étant la constante des gaz parfaits), et p_2 est la pression hydrodynamique associée au respect de l'équation de continuité. Le modèle s'écrit :

$$\left\{ \begin{array}{l} \nabla \cdot \mathbf{v} = \frac{1}{T} \frac{DT}{Dt} - \frac{1}{P} \frac{dP}{dt} \\ \rho \left(\frac{\partial \mathbf{v}}{\partial t} + \mathbf{v} \cdot \nabla \mathbf{v} \right) = -\nabla p_2 + \nabla \cdot \boldsymbol{\tau} + \rho \mathbf{g} \\ \frac{\partial T}{\partial t} + \mathbf{v} \cdot \nabla T = \frac{1}{\rho c_p} \nabla \cdot (k \nabla T) + \frac{\gamma - 1}{\gamma} \frac{T}{P} \frac{dP}{dt} \\ P = \rho r T \end{array} \right. \quad (25)$$

Les équations sont donc couplées à travers la pression thermodynamique, sauf pour l'équation de quantité de mouvement qui reste inchangée par rapport au modèle incompressible. Pour modéliser notre problème diphasique liquide (écoulement incompressible) - vapeur (écoulement compressible faible Mach), nous introduisons une fonction indicatrice de phase $H(\mathbf{x}, t)$, telle que $H = 1$ dans le gaz et $H = 0$ dans le liquide. Dans ce travail, le changement de phase

n'est pas pris en compte, et donc la dynamique de l'interface peut être décrite par une simple équation d'advection :

$$\frac{\partial H}{\partial t} + \mathbf{v} \cdot \nabla H = 0 \quad (26)$$

Le modèle composite MC est obtenu en écrivant $MC = H \times FM + (1 - H) \times MI$, en désignant par FM le modèle faible Mach (25) et par MI le modèle incompressible (24).

Considérons le cas d'un domaine fermé, dans lequel un liquide enferme plusieurs inclusions gazeuses (bulles). Chaque bulle, numérotée j , est repérée par sa propre fonction indicatrice $H_j(\mathbf{x}, t)$, et possède sa propre pression thermodynamique P_j uniforme dans la bulle. Les fonctions indicatrices obéissent chacune à l'équation d'advection $\frac{\partial H_j}{\partial t} + \mathbf{v} \cdot \nabla H_j = 0$. Traiter ce problème implique de raccorder les deux modèles, incompressible et faible Mach, sur les interfaces. Pour cela, il faut s'intéresser à la pression. Si les bulles sont à des pressions thermodynamiques différentes, cela va induire un gradient de pression et donc une accélération dans le liquide. Il manque donc un terme de l'ordre de la pression thermodynamique dans l'équation de quantité de mouvement du modèle composite. Pour réintégrer ce terme, remarquons que $\nabla p_2 = \nabla(p_2 + P_j)$ dans chaque bulle. Les relations de saut à travers l'interface impliquent alors que $p_2 + P_j = p_l$, où p_l est la pression dans le liquide. La décomposition de la pression dans le gaz suggère une décomposition similaire dans le liquide, soit $p_l = P_l + \pi_l$, P_l étant du même ordre de grandeur que P_j , et π_l que p_2 , et on impose $P_j = P_l$ et $p_2 = \pi_l$ sur chaque interface. Dans le liquide, la pression P_l n'est pas uniforme puisqu'elle doit raccorder les pressions P_j dans les différentes bulles, mais elle doit être harmonique pour satisfaire la condition d'incompressibilité, soit $\nabla^2 P_l = 0$.

Finalement on a construit deux champs de pression définis dans tout le domaine, dont la somme donne les relations de saut correctes aux interfaces. Si l'on note P_e (pression thermodynamique étendue) le champ égal à P_j dans les bulles et égal à P_l dans le liquide, on peut construire l'équation vérifiée par P_e dans tout le domaine (pour N inclusions gazeuses) :

$$\frac{1}{\eta^2} P_e(\mathbf{x}, t) \cdot H(\mathbf{x}, t) + (1 - H(\mathbf{x}, t)) \cdot \nabla^2 P_e(\mathbf{x}, t) = \sum_{j=1}^N H_j(\mathbf{x}, t) \cdot \frac{1}{\eta^2} P_j(t) \quad (27)$$

La quantité η , homogène à une longueur, assure la consistance dimensionnelle de l'équation (27). Elle est liée à la représentation numérique étalée sur quelques mailles de l'interface, et doit être de l'ordre de cette épaisseur comme cela est démontré dans [21]. On note aussi π la pression hydrodynamique étendue, égale à p_2 dans le gaz et à π_l dans le liquide.

Le modèle composite s'écrit finalement :

$$\left\{ \begin{array}{l} \nabla \cdot \mathbf{v} = H(\mathbf{x}, t) \frac{1}{T} \frac{DT}{Dt} - \sum_{j=1}^N H_j(\mathbf{x}, t) \frac{1}{P_j} \frac{dP_j}{dt} \\ \frac{D\mathbf{v}}{Dt} = -\frac{1}{\rho} \nabla \pi - \frac{1}{\rho} \nabla P_e + \frac{1}{\rho} \nabla \cdot \boldsymbol{\tau} + \mathbf{g} \\ \frac{DT}{Dt} = \frac{1}{\rho c_p} \nabla \cdot (k \nabla T) + \frac{\gamma - 1}{\gamma} T \sum_{j=1}^N H_j(\mathbf{x}, t) \frac{1}{P_j} \frac{dP_j}{dt} \\ \rho(\mathbf{x}, t) = \sum_{j=1}^N H_j(\mathbf{x}, t) \frac{P_j(t)}{rT(\mathbf{x}, t)} + (1 - H(\mathbf{x}, t)) \rho_l \end{array} \right. \quad \begin{array}{l} (a) \\ (b) \\ (c) \\ (d) \end{array} \quad (28)$$

complété de l'équation (27) pour le calcul de P_e . Les pressions P_j sont calculées en intégrant l'équation de continuité sur un contour entourant chaque bulle.

Dans la méthode numérique telle qu'elle a été implementée dans [21], une méthode de front-tracking [105, 104, 44] était utilisée pour le suivi de l'interface. Une première comparaison avec

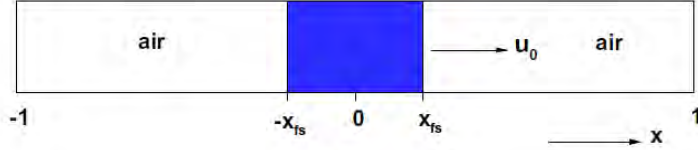


FIGURE 26 – Conditions initiales pour le cas test de la colonne d'eau oscillante.

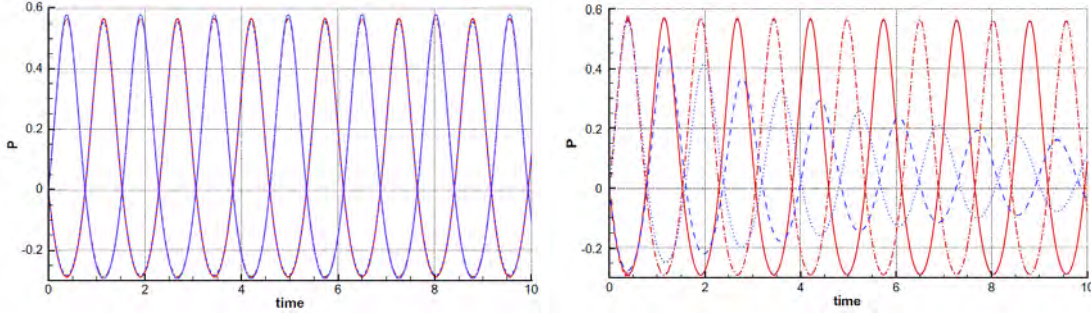


FIGURE 27 – Evolution temporelle des coefficients de pression dans les zones gazeuses de gauche et de droite (lignes rouges continue et pointillée frontières gauche et droite $CFL = 1$, lignes bleues tireté et pointillé frontières gauche et droite $CFL = 100$). À gauche, méthode faible Mach, à droite méthode à une seule pression ("all Mach").

un modèle de type "all Mach" a été effectuée sur un cas test 1D consistant en l'oscillation d'une colonne d'eau incluse entre deux zones gazeuses (figure 26). Les fluides sont considérés non visqueux. Une vitesse initiale étant imposée à tout le fluide, la zone gazeuse de droite est d'abord compressée, puis le système se met à osciller sans amortissement. La zone liquide se comporte comme un corps solide ici, sa vitesse étant uniforme du fait de l'incompressibilité du liquide. L'évolution temporelle des coefficients de pression, définis par $C_P(t) = (p(x_p, t) - p_0)/p_0$ où p_0 est la pression initiale et x_p la position sur les parois, est représentée sur la figure 27, pour l'algorithme faible Mach à deux pressions développé ici (à gauche), et un algorithme "all Mach" faisant intervenir une pression unique (à droite). Deux valeurs du pas de temps sont utilisées ici, la première ($CFL = 1$) correspondant à une condition de stabilité basée sur la vitesse acoustique, la seconde ($CFL = 100$, donc un pas de temps 100 fois plus grand) correspondant à une condition de stabilité basée sur la vitesse du fluide, naturelle ici. On constate que pour $CFL = 1$, les solutions données par les deux méthodes concordent. Dans le cas $CFL = 100$ en revanche, la solution "all Mach" est très fortement dégradée, alors que la solution donnée par la méthode faible Mach est quasiment identique à celle obtenue pour $CFL = 1$. De plus la masse totale d'air décroît pour le cas "all Mach", ce qui signifie que l'air est converti en eau [21]. Cela indique donc que pour la méthode "all Mach", le pas de temps utilisé dans la simulation numérique doit rester de l'ordre du pas de temps acoustique pour des raisons de précision. Si l'on rappelle que le rapport entre les pas de temps acoustique et convectif est égal au nombre de Mach M , on voit que la méthode faible Mach sera d'autant plus efficace par rapport à la méthode "all Mach" que le nombre de Mach est petit.

Pour illustrer le bon comportement de la méthode dans le cas multidimensionnel, nous avons traité le cas 2D suivant : dans un liquide initialement au repos, à la pression atmosphérique à l'intérieur d'une enceinte fermée, on place 6 bulles d'air de même surface, dont 3 sont initialement en surpression. La viscosité et la tension de surface sont prises en compte. Le système commence alors à osciller, avec dans le liquide des vitesses observées de l'ordre de 1 m/s aux

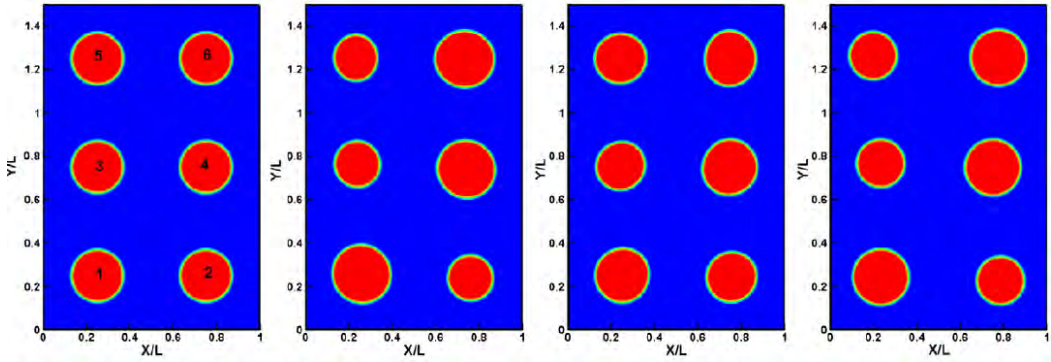


FIGURE 28 – Evolution de H à $t = 0, 3, 6\mu\text{s}$ et t_{mech} . Les bulles 1, 4, 6 sont initialement en surpression (1.4 atm).

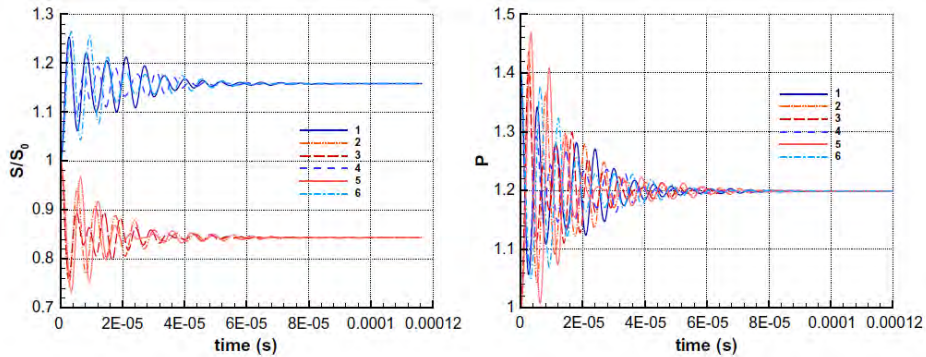


FIGURE 29 – Evolution temporelle de la surface relative (gauche) et de la pression thermodynamique ($\text{Pa}/10^5$) des bulles.

premiers instants, avant de se stabiliser mécaniquement à $t_{\text{mech}} \approx 100\mu\text{s}$ (figure 28). Les bulles n'ont alors plus la même surface, la surface des bulles initialement en surpression ayant augmenté, tandis celle des autres est réduite. L'évolution temporelle de la surface des bulles ainsi que de leur pression thermodynamique est représentée figure 29. Elle montre le mécanisme oscillatoire couplé de la surface et de la pression thermodynamique des bulles. Lorsque l'écoulement est stabilisé, la pression thermodynamique devient uniforme.

Sur la figure 30 sont représentées les deux pressions étendues du modèle, pression thermodynamique à gauche et pression hydrodynamique à droite, au début de l'évolution instationnaire. Comme attendu, les deux pressions (en $\text{Pa}/10^5$) sont d'un ordre de grandeur très différent : 1 pour la pression thermodynamique, et 10^{-2} pour la pression hydrodynamique (d'ordre de grandeur $\rho_l|\mathbf{v}|^2$). On observe une discontinuité de la pression hydrodynamique aux interfaces, due à la tension de surface (loi de Laplace). La pression thermodynamique est bien uniforme dans les bulles, et continue aux interfaces, avec une variation régulière dans le liquide.

Par la suite je n'ai pas poursuivi mes travaux sur les écoulements diphasiques, et j'ai plutôt, à partir de 2009, commencé à m'intéresser au streaming acoustique rencontré dans les machines thermoacoustiques.

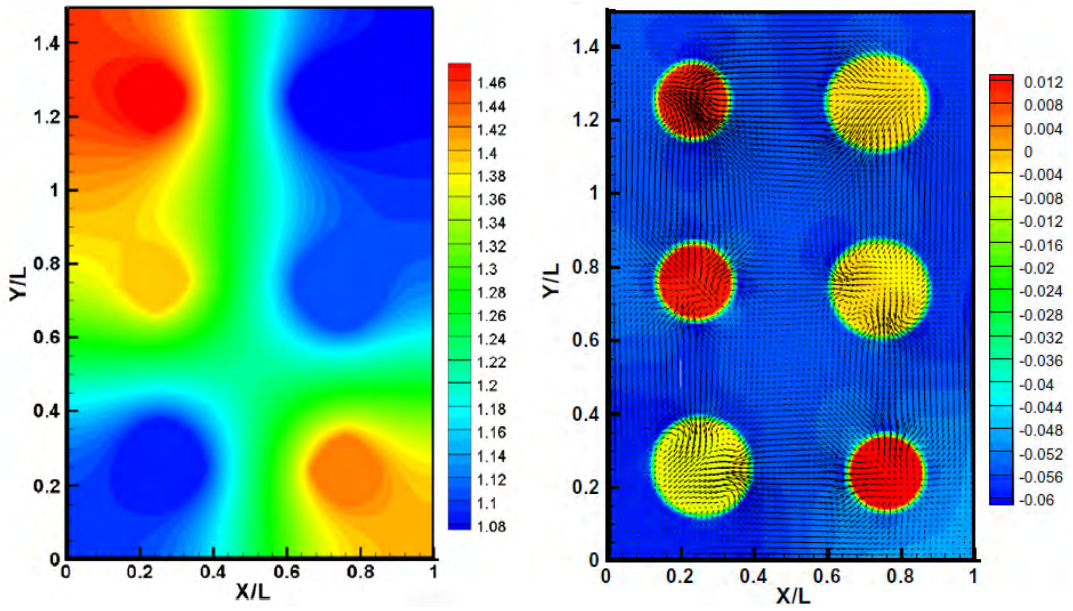


FIGURE 30 – Pressions au temps $t = 3\mu\text{s}$. À gauche : pression thermodynamique étendue ($\text{Pa}/10^5$), à droite : pression hydrodynamique étendue ($\text{Pa}/10^5$) et champ de vitesse.

4 Streaming acoustique.

Le streaming acoustique, ou "vent acoustique", est un écoulement secondaire moyen qui apparaît soit lorsqu'un écoulement oscillant (par exemple une onde acoustique) interagit avec une paroi (streaming de Rayleigh), soit en raison de l'absorption dans l'écoulement principal d'un faisceau sonore irrotationnel (streaming d'Eckart). En lien avec les études expérimentales et numériques menées au LIMSI depuis de nombreuses années sur les machines thermoacoustiques, j'ai commencé à m'intéresser au streaming de Rayleigh, en collaboration avec Diana Baltean-Carlès et Catherine Weisman. Le streaming acoustique est identifié comme l'une des sources principales de pertes thermiques dans les machines thermoacoustiques [4], et il est nécessaire d'en avoir une connaissance précise pour en contrôler les causes et les effets et optimiser le fonctionnement des machines. Une machine thermoacoustique est constituée d'un résonateur, renfermant un stack (plaques parallèles ou milieu poreux) et des échangeurs, à l'intérieur duquel on installe une onde acoustique stationnaire ou progressive. L'interaction de l'onde avec les parois (du stack mais aussi du résonateur) produit l'effet thermoacoustique, correspondant à un flux de transport de la température moyenne dans le sens inverse de la loi de Fourier (du froid vers le chaud). L'effet thermoacoustique est produit près des parois dans une zone de quelques épaisseurs δ_ν , avec $\delta_\nu = \sqrt{\frac{2\mu}{\rho_0\omega}}$ l'épaisseur de couche limite, où ω est la pulsation de l'onde. Cet effet thermoacoustique est illustré sur la figure 31, qui montre le flux de chaleur thermoacoustique dans une section radiale d'un résonateur, ainsi que le champ de température moyenne associé. On voit que le fluide est refroidi dans la partie centrale, et chauffé près des bords latéraux.

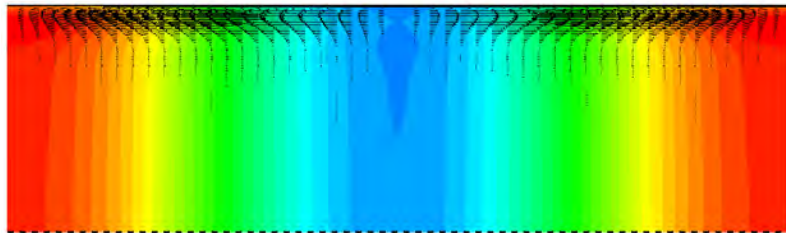


FIGURE 31 – Flux de chaleur thermoacoustique superposé au champ de température moyenne, entre l'axe du résonateur (en bas) et la paroi (en haut). Code de couleur : rouge=chaud, bleu=froid.

Dans le résonateur un écoulement moyen est produit, le streaming (ici de Rayleigh), qui se superpose à l'écoulement acoustique. Il s'agit d'un écoulement stationnaire, du second ordre en nombre de Mach. Pour une onde stationnaire, et si le résonateur est assez large, cet écoulement de streaming est séparé en deux zones, une zone dite "intérieure" en proche paroi (streaming intérieur ou de couche limite), et une zone dite "extérieure" dans la partie centrale du résonateur (streaming extérieur). La taille de la zone intérieure est d'environ trois épaisseurs de couche limite. Dans chacune des zones, le streaming est caractérisé (dans le cas plan) par quatre tourbillons contrarotatifs stables dans une demi-longueur d'onde de l'onde stationnaire (tourbillons "extérieurs" dans la zone extérieure, et "intérieurs" dans la zone proche paroi). Si la largeur du guide est petite (inférieure à quelques épaisseurs de couche limite), les tourbillons extérieurs peuvent ne pas exister. Lorsqu'ils existent, l'écoulement de streaming est orienté depuis les nœuds vers les ventres de vitesse acoustique le long de l'axe central du guide. Un exemple est représenté figure 32, qui montre la vitesse acoustique sur l'axe d'un résonateur de longueur $L = \lambda/2$ (où λ est la longueur d'onde) et de largeur $2R \gg \delta_\nu$ à plusieurs instants dans une

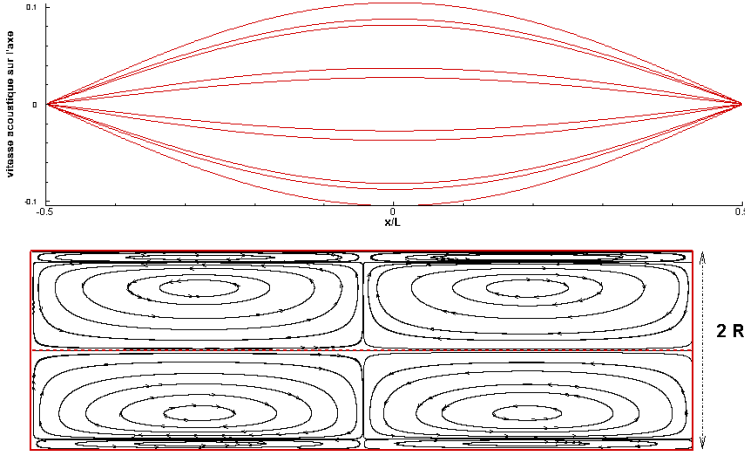


FIGURE 32 – En haut : vitesse acoustique sur l’axe du résonateur. En bas : lignes de courant de l’écoulement de streaming acoustique.

période, et les lignes de courant du champ de vitesse du streaming associé.

Dans le cas d’une onde acoustique de faible amplitude, cet écoulement est bien analysé et connu. Il a fait l’objet de nombreux travaux théoriques dont Rayleigh a été le précurseur [80], suivi notamment par [69] et [112] (approche RNW - Rayleigh, Nyborg, Westervelt) qui ont donné une solution analytique complète au problème proposé par Rayleigh. Dans ce problème, une hypothèse fondamentale est que $R \ll L$ (résonateur très allongé), et donc que l’onde acoustique est plane. On suppose aussi que les tourbillons extérieurs existent, ce qui implique que la largeur du guide doit être grande devant δ_ν , $\hat{R} = R/\delta_\nu \gg 1$. Ce problème est donc relatif au streaming à l’intérieur du résonateur d’une machine thermoacoustique, et non à celui qui existe à l’intérieur du stack. Enfin l’onde acoustique est supposée de faible amplitude et monochromatique. Le champ acoustique peut ainsi être calculé en résolvant les équations de l’acoustique linéaire, obtenues à partir d’un développement asymptotique au premier ordre en nombre de Mach. Les équations gouvernant l’écoulement de streaming sont ensuite établies en moyennant les équations de Navier-Stokes sur une période, puis en linéarisant. Chaque grandeur ϕ est décomposée en une partie moyenne $\bar{\phi}$ (le streaming) et une partie fluctuante ϕ' (l’acoustique) : $\phi = \bar{\phi} + \phi'$. On a alors pour tous ϕ et ψ : $\bar{\phi}\bar{\psi} = \bar{\phi}\bar{\psi} + \bar{\phi}'\bar{\psi}'$. Si x est la direction axiale et y la direction transverse, l’hypothèse $R \ll L$ implique $\frac{\partial^2}{\partial x^2} \ll \frac{\partial^2}{\partial y^2}$ et permet de simplifier les équations résultantes pour le champ moyen, qui s’écrivent dans le cas 2D plan (pour le problème dynamique) :

$$\left\{ \begin{array}{l} \rho_0 \left(\frac{\partial \bar{u}}{\partial x} + \frac{\partial \bar{v}}{\partial y} \right) = - \frac{\partial}{\partial x} (\bar{\rho} u') - \frac{\partial}{\partial y} (\bar{\rho} v') \quad a) \\ \mu \frac{\partial^2 \bar{u}}{\partial y^2} = \frac{\partial \bar{p}}{\partial x} + \rho_0 \frac{\partial}{\partial x} (\bar{u} u') + \rho_0 \frac{\partial}{\partial y} (\bar{u} v') \quad b) \\ \mu \frac{\partial^2 \bar{v}}{\partial y^2} = \frac{\partial \bar{p}}{\partial y} + \rho_0 \frac{\partial}{\partial x} (\bar{u} v') + \rho_0 \frac{\partial}{\partial y} (\bar{v} v') \quad c) \end{array} \right. \quad (29)$$

Ici \bar{u} , \bar{v} et \bar{p} sont les composantes axiale et transverse de la vitesse moyenne et la pression moyenne, et u' et v' sont les composantes axiale et transverse de la vitesse acoustique. Les termes moyennés $\bar{u}u'$, $\bar{u}v'$ et $\bar{v}v'$, d’ordre 2 en Mach, sont les contraintes de Reynolds, qui sont à l’origine de l’écoulement de streaming. Ainsi linéarisées et simplifiées, les équations (29) peuvent être résolues analytiquement. Le long de l’axe du résonateur ($y = 0$), la solution

de Rayleigh donne la vitesse moyenne axiale \bar{u}_R suivante :

$$\bar{u}_R = -\frac{3}{16} \frac{U_{ac}^2}{c_0} \sin(2\pi x/L), \quad -L/2 \leq x \leq L/2, \quad (30)$$

où U_{ac} est la vitesse acoustique au centre de l'onde sur l'axe du résonateur, et c_0 est la vitesse du son. Dans le cas d'un résonateur cylindrique, la structure de l'écoulement de streaming est analogue, les tourbillons intérieurs et extérieurs étant alors toroïdaux. La vitesse de streaming sur l'axe devient [92] :

$$\bar{u}_R = -\frac{3}{8} \frac{U_{ac}^2}{c_0} \sin(2\pi x/L), \quad -L/2 \leq x \leq L/2,$$

donc d'amplitude double par rapport au cas plan.

Dans l'approche RNW, les contraintes de Reynolds figurant dans l'équation de la vitesse transverse (29-c) sont usuellement négligées, étant considérées d'un ordre de grandeur plus faible. Or nous avons récemment montré, dans l'article [5] (qui figure en annexe), que l'une de ces contraintes (le terme $\frac{\partial}{\partial x}(\bar{u}'v')$) peut dans certains cas avoir un effet important. Dans cet article, nous avons résolu analytiquement le système complet (29), en utilisant le logiciel de calcul formel Mathematica. Nous avons ainsi quantifié la dépendance du streaming de Rayleigh à la largeur du guide \hat{R} , et montré que la contrainte de Reynolds supplémentaire considérée peut modifier drastiquement sa configuration dans certaines géométries. En effet le champ de vitesse moyen est obtenu par intégrations successives des contraintes de Reynolds dans (29), et la dépendance en y/R (ou r/R) des champs acoustiques influe beaucoup sur le résultat de l'intégration. La vitesse de streaming sur l'axe obtenue en prenant en compte toutes les contraintes de Reynolds, normalisée par la vitesse de Rayleigh (30), s'écrit ainsi :

$$\frac{\bar{u}(\hat{x}, 0)}{\bar{u}_R} = 1 - \frac{29}{6} \frac{1}{\hat{R}} - \frac{2\pi^2}{45} \frac{\hat{R}^3}{\hat{L}^2} \left[1 + \frac{73}{2\hat{R}} - \frac{585}{4\hat{R}^2} + \frac{180}{\hat{R}^3} \right]. \quad (31)$$

avec $\hat{L} = L/\delta_\nu$. Dans (31), le deuxième terme du membre de droite est la correction due à l'influence de la largeur du résonateur, et le troisième terme résulte de la prise en compte de la contrainte $\frac{\partial}{\partial x}(\bar{u}'v')$. Ce dernier terme est toujours négatif, et produit donc un écoulement en sens inverse du streaming de Rayleigh. Le streaming total résultant peut ainsi devenir négatif sur l'axe selon les valeurs des paramètres géométriques \hat{R} et \hat{L} . Si le fluide de travail est de l'air à conditions standard, on montre que cela se produit pour des guides de dimensions millimétriques et de rapport L/R de l'ordre de 10 ou moins. Cela peut donc concerter les systèmes microfluidiques qui font l'objet de beaucoup de développements à l'heure actuelle.

Si le streaming acoustique est bien analysé lorsque l'amplitude acoustique est faible (streaming dit linéaire), il n'en va pas de même quand le niveau acoustique augmente (et donc le nombre de Mach $M = \frac{U_{ac}}{c_0}$). On parle alors de streaming rapide ou non linéaire. C'est à ce type de streaming que nous nous intéressons depuis 2009. Menguy et Gilbert [60] ont mené une analyse théorique dans le cas isentropique, et introduit le nombre de Reynolds $Re_{NL} = M^2 \hat{R}^2$, qui caractérise le rapport entre les forces d'inertie et les forces visqueuses dans l'écoulement de streaming. À fort niveau acoustique, Re_{NL} devient plus grand que 1 et donc les effets d'inertie ne peuvent plus être négligés. L'étude [60] montre que le streaming est déformé si Re_{NL} augmente. Cependant cette étude était limitée à des valeurs de Re_{NL} faibles, inférieures à 6. Plus tard il a été montré expérimentalement [103, 66, 84] que les tourbillons extérieurs s'atténuent avec l'augmentation de Re_{NL} , et qu'éventuellement de nouveaux tourbillons contra-rotatifs peuvent apparaître près de l'axe du résonateur pour Re_{NL} assez grand (entre 30 et 150 dans les expériences de [84]).

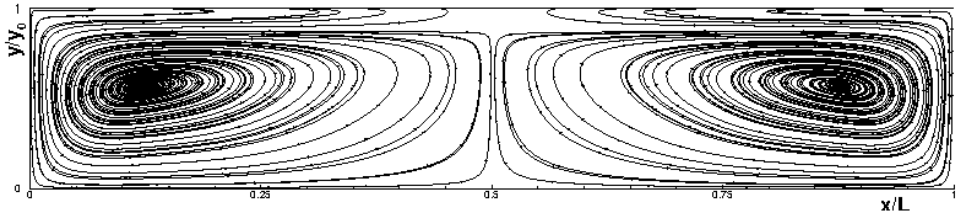


FIGURE 33 – Lignes de courant de l’écoulement de streaming entre l’axe (en bas) et la paroi (en haut) du résonateur, $Re_{NL} = 12$. Tiré de [22].

Nos premiers travaux sur le streaming rapide ont commencé avec la simulation numérique directe (DNS) de l’écoulement d’air dans un résonateur plan, à l’intérieur duquel on installe une onde plane par "secouage" (*i.e.* ajout d’un terme source dans les équations de Navier-Stokes résolues dans le référentiel lié au résonateur). L’écoulement est simulé dans son ensemble, et l’écoulement de streaming est obtenu en moyennant les champs instantanés sur chaque période acoustique. Le schéma numérique étant explicite, le pas de temps est limité à des valeurs très petites du fait de la condition de stabilité (liée à l’acoustique), et plusieurs centaines de milliers de pas de temps sont nécessaires pour que l’écoulement de streaming se stabilise. Du fait des coûts de calcul, la longueur du résonateur était beaucoup plus petite que dans les expériences de référence, correspondant à une fréquence acoustique beaucoup plus grande ($L = \frac{1}{2} \frac{c_0}{f}$, avec f la fréquence, égale à 20000 Hz dans les simulations, et de l’ordre de 250 Hz dans les expériences). Avec le stage de Master 2 de Gurunath Gandikota en 2009-2010 au LIMSI, nous avons mis en place la méthodologie numérique adaptée pour traiter ce cas, à partir de mon code 2D basé sur le schéma OSMP (convergence en maillage, ordre du schéma numérique pertinent pour minimiser les coûts de calcul, calcul des moyennes temporelles...). Nous avons fait des simulations pour des valeurs de Re_{NL} entre 0.041 et 27. Les résultats dans le cas du streaming linéaire ($Re_{NL}=0.041$) ont permis de valider nos simulations numériques, en montrant une bonne adéquation avec les études théoriques [80, 30, 31]. Dans le régime rapide, l’évolution observée du streaming avec l’augmentation de Re_{NL} était cohérente avec les mesures LDV de [103] pour $Re_{NL} \leq 20$, $Re_{NL} = 20$ étant la plus grande valeur considérée dans [103]. Les lignes de courant de l’écoulement de streaming calculé numériquement pour $Re_{NL} = 12$ sont représentées figure 33. Les tourbillons extérieurs sont déformés, et la vitesse sur l’axe dans la partie centrale du guide est plus faible que la vitesse théorique de Rayleigh. En augmentant Re_{NL} , on observait que la vitesse sur l’axe, normalisée par (30), continuait de décroître, puis que de nouveaux tourbillons apparaissaient près du centre du résonateur. Une interaction complexe entre le streaming et le champ de température moyen, lui aussi fortement modifié à grand Re_{NL} , était mise en évidence, comme cela avait aussi été remarqué dans [103]. Cependant dans les simulations numériques en tube droit, des ondes de choc apparaissent dans l’écoulement instantané à partir de valeurs de Re_{NL} assez faibles (de l’ordre de 5), ce qui a priori a une forte influence sur la température. Dans les expériences il n’y pas d’ondes de choc, et on peut donc s’attendre à des effets thermiques très différents dans les deux cas. Ces premières simulations ont été publiées dans [22].

En décembre 2011 nous avons participé au GDR thermoacoustique regroupant les laboratoires français travaillant sur ce thème. À cette occasion nous avons assisté à la présentation d’Ida Reyt, qui à l’époque était doctorante au laboratoire Pprime à Poitiers, sous la direction d’Hélène Bailliet. Il est apparu que nous travaillions sur le même thème, le streaming rapide, nous par simulation numérique et elles par expérimentations (LDV et PIV). Nos résultats étaient en bon accord, montrant une évolution similaire du streaming avec l’augmentation du nombre

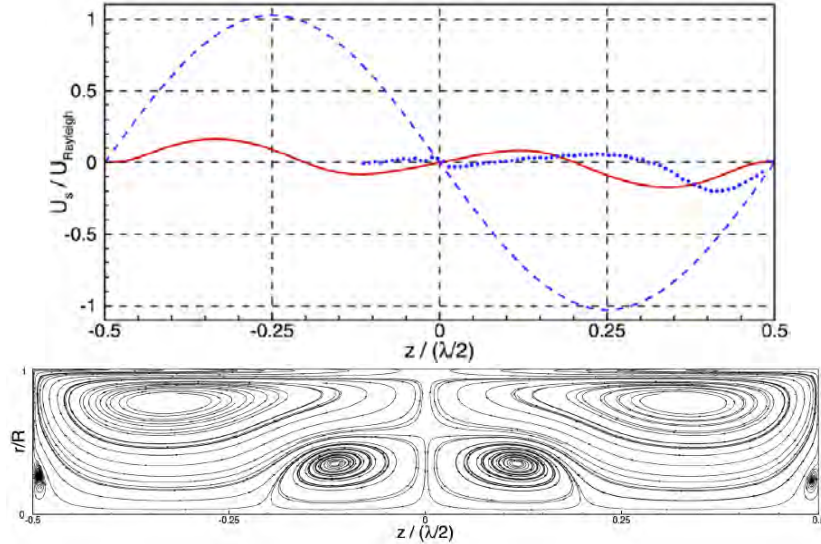


FIGURE 34 – En haut : variation de la vitesse de streaming normalisée par la solution de Rayleigh le long de l’axe du résonateur. Ligne rouge continue : simulation numérique $Re_{NL} = 38.6$; pointillés bleus : expérience $Re_{NL} = 31.8$; tirets bleus : solution de Rayleigh. En bas : lignes de courant de l’écoulement de streaming dans une section radiale du résonateur (simulation numérique, $Re_{NL} = 38.6$).

de Mach. Cela a marqué le début d’une collaboration qui dure encore aujourd’hui. Ida ayant soutenu sa thèse fin 2012, elle est venue comme ATER à l’université Paris-Sud en 2012-2013, puis à l’Ensam en 2013-2014. Nous avons alors publié un article dans le JASA [85] présentant la comparaison entre les expériences menées dans la thèse d’Ida et nos simulations numériques (effectuées en coordonnées cylindriques). Malgré la grande différence des géométries considérées (rapport de longueurs de résonateur expériences/simulations égal à 82), on observait dans les deux cas qu’à partir de $Re_{NL} \approx 30$ le streaming sur l’axe était fortement diminué et que de nouveaux tourbillons contre-rotatifs de faible intensité apparaissaient près du ventre acoustique. On le voit sur la figure 34 (extraite de [85]) qui montre (en haut) la vitesse de streaming sur l’axe du résonateur obtenue expérimentalement ($Re_{NL} = 31.8$) et numériquement ($Re_{NL} = 38.6$). La vitesse change de signe trois fois le long de l’axe, montrant l’existence de deux tourbillons supplémentaires par rapport à la solution de Rayleigh. Les lignes de courant de l’écoulement simulé numériquement (en bas), montrent que les nouveaux tourbillons sont concentrés sur l’axe près du ventre de vitesse acoustique, et s’étendent radialement sur une partie de la section du résonateur.

À partir de ces premiers résultats, nous avons essayé de comprendre les mécanismes à l’oeuvre dans cette évolution du streaming à forte amplitude acoustique. Plusieurs phénomènes, éventuellement couplés, peuvent avoir une influence : les effets d’inertie, les effets d’acoustique non linéaire (harmoniques et ondes de choc), les effets thermiques et une éventuelle interaction acoustique/streaming. Les effets d’acoustique non linéaire sont très faibles dans les expérimentations, pour lesquelles il est reporté toujours moins de 10% d’harmoniques supérieurs. Ils sont forts en revanche dans les simulations numériques (jusqu’à 40% pour le premier harmonique), où des ondes de choc apparaissent très rapidement quand on augmente l’amplitude acoustique. On peut donc supposer qu’ils n’ont une éventuelle influence sur le streaming que par les effets thermiques induits. En tout cas ils ne sont pas à l’origine de la réorganisation du streaming.

Afin d’étudier séparément l’influence de ces différents phénomènes, nous avons utilisé plusieurs stratégies, ce que permet la simulation numérique. Dans un premier temps, nous avons

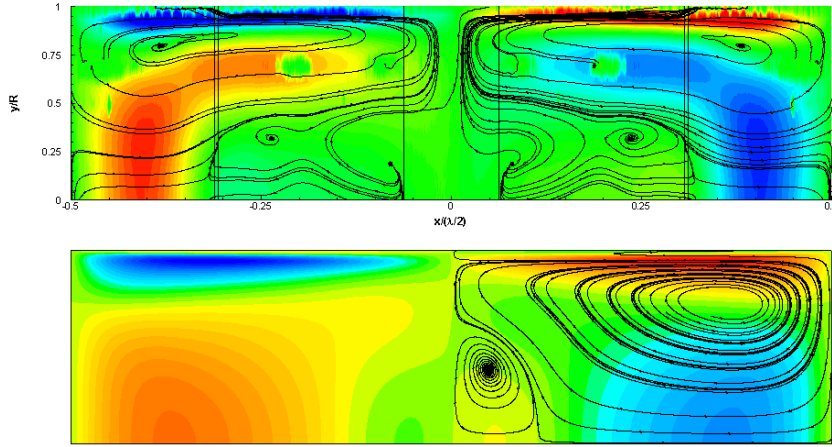


FIGURE 35 – Isocontours de la vitesse axiale de streaming et lignes de courant de l’écoulement. En haut : résultats expérimentaux PIV tirés de [83], $Re_{NL} = 30$, $\hat{R} = 140$; en bas : résultats numériques en isentropique, $Re_{NL} = 111$, $\hat{R} = 50$.

écarté les effets thermiques, en développant une version isentropique du code DNS. Par ailleurs une version moyennée du code isentropique (code "AMS") a aussi été développée, dans laquelle on résout directement les équations moyennées (29), en imposant des contraintes de Reynolds calculées par ailleurs ou données analytiquement. Cela permet notamment d’étudier le streaming produit par une onde acoustique monochromatique de forte intensité, ce qui n’est pas possible dans la simulation directe. Les résultats obtenus dans ce cadre ont fait l’objet des publications [23, 24] (l’article [24] figure en annexe).

Les principales conclusions reportées dans ces articles sont les suivantes : en premier lieu le modèle isentropique produit des résultats analogues pour le streaming à fort niveau acoustique, mais pour de plus grandes valeurs de Re_{NL} . Par exemple, dans [23] l’apparition de la nouvelle cellule sur l’axe se produit pour $Re_{NL} > 80$. La comparaison des résultats numériques et expérimentaux sur la figure 35 montre des champs très similaires dans la zone de couche limite, mais aussi que l’effet de diminution de la vitesse de streaming dans la zone centrale du résonateur est moins accentué dans le cas numérique.

Ensuite, nous avons montré qu’à forte amplitude acoustique, la vitesse maximum de streaming sur l’axe \bar{U}_s change de régime. Pour de faibles valeurs de U_{ac} , \bar{U}_s est classiquement une fonction quadratique de U_{ac} . Lorsque U_{ac} augmente, cette dépendance devient linéaire à partir d’une certaine valeur, comme on l’observe sur la figure 36. Cette figure est intéressante car elle montre que ce changement de régime est observé aussi bien sur les résultats numériques que dans les expérimentations, bien que le modèle numérique soit isentropique.

Les simulations numériques utilisant le code AMS nous ont aussi permis de montrer que l’établissement de l’écoulement de streaming se fait de la même manière que dans le célèbre problème de la cavité entraînée : un écoulement produit dans une cavité par l’entraînement de la paroi supérieure à laquelle on impose une vitesse de déplacement. Dans le cas du streaming linéaire, les tourbillons extérieurs sont donc produits uniquement par diffusion de la quantité de mouvement à partir de la vitesse dans la couche limite (qui s’établit presque immédiatement), en cohérence avec l’analyse de Rayleigh. On observe de plus que, à fort niveau acoustique, on peut analyser l’évolution temporelle de l’écoulement par le double effet de la diffusion et de la convection, dont les temps caractéristiques sont différents. Cette évolution temporelle se produit de manière similaire dans le problème de la cavité entraînée et dans le problème

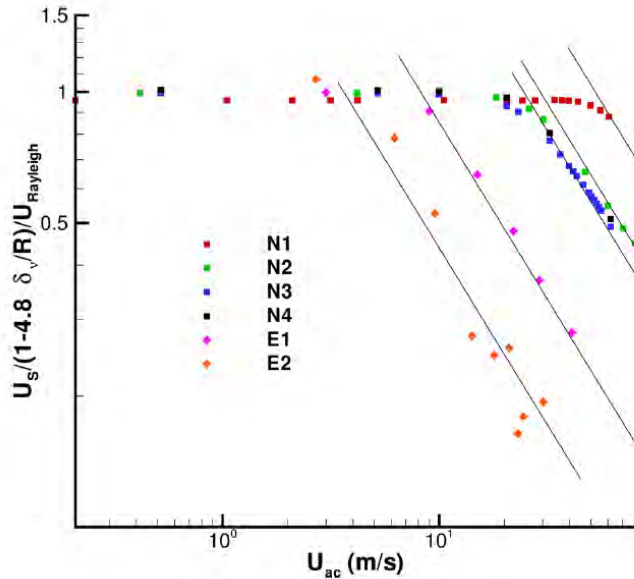


FIGURE 36 – Représentation log-log de la vitesse de streaming normalisée sur l'axe. Les données N1 à N4 sont des résultats numériques, les données E1 et E2 des résultats expérimentaux tirés de la thèse d'Ida Rey [83], pour plusieurs valeurs de la fréquence acoustique et de R/δ_ν . Définition des cas : N1 : $f = 20,000$ Hz, $\hat{R} = 20$; N2 : $f = 20,000$ Hz, $\hat{R} = 40$; N3 : $f = 20,000$ Hz, $\hat{R} = 50$; N4 : $f = 5,000$ Hz, $\hat{R} = 50$; E1 : $f = 88$ Hz, $\hat{R} = 84$; E2 : $f = 240$ Hz, $\hat{R} = 138$. Figure tirée de [24].

du résonateur (en considérant pour la cavité entraînée une vitesse de paroi correspondant à la vitesse en bordure de couche limite dans le résonateur). En revanche, dans le cas de la cavité entraînée, la vitesse de l'écoulement sur l'axe est plus grande que dans le cas du résonateur, et on ne voit pas apparaître de nouveaux tourbillons.

Le code AMS a ensuite permis d'étudier le streaming en considérant une onde acoustique monochromatique de forte intensité, obtenue analytiquement à partir de la solution théorique dans le cas linéaire. Cette onde n'est ainsi pas soumise à une éventuelle interaction avec le streaming. Les simulations ont montré une évolution du streaming identique à celle observée pour l'écoulement dans la cavité entraînée à grande vitesse. Les résultats obtenus se sont également révélés conformes aux prédictions de l'étude [60], ce qui est cohérent puisque cette étude était basée sur les mêmes hypothèses (écoulement isentropique et onde acoustique monochromatique de forte intensité). Cela est illustré sur la figure 37 qui montre la vitesse de streaming sur l'axe pour plusieurs valeurs de Re_{NL} , obtenue par Menguy et Gilbert [60] (à gauche), et dans les simulations AMS (à droite). On constate que la déformation du streaming entraînée par les seuls effets d'inertie (simulations AMS ou modèle [60]) n'est pas du tout en adéquation avec celle observée dans la simulation numérique directe ou dans les expérimentations, comme on le voit sur la figure 38, qui montre la comparaison entre les résultats AMS et DNS pour un nombre de Reynolds $Re_{NL} \approx 81$. Les effets d'inertie produisent seulement un classique "raissement" du profil de vitesse dans la direction de l'écoulement, mais très peu d'atténuation et pas d'apparition de nouveaux tourbillons.

On conclut donc de ces résultats que les effets d'inertie ne constituent pas un mécanisme suffisant pour expliquer à eux seuls l'évolution du streaming, et qu'à fort niveau acoustique il faut prendre en compte l'interaction non linéaire entre le champ acoustique et le streaming. Les simulations numériques directes montrent en effet que dans ce cas la vitesse radiale acoustique

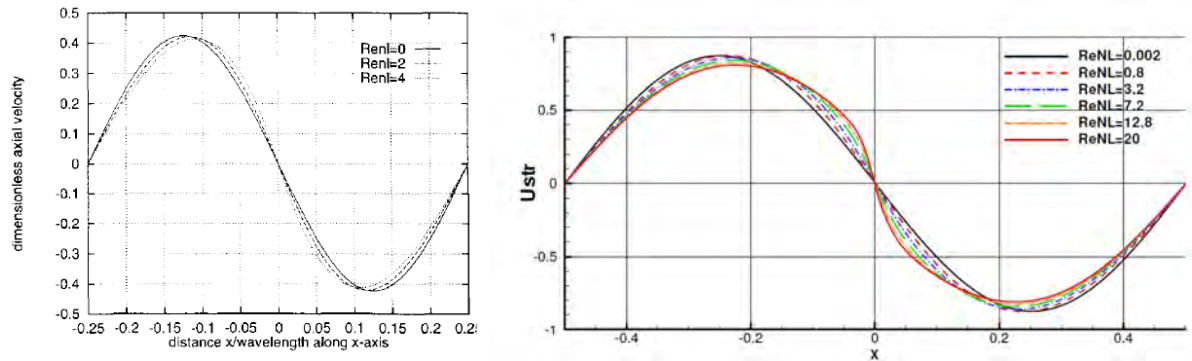


FIGURE 37 – Vitesse de streaming adimensionnée sur l’axe pour plusieurs valeurs de Re_{NL} . À gauche : figure tirée de [60]. À droite : résultats numériques donnés par le code AMS. La vitesse de référence est $M^2 c_0$ à gauche, $3/8 M^2 c_0$ à droite).

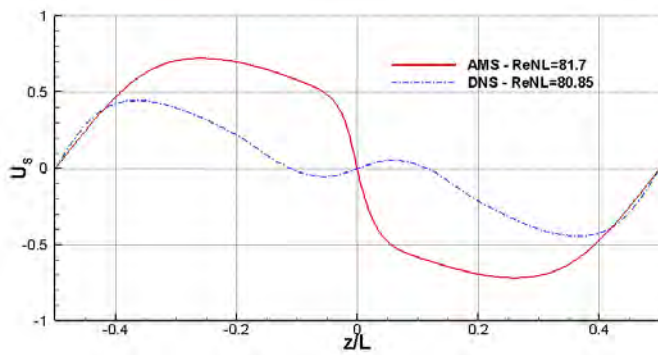


FIGURE 38 – Comparaison de la vitesse de streaming adimensionnée sur l’axe pour les simulations AMS et DNS, $Re_{NL} \approx 81$.

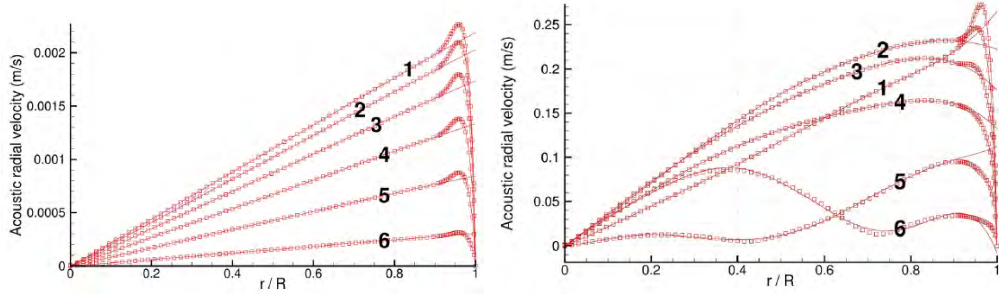


FIGURE 39 – Vitesse radiale acoustique en plusieurs positions axiales sur une cellule de streaming. À gauche, $Re_{NL} = 0.006$, à droite $Re_{NL} = 81$. Les positions axiales sont numérotées de 1 (près du noeud acoustique) à 6 (près du ventre acoustique).

est significativement modifiée par cette interaction. La figure 39, tirée de [24], montre les profils radiaux de vitesse acoustique radiale obtenus par DNS à faible et fort niveau acoustique. À faible niveau acoustique, la vitesse radiale varie linéairement en r entre l'axe du résonateur et le bord de la couche limite, comme prévu par la théorie. À fort niveau acoustique au contraire, la vitesse radiale acoustique varie comme un polynôme d'ordre 6 en r . La vitesse acoustique axiale, elle, n'est que très peu modifiée par l'interaction avec le streaming. Une simulation numérique DNS a été menée dans les mêmes conditions, dans laquelle à chaque période temporelle on soustrait le champ de streaming au champ instantané. Cela permet d'éliminer artificiellement l'influence du streaming sur l'acoustique. Le résultat montre que la composante de vitesse acoustique radiale recouvre une variation radiale linéaire dans la partie centrale du résonateur [24], ce qui démontre que c'est bien l'interaction avec le streaming qui modifie la vitesse acoustique.

En fait la comparaison des ordres de grandeur des vitesses radiales montre que la vitesse radiale de streaming (qui varie en U_{ac}^2) devient plus grande que la vitesse radiale acoustique (qui varie en U_{ac}) à partir d'une certaine valeur de U_{ac} , ce qui explique la forte interaction entre les deux écoulements. Cette valeur diminue lorsque \hat{R} augmente. Cela est observé dans les simulations numériques et dans les expérimentations [24], et peut aussi être démontré théoriquement à partir du modèle analytique (résolu à l'aide de Mathematica) développé dans [5]. L'interaction entre les deux écoulements, l'écoulement principal acoustique et l'écoulement secondaire de streaming, joue donc un grand rôle à forte amplitude acoustique et est à l'origine d'un changement de configuration du streaming. Il ressort aussi de ces résultats qu'une petite modification du champ acoustique a d'importantes répercussions sur le streaming.

Nos derniers travaux sur le streaming rapide concernent la prise en compte des effets thermiques. L'existence d'une stratification axiale de température a fait l'objet de beaucoup d'études dans le contexte de la thermoacoustique [89, 71], sans mettre en évidence une modification associée importante du streaming. En revanche de récents articles [11, 12, 62] ont fait apparaître le très important effet d'une stratification transverse de température. Dans notre cas, lorsque le transport convectif de la température par le streaming devient significatif, l'organisation du champ de température induit par effet thermoacoustique est modifiée. Le fluide chaud est entraîné par convection le long de l'axe du résonateur vers le ventre acoustique, et le fluide froid près de la paroi vers les noeuds, donnant lieu à une stratification transverse du champ de température (figure 40).

Dans [12] des simulations numériques ont été effectuées en imposant un profil de température à la paroi du résonateur et en étudiant l'effet du gradient radial de température résultant du transport convectif. Cette étude, limitée à de faibles valeurs de Re_{NL} pour des raisons de

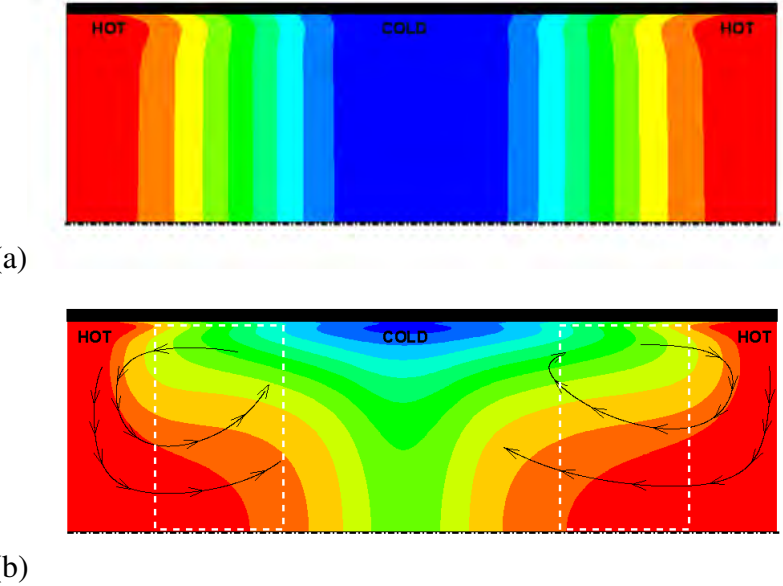


FIGURE 40 – Représentation schématique des lignes isothermes dans le résonateur à (a) faible niveau acoustique et (b) fort niveau acoustique. Les rectangles en tirets blancs indiquent les zones de température stratifiées radialement. Figure tirée de [25].

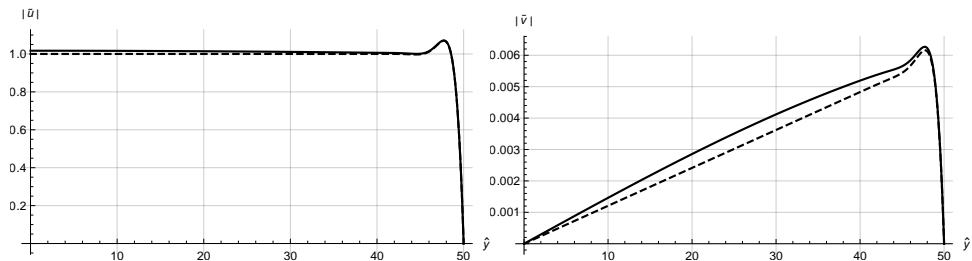


FIGURE 41 – Profil transverse de vitesse acoustique axiale ($\hat{x} = 0$, gauche) et transverse ($\hat{x} = -1/2$, droite), m/s, $\hat{R} = 50$. Différence de température axe-paroi $\Delta T = 5$ K (lignes continues), $\Delta T = 0$ K (tirets). $U_{ac} = 1$ m/s, air.

stabilité numérique, montrait que de très petites différences de température peuvent modifier en profondeur l’organisation de l’écoulement de streaming.

Afin d’étudier quantitativement ce phénomène, nous avons étendu le modèle analytique développé dans [5] pour prendre en compte l’existence d’un champ de température stratifié dans la direction transverse du résonateur. L’hypothèse centrale dans cette étude est que le streaming rapide peut être étudié théoriquement de façon adéquate en résolvant les équations linéaires, à la fois pour l’acoustique et le streaming, avec une distribution transverse de température imposée. La différence de température ΔT entre la paroi et l’axe est supposée petite, $\Theta = \Delta T/T_0 \ll 1$ (T_0 étant la température de l’état de référence). Le calcul du champ acoustique montre que la vitesse acoustique est modifiée par cette distribution de température en dehors de la couche limite, mais les modifications sont faibles (figure 41). Cependant, comme dans le cas de l’interaction acoustique-streaming, ces petites modifications de l’acoustique ont un effet important sur le streaming.

Le calcul de l’écoulement de streaming associé à ce champ de vitesse acoustique donne la solution suivante pour la vitesse axiale le long de l’axe, adimensionnée par la vitesse de

Rayleigh (30) :

$$\frac{\bar{u}(x/L, 0)}{\bar{u}_R} = 1 + \frac{2}{3} \frac{(\gamma - 1)\sqrt{Pr}}{1 + Pr} - \frac{2}{45} \Theta \hat{R}^2 \quad (32)$$

où les termes d'ordre $1/\hat{R}$ et plus petits ont été négligés, et Pr est le nombre de Prandtl du fluide. Dans cette équation, les deux premiers termes du membre de droite correspondent à la solution classique obtenue en prenant l'équation de l'énergie en compte et en considérant que le fluide obéit à une loi d'état de gaz parfait [89]. Le dernier terme exprime l'influence du gradient de température transverse sur le streaming. Ce terme est négatif et donc s'oppose au streaming de Rayleigh si $\Theta > 0$, c'est à dire si la température est plus élevée sur l'axe que sur la paroi. Ce cas correspond à la situation décrite par la figure 40-b). En fonction de la valeur de $\Theta \hat{R}^2$, le streaming sur l'axe diminue et peut même devenir négatif (tourbillons tournant en sens inverse des tourbillons extérieurs de Rayleigh). De plus, la variation de ce terme en \hat{R}^2 implique qu'une très petite valeur de Θ peut provoquer une modification importante du streaming, puisque $\hat{R} \gg 1$.

En calculant par ailleurs la température à la paroi (obtenue en intégrant l'équation de l'énergie entre l'axe et la paroi), nous avons pu exhiber un critère qui permet de prédire l'évolution du streaming en fonction de Re_{NL} , et des caractéristiques du fluide et de la paroi. La paroi est supposée conductrice, d'épaisseur w , et les échanges avec l'air extérieur sont pris en compte par une loi de Newton.

Ce critère s'écrit :

$$Re_{NL} \geq K_C \quad (33)$$

avec

$$K_C = 30 \frac{k_s/k}{\hat{w} + k_s/(h\delta_\nu)} \left(1 + \frac{3}{2} \frac{1 + Pr}{(\gamma - 1)\sqrt{Pr}} \right) \frac{1}{(1 - Pr^{3/2})}. \quad (34)$$

Ici k et k_s sont les conductivités thermiques du fluide et du solide constituant la paroi du résonateur, $\hat{w} = w/\delta_\nu$ est le rapport entre l'épaisseur de la paroi et l'épaisseur de couche limite et h est le coefficient de transfert (loi de Newton) entre le résonateur et l'air extérieur. Si la paroi extérieure du résonateur est isotherme, le coefficient $\frac{k_s/k}{\hat{w} + k_s/(h\delta_\nu)}$ dans (34) doit être remplacé par $\frac{k_s/k}{\hat{w}}$.

Ce critère se révèle en bon accord avec les expérimentations disponibles [103, 84]. Il permet également d'expliquer l'influence des conditions aux limites thermiques à la paroi, qui se révèlent primordiales. En effet dans [89] il est montré que le streaming est fortement modifié dans le cas de conditions "non contrôlées" (c'est à dire lorsqu'il y a un échange thermique libre entre la paroi et l'air extérieur), alors qu'il l'est très peu pour des conditions isothermes. Ce travail récent a été soumis au Journal of Fluid Mechanics en février 2020 [25]. L'article figure en annexe.

La conclusion générale de cette étude sur le streaming non linéaire est donc la suivante : les effets d'inertie n'ont une réelle influence sur l'écoulement moyen qu'à travers la réorganisation, par transport convectif, du champ de température créé par effet thermoacoustique près de la paroi du résonateur. La stratification transverse de température qui en résulte modifie les vitesses acoustiques, ce qui a un fort impact sur l'écoulement de streaming. L'interaction non linéaire entre l'acoustique et le streaming joue également un grand rôle, en modifiant fortement la composante radiale de la vitesse acoustique, ce qui en retour modifie la configuration du streaming. Dans les deux cas, c'est bien l'interaction du champ moyen avec le champ acoustique qui est à l'oeuvre. De manière générale, il ressort que de petites modifications du champ acoustique peuvent modifier en profondeur l'organisation de l'écoulement de streaming. Les deux effets ont une influence analogue sur le champ de streaming résultant et s'ajoutent a priori, mais les

effets dus à la thermique sont prépondérants dans le cas de conditions aux limites thermiques non contrôlées.

Ce travail se poursuit avec le développement de simulations numériques venant à l'appui de l'étude théorique développée dans [25].

IV | Perspectives

Dans les années qui viennent, je compte continuer à travailler sur le streaming acoustique et la thermoacoustique, en collaboration avec Diana Baltean-Carlès et Catherine Weisman au LIMSI, et Hélène Bailliet à l’Institut Pprime. Cette collaboration, qui dure depuis une dizaine d’années, est je trouve idéale du fait de sa complémentarité, permettant une triple approche théorique, numérique et expérimentale (ce qui est une force rare), ainsi que des excellents rapports humains que nous entretenons.

D’un point de vue scientifique, la thermoacoustique est une source particulièrement riche et intéressante de thèmes de recherche combinant l’acoustique, la mécanique des fluides et la thermique, qui sans nul doute m’occuperont jusqu’à la retraite... Du point de vue sociétal, c’est une technologie qui a toute sa place dans le contexte actuel du changement climatique et de la transition énergétique. En effet, les machines thermoacoustiques n’utilisent pas de gaz à effet de serre, et peuvent utiliser des énergies non fossiles, comme l’énergie solaire, le vent ou la biomasse. Elles peuvent aussi être utilisées pour récupérer la chaleur perdue à basse température (chaleur fatale) dans les procédés industriels. Bien que des efforts de recherche importants aient été consacrés à la mise au point de ces machines, il reste encore beaucoup de connaissances fondamentales à acquérir pour optimiser leur fonctionnement.

Notre étude théorique du streaming en résonateur a récemment amené de nouveaux résultats avec l’étude complète, dans le cas linéaire (faible niveau acoustique), de tous les termes sources (contraintes de Reynolds) à l’origine de cet écoulement [5]. Dans le cas du streaming rapide (fort niveau acoustique), l’intégration des effets thermiques a permis le développement d’un critère qui semble bien prédire l’évolution du streaming quand le niveau acoustique augmente [25]. Quelques développements supplémentaires sont prévus, notamment pour étudier l’effet du frottement visqueux, qui est toujours négligé dans les modèles.

La dernière étape en cours dans l’étude du streaming rapide est d’effectuer des simulations numériques dans une configuration analogue à celle de l’expérience, afin de reproduire et analyser l’écoulement de streaming dans son ensemble. La simulation numérique en vraie grandeur n’étant pas accessible pour des raisons de coût de calcul, elle doit nécessairement être menée sur un système plus petit. Les résultats de nos études théoriques prennent ici toute leur importance, en permettant de définir les paramètres de la simulation numérique en similitude avec les expérimentations. Du point de vue numérique, une des difficultés principales tient au fait que lorsqu’on augmente l’intensité de l’onde acoustique, des ondes de choc (de faible intensité) se développent rapidement dans l’écoulement. Or l’existence d’ondes de choc modifie fortement le champ de température dans l’écoulement [61]. Dans le cas expérimental, l’apparition d’ondes de choc dans l’écoulement est évitée grâce à une modification de la géométrie du résonateur. Celui-ci est en effet connecté à des convergents, qui inhibent la génération d’harmoniques. Pour comparer les résultats théoriques et expérimentaux, et valider notre théorie sur l’évolution du streaming à forte amplitude acoustique liée aux effets thermiques (menée rappelons-le dans le cas linéaire), il est nécessaire de mettre en oeuvre une approche numérique qui empêche le développement d’ondes de choc, à la manière de ce qui est fait en expérimental. Ainsi, l’approche selon laquelle l’onde acoustique est créée en secouant un tube droit doit être revue. Il faut aussi prendre en compte une paroi conductrice d’épaisseur non nulle, dont l’étude [25] a mis en évidence l’importance. On s’attend alors à voir apparaître une échelle de temps supplémentaire liée à la conduction thermique ($\tau = l^2/\kappa$, où l est une longueur caractéristique du système, et κ la diffusivité thermique du fluide ou du solide constituant la paroi). Dans le cas isentropique, les échelles de temps acoustique et convective sont déjà très différentes (le nombre de Mach est petit dans ce type d’écoulement). Cette co-existence de deux échelles de temps très différentes rend la simulation numérique directe très coûteuse en temps CPU. Typiquement, dans le cas isentropique, plusieurs centaines de périodes temporelles (soit plus d’un million d’itérations en temps) sont nécessaires pour obtenir un champ de streaming convergé (stationnaire).

Avec l'introduction de l'échelle supplémentaire τ , le problème prend une autre ampleur et on s'attend à devoir effectuer un nombre de périodes beaucoup plus important (plusieurs milliers) pour obtenir un champ de streaming stationnaire. La première étape pour rendre ce type de simulation abordable réside donc dans la parallélisation de mon code, qui jusqu'à présent était monoprocессeur, et son optimisation. Ce travail est en cours. Il faut ensuite adapter le code pour considérer une géométrie analogue à la géométrie expérimentale, en prenant en compte des sections convergentes supplémentaires connectées au tube droit. Afin de se rapprocher au plus de l'expérience, la méthode d'excitation pour la génération de l'onde acoustique sera également modifiée, en développant une méthode basée sur le déplacement de pistons dans les parties convergentes. La figure 42 montre la géométrie qui sera considérée. Comme dans le cas expérimental, on considérera une longueur de résonateur $L = 3\lambda/2$, donnant lieu au développement de six cellules de streaming extérieur. Cela permet d'obtenir quatre cellules de streaming peu influencées par les convergents.

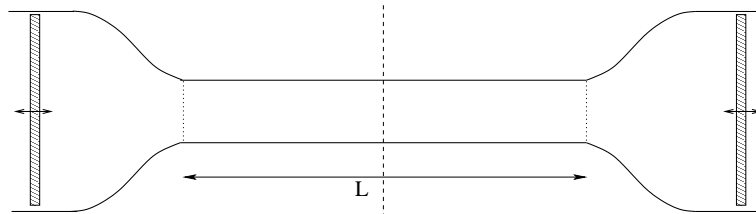


FIGURE 42 – Géométrie considérée dans les simulations numériques pour se rapprocher des conditions expérimentales. Le résonateur de longueur L est inséré entre deux convergents à l'intérieur desquels des pistons engendrent l'onde acoustique. Le problème est symétrique par rapport à un axe vertical passant au centre du résonateur.

Je compte faire ces développements dans le cadre d'une méthode de type "frontières immergées", où le maillage est fixe et cartésien. J'ai une expérience de ce type de méthodes, acquise au cours de la thèse de Laurent Monasse. Les résultats obtenus devraient aussi nous permettre d'évaluer l'effet des ondes de choc sur l'écoulement de streaming, qui n'est pas quantifié dans les études numériques existantes [55].

Par la suite je pense aborder la simulation d'une machine thermoacoustique simplifiée, obtenue en intégrant dans le résonateur un empilement de plaques ou/et un milieu poreux. La mise au point d'un modèle de milieu poreux adapté pour le compressible sera l'un des aspects intéressants de cette étude. L'effet de la gravité pourra aussi être étudié dans le cas 2D.

Je participe également à l'ANR TACOT (2018-2021). L'objectif de ce projet, qui rassemble quatre laboratoires de recherche (PPRIME, LAUM, LMFA, LIMSI) et le constructeur automobile PSA, est de démontrer l'applicabilité de la thermoacoustique pour la climatisation automobile. Il est prévu de concevoir, construire et étudier les performances d'un système thermoacoustique coaxial compact proposé à l'origine dans [75, 76]. Il s'agit d'un système très différent des systèmes habituels, qui en général comportent un résonateur de longueur comparable à la longueur d'onde acoustique. La machine TACOT, qui ne comprend pas de résonateur, fonctionne suivant le principe d'une onde progressive, engendrée par deux sources acoustiques dont l'une crée le champ de pression et l'autre le champ de déplacement (figure 43). On ne s'attend pas dans cette configuration à voir apparaître d'écoulement de streaming significatif, mais cela reste une question ouverte.

Le LIMSI intervient dans ce projet en tant que laboratoire spécialiste de modélisation et simulation numérique. Nous nous intéressons en particulier aux phénomènes liés à la gravité (convection naturelle) ou au streaming dans un modèle simplifié du dispositif. Des simulations

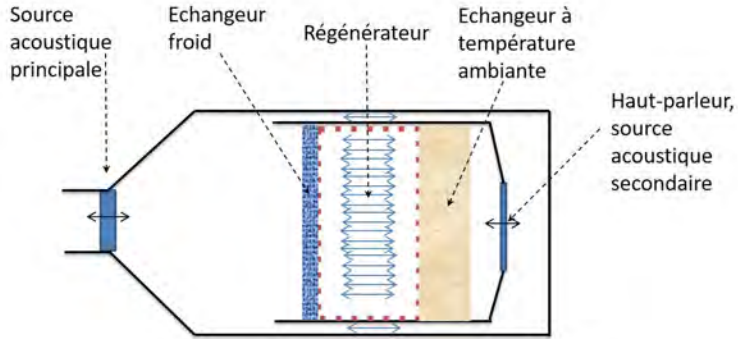


FIGURE 43 – Géométrie simplifiée du prototype TACOT. La source acoustique principale crée la pression, la source secondaire la vitesse. Un stack (régénérateur) est positionné dans le rectangle intérieur en tirets.

3D en cavité thermoacoustique comprenant un milieu poreux ont été effectuées et comparées avec un très bon accord avec des expérimentations menées à Pprime [37]. Dans cette étude préliminaire cependant le modèle d'écoulement était incompressible, il n'y avait pas de champ acoustique et seuls les effets thermiques étaient étudiés. La prise en compte de l'acoustique fait l'objet de nos réflexions actuelles. Du fait de la géométrie du problème, le régime d'écoulement est très différent de celui observé dans une machine thermoacoustique classique comportant un résonateur dont la longueur est du même ordre de grandeur que la longueur d'onde acoustique. En effet, on se trouve maintenant dans une configuration pour laquelle la longueur caractéristique de la machine $L \approx 20$ cm et la fréquence d'excitation du système $f \approx 50$ Hz. En conditions thermodynamiques standard on a donc $L/\lambda = 0.03 \ll 1$ si $\lambda = c_0/f$ est la longueur d'onde acoustique. Un modèle faible Mach tel que celui décrit en section 3.4 semble alors approprié pour décrire ce type d'écoulement. En collaboration également avec Yann Fraigneau au LIMSI, nous nous intéressons pour le projet TACOT à la comparaison des deux approches, compressible (telle que celle mise en oeuvre pour nos études sur le streaming) et faible Mach, en domaine de volume variable traité par une méthode de type "frontières immergées". Une des difficultés tient à la représentation en maillage fixe de la variation de volume du domaine dans l'approche faible Mach. D'autre part la machine comporte deux sources acoustiques, dont l'une se situe à l'intérieur de la machine, ce qui représente une difficulté de modélisation supplémentaire. Le LIMSI a une grande expérience du modèle faible Mach [51, 74, 36, 57]. Un code 3D implémentant ce modèle, appelé SUNFLUIDH, a été développé par Yann Fraigneau. Les études [51, 74] montrant l'efficacité de l'approche faible Mach concernaient des écoulements de convection naturelle, en domaine fixe. Ici on s'intéresse à une configuration beaucoup plus complexe, comportant un écoulement oscillant en domaine de volume variable, superposé à un écoulement moyen de streaming et de convection naturelle dont l'intensité reste à déterminer. Le modèle faible Mach, si il est validé dans ce contexte, pourra nous permettre d'effectuer des simulation numériques 3D d'un modèle simplifié de la machine, et d'en tirer une connaissance fine de son fonctionnement.

Bibliographie

- [1] T. Abadie, J. Aubin, D. Legendre, "On the combined effects of surface tension force calculation and interface advection on spurious currents within Volume of Fluid and Level Set frameworks", *Journal of Computational Physics*, **297**, 611–636 (2015).
- [2] M. O. Abu-Al-Saud, S. Popinet, H. A. Tchelepi, "A conservative and well-balanced surface tension model". *J. Comput. Phys.* **371**, 896–913 (2018).
- [3] Attenborough K., Taherzadeh S., et al : "Benchmark cases for outdoor sound propagation models", *J. Acoust. Soc. Am.*, **97**, 1, 173–191 (1995).
- [4] S. Backhaus and G. W. Swift : "A thermoacoustic-Stirling heat engine : Detailed study", *J. Acoust. Soc. Am.*, **107**(6), 3148–3166 (2000).
- [5] D. Baltean-Carlès, V. Daru, C. Weisman, S. Tabakova, H. Bailliet, "An unexpected balance between outer Rayleigh streaming sources", *J. Fluid Mech.* **867**, 985-1011 (2019).
- [6] C. Bogey, C. Bailly, "A family of low dispersive and low dissipative explicit schemes for noise computation", *Journal of Computational Physics*, **194**(1), 194–214 (2004).
- [7] C. Bogey, N. de Carqueray, C. Bailly, "A shock-capturing methododology based on adaptative spatial filtering for high-order non-linear computations", *Journal of Computational Physics*, **228**, 1447–1465 (2009).
- [8] L. Biamino, G. Jourdan, C. Mariani, O. Igra, A. Massol & L. Houas, "Experimental investigation of door dynamic opening caused by impinging shock wave", *Shock Waves* **21**, p. 19-28 (2011).
- [9] Blanken, H., Tremblay, L.B., Gaskin, S., Slavin, A., "Modelling the long-term evolution of worst-case Arctic oil spills", *Marine Pollution Bulletin*, **116**(1-2), 315–331 (2017).
- [10] T. Bonometti and J. Magnaudet, "An interface capturing method for incompressible two-phase flows : Validation and application to bubble dynamics", *Int. J. Multiphase Flow* **33**, 139 (2007).
- [11] Cervenka, M. & Bednarrik, M., "Effect of inhomogeneous temperature fields on acoustic streaming structures in resonators". *J. Acoust. Soc. Am.* **141**, 4418–4426 (2017).
- [12] Cervenka, M. & Bednarrik, M., "Numerical study of the influence of the convective heat transport on acoustic streaming in a standing wave". *J. Acoust. Soc. Am.* **143**, 727 (2018).
- [13] A. J. Chorin, "A numerical method for solving incompressible viscous flow problems", *J. Comput. Phys.*, **2**, 12 (1967)
- [14] Daru V. and Lerat A., "An implicit centered scheme which gives non-oscillatory steady shocks", Nonlinear hyperbolic problems, *Lecture Notes in Mathematics*, Vol. 1270, pp. 115-17, 1987.
- [15] Daru V. and Lerat A., "Analysis of an implicit solver", *Numerical methods for the Euler equations of fluid dynamics*, Angrand et al. eds., Philadelphia : SIAM Publications (1985).
- [16] V. Daru, C. Tenaud, "Evaluation of TVD high resolution schemes for unsteady viscous shocked flows", *Computers and Fluids*, **30**, 89–113 (2001).

- [17] V. Daru, C. Tenaud : "High order one-step monotonicity-preserving schemes for unsteady compressible flows calculations", *Journal of Computational Physics*, **193**, 563–594 (2004).
- [18] V. Daru, X. Gloerfelt, "Aeroacoustic computations using a high order shock-capturing scheme", *AIAA Journal*, **45**(10) : 2474–2486 (2007).
- [19] Daru V., Millet C., Majorcrys J.-P., "Application of a high resolution monotonicity preserving scheme to wave propagation in the atmosphere", *18th International Shock Interaction Symposium (ISIS18)*, 15-18 Juillet 2008, Rouen (France).
- [20] V. Daru, C. Tenaud, "Numerical simulation of the viscous shock tube problem by using a high resolution monotonicity preserving scheme", *Computers and Fluids*, **38**(3) : 664–676 (2009).
- [21] V. Daru, P. Le Quéré, M.-C. Duluc, O. Le Maître, "A numerical method for the simulation of low Mach number liquid-gas flows", *Journal of Computational Physics*, **229**(23) : 8844–8867 (2010).
- [22] Daru, V., Baltean-Carlès, D., Weisman, C., Debasse, P. & Gandikota, G., "Two-dimensional numerical simulations of nonlinear acoustic streaming in standing waves". *Wave Motion* **50**, 955–96 (2013).
- [23] V. Daru, C. Weisman, D. Baltean-Carlès, I. Reyt, H. Bailliet, "Inertial effects on acoustic Rayleigh streaming flow : Transient and established regimes", *Wave Motion*, Volume 74, Pages 1-17 (2017).
- [24] Daru, V., Reyt, I., Bailliet, H., Weisman, C., Baltean-Carlès, D., "Acoustic and streaming velocity components in a resonant waveguide at high acoustic levels", *Journal of the Acoustical Society of America*, 141 (1), pp. 563-574, (2017).
- [25] Virginie Daru, Catherine Weisman, Diana Baltean-Carlès, Hélène Bailliet, "Thermal effects on fast acoustic streaming inside a resonator", soumis à *J. Fluid Mech* (2020).
- [26] Fabian Denner, Fabien Evrard, Berend G.M. van Wachem, "Conservative finite-volume framework and pressure-based algorithm for flows of incompressible, ideal-gas and real-gas fluids at all speeds", *Journal of Computational Physics*, **409**, 109348 (2020).
- [27] J. Falcovitz, G. Alfandary & G. Hanoch, "A two-dimensional conservation laws scheme for compressible flows with moving boundaries", *J. Comput. Phys.* 138 (1997), p. 83-102.
- [28] Flexas, M.M., Thompson, A.F., Torres, H.S., Klein, P., Farrar, J.T., Zhang, H., Menemenlis D., "Global Estimates of the Energy Transfer From the Wind to the Ocean, With Emphasis on Near-Inertial Oscillations", *Journal of Geophysical Research : Oceans*, **124**(8), 5723-5746 (2019).
- [29] Forester, C., Emery, A., "A computational method for low mach number unsteady compressible free convective flows". *J. Comput. Physics* **10**(3), 487–502 (1972)
- [30] Hamilton, M. F., Ilinskii, Y. A. & Zabolotskaya, E. A., "Acoustic streaming generated by standing waves in two-dimensional channels of arbitrary width". *J. Acoust. Soc. Am.* **113**(1), 153–160, 2003.
- [31] Hamilton, M. F., Ilinskii, Y. A. & Zabolotskaya, E. A., "Thermal effects on acoustic streaming in standing waves". *J. Acoust. Soc. Am.* **114**(6), 3092–3101, 2003.
- [32] F.H. Harlow, A.A. Amsden, "A numerical fluid dynamics calculation method for all flow speeds", *Journal of Computational Physics*, **8**, 197–213 (1971).
- [33] A. Harten, "High resolution schemes for hyperbolic conservation laws", *Journal of Computational Physics*, **49**, 357–393 (1983).

- [34] A. Harten, "On a class of high resolution total variation stable finite differences schemes", *SIAM Journal of Numerical Analysis*, **21**, 1–23 (1984).
- [35] A. Harten, B. Engquist, S. Osher and S. Chakravarthy, "Uniformly high order essentially non-oscillatory schemes, III", *Journal of Computational Physics*, **71**, 231–303 (1987). Aussi (reprint) : *Journal of Computational Physics*, **131**, 3–47 (1997)
- [36] O. Hireche, C. Weisman, D. Baltean-Carlès, P. Le Quéré, L. Bauwens, "Low Mach number analysis of idealized thermoacoustic engines with numerical solution", *J. Acoust. Soc. Am.* **128** (6), 3438–3448 (2010).
- [37] Omar Hireche, Islam Ramadan, Catherine Weisman, Hélène Bailliet, Yann Fraigneau, Diana Baltean-Carlès, Virginie Daru, "Experimental and numerical investigation of natural convection flows in two horizontal thermoacoustic cavities", *Int. J. Heat Mass Transfer* **149**, 119195 (2020).
- [38] C. W. Hirt, B.D. Nichols, "Volume of fluid (VOF) method for the dynamics of free boundaries", *Journal of Computational Physics*, **39**, 201-225 (1981).
- [39] X. Y. Hu, B. C. Khoo, N. A. Adams & F. L. Huang, "A conservative interface method for compressible flows", *J. Comput. Phys.* **219**, no. 2, p. 553-578 (2006).
- [40] A. Jameson, W. Schmidt, E. Turkel, "Numerical simulation of the Euler equations by finite volume methods using Runge-Kutta time stepping schemes", *AIAA Paper 81-1259*, AIAA 5th Computational Fluid Dynamics Conference (1981).
- [41] A. Jameson, "Transonic aerofoil calculations using the Euler equations", In P.L Roe (ed.), *Numerical Methods in Aeronautical Fluid Dynamics*, New York, Academic Press (1982).
- [42] G.S. Jiang, C.W. Shu, "Efficient implementation of weighted ENO schemes", *Journal of Computational Physics*, **126**, 202–228 (1996).
- [43] Josserand and S. Zaleski, "Droplet splashing on a thin liquid film", *Phys. Fluids* **15**, 1650 (2003).
- [44] D. Juric, G. Tryggvason, "Computations of boiling flows", *Int. J. Multiphase Flow* **24** (3) 387–410 (1998).
- [45] K. H. Kim, C. Kil, "Accurate, efficient and monotonic numerical methods for multidimensional compressible flows. Part II : Multidimensional limiting process.", *Journal of Computational Physics*, **126**, 570–615 (2005).
- [46] P. Kuszla and V. Daru, "Multifluid computation of droplets impact", *Sixteenth International Conference on Numerical Methods in Fluid Dynamics*, Lecture Notes in Physics Vol. 515, C.H. Bruneau ed., Springer (1998).
- [47] P. Kuszla and V. Daru, " Numerical simulation of high speed liquid jets", *4th World Congress on Computational Mechanics*, Buenos-Aires, Argentine, Juin 1998. Actes publiés sous la forme d'un CD-ROM (Computational Mechanics, S.R. Idelsohn et al eds., CIMNE-IACM).
- [48] P. D. Lax, B. Wendroff, "Systems of Conservation Laws", *Communications on Pure and Applied Mathematics*, **13**, 217–237 (1960).
- [49] B.P. Leonard, "The ULTIMATE conservative difference scheme applied to unsteady one-dimensional advection", *Computer Methods in Applied Mechanics and Engineering*, **88**, 17–74 (1991).
- [50] Le Quéré, P., Masson, R., Perrot, P., "A chebyshev collocation algorithm for 2d non-boussinesq convection". *J. Comput. Physics* **103**(2), 320–335 (1992)

- [51] P. Le Quéré, C. Weisman, H. Paillère, J. Vierendeels, E. Dick, R. Becker, M. Braack, J. Locke, "Modelling of natural convection flows with large temperature differences. Part 1 : reference solutions", *Math. Model. Numer. Anal.* **39** (3) 609–616 (2005).
- [52] A. Lerat, C. Corre, "A Residual-Based Compact Scheme for the Compressible Navier-Stokes Equations", *Journal of Computational Physics*, **170**, 642-675 (2001).
- [53] A. Lerat, C. Corre, "Residual-based compact schemes for multidimensional hyperbolic systems of conservation laws", *Computers & Fluids*, **31**, 639-661 (2002).
- [54] Lerat A., Sidès J., Daru V., "Efficient computation of steady and unsteady transonic flows by an implicit solver", *Advances in Computational Transonics*, W.G. Habashi ed., London : Pineridge Press (1985).
- [55] Lin, Y. & Farouk, B., "Heat transfer in a rectangular chamber with differentially heated horizontal walls : Effects of a vibrating sidewall". *Int. J. Heat Mass Transfer* **51**, 3179–3189 (2008).
- [56] Liu, X.-D., Osher, S. & Chan, T., "Weighted essentially non-oscillatory schemes", *Journal of Computational Physics* **115** : 200–212 (1994) .
- [57] L. Ma, C. Weisman, D. Baltean-Carlès, I. Delbende, L. Bauwens, "Effect of a resistive load on the starting performance of a standing wave thermoacoustic engine : A numerical study", *J. Acoust. Soc. Am.* **138** (2), 847–857 (2015).
- [58] Mardsen, O., Bailly, C. & Bogey, C. , "A study of infrasound propagation based on high-order finite difference solutions of the Navier–Stokes equations", *J. Acoust. Soc. Am.* **135**, 1083–1095 (2014).
- [59] C. Mariotti, "Lamb's problem with the lattice model Mka3D", *Geophys. J. Int.* **171**, p. 857-864 (2007).
- [60] Menguy, L. & Gilbert, J., "Non-linear Acoustic Streaming Accompanying a Plane Stationary Wave in a Guide". *Acta Acustica united with Acustica* **86** , 249–259 (2000).
- [61] Merkli, P. & Thomann, H., "Thermoacoustic effects in a resonance tube". *J. Fluid Mech.* **70** , 161–177 (1975).
- [62] Michel, G. & Chini, G. P., "Strong wave-mean-flow coupling in baroclinic acoustic streaming". *J. Fluid Mech.* **858**, 536–564 (2019).
- [63] Millet C., Robinet J.-C., Roblin C., "On using computational aeroacoustics for long-range propagation of infrasounds in realistic atmospheres", *Geophysical Research Letters*, **34**,L14814 (2007).
- [64] Christophe Millet, Virginie Daru, "Nonlinear propagation of acoustic-gravity waves from explosive sources in the atmosphere", *61st Annual Meeting of the APS Division of Fluid Dynamics*, November 23-25 2008, San Antonio, Texas, USA.
- [65] L. Monasse, V. Daru, C. Mariotti, S. Piperno, C. Tenaud, "A conservative coupling algorithm between a compressible flow and a rigid body using an Embedded Boundary method", *Journal of Computational Physics*, **231**, p. 2977–2994 (2012).
- [66] Solenn Moreau, Hélène Bailliet & Jean-Christophe Valière, "Measurements of inner and outer streaming vortices in a standing waveguide using laser doppler velocimetry", *J. Ac. Soc. America*, **123**, p. 640 (2008).
- [67] A. Mongruel, V. Daru, F. Feuillebois, S. Tabakova, "Early post-impact times dynamics of viscous drops onto a solid dry surface", *Physics of Fluids*, **21** : 032101(1-13) (2009).
- [68] W. F. Noh, "Fundamental methods of hydrodynamics", *Methods of computational physics*, vol. 3, p. 117-179, Methods of computational physics, Academic Press, New York/London, 1964.

- [69] Nyborg, W. L., "Acoustic streaming due to attenuated plane waves". *J. Acoust. Soc. Am.* **25**, 68–75 (1953)
- [70] Taku Ohwada, Yuki Shibata, Takuma Kato, Taichi Nakamura, "A simple, robust and efficient high-order accurate shock-capturing scheme for compressible flows : Towards minimalism", *Journal of Computational Physics*, **362**(1), 131-162 (2018).
- [71] Olson, J. R. & Swift, G. W., "Acoustic streaming in pulse tube refrigerators : Tapered pulse tubes", *Cryogenics*. **37**, 769–776 (1997).
- [72] Paolucci, S., "On filtering of sound from the Navier-Stokes equations", Sandia National lab. Report SAND 82-8257. Unpublished (1982)
- [73] C.S. Peskin, "Numerical analysis of blood flow in the heart", *J. Comput. Phys.* **25** 220–252 (1977).
- [74] H. Paillère, P. Le Quéré, C. Weisman, J. Vierendeels, E. Dick, "Modelling of natural convection flows with large temperature differences. Part 2 : contributions", *Math. Model. Numer. Anal.* **39** (3) 617–621 (2005).
- [75] Poignand, G., Lihoreau, B., Lotton, P., Gaviot, E., Bruneau, M., Gusev, V., "Optimal acoustic fields in compact thermoacoustic refrigerators". *Applied Acoustics* 68, 642–659 (2007).
- [76] Poignand, G., Lotton, P., Penelet, G., Bruneau, M., "Thermoacoustic, Small Cavity Excitation to Achieve Optimal Performance". *Acta Acustica united with Acustica* 97, 926–932 (2011).
- [77] Popinet S, Zaleski S., "A front-tracking algorithm for accurate representation of surface tension". *Int. J. Numer. Methods Fluids* **30**, 775–93 (1999).
- [78] Popinet S., "Numerical Models of Surface Tension", *Annual Review of Fluid Mechanics* **50**, 49–76 (2018).
- [79] Puscas M.A., Monasse L., Ern A., Tenaud C., Mariotti C., Daru V., "A time semi-implicit scheme for the energy-balanced coupling of a shocked fluid flow with a deformable structure". *J. Comput. Phys.*, 296 :241–262 (2015).
- [80] Lord Rayleigh, "On the circulation of air observed in Kundt tubes, and on some allied acoustical problems". *Philos. Trans. R. Soc. London* **175**, 1–21 (1884).
- [81] Reed J.W., Church H.W., Huck T.W., "Misty Picture weather-watch and microbarograph project", SAND87-2978C (1987).
- [82] Renardy Y., Renardy M., "PROST : a parabolic reconstruction of surface tension for the volume-of-fluid method", *J. Comput. Phys.* **183** 400–421 (2002).
- [83] Reyt Ida, "Écoulements induits en guide d'onde acoustique fort niveau", Thèse de Doctorat de l'Université de Poitiers, novembre 2012.
- [84] Reyt, I., Bailliet, H. & Valière, J.-C., "Experimental investigation of acoustic streaming in a cylindrical wave guide up to high streaming Reynolds numbers". *J. Acoust. Soc. Am.* **135** (1), 27–37 (2014).
- [85] Ida Reyt, Hélène Bailliet, Diana Baltean-Carlès, Virginie Daru, Solène Moreau, Jean-Christophe Valière, and Catherine Weisman, "Fast acoustic streaming in standing waves : Generation of an additional outer streaming cell", *Journal of the Acoustical Society of America*, **134**(3) : 1791–1801 (2013).
- [86] R. Rioboo, M. Marengo, C. Tropea, "Time evolution of liquid drop impact onto solid, dry surfaces", *Experiments in Fluids*, **33**, 112–124 (2002).

- [87] J.-Ch. Robinet, V. Daru and Ch. Tenaud, "Two-dimensional laminar shock wave / boundary layer interaction". *BAIL2004*, Toulouse, Juillet 2004.
- [88] P. L. Roe, "Approximate Riemann solvers, parameter vectors and difference schemes", *Journal of Computational Physics*, **43**, 357–372 (1981).
- [89] Rott, N., "The influence of heat conduction on acoustic streaming". *Zeitschrift für Angewandte Mathematik und Physik (ZAMP)* **25**, 417–421 (1974).
- [90] R. Sabatini, O. Mardsen, C. Bailly and O. Gainville, "Three-dimensional direct numerical simulation of infrasound propagation in the Earth's atmosphere", *Journal Fluid Mechanics*, **859**, p. 754–789 (2019).
- [91] Richard Saurel, Rémi Abgrall, "A Multiphase Godunov Method for Compressible Multi-fluid and Multiphase Flows", *Journal of Computational Physics*, **175**, 425–467 (1999).
- [92] Schuster, V. K. & Matz, W., "Über stationare Strömungen im Kundtschen Rohr (On Stationary Streaming in Kundt Tubes)". *Akust. Zeitschrift* **5**, 349–352 (1940).
- [93] Sethian J. A., "Level Set Methods : Evolving Interfaces in Geometry, Fluid Mechanics, Computer Vision and Materials Sciences", Cambridge University Press, 1999.
- [94] Seungwon Shin, S. I. Abdel-Khalik, Virginie Daru and Damir Juric, "Accurate representation of surface tension using the level contour reconstruction method", *Journal of Computational Physics*, **203** : 493–516 (2005).
- [95] C.W. Shu, S. Osher, "Efficient Implementation of Essentially Non-Oscillatory Shock-Capturing Schemes", *Journal of Computational Physics*, **77**, 439–471 (1988).
- [96] C.W. Shu, "Essentially Non-Oscillatory and Weighted Essentially Non-Oscillatory Schemes for Hyperbolic Conservation Laws", NASA/CR-97-206253 and ICASE Report 97-65 (1997).
- [97] S. Sikalo, C. Tropea, and E. N. Ganic, "Dynamic wetting angle of a spreading droplet", *Exp. Therm. Fluid Sci.* **29**, 795 (2005).
- [98] B. Sjogreen, H.C. Yee, "Grid convergence of high order methods for multiscale complex unsteady viscous compressible flows", *Journal of Computational Physics*, **185**, 1–26 (2003).
- [99] G. Strang, "On the construction and comparison of difference schemes", *SIAM Journal Numer. Anal.*, **5**, 506–517 (1968).
- [100] A. Suresh, H.T. Huynh, "Accurate Monotonicity-Preserving Schemes with Runge-Kutta Time Stepping", *Journal of Computational Physics*, **136**, 83–99 (1997).
- [101] S. Tekam, V. Daru, M. Demoulin, "Prediction of the efficiency of an automotive oil separator : comparison of numerical simulations with experiments", Diesel Particulate Systems, Engines and Components, and Performance Additives 2004, *SAE International Special Publication 1898*, 2004. Aussi SAE Technical Papers Series 2004-01-3019 (2004).
- [102] Tenaud, C., Podvin, B., Fraigneau, Y., Daru, V., "On wall pressure fluctuations and their coupling with vortex dynamics in a separated–reattached turbulent flow over a blunt flat plate", *International Journal of Heat and Fluid Flow*, **61**, pp. 730-748, (2016).
- [103] Thompson, M. W., Atchley, A. A. & Maccarone, M. J., "Influences of a temperature gradient and fluid inertia on acoustic streaming in a standing wave". *J. Acoust. Soc. Am.* **117**(4) 1839–1849 (2005).
- [104] Tryggvason G, Bunner B, Esmaeeli A, Juric D, Al-Rawahi N, et al., "A front-tracking method for the computations of multiphase flow". *J. Comput. Phys.*, **169** :708–59 (2001).
- [105] Unverdi SO, Tryggvason G., "A front-tracking method for viscous, incompressible, multi-fluid flows". *J. Comput. Phys.* **100** :25–37 (1992).

- [106] B. Van Leer, "Towards the Ultimate Conservative Difference Scheme. I. The Quest of Monotonicity.", in *Third International Conference on Numerical Methods in Fluid Mechanics*, Lecture Notes in Physics **18**, 163–168, Springer Verlag (1973).
- [107] B. Van Leer, "Towards the Ultimate Conservative Difference Scheme. II. Monotonicity and Conservation Combined in a Second-Order Scheme.", *Journal of Computational Physics* **14**, 361–370, (1974).
- [108] B. Van Leer, "Towards the Ultimate Conservative Difference Scheme. III. Upstream-Centered Finite Difference Schemes for Ideal Compressible Flow.", *Journal of Computational Physics* **23**, 263–275, (1977).
- [109] B. Van Leer, "Towards the Ultimate Conservative Difference Scheme. IV. A new approach to numerical convection.", *Journal of Computational Physics* **23**, 276–299, (1977).
- [110] B. Van Leer, "Towards the Ultimate Conservative Difference Scheme. V. A second order sequel to Godunov's method.", *Journal of Computational Physics* **32**, 101–136, (1979).
- [111] J. Von Neumann, R. D. Richtmyer, "A method for the numerical calculations of hydro-dynamical shocks", *Journal of Mathematical Physics*, **21** (1950).
- [112] Westervelt, P. J., "The Theory of Steady Rotational Flow Generated by a Sound Field". *J. Acoust. Soc. Am.* **25**, 60–67 (1953).
- [113] Yarin, A. L., "Drop impact dynamics : splashing, spreading, receding, bouncing...", *Ann. Rev. Fluid Mech.*, **38**, 159–192 (2006).

P. Kuszla, V. Daru.

" Numerical simulation of high-speed liquid jets ".

Computational Mechanics, New trends and applications, S. Idelsohn, E. Oñate and E. Dvorkin
(Eds.), CIMNE, ©Barcelona, Spain (1998).

NUMERICAL SIMULATION OF HIGH-SPEED LIQUID JETS

Patrick Kuszla, Virginie Daru

Laboratoire SINUMEF
Ecole Nationale Supérieure d'Arts et Métiers
151 Bd. de l'Hôpital, 75013 Paris, France
e-mail : kuszla@paris.ensam.fr, daru@paris.ensam.fr

Key Words: interface, numerical simulation, jet, impact, HLLE scheme

Abstract. *We propose a numerical method to calculate high speed liquid jets used in industrial applications. High speeds and pressures observed in jet cleaning or cutting lead us to consider the compressibility of the liquid. The flow is thus modelized using the Euler compressible equations. A stiffened gas equation of state is used for both the liquid, the ambient air and the material impacted by the jet.*

The numerical approach is fully Eulerian and captures automatically the interfaces. It is based on the method proposed by Abgrall [1] in the 1D case for multi-species perfect gases, which is here extended to take into account a stiffened gas equation of state in the multi-dimensional case.

Due to the large density ratios between liquids and gases, a robust and positively conservative scheme must be used to avoid the occurrence of unphysical values of the pressure. The HLLE scheme [2] is a good candidate, and is here extended in this multi-fluid context.

The multi-dimensional formulation uses a time splitting approach, solving alternately one-dimensional problems in each space direction. The energy equation is modified into a conservation equation for the longitudinal energy, avoiding numerical oscillations that can arise along slip lines.

The numerical method allows the computation of free and impacting jets. The results show a Mach 2.3 free jet and a jet impacting an aluminium plate.

1 INTRODUCTION

Since the fifties, high pressure and high speed jets prove their efficiency in many industrial fields. Technical advances allow the use of increasing jet pressures and velocities and even abrasive or liquid CO₂ jets [1]. The study of such jets, abrasive or not, and also of their impact is of great interest in many areas such as cutting (metal, wood, food, glass, explosives ...), cleaning (concrete, nuclear waste...), mining, rain erosion or surgery.

In [2] an experimental and theoretical investigation of compressible supersonic jets (referring to the speed of sound in the liquid) is presented. Such jets are produced by impulsively accelerating a packet of liquid through a nozzle [3]. For that kind of flow (which will be considered in the following), Field and Lesser describe the waves inside and outside the jet, its profile, the Taylor instability phenomenon and the Stokes drag on the droplet cloud surrounding the jet.

The numerical methods developed to calculate such flows are of two kinds : *front capturing* methods which treat automatically the interfaces without extra manipulations and *front tracking* methods which emphasize their Lagrangian aspect and explicitly follow the evolution of the topology.

Front tracking methods attempt to reduce the numerical diffusion by locating precisely the interfaces. The common characteristic of such methods is to point out the Lagrangian aspect of an interface whereas the other features of the flow are very often calculated in an Eulerian frame. Other methods adopt a fully Eulerian approach by using front capturing methods. We will retain this last option.

The direct extension of the numerical methods usually used in the context of gas dynamics to more complicated systems of conservation laws is not a trivial task. In multi-fluid flow calculations, two problems are typically encountered : oscillations around the interface even with a TVD (Total Variation Diminishing) scheme and non-positivity of the mass fractions. In [4], Larrouy proposed a solution to preserve the mass fraction positivity based on the structure of the exact solution of the Riemann problem. Karni [5] solved the two problems using a non conservative approach but which cannot handle strong shocks. Jenny, Müller and Thomann [6] used an *a posteriori* correction of the total energy using the primitive variables decoded from the fluxes values at the interfaces of the cells.

Abgrall [7] proposed a *quasi-conservative* approach. Observing a contact discontinuity, he showed that the oscillations come from a numerical incompatibility between the energy equation and the transport equation of the interface written in conservative form. He then proposed to solve the transport equation in non-conservative form in order to remove this incompatibility.

In the following we will extend this approach to fluids described by a stiffened gas equation of state in two and three dimensions.

2 GOVERNING EQUATIONS

We are interested in high-speed liquid jets such as those described in [2]. With such extreme pressures (more than 1000 bars) and speeds (1000 to 4000 ms⁻¹), the compressibility effects become noticeable and the most important physical process is the decompression of the compressed liquid. In such conditions, viscous and capillary effects will be neglected. Such a flow can be modeled using the compressible Euler equations. We hence solve three conservation laws for the mass (1), the momentum (2) and the total energy (3) :

$$\partial_t \rho + \nabla \cdot (\rho \mathbf{q}) = 0 \quad (1)$$

$$\partial_t (\rho \mathbf{q}) + \nabla \cdot (\rho \mathbf{q} \otimes \mathbf{q} + p \mathbb{I}) = 0 \quad (2)$$

$$\partial_t (\rho E) + \nabla \cdot (\rho (E + p) \mathbf{q}) = 0 \quad (3)$$

where ρ is the specific mass of the fluid, \mathbf{q} is its velocity which components are (u, v, w) , E is the total specific energy related to the internal specific energy by $E = e + \frac{1}{2} \mathbf{q} \cdot \mathbf{q}$ and p is the pressure.

This system of conservation laws must be closed by the choice of a suitable equation of state and by kinematic equations describing the motion of the interface. A stiffened gas equation of state will be used :

$$p + \gamma p_\infty = (\gamma - 1) \rho e \quad (4)$$

where p_∞ and γ are two constants specific to each material. This equation of state describes correctly the liquids and many other materials such as the metal impacted by the jet once in the plasticity domain. Moreover, the classical perfect gas equation of state is included in the stiffened gas equation by setting $p_\infty = 0$. Table 1 gives some examples of the values used to modelize different materials.

Air :	$p_\infty = 0$ Pa	$\gamma = 1.4$
Water :	$p_\infty = 6.00 \cdot 10^8$ Pa	$\gamma = 4.4$
Al :	$p_\infty = 2.63 \cdot 10^{10}$ Pa	$\gamma = 3.0$
Steel :	$p_\infty = 5.20 \cdot 10^{10}$ Pa	$\gamma = 3.17$

Table 1: Values of γ and p_∞ for different materials

Two parameters are needed to evaluate the pressure through this equation of state : γ and p_∞ . With the proposed modelization, the interface is only advected by the flow, therefore we must set two transport equations related to these two variables. The mixing of two different fluids in one cell is the source of a well known problem of fully conservative formulations ([5],[7]). With conservative kinematic equations, pressure oscillations around the interface may be responsible for the failure of the computations when they lead to non-physical values of the pressure. We will thus try to find two equations in non-conservative

form. As a guideline for the choice of these equations, we study the behaviour of a planar contact discontinuity, normal to the first space direction with null transverse velocities (*i.e* $v = w = 0$). In that case, all the y and z derivatives vanish and $\partial_t p = \partial_t u = \partial_x p = \partial_x u = 0$. Therefore the energy equation reduces to :

$$\partial_t \left(\frac{1}{\gamma - 1} \right) + u \partial_x \left(\frac{1}{\gamma - 1} \right) + \partial_t \left(\frac{\gamma p_\infty}{\gamma - 1} \right) + u \partial_x \left(\frac{\gamma p_\infty}{\gamma - 1} \right) = 0 \quad (5)$$

We can reproduce such a calculation for the other space directions, and the above equation suggests to solve the following transport equations :

$$\partial_t(\phi) + \mathbf{q} \nabla \cdot (\phi) = 0 \quad (6)$$

$$\partial_t(\Pi) + \mathbf{q} \nabla \cdot (\Pi) = 0 \quad (7)$$

where $\phi = \frac{1}{\gamma - 1}$ and $\Pi = \frac{\gamma p_\infty}{\gamma - 1}$.

Finally, the set of equations to solve is made of the three conservation laws (1) (2) and (3) and the kinematic equations (6),(7) which must be discretized so as to be consistent with the discretization of the energy equation. Moreover, we will see in the following that the conservation of total energy is numerically problematic and will not be maintained.

3 1-D NUMERICAL METHOD

We first address the mono-dimensional problem and assume $v = w = 0$ everywhere :

$$\partial_t W + \partial_x f(W) = 0 \quad (8)$$

with

$$W = \begin{Bmatrix} \rho \\ \rho u \\ \rho E \end{Bmatrix} \quad f(W) = \begin{Bmatrix} \rho u \\ \rho u^2 + p \\ (\rho E + p)u \end{Bmatrix}$$

and the kinematic equations are :

$$\partial_t \phi + u \partial_x \phi = 0 \quad (9)$$

$$\partial_t \Pi + u \partial_x \Pi = 0 \quad (10)$$

The system formed by the equations (8) and the kinematic equations (9,10) is hyperbolic and the eigenvalues of its Jacobian matrix are $\{u - a, u, u, u, u + a\}$, where a is the sound speed defined by :

$$a^2 = \frac{\gamma(p + p_\infty)}{\rho} \quad (11)$$

The choice of a numerical scheme is crucial, a fundamental property of the desired scheme is to keep all the variables in their domain of validity. This condition may be seen

as a kind of stability condition. Some experiments, with Roe's scheme [8] for example, revealed a domain of stability which cannot handle important density ratios in the general case. Roe's scheme exhibits non-physical states when solving liquid-gas shock tubes leading to negative pressures in gases. Therefore we must choose a more robust and positively conservative scheme. The HLLE scheme ([9],[10]) is a good candidate regarding to the expected properties.

We denote W_i^n the state vector at time $t_0+n\Delta t$ in the i^{th} cell, Δt and Δx are respectively the time and space steps. The HLLE scheme is written :

$$W_i^{n+1} = W_i^n - \frac{\Delta t}{\Delta x} \left(\tilde{f}_{i+\frac{1}{2}} - \tilde{f}_{i-\frac{1}{2}} \right) \quad (12)$$

where the numerical flux \tilde{f} is defined by :

$$\tilde{f}_{i+\frac{1}{2}} = \frac{b_{i+\frac{1}{2}}^+ f(W_i) - b_{i+\frac{1}{2}}^- f(W_{i+1})}{b_{i+\frac{1}{2}}^+ - b_{i+\frac{1}{2}}^-} + \frac{b_{i+\frac{1}{2}}^+ b_{i+\frac{1}{2}}^- (W_{i+1} - W_i)}{b_{i+\frac{1}{2}}^+ - b_{i+\frac{1}{2}}^-} \quad (13)$$

with

$$b_{i+\frac{1}{2}}^+ = \max\{b_{i+\frac{1}{2}}^r, 0\} \quad \text{et} \quad b_{i+\frac{1}{2}}^- = \min\{b_{i+\frac{1}{2}}^l, 0\} \quad (14)$$

$b_{i+\frac{1}{2}}^l$ and $b_{i+\frac{1}{2}}^r$ are an approximation of respectively the smallest and the largest wave speed of the exact solution of the Riemann problem solved at the interface $i + \frac{1}{2}$ (see for example [10] for the evaluation of these speeds in a perfect gas flow).

In our computations, the wave velocities were taken as :

$$b_{i+\frac{1}{2}}^l = \min\{u_{i+\frac{1}{2}}^{Roe} - c_{i+\frac{1}{2}}^{Roe}, u_i - c_i\} \quad \text{and} \quad b_{i+\frac{1}{2}}^r = \max\{u_{i+\frac{1}{2}}^{Roe} + c_{i+\frac{1}{2}}^{Roe}, u_{i+1} + c_{i+1}\} \quad (15)$$

where $u_{i+\frac{1}{2}}^{Roe}$ and $c_{i+\frac{1}{2}}^{Roe}$ are derived from the usual Roe averages $\bar{\alpha}_{i+\frac{1}{2}} = \frac{\sqrt{\rho_i} \alpha_i + \sqrt{\rho_{i+1}} \alpha_{i+1}}{\sqrt{\rho_i} + \sqrt{\rho_{i+1}}}$:

$$u_{i+\frac{1}{2}}^{Roe} = \bar{u}_{i+\frac{1}{2}} \quad \text{and} \quad \left(c_{i+\frac{1}{2}}^{Roe} \right)^2 = \frac{\bar{H}_{i+\frac{1}{2}} - \frac{1}{2} \bar{u}_{i+\frac{1}{2}}^2}{\bar{\phi}_{i+\frac{1}{2}}} \quad (16)$$

where H denotes the total enthalpy $H = E + p/\rho$.

We now need a proper discretization of the kinematic equations written in non-conservative form. To this end, we consider the particular case of an interface located at $x_{i+\frac{1}{2}}$ at time $t_0 + n\delta t$, *i. e.* the velocity u and the pressure p are constant. We denote δ^b the difference operator $\delta_{i+\frac{1}{2}}^b \alpha = b_{i+\frac{1}{2}}^+ \alpha_i - b_{i+\frac{1}{2}}^- \alpha_{i+1}$ and we observe the evolution of this interface after one time step, keeping in mind that p et u must remain constant. From the continuity equation and the momentum equation we can conclude that

$$u_i^{n+1} = u_i^n = u \quad (17)$$

The energy equation, setting all the simplifications due to the particular case of an interface, reads :

$$\begin{aligned} \left[\begin{array}{c} p\phi \\ +\Pi \end{array} \right]_i^{n+1} &= \left[\begin{array}{c} p\phi \\ +\Pi \end{array} \right]_i^n \\ -\frac{\Delta t}{\Delta x} \left\{ \left[\begin{array}{c} up\delta^b(\phi)_{i+\frac{1}{2}} + pb_{i+\frac{1}{2}}^+ b_{i+\frac{1}{2}}^- \delta(\phi)_{i+\frac{1}{2}} \\ +u\delta^b(\Pi)_{i+\frac{1}{2}} + b_{i+\frac{1}{2}}^+ b_{i+\frac{1}{2}}^- p\delta(\Pi)_{i+\frac{1}{2}} \end{array} \right] \frac{1}{b_{i+\frac{1}{2}}^+ - b_{i+\frac{1}{2}}^-} \right. \\ &\quad \left. - \left[\begin{array}{c} up\delta^b(\phi)_{i-\frac{1}{2}} + pb_{i-\frac{1}{2}}^+ b_{i-\frac{1}{2}}^- \delta(\phi)_{i-\frac{1}{2}} \\ +u\delta^b(\Pi)_{i-\frac{1}{2}} + b_{i-\frac{1}{2}}^+ b_{i-\frac{1}{2}}^- p\delta(\Pi)_{i-\frac{1}{2}} \end{array} \right] \frac{1}{b_{i-\frac{1}{2}}^+ - b_{i-\frac{1}{2}}^-} \right\} \end{aligned} \quad (18)$$

(18) shows that the pressure may be kept constant provided that the kinematic equations are discretized in the following way :

$$(\phi)_i^{n+1} = (\phi)_i^n - \frac{\Delta t}{\Delta x} \left\{ \frac{u_i \delta^b(\phi)_{i+\frac{1}{2}} + b_{i+\frac{1}{2}}^+ b_{i+\frac{1}{2}}^- \delta(\phi)_{i+\frac{1}{2}}}{b_{i+\frac{1}{2}}^+ - b_{i+\frac{1}{2}}^-} - \frac{u_i \delta^b(\phi)_{i-\frac{1}{2}} + b_{i-\frac{1}{2}}^+ b_{i-\frac{1}{2}}^- \delta(\phi)_{i-\frac{1}{2}}}{b_{i-\frac{1}{2}}^+ - b_{i-\frac{1}{2}}^-} \right\} \quad (19)$$

$$(\Pi)_i^{n+1} = (\Pi)_i^n - \frac{\Delta t}{\Delta x} \left\{ \frac{u_i \delta^b(\Pi)_{i+\frac{1}{2}} + b_{i+\frac{1}{2}}^+ b_{i+\frac{1}{2}}^- \delta(\Pi)_{i+\frac{1}{2}}}{b_{i+\frac{1}{2}}^+ - b_{i+\frac{1}{2}}^-} - \frac{u_i \delta^b(\Pi)_{i-\frac{1}{2}} + b_{i-\frac{1}{2}}^+ b_{i-\frac{1}{2}}^- \delta(\Pi)_{i-\frac{1}{2}}}{b_{i-\frac{1}{2}}^+ - b_{i-\frac{1}{2}}^-} \right\} \quad (20)$$

4 EXTENSION TO MULTI-DIMENSIONS

The extension to multi-dimensions uses a time splitting approach, leading to solve alternately 1-D problems in each space direction. In this part we will consider the first operator in the x direction (the same results can be derived for the other operators). It reads :

$$\partial_t W + \partial_x f(W) = 0 \quad (21)$$

with

$$W = \begin{Bmatrix} \rho \\ \rho u \\ \rho v \\ \rho w \\ \rho E \end{Bmatrix} \quad f(W) = \begin{Bmatrix} \rho u \\ \rho u^2 + p \\ \rho uv \\ \rho uw \\ (\rho E + p)u \end{Bmatrix}$$

and the kinematic equations are :

$$\partial_t \phi + u \partial_x \phi = 0 \quad (22)$$

$$\partial_t \Pi + u \partial_x \Pi = 0 \quad (23)$$

The system formed by (21) and (22,23) is hyperbolic and the eigenvalues of its Jacobian matrix are $\{u - a, u, u, u, u, u, u + a\}$.

In the multi-dimensional case, we encounter another numerical difficulty when dealing with slip lines (which already exists in the single fluid case). To illustrate it, we consider a planar interface orthogonal to the x axis located at $x_{i+\frac{1}{2}}$, the transverse velocities v and w are now non-zero and can be different on each side of the interface. The conservation of energy equation is hence written :

$$\partial_t \left(\frac{v^2 + w^2}{2} + \frac{p}{\gamma - 1} + \frac{\gamma p_\infty}{\gamma - 1} \right) + u \partial_x \left(\frac{v^2 + w^2}{2} + \frac{p}{\gamma - 1} + \frac{\gamma p_\infty}{\gamma - 1} \right) = 0 \quad (24)$$

Equation (24) exhibits a non-linear term that will be referred as the transverse kinetic energy : $e_{ct} = \frac{v^2 + w^2}{2}$ whereas $e_{cl} = \frac{u^2}{2}$ will be called the longitudinal kinetic energy. Those transverse terms are the cause of oscillations along slip lines. This problem, mentionned in [7] by Abgrall can be eliminated by solving an additional transport equation for e_{ct} ¹ as proposed by Saurel [11]. Figure 1 explains the origin of these oscillations : we consider a moving slip plane orthogonal to the x axis with transverse velocities v_1 and $-v_2$. After a few time steps, the velocity field exhibits a diffused profile and a corresponding diffused profile of transverse kinetic energy. But if a transport equation for e_{ct} is used, the profile of transverse kinetic energy obtained is generally different.

Instead of solving an additional equation for e_{ct} , we here propose a simpler approach, in which we subtract the tranport equation for e_{ct} from the energy equation. This results in solving a conservation equation for the "longitudinal" total energy :

$$\partial_t (\rho E_l) + \partial_x ((\rho E_l + p) u) = 0 \quad (25)$$

where $E_l = e + \frac{u^2}{2} = E - e_{ct}$.

The vectors W and $f(W)$ become:

$$W = \begin{Bmatrix} \rho \\ \rho u \\ \rho v \\ \rho w \\ \rho E_l \end{Bmatrix} \quad f(W) = \begin{Bmatrix} \rho u \\ \rho u^2 + p \\ \rho u v \\ \rho u w \\ (\rho E_l + p) u \end{Bmatrix}$$

With these equations, the diffusion of the transverse velocities does not pollute the total energy. Hence the slip lines are correctly captured which is far for being true with an equation for the complete total energy. In fact, numerical experiments in the case of shock tubes show that this formulation allow the correct restitution of the shock

¹From the actually solved equations $\partial_t(\rho v) + \partial_x(\rho u v) = 0$ and $\partial_t(\rho w) + \partial_x(\rho u w) = 0$ one can derive the transport equation of e_{ct} : $\partial_t(\rho e_{ct}) + \partial_x(\rho u e_{ct}) = 0$.

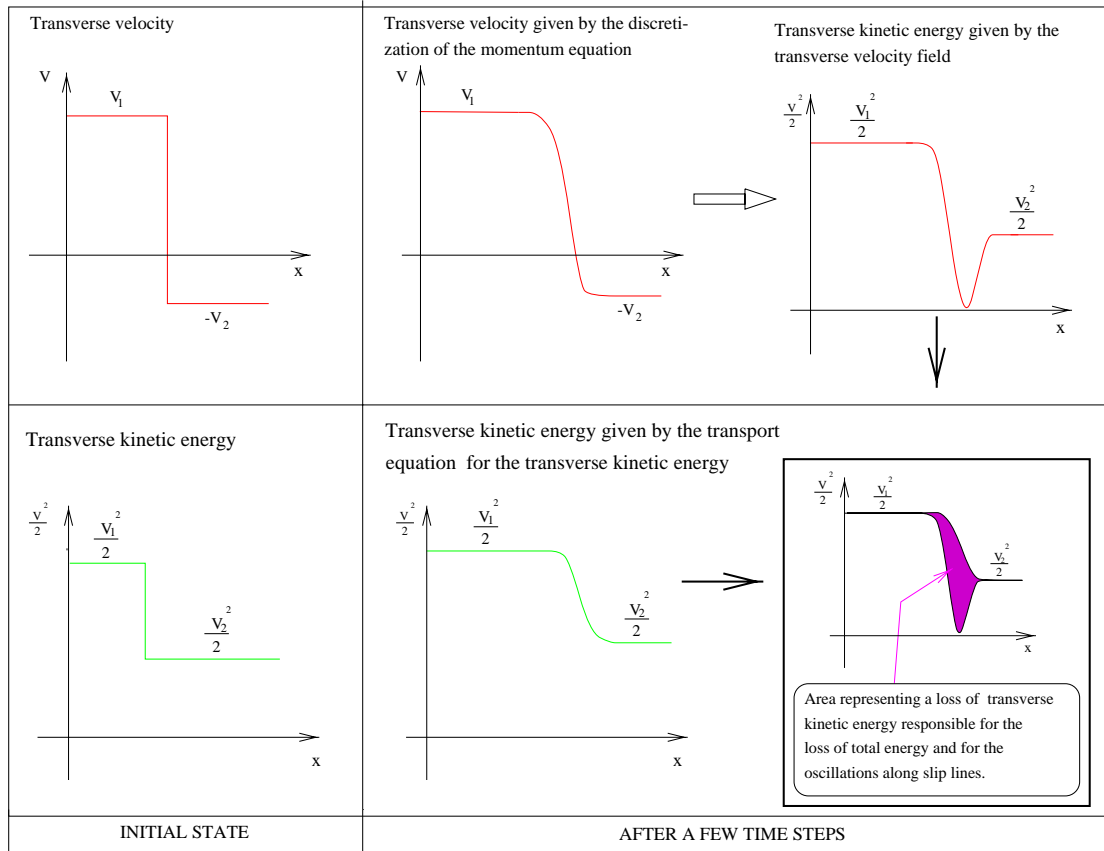


Figure 1: Comparison between the transverse kinetic energy fields obtained with a transport equation for e_{ct} and with the transverse velocity field coming from the the momentum equation. Case of a slip plane orthogonal to the x axis with transverse velocities v_1 and $-v_2$.

velocities whereas the conservation of total energy leads to wrong shock velocities and strong oscillations around slip lines.

Each splitted operator has a different longitudinal total energy (respectively $e + \frac{u^2}{2}$, $e + \frac{v^2}{2}$ and $e + \frac{w^2}{2}$). As a consequence this energy must be set before each spatial step. In these conditions the total energy E cannot be conserved. The loss of energy is due precisely to the difference between the transverse kinetic energy given by a transport equation and the transverse kinetic energy coming from the velocity field as is illustrated in figure (1).

5 RESULTS

5.1 Free water jet

We compute the flow of a 2-D supersonic water jet. The first order HLLE scheme is extended to second order via MUSCL extrapolation as in [7]. A detailed description of the wave pattern observed inside and outside the jet is given in [2]. In figure 2 are depicted the main features of the early time behaviour of a supersonic jet. The frontal and side relief waves carry the decompression from the ambient state around the jet to the liquid interior. One can also notice two corner waves coming from the edges of the jet. A shock wave propagates in the air surrounding the jet.

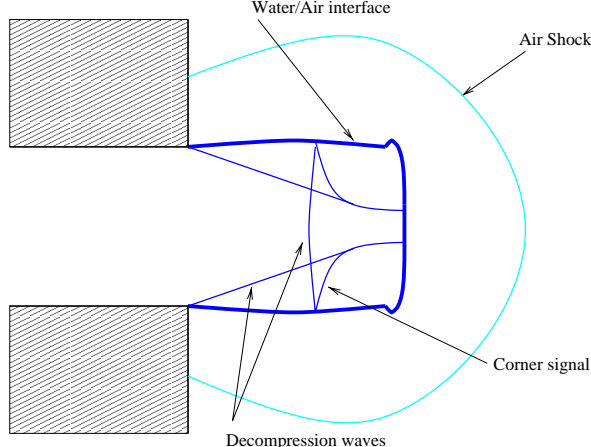


Figure 2: Wave pattern of a supersonic jet

The initial conditions for this case are :

	ρ (kg m ⁻³)	u (ms ⁻¹)	v (ms ⁻¹)	p (Pa)	γ	p_∞ (Pa)
Jet entry	1040.0	4000.0	0.0	10^8	4.4	$6.0 \cdot 10^8$
Air	1.2	0.0	0.0	10^5	1.4	0.0

The results presented in figure 3 are in good agreement with the expected wave pattern described by Field and Lesser. The gradient of the density is plotted, simulating numerically the Schlieren images that could be obtained experimentally. The frontal decompression wave presents some oscillations that are increasing with the time step. The interface is smeared over about 10 cells since the HLLE scheme is very diffusive.

5.2 Impacting water jet

We now compute the flow of a 2-D supersonic water jet impacting an aluminum plate. The initial conditions for this case are :

	ρ (kg m ⁻³)	u (ms ⁻¹)	v (ms ⁻¹)	p (Pa)	γ	p_∞ (Pa)
Jet entry	1040.0	1800.0	0.0	10^8	4.4	$6.0 \cdot 10^8$
Aluminum plate	2785.0	0.0	0.0	10^5	3.0	$2.63 \cdot 10^{10}$
Air	1.2	0.0	0.0	10^5	1.4	0.0

The results for this case are presented in figure 4. As expected the wave pattern inside the jet is similar to the previous case. The corner waves and the decompression waves are visible. The impact of the jet give rise to two shock waves. One is clearly visible and is propagating upstream in the jet. The second one is propagating inside the aluminum plate and is visible at $t = 2.6148 \cdot 10^{-4}$ s. The deformation of the plate is accompanied by lateral jets which trajectory is deviated by the shape of the impacted plate.

6 CONCLUSION

We proposed a numerical method to calculate multi-fluid flows involving materials described by a stiffened gas equation of state. The problem of the pressure oscillations occurring at the interfaces was solved generalizing the quasi-conservative approach proposed in [7]. The HLLE scheme was extended to this context allowing the computation of flows with large density ratios and avoiding problematic non-physical states. The application to free and impacting supersonic water jets gives encouraging results.

However, our computations did not take into account any phase change since cavitation zones may appear in the jet. In fact, the pressure field allows us to detect the regions where one can expect the onset of cavitation.

The main drawback of the method is the numerical diffusion of the selected scheme which is a counterpart of its robustness. The calculated interfaces may be 10 cells wide or more. This phenomenon limits the efficiency of the code but could be limited by the use of an adaptative mesh refinement strategy. With such an approach, the grid is refined only where the solution needs it and evolves according to it.

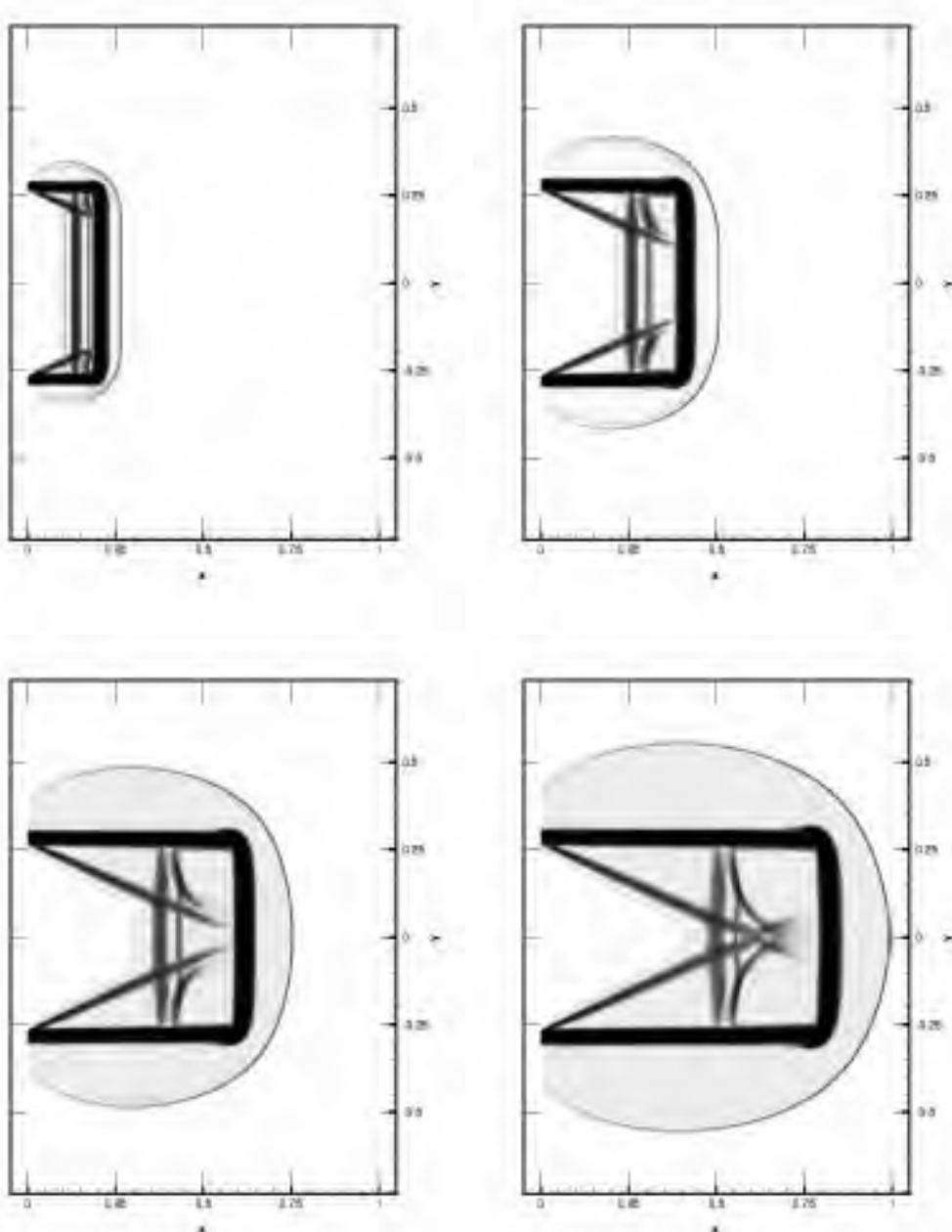


Figure 3: Numerical Schlieren images of a Mach 2.3 free jet from $t = 4.97 \cdot 10^{-5} s$ to $t = 2.21 \cdot 10^{-4} s$, (400x400 grid for a half domain)

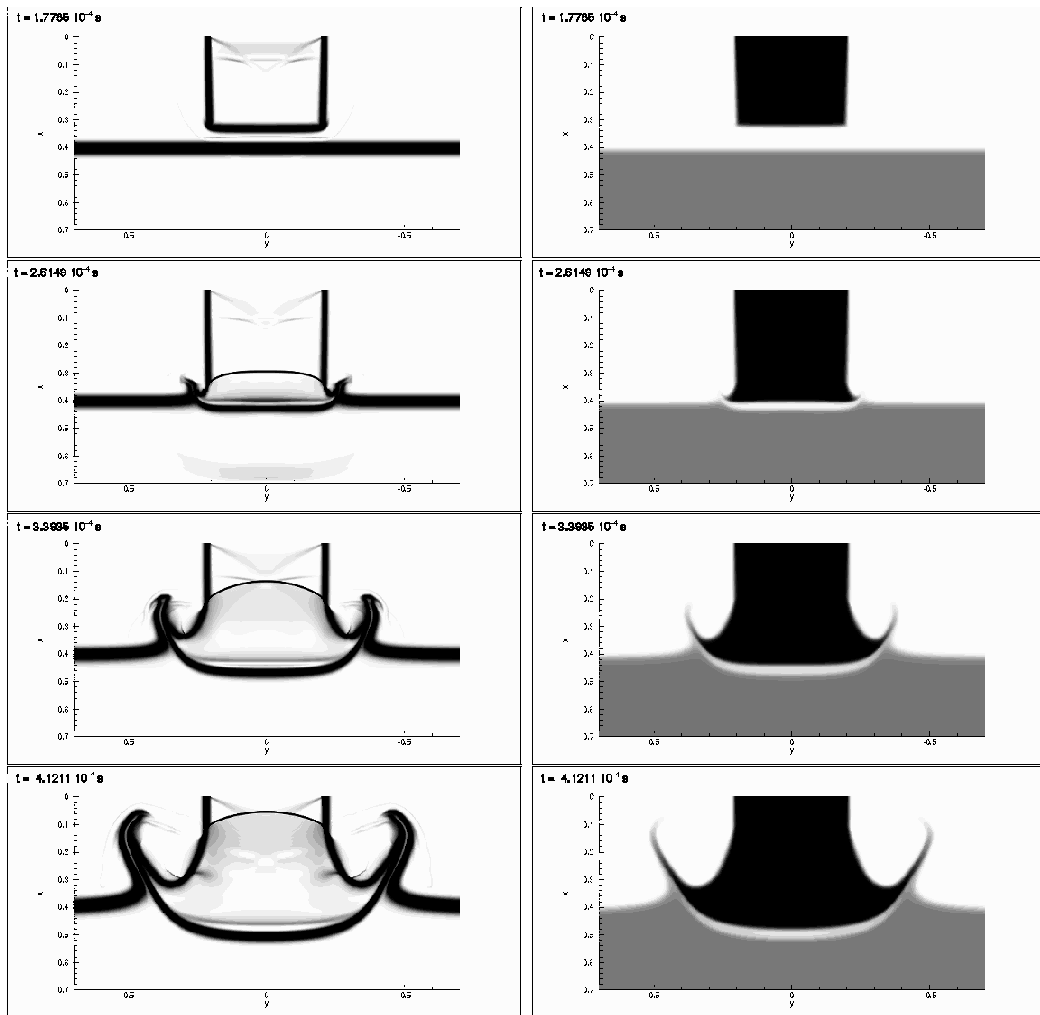


Figure 4: Numerical Schlieren images (on the left) and isovalues of γ (on the right) of a water jet impacting an aluminum plate (400x400 grid for a half domain)

REFERENCES

- [1] Summers D. From brute force to intelligent use - the birth of a new technology. *Proceeding of 13th International Conference on Jet Cutting Technology*, pages 183–192 (1996).
- [2] Field J. E. et Lesser M. B. On the mechanics of high speed liquid jets. *Proc. R. Soc. Lond.*, **357**, 143–162 (1977).
- [3] Glenn L. A. The mechanics of the impulsive water cannon. *Computers and Fluids*, **3**, 197–215 (1977).
- [4] Larroutrou B. How to preserve the mass fractions positivity when computing compressible multi-component flows. *J. Comput. Phys.*, **95**, 59–84 (1991).
- [5] Karni S. Multi-component flow calculations by a consistent primitive algorithm. *J. Comput. Phys.*, **112**, 31–43 (1994).
- [6] Thomann H. Jenny p., Müller B. Correction of conservative euler solvers for gas mixtures. *J. Comput. Phys.*, **132**, 91–107 (1997).
- [7] Abgrall R. How to prevent pressure oscillations in multicomponent flow calculations : a quasi-conservative approach. *J. Comput. Phys.*, **125**, 150–160 (1996).
- [8] Roe P. L. Approximate riemann solvers, parameter vectors and difference schemes. *J. Comput. Phys.*, **53**, 357–372 (1981).
- [9] Einfeldt B. On godunov methods for gas dynamics. *SIAM J. Numer. Anal.*, **25**, 294–318 (1988).
- [10] Munz C. D. Einfeldt B. and Sjögreen B. Godunov-type methods near low densities. *J. Comput. Phys.*, **92**, 273–295 (1991).
- [11] Saurel R. Private communication. (1997).

V. Daru, C. Tenaud.

" High order one-step monotonicity-preserving schemes for unsteady compressible flows calculations ".

Journal of Computational Physics 193, p. 563-594 (2004).



Available online at www.sciencedirect.com

SCIENCE @ DIRECT®

Journal of Computational Physics 193 (2004) 563–594

JOURNAL OF
COMPUTATIONAL
PHYSICS

www.elsevier.com/locate/jcp

High order one-step monotonicity-preserving schemes for unsteady compressible flow calculations

V. Daru ^{a,b}, C. Tenaud ^{b,*}

^a ENSAM, 151 Boulevard de l'Hôpital, 75013 Paris, France

^b LIMSI – CNRS, B.P. 133, Campus d'Orsay, F-91403 Orsay Cedex, France

Received 12 November 2002; received in revised form 12 August 2003; accepted 14 August 2003

Abstract

This paper deals with the development of accurate one-step schemes for the numerical simulation of unsteady compressible flows. Pursuing our work in Daru and Tenaud [V. Daru, C. Tenaud, Comput. Fluids 30 (2001) 89] where third-order schemes were considered, we follow the Lax-Wendroff approach to develop high order TVD combined time-space schemes by correcting the successive modified equations. In the scalar case, TVD schemes accurate up to seventh order (OSTVD7) in time and space are obtained (in smooth regions and away from extrema). To avoid the clipping and the loss of accuracy that is common to the TVD schemes near extrema, we develop monotonicity-preserving (MP) conditions derived from Suresh and Huynh [A. Suresh, H.T. Huynh, J. Comput. Phys. 136 (1997) 83] to locally relax the TVD limitation for this family of one-step schemes. Numerical results for long time integration in the scalar case show that the MP one-step approach gives the best results compared to several multistage schemes, including WENO schemes. The extension to systems and to the multidimensional case is done in a simplified way which does not preserve the scalar order of accuracy. However we show that the resulting schemes have a very low level of error. For validation, the present algorithm has been checked on several classical one-dimensional and multidimensional test cases, including both viscous and inviscid flows: a moving shock wave interacting with a sine wave, the Lax shock tube problem, the 2D inviscid double Mach reflection and the 2D viscous shock wave-vortex interaction. By computing these various test cases, we demonstrate that very accurate results can be obtained by using the one-step MP approach which is very competitive compared to multistage high order schemes.

© 2003 Elsevier B.V. All rights reserved.

Keywords: High order scheme; Unsteady flows; Compressible flows; Shock capturing scheme

1. Introduction

In the high speed flow regime, many aerodynamic configurations involve interactions between shock waves and turbulence such as, for instance, within air intakes where shock wave-turbulent boundary

* Corresponding author. Tel.: +33-1-6985-8130; fax: +33-1-6985-8088.

E-mail address: tenaud@limsi.fr (C. Tenaud).

layer or shock wave-shear layer interactions occur. An accurate prediction of such interactions is of importance in effective design of supersonic vehicles since they greatly affect the aerodynamic loads. At the present time, it is commonly admitted that large Eddy simulation (LES) is a highly promising technique for the prediction of complex shock wave turbulence interactions including large-scale flow phenomena such as those encountered in engineering applications [8,12]. Recent CFD predictions of shock wave turbulent boundary layer interactions is summarized in [12]. A review of the LES of compressible flows can also be found in [16]. It is well known that, in the LES approach, the numerical scheme must have low dissipation to minimize the interaction with the subgrid scale model. In the past, high order accurate schemes, like spectral ([3,4,18]) or Padé schemes ([14,17]), have been identified as suitable tools for LES. Nevertheless, in the transonic and supersonic flow regimes when dealing with flows involving shock waves, one must use a numerical scheme which can both represent small scale structures with the minimum of numerical dissipation, and capture discontinuities with the robustness that is common to Godunov-type methods. To achieve this dual objective, high order accurate shock capturing schemes must be employed. However, as pointed out by Titarev and Toro [26], the design of high order accurate numerical schemes for hyperbolic conservation laws is a formidable task since three major difficulties have to be overcome: ensuring the conservation property, preserving the high order of accuracy in both time and space and controlling the generation of the spurious oscillations in the vicinity of discontinuities.

At present, the numerical methods generally employed can basically be divided into two approaches: a coupled time and space (one-step) approach and separate time and space integrations. On the one hand, the methods for which time and space are considered separately, are generally based on a multistage time integration. The most recent highly accurate separate time-space methods use a Runge–Kutta type time discretization. In each stage of the time integration, a high order spatial discretization equipped with a shock capturing technique is applied ensuring non-oscillatory and conservation properties. As the spatial support of the high order reconstruction is relatively large, the global stencil of a decoupled time-space scheme is much larger than that of a coupled time-space approach for the same order of accuracy since the space discretization is applied in each sub-step of the time integration. Following that approach, one does not control the total truncation error of the scheme and the limiting process acts only on the space discretization while the time integration stays invariant. Moreover, it is not possible to reach very high order of accuracy in time without introducing spurious oscillations. For instance, using a Runge–Kutta method, the TVD property cannot be recovered for an accuracy greater than fifth order. To recover the TVD property for the fourth and fifth order, one needs to solve adjoint problems during the sub-steps, which is very expensive. On the other hand, the coupled time and space schemes are preferably developed on a Lax–Wendroff type approach. The schemes constructed in this way use a minimum stencil. As will be shown, this approach is also very attractive for controlling the total truncation error (at least in the scalar case), and deriving optimal non-oscillatory conditions. However the extension to non-linear systems of equations is not trivial, and the integration of source terms is delicate.

Whatever the approach (coupled or decoupled), an ad hoc discontinuity-capturing feature must be employed to limit the spurious oscillations in the vicinity of the strong gradient regions. Among the shock capturing techniques found in the literature, total variation diminishing (TVD) schemes are generally considered to be well suited for the capture of shock waves but too diffusive in smooth regions, due to the limitation of the accuracy to first order near extrema. More recent schemes like the ENO/WENO [10,20–23] family are very accurate in smooth regions but show a diffusive behavior in the vicinity of discontinuities. Also, these schemes are very expensive in terms of CPU time (for example the high order WENO schemes turns out to be too costly to be used for grid convergence studies in several cases reported in [24]). A WENO reconstruction was also used recently in the ADER approach by Titarev and Toro [26], together with a coupled time-space integration. However, it is likely that the scheme might suffer from the same drawbacks as the WENO schemes.

Another successful approach has recently been developed in [25] to enlarge the TVD constraint for a better representation near extrema. The development has been performed on a separate time and space integration by using a high order polynomial fixed stencil reconstruction and Runge–Kutta time stepping. The reconstructed values at the interfaces of the mesh cells are then limited such as to preserve both monotonicity and high order accuracy. This is achieved by using local geometrical considerations to relax the monotonicity constraints near extrema. This limiting strategy has then been extended to the WENO family of schemes in [2], in order to avoid the oscillations which sometimes can develop with high order WENO reconstructions. However, in some sense this negates the key ingredient of the WENO schemes, which is the use of a variable stencil to obtain a non-oscillatory reconstruction.

In this paper, our aim is to show that, contrary to the commonly admitted opinion, very accurate and efficient one-step schemes can be developed in the TVD framework. We retain the coupled time and space approach and a fixed stencil to develop highly accurate numerical schemes that can be rendered TVD or monotonicity preserving with control over the total truncation error. Being one-step, these schemes are very efficient. Pursuing our work in [7] where third-order schemes were considered, we obtain higher order schemes by correcting the error terms at the desired order in the equivalent equation. The implementation of these schemes is very simple as the increase of accuracy can be obtained via a change of an “accuracy function” applied to a classical second-order scheme. The schemes can then recover the TVD property by applying a limitation on this specific function. In the scalar case, TVD schemes accurate up to the seventh order in time and space are obtained in smooth regions and away from extrema. These schemes have however a tendency to clip extrema, a drawback which is inherent in all TVD schemes. By highlighting the geometric significance of the TVD constraints, we develop monotonicity-preserving (MP) conditions derived from [25] to relax the TVD limitation near extrema for this family of one-step schemes. We thus obtain very accurate non-oscillatory results. Comparisons are made in the scalar case with the Runge–Kutta scheme developed in [25], which turn out in favor of the one-step approach. The latter has better control over the total dissipation of the scheme, while a multistage approach controls only the spatial dissipation. Moreover, the cost (in terms of CPU time) of the one-step scheme is much lower. In the 1D scalar case, it appears that our one-step schemes are very similar to those proposed by Leonard [15] for solving the advection equation, although the formulation and the method of construction are quite different (Leonard uses high order characteristic interpolations). To our knowledge, this study has however remained restricted to the 1D linear scalar case, and was not extended to flow computations. We also believe that the TVD formulation that we use here is better adapted for generalizations to the case of non-linear systems. Though the extensions to systems of equations and to multidimensions are not trivial when using a coupled time and space integration, we propose an extension of the present scheme to the Euler and Navier–Stokes equations, based on the classical Roe flux difference splitting and dimensional splitting. The resulting schemes are only second-order accurate, but they are very economical in terms of CPU time and their level of error is very low as shown by convergence studies, making them attractive for use in cases where it is not possible to use very fine meshes (for example in LES calculations where all the length scales are not fully resolved).

This study is limited to uniform cartesian meshes. The extension of the one-step schemes to general curvilinear meshes can be done using a classical coordinate transformation. If the transformation is not sufficiently smooth, the good properties of the schemes can of course deteriorate, but this is a problem common to all approaches (for example the high order finite difference ENO/WENO schemes can apply only to uniform or smoothly varying grids; multidimensional finite volume schemes do not share this drawback but are very complicated and costly, see [5,23]). The dimensional splitting we use in the multi-dimensional case is not applicable to unstructured meshes. This is indeed a disadvantage, but structured meshes are still widely used for CFD studies.

The paper is organized as follows: in Section 2, we consider the scalar case. We construct the one-step high order schemes, and derive the TVD and MP versions of these schemes. The multistage approach is also

presented in the TVD context for comparison. We then extend the one-step scheme to the Euler and Navier–Stokes equations in Section 3. In Section 4 convergence studies and numerical results for various 1D and 2D test cases are presented, demonstrating that very accurate results can be obtained by using the one-step MP approach.

2. High order schemes: the scalar case

To present the numerical schemes we developed in this study, we first focus on the solution $u(x, t)$ of the linear scalar transport equation

$$u_t + f(u)_x = 0 \quad (1)$$

with $f(u) = au$, a being the velocity which is supposed to be constant. For simplicity, we will suppose in the following that $a > 0$. The case $a < 0$ can however be treated by symmetry relative to each cell interface. In view of the discretization of this equation, we will denote by δt and δx the time step and cell width, respectively. u_j^n will denote the numerical solution at time $t = t_0 + n \cdot \delta t$ and position $x = x_0 + j \cdot \delta x$.

In the following, we present the development of the coupled time–space one-step schemes. In order to draw a parallel with the one-step scheme and to also highlight the differences, the separate space-time discretization will also be presented though this is a classical approach.

2.1. Development of high order one-step schemes

2.1.1. Unlimited schemes

The one-step approach is of the Lax–Wendroff type [13], i.e., the time Taylor series expansion is used to express u_j^{n+1} and the time derivatives are substituted with space derivatives using the exact equation. The construction of such schemes can equivalently be obtained by correcting the successive error terms of the modified equations to increase the order of accuracy of the schemes. In this way, we obtain high order accurate schemes relative to both time and space. To begin, let us consider the Lax–Wendroff scheme:

$$u_j^{n+1} = u_j^n - \frac{\delta t}{\delta x} (F_{j+1/2}^{lw} - F_{j-1/2}^{lw}), \quad (2)$$

where $F_{j+1/2}^{lw}$ is the numerical flux:

$$F_{j+1/2}^{lw} = f_j^n + \frac{(1-v)}{2} (f_{j+1}^n - f_j^n) \quad (3)$$

and v is the CFL number $v = a(\delta t/\delta x)$. The modified equation for this scheme reads:

$$u_t + f(u)_x = a \frac{\delta x^2}{6} (v^2 - 1) u_{xxx}. \quad (4)$$

By subtracting from the Lax–Wendroff scheme an upwind term formed by discretizing the right-hand side of (4), one obtains the classical third-order upwind-biased scheme with a numerical flux which can be written:

$$F_{j+1/2}^3 = f_j^n + \frac{(1-v)}{2} \left(f_{j+1}^n - f_j^n - \frac{1+v}{3} (f_{j+1}^n - 2f_j^n + f_{j-1}^n) \right). \quad (5)$$

For convenience, this numerical flux can be recast in the following form:

$$F_{j+1/2}^3 = f_j^n + \Phi_{j+1/2}^3 \frac{(1-v)}{2} (f_{j+1}^n - f_j^n) \quad (6)$$

with

$$\Phi_{j+1/2}^3 = 1 - \frac{1+v}{3}(1 - r_{j+1/2}) \quad (7)$$

and $r_{j+1/2} = (u_j^n - u_{j-1}^n)/(u_{j+1}^n - u_j^n)$. Thus, the third-order scheme is expressed in the usual form of a second-order flux limiter scheme, and the Φ function plays the role of an accuracy function.

Following such successive corrections of the higher order error terms, one can construct schemes of arbitrarily high o-th order of accuracy, whose numerical flux can be written in the generic form

$$F_{j+1/2}^o = f_j^n + \Phi_{j+1/2}^o \frac{(1-v)}{2} (f_{j+1}^n - f_j^n) \quad (8)$$

depending only on the function $\Phi_{j+1/2}^o$ which drives the o-th order of accuracy of the scheme.

For example, to construct the function Φ^4 , we derive the modified equation of the third-order scheme, which reads:

$$u_t + f(u)_x = a \frac{\delta x^3}{24} (v^2 - 1)(2 - v) u_{xxxx} \quad (9)$$

and subtract from the scheme a term formed by discretizing the RHS of (9). In this way we obtain the function Φ^4 corresponding to a fourth-order (in time and space) scheme:

$$\Phi_{j+1/2}^4 = \Phi_{j+1/2}^3 + \frac{1+v}{3} \cdot \frac{v-2}{4} (1 - 2 r_{j+1/2} + r_{j+1/2} r_{j-1/2}). \quad (10)$$

We have performed the successive derivations of the modified equations up to sixth order. We only give here the functions Φ^5 , Φ^6 and Φ^7 corresponding to the fifth-, sixth- and seventh-order numerical schemes obtained by correcting these modified equations:

$$\begin{aligned} \Phi_{j+1/2}^5 &= \Phi_{j+1/2}^4 - \frac{1+v}{3} \cdot \frac{v-2}{4} \cdot \frac{v-3}{5} \cdot \left(\frac{1}{r_{j+3/2}} - 3 + 3 r_{j+1/2} - r_{j+1/2} r_{j-1/2} \right), \\ \Phi_{j+1/2}^6 &= \Phi_{j+1/2}^5 + \frac{1+v}{3} \cdot \frac{v-2}{4} \cdot \frac{v-3}{5} \cdot \frac{v+2}{6} \\ &\quad \cdot \left(\frac{1}{r_{j+3/2} r_{j+5/2}} - \frac{4}{r_{j+3/2}} + 6 - 4 r_{j+1/2} + r_{j+1/2} r_{j-1/2} \right), \\ \Phi_{j+1/2}^7 &= \Phi_{j+1/2}^6 - \frac{1+v}{3} \cdot \frac{v-2}{4} \cdot \frac{v-3}{5} \cdot \frac{v+2}{6} \cdot \frac{v+3}{7} \\ &\quad \cdot \left(\frac{1}{r_{j+3/2} r_{j+5/2}} - \frac{5}{r_{j+3/2}} + 10 - 10 r_{j+1/2} + 5 r_{j+1/2} r_{j-1/2} - r_{j+1/2} r_{j-1/2} r_{j-3/2} \right). \end{aligned} \quad (11)$$

Let us emphasize that the numerical schemes constructed in this way always have the same order of accuracy in time and space. The most interesting functions are the odd ones because they correspond to schemes having a dominant dissipative error (even derivative in the right-hand side of the modified equation). The dispersive error being one-order lower, the corresponding schemes have a nearly symmetric behavior.

Comparing the stencil of this scheme to the Runge–Kutta high order scheme described in the following (Section 2.1.6), here we use a stencil of only eight points to get a seventh-order scheme relative to both time and space. Also notice that this kind of scheme has the property, which seems desirable, of giving the exact solution if the CFL number is equal to 1 (the schemes have a classical CFL stability condition $0 \leq v \leq 1$).

2.1.2. TVD schemes

The general constraint for a one-step scheme to be TVD, following the criteria developed by Harten, is:

$$-\frac{2}{v} \leq \Phi_{j+1/2} - \Phi_{j+1/2}/r_{j+1/2} \leq \frac{2}{1-v}. \quad (12)$$

If, as usual, Φ is set to zero for negative values of r , this leads to:

$$\begin{cases} 0 \leq \Phi_{j+1/2} \leq \frac{2}{1-v}, \\ 0 \leq \Phi_{j+1/2} \leq \frac{2r_{j+1/2}}{v}. \end{cases} \quad (13)$$

The upper bound of these limits is

$$\max \left(0, \min \left(\frac{2}{1-v}, \Phi_{j+1/2}, \frac{2r_{j+1/2}}{v} \right) \right).$$

The most usual limiters use the most restrictive of these values under a CFL condition $0 \leq v \leq 1$, that is:

$$\begin{cases} 0 \leq \Phi_{j+1/2} \leq 2, \\ 0 \leq \Phi_{j+1/2} \leq 2r_{j+1/2}. \end{cases} \quad (14)$$

In fact, there is no real necessity to restrict the constraints except in the case where a steady solution is searched, which should be independent of the CFL number. In the general unsteady case, it is worth keeping the original constraints. In such a way, it is possible to construct higher than second-order TVD schemes. In [1], such a third-order TVD scheme was proposed. The limiter function was

$$\Phi^{3\text{-TVD}} = \max \left(0, \min \left(\frac{2}{1-v}, \Phi^3, \frac{2r_{j+1/2}}{v} \right) \right). \quad (15)$$

This limiter was also used in [7] to compute a viscous flow in a shock tube.

The principle can naturally be extended to higher order schemes, using the Φ function described above. As a general rule, a o -th order TVD scheme will be obtained by taking Φ as $\Phi^{o\text{-TVD}}$, where

$$\Phi^{o\text{-TVD}} = \max \left(0, \min \left(\frac{2}{1-v}, \Phi^o, \frac{2r_{j+1/2}}{v} \right) \right). \quad (16)$$

The resulting scheme will be o -th order accurate almost everywhere, except around extrema and discontinuities where it becomes first-order accurate, as is the case for all TVD schemes. This is a serious drawback that needs correction for our purpose.

2.1.3. Geometrical interpretation of the TVD conditions

We would like here to introduce an original geometrical interpretation of the TVD conditions previously presented. This will establish the link between TVD schemes and the monotonicity preserving constraints developed in [25]. Let us write the numerical flux of a one-step scheme as:

$$F_{j+1/2} = f_j^n + \Phi_{j+1/2} \frac{(1-v)}{2} (f_{j+1}^n - f_j^n) = f_j^n + \gamma^+ (f_{j+1}^n - f_j^n) \quad (17)$$

with

$$\gamma^+ = \Phi_{j+1/2} \frac{(1-v)}{2}. \quad (18)$$

The first TVD constraint $0 \leq \Phi_{j+1/2} \leq 2/(1 - v)$ is equivalent to $0 \leq \gamma^+ \leq 1$, so this amounts to saying that the numerical flux $F_{j+1/2}$ must belong to the interval $[f_j^n, f_{j+1}^n]$.

In regard to the second TVD constraint, let us now introduce the numerical flux defining an upper limit:

$$f_j^{\text{ul}} = f_j^n + \frac{1-v}{v} (f_j^n - f_{j-1}^n) \quad (19)$$

and rewrite the flux $F_{j+1/2}$ as:

$$F_{j+1/2} = f_j^n + \Phi_{j+1/2} \frac{v}{2 r_{j+1/2}} (f_j^{\text{ul}} - f_j^n) = f_j^n + \gamma^- (f_j^{\text{ul}} - f_j^n) \quad (20)$$

with

$$\gamma^- = \Phi_{j+1/2} \frac{v}{2 r_{j+1/2}}. \quad (21)$$

The second TVD constraint $0 \leq \Phi_{j+1/2} \leq (2 r_{j+1/2})/v$ amounts here to saying that the coefficient γ^- must take values in between 0 and 1, i.e. the numerical flux $F_{j+1/2}$ must belong to the interval $[f_j^n, f_j^{\text{ul}}]$.

Finally the TVD conditions can be expressed by enforcing the interface numerical flux value $F_{j+1/2}$ in the intersection of the two intervals $[f_j^n, f_{j+1}^n]$ and $[f_j^n, f_j^{\text{ul}}]$. This shows that the TVD conditions are identical to the first-order geometrical constraints derived in [25] for the multistage case.

2.1.4. Monotonicity-preserving schemes

We now would like to enlarge the intervals defined above in order to avoid the loss of accuracy near extrema that is common to TVD schemes. To recover an accurate value of the numerical flux near an extremum, the TVD constraint should not be activated. To this end, we here adapt the method derived in [25] to be optimum for the one step schemes.

We note by $[f^1, f^2, \dots, f^k]$ the interval $[\min(f^1, f^2, \dots, f^k), \max(f^1, f^2, \dots, f^k)]$. In [25], the first interval $[f_j^n, f_{j+1}^n]$ is enlarged to $[f_j^n, f_{j+1}^n, f_j^{\text{md}}]$, where:

$$f_j^{\text{md}} = \frac{1}{2} (f_j^n + f_{j+1}^n) - \frac{1}{2} d_{j+1/2} \quad (22)$$

and the second interval $[f_j^n, f_j^{\text{ul}}]$ is enlarged to $[f_j^n, f_j^{\text{ul}}, f_j^{\text{lc}}]$ where:

$$f_j^{\text{lc}} = f_j^n + \frac{1}{2} (f_j^n - f_{j-1}^n) + \frac{\beta}{3} d_{j-1/2} \quad (23)$$

with $d_{j+1/2} = d_{j+1/2}^{\text{MM}} = \text{minmod}(d_j, d_{j+1})$ and $d_j = f_{j+1}^n - 2f_j^n + f_{j-1}^n$ is a measurement of the local curvature of the flux function (we work here directly with the fluxes, contrary to [25] where reconstructed values at the interface are used). The coefficient β is a heuristic factor giving freedom for the value of the local curvature.

In order to satisfy the monotonicity preserving criteria, the numerical flux $F_{j+1/2}$ must belong to the intersection of the enlarged intervals $[f_j^n, f_{j+1}^n, f_j^{\text{md}}]$ and $[f_j^n, f_j^{\text{ul}}, f_j^{\text{lc}}]$. This provides room for the numerical flux to maintain an accurate value.

In the context of our TVD flux limiter one step schemes, we follow the same procedure but rather use the following value for f_j^{lc} :

$$f_j^{\text{lc}} = f_j^n + \frac{1}{2} \left(1 + \frac{d_{j-1/2}}{f_j^n - f_{j-1}^n} \right) (f_j^{\text{ul}} - f_j^n) = f_j^n + \gamma_{\text{lc}}^- (f_j^{\text{ul}} - f_j^n), \quad (24)$$

where

$$\gamma_{lc}^- = \frac{1}{2} \left(1 + \frac{d_{j-1/2}}{f_j^n - f_{j-1}^n} \right). \quad (25)$$

This choice for f_j^{lc} is more natural as expressed in terms of f_j^{ul} , and also suppresses the need for the coefficient β .

Let us also rewrite f_j^{md} in a similar form:

$$f_j^{md} = f_j^n + \gamma_{md}^+ (f_{j+1}^n - f_j^n), \quad (26)$$

where

$$\gamma_{md}^+ = \frac{1}{2} \left(1 - \frac{d_{j+1/2}}{f_{j+1}^n - f_j^n} \right). \quad (27)$$

Now we can see that if $0 \leq \gamma_{md}^+ \leq 1$ and $0 \leq \gamma_{lc}^- \leq 1$, then f_j^{md} and f_j^{lc} belong to the TVD intervals. Thus the TVD conditions are not modified in this case. The first inequality $0 \leq \gamma_{md}^+ \leq 1$ gives:

$$0 \leq \frac{1}{2} \left(1 - \frac{d_{j+1/2}}{f_{j+1}^n - f_j^n} \right) \leq 1 \quad (28)$$

or equivalently:

$$\left| \frac{d_{j+1/2}}{f_{j+1}^n - f_j^n} \right| \leq 1. \quad (29)$$

The second inequality $0 \leq \gamma_{lc}^- \leq 1$ gives:

$$0 \leq \frac{1}{2} \left(1 + \frac{d_{j-1/2}}{f_j^n - f_{j-1}^n} \right) \leq 1 \quad (30)$$

or equivalently:

$$\left| \frac{d_{j-1/2}}{f_j^n - f_{j-1}^n} \right| \leq 1. \quad (31)$$

This shows that the two inequalities are identical. Next let us show that the inequality (29) is always verified in the case where the numerical values f_{j+l} , $l \in \{-1, 0, 1, 2\}$ are monotone. Without loss of generality, we can suppose increasing values. If d_j and d_{j+1} have opposite signs, $d_{j+1/2}$ is equal to zero and the conclusion is trivial. Let us suppose that $d_j \geq 0$ and $d_{j+1} \geq 0$. Eq. (29) can be developed as

$$\min \left(\left| \frac{f_{j+2}^n - f_{j+1}^n}{f_{j+1}^n - f_j^n} - 1 \right|, \left| 1 - \frac{f_j^n - f_{j-1}^n}{f_{j+1}^n - f_j^n} \right| \right) \leq 1. \quad (32)$$

If $d_j \geq 0$, then $f_{j+1}^n - f_j^n \geq f_j^n - f_{j-1}^n \geq 0$, implying that $0 \leq 1 - (f_j^n - f_{j-1}^n)/(f_{j+1}^n - f_j^n) \leq 1$. The case where $d_j \leq 0$ and $d_{j+1} \leq 0$ is symmetrical. This shows that (29) is always verified for monotone numerical data. The enlarged intervals being identical to the TVD intervals, the numerical scheme is MP.

To remain in the TVD framework, we also can express the MP conditions that the numerical flux $F_{j+1/2}$ must belong to the intersection of the enlarged intervals $[f_j^n, f_{j+1}^n, f_j^{md}]$ and $[f_j^n, f_j^{ul}, f_j^{lc}]$ directly as constraints on Φ , namely:

$$\min(0, \Phi^{\text{md}}) \leq \Phi \leq \max\left(\frac{2}{1-v}, \Phi^{\text{md}}\right), \quad (33)$$

where

$$\Phi_{j+1/2}^{\text{md}} = \left(\frac{2}{1-v}\right)\gamma_{\text{md}}^+ = \frac{2}{1-v} \frac{f_j^{\text{md}} - f_j^n}{f_{j+1}^n - f_j^n} \quad (34)$$

for the first condition, and

$$\min\left(0, \frac{2r}{v}, \Phi^{\text{lc}}\right) \leq \Phi \leq \max\left(0, \frac{2r}{v}, \Phi^{\text{lc}}\right), \quad (35)$$

where

$$\Phi_{j+1/2}^{\text{lc}} = \left(\frac{2 r_{j+1/2}}{v}\right)\gamma_{\text{lc}}^- = \frac{2 r_{j+1/2}}{v} \frac{f_j^{\text{lc}} - f_j^n}{f_j^{\text{ul}} - f_j^n} \quad (36)$$

for the second condition.

Finally the MP constraint which preserves accuracy takes the form:

$$\Phi^{o\text{-MP}} = \max(\Phi^{\text{min}}, \min(\Phi^o, \Phi^{\text{max}})), \quad (37)$$

where

$$\Phi^{\text{min}} = \max\left(\min(0, \Phi^{\text{md}}), \min\left(0, \frac{2r}{v}, \Phi^{\text{lc}}\right)\right) \quad (38)$$

and

$$\Phi^{\text{max}} = \min\left(\max\left(\frac{2}{1-v}, \Phi^{\text{md}}\right), \max\left(0, \frac{2r}{v}, \Phi^{\text{lc}}\right)\right). \quad (39)$$

In practice, as was done in [25], the criteria is strengthened by choosing a different definition for the curvature measurement $d_{j+1/2}$, namely

$$d_{j+1/2} = d_{j+1/2}^{\text{M4}} = \text{minmod}(4d_j - d_{j+1}, 4d_{j+1} - d_j, d_j, d_{j+1}). \quad (40)$$

This reduces the range of values left to $\Phi^{o\text{-MP}}$ in the case of a non-monotone discontinuity.

To conclude this section, let us remark that MP schemes are close to TVB (Total Variation Bounded) schemes (see [19]) in the sense that the Total Variation of the numerical solution is allowed to increase for an amount $O(\delta x)$ in both cases. The essential difference is that MP schemes allow this increase only for non-monotone data, and are TVD for monotone data such that the scheme is not oscillatory around discontinuities. In the TVB case, the Total Variation is allowed to increase everywhere, and oscillations can develop whose amplitude is controlled by an heuristic factor.

2.1.5. Extension to the non-linear case

In the non-linear scalar case, the one-step scheme can be extended in order to preserve the high order of accuracy in both time and space, in the case where the flux function f depends only on u . We can show that the Jacobian $a(u) = df/du$ verifies the same equation as the variable u , that is:

$$a_t + a(u)a_x = 0. \quad (41)$$

This is easily shown by deriving:

$$a_t + a(u)a_x = \frac{da}{du}(u_t + a(u)u_x) = 0. \quad (42)$$

Following these equations, the time derivatives can then be replaced by the space derivatives in the Lax–Wendroff procedure. For instance, let us write down the first through third derivatives in time by using successive derivatives of the exact equation:

$$\begin{cases} u_t = -f_x, \\ u_{tt} = (a f_x)_x, \\ u_{ttt} = (a f_x)_{xt} = (a_t f_x + a f_{tx})_x, \\ = (a_t f_x - a (a f_x)_x)_x, \\ = ((a_t + a a_x)f_x - (a^2 f_x)_x)_x, \\ = -(a^3 u_x)_{xx}. \end{cases} \quad (43)$$

Similarly, we can show that in general we get for the m th time derivative:

$$u_{mt} = ((-a)^m u_x)_{(m-1)x}. \quad (44)$$

Following this relation, the successive modified equation that we established in the linear case takes the general form in the non-linear case:

$$u_t + f(u)_x = \frac{\delta x^{m-1}}{m!} (\omega(v)a(u)u_x)_{(m-1)x}, \quad (45)$$

where $\omega(v)$ is a polynomial function of $v = a(u)\delta t/\delta x$. In this way, the only modification we have to include in the expression of the high order terms is to include $\omega(v)$ in the difference formulae. Let us illustrate the present development on the third order flux (see (5) in the linear case), which then is in the non-linear case written:

$$F_{j+1/2}^3 = f_j^n + \frac{(1-v)_{j+1/2}}{2} (f_{j+1}^n - f_j^n) - \left(\frac{(1-v^2)_{j+1/2}}{6} (f_{j+1}^n - f_j^n) - \frac{(1-v^2)_{j-1/2}}{6} (f_j^n - f_{j-1}^n) \right). \quad (46)$$

The flux is written for the case where $a(u) > 0$, but it is easily generalized by symmetry. The function $\Phi_{j+1/2}^3$ becomes:

$$\Phi_{j+1/2}^3 = 1 - \frac{1}{3} \frac{(1-v^2)_{j+1/2} (f_{j+1}^n - f_j^n) - (1-v^2)_{j-1/2} (f_j^n - f_{j-1}^n)}{(1-v)_{j+1/2} (f_{j+1}^n - f_j^n)} \quad (47)$$

or equivalently:

$$\Phi_{j+1/2}^3 = 1 - \frac{1}{3} \frac{(1-v^2)_{j+1/2} - (1-v^2)_{j-1/2}}{(1-v)_{j+1/2}} r_{j+1/2}. \quad (48)$$

The present procedure can be pursued to achieve higher order schemes. In this way, the high order accuracy of the schemes can be maintained in both time and space.

Following Harten's general TVD necessary conditions, the TVD constraints should be expressed by:

$$\Phi_{j+1/2}^{o\text{-TVD}} = \max \left(0, \min \left(\frac{2 r_{j+1/2}}{|v_{j+1/2}|}, \frac{1 - |v_{j-1/2}|}{1 - |v_{j+1/2}|}, \Phi_{j+1/2}^o, \frac{2}{1 - |v_{j+1/2}|} \right) \right). \quad (49)$$

Note that, in a similar way, the extension of the MP constraint is straightforward.

2.1.6. Multistage TVD and MP schemes

In this approach (the so-called method of lines), the space and time discretizations are performed separately. The most widely used time integration schemes for unsteady computations are Runge–Kutta type ODE solvers. Beside the classical Runge–Kutta solvers, Shu and Osher [22] have derived explicit Runge–Kutta methods up to the fourth order which possess the desirable property of being TVD. Unfortunately, only the second and third-order methods do not necessitate the use of the x -reversed operator (i.e. solving $u_t - f(u)_x = 0$). Their third-order TVD RK3 time integration is widely used. It is written:

$$\begin{cases} u^1 = u^n + \delta t L_{\delta x}(u^n), \\ u^2 = \frac{3}{4} u^n + \frac{1}{4} u^1 + \frac{\delta t}{4} L_{\delta x}(u^1), \\ u^{n+1} = \frac{1}{3} u^n + \frac{2}{3} u^2 + \frac{2}{3} \delta t L_{\delta x}(u^2) \end{cases} \quad (50)$$

with $L_{\delta x}$ being a discrete approximation of $L(u) = -f(u)_x$.

As this specific Runge–Kutta scheme is made up of repeated applications of a single stage scheme given by $u^{k+1} = u^k + \delta t L_{\delta x}(u^k)$, the scheme is completed once $L_{\delta x}$ is chosen. Integrating the single stage scheme over the cell $[x_{j-1/2}, x_{j+1/2}]$, this amounts to approximating the interface value of the flux $f(u^k(x_{j+1/2}))$. Let $F_{j+1/2}$ be the numerical flux approximating this interface flux (the reconstruction step). We will here briefly recall and discuss several different approaches.

The widely used MUSCL reconstruction uses the local slope $\Delta_{j+1/2}$ to express the interface value:

$$F_{j+1/2} = f_j + \frac{1}{2} \Delta_{j+1/2}. \quad (51)$$

Depending on the value given to $\Delta_{j+1/2}$, different schemes can be obtained. A linear combination of $f_{j+1} - f_j$ and $f_j - f_{j-1}$ is classically used, giving a second or third-order space accuracy. To increase the order of accuracy, one can use a larger stencil to express the slope. In [25] for example, the slope $\Delta_{j+1/2}$ is chosen as:

$$\Delta_{j+1/2} = (2f_{j-2} - 13f_{j-1} - 13f_j + 27f_{j+1} - 3f_{j+2})/30, \quad (52)$$

which gives a spatially fifth-order scheme, or:

$$\Delta_{j+1/2} = (-3f_{j-3} + 25f_{j-2} - 101f_{j-1} - 101f_j + 214f_{j+1} - 38f_{j+2} + 4f_{j+3})/210, \quad (53)$$

which gives a spatially seventh-order scheme. The fifth-order scheme uses a six point stencil per Runge–Kutta sub-step, that gives a total stencil of sixteen points per time step. The seventh-order scheme uses an eight point stencil per Runge–Kutta sub-step giving a total stencil of 22 points per time iteration.

Equivalently, as was done in the one-step case, the numerical flux can also be written in the different form:

$$F_{j+1/2} = f_j + \frac{1}{2} \Psi_{j+1/2}^o (f_{j+1}^n - f_j^n), \quad (54)$$

where, for example, the spatially fifth-order scheme corresponds to:

$$\Psi_{j+1/2}^5 = \left(2r_{j-1/2}r_{j+1/2} - 11r_{j+1/2} + 24 - \frac{3}{r_{j+3/2}} \right) / 30. \quad (55)$$

The slope $\Delta_{j+1/2}$ becomes $\Delta_{j+1/2} = \Psi_{j+1/2}^o (f_{j+1}^n - f_j^n)$, and Ψ is the accuracy function. The above reconstruction methods use a fixed stencil. By contrast, the family of ENO–WENO schemes [10,20–23] is based on the use of a variable stencil to perform the reconstruction, with the idea of selecting the stencil giving the smoothest interpolation.

To recover the TVD property for a multistage scheme, both the Runge–Kutta solver and each space-discretized step of the Runge–Kutta solver are required to be TVD. As the Runge–Kutta scheme is made up of repeated applications of the same single stage scheme, we only have to consider one stage. The corresponding numerical flux was written above as:

$$F_{j+1/2} = f_j + \frac{1}{2} \Psi_{j+1/2} (f_{j+1}^n - f_j^n). \quad (56)$$

The slope must then be limited in order to get a TVD scheme. This can be obtained by applying the TVD constraints on the Ψ function. We obtain:

$$\begin{cases} 0 \leq \Psi_{j+1/2} \leq 2r_{j+1/2} \frac{1-v}{v}, \\ 0 \leq \Psi_{j+1/2} \leq 2. \end{cases} \quad (57)$$

If one wants to keep the order of accuracy at least equal to 2, it is necessary that $\Psi = 1$ when $r_{j+1/2}$ is equal to 1. This implies that the CFL value must be restricted such as:

$$1 \leq 2 \frac{1-v}{v} \quad (58)$$

giving the CFL condition

$$v \leq \frac{2}{3}. \quad (59)$$

The upper bound value of the limited Ψ function is then:

$$\Psi^{\text{TVD}} = \max \left(0, \min \left(2 r_{j+1/2} \frac{1-v}{v}, \Psi, 2 \right) \right). \quad (60)$$

Let us remark that this condition is more restrictive than the one-step condition (16) for all values of v . One can either use this formula, or fix the coefficient $\alpha = (1-v)/v$ to its minimum value. For example, for CFL values lower than 0.5, we have $\alpha_{\min} = 1$ and one can take $\Psi^{\text{TVD}} = \max(0, \min(2 r_{j+1/2}, \Psi, 2))$ which allows all the classical (second-order accurate) limiters to be used to express Ψ^{TVD} .

In the followings, we will denote by Ψ_α^{TVD} the function

$$\Psi_\alpha^{\text{TVD}} = \max(0, \min(2 \alpha r_{j+1/2}, \Psi, 2)). \quad (61)$$

In order to obtain a TVD scheme at each step of the Runge–Kutta solver, v must then be restricted such that $v \leq 1/(1+\alpha)$.

These TVD conditions, identical to the non-relaxed geometrical conditions in [25], correspond to

$$\gamma^+ = \frac{1}{2} \Psi_{j+1/2} \quad \text{and} \quad \gamma^- = \frac{1}{2} \Psi_{j+1/2} \frac{1}{r_{j+1/2}} \frac{v}{1-v}$$

in (18) and (21).

This shows that the MP conditions derived in [25] can be expressed as constraints acting on the Ψ function. The procedure is similar to the one followed in the one-step scheme by replacing the function Φ by Ψ , and must be performed for each stage of the Runge–Kutta scheme.

3. Extension of the one-step scheme to the Euler and Navier–Stokes equations

3.1. One dimension

The Euler system for 1D gas dynamics is written:

$$\frac{\partial w}{\partial t} + \frac{\partial f(w)}{\partial x} = 0, \quad (62)$$

where $w = (\rho, \rho u, \rho E)^T$ is the vector of conservative variables, ρ being the density, u the velocity, E the total energy linked to the pressure p by the perfect gas equation of state $p = (\gamma - 1)\rho(E - \frac{1}{2}u^2)$ (the specific heat ratio γ is constant and equal to 1.4). The flux $f(w)$ is the vector $(\rho u, \rho u^2 + p, (\rho E + p)u)^T$.

In the following, we present the extension of the high order coupled time–space approach to the system of equations, by using the Roe flux difference splitting. We then describe the extension of the related TVD and MP constraints.

3.1.1. OSo scheme

The one-step scheme reads:

$$w_j^{n+1} = w_j^n - \frac{\delta t}{\delta x} (F_{j+1/2} - F_{j-1/2}), \quad (63)$$

where w_j^n is the local value of w in cell j at time $t = n\delta t$ and $F_{j+1/2}$ is the numerical flux of the scheme which is given by:

$$F_{j+1/2} = F_{j+1/2}^{\text{Roe}} + \frac{1}{2} \sum_{k=1}^3 (\Phi_k^o(1 - |v_k|) \delta |f_k| \mathbf{r}_k)_{j+1/2} \quad (64)$$

with the first-order Roe flux defined as follows:

$$F_{j+1/2}^{\text{Roe}} = \frac{1}{2} (f_j + f_{j+1}) - \frac{1}{2} \sum_k (\delta |f_k| \mathbf{r}_k)_{j+1/2} \quad (65)$$

with

$$\delta |f_k| = |\lambda_k| \delta \alpha_k,$$

where δ is the forward difference operator ($\delta z_{i+1/2} = z_{i+1} - z_i$), λ_k and \mathbf{r}_k are the eigenvalues and right eigenvectors of the Roe-averaged jacobian matrix $A = df/dw$, $\delta \alpha_k$ is the k th Riemann invariant and $v_k = (\delta t/\delta x)\lambda_k$. Let us mention that, for clarity, the superscript n has been omitted in the expression of the fluxes.

The most direct way to extend the high order one step scheme to the non-linear system case uses a classical direct extension of the formula (11) with respect to each k th wave of the system, where v is replaced by $|v_k|$ and $r_{j+1/2}$ is replaced by $r_{j+1/2,k}^s$ with $s = \text{sign}(\lambda_k)$. The ratio of the wave strengths $r_{j+1/2,k}^s$ is then defined as:

$$r_{j+1/2,k}^s = \frac{\delta \alpha_{k,j-s+1/2}}{\delta \alpha_{k,j+1/2}}.$$

This is the simplest and cheapest way to extend the scheme, but the drawback is that the formal order of accuracy in space is now only two, as we work in the eigenvector basis of the considered interface, i.e., we locally linearize the equations. The order of accuracy in time is also no more than two in this way, as we do not take into account the complicated non-linear terms that arise in the derivation of the modified equation of the Lax–Wendroff scheme.

Another way to extend the scheme would be to use the Cauchy–Kowalewski procedure for substituting time derivatives by space derivatives in the derivation of the successive modified equations. This procedure, described in [9], should allow the extension of the scheme to the non-linear system case while keeping the same order of accuracy. However, the procedure is very complex, especially in the multidimensional case. Also, the TVD (and MP as a consequence) conditions are not directly extensible in 2D, except if a time splitting strategy is used. In view of these problems, we choose here to keep the level of complexity of the scheme comparable to classical second-order TVD schemes. This point could be the subject of further studies, but as we will show in the following we have obtained very good numerical results using this simple method of extension.

3.1.2. OSTVDo scheme

The TVD constraints are written for each characteristic field as in the non-linear scalar case

$$\Phi_{j+1/2,k}^{\text{o-TVD}} = \max \left(0, \min \left(\frac{2r_{j+1/2,k}^s}{|v_{j+1/2,k}|}, \frac{1 - |v_{j-s+1/2,k}|}{1 - |v_{j+1/2,k}|}, \Phi_{j+1/2,k}^o, \frac{2}{1 - |v_{j+1/2,k}|} \right) \right). \quad (66)$$

3.1.3. OSMPo scheme

The monotonicity constraints are extended by rather working on the flux difference components:

$$\delta F_{j+1/2,k} = F_{j+1/2,k} - F_{j+1/2,k}^{\text{Roe}} = \frac{1}{2} \Phi_{j+1/2,k}^o (1 - |v_{j+1/2,k}|) \delta |f_{j+1/2,k}|. \quad (67)$$

We also express the values defining the monotonicity intervals as flux differences, following the work previously performed on the scalar case:

$$\delta f_{j+1/2,k}^{\text{ul}} = \frac{r_{j+1/2,k}^s}{|v_{j+1/2,k}|} (1 - |v_{j-s+1/2,k}|) \delta |f_{j+1/2,k}|, \quad (68)$$

$$\delta f_{j+1/2,k}^{\text{md}} = \frac{1}{2} \delta |f_{j+1/2,k}| - \frac{1}{2} d_{j+1/2,k}, \quad (69)$$

$$\delta f_{j+1/2,k}^{\text{lc}} = \frac{1}{2} \delta f_{j+1/2,k}^{\text{ul}} + \frac{1}{2} \frac{1 - |v_{j-s+1/2,k}|}{|v_{j+1/2,k}|} d_{j-s+1/2,k}, \quad (70)$$

where $d_{j+1/2,k}$ is given by (40) with however:

$$d_{j,k} = \lambda_{j+1/2,k} \delta \alpha_{j+1/2,k} - \lambda_{j-1/2,k} \delta \alpha_{j-1/2,k}. \quad (71)$$

Finally the values $\Phi_{j+1/2,k}^{\text{md}}$ and $\Phi_{j+1/2,k}^{\text{lc}}$ are given by:

$$\Phi_{j+1/2,k}^{\text{md}} = \frac{2}{1 - |v_{j+1/2,k}|} \frac{\delta f_{j+1/2,k}^{\text{md}}}{\delta |f_{j+1/2,k}|}$$

and

$$\Phi_{j+1/2,k}^{\text{lc}} = \frac{2r_{j+1/2,k}^s}{|v_{j+1/2,k}|} \frac{1 - |v_{j-s+1/2,k}|}{1 - |v_{j+1/2,k}|} \frac{\delta f_{j+1/2,k}^{\text{lc}}}{\delta f_{j+1/2,k}^{\text{ul}}}.$$

This completes the extension to systems.

3.2. Two dimensions

The treatment of the multidimensional case is straightforward in the case of separate time–space discretization, if treated dimension by dimension (see [25]). However, the MP conditions rely on TVD conditions as we have shown in the preceding section. TVD conditions are not directly extensible in the multidimensional case, and Locally Extremum Diminishing conditions should rather be considered, but this would lead to additional stability restrictions. This implies that the direct extension of the MP conditions does not guarantee that the resulting scheme will be non-oscillatory.

Following the one-step approach, the multidimensional extension is even more delicate, since we have to consider cross derivative terms that appear in the second and higher order terms, which are left uncontrolled if one applies a direction by direction TVD correction to a Lax–Wendroff unsplit scheme. A Locally Extremum Diminishing scheme can be obtained if one discretizes the mixed terms using upwind formulae, but it is very difficult to implement and our preliminary numerical experiments in this way did not give good results. The simplest way to avoid the problem of cross derivatives and to recover the good properties of the 1D scheme is to use a Strang directional splitting strategy, which is only second-order accurate. In two dimensions, the Euler system is written:

$$\frac{\partial w}{\partial t} + \frac{\partial f(w)}{\partial x} + \frac{\partial g(w)}{\partial y} = 0, \quad (72)$$

where f and g are the fluxes in each direction. We implement the splitting as follows:

$$w_j^{n+2} = L_{\delta x} L_{\delta y} L_{\delta y} L_{\delta x} w_j^n, \quad (73)$$

where $L_{\delta x}$ (resp. $L_{\delta y}$) being a discrete approximation of $L_x(w) = -f(w)_x$ (resp. $L_y(w) = -g(w)_y$). In such a way, the second-order accuracy is recovered every two time steps.

4. Numerical results

4.1. The 1D scalar case

4.1.1. A convergence study for a smooth initial profile

We solve the advection Eq. (1) on the domain $[-1, 1]$ with initial condition $u_0(x) = \sin^4(\pi x)$ and periodic boundary conditions. The computed L_1 error and order of accuracy are listed in Table 1 (the CFL number is equal to 0.5). The results for the OSTVD7 scheme show that the TVD constraints lower the order of accuracy to around 2.5. We note that the OSMP7 scheme equipped with $d_{j+1/2} = d_{j+1/2}^{\text{MM}}$ gives the same results as the OS7 scheme, and that both schemes reach the theoretical seventh order of accuracy. The use of $d_{j+1/2} = d_{j+1/2}^{\text{M4}}$ has the effect of lowering the order for the finest meshes. Compared to the results given in [2] for this test case, the OSMP7 scheme has errors at least one order of magnitude lower than the MPWENO5 scheme.

4.1.2. Advection of an initial profile with discontinuities

We now consider the classical test case of the advection of an initial profile composed of a Gaussian wave, a square wave, a triangular wave and an ellipse. This is a difficult test case because it includes discontinuities as well as smooth portions of curves and extrema. The initial condition $u_0(x)$ is defined on the interval $x \in [-1, 1]$ as:

Table 1

Advection of the initial condition $u_0(x) = \sin^4(\pi x)$: L_1 error and order of accuracy for the one-step schemes

Method	Number of grid points	L_1 error	L_1 order
OS7	20	5.16494×10^{-3}	
OSMP7	40	5.66989×10^{-5}	6.51
$d_{j+1/2} = d_{j+1/2}^{\text{MM}}$	80	4.74407×10^{-7}	6.90
	160	3.76700×10^{-9}	6.98
	320	2.95501×10^{-11}	6.99
OSMP7	20	5.08530×10^{-3}	
$d_{j+1/2} = d_{j+1/2}^{\text{M4}}$	40	5.67752×10^{-5}	6.48
	80	6.84954×10^{-7}	6.37
	160	2.19588×10^{-8}	4.96
	320	1.33241×10^{-9}	4.04
OSTVD7	20	2.13730×10^{-2}	
	40	3.85456×10^{-3}	2.47
	80	7.78303×10^{-4}	2.31
	160	1.47891×10^{-4}	2.40
	320	2.73871×10^{-5}	2.43

$$\begin{cases} u_0(x) = \exp(-\log(2)(x + 0.7)^2/0.0009) & \text{if } -0.8 \leq x \leq -0.6, \\ u_0(x) = 1 & \text{if } -0.4 \leq x \leq -0.2, \\ u_0(x) = 1 - |10(x - 0.1)| & \text{if } 0 \leq x \leq 0.2, \\ u_0(x) = (1 - 100(x - 0.5)^2)^{1/2} & \text{if } 0.4 \leq x \leq 0.6, \\ u_0(x) = 0 & \text{otherwise} \end{cases} \quad (74)$$

and periodic boundary conditions are prescribed. We use a uniform grid composed of 200 mesh-cells. The solutions obtained at two dimensionless times $t = 20$ (10 periods) and $t = 100$ (50 periods) are shown in Figs. 1–5. Let us emphasize that this corresponds to long time integration, as usually only 10 periods are presented for this test case.

Among the schemes described above, we present the results obtained using three of them (and their TVD and monotonicity-preserving variants): the one-step seventh-order scheme (named OS7), and the multistage RK3 scheme associated with a fifth order (RK3/5) and a seventh order (RK3/7) in space discretization. We will denote by OSTVD7 and OSMP7, respectively, the TVD and monotonicity-preserving variants of the OS7 scheme. We will also denote by RK3/TVD5(α) (respectively RK3/TVD7(α)) the TVD versions of the multistage schemes, and by RK3/MP5(α) (respectively RK3/MP7(α)) their MP versions; here the notation (α) is relative to the coefficient of the limited function Ψ_α^{TVD} . For comparison, we have also performed a calculation using a RK3/WENO($r = 5$) [10] scheme.

Let us first compare the CPU times needed for each scheme to compute 20,000 time steps, it takes: 22.83 s using the OS7 scheme, 25.31 s for the OSTVD7 scheme, 33.77 s for the OSMP7 scheme, 39.37 s for the RK3/TVD5 scheme and 46.23 s for the RK3/TVD7 scheme. This means that it takes nearly twice the time to get a seventh order in space approximation using a multistage scheme compared to a one-step scheme (and a larger stencil is necessary).

Fig. 1 shows the results obtained for the three versions of the one step seventh-order scheme and the RK3/WENO5 scheme, using a CFL number equal to 0.1. The OS7 gives very good results, except for numerical oscillations in the discontinuous regions. The TVD correction does a very good job of eliminating these oscillations, but tends to smooth extrema, although this is very localized. The MP correction is almost perfect, keeping the properties of the TVD correction while leaving unchanged the extrema compared to the original scheme. The discontinuities are represented over six points, which is rather low

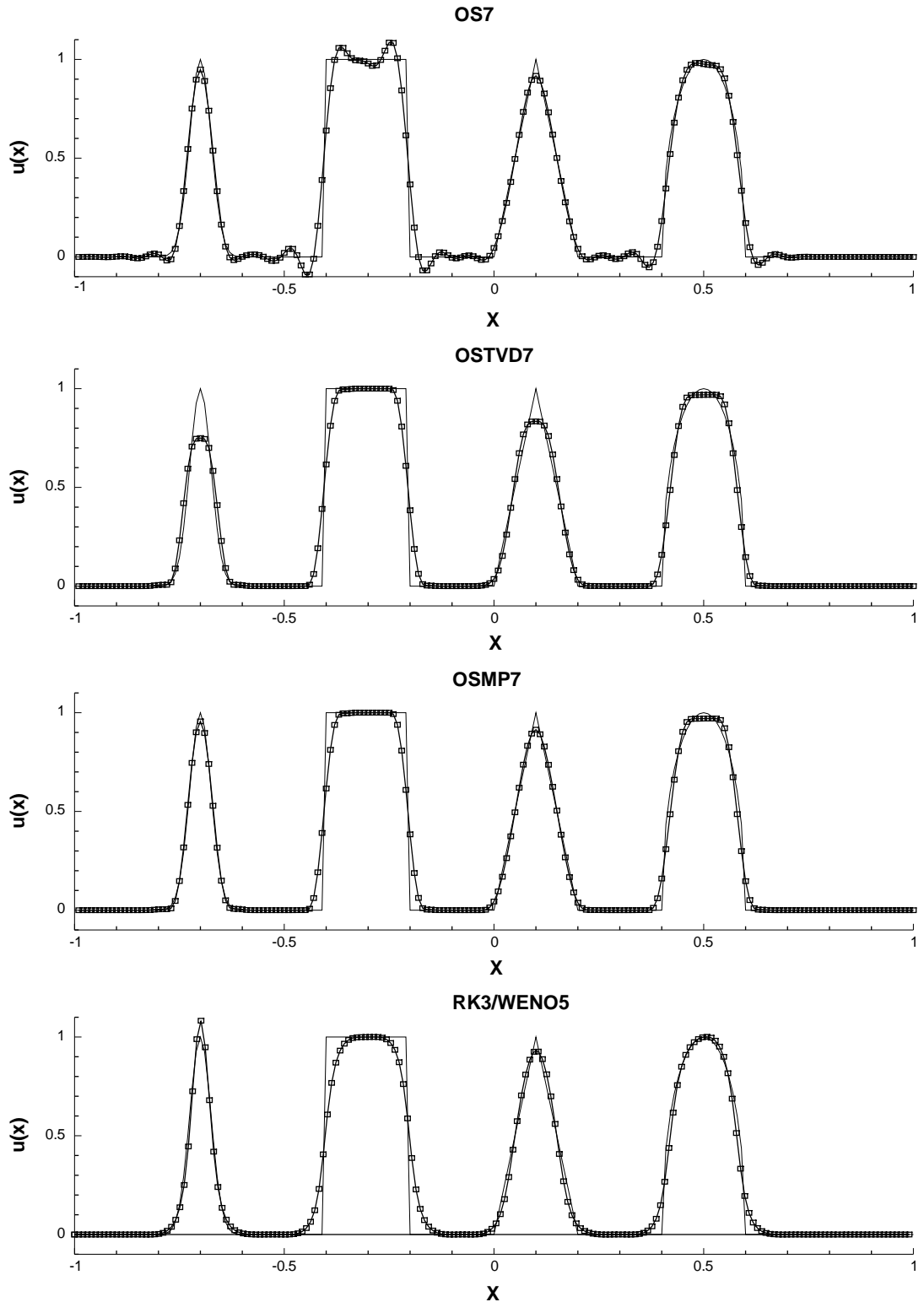


Fig. 1. Advection over 10 periods ($t = 20$). From top to bottom: Seventh-order one-step scheme (OS7), the corresponding TVD (OSTVD7) and MP (OSMP7) schemes, a RK3/WENO5 scheme. All the schemes are used with $CFL = 0.1$.

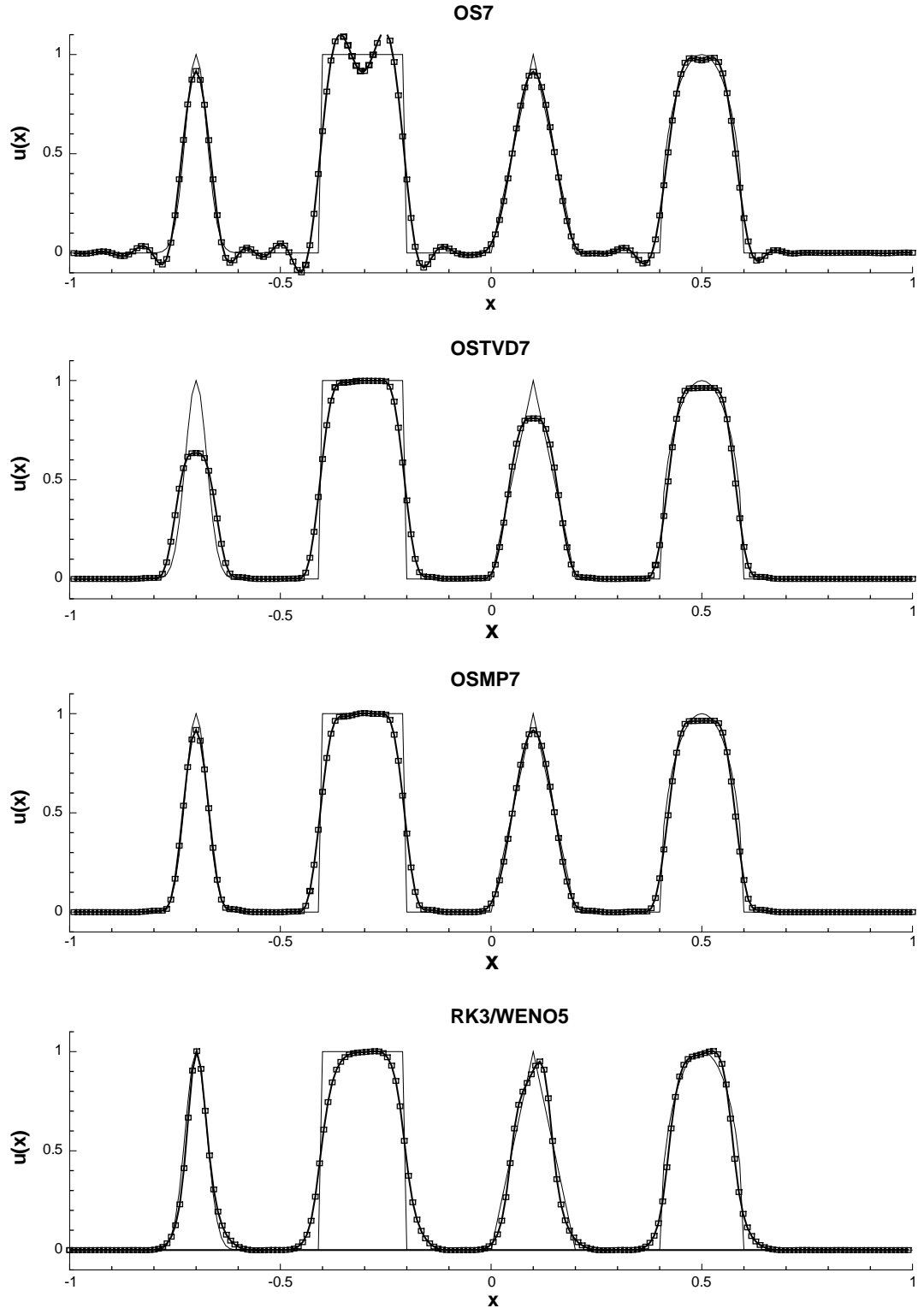


Fig. 2. Advection over 50 periods ($t = 100$). From top to bottom: Seventh-order one-step scheme (OS7), the corresponding TVD (OSTVD7) and MP (OSMP7) schemes, a RK3/WENO5 scheme. All the schemes are used with $CFL = 0.1$.

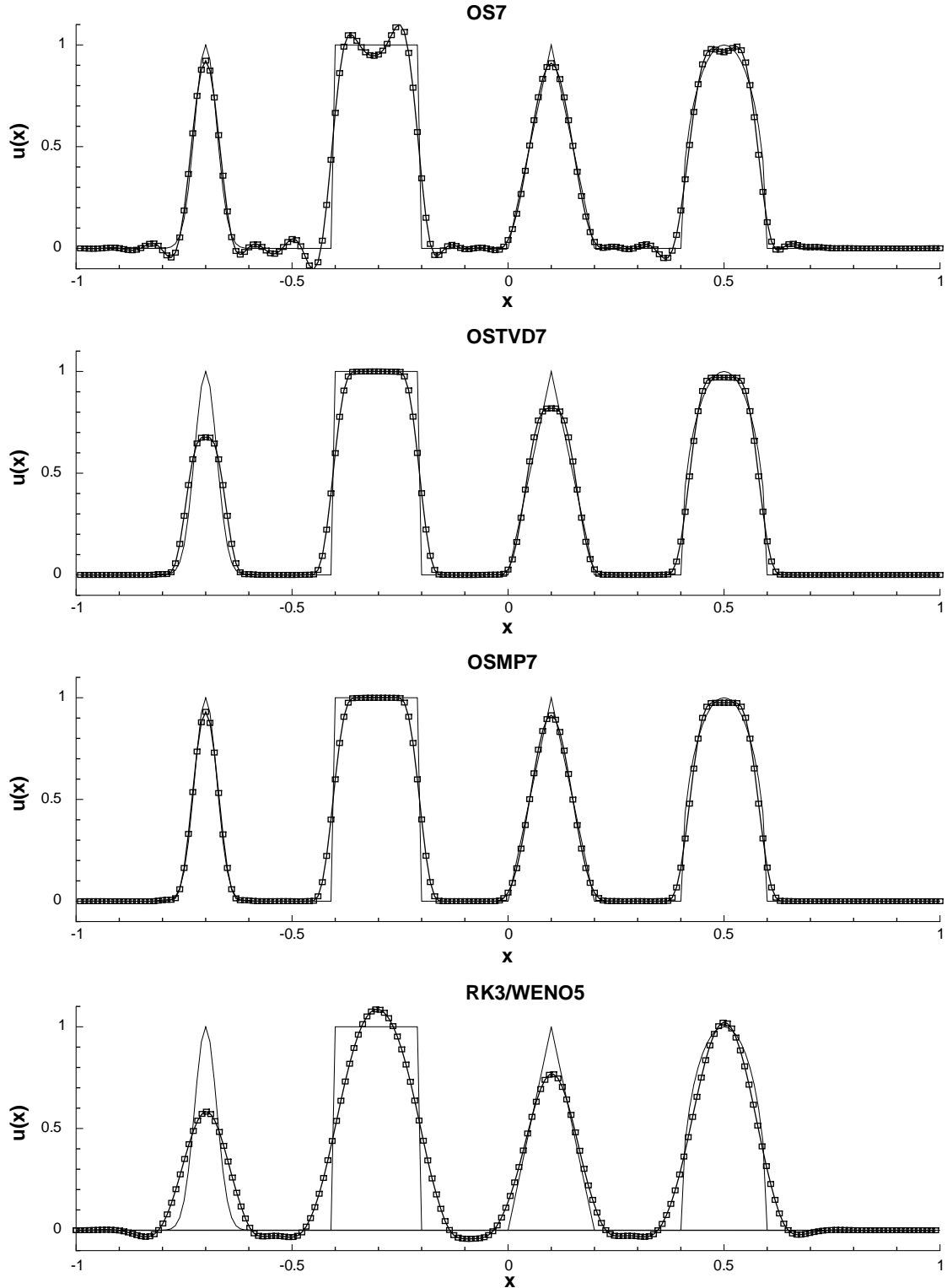


Fig. 3. Advection over 50 periods ($t = 100$). From top to bottom: Seventh-order one-step scheme (OS7), the corresponding TVD (OSTVD7) and MP (OSMP7) schemes, a RK3/WENO5 scheme. All the schemes are used with $CFL = 0.5$.

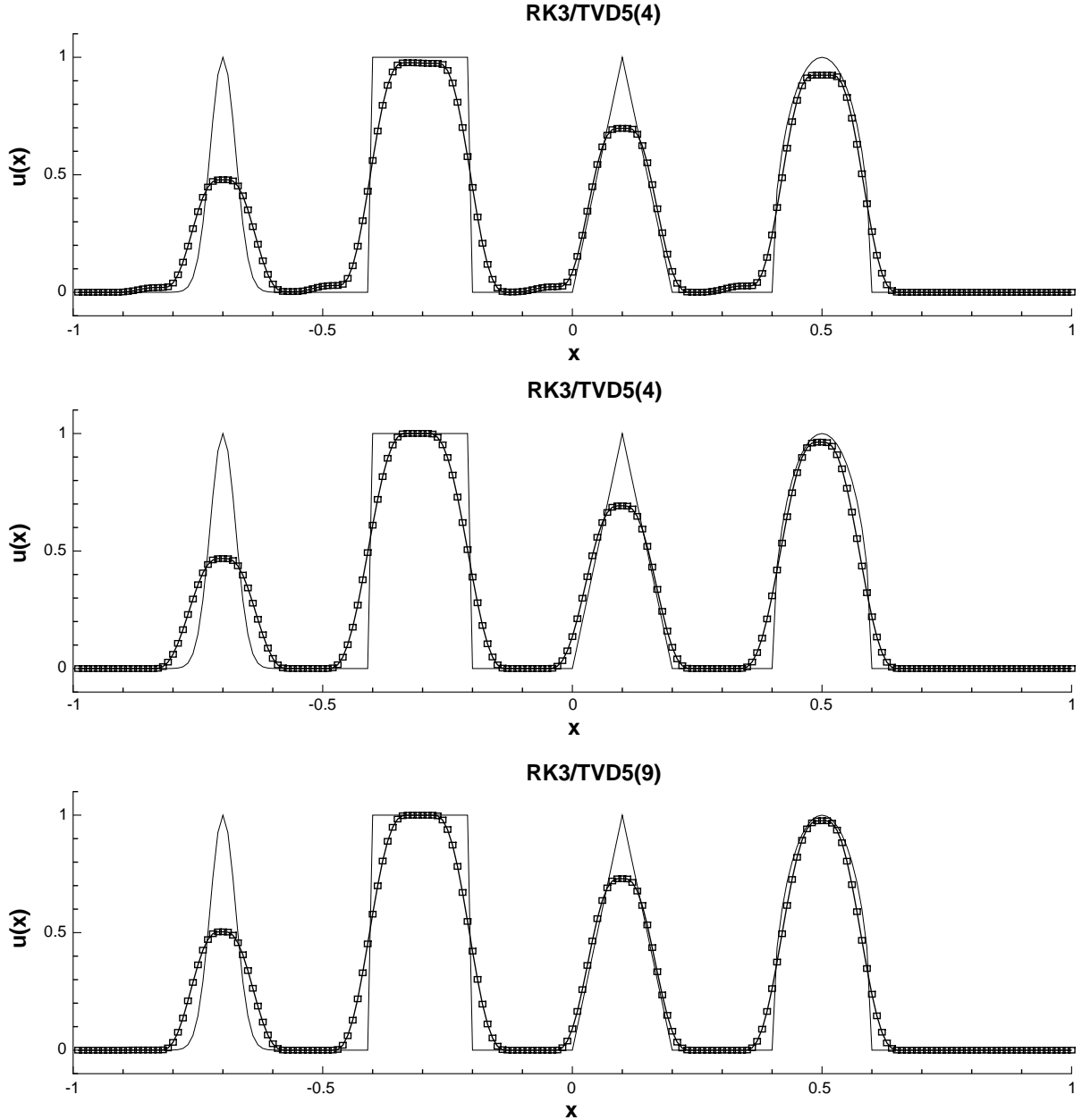


Fig. 4. Advection over 50 periods ($t = 100$). Fifth-order TVD multistage scheme: RK3/TVD5(4) with $CFL = 0.1$ (top) and $CFL = 0.4$ (middle), RK3/TVD5(9) with $CFL = 0.1$ (bottom).

after 20,000 time iterations. The same conclusions can be made after 50 periods (Fig. 2). The discontinuities are a little more smeared (eight points), and one can notice a small staircasing effect around the corners which is due to diffusive effects at low CFL numbers. But the solution can still be considered of excellent quality. The quality of the results given by the OSMP7 scheme is even better at higher CFL number as shown in Fig. 3 for $CFL = 0.5$. If we now compare these results with those given by the RK3/WENO5 scheme, it is apparent that, while the WENO scheme is very successful in representing extrema (sometimes without control as can be seen in Fig. 1), it is more diffusive around discontinuities and tends

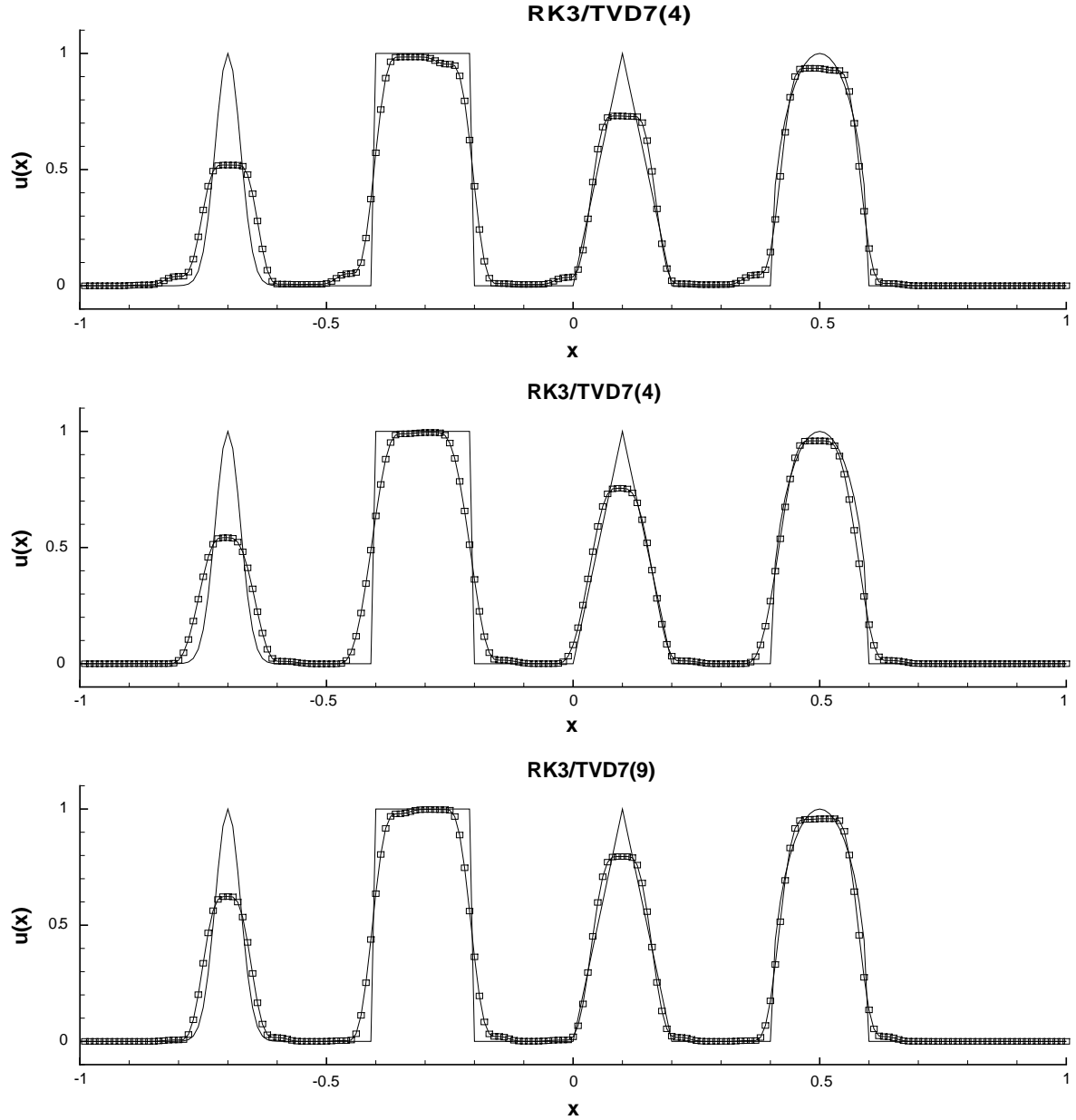


Fig. 5. Advection over 50 periods ($t = 100$). Seventh-order TVD multistage scheme: RK3/TVD7(4) with $CFL = 0.1$ (top) and $CFL = 0.4$ (middle), RK3/TVD7(9) with $CFL = 0.1$ (bottom).

to round the corners. One can also remark that the error of this scheme increases with the CFL number (Fig. 3), unlike the OS7 scheme.

Let us now compare these results with those obtained using the RK3/TVD and MP schemes. Figs. 4 and 5 show the numerical solution after 50 periods given by the RK3/TVD5 and TVD7 schemes, using the two values $\alpha = 4$ and $\alpha = 9$. For the case $\alpha = 4$, the scheme will be TVD provided that $v \leq 0.2$. In fact, as can be seen on the results, this CFL constraint is too restrictive, as it does not take into account the dissipation added by the temporal scheme. The results are better using $CFL = 0.4$ than $CFL = 0.1$, which means that the errors of the spatial and temporal scheme compensate for $CFL = 0.4$, while the total dissipative error is

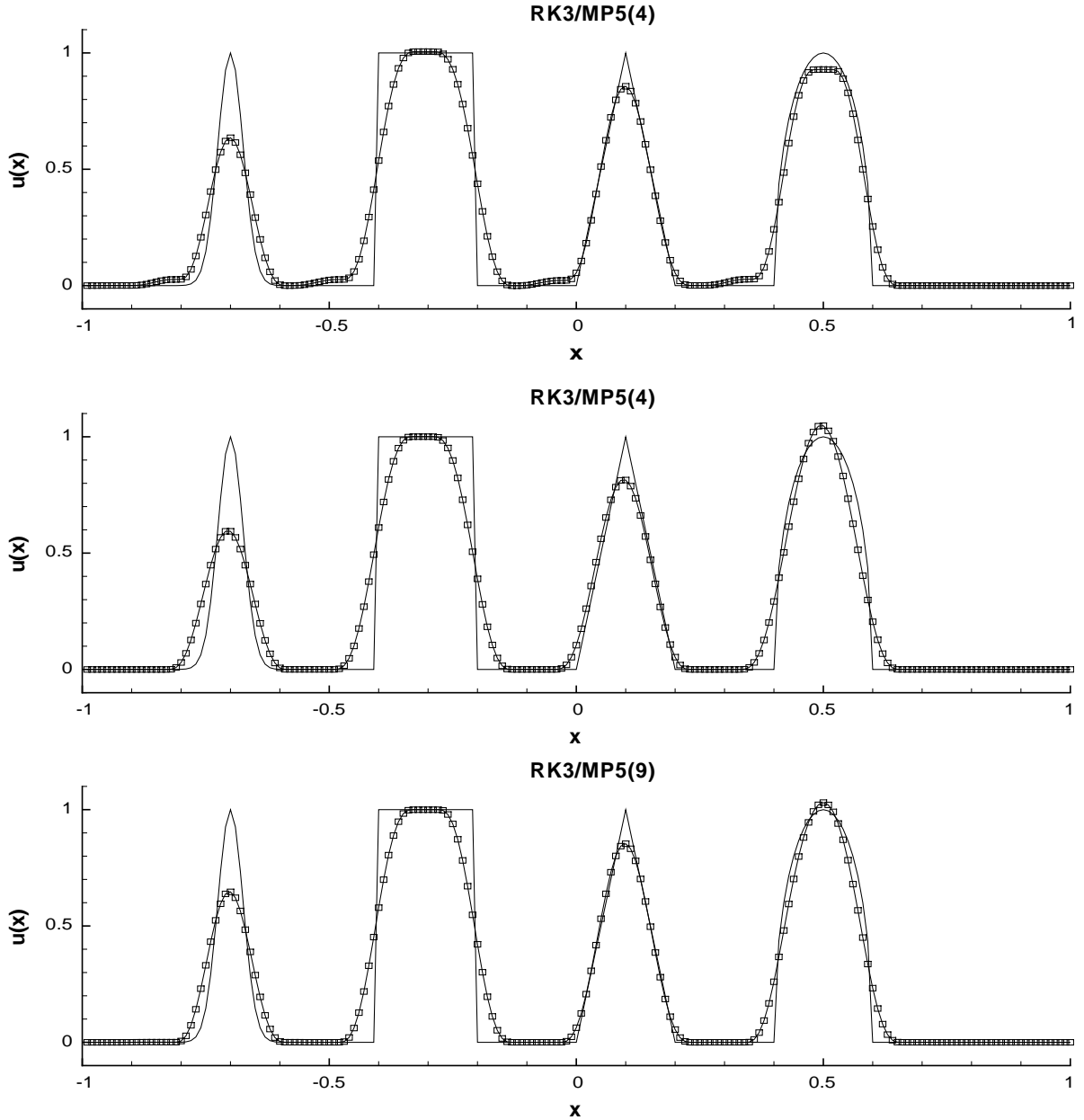


Fig. 6. Advection over 50 periods ($t = 100$). Fifth-order MP multistage scheme: RK3/MP5(4) with $CFL = 0.1$ (top) and $CFL = 0.4$ (middle), RK3/MP5(9) with $CFL = 0.1$ (bottom).

too large if the scheme is step by step TVD. More precisely, in the multistage approach the dissipation added by the temporal scheme is not included in the derivation of the TVD or MP constraints. As a consequence, the TVD/MP corrections will be switched on more often than would really be necessary, contrary to what happens in the one-step approach. This phenomenon is accentuated when the spatial order of the scheme is increased, as can be seen by comparing the fifth- and seventh-order results, showing that the staircasing due to the dissipative error is greater in the seventh-order case. Let us also remark that it is interesting to increase the value of α to improve the results (see the results using $\alpha = 9$), but this implies a lowering of the CFL number (the scheme is TVD at each time step if $v \leqslant 0.1$ for $\alpha = 9$). Finally, Fig. 6 shows the results obtained by using the RK3/MP5 scheme. While these results are much better than the

corresponding TVD results shown in Fig. 4, the same remark can be made for the role of the dissipative temporal error.

In conclusion, among the schemes we compared, the one-step scheme gives the best results, at the lowest cost. The control of the total truncation error allowed by the one step approach leads to the derivation of optimal non-oscillatory conditions.

4.2. 1D Euler equations

4.2.1. Shock wave interacting with a density disturbance

In this test case, which was proposed in [21], a moving Mach 3 shock wave interacts with a sinusoidal density profile. It is a difficult test case because it involves both a shock and smooth structures. The 1D Euler equations are solved on the spatial domain $x \in [0, 10]$. The solution is initially prescribed as

$$\begin{cases} \rho = 3.857, & u = 2.629, & p = 10.3333 & \text{when } x < 1, \\ \rho = 1 + 0.2 \sin(5x), & u = 0, & p = 1 & \text{when } x \geq 1. \end{cases}$$

The computation is stopped at a dimensional time $t = 1.8$. Fig. 7 presents the results obtained by using the three versions of the OS7 scheme (OS7, OSTVD7, OSMP7) and the RK3/WENO5 scheme [10], for 200

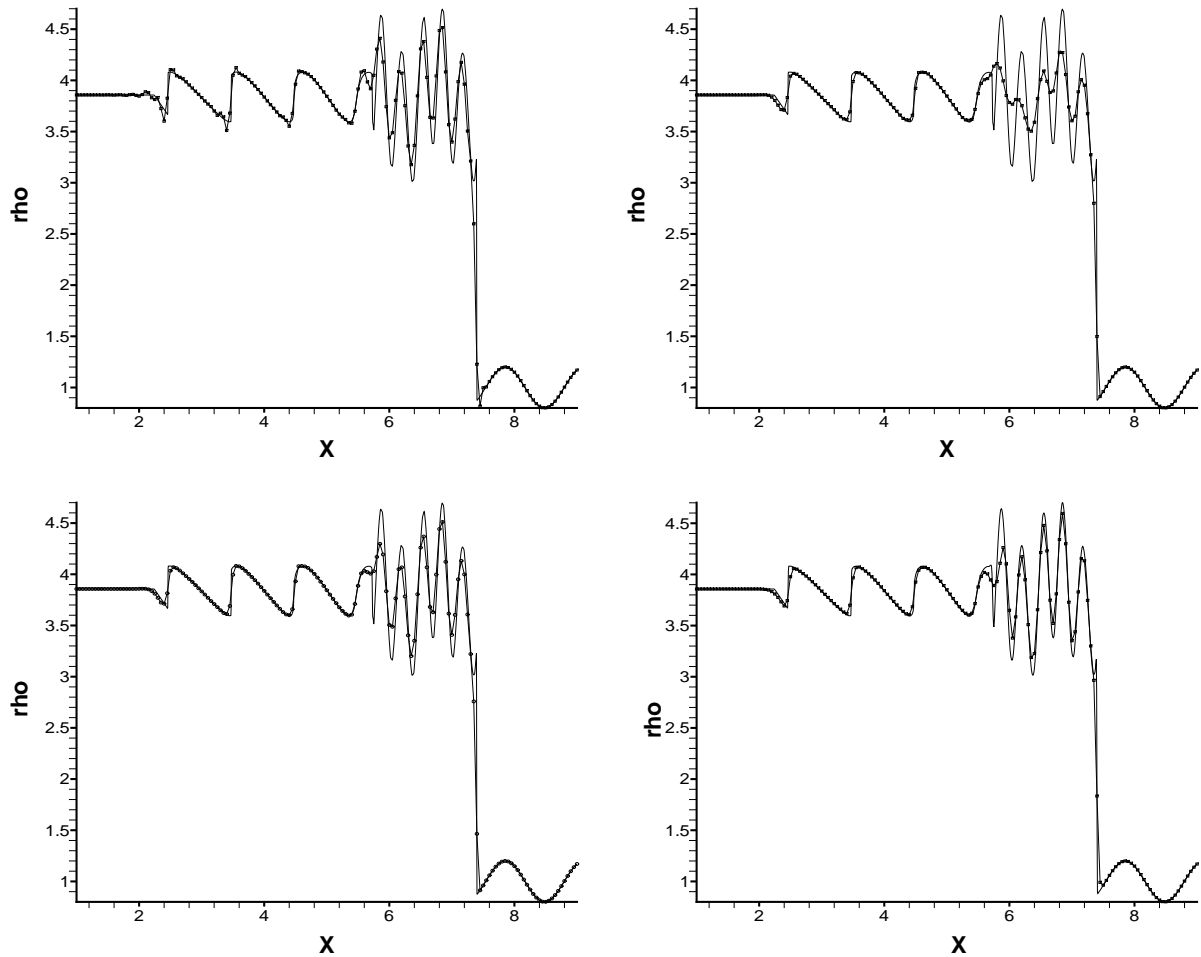


Fig. 7. Density distribution for the first Shu–Osher test case at $t = 1.8$, 200 grid points, CFL = 0.5. Top left: OS7 scheme, top right: OSTVD7 scheme, bottom left: OSMP7 scheme, bottom right: RK3/WENO5 scheme.

grid cells. This is a very coarse grid in which classical TVD schemes retain almost none of the structures immediately behind the shock wave. We can see here that the OSMP7 does a very good job, by eliminating the spurious oscillations generated by the OS7 base scheme, while relaxing the TVD constraints where they are not useful and “clip” the extrema. The OSMP7 results here are very close to those given by the RK3/WENO5 scheme, which is very good for this test case.

In Fig. 8 are compared the results for the OSMP7 and RK3/WENO5 schemes using 400 grid cells. One can conclude that both schemes have practically converged on this mesh, but at a lower cost for the OSMP7 scheme which is about five–six times less expensive than the RK3/WENO5 scheme. To be more precise, we have counted the number N of floating point operations needed per grid point and per time iteration in each case. The results are the following: the value of N is 1641 for RK3/WENO3, 3725 for RK3/WENO5, 541 for OSTVD7, 670 for OSMP7 and 354 for a one-step Van Leer second-order flux limiter scheme. Each stage of the RK3/WENO5 scheme costs roughly twice a time iteration of the OSTVD7 scheme. The added cost for the MP algorithm can be approximated by the difference $N(\text{OSMP7}) - N(\text{OSTVD7})$, so we can estimate a N -value close to 4100 for the RK3/MPWENO5 scheme, six times that of the OSMP7 scheme.

Let us also present the results we obtained for a variant of this test case that is often considered in place of the first one. The spatial domain is now the interval $[-1, 1]$ and the initial state is

$$\begin{cases} \rho = 3.857, & u = 2.629, \quad p = 10.3333 \quad \text{when } x < -0.8, \\ \rho = 1 + 0.2 \sin(5\pi x), & u = 0, \quad p = 1 \quad \text{when } x \geq -0.8. \end{cases}$$

The computation is stopped at a dimensional time $t = 0.47$. A grid with 200 zones is used. This test case is for example treated using a RK3/MPWENO5 scheme in [2]. We can compare this result in [2] (Fig. 4(a)) to the OSMP7 result shown in Fig. 9, and conclude that they are quite similar. We also have shown in Fig. 9 the result given by a classical second-order TVD scheme equipped with a Van Leer limiter, in order to highlight the increase of accuracy due to the OSMP7 scheme.

4.2.2. Lax shock tube

The previous test case is not very demanding of the robustness of the scheme, as the shock wave is rather weak. This is not the case for Lax’s problem, which we have treated to highlight this point. The spatial domain is $[0, 2]$ and the initial conditions are defined as:

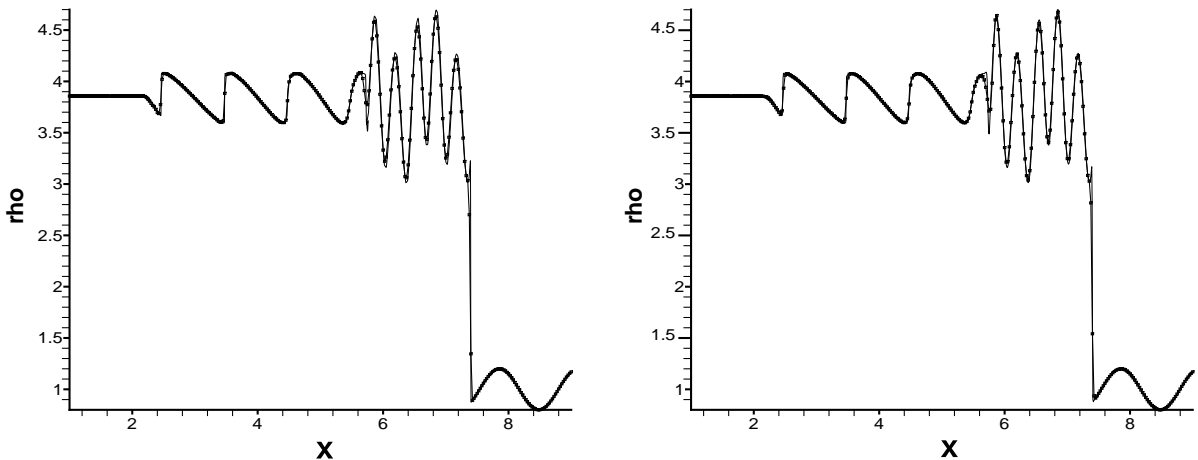


Fig. 8. Density distribution for the first Shu–Osher test case at $t = 1.8$, 400 grid points, $\text{CFL} = 0.5$. Left: OSMP7 scheme, right: RK3/WENO5 scheme.

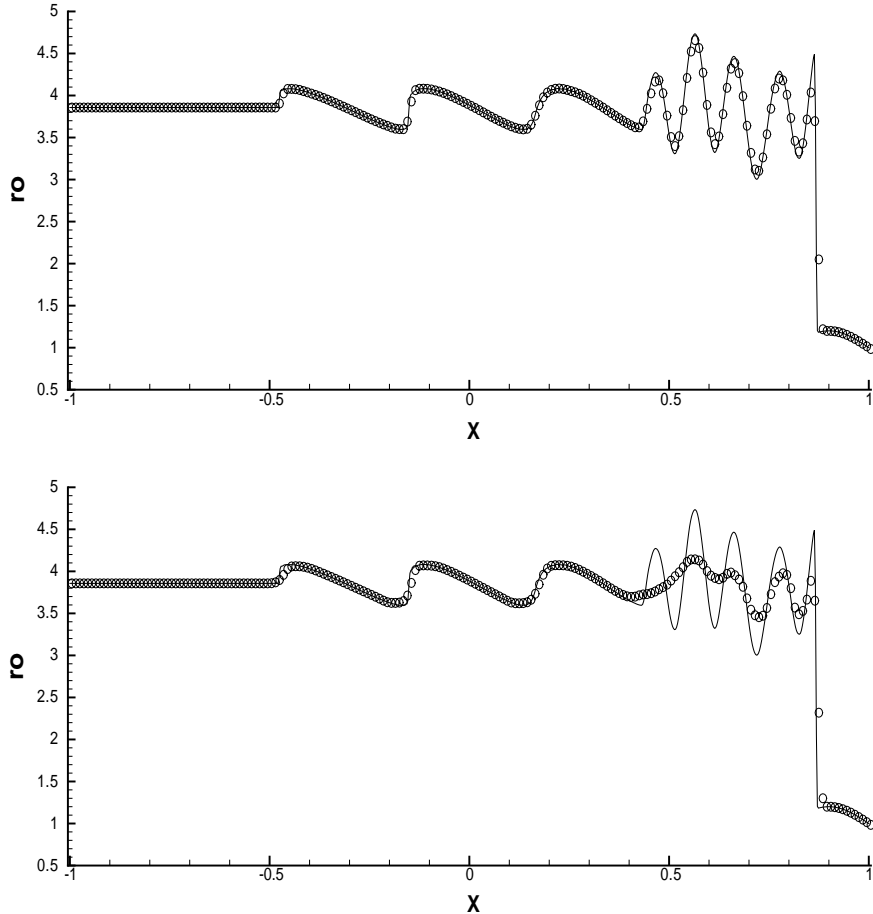


Fig. 9. Density distribution for the second Shu–Osher test case at $t = 0.47$, 200 grid points, $\text{CFL} = 0.5$. Top: OSMP7 scheme, bottom: TVD/Van Leer second-order scheme.

$$\begin{cases} \rho = 0.445, & u = 0.698, & p = 3.528 & \text{when } x < 1, \\ \rho = 0.5, & u = 0, & p = 0.571 & \text{when } x \geq 1. \end{cases}$$

The results are shown in Fig. 10 at time 0.32, for the OSMP7 scheme and three RK3/WENO3/5/7 schemes. One can observe that the best results are given by the OSMP7 scheme, the WENO results being more diffusive around the discontinuities or oscillatory for the WENO7. The MP strategy should give good results here applied to the WENO scheme as was done in [2], but with a higher computational effort.

4.3. 2D Euler and Navier–Stokes equations

4.3.1. Convergence study for a 2D Euler case

We consider the test case, treated in [2], of the propagation at 45° to the grid lines of a strong vortex at a supersonic Mach number. The vortex is initially centered in a domain $[-5, 5] \times [-5, 5]$. It is defined as a fluctuation to an unperturbed flow with $(\rho, p, u, v) = (1, 1, 1, 1)$, given by

$$(\delta u, \delta v) = \frac{\epsilon}{2\pi} e^{0.5(1-r^2)}(-y, x), \quad \delta T = -\frac{(\gamma - 1)\epsilon^2}{8\gamma\pi^2} e^{(1-r^2)}, \quad \delta S = 0,$$

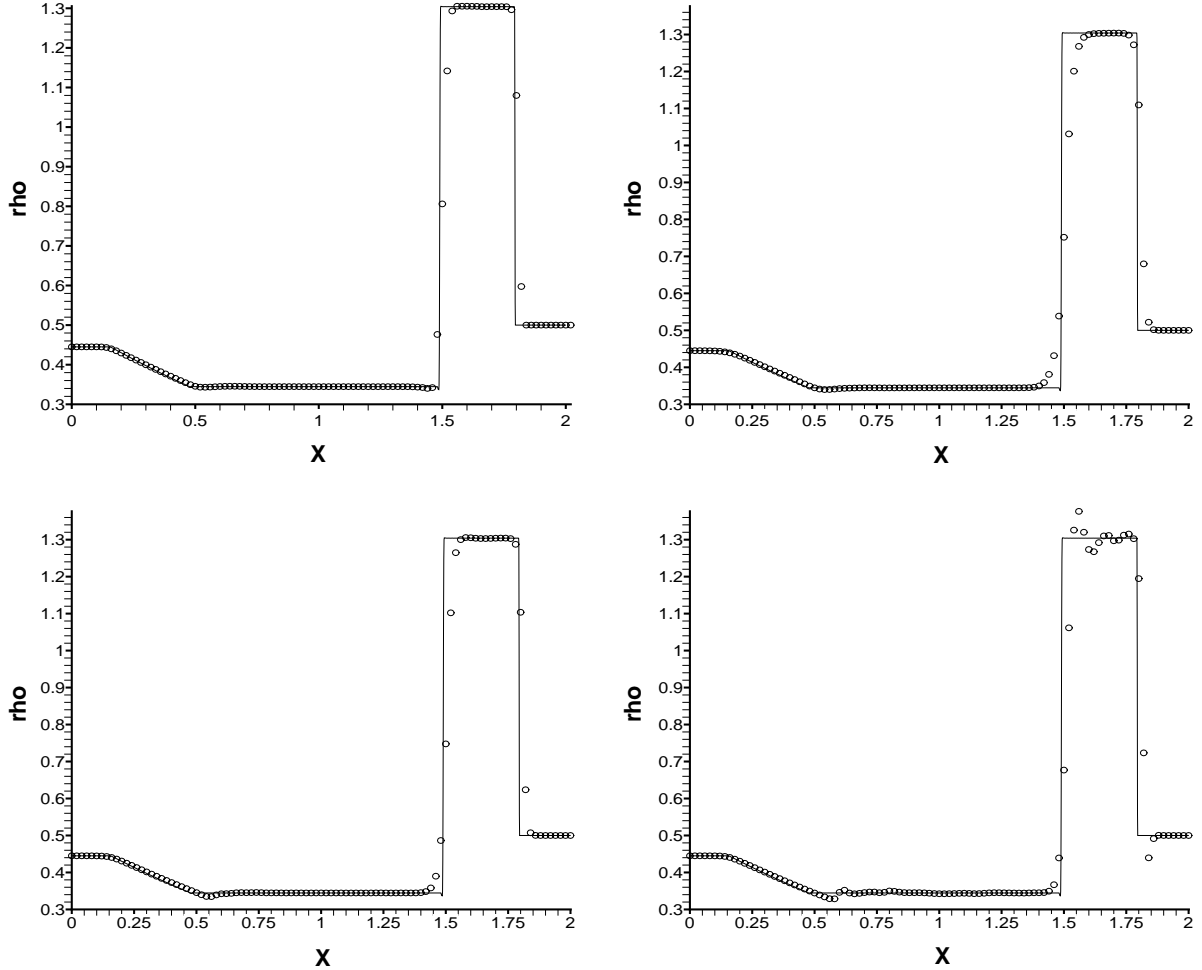


Fig. 10. Density distribution for the Lax test case at $t = 0.32$, 100 grid points, $CFL = 0.5$. Top, left: OSMP7 scheme, right: RK3/WENO3 scheme. Bottom, left: RK3/WENO5 scheme, right: RK3/WENO7 scheme.

where $r^2 = x^2 + y^2$, $S = p/\rho^\gamma$ is the entropy and $T = p/\rho$ is the temperature, $\gamma = 1.4$, $\epsilon = 5$ is the vortex strength. Periodic boundary conditions are imposed. The exact solution of this problem is just the passive convection of the vortex. The errors are calculated at time $t = 10$.

In Table 2 are listed the L_1 and L_∞ errors, together with the L_1 order of accuracy, obtained using the OSMP7 with $d_{j+1/2} = d_{j+1/2}^{M4}$. One can see that the scheme is only second-order accurate, due to the simplified extension to the non-linear system case. Nevertheless, as we have seen in the 1D Euler case, the quantitative values of the error are indeed much lower than for a classical second-order scheme. In Fig. 11 are represented the convergence curves associated with several schemes. The values for the WENO schemes are taken from [2]. One can see that, although the WENO schemes keep a high order of accuracy even in the 2D non-linear system case, their level of error is higher when the mesh is coarse. This implies that the OSMP7 scheme is more accurate than the WENO3 scheme for all the considered meshes. The MPWENO5 scheme has a lower error than the OSMP7 scheme for meshes finer than about 60×60 . Considering also the lower cost of the OSMP7 scheme, this shows that it can be profitable to use the OSMP7 scheme, in cases where it is not possible to use very fine meshes (which is a very standard case, for example in LES calculations where all the length scales are not fully resolved). Using the argument developed in [2] that the flow features should be simulated with at least 1% accuracy for the purpose of LES calculations, we can see

Table 2

Transport of a strong vortex in supersonic flow: L_1 error and order of accuracy, L_∞ error for the OSMP7 scheme

Method	Number of grid points	L_1 error	L_1 order	L_∞ error
OSMP7 $d_{j+1/2} = d_{j+1/2}^{M4}$	25×25	1.37×10^{-3}		1.67×10^{-2}
	50×50	3.13×10^{-4}	2.13	3.55×10^{-3}
	75×75	1.38×10^{-4}	2.02	1.66×10^{-3}
	100×100	7.73×10^{-5}	2.01	9.11×10^{-4}

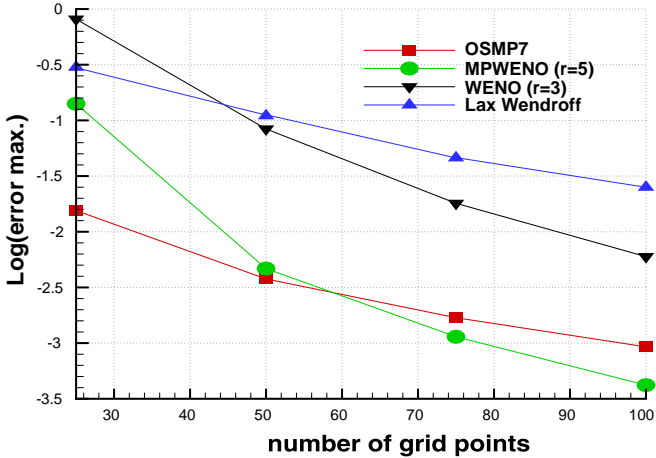


Fig. 11. Convergence curves for several schemes.

that the OSMP7 scheme achieves this level of error on the coarsest 25×25 grid (all flow variables are of the order of unity).

4.3.2. Double Mach reflection

This test case was solved using several numerical schemes for comparison in [28]. Solutions obtained using very fine meshes can also be found in [6]. The domain has a dimension $[0, 4] \times [0, 1]$. The problem involves a Mach 10 shock wave in air ($\gamma = 1.4$), which initially makes a 60° angle with the horizontal axis. The shock intersects the axis at $x = 1/6$. The region from $x = 0$ to $x = 1/6$ is always assigned the initial values. The region $x \in [1/6, 4]$ is a reflecting wall. The exact solution is set up and driven at the top of the domain. The computation stops at time 0.2. It is a difficult test case, involving both strong shocks and multiple stems. A jet forms along the wall, which is also very difficult to compute properly.

The results for this test case are shown in Fig. 12, where the density contours obtained using four grids with increasing resolution are represented. One can remark that all the features of the flow are captured at the correct position in the coarsest mesh. The shocks are very sharply captured, including the weak shock in the secondary Mach stem. There are some small oscillations in the nearly stationary zone underneath the curved shock wave, which is inherent to all schemes whose dissipation vanishes with zero flow velocity. If we compare our results with those in [25], for the 240×60 grid, we can conclude that they are very similar except that the wall jet is better represented in our calculation, if we refer to the results obtained using the finest grids.

As was pointed out in [2], this test case is difficult for schemes having Roe's scheme as the underlying first-order scheme. In fact, Roe's scheme systematically produces a carbuncle-type effect around the point

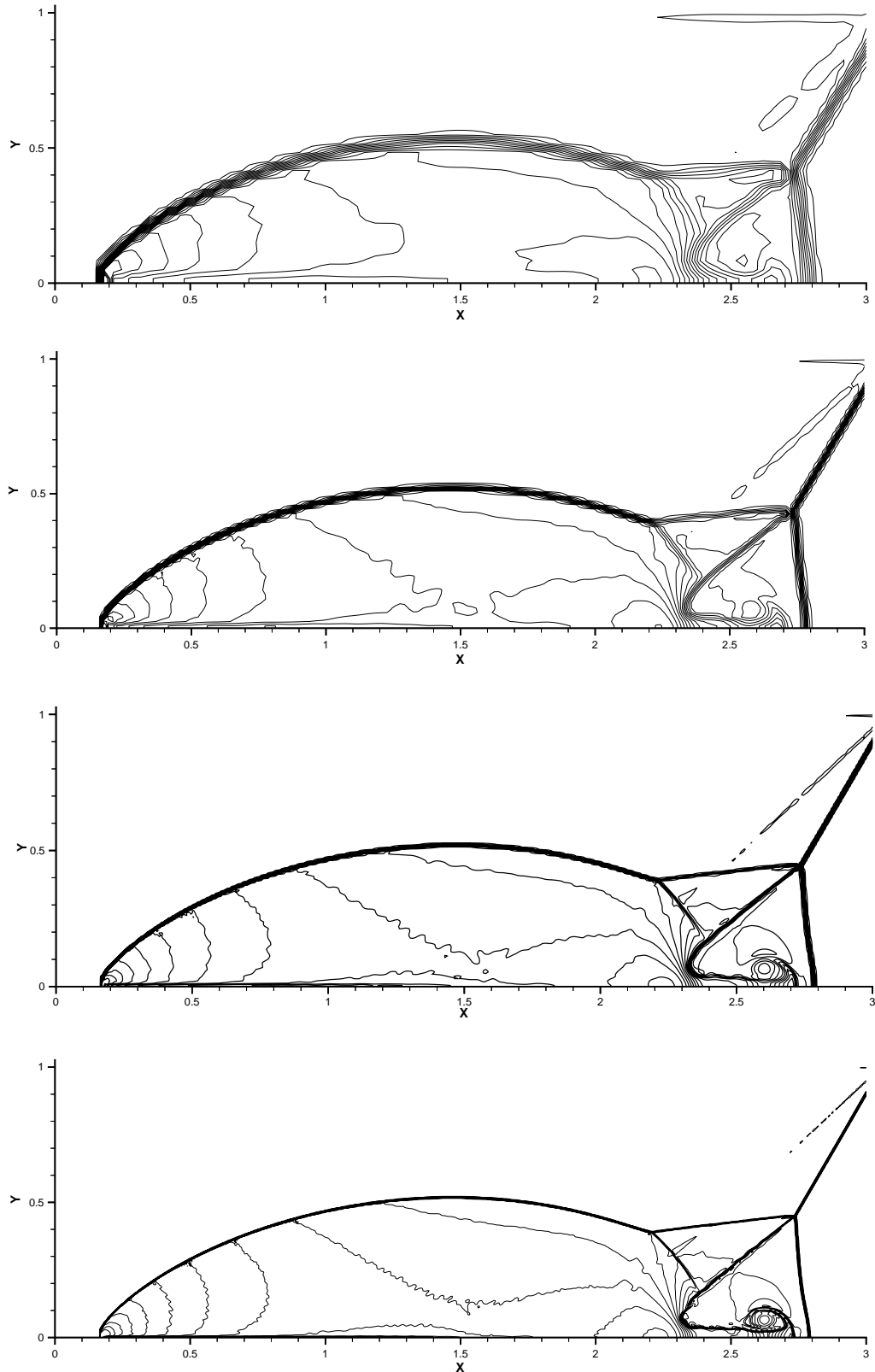


Fig. 12. Double Mach reflection, OSMP7 scheme. Density, 30 contours from 1.73 to 21, 120×30 grid, 240×60 grid, 480×120 grid, 960×240 grid from top to middle.

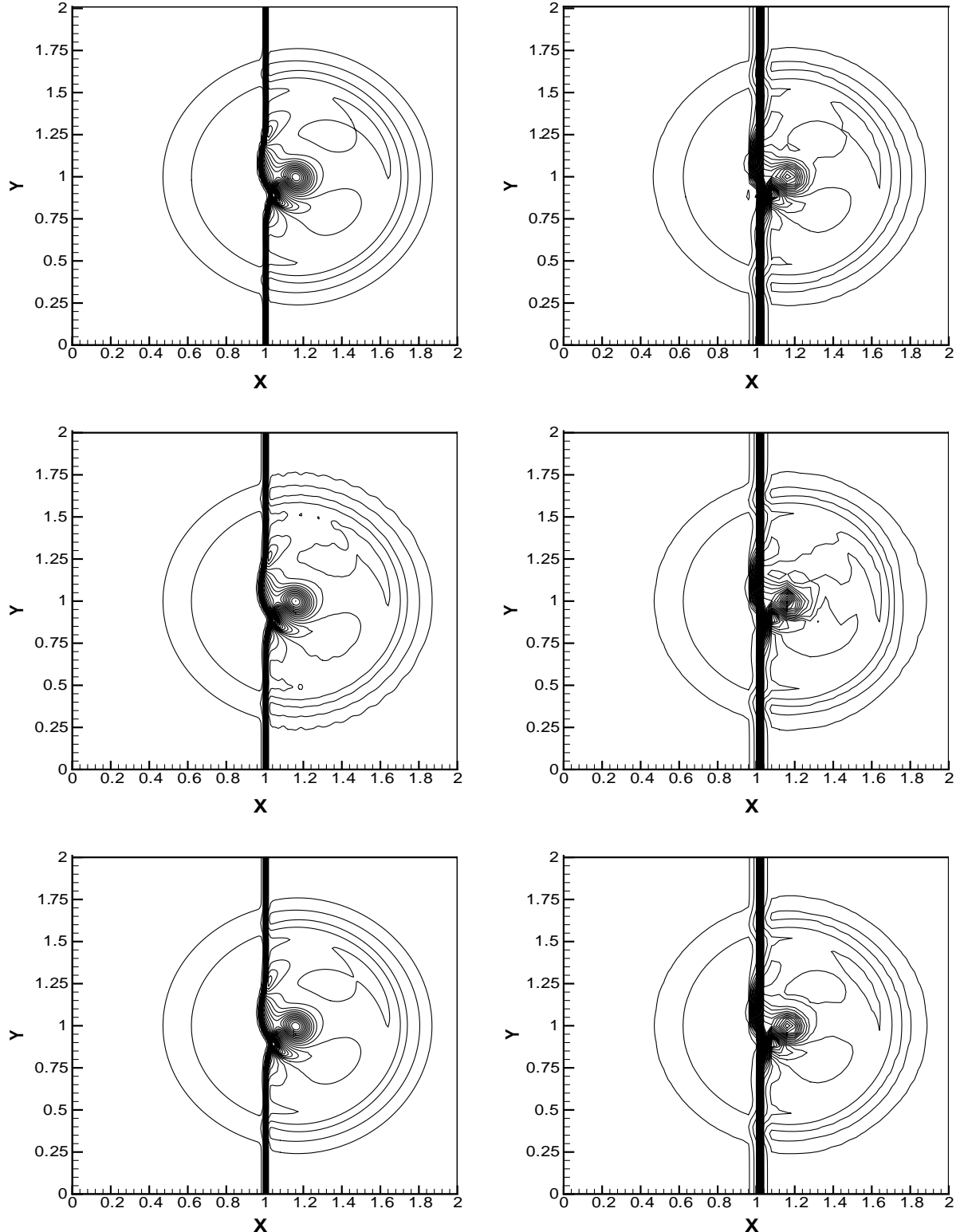


Fig. 13. Pressure contours for the 2D shock–vortex interaction at $t = 0.7$, $CFL = 0.5$ (49 contours from 0.527 to 0.845). Left: 200×200 grid points, right: 50×50 grid points. Top ,OSMP7 scheme; middle, RK3/WENO5 scheme; bottom, RK3/WENO7 scheme.

where the normal shock meets the wall. Curiously, this kind of problem was not encountered using the OSMP7 scheme in all the meshes we considered, whereas we could not obtain a correct solution using the WENO–Roe schemes in any grid (let us notice that we have added an entropy correction ([11]) to our OS scheme, which has a favorable effect on the problem). In [2] the Lax–Friedrichs (LF) scheme was used instead of Roe's scheme in order to avoid the problem (it is well known that the LF scheme is not prone to this phenomenon).

4.3.3. 2D viscous shock–vortex interaction

This test case, treated in [27], considers the viscous ($Re = 2000$) interaction of a plane weak shock with a single isentropic vortex. During the interaction, acoustic waves are produced, and we investigate the ability of the numerical scheme to predict and transport these waves. As this is a viscous flow, the Navier–Stokes equations are solved. In order to take the viscous terms easily into account, the one-step scheme is implemented as a Mac Cormack scheme followed by a correction, as was done in [7]. The viscous terms are discretized using centered second-order formulae.

The domain has a dimension $[0, 2L_0] \times [0, 2L_0]$, where L_0 is a reference length scale. The dimensionless computational domain is $[0, 2] \times [0, 2]$. A stationary plane shock is located at $x = 1$. The prescribed pressure jump through the shock is $\Delta P/P_\infty = 0.4$, where P_∞ is the static pressure at infinity, corresponding to a reference Mach number $M_0 = 1.1588$. The reference density and velocity are those of the free uniform flow at infinity. The Reynolds number, based on the reference length scale, density and velocity, is $Re = 2000$. An isolated Taylor vortex centered at $x_0 = \frac{1}{2}$, $y_0 = 1$ is initially superimposed on the base flow. The tangential velocity in the vortex is given by:

$$V_\theta(r) = C_1 r \cdot e^{-C_2 r^2} \quad (75)$$

with

$$C_1 = \frac{U_c}{r_c}, \quad C_2 = \frac{1}{2r_c^2}, \quad r = \sqrt{(x - x_0)^2 + (y - y_0)^2}.$$

The calculations were performed for $r_c = 0.075$ and $U_c = 0.25$. Periodic boundary conditions are applied in the y direction. The computations stopped at a dimensionless time $t = 0.7$.

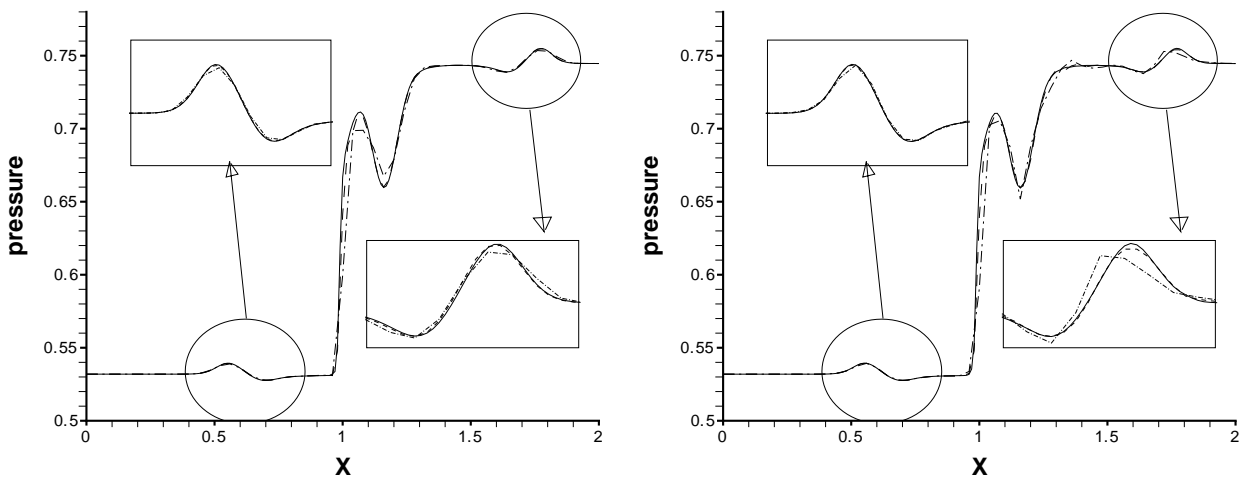


Fig. 14. Pressure along the line $y = 1$, 50×50 grid (dash-dotted line), 100×100 grid (dashed line), 200×200 grid (solid line); left: OSMP7 scheme, right: RK3/WENO5 scheme.

The pressure field contours obtained by using the OSMP7, RK3/WENO5 and RK3/WENO7 schemes are shown in Fig. 13, using 200×200 grid cells and 50×50 grid cells. One can notice the OSMP7 result is quite accurate even on a coarse grid and comparable to the WENO7 result. Curiously, the WENO5 scheme exhibits a slightly oscillatory behavior, which is not found in the WENO7 results. This can be seen more precisely on the pressure distribution along the line $y = 1$ (Fig. 14), which shows the high accuracy of the OSMP7 scheme in capturing the acoustic wave even on the coarsest grid. For this problem, the WENO5 scheme is seen to be insufficiently accurate on the coarse grid.

5. Conclusion

For the numerical simulation of unsteady compressible flows, we developed accurate numerical schemes based on a coupled time–space approach, which offer a compromise between high accuracy in smooth regions and an efficient shock capturing technique. We have shown that a coupled time and space approach for the solution of hyperbolic equations provides a very competitive numerical method compared to the state-of-the-art high resolution schemes (WENO, Runge–Kutta MP schemes). In the scalar case, a seventh-order accurate in time and space one-step scheme has been derived. When combined with MP conditions, the scheme has been shown to give very high quality results for long time integration. The MP conditions have then been extended from ([25]) to the case of a one-step scheme, and reinterpreted as TVD-like conditions in a flux limiting approach.

The extension of the one-step MP scheme to Euler and Navier–Stokes equations has been performed by using local linearization and dimensional splitting in the multidimensional case. Although this approach does not preserve the formal high order of accuracy of the scheme, it is shown to give very accurate results which compare well to high order WENO schemes, at a lower cost.

The investigated MP one-step schemes yield accurate results for the selected relevant test cases. However, one of the classical drawbacks associated with dimensional splitting is related to the treatment of boundary conditions for the intermediate step for bounded viscous flow calculations. This point is currently under investigation.

References

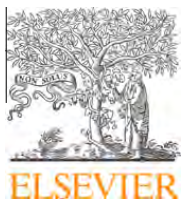
- [1] M. Arora, P.L. Roe, A well behaved TVD limiter for high-resolution calculations of unsteady flows, *Journal of Computational Physics* 132 (1997) 2–11.
- [2] D.S. Balsara, C.W. Shu, Monotonicity preserving weighted essentially non-oscillatory schemes with increasingly high order of accuracy, *Journal of Computational Physics* 160 (2000) 405–452.
- [3] C. Bernardi, Y. Maday, Approximations spectrales de problèmes aux limites elliptiques, in: J.M. Ghidagliaet, P. Lascaux (Eds.), *Collection Mathématiques & Applications*, Springer, Berlin, 1992.
- [4] C. Canuto, M.Y. Hussaini, A. Quarteroni, T.A. Zang, *Spectral Methods in Fluid Dynamics*, Springer, New York, 1988.
- [5] J. Casper, Finite-volume implementation of high-order essentially nonoscillatory schemes in two dimensions, *AIAA Journal* 30 (1992) 2829–2835.
- [6] B. Cockburn, C.W. Shu, The Runge–Kutta discontinuous Galerkin method for conservation laws V, *Journal of Computational Physics* 141 (1998) 199–224.
- [7] V. Daru, C. Tenaud, Evaluation of TVD high resolution schemes for unsteady viscous shocked flows, *Computers and Fluids* 30 (2001) 89–113.
- [8] F. Ducros, V. Ferrand, F. Nicoud, C. Weber, D. Darracq, C. Gachereau, T. Poinsot, Large Eddy simulation of shock/turbulence interaction, *Journal of Computational Physics* 152 (1999) 517–549.
- [9] A. Harten, B. Engquist, S. Osher, S. Chakravarthy, Uniformly high order essentially non-oscillatory schemes, III, *Journal of Computational Physics* 71 (1987) 231–303.
- [10] G.S. Jiang, C.W. Shu, Efficient implementation of weighted ENO schemes, *Journal of Computational Physics* 12 (1996) 202–228.
- [11] K. Khalfallah, A. Lerat, Correction d'entropie pour des schémas numériques approchant un système hyperbolique', *Comptes Rendus à l'Académie des Sciences* 308 II (1989) 815–820.

- [12] D. Knight, H. Yan, A.G. Panaras, A. Zheltovodov, Advances in CFD prediction of shock wave turbulent boundary layer interactions, *Progress in Aerospace Sciences* 39 (2003) 121–184.
- [13] D. Lax, B. Wendroff, Systems of conservation laws, *Communications on Pure and Applied Mathematics* 13 (1960) 217–237.
- [14] S.K. Lele, Compact finite difference schemes with spectral-like resolution, *Journal of Computational Physics* 103 (1992) 16–42.
- [15] B.P. Leonard, The ULTIMATE conservative difference scheme applied to unsteady one-dimensional advection, *Computer Methods in Applied Mechanics and Engineering* 88 (1991) 17–74.
- [16] M. Lesieur, P. Comte, Large Eddy simulations of compressible turbulent flows, in: *Cours AGARD-VKI, Turbulence in Compressible Flows*, 1997.
- [17] K. Mahesh, A family of high-order finite difference schemes with good spectral resolution, *Journal of Computational Physics* 145 (1998) 332–358.
- [18] R. Peyret, *Spectral Methods With Application to Incompressible Viscous Flow*, Springer, Berlin, 2002.
- [19] C.W. Shu, TVB uniformly high order schemes for conservation laws, *Mathematics of Computation* 49 (1987) 105–121.
- [20] C.W. Shu, S. Osher, Efficient implementation of essentially non-oscillatory shock-capturing schemes, *Journal of Computational Physics* 77 (1988) 439–471.
- [21] C.W. Shu, S. Osher, Efficient implementation of essentially non-oscillatory shock-capturing schemes, II, *Journal of Computational Physics* 83 (1989) 32–79.
- [22] C.W. Shu, T.A. Zang, G. Erlebacher, D. Whitaker, S. Osher, High order ENO schemes applied to two- and three-dimensional compressible flows, *Applied Numerical Mathematics: Transactions of IMACS* 9 (1992) 45–71.
- [23] C.W. Shu, Essentially non-oscillatory and weighted essentially non-oscillatory schemes for hyperbolic conservation laws, NASA/CR-97-206253 and ICASE Report, 1997 pp. 97–65.
- [24] B. Sjogreen, H.C. Yee, Grid convergence of high order methods for multiscale complex unsteady viscous compressible flows, *Journal of Computational Physics* 185 (2003) 1–26.
- [25] A. Suresh, H.T. Huynh, Accurate monotonicity-preserving schemes with Runge–Kutta time stepping, *Journal of Computational Physics* 136 (1997) 83–99.
- [26] V.A. Titarev, E.F. Toro, ADER: arbitrary high order Godunov approach, *Journal of Scientific Computing* 17 (1–4) (2002) 609–618.
- [27] C. Tenaud, E. Garnier, P. Sagaut, Evaluation of some high-order shock capturing schemes for direct numerical simulation of unsteady two-dimensional free flows, *International Journal for Numerical Methods in Fluids* 126 (2000) 202–228.
- [28] P. Woodward, P. Colella, The numerical simulation of two-dimensional fluid flow with strong shocks, *Journal of Computational Physics* 54 (1984) 115–173.

V. Daru, P. Le Quéré, M.-C. Duluc, O. Le Maitre

" A numerical method for the simulation of low Mach number liquid-gas flows ".

Journal of Computational Physics, 229(23), p. 8844-8867 (2010).



A numerical method for the simulation of low Mach number liquid–gas flows

V. Daru ^{a,b,*}, P. Le Quéré ^a, M.-C. Duluc ^{a,c}, O. Le Maître ^a

^aLIMSI-UPR CNRS 3251, BP 133, 91403 ORSAY Cedex, France

^bArts et Métiers ParisTech, DynFluid Lab., 151 Bd de l'Hôpital, 75013 Paris, France

^cCNAM, 292 Rue Saint Martin, 75141 Paris Cedex 03, France

ARTICLE INFO

Article history:

Received 20 October 2009

Received in revised form 29 July 2010

Accepted 11 August 2010

Available online 17 August 2010

Keywords:

Two-phase flow

Front-tracking

Low Mach number flow

Compressibility

ABSTRACT

This work is devoted to the numerical simulation of liquid–gas flows. The liquid phase is considered as incompressible, while the gas phase is treated as compressible in the low Mach number approximation. A single fluid two pressure model is developed and the front-tracking method is used to track the interface. Navier–Stokes equations coupled with that of temperature are solved in the whole computational domain. Velocity, pressure and temperature fields are computed yielding a complete description of the dynamics for both phases. We show that our method is much more efficient than the so-called all-Mach methods involving a single pressure, since large time steps can be used while retaining time accuracy. The model is first validated on a reference test problem solved using an accurate ALE technique to track the interface. Numerical examples in two space dimensions are next presented. They consist of air bubbles immersed in a closed cavity filled up with liquid water. The forced oscillations of the system consisting of the air bubbles and the liquid water are investigated. They are driven by a heat supply or a thermodynamic pressure difference between the bubbles.

© 2010 Elsevier Inc. All rights reserved.

1. Introduction

The numerical simulation of two-phase flow and related phenomena raises many different and difficult issues, from both modeling and computational standpoints. Several of these difficulties, such as dealing with the interface between two phases, tracking of the interface, implementing surface tension, coalescence, etc. are common to the simulation of flows of isothermal and incompressible multiphase fluids. Early attempts have made use of boundary fitted co-ordinates to simulate the flow around isolated bubbles of stationary or unsteady shapes [26]. These techniques allow one to impose very precisely the full interface conditions, but are limited to weak deformations and can hardly be extended to configurations involving many bubbles. These limitations have led to the development of Eulerian approaches, which have received much attention in the recent past and are still the subject of intensive ongoing research. Many types of numerical techniques have been developed to follow the interfaces, amongst which the VOF method [23,37], the level set method [42,38,43], the front-tracking method [44,40], interface capturing methods [1], and mixed methods [29]. A unified perspective of most of these methods can be found in [35].

One of the promising field of application of these techniques is the simulation of two-phase boiling flows that occur in confined environments. These simulations can be used to study various local dynamics processes and related heat transfer

* Corresponding author at: Arts et Métiers ParisTech, DynFluid Lab., 151 Bd de l'Hôpital, 75013 Paris, France.

E-mail address: Virginie.Daru@paris.ensam.fr (V. Daru).

such as bubble growth or collapse, interaction between several bubbles, in the aim of deriving macroscopic interaction laws between phases used in more conventional modeling techniques, in which each of the two phases is defined as a local volume or mass fraction. One specific issue in the simulation of these boiling phenomena is the coexistence of a liquid and a gas phase in a non-isothermal environment, the gas being made up totally or partially of the liquid vapor. An additional difficulty arises in the case of confined flows, for which the variations of the thermodynamic pressure in the gaseous phase play an important role and must be taken into account. For instance, in situations like in a pressure cooker, it is the fact that the mean pressure in the vessel can rise above the atmospheric pressure that allows the liquid-vapor phase change to take place at temperatures well above 100 °C, improving the Carnot efficiency or reducing the cooking time. The present work is devoted to the design of such a model and its numerical implementation providing a way to give access to some value of the thermodynamic pressure.

One way to give access to the thermodynamic pressure is to treat all fluid phases as fully compressible. For high speed flows, this has promoted the development of explicit algorithms in which both the liquid and the gas phases are modeled with the fully compressible Navier–Stokes equations [20,41,36]. Let us also cite the work of Caiden et al. [5], considering two-phase flow consisting of separate incompressible and high speed compressible regions. However, in many applications like those mentioned above, the velocities in the gas are very small, and the fully compressible approach raises different difficulties or issues of modeling or numerical nature. For low speed flows, one of these difficulties is linked to numerical representation of the pressure. Dynamic pressure variations corresponding to flow speeds of velocity V are of order ρV^2 which can be very small for flows of light low speed fluids and this raises the issue of finite precision arithmetic used in digital computers. For instance air flow velocities of 10^{-2} ms^{-1} correspond to differences in pressure of 10^{-4} Pa , which cannot be represented in single precision arithmetic within a pressure field whose mean value is equal to the atmospheric pressure $\approx 10^5 \text{ Pa}$, independently of the poor conditioning of the Jacobian matrix.

For fully compressible explicit methods, another major difficulty is linked to the severe limitation of the time step induced by the large value of sound velocity in the liquid. The speed of sound in a liquid can be more than 10^4 or 10^5 times larger than the convection velocity. For natural convection configurations where one has to integrate the equations on the order of a viscous or diffusion time scales, this limitation makes virtually impossible to attain the asymptotic flow regime. Alleviating this limitation leads one to promote an approach where the liquid is treated as completely incompressible. However, in many applications like those mentioned above, the velocities in the gas are very small, and the limitation of the time step based on the speed of sound (acoustic time step) in the gas remains severe. The so-called all-Mach or Mach-uniform methods that have received much attention in recent years are aimed at remedying this problem. These algorithms fall into two classes: density-based methods which we do not consider here as time accuracy is difficult to recover, and pressure based methods. The latter are derived from projection methods that are classically used for incompressible flows. They use an implicit algorithm for the calculation of pressure, which integrate the acoustic wave related part in the governing equations. Thereby the stability limitation of the time step due to acoustic propagation is avoided. Pressure-based methods also have the interesting property of being capable of handling both incompressible and compressible flows, as the pressure equation reduces to the usual Poisson equation when the Mach number tends to zero. This class of methods has been developed in several articles. Yabe et al. [47] utilize a Cubic Interpolated Polynomial (CIP) based time splitting predictor–corrector technique, separating advection and non-advection parts in the governing equations. Xiao [45,46] brings several improvements to the method and proposes a conservative algorithm. Ida [16] incorporates into the CIP algorithm a multi-time step integration involving sub-iterations for solving the components of different time scales of the Navier–Stokes equations. In [18] a fully conservative method that uses a second order ENO method for the non-oscillatory treatment of discontinuities is developed. The work in [22] presents a method quite similar but that rather uses a staggered MAC grid discretization.

Although this kind of methods may be thought of as a good candidate for our problem, the analysis in the literature shows that for unsteady calculations time steps of the order of the acoustic time step are generally used for accuracy reasons. In [16] is treated a case of bubble dynamics in an acoustic field, where it is shown that acoustics must be solved accurately for the entire flow accuracy, thus limiting the time step in the acoustic part of the solver to values close to the explicit value. The unsteady Oscillating Water Column test case is treated in [18] using an acoustic CFL number of 3 at most. In [22] a low Mach unsteady flow case is reported using again an acoustic CFL number of 3 for time accuracy of the solution. The conclusion that seems to emerge is that although the time step is not limited by a stability condition, it is still limited to values close to the explicit one for time accuracy reasons. This is also our finding, as we demonstrate below treating the Oscillating Water Column test case.

Although not subject to stability restrictions owing to their implicit nature, all Mach pressure based methods still consider the fully compressible model involving acoustics. However, for applications where the velocities in the gas are very small, a low Mach number model seems well adapted. In such an approach, acoustics is removed beforehand from the equations. The use of this approach was already proposed by [9] in the context of multicomponent gaseous flows, in the case of a potential approximation. Those methods were initially designed to handle low speed gas flows which can experience large variations of the mean pressure such as discharging flows from pressurized vessels [13] or natural convection flows due to very large temperature differences for which the Boussinesq approximation is no longer valid [33,24]. In these methods the pressure is split into a mean pressure that can evolve in time and an additional component which is responsible for satisfying the continuity equation. This pressure splitting inhibits the local coupling between pressure and density, thus avoiding the simulation of acoustic waves and alleviating the corresponding stability criteria. Indeed, low Mach number approaches have

been shown to be much more efficient and reliable than fully compressible models for the computation of natural convection flows in closed cavities [25,32].

Another question to be addressed concerns the appropriate description of the dynamics of the flow within the gas phase. One strategy is to neglect the flow within each gaseous inclusion, which is then just described by its shape, mean pressure and temperature. Such an approach was followed by Caboussat et al. [4,3] in the isothermal case to handle mould filling. The case of bubbles with uniform but time dependent temperatures was largely investigated by Prosperetti's group, considering a gas bubble in a small tube [14] or a vapour bubble in a micro-channel [48]. The physical description considers uniform properties in the bubble (pressure, temperature, density). The liquid description is performed using an approximate potential flow [30] or the complete Navier–Stokes equations [31]. At the interface, the connection with bubble properties is achieved through standard jump equations while the numerical description performed in [31] makes use of free surface techniques.

Neglecting the gas dynamics may result in the impossibility to describe physical phenomena such as thermal convection effects for instance. In the microfluidic context, some operations like pumping or mixing rely on the gas dilatability to impose the liquid motion. We have shown that in such configurations the complete description of the flow in the gas is indeed necessary [7,10].

In this work we report the development and numerical implementation of a physical model dedicated to the simulation of low speed non-isothermal two-phase flows in closed vessels. To be specific, amongst the type of configurations we have in mind we can list a steam engine or a pressure cooker, or microfluidic devices like thermopneumatic actuators. To this aim, we propose a numerical algorithm in which both the liquid and gaseous phases are governed by their corresponding momentum and energy equations, the liquid phase being truly incompressible while the gaseous phase follows a low Mach number approximation. A single field formulation is derived that can describe the whole flow field. The two phases are separated by a dynamic interface across which the physical properties of both phases are discontinuous, and on which surface tension forces are taken into account. Phase change however is not considered in the present article, and is the object of ongoing work. The numerical integration of the single field model is based on front tracking techniques that have been developed for purely incompressible flows in [44,17,40].

The paper is organized as follows: Section 2 is devoted to the physical modeling equations, considering the case of multiple gaseous inclusions in an incompressible liquid. A single field formulation of such multiphase flows is derived. In this section we also discuss some specific details concerning the link between the thermodynamic pressure in the bubbles and the pressure in the liquid phase. Numerical methods are presented in Section 3. A comparison with a single pressure method on an isentropic classical test case is provided in Section 4, illustrating the high efficiency of our low Mach method. Section 5 presents numerical results for several non-isothermal cases. A validation study performed on a reference 1D case is first presented. Next are investigated 2D cases consisting of air bubbles embedded in a closed cavity filled with liquid water. Conclusions and perspectives will finally be drawn in Section 6.

2. Physical modeling and governing equations

2.1. Specific models for each phase

In this section we develop a single field formulation of a multiphase flow involving a strictly incompressible liquid phase and a compressible gaseous phase, the latter being considered under the low Mach number assumption. We consider a volume region of interest, \mathfrak{R} , containing a liquid phase (volume Ω_l) and N gaseous inclusions. The volume of each bubble is $\Omega_k(t)$ ($k = 1, 2, \dots, N$). No mass transfer occurs at the gas–liquid interfaces noted $\Sigma_k(t)$. Neglecting viscous loss in the energy balance, the following Navier–Stokes equations allow the description of the flow in the liquid and in the gas bubbles:

$$\begin{cases} \frac{\partial \rho}{\partial t} + \nabla \cdot (\rho \mathbf{v}) = 0 \\ \rho \left(\frac{\partial \mathbf{v}}{\partial t} + \mathbf{v} \cdot \nabla \mathbf{v} \right) = -\nabla p + \nabla \cdot \boldsymbol{\tau} + \rho \mathbf{g} \\ \rho c_p \left(\frac{\partial T}{\partial t} + \mathbf{v} \cdot \nabla T \right) = \nabla \cdot (k \nabla T) - \frac{T}{\rho} \left(\frac{\partial \rho}{\partial T} \right)_p \frac{Dp}{Dt} \\ p = f(\rho, T) \end{cases} \quad (1)$$

where $p(x,t)$ is the pressure, ρ the density, \mathbf{v} the velocity, T the temperature, c_p the specific heat, k the thermal conductivity and \mathbf{g} the gravitational acceleration. The viscous tensor $\boldsymbol{\tau}$ is equal to $\lambda \nabla \cdot \mathbf{v} \mathbf{I} + 2\mu \mathbf{D}$ with Lamé coefficients λ and μ , \mathbf{D} being the strain rate tensor and \mathbf{I} the identity tensor. The material derivative is denoted by $\frac{D}{Dt} = \frac{\partial}{\partial t} + \mathbf{v} \cdot \nabla$.

The interfaces between the liquid and the gas inclusions act as surfaces of discontinuity and jump conditions have to be used [8,12]. As no mass transfer is considered in the present case, these conditions read:

$$\begin{cases} \mathbf{v}_l \cdot \mathbf{n} = \mathbf{v}_g \cdot \mathbf{n} & (a) \\ (p_g - p_l) \mathbf{I} \cdot \mathbf{n} = (\boldsymbol{\tau}_g - \boldsymbol{\tau}_l) \cdot \mathbf{n} + \sigma \kappa \mathbf{n} & (b) \\ (\mathbf{q}_g - \mathbf{q}_l) \cdot \mathbf{n} = 0 & (c) \end{cases} \quad (2)$$

where σ is the surface tension coefficient, κ is twice the mean interface curvature which is positive when the center of curvature lies in the gas, \mathbf{n} is the unit normal to the interface, defined to point outside the gaseous phase and \mathbf{q} is the heat flux. In (2) the subscripts l and g denote the values on the liquid and gaseous sides of the interface.

We will consider in the present paper two-phase systems where an incompressible liquid is in contact with various gas bubbles, each one of them having its own pressure. For the liquid phase of constant density ρ_l , the Navier–Stokes equations (1) reduce to:

$$\begin{cases} \nabla \cdot \mathbf{v} = 0 & (a) \\ \rho_l \left(\frac{\partial \mathbf{v}}{\partial t} + \mathbf{v} \cdot \nabla \mathbf{v} \right) = -\nabla p + \nabla \cdot \boldsymbol{\tau} + \rho_l \mathbf{g} & (b) \\ \rho_l c_p \left(\frac{\partial T}{\partial t} + \mathbf{v} \cdot \nabla T \right) = \nabla \cdot (k \nabla T) & (c) \end{cases} \quad (3)$$

Now considering that bubbles are made of the same perfect gas, the Navier–Stokes equations (1) read in the gaseous phase:

$$\begin{cases} \frac{\partial \rho}{\partial t} + \nabla \cdot (\rho \mathbf{v}) = 0 \\ \rho \left(\frac{\partial \mathbf{v}}{\partial t} + \mathbf{v} \cdot \nabla \mathbf{v} \right) = -\nabla p + \nabla \cdot \boldsymbol{\tau} + \rho \mathbf{g} \\ \frac{\partial T}{\partial t} + \mathbf{v} \cdot \nabla T = \frac{1}{\rho c_p} \nabla \cdot (k \nabla T) + \frac{\gamma-1}{\gamma} \frac{T}{p} \frac{Dp}{Dt} \\ p = \rho r T \end{cases} \quad (4)$$

where r is the ideal gas constant $r = c_p - c_v$ and $\gamma = c_p/c_v$ is the ratio of specific heats.

The jump equations given by (2) are unchanged. The linear momentum jump condition notably shows that pressure is continuous through the interface provided that viscous and surface tension effects be negligible. Velocity should also be continuous at the interfaces by virtue of the continuity equation.

In this paper are solely considered gas liquid two-phase flows and small velocities. In this particular case, the Mach number in the compressible gaseous phase is small. The flow in the bubbles may then be described using a low Mach model [33,6,24]. Such a model is derived from the fully compressible Navier–Stokes equations (1) expanding each variable into a power series of the Mach number M_0 , and taking the asymptotic limit for M_0 going to zero. For each variable, the lowest order term remains in the equations, except for the pressure $p(\mathbf{x},t)$ which is split in two components, a thermodynamic pressure, uniform in space $P(t)$ and a hydrodynamic pressure $p_2(\mathbf{x},t)$. One has $p(\mathbf{x},t) \simeq P(t) + p_2(\mathbf{x},t)$. As the ratio $p_2(\mathbf{x},t)/P(t) \sim M_0^2$, the hydrodynamic pressure $p_2(\mathbf{x},t)$ is much smaller than the thermodynamic pressure $P(t)$. For a single-phase compressible flow of a perfect gas, the low Mach model can be written, expressing the conservation of mass, momentum and energy (viscous loss is neglected in the energy balance):

$$\begin{cases} \frac{\partial \rho}{\partial t} + \nabla \cdot (\rho \mathbf{v}) = 0 & (a) \\ \rho \left(\frac{\partial \mathbf{v}}{\partial t} + \mathbf{v} \cdot \nabla \mathbf{v} \right) = -\nabla p_2 + \nabla \cdot \boldsymbol{\tau} + \rho \mathbf{g} & (b) \\ \frac{\partial T}{\partial t} + \mathbf{v} \cdot \nabla T = \frac{1}{\rho c_p} \nabla \cdot (k \nabla T) + \frac{\gamma-1}{\gamma} \frac{T}{P} \frac{dP}{dt} & (c) \\ P = \rho r T & (d) \end{cases} \quad (5)$$

Using the ideal gas law $P(t) = \rho(\mathbf{x},t)rT(\mathbf{x},t)$, the continuity equation in (5) may also be written:

$$\nabla \cdot \mathbf{v} = -\frac{1}{\rho} \frac{D\rho}{Dt} = \frac{1}{T} \frac{DT}{Dt} - \frac{1}{P} \frac{dP}{dt} \quad (6)$$

2.2. Derivation of a single field formulation

We now have to build a single set of governing equations that can represent both phases. As our aim is to model the liquid phase as incompressible and the gas phase as compressible under the low Mach approximation, this set of equations must be consistent with Eqs. (2), (3) and (5). In order to develop a generalized single field model, let us classically introduce a Heaviside function $H(\mathbf{x},t)$, which is the characteristic function of the gaseous phase (H is equal to 1 in the gas, and equal to 0 in the liquid phase). If N bubbles of volume Ω_j , $j = 1, 2, \dots, N$ are present in \mathfrak{R} , each one is marked by its own characteristic function $H_j(\mathbf{x},t)$ and its own thermodynamic pressure $P_j(t)$. The gas characteristic function $H(\mathbf{x},t)$ is given by $H = \sum_{j=1}^N H_j$ since $\Omega_j \cap \Omega_i = \emptyset$ for $i \neq j$.

As no phase change is considered in the present paper, H is simply advected by the flow, and thus obeys to the following transport equation (although this equation is not directly solved in the front-tracking method that we use for interface treatment):

$$\frac{\partial H}{\partial t} + \mathbf{v} \cdot \nabla H = 0 \quad (7)$$

2.2.1. Continuity and energy equations

We also must define a generalized equation of state valid for the two phases. The liquid assumed to be incompressible has a constant density ρ_l . Using the perfect gas law, a two-phase generalized equation of state can be written as:

$$\rho(\mathbf{x},t) = \sum_{j=1}^N H_j(\mathbf{x},t) \frac{P_j(t)}{rT(\mathbf{x},t)} + (1 - H(\mathbf{x},t))\rho_l \quad (8)$$

Using (6)–(8), it is now possible to establish a generalized continuity equation valid in both liquid ($H = 0$) and gas ($H = 1$) phases:

$$\nabla \cdot \mathbf{v} = H(\mathbf{x}, t) \frac{1}{T} \frac{DT}{Dt} - \sum_{j=1}^N H_j(\mathbf{x}, t) \frac{1}{P_j} \frac{dP_j}{dt} \quad (9)$$

Similarly is established a generalized energy equation:

$$\left(\frac{\partial T}{\partial t} + \mathbf{v} \cdot \nabla T \right) = \frac{1}{\rho c_p} \nabla \cdot (k \nabla T) + \frac{\gamma - 1}{\gamma} T \sum_{j=1}^N H_j(\mathbf{x}, t) \frac{1}{P_j} \frac{dP_j}{dt} \quad (10)$$

The thermodynamic pressure may be calculated using an integral relation that is now derived. Let us suppose that the gaseous phase $\Omega_j(t)$ is enclosed by walls or by the liquid phase (case of a bubble for example), and let us denote by \mathbf{n} the unit outward normal to the bounding surface $\Sigma_j(t)$. We integrate the mass Eq. (9) over $\Omega_j(t)$ to obtain:

$$\frac{1}{P_j} \frac{dP_j}{dt} = \frac{1}{\int_{\Omega_j(t)} d\mathbf{x}} \left(\int_{\Omega_j(t)} \frac{1}{T} \frac{DT}{Dt} d\mathbf{x} - \int_{\Omega_j(t)} \nabla \cdot \mathbf{v} d\mathbf{x} \right) \quad (11)$$

or equivalently:

$$\frac{1}{P_j} \frac{dP_j}{dt} = \frac{1}{\int_{\mathfrak{R}} H_j d\mathbf{x}} \left(\int_{\mathfrak{R}} H_j \frac{1}{T} \frac{DT}{Dt} d\mathbf{x} - \int_{\Sigma_j(t)} \mathbf{v} \cdot \mathbf{n} ds \right) \quad (12)$$

This formulation allows for the calculation of the source term $\frac{1}{P_j} \frac{dP_j}{dt}$ in the energy Eq. (10). Once $\frac{1}{P_j} \frac{dP_j}{dt}$ is known, the pressure $P_j(t)$ can be obtained directly from a time integration, i.e.:

$$P_j(t) = P_j(t_0) \cdot \exp \int_{t_0}^t \left(\frac{1}{P_j} \frac{dP_j}{dt'} \right) dt' \quad (13)$$

Let us note for further usage that, owing to incompressibility, the surface term integration in (12) can be done over any closed contour in the liquid enclosing the gaseous zone $\Omega_j(t)$.

An important point to emphasize concerning the above model is that, in addition to the increased accuracy that can be expected from the splitting of the pressure into two components of different magnitudes, the calculation of the thermodynamic pressure using the integral relation (11) constitutes a means of imposing mass conservation of the gaseous phase separately. This is a very important advantage over other methods based on the use of a single pressure field, as will be illustrated on 1D numerical results (Section 4).

2.2.2. Momentum equation and pressure issues

We now have to consider the momentum equation issue. Its treatment cannot be as straightforward as for continuity and energy equations and deserves a few preliminary comments. Even though the momentum equations as written in (3b) and (5b) appear to be very similar, an essential difference arises due to the pressure gradient term. Let us recall that the problems of interest in the present paper concern a liquid volume with several gaseous inclusions, each one having its own (thermodynamic) pressure. The linear momentum jump Eq. (2b) shows that for any interface, the local pressure is the same on both gaseous and liquid sides (viscous and surface tension effects are disregarded here for the sake of comprehension). The difference in the bubbles' pressure therefore generates a pressure gradient in the liquid volume which induces in turn an acceleration of the liquid. This pressure gradient, ∇p in Eq. (3b), is expected to scale as P_0/L_0 where L_0 and P_0 are respectively the characteristic values for the liquid dimension and for the thermodynamic pressure in the bubbles. On the other hand, the pressure p_2 defined in the low Mach model (5) scales as $M_0^2 P_0$ leading the pressure gradient in Eq. (5b) to scale as $M_0^2 P_0/L_0$. At that point, it is obvious that a proper description of the incompressible liquid flow cannot be achieved through momentum Eq. (5b). It is clear however that the problem does not arise if the thermodynamic pressure, although being constant, is retained in the momentum equation of the low Mach model Eq. (5b), that can equivalently be written:

$$\rho \left(\frac{\partial \mathbf{v}}{\partial t} + \mathbf{v} \cdot \nabla \mathbf{v} \right) = -\nabla(p_2 + P) + \nabla \cdot \boldsymbol{\tau} + \rho \mathbf{g} \quad (14)$$

When using Eq. (14) to derive the momentum jump equation at the interfaces, which now reads:

$$((p_2 + P)_g - p_l) \mathbf{I} \cdot \mathbf{n} = (\boldsymbol{\tau}_g - \boldsymbol{\tau}_l) \cdot \mathbf{n} + \sigma \kappa \mathbf{n} \quad (15)$$

then the total pressure at the gas side has the proper magnitude.

The splitting of pressure in the gas suggests a corresponding splitting of pressure in the liquid, aimed at providing a single momentum equation valid for both phases. We thus propose to split the liquid pressure field into two components P_l and π_l that is:

$$p(\mathbf{x}, t) = \pi_l(\mathbf{x}, t) + P_l(\mathbf{x}, t) \quad (16)$$

in the liquid.

We choose to define the respective components of the pressure in such a way that the momentum jump relations split like:

$$\begin{cases} (p_{2g} - \pi_l) \mathbf{I} \cdot \mathbf{n} = (\boldsymbol{\tau}_g - \boldsymbol{\tau}_l) \cdot \mathbf{n} + \sigma \kappa \mathbf{n} & (a) \\ (P_g - P_l) \mathbf{I} \cdot \mathbf{n} = 0 & (b) \end{cases} \quad (17)$$

i.e. the jump relations due to surface tension and viscous tensor are ascribed to p_{2g} and π_l whereas P_g and P_l are equal at the liquid gas interface.

In addition, in the same way as p_2 is the Lagrangian multiplier of the continuity equation in the gas, we ascribe to π_l its respective role of Lagrangian multiplier of the divergence free continuity equation in the liquid. This will later be used to solve simultaneously for p_2 and π_l in the framework of a single field equation in the projection step of the time stepping algorithm. This is achieved by requiring that P_l be harmonic in the liquid since the divergence of its gradient is then identically zero.

Finally let us call $P_e(\mathbf{x}, t)$ (extended thermodynamic pressure field) the pressure field that is equal to $P_j(t)$ in each bubble and to $P_l(\mathbf{x}, t)$ in the liquid. P_e is continuous at the interfaces from (17b). Similarly we call π the hydrodynamic pressure field that is equal to p_2 in the gas, and to π_l in the liquid. We thus have built two pressure fields defined in the whole domain, their sum giving the correct jump relations at the interfaces. Using these two pressure fields a single field momentum equation capable of treating both phases can be written as:

$$\rho \left(\frac{\partial \mathbf{v}}{\partial t} + \mathbf{v} \cdot \nabla \mathbf{v} \right) = -\nabla \pi - \nabla P_e + \nabla \cdot \boldsymbol{\tau} + \rho \mathbf{g} \quad (18)$$

Let us now construct the equation for this auxiliary field $P_e(\mathbf{x}, t)$. As said above, P_e satisfies:

$$\begin{cases} \nabla^2 P_e(\mathbf{x}, t) = 0, & \text{in the liquid} \\ P_e(\mathbf{x}, t) = P_j(t), & \text{in each gas bubble} \end{cases} \quad (19)$$

Moreover, since this auxiliary pressure field should not modify the velocity at the domain boundaries, $P_e(\mathbf{x}, t)$ satisfies an homogeneous Neumann boundary condition on the walls of any closed domain. The above constraints are summarized in the following equation for P_e :

$$\frac{1}{\eta^2} P_e(\mathbf{x}, t) \cdot H(\mathbf{x}, t) + (1 - H(\mathbf{x}, t)) \cdot \nabla^2 P_e(\mathbf{x}, t) = \sum_{j=1}^N H_j(\mathbf{x}, t) \cdot \frac{1}{\eta^2} P_j(t) \quad (20)$$

supplemented with homogeneous Neumann boundary conditions on the walls. The quantity η , which is homogeneous to a length, is introduced in the composite Eq. (20) for dimensional consistency. If the Heaviside function H was strictly a characteristic function equal to either 0 or 1, the value of η would have no influence on the solution. However, in the numerical implementation of the model, H is smoothed over a few mesh cells, leading to the existence of a transition zone (of fixed width) between the two pure phases where H can take values between 0 and 1 (see Section 3.1). The influence of η on the numerical solution is analyzed in Section 3.2.

As a summary, the governing equations of the single field model are now:

$$\begin{cases} \nabla \cdot \mathbf{v} = H(\mathbf{x}, t) \frac{1}{T} \frac{DT}{Dt} - \sum_{j=1}^N H_j(\mathbf{x}, t) \frac{1}{P_j} \frac{dP_j}{dt} & (a) \\ \frac{D\mathbf{v}}{Dt} = -\frac{1}{\rho} \nabla \pi - \frac{1}{\rho} \nabla P_e + \frac{1}{\rho} \nabla \cdot \boldsymbol{\tau} + \mathbf{g} & (b) \\ \frac{DT}{Dt} = \frac{1}{\rho c_p} \nabla \cdot (k \nabla T) + \frac{\gamma-1}{\gamma} T \sum_{j=1}^N H_j(\mathbf{x}, t) \frac{1}{P_j} \frac{dP_j}{dt} & (c) \end{cases} \quad (21)$$

Surface tension was not included so far. It can be taken into account by adding in the right hand side of the momentum Eq. (21b) the following integral source term acting on the interface:

$$-\frac{1}{\rho} \int_{\Sigma(t)} \sigma \kappa \mathbf{n} \delta(\mathbf{x} - \mathbf{x}_s) ds \quad (22)$$

where $\mathbf{x}_s = \mathbf{x}(s, t)$ is a parametrization of $\Sigma(t)$. The function $\delta(\mathbf{x} - \mathbf{x}_s)$ is a three-dimensional delta function that is non-zero only where $\mathbf{x} = \mathbf{x}_s$. We also use H to construct the material property fields of the fluid for both the liquid and gaseous phases. For example, one way to construct the viscosity field is given by:

$$\mu(\mathbf{x}, t) = \mu_l + (\mu_g - \mu_l) H(\mathbf{x}, t) \quad (23)$$

where the subscripts g and l refer to the gas and liquid phases respectively. Similar equations can be written for the thermal conductivity, k , constant volume, c_v , or constant pressure, c_p , specific heats.

The jump conditions associated to system (21) are given by Eqs. (2a), (2c), (17). These conditions are not explicitly needed for our formulation, and are not used in the numerical method. However we will check that they are indeed satisfied by the numerical solution.

2.3. Illustration on a 1D Cartesian case

As an illustration, we apply this model on a simple 1D Cartesian case consisting of a moving liquid zone $\Omega_l = [x_1, x_2]$ of constant length $L = x_2 - x_1$, enclosed between two gaseous zones Ω_1 and Ω_2 of variable length. This case was investigated in detail in [10], using an ALE approach where liquid and gaseous domains were considered separately. The thermodynamic pressures in the gaseous zones are $P_1(t)$ and $P_2(t)$. We consider here a simplified problem with no gravity and no viscous effects. Following (3), the formulation of the dynamic problem in the liquid is:

$$\begin{cases} \frac{\partial u_l}{\partial x} = 0 \\ \frac{\partial u_l}{\partial t} + u_l \frac{\partial u_l}{\partial x} = -\frac{1}{\rho_l} \frac{\partial p_l}{\partial x} \end{cases} \quad (24)$$

The continuity equation shows that $u_l(x, t) = u_l(t)$. The pressure gradient is thus uniform in the liquid and may be written:

$$\frac{\partial p_l}{\partial x} = \frac{p_l(x_2, t) - p_l(x_1, t)}{L} \quad (25)$$

In 1D Cartesian co-ordinates, the momentum jump Eq. (2b) reduces to:

$$p_g(x_k, t) = p_l(x_k, t) \quad k = 1, 2 \quad (26)$$

Using a low Mach model for the gas description, the pressure on the gaseous side of any interface reads:

$$p_g(x_k, t) = P_k(t) + \pi_g(x_k, t) \quad k = 1, 2 \quad (27)$$

Splitting the pressure p_l in two components P_e and π_l , it comes:

$$\frac{\partial p_l}{\partial x} = \frac{\partial P_e}{\partial x} + \frac{\partial \pi_l}{\partial x} \quad (28)$$

Both terms in the r.h.s. are next identified using Eqs. (25)–(28):

$$\begin{aligned} \frac{\partial P_e}{\partial x} &= \frac{P_2(t) - P_1(t)}{L} \\ \frac{\partial \pi_l}{\partial x} &= \frac{\pi_l(x_2, t) - \pi_l(x_1, t)}{L} \end{aligned} \quad (29)$$

In this particular 1D Cartesian case, both pressure fields P_e and π are linear in the liquid. Using Eqs. (24)–(27), the momentum equation in the liquid may also be written:

$$\rho_l L \frac{du_l}{dt} = [P_1(t) + \pi_g(x_1, t)] - [P_2(t) + \pi_g(x_2, t)] \quad (30)$$

$$\rho_l L \frac{du_l}{dt} \cong P_1(t) - P_2(t) \quad (31)$$

One recognizes here the second law of Newton applied to the whole liquid domain Ω_l . It states that a liquid acceleration arises from the difference between the (thermodynamic) pressure forces in the two gaseous media.

3. Numerical method

3.1. Interface treatment

The model described above must be coupled to a specific method for tracking the liquid–gas interface. Among the existing methods, we have chosen here to use the Lagrangian front-tracking method developed in [11,17,44] and subsequent papers. A robust and connectivity free method to reconstruct the interface for both two and three-dimensional flows is discussed in [40]. This method uses a Lagrangian discretization and movement of the interface. The interface is represented by separate, non-stationary computational elements (straight lines in 2D, triangles in 3D) which are physically connected at their vertices to form a Lagrangian interface mesh which lies within a stationary Eulerian finite-difference mesh. The interface elements are used to calculate geometric information and their vertices are advected in an explicit Lagrangian way, by integrating:

$$\frac{d\mathbf{x}_s}{dt} = \mathbf{v} \quad (32)$$

A Heaviside function $H(\mathbf{x}, t)$, defined on the Eulerian grid, is found from the Lagrangian definition of the interface at each time step, by solving the following Poisson equation:

$$\nabla^2 H = \nabla \cdot \int_{\Sigma(t)} \mathbf{n} \delta(\mathbf{x} - \mathbf{x}_s) ds. \quad (33)$$

using the definitions introduced in Section 2. Once $H(\mathbf{x},t)$ has been determined from \mathbf{x}_s we can use it to construct values for the material property fields of the fluid for both the liquid and gaseous phases, using Eq. (23) and similar equations for k and c_p .

At each time step, information must be passed between the moving Lagrangian interface and the stationary Eulerian grid since the Lagrangian interface points do not necessarily coincide with the Eulerian grid points. This is done by a method that has become known as the Immersed Boundary Technique which was introduced by Peskin [34] for the analysis of blood flow in the heart. With this technique, the infinitely thin interface is approximated by a smooth distribution function that is used to distribute the forces at the interface over grid points nearest the interface. In a similar manner, this function is used to interpolate field variables from the stationary grid to the interface. In this way, the front is given a finite thickness on the order of the mesh size to provide stability and smoothness. This leads to the existence of a “mixing” zone between the two fluids, where the model has no real physical meaning. Although the interface is smoothed, the method however is free from numerical diffusion since the interface thickness remains constant for all time, as it is directly controlled through the definition of the smoothed delta function, which is built on the Lagrangian definition of the interface. The question of the convergence of the method was considered, for example, in [11,44]. Surface tension is treated using the method developed in [39], which was shown to minimize the parasitic currents that are commonly generated by inadequate numerical representation of surface tension.

3.2. Fixing the parameter η in the equation for extended pressure

In this section we study the behavior of the function P_e in the transition zone that is created at the interfaces by the Immersed Boundary Technique. Without loss of generality, we restrict our study to the one-dimensional case for clarity reasons. Let us consider an isolated transition zone of width l between gas at the left, at thermodynamic pressure $P_0(t)$, and liquid at the right. Let $y = x/l$ be the non-dimensional abscissa describing the zone ($0 \leq y \leq 1$) ($x = 0$ corresponding to the left boundary of the transition zone). Setting $\chi(y) = H(x,t)$ and $f(y) = P_e(y,t) - P_0(t)$, Eq. (20) reads:

$$\chi(y)f(y) + (1 - \chi(y)) \frac{\eta^2}{l^2} f'' = 0 \quad (34)$$

The boundary conditions associated to (34) are: $f(0) = 0, f(1) = l g_P$, where g_P is the thermodynamic pressure gradient across the liquid imposed by the existence of another separated gaseous area (the extended pressure profile being harmonic is linear in the liquid in the 1D case). Although Eq. (34) can be solved only for simple χ profiles, it is interesting to study its behavior for extreme values of the parameter $\epsilon = \eta/l$. For $\epsilon \ll 1$, we get $f(y) \approx 0$, that is $P_e(x,t) \approx P_0(t)$ in the transition zone. For $\epsilon \gg 1$ we get $f(y) \approx l g_P y$, that is $P_e(x,t) \approx P_0(t) + g_P x$. This leads to conclude that the difference between the two values of ϵ results in a shift of the global P_e profile by the length l , the linear part starting at the gaseous side in the case $\epsilon \gg 1$ and at the liquid side in the case $\epsilon \ll 1$. In the case where ϵ takes intermediate values, for instance $\epsilon = 1$, the profile of P_e will result in an intermediate curve, with the same gradient at the liquid side (see Fig. 1 left).

The question is now to analyze whether what happens in the transition zone has some influence on the gradient of the calculated field P_e . To this end we must take into account a second gaseous zone that we suppose at thermodynamic pressure

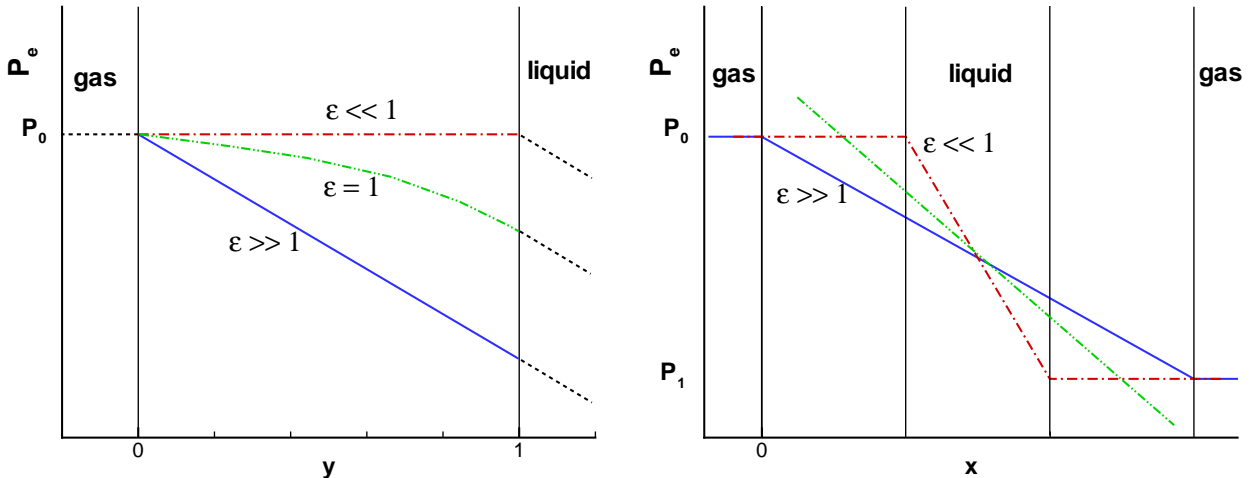


Fig. 1. Extended pressure profile. Left: inside a transition zone, for different values of ϵ . Right: global for two gaseous zones (the green dash-dot-dot line shows the exact slope in the liquid). (For interpretation of the references to color in this figure legend, the reader is referred to the web version of this article.)

P_1 , which will fix the extended pressure gradient inside the liquid. Considering the previous analysis, we can conclude that, in function of the value of ϵ , the linear variation of the calculated P_e takes place between the two gaseous sides ($\epsilon \gg 1$), or between the two liquid sides ($\epsilon \ll 1$). This will change the extended pressure gradient of an amount proportional to the width of the transition zone (thus on the order of the mesh size) as is illustrated in Fig. 1(right). The exact value of the gradient will be obtained if the linear part of P_e originates at the interface, that is in the middle of the transition zone. Indeed the error will be reduced with mesh refinement. The error also decreases when the ratio of the transition zone length to liquid width is small.

From the previous analysis we can conclude that η should be of the same order than l , although any other value will give the correct result at grid convergence. In results presented in the following, we fixed $\eta = l = 4\delta x$, δx being the grid cell size.

3.3. Discretization and projection method

The spatial discretization of model (21), (11), (20) is based on centered finite differences for both the convection and diffusion terms. A staggered mesh is used, where density, hydrodynamic pressure, extended pressure and temperature are located at the center of the cells, while the components of the velocity are located on the faces. We have used here a first order explicit temporal discretization, but the extension to semi-implicit second order should be considered in the future. A classical prediction–projection algorithm is used to compute the velocities [15]. The predicted velocity \mathbf{v}^* is calculated from:

$$\frac{\mathbf{v}^* - \mathbf{v}^n}{\delta t} = -\mathbf{v}^n \cdot \nabla \mathbf{v}^n + \frac{1}{\rho^{n+1}} \nabla \cdot \boldsymbol{\tau}^n - \frac{1}{\rho^{n+1}} \nabla \pi^n - \frac{1}{\rho^{n+1}} \nabla P_e^n + \mathbf{g} \quad (35)$$

Calculating \mathbf{v}^* from Eq. (35) needs to calculate first the extended thermodynamic pressure field P_e . To this end Eq. (20) is solved using a BiCGStab solver.

Once \mathbf{v}^* is known, the projection step consists in extracting \mathbf{v}^{n+1} from \mathbf{v}^* in such a way that $\nabla \cdot \mathbf{v}^{n+1}$ is zero in the liquid, and equal to its specified value in the gas. This amounts to solving the following Poisson equation for the hydrodynamic pressure:

$$\nabla \cdot \left(\frac{1}{\rho^{n+1}} \nabla \phi \right) = \frac{1}{\delta t} (\nabla \cdot \mathbf{v}^* - \nabla \cdot \mathbf{v}^{n+1}) \quad (36)$$

where $\phi = \pi^{n+1} - \pi^n$ is the pressure increment. In the r.h.s. of Eq. (36), $\nabla \cdot \mathbf{v}^{n+1}$ is obtained using the mass conservation Eq. (21a), after the temperature field and $\frac{1}{P_j} \frac{dP_j}{dt}$ in each gaseous inclusion have been calculated. The latter are calculated using a more convenient form of Eq. (11):

$$\frac{1}{P_j} \frac{dP_j}{dt} = \frac{1}{\int_{\mathcal{R}} H_j d\mathbf{x}} \left(\int_{\mathcal{R}} H_j \frac{1}{T} \frac{DT}{Dt} d\mathbf{x} - \int_{\mathcal{R}} H_j \nabla \cdot \mathbf{v} d\mathbf{x} \right) \quad (37)$$

The solution of (36) requires a robust matrix solver as the coefficients $1/\rho$ are discontinuous, the ratio between the gas and liquid density being generally very large (around 1000 for air–water, much more for example if the liquid is molten glass). To this end, we have used a multigrid method that is described in Appendix A.

Once the hydrodynamic pressure is obtained, the velocity is calculated from:

$$\mathbf{v}^{n+1} = \mathbf{v}^* - \delta t \frac{1}{\rho^{n+1}} \nabla \phi \quad (38)$$

and the hydrodynamic pressure field is updated by:

$$\pi^{n+1} = \pi^n + \phi \quad (39)$$

Let us now sum up the complete numerical methodology for the determination of the solution at time $t = (n + 1)\delta t$, assuming the solution known at time $t = n\delta t$. Due to the non-linear coupling of the equations, iterations are necessary within each time step. Indeed, the calculation of $(\frac{1}{P} \frac{dP}{dt})_j^{n+1}$ using Eq. (37) makes use of the velocity \mathbf{v}^{n+1} which is unknown at the first iteration. A convenient first guess for \mathbf{v}^{n+1} can be obtained from the discretization of a simplified momentum equation, where only the external forces (extended thermodynamic and gravity forces) are taken into account. It is important to include the extended pressure force in the first guess in order to avoid selecting the trivial solution consisting of fluid at rest. For this solution, in the absence of gravity, the hydrodynamic pressure field is obtained as the opposite of the thermodynamic pressure field.

The whole procedure is then:

- (1) using the front-tracking method, calculate H_j^{n+1} in each gaseous zone, $H^{n+1} = \sum_{j=1}^N H_j^{n+1}$ and the new values of k , c_p .
- (2) Set guessed estimates $P_j^{n+1} = P_j^n$, $(\frac{1}{P} \frac{dP}{dt})_j^{n+1} = (\frac{1}{P} \frac{dP}{dt})_j^n$, $\rho^{n+1} = \rho^n$, $\mathbf{v}^{n+1} = \mathbf{v}^n - \delta t \frac{1}{\rho^n} \nabla P_e^n + \delta t \mathbf{g}$.
- (3)
 - solve Eq. (21c) for T^{n+1} using $(\frac{1}{P} \frac{dP}{dt})_j^{n+1}$;
 - calculate the new value of $(\frac{1}{P} \frac{dP}{dt})_j^{n+1}$ and P_j^{n+1} in each gaseous zone using \mathbf{v}^{n+1} , H^{n+1} and T^{n+1} in (37) and (13);

- calculate ρ^{n+1} using (8);
 - calculate the extended thermodynamic pressure $P_e^{n+1}(\mathbf{x}, t)$ from (20) using P_j^{n+1} , H_j^{n+1} ;
 - calculate $\nabla \cdot \mathbf{v}^{n+1}$ for the Poisson equation using the mass Eq. (21a);
 - calculate the predicted velocities \mathbf{v}^* from (35);
 - solve (36) for the hydrodynamic pressure increment ϕ (multigrid);
 - project the velocity by (38);
 - increment the hydrodynamic pressure by (39).
- (4) If the computed thermodynamical pressure, density and velocity are different from the ones used at the beginning of step 3, restart from step 3 for a new iteration.

In the computations presented in this study, two to four iterations were needed for the convergence of the thermodynamical pressure. However the results with or without internal iterations were indistinguishable. This might not be true for other types of flows.

For closed gaseous zones, an important point to emphasize is the compatibility relation that must be satisfied when processing the integration of (37) to calculate $(\frac{1}{P} \frac{dP}{dt})^{n+1}$ in each gaseous zone. In the case where the fluid domain is bounded by walls and includes N closed gaseous zones, replacing the N Eq. (37) in (21a) and integrating over the whole domain results in the following relation:

$$\sum_{j=1}^N \int_{\Omega_j(t)} \nabla \cdot \mathbf{v} d\mathbf{x} = 0 \quad (40)$$

However, in the front-tracking method, as already mentioned, there exists a mixing zone, a few cells thick, inside which the velocity results from the blending of the liquid velocity, which is divergence free, and the gas velocity which is not. Thus there is no chance that the global balances (40) be zero if the contour of integration for each gaseous zone is located inside this mixing zone. In fact the contour of integration must include the mixing zone up to the liquid, or equivalently the volume integral in (40) must take into account all grid cells for which H_j is not zero. To do this we define an “enlarged” function H_j^{ext} , such that:

$$\begin{cases} H_j^{ext}(\mathbf{x}, t) = 1, & \text{if } H_j(\mathbf{x}, t) \neq 0 \\ H_j^{ext}(\mathbf{x}, t) = 0, & \text{if } H_j(\mathbf{x}, t) = 0 \end{cases} \quad (41)$$

This enlarged characteristic function is used for the integration of (37) that becomes:

$$\frac{1}{P_j} \frac{dP_j}{dt} = \frac{1}{\int_{\mathfrak{R}} H_j d\mathbf{x}} \left(\int_{\mathfrak{R}} H_j \frac{1}{T} \frac{DT}{Dt} d\mathbf{x} - \int_{\mathfrak{R}} H_j^{ext} \nabla \cdot \mathbf{v} d\mathbf{x} \right) \quad (42)$$

4. Comparison of the 1D low Mach method with a single pressure method on the oscillating water column test case

In this section we highlight the capability of our low Mach method to produce accurate results, even when the time step is of the order of the convective time step, *i.e.* large compared to an explicit acoustic stability criteria. On the opposite, we show that a method involving a single pressure (falling in the class of all-Mach methods) needs to be used with small time steps, as it produces very large numerical diffusion when too large time steps are used. It is likely that other single pressure methods, which use more or less the same equation for the pressure, will lead to similar conclusions. This demonstrates that a very significant gain in efficiency is obtained using our low Mach method. Moreover the gain is expected to be inversely proportional to the Mach number.

We consider the oscillating water column, a 1D isentropic problem that is treated in [19,18]. The problem is as follows: a closed 1D tube is filled with a column of water in between of two columns of air. We use the same physical settings as in [19,18] (see Fig. 2). At initial state, $x_{fs} = 0.1$ and all three columns flow to the right at constant speed $u_0 = 1$ and constant pressure $p_0 = 1$. Starting from initial state, the air to the right is compressed by the water while the air to the left expands, generating a pressure difference across the water column. The water column then starts to oscillate. In the following results we use the isentropic equation of state for air:

$$p/p_0 = (\rho/\rho_0)^{1/\gamma} \quad (43)$$

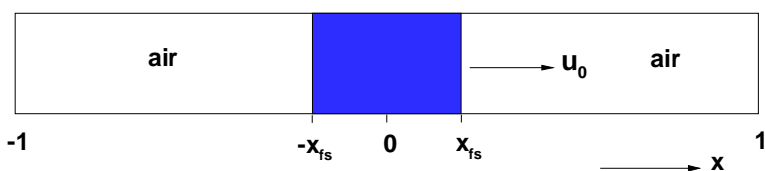


Fig. 2. Initial conditions for the Oscillatory Water Column test case.

with $\gamma = 1.4$, and initial value $\rho_0 = 0.001$. This also sets the reference speed of sound value in air $c_a = (\gamma p_0 / \rho_0)^{1/2} = 37.42$. Water is considered as incompressible, of constant density $\rho_w = 1$, and the fluid viscosities are set to zero. In our low Mach model, the thermodynamic pressure P is used in (43). Let us notice that in this problem the Mach number in the gas never exceeds 0.03 as we have verified, justifying the low Mach assumption.

In [19], water and air are both treated as compressible fluids, and an explicit method is used. The work in [18] also treats the water as compressible, and makes use of a single pressure implicit method aimed at solving all speed multiphase flows, where a Helmholtz equation comparable to the one in [7] is solved for pressure. However in [18] the gas-dynamics equations are not solved in the gas, avoiding the difficulties of a real two-phase flow computation.

Let us briefly describe the single pressure method that we use for these computations. The flow model is a single pressure isentropic version of (21), that writes:

$$\begin{cases} \nabla \cdot \mathbf{v} = -H(\mathbf{x}, t) \frac{1}{\rho} \frac{D\rho}{Dt} = -H(\mathbf{x}, t) \frac{1}{\gamma p} \frac{Dp}{Dt} \\ \frac{\partial \mathbf{v}}{\partial t} + \mathbf{v} \cdot \nabla \mathbf{v} + \frac{1}{\rho} \nabla p = \frac{1}{\rho} \nabla \cdot \boldsymbol{\tau} + \mathbf{g} \end{cases} \quad (44)$$

where p is the (unique) pressure that is involved in the equation of state. We first approximate the continuity equation by:

$$\nabla \cdot \mathbf{v}^{n+1} = -H^{n+1} \frac{1}{\gamma p^*} \left(\frac{p^{n+1} - p^n}{\delta t} + \mathbf{v}^* \nabla p^{n+1} \right) \quad (45)$$

\mathbf{v}^* being the predicted velocity and p^* obtained by second order backward time extrapolation. This results in the following equation for the pressure:

$$\nabla \cdot \left(\frac{1}{\rho^*} \nabla \phi \right) - \frac{1}{\delta t^2} \frac{H^{n+1}}{\gamma p^*} \phi - \frac{1}{\delta t} \frac{H^{n+1}}{\gamma p^*} \mathbf{v}^* \nabla \phi = \frac{1}{\delta t} \nabla \cdot \mathbf{v}^* + \frac{1}{\delta t} \frac{H^{n+1}}{\gamma p^*} \mathbf{v}^* \nabla p^n \quad (46)$$

with $\rho^* = H^{n+1} \rho_0 (p^*/p_0)^\gamma + (1 - H^{n+1}) \rho_w$.

We first present the results obtained using our two-pressure low Mach method. For comparison with an explicit method and the results in [19,18], the time step is calculated as a multiple of the one obtained by using the stability criteria in [19]:

$$\delta t = \text{CFL} \frac{\delta x}{\max_j |u_j| + c_w} \quad (47)$$

where c_w is the value of speed of sound in water used in [19], $c_w = 144.94$. In the explicit case the stability criterion is $\text{CFL} \leq 1$, while a stability criterion based on the convective velocity would allow values of CFL of the order of 100.

We present results for a uniform grid with $\delta x = 1/40$. Fig. 3 presents the time evolution of the pressure coefficients obtained using our low Mach model, for two values of the CFL number, $\text{CFL} = 1$ and $\text{CFL} = 100$. The pressure coefficients are defined as

$$P(t) = \frac{p(x_{wall}, t) - p_0}{p_0} \quad (48)$$

where x_{wall} denote the positions at the left and right walls. The pressure p in (48) is taken as the thermodynamic pressure for the low Mach method. One can remark that the curves corresponding to $\text{CFL} = 1$ and $\text{CFL} = 100$ are nearly superimposed,

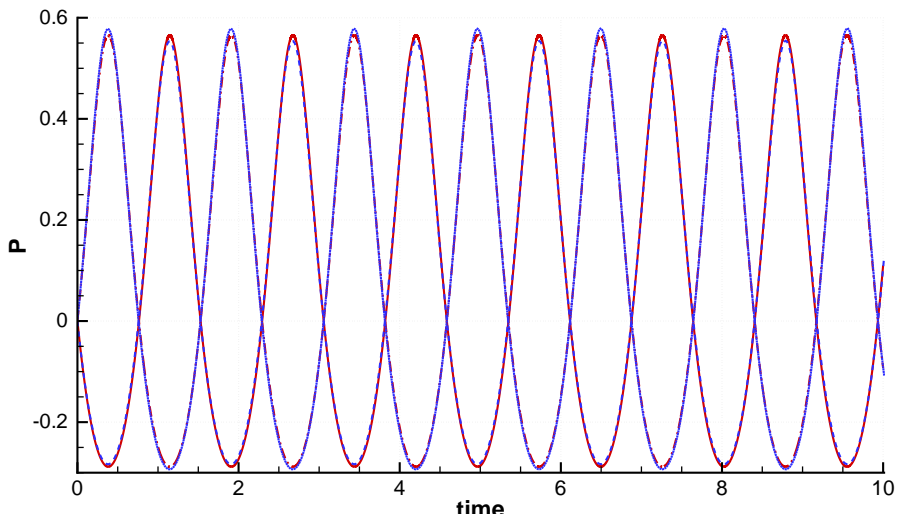


Fig. 3. Low Mach method. Time evolution of the pressure coefficients at left and right air columns (red solid and dash-dotted lines, left and right boundaries, $\text{CFL} = 1$, blue dashed and dotted lines, left and right boundaries, $\text{CFL} = 100$). (For interpretation of the references to color in this figure legend, the reader is referred to the web version of this article.)

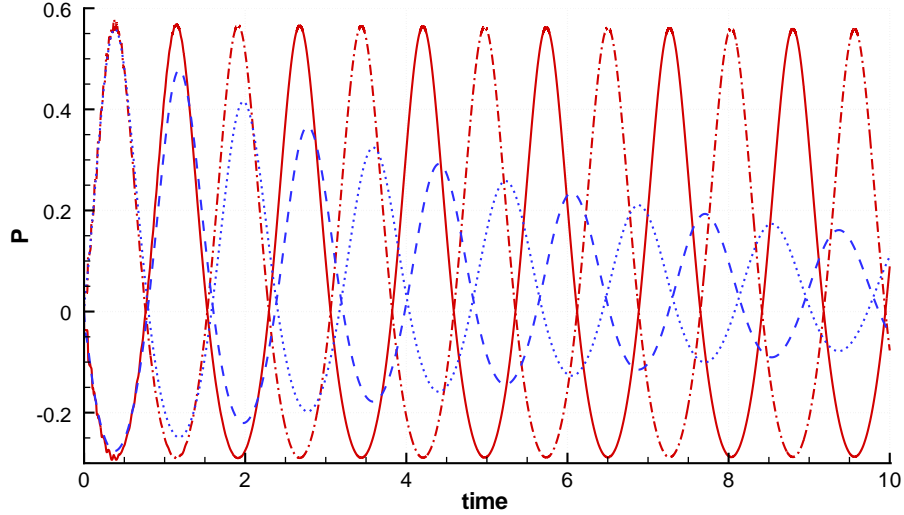


Fig. 4. Single pressure method. Time evolution of the pressure coefficients at left and right air columns (red solid and dash-dotted lines, left and right boundaries, $CFL = 1$, blue dashed and dotted lines, left and right boundaries, $CFL = 100$). (For interpretation of the references to color in this figure legend, the reader is referred to the web version of this article.)

indicating that the method is accurate even using large time steps. Surprisingly, the pressure levels are the same as in [18], which are different from those in [19], although we use a two-fluid model. On the contrary, corresponding results using the single pressure method, presented in Fig. 4, exhibit a very large dependence on the time step. For $CFL = 1$, the results coincide with those given by the low Mach method. For $CFL = 100$, the oscillation of the flow decays due to significant numerical dissipation. This implies that the single pressure method can be used only with small values of the CFL number based on acoustic speed, leading to poor efficiency.

Figs. 5 and 6 present the time evolution of the relative error of total mass of air in the tube for the two methods. The error presents a similar amplitude, about 10^{-3} , for the two methods at $CFL = 1$. This value is close to the one reported in [19]. It is much higher than the mass conservation error reported in [18] (10^{-7}). However in this work the interface was considered as a moving boundary, described using a level set method combined with a ghost fluid treatment that avoids the errors due to the jump of the fluids properties. For $CFL = 100$, the error of the low Mach method is only about 3–4 times the error for $CFL = 1$, which shows that the gain in efficiency is not accompanied by an error increase in the same proportions. On the contrary, the single pressure method generates much larger mass conservation errors for large CFL values. Moreover the total mass of air is decreasing, meaning that air is converted into water. This phenomenon, that was also observed in [19], does not appear when using the low Mach method, the mass of each fluid being conserved separately.

We conclude this section with a grid convergence study of the low Mach method for $CFL = 100$. Fig. 7 presents the velocity fields at time $t = 10$, obtained for increasing grid resolution: $\delta x = 1/40$, $\delta x = 1/80$, $\delta x = 1/160$, $\delta x = 1/320$. In the liquid column the velocity is uniform due to incompressibility, while it is linear in the gaseous columns. One can notice that the differences

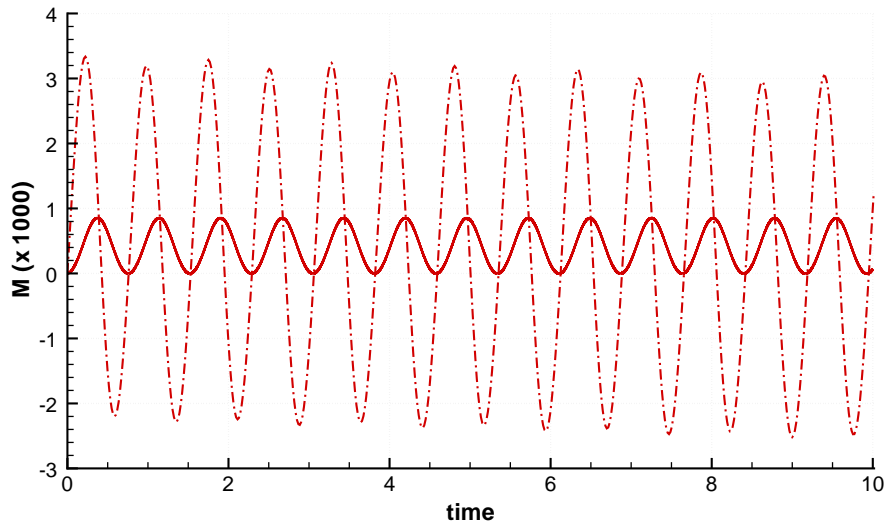


Fig. 5. Low Mach method. Time evolution of relative error in total mass of air. Solid line: $CFL = 1$, dash-dotted line: $CFL = 100$.

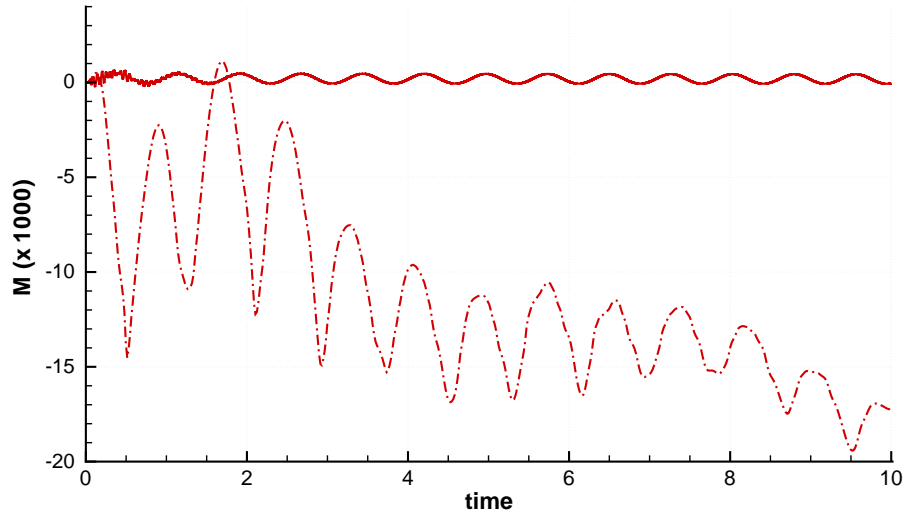


Fig. 6. Single pressure method. Time evolution of relative error in total mass of air. Solid line: $CFL = 1$, dash-dotted line: $CFL = 100$.

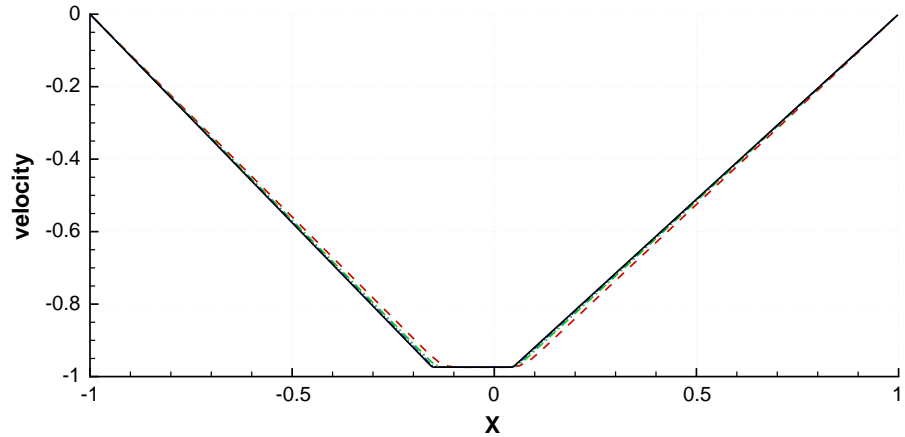


Fig. 7. Low Mach method, $CFL = 100$. Grid convergence of the velocity field at time $t = 10$. Solid black line $\delta x = 1/320$, blue dash-dot-dotted $\delta x = 1/160$, green dash-dot $\delta x = 1/80$, red dashed $\delta x = 1/40$. (For interpretation of the references to color in this figure legend, the reader is referred to the web version of this article.)

between the four grids are small, and that convergence is nearly reached for $\delta x = 1/80$. Moreover the velocity appears continuous at the interfaces, showing that the jump relations are indeed satisfied.

5. Investigations of air–water configurations using the low Mach method

All the simulations presented below involve water and air as the incompressible and compressible fluid respectively. Surface tension is taken into account in the 2D case, except for case 1. For water, the physical characteristics are the following: density $\rho_l = 1000 \text{ kg/m}^3$, dynamic viscosity $\mu_l = 0.001 \text{ Pa s}$, thermal conductivity $k_l = 0.6 \text{ W m}^{-1} \text{ K}^{-1}$, specific heat $c_{pl} = 4184 \text{ J K}^{-1} \text{ kg}^{-1}$. For air, considered as a perfect gas, the values are: dynamic viscosity $\mu_g = 1.82 \times 10^{-5} \text{ Pa s}$, thermal conductivity $k_g = 0.0256 \text{ W m}^{-1} \text{ K}^{-1}$, specific heat at constant pressure $c_{pg} = 1004.5 \text{ J K}^{-1} \text{ kg}^{-1}$, specific heat ratio $\gamma = 1.4$. For air/water interfaces the surface tension coefficient is $\sigma = 0.07 \text{ N m}^{-1}$.

The time step that is used in these simulations is restricted by the explicit stability condition imposed by the diffusive part of the equations: viscous and thermal conduction effects, the latest being generally the most restrictive. Thus the time step is taken as $\delta t = 0.25 \delta x^2 / \max(k/\rho c_p)$. Using an implicit scheme for the diffusive terms of the Navier–Stokes equations would remove this restriction and allow for the use of a convective time step.

5.1. Numerical results for a 1D non-isothermal problem

A one-dimensional fluid system consisting of two layers of gas (air) enclosing a layer of liquid (water) is considered. The system is closed by two walls. The total length of the system is $100 \mu\text{m}$, the length of the liquid layer is $10 \mu\text{m}$, the latter

being initially situated at the center of the system. The initial thermodynamic conditions are $P_0 = 101,325 \text{ Pa}$, $T_0 = 293.15 \text{ K}$. At initial time, the left wall is heated to $T_w = 373.15 \text{ K}$, the right wall being insulated. After a transient evolution, a steady state establishes where the initial positions of the liquid–gas interfaces are recovered, due to mass conservation. In the gas, the density at steady state is unchanged, $T_f = T_w$ everywhere, and $P_f = P_0 T_f / T_0 = 128,976.37 \text{ Pa}$ following the perfect gas equation of state. This test case was treated in [10], based on a Arbitrary Lagrangian Eulerian (ALE) method (moving mesh). In this way, the interfaces between liquid and gas are real discontinuities, and there are no errors that could be attributed to the front-tracking method and the existence of a mixing zone. Using an accurate discretization, we can consider the results given by this code as reference results (see [10] for more details about the ALE procedure).

The domain is discretized using 100 grid points. The time step is equal to 10^{-8} s , due to stability limits. Fig. 8 presents trajectories of the two liquid–gas interfaces. The first remark that can be done is that those trajectories are parallel (the liquid has a rigid body motion), and that the initial positions are well recovered. This last point is a very important and demanding test for mass conservation for the method.

A logarithmic representation of the interface trajectory reveals that in the early stages right after the heating of the left wall, an oscillatory motion of the liquid zone is observed. This effect is entirely due to the gas compressibility and was analyzed in detail in [10]. The corresponding thermodynamic pressure history is shown in Fig. 9, in linear and logarithmic scales. As the pressures in the two gaseous zones are not equal, the liquid undergoes an acceleration. Fig. 10 shows the fluid velocity in the whole domain, for two successive times. One can remark that the velocity is constant in the liquid, showing again that it behaves as a rigid body in this 1D case, whereas it is not the case in the gas due to compressibility effects. In the first microseconds, high velocities can be attained. The hydrodynamic pressure at $t = 1 \mu\text{s}$ is shown in Fig. 11(left). The temperature fields for several successive times are shown in Fig. 11(right) and reveal that after an initial transient where a piston effect can be observed in the rightmost part of the left gaseous zone [28], a purely conductive regime establishes in the left gaseous zone while temperature is nearly uniform in the right gaseous zone due to the adiabatic wall condition. The relative total mass variation in the cavity never exceeds 0.5% throughout the entire evolution, demonstrating good mass conservation properties of the algorithm.

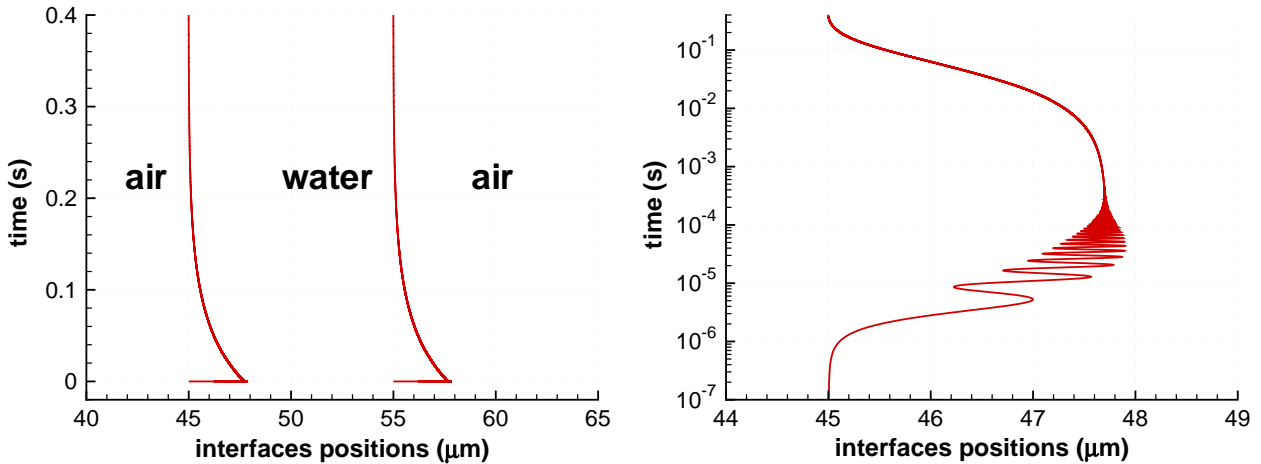


Fig. 8. Trajectories of interfaces, in natural time scale (left), log scale (right).

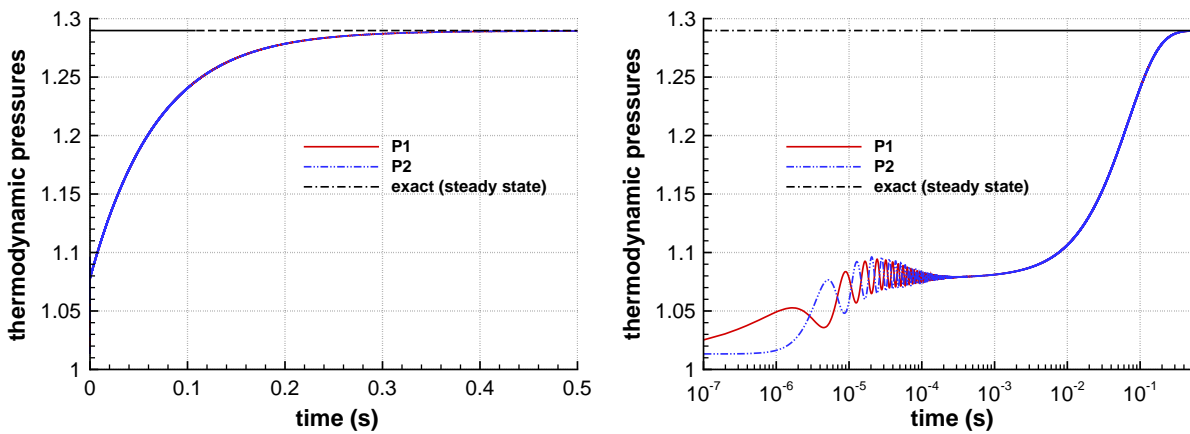


Fig. 9. Thermodynamic pressures (atm) in the gas zones, in natural time scale (left), log scale (right).

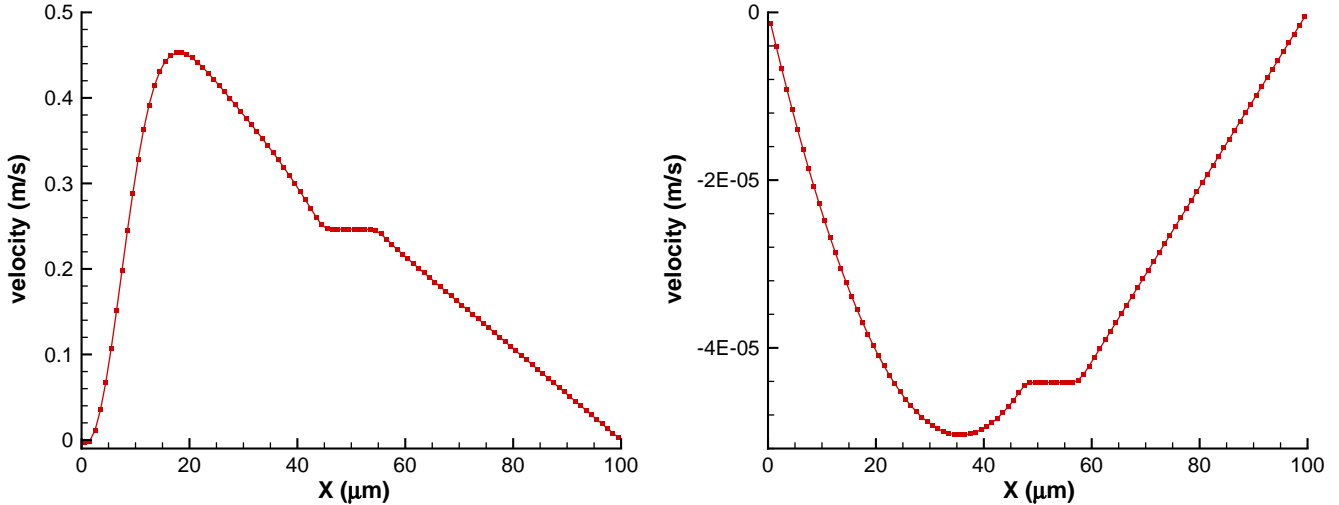


Fig. 10. Velocity in the domain, $t = 1 \mu\text{s}$ (left), $t = 1 \text{ ms}$ (right).

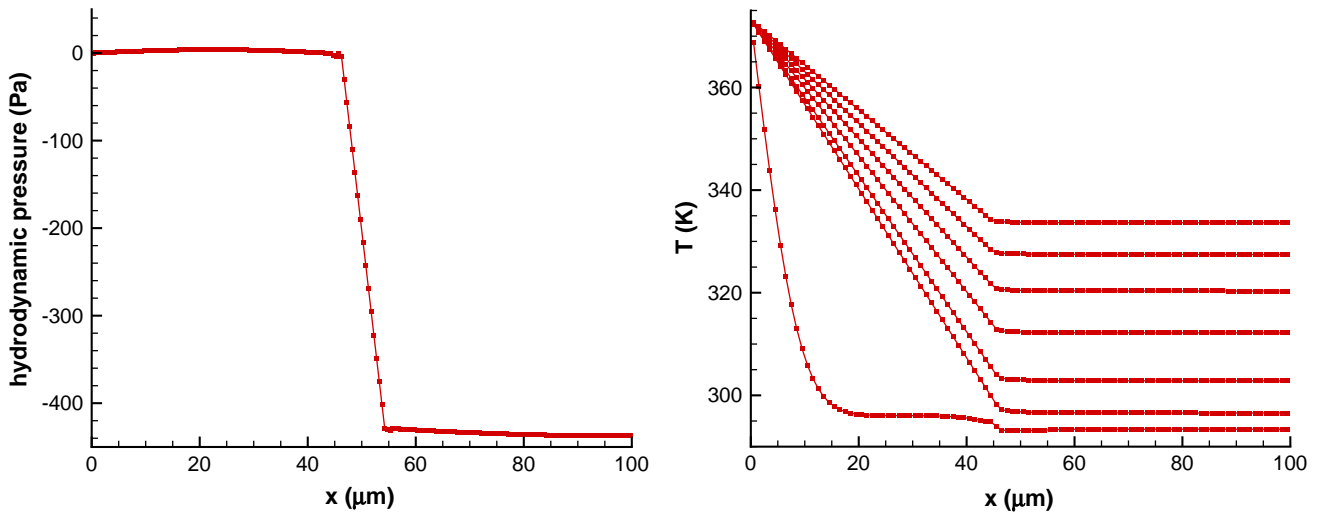


Fig. 11. Left: hydrodynamic pressure (Pa), $t = 1 \mu\text{s}$. Right: temperature (K), $t = 1 \mu\text{s}, t = 4, 5, 6, 7, 8, 9 \text{ ms}$.

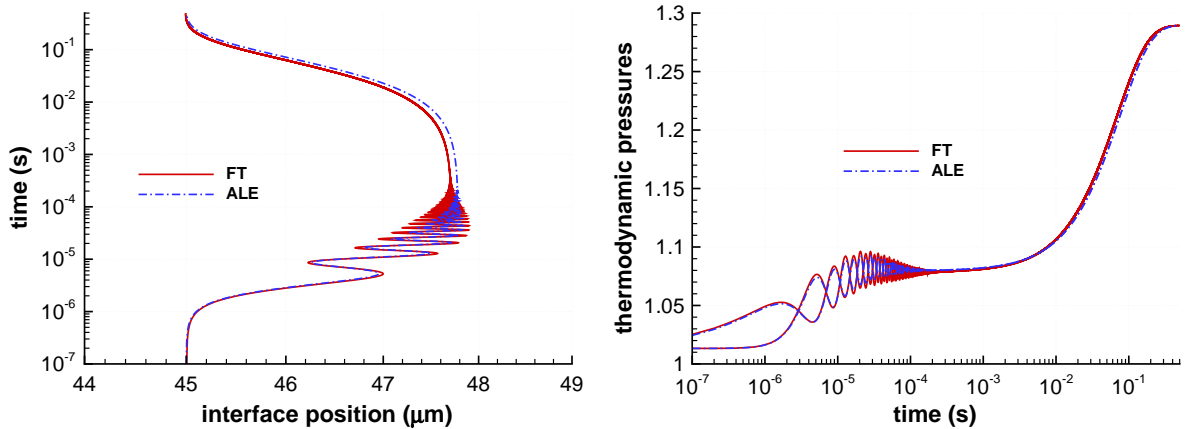


Fig. 12. Comparison of the front-tracking (FT) and ALE results. Left: left interface trajectory. Right: thermodynamic pressures (atm).

Finally, in Fig. 12 we compare the results given by the front-tracking algorithm and the ALE approach, the latter being considered as reference. It can be seen, from the trajectories and the pressures history, that the results are very close,

although the front-tracking algorithm is only first order in time. This validates the low Mach compressible/incompressible approach in the front-tracking framework.

5.2. 2D numerical results

5.2.1. Case 1: a bubble in water in a heated box

We now consider a two-phase system: a circular air bubble trapped in the middle of a hundred micron square container of water. The radius of the bubble is 30 μm . A uniform 32×32 grid is used. The initial characteristic H function is presented in Fig. 13. To focus on the phenomena of interest, buoyancy effects are neglected, and surface tension is not taken into account. Initially the fluid is at temperature $T_0 = 293.15$ K, and the thermodynamic pressure in air is $P_0 = 101,325$ Pa. At initial time, the walls are heated at temperature $T_1 = 373.15$ K. In water, heating does not induce any flow. However, as soon as the heat flux becomes significant at the interface, the thermodynamic pressure increases in the air bubble. Some results are presented in Figs. 14 and 15. The time variation of the mean pressure in Fig. 15 clearly shows the mean pressure rise in the container as a result of the corresponding increase in the temperature of the air bubble. It is interesting to note the initially constant mean pressure during the phase of heat diffusion in the liquid. Fig. 15 also shows the evolution of the mean velocity modulus in time, which reaches a maximum value of the order of 10^{-6} ms^{-1} , justifying the low Mach flow hypothesis that was made. Fig. 14 shows the velocity field superimposed on the temperature field and on the velocity divergence field at

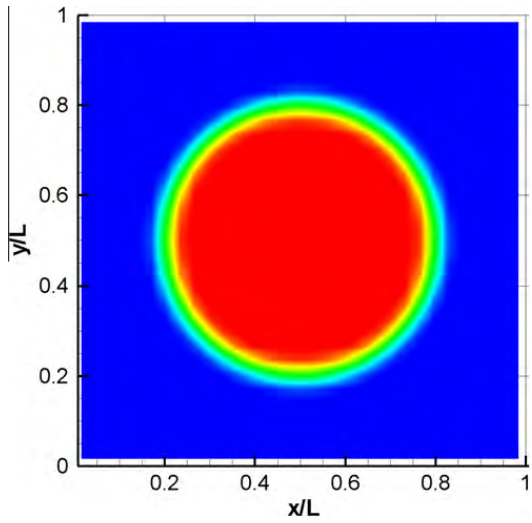


Fig. 13. Heated square box. Initial H function. Reference length $L = 100 \mu\text{m}$.

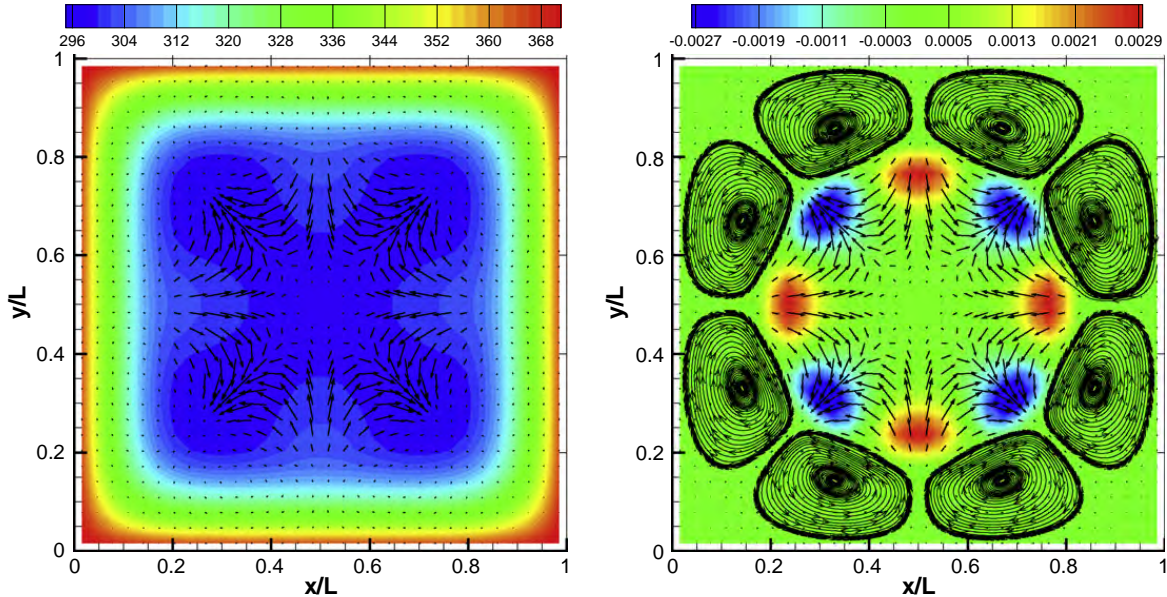


Fig. 14. Heated square box, $t = 4$ s. Left: temperature and velocity fields. Right: divergence and velocity fields, streamlines superimposed in the liquid.

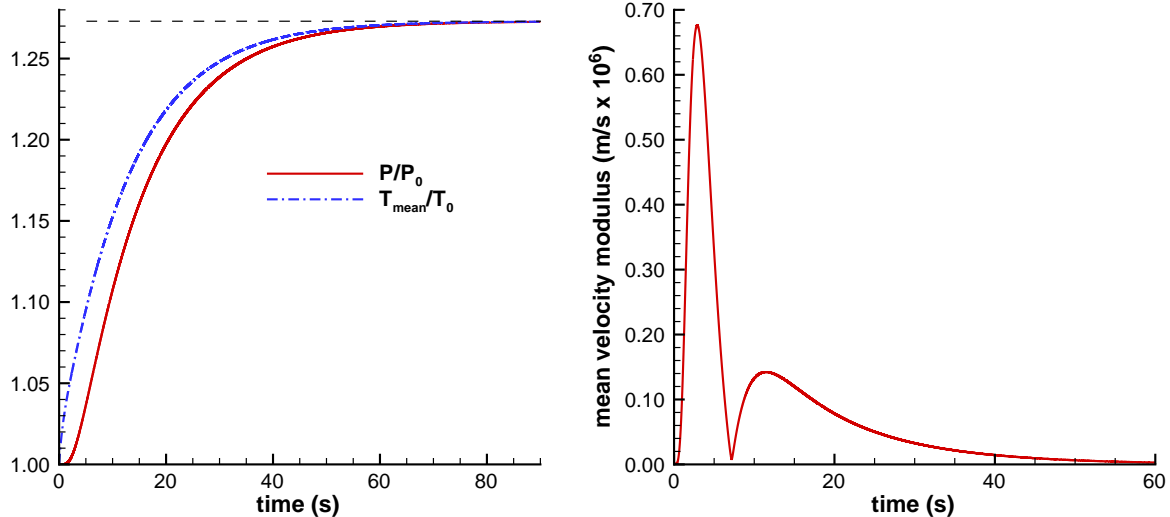


Fig. 15. Heated square box. Left: normalized thermodynamic pressure in the bubble and mean temperature in the box versus time. The dashed straight line shows the steady exact value. Right: mean velocity modulus versus time.

time equal 4 s. The heat amount received by the bubble induces a compression flow inside of it. The water is not completely motionless as the air flow is not axisymmetric, due to the square shape of the cavity. Streamlines in the water show the development of eight vortices around the bubble (Fig. 14). After a transient period, steady state is reached, where temperature is at uniform value T_1 in the cavity, and by virtue of mass conservation the thermodynamic pressure in air satisfies $P_1/P_0 = T_1/T_0 = 1.273$.

5.2.2. Case 2: two bubbles in water with initial thermodynamic pressure difference

We consider a $50 \mu\text{m} \times 100 \mu\text{m}$ rectangular closed box. The box walls are insulated. Two circular bubbles of air with initial radius $R_1 = 12 \mu\text{m}$ and $R_2 = 12 \times \sqrt{1.4} \mu\text{m}$ are included inside the liquid, centered at positions $(25 \mu\text{m}, 25 \mu\text{m})$ and $(75 \mu\text{m}, 25 \mu\text{m})$. The initial surface ratio of the bubbles S_2/S_1 is thus equal to 1.4. The fluid is initially at rest, and uniformly at a temperature $T_0 = 293.15 \text{ K}$. At initial state, the two bubbles are at different thermodynamic pressures, $P_1 = 1.4 \text{ atm}$ and $P_2 = 1 \text{ atm}$. When time goes on, this initial pressure difference induces an oscillatory movement in the liquid, in the same way as in the above one-dimensional case: the bubble at the higher pressure expands, the other shrinks, this being allowed by compressibility of the bubbles. As a consequence of the inertia of the incompressible fluid flow between the two bubbles, the pressure in first bubble decreases below the equilibrium pressure whereas that in the second bubble rises above equilibrium. This reverses the direction of the flow, and after that the bubbles undergo an oscillatory process involving alternate expansions and compressions. Mechanical equilibrium is observed in a short time delay, of about $t_{\text{mech}} = 150 \mu\text{s}$. Once the mechanical equilibrium is achieved, the system evolves very slowly towards steady-state due to the viscous and heat conduction effects. Indeed, the time period required to achieve thermal equilibrium is much longer due to the large time constant associated with heat transfer in the liquid phase. While the total area of gas should remain constant, the area of each bubble varies with expansions and compressions. At steady state, thermodynamic pressure P_f and temperature T_f are uniform. Let us denote by M_1 and M_2 the masses of gas in each bubble, that stay constant all over the evolution. Then we can write:

$$\begin{cases} M_1 = \frac{P_1}{RT_0} S_1 = \frac{P_f}{RT_f} S_{1f} \\ M_2 = \frac{P_2}{RT_0} S_2 = \frac{P_f}{RT_f} S_{2f} \end{cases} \quad (49)$$

S_{1f} and S_{2f} being the final surfaces of the bubbles, such that the final ratio of the surface of the bubbles is:

$$\frac{S_{2f}}{S_{1f}} = \frac{M_2}{M_1} = \frac{P_2}{P_1} \cdot \frac{S_2}{S_1} \quad (50)$$

In the same time, we can calculate the final pressure P_f in the bubbles. The walls being adiabatic and rigid, the total energy in the box remains constant, implying that the final temperature T_f is equal to T_0 as the total surface of gas and the mass of gas in each bubble is constant. Thus we can write:

$$M_1 + M_2 = \frac{P_f}{RT_0} (S_1 + S_2) \quad (51)$$

yielding:

$$P_f = \frac{P_1/P_2 + S_2/S_1}{1 + S_2/S_1} \cdot P_2 \quad (52)$$

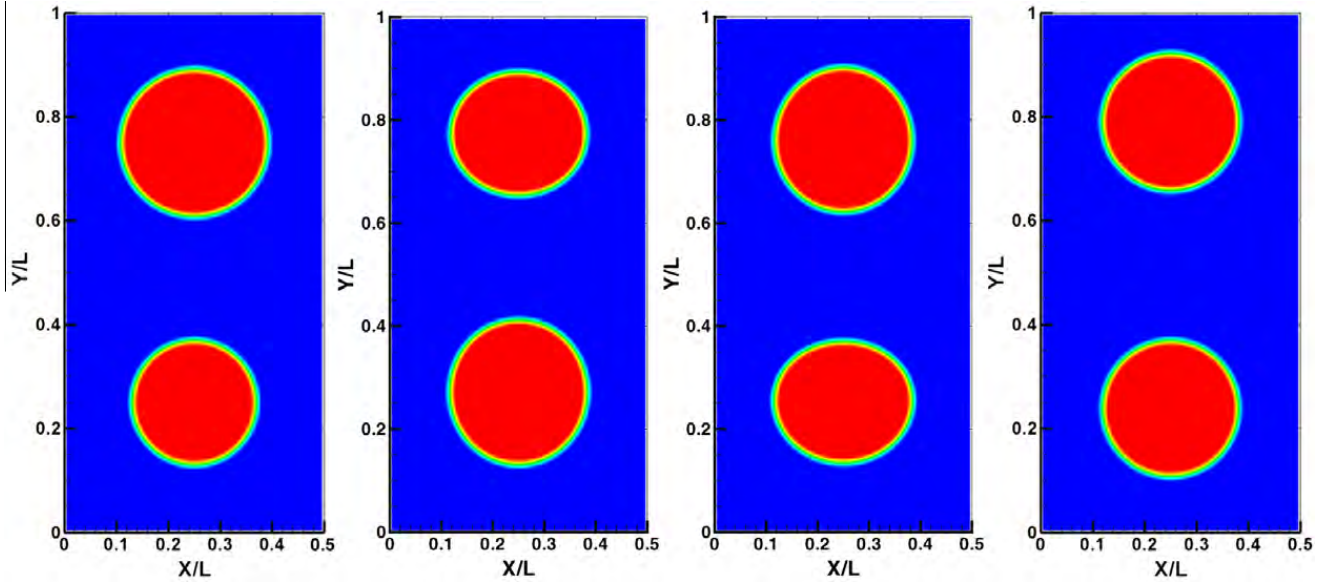


Fig. 16. 64×128 grid. H , $t = 0, 4, 8 \mu\text{s}$ and steady state. Reference length $L = 100 \mu\text{m}$.

In the present case we obtain $S_{2f} = S_{1f}$ and $P_f = \frac{7}{6}P_2 = 118, 212.5 \text{ Pa}$ at steady state.

The results obtained using a 64×128 grid are shown in Figs. 16 and 17. The characteristic function of the bubbles at several successive times is presented in Fig. 16. The variation of the shape and surface of the bubbles induced by the thermodynamic pressure variations is clearly seen here. In Fig. 17 are presented the time variations of several quantities, showing the damped oscillating motion of the system. Fig. 17(a) shows the surface ratio of the bubble, which should converge to 1 at steady state. An error of about 2% is visible. The thermodynamic pressures in the two bubbles, shown in Fig. 17(b), oscillate out of phase and converge to the same value after 0.15 ms. In Fig. 17(c) one can see that the mean velocity modulus in the field reaches a value close to 1 ms^{-1} . Local velocities in the flow can reach 3 ms^{-1} , and very high accelerations are given to the fluid during the oscillatory period. Fig. 17(d) shows the normalized total gas area during time evolution, which should stay constant as the mass of gas is constant. One can notice that the mass conservation error remains very small all over the system evolution.

In order to quantify the grid convergence of the method, we have reproduced the same calculations for three different grids: 32×64 , 64×128 and 128×256 . Fig. 18 shows the time evolution of the surface ratio of the bubbles and the total gas area for the three grids. It can be noticed that the frequency of the oscillations slightly increases as the mesh is refined, and in the same time the damping time scale decreases. This effect could be related to the antidissipative nature of a first order time discretization. The solution on the middle mesh is close to that on the finer mesh, indicating that convergence is almost reached.

Knowing the exact steady values, we have calculated for each mesh the numerical error that is committed at steady state for the three quantities: S_{2f}/S_{1f} , total gaseous area and P_f . The relative errors in percentage are compiled in Table 1. The quantity S_{2f}/S_{1f} is seen to converge with first order accuracy, which is consistent with the first order accuracy in time of the scheme. However the convergence rate of the thermodynamic pressure is close to second order, while it is not regular for the total gaseous area. The reason why convergent rates are not the same for all variables remains unclear. The front-tracking method also has some influence which is difficult to quantify precisely.

5.2.3. Case 3: six bubbles in water with initial thermodynamic pressure difference

We consider a $100 \mu\text{m} \times 150 \mu\text{m}$ square closed box. A uniform 128×192 grid is used. The box is filled with liquid water. Six identical circular air bubbles, $12 \mu\text{m}$ in radius are regularly distributed in the liquid, as shown in Fig. 19(left) which presents the initial field of the characteristic function H . The fluid is initially at rest with a uniform temperature $T_0 = 293.15\text{K}$; different values of the thermodynamic pressure are imposed inside the bubbles as $P_{j0} = 1.4 \text{ atm}$ for $j = 1, 4, 6$ and $P_{j0} = 1 \text{ atm}$ for $j = 2, 3, 5$, where the subscript j represents the bubble's number and the subscript 0 stands for initial conditions (see Fig. 19(left) for the numbering of the bubbles). At the very beginning of the transient process, the three bubbles with the highest pressures expand leading to the subsequent shrinkage of the three other bubbles. Mutual interactions then produce a complex multimodal oscillatory process until mechanical equilibrium is observed. This happens in a short time delay, of about $t_{\text{mech}} = 100 \mu\text{s}$. At that time, thermodynamic pressure is the same in all six bubbles as illustrated in Fig. 22(right). Computed data show that at time t_{mech} , the temperatures within the bubbles are almost equal to T_0 and that only small superheats are noticeable in the liquid, close to the bubble's interfaces. Then combining in a first approximation, mass conservation and the equation of state for all six bubbles, one may estimate the thermodynamic pressure at time t_{mech} :

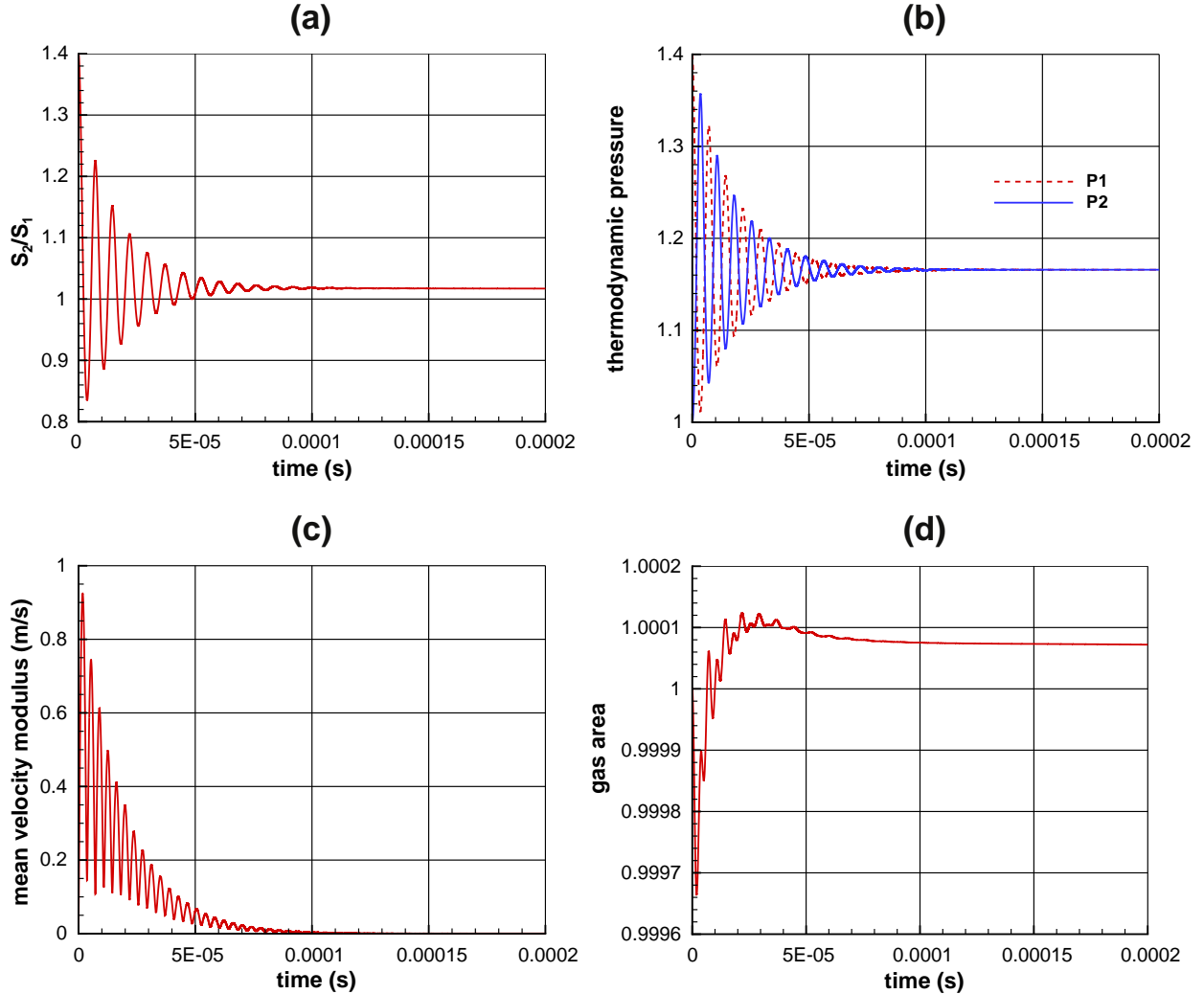


Fig. 17. Time evolution for the 64×128 grid. (a): surface ratio of the bubbles, (b): thermodynamic pressures (atm), (c): mean velocity modulus over the box, (d) total bubbles area normalized by the initial area.

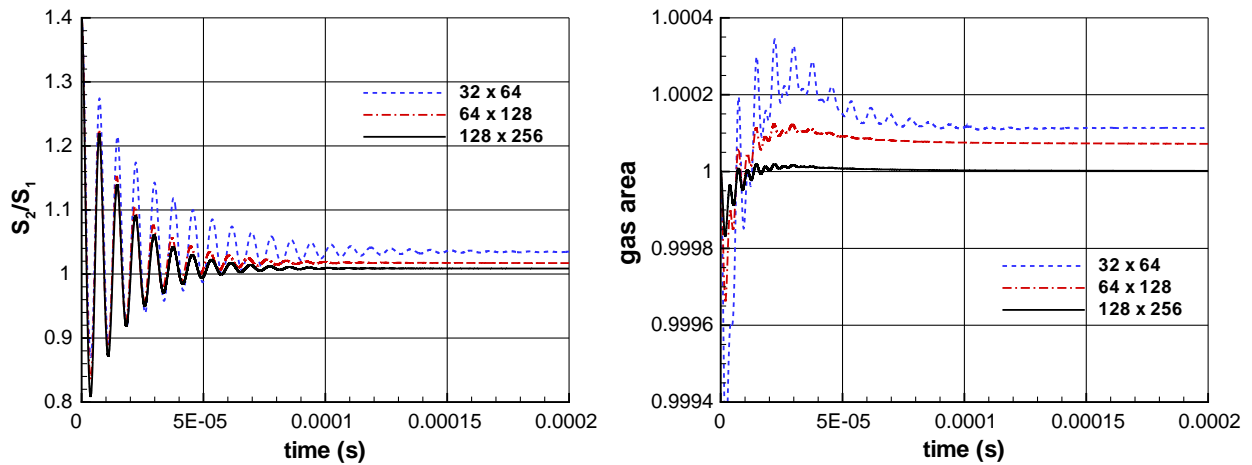


Fig. 18. Grid convergence of the bubbles surface ratio (left) and normalized gas area (right).

$$P_f = \frac{\sum_{j=1}^6 (P_{j0} S_{j0})}{\sum_{j=1}^6 S_{j0}} = \frac{\sum_{j=1}^6 (P_{j0})}{6} = 1.2 \text{ atm} \quad (53)$$

Table 1

Convergence study: relative errors at steady state as a function of the grid size (in %).

Grid size	S_{2f}/S_{1f}	Total gaseous area	P_f
32×64	3.2	0.009	0.21
64×128	1.6	0.007	0.067
128×256	0.83	0.0001	0.022

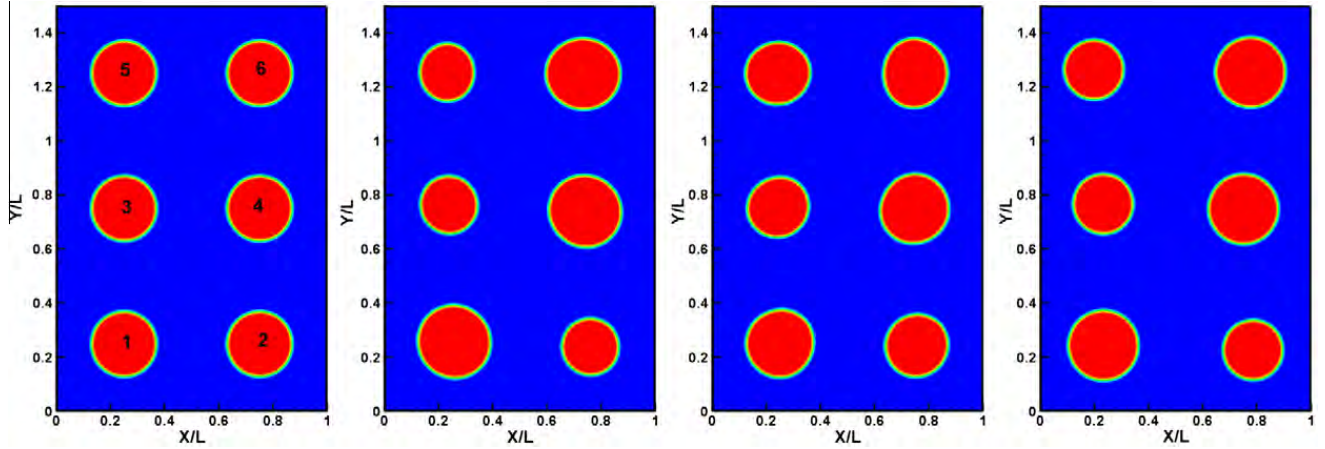


Fig. 19. Rectangular box with six bubbles at different initial thermodynamic pressures. From left to right: H at times 0, 3, 6 μs and t_{mech} . Reference length $L = 100 \mu\text{m}$.

The bubble surface at time t_{mech} reads:

$$\frac{S_{jf}}{S_0} = \frac{P_{j0}}{P_f} \quad \text{for } j = 1, 2, \dots, 6 \quad (54)$$

Numerical values are $\frac{S_{jf}}{S_0} = \frac{7}{6}$ for $j = 1, 4, 6$ and $\frac{S_{jf}}{S_0} = \frac{5}{6}$ for $j = 2, 3, 5$. Computed data presented in Fig. 22 are in close agreement with these estimated theoretical values.

The transient oscillating process (*i.e.* $t < t_{\text{mech}}$) is now discussed. In Fig. 19, the characteristic functions of the bubbles are presented for several successive times including t_{mech} . In addition, in Figs. 20 and 21 are also displayed for time $t = 3 \mu\text{s}$ the

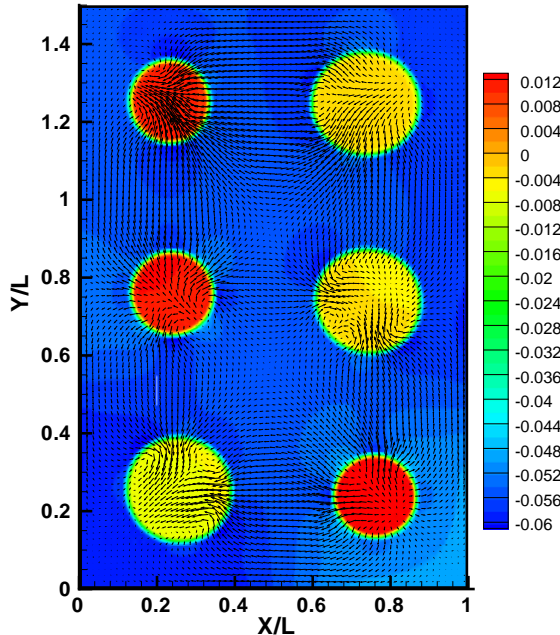


Fig. 20. Rectangular box with six bubbles at time 3 μs . Hydrodynamic pressure π ($\text{Pa}/10^5$) with velocity field superimposed (only one vector out of four is shown). Reference length $L = 100 \mu\text{m}$.

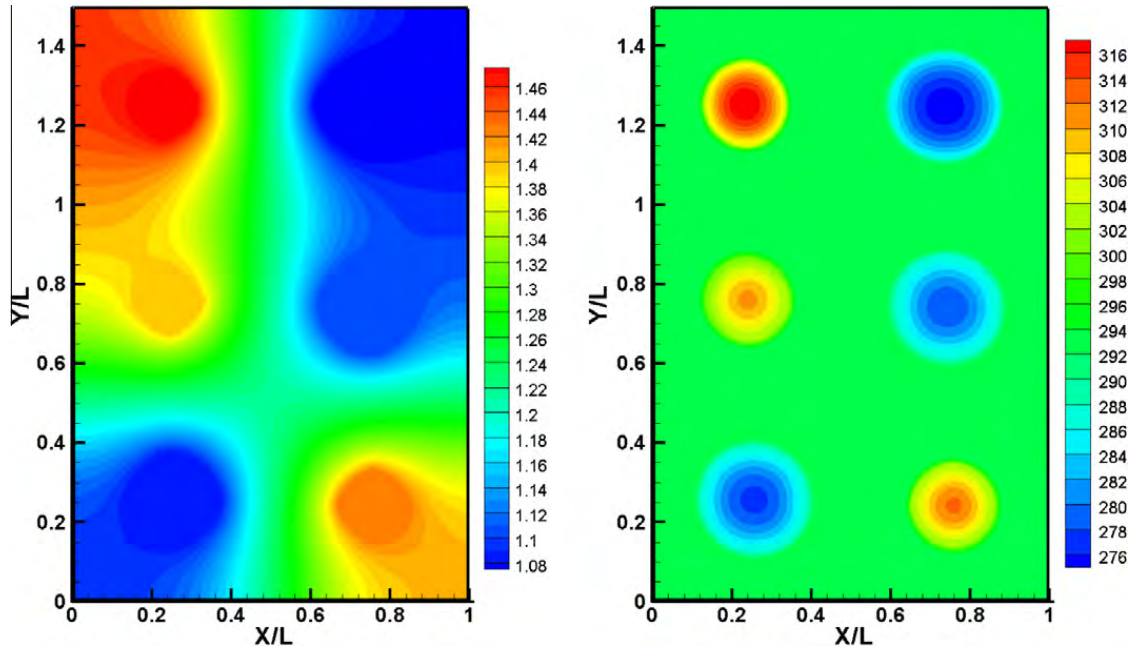


Fig. 21. Rectangular box with six bubbles at time 3 μ s. Left: extended thermodynamic pressure P_e ($\text{Pa}/10^5$), right: temperature (K). Reference length $L = 100 \mu\text{m}$.

velocity field superimposed on the hydrodynamic pressure field, the extended thermodynamic pressure field as derived from Eq. (20) and the temperature field.

During the transient process, interactions between bubbles lead to deviations from the initial circular shape. The circular shape is however recovered at time t_{mech} due to surface tension effects.

The hydrodynamic pressure (π) presented in Fig. 20 and the extended thermodynamic (P_e) pressure fields presented in Fig. 21 show, as expected, that these two quantities are very different in magnitude. Pressure π is discontinuous at the bubble's interface due to surface tension, its value inside the bubbles being higher than in the liquid. Spatial variations of the hydrodynamic pressure are about $\rho_l V^2$ in magnitude. Concerning the extended thermodynamic pressure field P_e , it is reminded here that values inside the bubbles are the uniform thermodynamic pressures, their magnitude being about 10^5 Pa .

The velocity field, superimposed with the hydrodynamic pressure field in Fig. 20, reveals 2D complex flows in both the liquid and gaseous phases. One can remark that the velocity field is smooth in the vicinity of the interfaces, although we consider large density ratio and real surface tension effects. The liquid motion induced by the bubbles' expansion or compression may be associated, in the early stages, to a velocity as large as 1 ms^{-1} .

At time 3 μ s, temperature is uniform in the liquid, equal to the initial value T_0 due to the high thermal mass. On the other hand, the temperature inside the six bubbles is modified. Three bubbles, i.e. # 1, 4, 6 are cooled due to the expansion process, their respective temperatures being lower than the initial value $T_0 = 293 \text{ K}$. In contrast, bubbles # 2, 3, 5 are heated due to the work supplied by compression. Their temperatures are thus higher than the initial value. One will note that temperature in the bubbles is not uniform as time $t = 3 \mu\text{s}$ is smaller than the characteristic time scale for heat diffusion in the gas, estimated to be about 7 μs .

6. Conclusions and perspectives

In this work, a single field model aimed at the numerical simulation of liquid–gas flows has been proposed. The liquid phase is considered as strictly incompressible, while compressibility effects are taken into account in the gas through a low Mach approach. In contrast with previous works, our model allows for the complete mechanical and thermal description for the dynamics of each the two phases. The interface is treated using a front-tracking approach. In the case of multiple gaseous inclusions, the single field approach raises the problem of taking into account thermodynamic pressure differences effects. We propose a solution to this problem via the definition of an extended thermodynamic pressure field, which allows to recover the correct interface jump conditions. In addition, our method has the advantage of avoiding arithmetic precision problems that could be encountered if the thermodynamic pressure was incorporated into the hydrodynamic pressure field, the latter being several orders of magnitude smaller.

Concerning the numerical solution, the unsteady momentum equations are advanced in time through a prediction–projection time stepping algorithm. The projection step is done with a multigrid algorithm capable of dealing efficiently with large fluid density ratios. It allows us to enforce the divergence free condition in the liquid phase, and the specified value of the velocity divergence in the gas phase. The algorithm enforces exactly compatibility conditions and the coherence between energy and continuity equations at the discrete level.

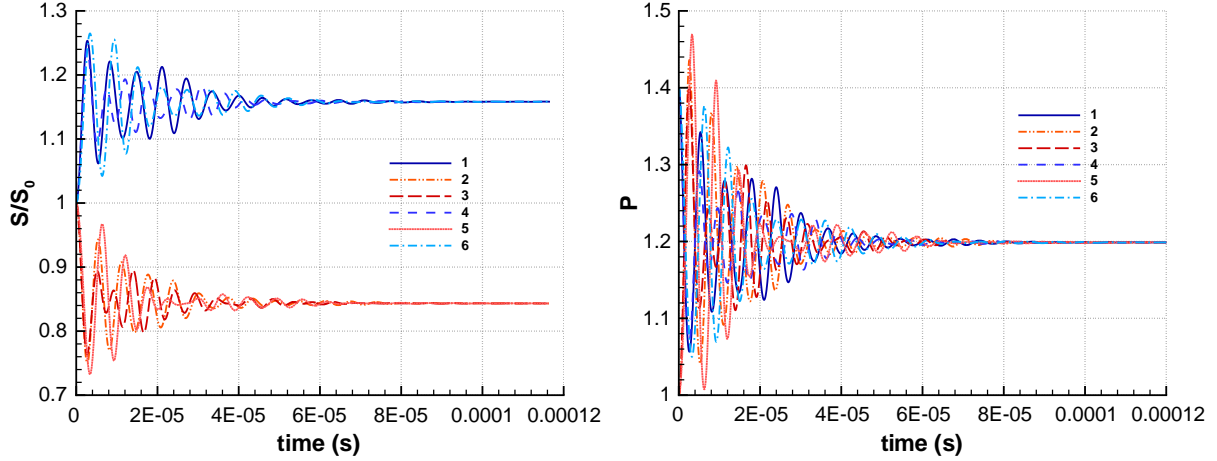


Fig. 22. Time evolution of the surface (left) and thermodynamic pressure (right) of the six bubbles.

To illustrate the efficiency of our method, the Oscillatory Water Column isentropic test case was considered and comparisons were made with a single pressure (all-Mach) method. We showed that the low Mach method allows the use of much larger time steps while maintaining time accuracy. Then the entire algorithm was first validated against a 1D reference non-isothermal case. Calculations were next performed for 2D test cases where the flow is driven by thermopneumatic effects. Time evolution of the dynamics of the flow is discussed, showing that the whole configuration relaxes in an oscillatory way towards steady state. Alternate compression and dilatation phases result in corresponding heating and cooling of the gas within each bubble. In all cases, real fluids were considered (water and air), showing the robustness of the method with respect to the large density ratio involved.

Current work concerns the implicitation of the numerical method and its extension to second order accuracy in time. This should allow gain in CPU time, as the present explicit scheme is somewhat time consuming due to the restrictive diffusive stability condition. This is especially important as we plan to consider 3D applications, for which the optimization of the numerical method will be crucial. From the physical point of view, the model will be extended to take into account phase change. An important feature of our model is that, in contrast with purely incompressible approaches [17], it will give the possibility to account for the saturation curve, which links pressure and temperature at the interface for liquid-vapor flows.

Acknowledgments

The authors thank Damir Juric for providing his 2D incompressible front tracking code, and Olivier Daube and Yann Fraigneau for many fruitful discussions about projection methods and low Mach models. The authors also wish to acknowledge the anonymous contribution of one referee, whose comments and suggestions greatly helped improving the description of the model.

Appendix A. Multigrid solver for the Poisson equation

The projection step consists in solving the equation

$$\nabla \cdot (\lambda \nabla f) = s \quad (55)$$

with homogeneous Neumann boundary conditions, where $\lambda = \frac{1}{\rho}$. For the two-phase flow configurations at hand, the density ρ is a discontinuous field with jumps of three orders of magnitude. Efficient solution of this type of equation has been the subject of intense research, as its solution can consume more than 80% of the total computing time, in particular when an explicit scheme is used for the prediction step. To this aim we use a multigrid solver along the lines of the algorithm proposed in [27,21]. It is not our purpose to discuss in detail the multigrid procedure which is well documented in several textbooks [2]. The ingredients of any multigrid procedure are the expression of the operator on the coarse grids, the relaxation scheme, the smoother, the coarse transfer operator that transfers the residual from a given grid to the next coarser grid and the fine transfer operator that transfers the correction from a grid to the next finer one to add it to the current estimate of the correction.

The computational domain Ω is covered with $N \times M$ cells of size $\Delta x_i \times \Delta z_j$, $i = 1, \dots, N$, $j = 1, \dots, M$. λ is defined by its values at the cell centers λ_{ij} . The solution is also sought at the cell centers. The finite volume discretization of the flux in (55) reads

$$\lambda_{i+1/2,j} \frac{f_{i+1,j} - f_{i,j}}{x_{i+1,j} - x_{i,j}}$$

at the east side of the cell with similar expressions for the other faces. Following [27,21], the main idea of the algorithm is to enforce continuity of fluxes at the cell interfaces. It is well known that this is achieved by defining $\lambda_{i+1/2,j}$ as the harmonic average of $\lambda_{i+1,j}$ and $\lambda_{i,j}$ that is

$$\frac{2}{\lambda_{i+1/2,j}} = \frac{1}{\lambda_{i+1,j}} + \frac{1}{\lambda_{i,j}}$$

The coarse grids are defined by merging together two cells in each direction, which sets the cell boundaries as guidelines to define the coarse grids. The cell centers are defined accordingly. Once the grid is defined, we define λ_{ij} on a grid from the weighted average of the four corresponding values on the next finer grid. Likewise, the residual restriction transfer operator is defined as the sum of the residuals of the 4 corresponding cells, which ensures conservativity of the mass unbalance.

The relaxation scheme is a simple SOR iteration whose acceleration parameter is adjusted empirically in order to produce the best convergence rate.

Concerning the interpolation operator for the correction of the error, it is also defined to ensure a constant flux interpolation in the following way: for each coarse cell, 8 constant flux interpolations are first produced from coarse cell neighbors, 4 at the middle of the faces, 4 at the corners. With straightforward notations,

$$f_e = \frac{\lambda_{i+1,j} f_{i+1,j} + \lambda_{i,j} f_{i,j}}{\lambda_{i+1,j} + \lambda_{i,j}}; \quad f_{en} = \frac{\lambda_{i+1,j+1} f_{i+1,j+1} + \lambda_{i,j} f_{i,j}}{\lambda_{i+1,j+1} + \lambda_{i,j}}$$

with similar expressions for the other values. For each coarse cell, the corresponding 4 fine cell values are then defined as the arithmetic mean of the interpolated coarse values at the four corresponding corners.

In addition, for other application purposes, we define a solid phase indicator allowing for the presence of solid parts. One has then to solve the pressure equation with the homogeneous Neumann boundary conditions imposed at the fluid solid interface. The difficulty is to take into account this boundary condition to construct the operator in a systematic way. To do this, we recursively define the solid indicator of the coarse grids with the following principle: a coarse grid is considered as liquid iff one of the four corresponding fine cells is liquid. With all the ingredients, all operators can be recursively defined on all grids, allowing for an automatic algorithm once the various indicator functions are defined on the finest grid.

References

- [1] T. Bonometti, J. Magnaudet, An interface-capturing method for incompressible two-phase flows. Validation and application to bubble dynamics, *Int. J. Multiphase Flows* 33 (2007) 109–133.
- [2] W.L. Briggs, V.E. Henson, S.F. McCormick, *A Multigrid Tutorial*, second ed., SIAM, 2000.
- [3] A. Caboussat, A numerical method for the simulation of free surface flows with surface tension, *Comput. Fluids* 35 (2006) 1205–1216.
- [4] A. Caboussat, M. Picasso, J. Rappaz, Numerical simulation of free surface incompressible liquid flows surrounded by compressible gas, *J. Comput. Phys.* 203 (2005) 626–649.
- [5] R. Caiden, R.P. Fedkiw, C. Anderson, A numerical method for two-phase flow consisting of separate compressible and incompressible regions, *J. Comput. Phys.* 166 (2001) 1–27.
- [6] D. Chenoweth, S. Paolucci, Natural convection in an enclosed vertical air layer with large horizontal temperature differences, *J. Fluid Mech.* 169 (1986) 173–210.
- [7] V. Daru, M.C. Duluc, O. Le Maître, D. Juric, P. Le Quéré, Modélisation et simulation numérique du changement de phase liquide-vapeur en cavité, *CRAS Mécanique* 224 (2006) 25–33.
- [8] J.M. Delhaye, Jump conditions and entropy sources in two-phase systems. Local instant formulation, *Int. J. Multiphase Flow* 1 (1974) 395–409.
- [9] S. Dellacherie, Numerical resolution of a potential diphasic low Mach number system, *J. Comput. Phys.* 223 (2007) 151–187.
- [10] M.C. Duluc, O. Le Maître, V. Daru, P. Le Quéré, Numerical study of liquid inclusion oscillations inside a closed 1-D microchannel filled with gas, *Microfluidics Nanofluidics* 6 (2009) 163–177.
- [11] A. Esmaeeli, G. Tryggvason, Direct numerical simulations of bubbly flows. Part 1. Low Reynolds number arrays, *J. Fluid Mech.* 377 (1998) 313–345.
- [12] A. Esmaeeli, G. Tryggvason, Computations of film boiling. Part I: numerical method, *Int. J. Heat Mass Transfer* 47 (2004) 5451–5461.
- [13] C. Forester, A. Emery, A computational method for low Mach number unsteady compressible free convective flows, *J. Comput. Phys.* 10 (3) (1972) 487–502.
- [14] X. Geng, H. Yuan, N. Oğuz, A. Prosperetti, The oscillation of gas bubbles in tubes: experimental results, *J. Acoust. Soc. Am.* 106 (2) (1999) 674–681.
- [15] K. Goda, A multistep technique with implicit difference schemes for calculating two- or three-dimensional cavity flows, *J. Comput. Phys.* 30 (1) (1979) 76–95.
- [16] M. Ida, An improved unified solver for compressible and incompressible fluids involving free surfaces. II. Multi-time-step integration and applications, *Comput. Phys. Comm.* 150 (3) (2003) 300–322.
- [17] D. Juric, G. Tryggvason, Computations of boiling flows, *Int. J. Multiphase Flow* 24 (3) (1998) 387–410.
- [18] S.Y. Kadioglu, M. Sussman, S. Osher, et al, A second order primitive preconditioner for solving all speed multi-phase flows, *J. Comput. Phys.* 209 (2) (2005) 477–503.
- [19] B. Koren, M.R. Lewis, E.H. van Brummelen, B. van Leer, Riemann-problem and level-set approaches for homentropic two-fluid flow computations, *J. Comput. Phys.* 181 (11) (2002) 654–674.
- [20] P. Kuszla, V. Daru, Multifluid computation of droplets impact, *Lecture Notes in Physics*, vol. 515, C.H. Bruneau ed., Springer, 1998, pp. 524–529.
- [21] D. Kwak, J. Lee, Multigrid algorithm for the cell-centered finite difference method II: discontinuous coefficient case, *Numer. Methods Partial Differential Equations* 20 (5) (2004) 742–764.
- [22] N. Kwatra, J. Su, J.T. Gretarsson, R. Fedkiw, A method for avoiding the acoustic time step restriction in compressible flow, *J. Comput. Phys.* 228 (11) (2009) 4146–4161.
- [23] B. Lafaurie, C. Nardone, R. Scardovelli, S. Zaleski, G. Zanetti, Modelling merging and fragmentation in multiphase flows with surfer, *J. Comput. Phys.* 113 (1994) 134–147.
- [24] P. Le Quéré, R. Masson, P. Perrot, A Chebyshev collocation algorithm for 2D non-Boussinesq convection, *J. Comput. Phys.* 103 (2) (1992) 320–335.
- [25] P. Le Quéré, C. Weisman, H. Paillère, J. Vierendeels, E. Dick, R. Becker, M. Braack, J. Locke, Modelling of natural convection flows with large temperature differences. Part 1: reference solutions, *Math. Model. Numer. Anal.* 39 (3) (2005) 609–616.

- [26] D. Legendre, J. Borée, J. Magnaudet, Thermal and dynamic evolution of a spherical bubble moving steadily in a superheated or subcooled liquid, *Phys. Fluids* 10 (1998) 1256–1272.
- [27] C. Liu, Z. Liu, S. McCormick, An efficient multigrid scheme for elliptic equations with discontinuous coefficients, *Comm. Appl. Numer. Methods* 8 (1992) 621–631.
- [28] Y. Masuda, T. Aizawa, M. Kanakubo, N. Saito, Y. Ikushima, Numerical simulation of two-dimensional piston effect and natural convection in a square cavity heated from one side, *Int. Comm. Heat Mass Transfer* 31 (2) (2004) 151–160.
- [29] T. Ménard, S. Tanguy, A. Berlemont, Coupling level set/vof/ghost fluid methods: validation and application to 3D simulation of the primary break-up of a liquid jet, *Int. J. Multiphase Flow* 33 (2007) 510–524.
- [30] N. Oğuz, A. Prosperetti, The natural frequency of oscillation of gas bubbles in tubes, *J. Acoust. Soc. Am.* 103 (6) (1998) 3301–3308.
- [31] E. Ory, H. Yuan, A. Prosperetti, S. Popinet, S. Zaleski, Growth and collapse of a vapour bubble in a narrow tube, *Phys. Fluids* 12 (6) (2000) 1268–1277.
- [32] H. Paillère, P. Le Quéré, C. Weisman, J. Vierendeels, E. Dick, Modelling of natural convection flows with large temperature differences. Part 2: contributions, *Math. Model. Numer. Anal.* 39 (3) (2005) 617–621.
- [33] S. Paolucci, Sandia National Lab., Report SAND 82-8257, 1982 (unpublished).
- [34] C.S. Peskin, Numerical analysis of blood flow in the heart, *J. Comput. Phys.* 25 (1977) 220–252.
- [35] A. Prosperetti, G. Tryggvason, *Computational Methods for Multiphase Flows*, Cambridge University Press, 2007.
- [36] R. Saurel, R. Abgrall, A multiphase Godunov method for compressible multifluid and multiphase flows, *J. Comput. Phys.* 150 (1999) 425–467.
- [37] R. Scardovelli, S. Zaleski, Direct numerical simulation of free surface and interfacial flow, *Ann. Rev. Fluid Mech.* 31 (1999) 567–603.
- [38] J. Sethian, *Level Set Methods and Fast Marching Methods*, Cambridge University Press, 1999.
- [39] S. Shin, S. Abdel-Khalik, V. Daru, D. Juric, Accurate representation of surface tension using the level contour reconstruction method, *J. Comput. Phys.* 203 (2) (2005) 493–516.
- [40] S. Shin, D. Juric, Modeling three-dimensional multiphase flow using a level contour reconstruction method for front-tracking without connectivity, *J. Comput. Phys.* 180 (2002) 427–470.
- [41] K.M. Shyue, An efficient shock-capturing algorithm for compressible multicomponent problems, *J. Comput. Phys.* 142 (1998) 208–242.
- [42] M. Sussman, P. Smereka, S. Osher, A level set approach for computing solutions in incompressible two-phase flows, *J. Comput. Phys.* 114 (1994) 146–159.
- [43] S. Tanguy, A. Berlemont, Application of a level set method for simulation of droplet collisions, *Int. J. Multiphase Flow* 31 (2005) 1015–1035.
- [44] G. Tryggvason, B. Bunner, A. Esmaeli, D. Juric, N. Al-Rawahi, W. Tauber, J. Han, S. Nas, Y. Jan, A front-tracking method for the computations of multiphase flow, *J. Comput. Phys.* 169 (2) (2001) 708–759.
- [45] F. Xiao, Unified formulation for compressible and incompressible flows by using multi-integrated moments I: one-dimensional inviscid compressible flow, *J. Comput. Phys.* 195 (2) (2004) 629–654.
- [46] F. Xiao, R. Akoh, S. Li, Unified formulation for compressible and incompressible flows by using multi-integrated moments II: multi-dimensional version for compressible and incompressible flows, *J. Comput. Phys.* 213 (1) (2006) 31–56.
- [47] T. Yabe, F. Xiao, T. Utsumi, The constrained interpolation profile method for multiphase analysis, *J. Comput. Phys.* 169 (2) (2001) 556–593.
- [48] Z. Yin, A. Prosperetti, A microfluidic ‘blinking bubble’ pump, *J. Micromech. Microeng.* 15 (2005) 643–651.

L. Monasse, V. Daru, C. Mariotti, S. Piperno, C. Tenaud

" A conservative coupling algorithm between a compressible flow and a rigid body using an
Embedded Boundary method ".
Journal of Computational Physics 231, p. 2977-2994, (2012).



A conservative coupling algorithm between a compressible flow and a rigid body using an Embedded Boundary method

L. Monasse^{a,b,c,*}, V. Daru^{c,d}, C. Mariotti^a, S. Piperno^b, C. Tenaud^c

^a CEA DIF, F-91297 Arpajon, France

^b Université Paris-Est, CERMICS, 77455 Marne-la-Vallée, France

^c LIMSI – CNRS, 91403 Orsay, France

^d Arts et Métiers Paris Tech, DynFluid Lab., 75013 Paris, France

ARTICLE INFO

Article history:

Received 23 December 2010

Received in revised form 13 September 2011

Accepted 2 January 2012

Available online 8 January 2012

Keywords:

Compressible flows

Shock capturing scheme

Discrete Element method

Fluid–structure interaction

Embedded Boundary method

ABSTRACT

This paper deals with a new solid–fluid coupling algorithm between a rigid body and an unsteady compressible fluid flow, using an Embedded Boundary method. The coupling with a rigid body is a first step towards the coupling with a Discrete Element method. The flow is computed using a finite volume approach on a Cartesian grid. The expression of numerical fluxes does not affect the general coupling algorithm and we use a one-step high-order scheme proposed by Daru and Tenaud [V. Daru, C. Tenaud, *J. Comput. Phys.* (2004)]. The Embedded Boundary method is used to integrate the presence of a solid boundary in the fluid. The coupling algorithm is totally explicit and ensures exact mass conservation and a balance of momentum and energy between the fluid and the solid. It is shown that the scheme preserves uniform movement of both fluid and solid and introduces no numerical boundary roughness. The efficiency of the method is demonstrated on challenging one- and two-dimensional benchmarks.

© 2012 Elsevier Inc. All rights reserved.

1. Introduction

This work is devoted to the development of a coupling method for fluid–structure interaction in the compressible case. We intend to simulate transient dynamics problems, such as the impact of shock waves onto a structure, with possible fracturing causing the ultimate breaking of the structure. An inviscid fluid flow model is considered, being convenient for treating such short time scale phenomena. The simulation of fluid–structure interaction problems is often computationally challenging due to the generally different numerical methods used for solids and fluids and the instability that may occur when coupling these methods. Monolithic methods have been employed, using an Eulerian formulation for both the solid and the fluid (for instance, the diffusive interface method [16,1]), or a Lagrangian formulation for both the fluid and the solid (for example, the PFEM method [26]), but in general, most solid solvers use Lagrangian formulations and fluid solvers use Eulerian formulations. In this paper we consider the coupling of a Lagrangian solid solver with an Eulerian fluid solver.

For the coupling in space, a possible choice is to deform the fluid domain in order to follow the movement of the solid boundary: the Arbitrary Lagrangian–Eulerian (ALE) method has been developed to that end. It has been widely used for incompressible [11,19] and compressible [15] fluid–structure interaction. However, when solid impact or fracture occur, ALE methods are faced with a change of topology in the fluid domain that requires remeshing and projection of the fluid state

* Corresponding author at: Université Paris-Est, CERMICS, 77455 Marne-la-Vallée, France.

E-mail address: monassel@cermics.enpc.fr (L. Monasse).

on the new mesh, which are costly and error prone procedures. Moreover remeshing is poorly adapted to load balancing for parallel computations.

In order to allow for easier fracturing of the solid, we instead choose a method based on fictitious domains that solves the fluid flow on a fixed Eulerian mesh, on which a Lagrangian solid body is superimposed. A special treatment is then applied on fluid cells near the boundary and inside the solid. Different types of fictitious domain methods have been developed over the last 30 years. They can roughly be classified in three main classes: penalization methods, interpolation methods and conservative methods. Among penalization methods, the Immersed Boundary method is certainly the best known and most widely used for fluid–structure interaction. It was originally introduced by Peskin for incompressible blood flows [44,45]. The solid boundaries deform under the action of the fluid velocity, and the presence of the solid adds forces in the fluid formulation that enforce the impermeability of the solid. However, Xu and Wang have pointed out some numerical leaking of fluid into the solid [49]. Following Leveque and Li [33,34], they advocate the use of the Immersed Interface method, which incorporates jump conditions in the finite differences used. However, the absence of fluid mass loss is still not ensured exactly. In a different approach, Olovsson et al. [40,2] couple an Eulerian and a Lagrangian method by penalizing the penetration of the solid into the fluid by a damped spring force. As the stiffness of the spring goes to infinity, the penetration goes to zero. Boiron et al. [5] and Paccou et al. [41] consider the solid as a porous medium, using a Brinkman porosity model. As the porosity goes to zero, the solid becomes impermeable. However, in both cases, as the stiffness grows or the porosity decreases, the use of implicit schemes is mandatory to avoid the severe stability condition of explicit schemes [5,41]. For the high speed phenomena we consider, we use explicit solid and fluid solvers and an explicit coupling algorithm is better suited in order to avoid costly iterative procedures.

A second class of fictitious domain methods consists in enforcing the boundary conditions through interpolations in the vicinity of the boundary, using the exact values taken by the fluid on the boundary [37,13]. The method seems to be very versatile, being used with incompressible Navier–Stokes [37,13], Reynolds-averaged Navier–Stokes [10,29,30], turbulent boundary layer laws [6] and compressible Navier–Stokes [42]. The Ghost Fluid method developed by Fedkiw et al. [18,17] relies on the same type of principle for compressible fluids. The interface is tracked using a level-set function, and conditions are applied on both sides of the interface to interpolate the boundary conditions. The advantage of these methods is that they do not suffer from additional time-step restriction due to stability, and the order of accuracy of the boundary conditions can be set *a priori*. However, the interpolation does not ensure the conservation of mass, momentum and energy in the system. This can cause problems when dealing with shock waves interacting with solids.

In this article, we rather consider the third class of conservative fictitious domain methods, which seems the most adequate framework to develop our coupling algorithm. These methods are generally referred to as Embedded Boundary methods, and they rely on a modified integration of the numerical fluid fluxes in the cells cut by the solid boundary [43,14,22,25]. The original idea of the method can be traced back to Noh's CEL code [39]. The new contribution of the present work consists in the coupling algorithm and its properties. The Embedded Boundary method that we use is essentially identical to previous works [43,14,22,25]. The different versions of the Embedded Boundary method mainly differ in the way the stability condition arising from small cut-cells is enforced and we develop here a slightly different procedure in order to deal with solid boundaries coming close to each other. The method can be implemented independently from the time integration scheme used for the fluid, whether based on space–time splitting or multi-level time integration. Conservative fictitious domain methods have proven to give satisfactory conservation results for inviscid compressible flows in the case of static solid boundaries. Nevertheless, to our knowledge, conservation issues of the coupling have not been studied in the case of moving solids. We establish new conservation results in such a case. Our coupling method is designed to be capable of treating the general case of moving deformable bodies. In the present work, however, we only consider non-deformable (rigid) solid bodies. The case of deformable bodies is the object of ongoing work.

The fluid and solid solvers that we consider were chosen according to their ability to deal with shock waves and fracturing solids. The solid solver is based on a Discrete Element method, implemented in a code named Mka3D in the CEA [35]. It can handle elasticity as well as fracture and impact of solids. Solids are discretized into polyhedral particles, which interact through well-designed forces and torques. The particles have a rigid-body motion, and fracture is treated in a straightforward way by removing the physical cohesion between particles. The work reported in this article is a first step towards the coupling with the Mka3D code. The time integration scheme used by Mka3D (Verlet for displacement of the center of mass and RATTLE for rotation [38]) is retained for the rigid body treatment. Concerning the fluid solver, we use a Cartesian grid explicit finite volume method, based on the high-order one-step monotonicity-preserving scheme developed in [8] and space time splitting. However we emphasize that our coupling method is independent from both the Discrete Element method (as long as a solid interface is defined) and the numerical scheme used for the fluid calculation.

The article is organized as follows: we first present briefly the solid and fluid methods in Section 2. In sections 3 and 4, we describe the proposed explicit coupling procedure between the fluid and the moving solid in the framework of an Embedded Boundary method. The analysis of the conservation properties of the coupling is reported in Section 5, where we show that mass, momentum and energy of the solid–fluid system are exactly preserved. In Section 6, we demonstrate results about the preservation on a discrete level of two solid–fluid systems in uniform movement. Finally, we illustrate the efficiency and accuracy of the method on one and two-dimensional static and dynamic benchmarks in Section 7.

2. Solid and fluid discretization methods

2.1. Solid time-discretization method

We consider a non-deformable solid (rigid body). The position and velocity of the solid are given, respectively, by the position of its center of mass \mathbf{X} , the rotation matrix Q , the velocity of the center of mass \mathbf{V} and the angular momentum matrix P . The physical characteristics of the solid are its mass m and its matrix of inertia R which, in the inertial frame, is a diagonal matrix with the principal moments of inertia I_1 , I_2 and I_3 on the diagonal. Here, we instead use the diagonal matrix $D = \text{diag}(d_1, d_2, d_3)$, where:

$$\forall i \in \{1, 2, 3\}, \quad d_i = \frac{I_1 + I_2 + I_3}{2} - I_i.$$

The angular momentum matrix P can be related to the usual angular velocity vector Ω by the relation $P = D\mathbf{j}(\Omega)Q$, where the map $j : \mathbb{R}^3 \rightarrow \mathbb{R}^{3 \times 3}$ is defined such that:

$$\forall \mathbf{x} \in \mathbb{R}^3, \quad \forall \mathbf{y} \in \mathbb{R}^3, \quad j(\mathbf{x}) \cdot \mathbf{y} = \mathbf{x} \wedge \mathbf{y}.$$

Let us denote by \mathbf{F} and \mathcal{M} the external forces and torques acting on the solid, and by Δt the time-step. In order to preserve the energy of the solid over time integration of the movement, we choose a symplectic second-order scheme for constrained Hamiltonian systems, the RATTLE scheme [23]:

$$\mathbf{V}^{n+\frac{1}{2}} = \mathbf{V}^n + \frac{\Delta t}{2m} \mathbf{F}^n, \quad (1)$$

$$\mathbf{X}^{n+1} = \mathbf{X}^n + \Delta t \mathbf{V}^{n+\frac{1}{2}}, \quad (2)$$

$$P^{n+\frac{1}{2}} = P^n + \frac{\Delta t}{4} j(\mathcal{M}^n) Q^n + \frac{\Delta t}{2} A^n Q^n, \quad (3)$$

$$Q^{n+1} = Q^n + \Delta t P^{n+\frac{1}{2}} D^{-1}, \quad (4)$$

$$\text{with } A^n \text{ such that } (Q^{n+1})^T Q^{n+1} = I, \quad (5)$$

$$\mathbf{V}^{n+1} = \mathbf{V}^{n+\frac{1}{2}} + \frac{\Delta t}{2m} \mathbf{F}^{n+1}, \quad (6)$$

$$P^{n+1} = P^{n+\frac{1}{2}} + \frac{\Delta t}{4} j(\mathcal{M}^{n+1}) Q^{n+1} + \frac{\Delta t}{2} \tilde{A}^{n+1} Q^{n+1}, \quad (7)$$

$$\text{with } \tilde{A}^{n+1} \text{ such that } (Q^{n+1})^T P^{n+1} D^{-1} + D^{-1} (P^{n+1})^T Q^{n+1} = 0. \quad (8)$$

The symmetric matrices A^n and \tilde{A}^{n+1} play the role of Lagrange multipliers for the constraints on matrices Q^{n+1} and P^{n+1} .

The scheme makes use of the velocity at half time-step $\mathbf{V}^{n+\frac{1}{2}}$, which is constant during the time-step. Let us now consider the angular velocity. For a rigid solid, we have for all points \mathbf{x} :

$$\mathbf{X} - \mathbf{x} = Q \cdot (\mathbf{X}^0 - \mathbf{x}^0),$$

\mathbf{X}^0 and \mathbf{x}^0 being material points of the solid at initial time. Using the identity $\Omega \wedge (Q\mathbf{x}) = PD^{-1}\mathbf{x}$ for all \mathbf{x} , the velocity at point \mathbf{x} can be written as:

$$\mathbf{V}(\mathbf{x}) = \mathbf{V} + PD^{-1} \cdot (\mathbf{X}^0 - \mathbf{x}^0)$$

which is more convenient for use in the time scheme. In analogy with displacement, we consider $P^{n+\frac{1}{2}}$ as constant during the time-step, and we define the velocity of point \mathbf{x} at half time-step $(n + \frac{1}{2})\Delta t$:

$$\mathbf{V}^{n+\frac{1}{2}}(\mathbf{x}) = \mathbf{V}^{n+\frac{1}{2}} + P^{n+\frac{1}{2}} D^{-1} \cdot (\mathbf{X}^0 - \mathbf{x}^0).$$

2.2. Fluid discretization method

The problem of the interaction of shock waves with solid surfaces can be at first studied using an inviscid fluid model. In this work, we consider inviscid compressible flows, which follow the Euler equations:

$$\mathbf{w}_t + \nabla \cdot \mathbf{f}(\mathbf{w}) = \mathbf{0},$$

where $\mathbf{w} = (\rho, \rho\mathbf{u}, \rho E)^T$ is the vector of the conservative variables, and $\mathbf{f}(\mathbf{w})$ is the Euler flux:

$$\mathbf{f} = \begin{pmatrix} \rho\mathbf{u} \\ \rho\mathbf{u} \otimes \mathbf{u} + pI \\ (\rho E + p)\mathbf{u} \end{pmatrix},$$

where the pressure p is given by a perfect gas law: $p = (\gamma - 1)(\rho E - \frac{1}{2}\rho\mathbf{u} \cdot \mathbf{u})$.

To solve these equations, we use the OSMP numerical scheme, which is a one-step high-order scheme developed in [8,9]. It is derived using a coupled space-time Lax-Wendroff approach, where the formal order of accuracy in the scalar case can be set at arbitrary order (in this paper, we use order 11, that is the OSMP11 scheme). Imposing the MP conditions (Monotonicity Preserving) prevents the appearance of numerical oscillations in the vicinity of discontinuities while simultaneously avoiding the numerical diffusion of extrema. In one space dimension, on a uniform mesh with step-size Δx , at order p , it can be written:

$$w_j^{n+1} = w_j^n - \frac{\Delta t}{\Delta x} \left(f_{j+\frac{1}{2}}^p - f_{j-\frac{1}{2}}^p \right),$$

where $f_{j+\frac{1}{2}}^p$ is the p th-order-accurate numerical flux of the scheme at the cell interface $(j + \frac{1}{2})$. Given the l eigenvectors of the Jacobian matrix of the flux \mathbf{r}_k and eigenvalues λ_k , the general expression of the numerical fluxes can be written:

$$f_{j+\frac{1}{2}}^p = f_{j+\frac{1}{2}}^{\text{Roe}} + \frac{1}{2} \sum_k (\psi^p \mathbf{r})_{kj+\frac{1}{2}}, \quad (9)$$

where, for clarity, the superscript n has been omitted. $f_{j+\frac{1}{2}}^{\text{Roe}}$ is the first order Roe flux defined as follows:

$$f_{j+\frac{1}{2}}^{\text{Roe}} = \frac{1}{2} (f_j + f_{j+1}) - \frac{1}{2} \sum_k (\delta |f| \mathbf{r})_{kj+\frac{1}{2}} \quad (10)$$

with

$$\delta |f|_{kj+1/2} = |\lambda|_{kj+1/2} \delta \alpha_{kj+1/2}$$

$\delta \alpha_{kj+\frac{1}{2}} = \mathbf{r}_k \cdot (w_{j+1}^n - w_j^n)$ being the k th Riemann invariant of the Jacobian matrix. The ψ^p are corrective terms to obtain order p . The function ψ can be decomposed in odd and even parts:

$$\psi_{kj+\frac{1}{2}}^p = \sum_{n=1}^m \psi_{kj+\frac{1}{2}}^{2n} + js \sum_{n=1}^{m1} \psi_{kj+\frac{1}{2}-\frac{js}{2}}^{2n+1}, \quad (11)$$

where $m = \lfloor \frac{p}{2} \rfloor$, $m1 = \lfloor \frac{(p-1)}{2} \rfloor$ ($\lfloor \cdot \rfloor$ is the integer division symbol), and $js = \text{sign}(\lambda_{kj+\frac{1}{2}})$. The odd and even ψ functions are given by the recurrence formulae (valid for $n \geq 1$):

$$\psi_{kj+\frac{1}{2}}^{2n} = \sum_{l=0}^{2n-2} (-1)^l \mathbf{C}_{2n-2}^l \cdot (c_{2n} \delta \alpha)_{kj+\frac{1}{2}+n-1-l}, \quad (12)$$

$$\psi_{kj+\frac{1}{2}}^{2n+1} = \sum_{l=0}^{2n-1} (-1)^l \mathbf{C}_{2n-1}^l \cdot (c_{2n+1} \delta \alpha)_{kj+\frac{1}{2}+(n-1-l)js}, \quad (13)$$

where $\mathbf{C}_r^s = \frac{r!}{\lfloor (r-s) \rfloor s!}$. The coefficients c_q depend on the local CFL number, $v_{kj+\frac{1}{2}} = \frac{\delta t}{\Delta x} \lambda_{kj+\frac{1}{2}}$, and are given by:

$$(c_2)_{kj+\frac{1}{2}} = |\lambda|_{kj+\frac{1}{2}} \left(1 - |v|_{kj+\frac{1}{2}} \right),$$

$$(c_{q+1})_{kj+\frac{1}{2}} = \frac{|v|_{kj+\frac{1}{2}} + (-1)^q \lfloor \frac{(q+1)}{2} \rfloor}{q+1} \cdot (c_q)_{kj+\frac{1}{2}}, \quad q \geq 2. \quad (14)$$

At order p , the stencil of the scheme uses $p+2$ points. Flux limiting TVD or MP constraints are then be applied to ψ^p to make the scheme non-oscillatory. The detail of the limiting procedure can be found in [9].

Near cut-cells, the existence of an adequate stencil of fluid points is not necessarily provided for. Two main types of solutions can be devised: either lower the order of accuracy and thus the stencil width, or construct fictitious fluid values in the solid. We resort to the second solution, with simple mirroring conditions with respect to the solid boundary. The solution is satisfactory as long as the solid is larger than the stencil of the scheme, which is the case for the numerical examples considered in this paper. In case this condition fails, we could resort to Ghost Fluid-type methods as in [18].

In two dimensions, the fluxes are computed using a directional Strang splitting [47] which is second-order accurate. However the error of the scheme remains very low [8]. This splitting procedure will be expressed in Section 4 devoted to the coupling algorithm.

3. Treatment of the cells cut by the solid boundary in the Embedded Boundary method

In this section, we recall the main ideas of the Embedded Boundary method as exposed in [43,14,25].

In order to take into account the position of the solid in the fluid domain, we rely on the Embedded Boundary method, which consists in modifying the fluid fluxes in cells that are cut by the solid boundary (named cut cells), as in [25,14]. At time t , for a cut cell C , we assume that the solid occupies a volume fraction α_c . We also assume that the density, velocity and pressure are constant in the cell. The fluid mass, momentum and energy quantities contained in the cell are therefore equal

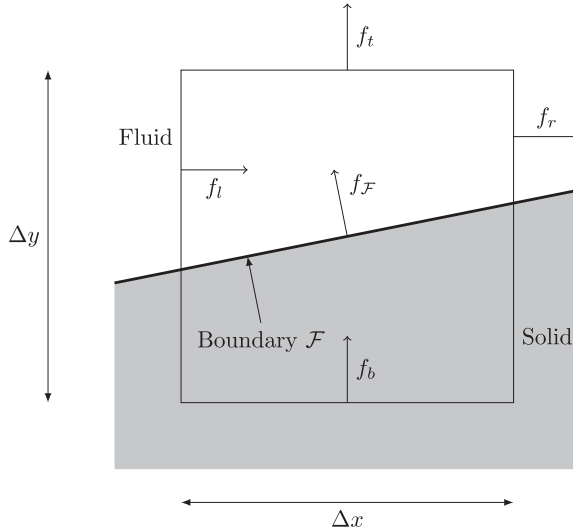


Fig. 1. Physical fluxes in a cut cell.

to their value at the center of the cell times the volume of the cell and the volume fraction of fluid $1 - \alpha_c$. In the same way, the computed fluxes are assumed to be constant on the faces of a cell. Denoting by $\kappa_{c_1 c_2}$ the solid surface fraction of the face between cells C_1 and C_2 , the effective flux between C_1 and C_2 is the computed flux times the surface of their interface times the fluid surface fraction $1 - \kappa_{c_1 c_2}$. Additional fluxes come from the presence of the moving solid boundary. These fluxes arise due to the change in surface fractions and the work of the fluid pressure on the solid surface. They are expressed in order to yield exact conservation of fluid mass and of the total momentum and energy of the system.

For the sake of simplicity, we limit ourselves to two space dimensions. However the three-dimensional case can be carried out in a similar way. Let us consider a fluid cell C cut by the boundary, as shown in Fig. 1. The indices l, r, t and b indicate respectively left, right, top and bottom in the sequel. Integrating the Euler equations on the cut cell and over the time interval $[n\Delta t, (n+1)\Delta t]$, and applying the divergence theorem, we get:

$$(1 - \alpha_c^{n+1})\Delta w_C = \Delta t \left(\frac{1 - \kappa_{cl}}{\Delta x} f_{cl} - \frac{1 - \kappa_{cr}}{\Delta x} f_{cr} + \frac{1 - \kappa_{cb}}{\Delta y} f_{cb} - \frac{1 - \kappa_{ct}}{\Delta y} f_{ct} \right) + \frac{\Delta t}{\Delta x \Delta y} X_{\mathcal{F}} + \sum_{\mathcal{F} \in C} \Delta w_{\mathcal{F}}^n, \quad (15)$$

where $\Delta w_C = w_C^{n+1} - w_C^n$ is the time increment and all fluxes are time-averaged over the time interval (the time averaging will be specified later). At the solid walls, pressure forces cause momentum and energy exchange between the solid and the fluid. They are taken into account through the exchange term $X_{\mathcal{F}}$. The detailed expression of $X_{\mathcal{F}}$ will be given in Section 4.4. Finally, the quantity $\Delta w_{\mathcal{F}}^n$ represents the amount of w^n swept by each solid boundary \mathcal{F} present in the cell during the time step. The solid boundary \mathcal{F} is the largest subsegment of the solid boundary which is contained in one single cell (not necessarily the same) at times $n\Delta t$ and $(n+1)\Delta t$. The precise definition of \mathcal{F} and the expression of $\Delta w_{\mathcal{F}}^n$ will be given in Section 4.3.

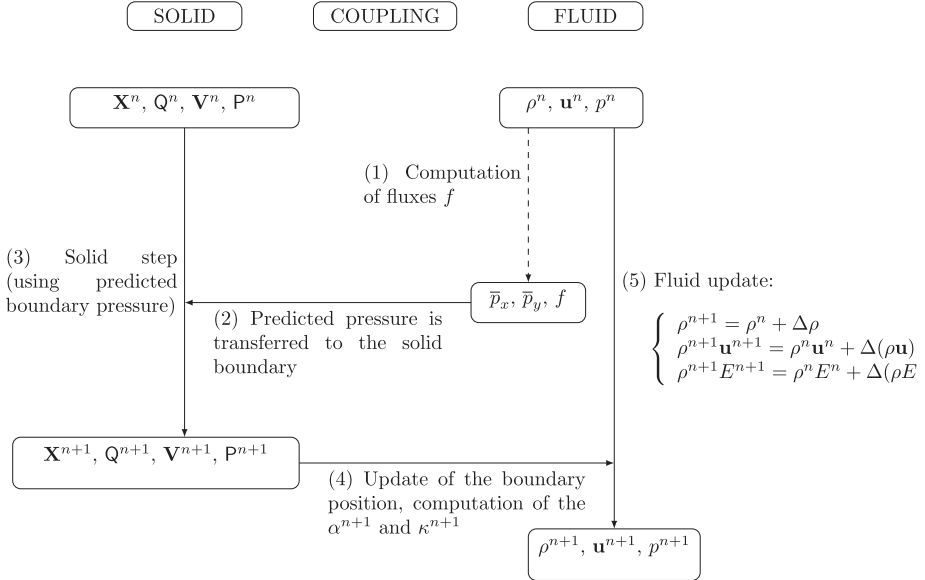
4. Coupling algorithm

Since the Discrete Element method is computationally expensive, the coupling algorithm should be explicit in order to avoid costly iterative procedures. In fact, the CFL condition of the explicit time-scheme gives the appropriate criterion for the capture of the high-frequency eigenmodes involved in the solid body fast dynamics. Moreover, as it is well known, explicit methods are more robust for impact problems. We choose the following general structure of the algorithm, which can be traced back to Noh [39]:

- The position of the solid and the density, velocity and pressure of the fluid are known at time t .
- The fluid exerts a pressure force on the solid boundaries: knowing the total forces applied on the solid, the position of the solid is advanced to time $t + \Delta t$.
- The density, velocity and pressure of the fluid are then computed at time $t + \Delta t$. This step takes into account the new position and velocity of the solid boundary, as well as the work of the forces of pressure on the boundary during the time step.

The choice of the coupling algorithm is guided by the conservation of the global momentum and energy of the system and the conservation of constant flows (see Section 6).

At the beginning of a time step, at time $n\Delta t$, the position and rotation of the solid particle ($\mathbf{X}^n, \mathbf{Q}^n$), the velocity and angular velocity of the solid particle ($\mathbf{V}^n, \boldsymbol{\Omega}^n$) and the fluid state \mathbf{w}^n are known. We choose the following general architecture for the algorithm:



Steps (1)–(5) of the algorithm are computed successively, and are detailed in the following subsections.

4.1. Computation of fluid fluxes and of the boundary pressure (steps (1) and (2))

Step (1) is a precomputation of fluxes without considering the presence of a solid boundary. As said above, the fluxes are computed in every cell using the OSMP11 scheme. However, we emphasize that the coupling algorithm does not depend on the choice of the numerical scheme. The fluxes are then stored for later use in step (5).

The other aim of this step is the computation of mean pressures in each cut-cell during the time-step in each direction \bar{p}_x and \bar{p}_y . These pressures, transferred to the solid boundary in step (2), account for the forces exerted by the fluid on the solid during the time-step. The same mean pressures will be used in step (5) to compute the momentum and energy exchanged between the solid and the fluid. In this way, the choice of \bar{p}_x and \bar{p}_y has no effect on the conservation of fluid mass, momentum or energy of the system. On the contrary it is a key ingredient for the exact conservation of constant flows (see Section 6). The explicit structure of our solid and fluid methods allows several possibilities for the choice of boundary pressures while maintaining the stability of the coupling algorithm. This is unusual in fluid–structure interaction.

The Strang directional splitting algorithm [47] is originally formulated as follows:

$$\mathbf{w}_j^{(n+1)} = L_x\left(\frac{\Delta t}{2}\right)L_y(\Delta t)L_x\left(\frac{\Delta t}{2}\right)\mathbf{w}_j^n,$$

where $L_x(\Delta t)$ and $L_y(\Delta t)$ are finite-difference approximation operators for the integration by a time-step Δt in directions x and y respectively. Here, this splitting procedure is implemented in a simplified form:

$$\mathbf{w}_j^{(n+2)} = L_x(\Delta t)L_y(\Delta t)L_y(\Delta t)L_x(\Delta t)\mathbf{w}_j^n,$$

that recovers the symmetry of the solution every two time steps. In our case, L_x and L_y involve the computation of a flux in the x or y direction using the state of fluid \mathbf{w} of the cells. The mean pressures \bar{p}_x and \bar{p}_y are then the pressures in the cell used for the computation of the fluxes by L_x and L_y , respectively. An analogous definition could be derived for other time integration methods, such as Runge–Kutta for instance. The directional splitting used for the fluid flux computation does not require

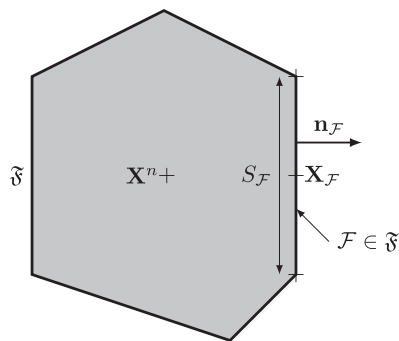


Fig. 2. Geometric description of the particles.

the solid body displacement to be split in x and y components. It is applied here only to recover second-order accuracy of the fluxes.

4.2. Computation of the solid step (step (3))

Step (3) consists mainly in the application of the time integration scheme for the rigid body motion described in Section 2.1. The essential difference with an uncoupled version lies in the integration of boundary pressure forces. As we consider an explicit coupling, the only boundary pressures available are \bar{p}_x and \bar{p}_y .

The solid is assumed to be polygonal (in two space dimensions) as described in Fig. 2. We denote by \mathfrak{F} the list of all faces of the solid in contact with fluid. For every face $\mathcal{F} \in \mathfrak{F}$, the position of the center of the face is given by vector $\mathbf{X}_{\mathcal{F}}$, and we denote by $S_{\mathcal{F}}$ its surface and $\mathbf{n}_{\mathcal{F}}$ its normal vector (oriented from the solid to the fluid). The fluid pressure force $\mathbf{F}_{\mathcal{F}}$ exerted on face $\mathcal{F} \in \mathfrak{F}$ is written as:

$$\mathbf{F}_{\mathcal{F}} \cdot \mathbf{e}_x = -\bar{p}_x S_{\mathcal{F}} n_{\mathcal{F}}^x, \quad (16)$$

$$\mathbf{F}_{\mathcal{F}} \cdot \mathbf{e}_y = -\bar{p}_y S_{\mathcal{F}} n_{\mathcal{F}}^y. \quad (17)$$

The total fluid pressure force \mathbf{F}_f^n is the sum of the contributions on each face:

$$\mathbf{F}_f^n = \sum_{\mathcal{F} \in \mathfrak{F}} \mathbf{F}_{\mathcal{F}}. \quad (18)$$

The fluid pressure torque \mathcal{M}_f^n is the sum of the torques of the pressure forces at the center of mass of the solid body:

$$\mathcal{M}_f^n = \sum_{\mathcal{F} \in \mathfrak{F}} \mathbf{F}_{\mathcal{F}} \wedge (\mathbf{X}^n - \mathbf{X}_{\mathcal{F}}).$$

The solid time-step is written as in Eqs. (1) to (8), with the only difference that the fluid pressure force and torque are taken constant during the whole time-step, equal to \mathbf{F}_f^n and \mathcal{M}_f^n (including in Eqs. (6) and (7)). The fact that \mathbf{F}_f^n , \mathcal{M}_f^n , $\mathbf{V}^{n+\frac{1}{2}}$ and $\mathbf{P}^{n+\frac{1}{2}}$ are constant during the time-step will be used in the conservation analysis in Section 5.

4.3. Update of the boundary and of the volume fractions (step (4))

Several tasks are carried out in step (4). For each cell C , the new solid volume fraction of the cell α_C^{n+1} and new surface fractions κ_C^{n+1} are computed. In addition, for each solid boundary \mathcal{F} , the pressures \bar{p}_x and \bar{p}_y are stored and the swept quantities $\Delta w_{\mathcal{F}}^n$ used in (15) are evaluated.

In two dimensions, the solid boundary is polygonal, and we therefore only have to deal with plane boundaries \mathcal{F} . In order to simplify the computation of the average of \bar{p}_x and \bar{p}_y on \mathcal{F} , we also assume that each boundary \mathcal{F} is contained only in one cell at time $n\Delta t$. The computation of the contribution of $\Delta w_{\mathcal{F}}^n$ to each cell is also easier if \mathcal{F} is entirely in the cell at time $(n+1)\Delta t$. We denote $\Phi_n(\mathcal{F})$ the position of boundary \mathcal{F} at time $n\Delta t$. We choose to define \mathcal{F} as the largest subsegment of the boundary polygon such that $\Phi_n(\mathcal{F})$ is contained in cell C_n at time $n\Delta t$ and $\Phi_{n+1}(\mathcal{F})$ is contained in cell C_{n+1} at time $(n+1)\Delta t$ (see Fig. 3). The two cells need not be necessarily different. \mathcal{F} may contain one or both vertices of the polygonal boundary at its ends, but we assume that each \mathcal{F} is contained in one single polygonal face. At each new time step, the polygonal boundary is subdivided into a new set of plane boundaries \mathcal{F} . Each newly computed boundary $\mathcal{F} \in \mathfrak{F}$ stores every variable necessary for the coupling: the surface $S_{\mathcal{F}}$ and the normal vector $\mathbf{n}_{\mathcal{F}}$ of $\Phi_n(\mathcal{F})$, the center of mass $\mathbf{X}_{\mathcal{F}}$ of \mathcal{F} , and we define $\mathbf{X}_{\mathcal{F}}^0 = \Phi_0(\mathbf{X}_{\mathcal{F}})$. The boundary also stores the pressures \bar{p}_x and \bar{p}_y in the cell occupied by $\Phi_n(\mathcal{F})$, and the velocity of the center of the boundary at time $(n + \frac{1}{2})\Delta t$, $\mathbf{V}_{\mathcal{F}}^{n+\frac{1}{2}}$, computed as:

$$\mathbf{V}_{\mathcal{F}}^{n+\frac{1}{2}} = \mathbf{V}^{n+\frac{1}{2}} + \mathbf{P}^{n+\frac{1}{2}} \mathbf{D}^{-1} \cdot (\mathbf{X}^0 - \mathbf{X}_{\mathcal{F}}^0). \quad (19)$$

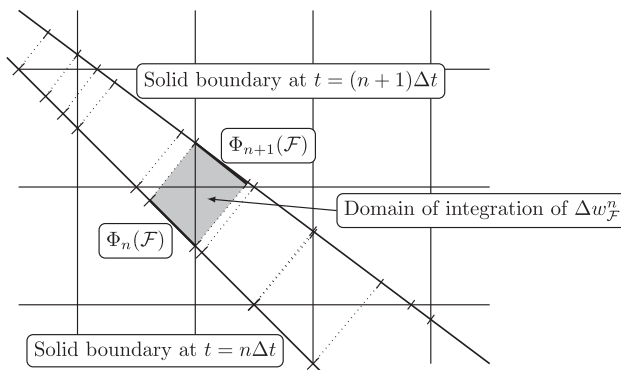


Fig. 3. Update of the boundary and computation of the $\Delta w_{\mathcal{F}}^n$.

The swept quantities $\Delta w_{\mathcal{F}}^n$ are computed as the integral of w^n in the quadrangle bounded by $\Phi_n(\mathcal{F})$ and $\Phi_{n+1}(\mathcal{F})$ (see Fig. 3). The condition

$$\sum_{\mathcal{F}} \Delta w_{\mathcal{F}}^n = \sum_{\mathcal{C}} (\alpha_c^{n+1} - \alpha_c^n) w_c^n \quad (20)$$

is then automatically satisfied as the set of such quadrangles is a partition of the volume swept by the solid during the time step.

The computation of α_c^{n+1} and κ_c^{n+1} involves the intersection of planes with rectangles, and can be carried out geometrically. The application of the divergence theorem to cell \mathcal{C} shows that the following relations are satisfied:

$$\kappa_{cl}^n = \kappa_{cr}^n + \sum_{\mathcal{F} \in \mathcal{C}} \frac{S_{\mathcal{F}}}{\Delta y} n_{\mathcal{F}}^x, \quad (21)$$

$$\kappa_{cb}^n = \kappa_{ct}^n + \sum_{\mathcal{F} \in \mathcal{C}} \frac{S_{\mathcal{F}}}{\Delta x} n_{\mathcal{F}}^y. \quad (22)$$

These conditions correspond to the geometric conservation laws (GCL) in ALE methods [32], and will be used in the analysis of the consistency of our method.

4.4. Modification of fluxes (step (5))

Step (5) of the algorithm consists mainly in the computation of the final values w_c^{n+1} in each cell, using a fully discrete expression of Eq. (15). It is the only part of the algorithm where the fluid “sees” the presence of a solid. The explicit fluid fluxes were pre-computed in step (1) on the Cartesian regular grid, and the modification of fluxes aims at conserving the mass of fluid and balancing the momentum and energy transferred to the solid during the time-step.

The exchange term in (15) can be written as

$$X_{\mathcal{F}} = \sum_{\mathcal{F} \in \mathcal{C}} S_{\mathcal{F}} f_{\mathcal{F}},$$

where $f_{\mathcal{F}}$ is the fluid flux at the solid boundary \mathcal{F} (see Fig. 1), that are approximated as:

$$f_{\mathcal{F}} = \frac{1}{S_{\mathcal{F}}} \left(0, \int_{\mathcal{F}} \bar{p}_x n_{\mathcal{F}}^x, \int_{\mathcal{F}} \bar{p}_y n_{\mathcal{F}}^y, \mathbf{V}_{\mathcal{F}}^{n+\frac{1}{2}} \cdot \int_{\mathcal{F}} \begin{pmatrix} \bar{p}_x n_{\mathcal{F}}^x \\ \bar{p}_y n_{\mathcal{F}}^y \end{pmatrix} \right)^T. \quad (23)$$

Here $\mathbf{V}_{\mathcal{F}}^{n+\frac{1}{2}}$ is the velocity of the center of the boundary and is defined in (19).

Using the fluid fluxes given by the OSMP11 scheme, we finally compute the time increment Δw_c from the following fully discrete version of Eq. (15):

$$(1 - \alpha_c^{n+1}) \Delta w_c = \Delta t \left(\frac{1 - \kappa_{cl}^{n+1}}{\Delta x} f_{cl} - \frac{1 - \kappa_{cr}^{n+1}}{\Delta x} f_{cr} + \frac{1 - \kappa_{cb}^{n+1}}{\Delta y} f_{cb} - \frac{1 - \kappa_{ct}^{n+1}}{\Delta y} f_{ct} \right) + \frac{\Delta t}{\Delta x \Delta y} \sum_{\mathcal{F} \in \mathcal{C}} S_{\mathcal{F}} f_{\mathcal{F}} + \sum_{\mathcal{F} \in \mathcal{C}} \Delta w_{\mathcal{F}}^n. \quad (24)$$

The value of w_c is then updated in every cell: $w_c^{n+1} = w_c^n + \Delta w_c$.

A main difference with [14] lies in the time integration of cell-face apertures $(1 - \kappa_c)$. Falcovitz et al. [14] use time-averaged cell-face apertures over the time step (at time $(n + \frac{1}{2})\Delta t$), ensuring consistency (in the sense that the uniform motion of a solid–fluid system is exactly preserved). In fact, a key ingredient in the consistency proof is the fact that conditions (21) and (22) are checked exactly. In [14], the consistent choice of time-averaged cell-face apertures $\kappa^{n+\frac{1}{2}}$ and solid surfaces in the fluid cell $\tilde{S}^{n+\frac{1}{2}}$ allows to check these conditions.

Here we instead take κ^{n+1} and recover consistency using the solid surface \tilde{S}^{n+1} present in the fluid cell at time $(n + 1)\Delta t$. This result is proved in section 6. Note that $\tilde{S}_c^{n+1} = \sum_{\Phi_{n+1}(\mathcal{F}) \in \mathcal{C}} S_{\mathcal{F}}^n$ as the solid is undeformable. This choice is motivated by the fact that the computation of time averaged $\kappa^{n+\frac{1}{2}}$ and $S^{n+\frac{1}{2}}$ is already complex in two dimensions and might become intractable in three dimensions. In addition, it requires an implicit resolution of $\tilde{S}^{n+\frac{1}{2}}$ in order to preserve the energy of the system. The choice of κ^{n+1} theoretically reduces the accuracy of the method in cut-cells. However, the accuracy of our numerical results did not advocate the use of the time-averaged $\kappa^{n+\frac{1}{2}}$ and the related added complexity in the algorithm.

In order to avoid the classical restriction of the time-step due to vanishing volumes:

$$\Delta t \leq \frac{(1 - \alpha_c) \min(\Delta x, \Delta y)}{\|\mathbf{u}\| + c},$$

where c is the local speed of sound, we resort to the mixing of small cut cells with their neighbors to prevent instabilities.

4.5. Conservative mixing of small cut cells

Two main methods have been developed to ensure the stability of conservative Embedded Boundary methods. A first method consists in computing a reference state using nonconservative interpolations, modified by redistributing the conservation error on neighboring cells [43,12,36]. A second method is to compute a fully conservative state using a formula similar

to (24). For stability reasons, small cells are merged with neighboring cells using a conservative procedure (originating from Glimm's idea [22]). We choose this second class of method, as [25] and [14].

Target cells need to be defined for small cells to be merged with them. [25] defines an equivalent normal vector to the boundary in the cell and mixes the cells preferentially in that direction. [14] rather merges newly exposed or newly covered cells with full neighbors having a face in common. In order to deal with cells occupied by several boundaries (impact of two solids), we cannot define a normal vector in every cell and we choose to improve the strategy applied in [14]. We define small cells as $\alpha_c > 0.5$. For mixing two cells \mathcal{C} and \mathcal{C}_T , so they have equal final value w , the following quantities are exchanged:

$$M_{\mathcal{C}\mathcal{C}_T} = \frac{\alpha_{\mathcal{C}_T}}{\alpha_{\mathcal{C}} + \alpha_{\mathcal{C}_T}} (w_{\mathcal{C}_T} - w_{\mathcal{C}}),$$

$$M_{\mathcal{C}_T\mathcal{C}} = \frac{\alpha_{\mathcal{C}}}{\alpha_{\mathcal{C}} + \alpha_{\mathcal{C}_T}} (w_{\mathcal{C}} - w_{\mathcal{C}_T}),$$

and it is easy to check that $w_{\mathcal{C}} + M_{\mathcal{C}\mathcal{C}_T} = w_{\mathcal{C}_T} + M_{\mathcal{C}_T\mathcal{C}}$. In the two dimensional case, we select the target cell \mathcal{C}_T as the fully-fluid cell ($\alpha_{\mathcal{C}_T} = 0$) nearest to \mathcal{C} , such that the path between the two cells does not cross a solid boundary. A recursive subroutine finds such a target cell in a small number of iterations, without any restriction on the geometry of the fluid domain.

5. Analysis of the conservation of mass, momentum and energy

In this section, we analyze the conservation properties of the coupling algorithm. These properties are verified for periodic boundary conditions or for an infinite domain.

5.1. Integration on the fluid domain

Integrating w on the fluid domain Ω_f^{n+1} at time $(n+1)\Delta t$, we obtain using (24) and the cancellation of fluxes on each cell face:

$$\frac{1}{\Delta x \Delta y} \int_{\Omega_f^{n+1}} w^{n+1} = \sum_c (1 - \alpha_c^{n+1}) w_c^n + \sum_c (1 - \alpha_c^{n+1}) \Delta w_c^n = \sum_c (1 - \alpha_c^{n+1}) w_c^n + \sum_{\mathcal{F}} \frac{\Delta t S_{\mathcal{F}}}{\Delta x \Delta y} f_{\mathcal{F}} + \sum_{\mathcal{F}} \Delta w_{\mathcal{F}}^n.$$

Using (20) we finally get:

$$\frac{1}{\Delta x \Delta y} \int_{\Omega_f^{n+1}} w^{n+1} = \sum_c (1 - \alpha_c^n) w_c^n + \sum_{\mathcal{F}} \frac{\Delta t S_{\mathcal{F}}}{\Delta x \Delta y} f_{\mathcal{F}} = \frac{1}{\Delta x \Delta y} \int_{\Omega_f^n} w^n + \frac{\Delta t}{\Delta x \Delta y} \sum_{\mathcal{F}} S_{\mathcal{F}} f_{\mathcal{F}} \quad (25)$$

the expression of $f_{\mathcal{F}}$ being given in Eq. (23).

The first component of system (25) expresses the fluid mass conservation. In order to proceed with the analysis of momentum and energy conservation, let us now turn to the solid part.

5.2. Solid conservation balance

Since the solid is treated using a Lagrangian method, the conservation of solid mass is straightforward. The fluid pressure force applied on the solid during the time step is given by (16)–(18). Let us consider a solid boundary $\mathcal{F} \in \mathfrak{F}$, and denote by $\Delta \mathcal{P}_{\mathcal{F}}$ the solid momentum variation induced by the pressure forces on \mathcal{F} , and $\Delta \mathcal{E}_{\mathcal{F}}$ the corresponding energy variation. Recalling that the pressure forces are kept constant during the time step, the balance of momentum and energy is given by:

$$\Delta \mathcal{P}_{\mathcal{F}} = \Delta t \mathbf{F}_{\mathcal{F}},$$

$$\Delta \mathcal{E}_{\mathcal{F}} = \Delta t \mathbf{F}_{\mathcal{F}} \cdot \left(\frac{1}{S_{\mathcal{F}}} \int_{\mathcal{F}} \mathbf{V}^{n+\frac{1}{2}}(\mathbf{x}) d\mathbf{x} \right) = \Delta t \mathbf{F}_{\mathcal{F}} \cdot \mathbf{V}_{\mathcal{F}}^{n+\frac{1}{2}}.$$

Finally, using the expression of forces $\mathbf{F}_{\mathcal{F}}$, we obtain:

$$\Delta \mathcal{P}_{\mathcal{F}}^x = -\Delta t \int_{\mathcal{F}} \bar{p}_x n_{\mathcal{F}}^x,$$

$$\Delta \mathcal{P}_{\mathcal{F}}^y = -\Delta t \int_{\mathcal{F}} \bar{p}_y n_{\mathcal{F}}^y,$$

$$\Delta \mathcal{E}_{\mathcal{F}} = -\Delta t \mathbf{V}_{\mathcal{F}}^{n+\frac{1}{2}} \cdot \int_{\mathcal{F}} \left(\bar{p}_x n_{\mathcal{F}}^x \right).$$

Comparing with Section 5.1, the balance of momentum and energy in the fluid domain results in:

$$\int_{\Omega_f^{n+1}} \rho^{n+1} \mathbf{u}^{n+1} + \sum_{\mathcal{F}} \Delta \mathcal{P}_{\mathcal{F}} = \int_{\Omega_f^n} \rho^n \mathbf{u}^n,$$

$$\int_{\Omega_f^{n+1}} \rho^{n+1} E^{n+1} + \sum_{\mathcal{F}} \Delta \mathcal{E}_{\mathcal{F}} = \int_{\Omega_f^n} \rho^n E^n.$$

This demonstrates the conservation of momentum and energy for the coupled system.

6. Conservation of constant flows

In this section we analyze the consistency of the coupling method, in the sense defined in [14], meaning exact conservation of uniform flows by the coupling algorithm. Two cases are analyzed. The first one, also considered in [14], consists of a solid immersed in a fluid and moving at the same velocity. This property is called “consistency” in [14]. The second one, not considered before, demonstrates the correct representation of the slip boundary condition along walls. These simple cases have been a guide to design the algorithm, as the preservation of such flows is a basic criterion for the quality of the method.

In the whole section, we consider a constant fluid state: $\rho^n = \rho_0$, $u^n = u_0$, $v^n = v_0$ and $p^n = p_0$ everywhere. The fluxes f are such that $f_r = f_l = (\rho_0 u_0, \rho_0 u_0^2 + p_0, \rho_0 u_0 v_0, (\rho_0 e_0 + p_0) u_0)^T$ and $f_t = f_b = (\rho_0 v_0, \rho_0 u_0 v_0, \rho_0 v_0^2 + p_0, (\rho_0 e_0 + p_0) u_0)^T$. In this case, the efficient pressures on the boundary of the solid are $\bar{p}_x = \bar{p}_y = p_0$.

6.1. Steady constant flow with moving boundaries

We consider an arbitrarily shaped rigid body, moving at constant velocity with no rotation, immersed in a uniform fluid flowing at the same velocity.

The solid is a closed set, and we denote by Ω_s^n the solid domain at initial time. We have:

$$\sum_{\mathcal{F}} S_{\mathcal{F}} \mathbf{n}_{\mathcal{F}} = \oint_{\partial \Omega_s^n} \mathbf{n} dS = \mathbf{0}.$$

Using (16) and (17), we obtain:

$$\sum_{\mathcal{F}} \mathbf{F}_{\mathcal{F}} = - \sum_{\mathcal{F}} p_0 S_{\mathcal{F}} \mathbf{n}_{\mathcal{F}} = \mathbf{0}.$$

This induces:

$$\mathbf{V}_i^{n+1} = \mathbf{V}_i^{n+\frac{1}{2}} = \mathbf{V}_i^n = (u_0, v_0)^T, \quad \mathbf{X}_i^{n+1} = \mathbf{X}_i^n + \Delta t (u_0, v_0)^T.$$

In the same way,

$$\sum_{\mathcal{F}} \mathcal{M}_{\mathcal{F}} = - \sum_{\mathcal{F}} p_0 S_{\mathcal{F}} \mathbf{n}_{\mathcal{F}} \wedge (\mathbf{X}_i^n - \mathbf{X}_{\mathcal{F}}) = p_0 \oint_{\partial \Omega_s} (\mathbf{X}_i^n - \mathbf{X}) \wedge \mathbf{n} dS = \mathbf{0}.$$

The volume swept by boundary \mathcal{F} is $\Delta t S_{\mathcal{F}} (u_0, v_0)^T \cdot \mathbf{n}_{\mathcal{F}}$. Since the initial state is constant, $\Delta w_{\mathcal{F}}^n$ is given by:

$$\Delta w_{\mathcal{F}}^n = \frac{\Delta t S_{\mathcal{F}}}{\Delta x \Delta y} (u_0 n_{\mathcal{F}}^x + v_0 n_{\mathcal{F}}^y) w_0.$$

In addition, as the solid translates without rotation, the normal vector $\mathbf{n}_{\mathcal{F}}$ to a boundary \mathcal{F} is constant in time. Using this property in Eqs. (21) and (22), we easily conclude that $(1 - \alpha_c) \Delta w_{\mathcal{F}}^n = 0$. Thus $w^{n+1} = w^n$, showing that the constant flow is left unchanged by the coupling algorithm and the mixing of small cells.

6.2. Free slip along a straight boundary

We consider an undeformable, fixed solid consisting in a semi-infinite half-space. The solid boundary is a straight planar boundary with a constant normal vector \mathbf{n} such that:

$$\mathbf{u}_0 \cdot \mathbf{n} = 0. \tag{26}$$

This initial state describes the free slip of the fluid along the straight boundary. In the inviscid case, no boundary layer should develop in the vicinity of the boundary. The conservation of such flows ensures that the boundary is not seen by the fluid as being artificially rough.

As the solid is fixed, α_c and κ_c remain constant over time and Δw_c^n is equal to zero. From Eq. (24), and using (21), (22) and (26), the components of Δw_c are calculated as:

$$(1 - \alpha_c)\Delta\rho_c = -\Delta t \sum_{\mathcal{F} \in \mathcal{C}} \frac{S_{\mathcal{F}}}{\Delta x \Delta y} \mathbf{n} \cdot \mathbf{u}_0 = 0,$$

$$(1 - \alpha_c)\Delta(\rho u)_c = -\Delta t \sum_{\mathcal{F} \in \mathcal{C}} \frac{S_{\mathcal{F}}}{\Delta x \Delta y} ((\mathbf{n} \cdot \mathbf{u}_0)u_0 + p_0 n_x) + \sum_{\mathcal{F} \in \mathcal{C}} \frac{\Delta t S_{\mathcal{F}}}{\Delta x \Delta y} p_0 n_x = 0,$$

$$(1 - \alpha_c)\Delta(\rho v)_c = -\Delta t \sum_{\mathcal{F} \in \mathcal{C}} \frac{S_{\mathcal{F}}}{\Delta x \Delta y} ((\mathbf{n} \cdot \mathbf{u}_0)v_0 + p_0 n_y) + \sum_{\mathcal{F} \in \mathcal{C}} \frac{\Delta t S_{\mathcal{F}}}{\Delta x \Delta y} p_0 n_y = 0,$$

$$(1 - \alpha_c)\Delta(\rho E)_c = -\Delta t \sum_{\mathcal{F} \in \mathcal{C}} \frac{S_{\mathcal{F}}}{\Delta x \Delta y} (\mathbf{n} \cdot \mathbf{u}_0)(\rho_0 e_0 + p_0) = 0.$$

This shows that the constant flow is preserved by step (5) of the algorithm. This result is not modified by the mixing procedure. We thus have shown the exact preservation of the free slip of the fluid along a straight boundary.

7. Numerical examples

In the following, we consider a perfect gas, with $\gamma = 1.4$. In all computations the CFL number was fixed equal to 0.5.

7.1. One-dimensional results

A piston of density 2 kg m^{-3} and length 0.5 m is initially centered at $x = 2 \text{ m}$, in a one-dimensional, 7 m-long tube, whose ends are connected by periodic boundary conditions which allow an easier comparison with ALE results. The gas initial pressure and density are equal to 10^6 Pa and 10 kg m^{-3} for $x \leq 2 \text{ m}$ and $x \geq 5 \text{ m}$ and to 10^5 Pa and 1 kg m^{-3} elsewhere. The system is initially at rest. The initial pressure difference between the two sides of the piston triggers its movement

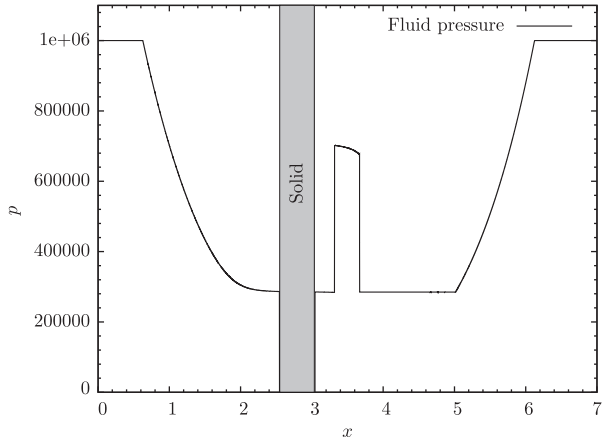


Fig. 4. Pressure at time $t = 0.003 \text{ s}$.

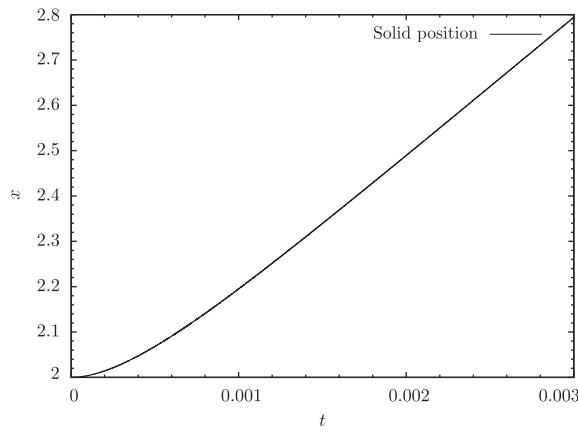


Fig. 5. Time evolution of the solid position.

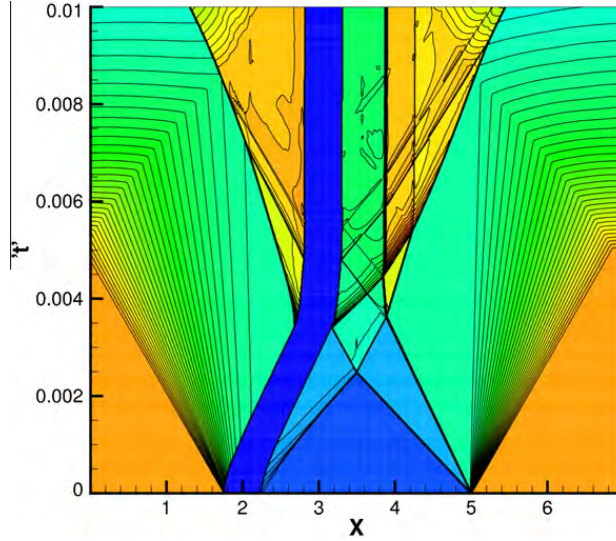


Fig. 6. x - t Diagram (the position of the solid is in deep blue). (For interpretation of the references to colour in this figure legend, the reader is referred to the web version of this article.)

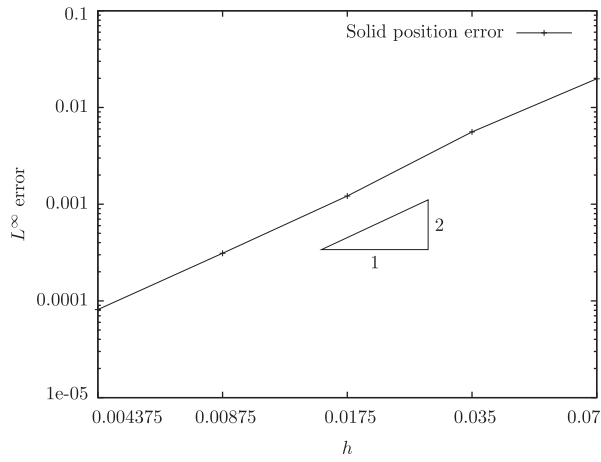


Fig. 7. Convergence of the solid position L^∞ -error.

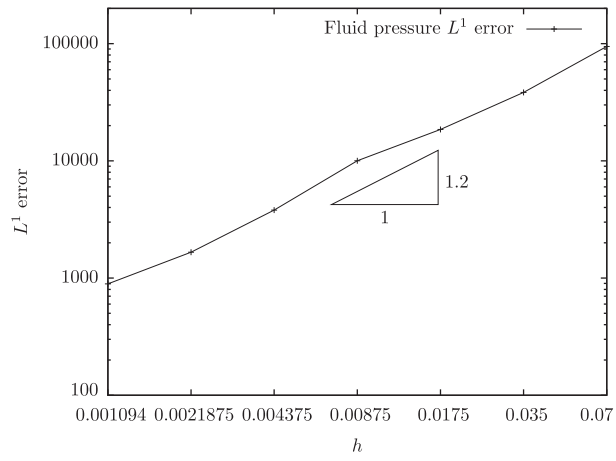


Fig. 8. Convergence of the fluid pressure L^1 -error.

and the propagation of waves in the fluid regions (a rarefaction in the left region and a shock wave in the right one). Wave interactions then occur at later time. The fluid pressure at time $t = 0.003$ s is shown in Fig. 4, and the trajectory of the solid is presented in Fig. 5. The x - t diagram over a longer time (0.01 s) is shown in Fig. 6.

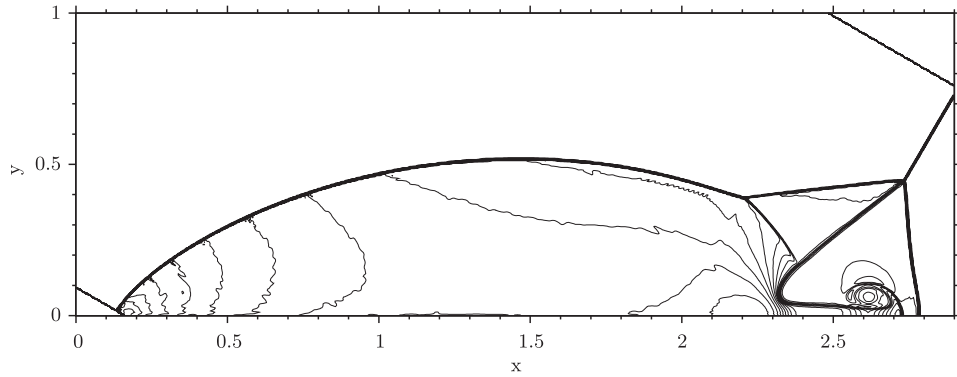


Fig. 9. Aligned case: 30 contours of fluid density from 1.73 to 21, $\Delta x = \Delta y = 1/220$.

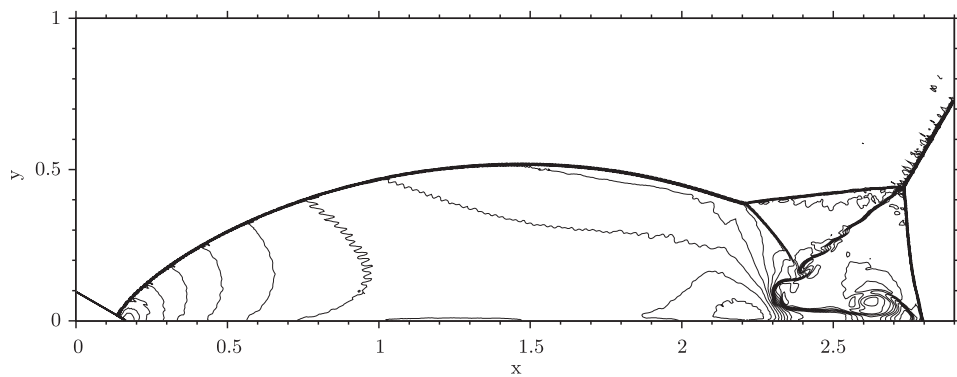


Fig. 10. Non-aligned grid case: 30 contours of fluid density from 1.73 to 21, $\Delta x = \Delta y = 1/220$.

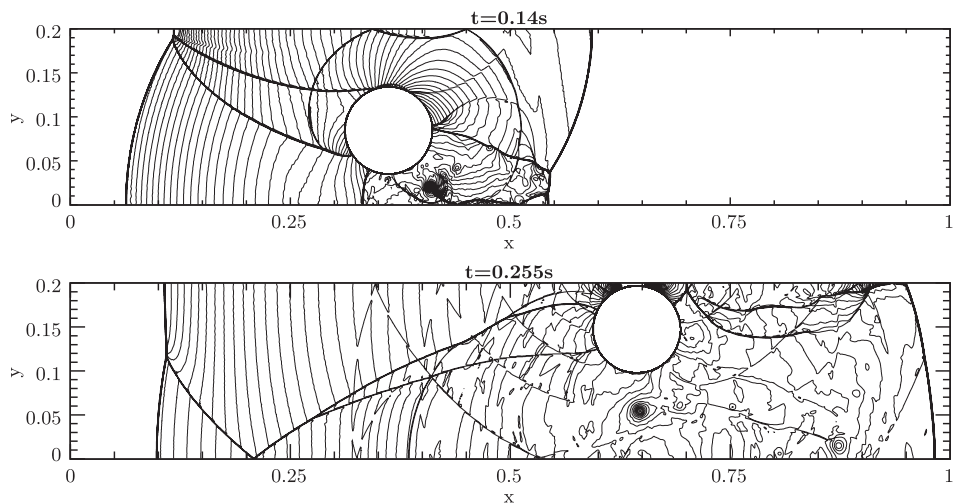


Fig. 11. 60 contours of fluid pressure from 0 to 28 at different times, $\Delta x = \Delta y = 6.25 \times 10^{-4}$.

An ALE computation was done for comparison, using a uniform grid moving at the solid velocity. The solid position and velocity are updated using the same second-order Verlet scheme. We compared the numerical results obtained through the Embedded Boundary method on 100, 200, 400, 800, 1600, 3200, 6400 and 12,800 points grids with a 51200-points ALE grid, considered as the reference solution. We observe a second-order convergence of the solid position (Fig. 7) and a super-linear convergence of order 1.2 of the fluid pressure (Fig. 8). The convergence rate is optimal for the solid (Verlet scheme is second-order accurate). The convergence rate for the fluid pressure is not optimal, due to the presence of discontinuities, but is not affected by the solid coupling.

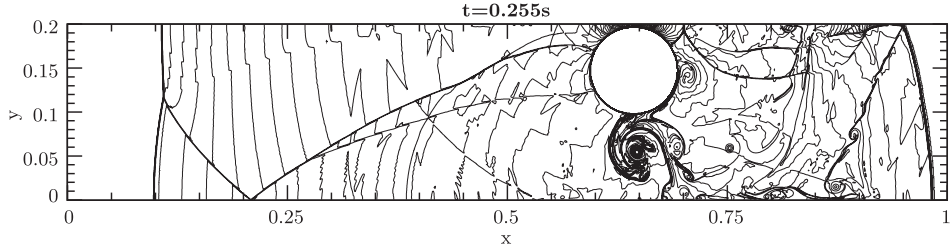


Fig. 12. 60 contours of fluid density from 0 to 12 at final time, $\Delta x = \Delta y = 6.25 \times 10^{-4}$.

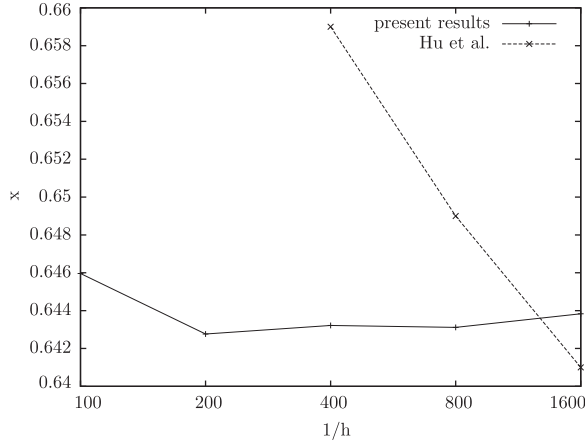


Fig. 13. Comparison of the convergence of the horizontal position of the center of mass of the cylinder with Hu et al. [25].

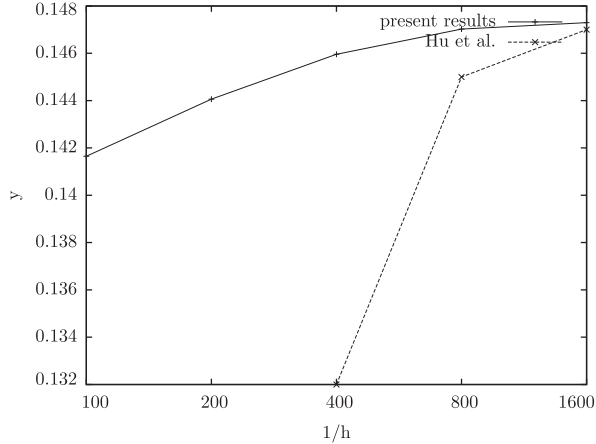


Fig. 14. Comparison of the convergence of the vertical position of the center of mass of the cylinder with Hu et al. [25].

7.2. Double Mach reflection

A Mach 10 planar shock wave reflects on a fixed 30° wedge, creating a Mach front, a reflected shock wave, and a contact discontinuity which develops into a jet along the solid boundary. This benchmark was first simulated on a Cartesian grid aligned with the solid boundary, using different finite volume methods [27,48,8]. Non-aligned grid methods were also tested on this benchmark, using Embedded Boundary methods [43,7], non-conservative Immersed Boundary methods [21], h -box methods [24], and kinetic schemes [31]. The position of the tip of the jet is an important characteristic of the accuracy of the results. The comparison with grid-aligned results shows that it is better recovered by conservative methods than non-conservative methods [43,7].

We have simulated the problem on a grid aligned with the wedge (aligned case, Fig. 9) and on a grid aligned with the incident shock wave (non-aligned case, Fig. 10). The two results are very similar, and agree with [7,43,27,8]. One can remark that all the features of the flow are captured at the correct position in the non-aligned case. The jet propagates along the wall

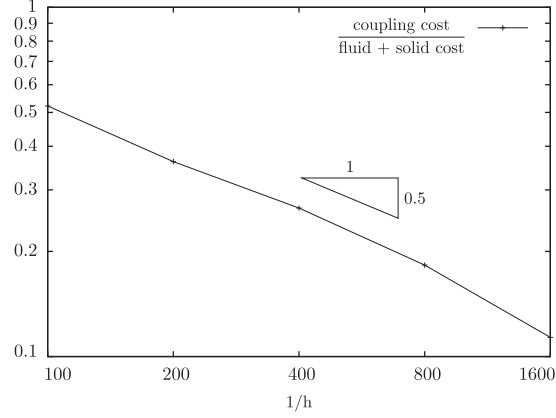


Fig. 15. Ratio between the coupling computation cost and the fluid and solid costs.

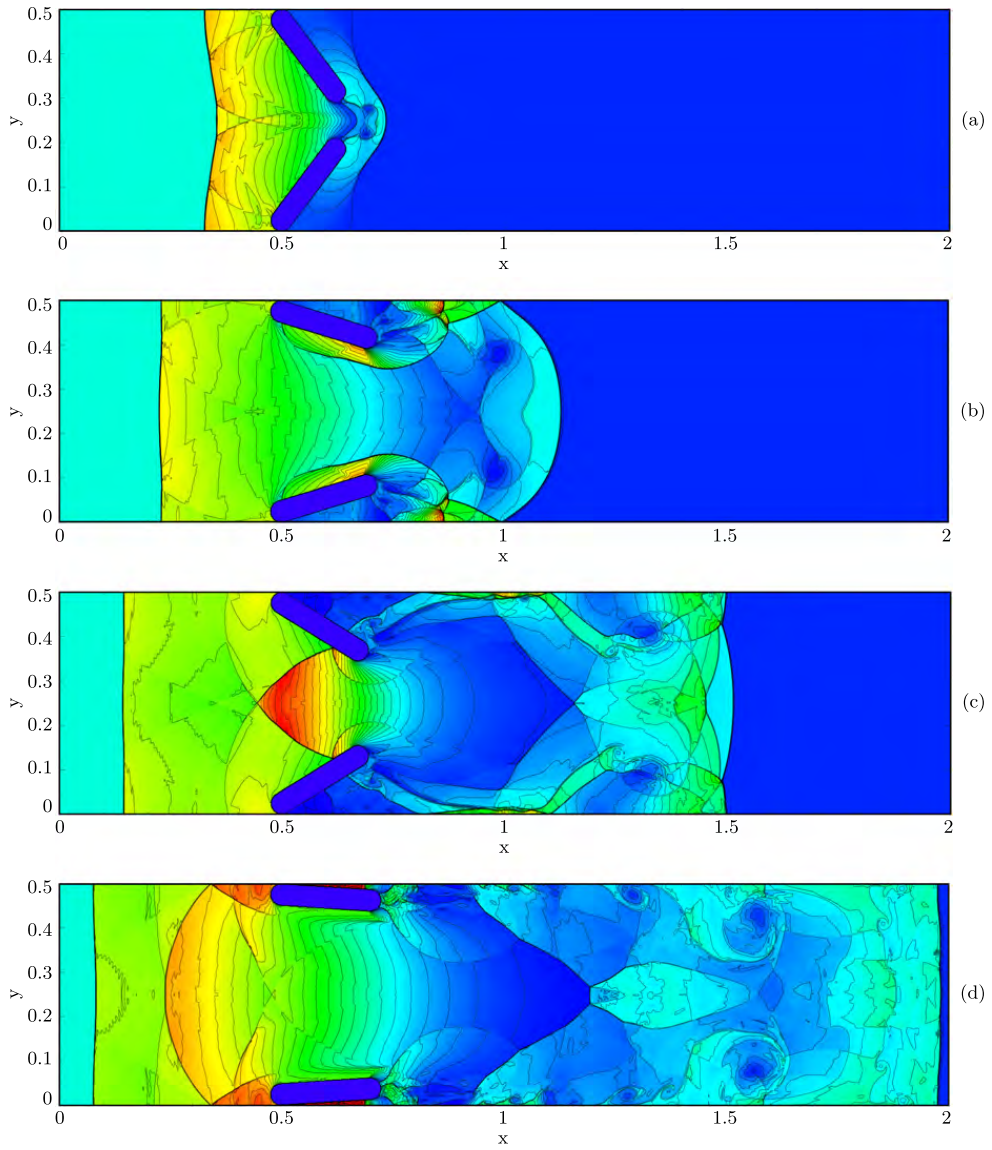


Fig. 16. Density contours at times $t = 0.125$ s (a), $t = 0.25$ s (b), $t = 0.375$ s (c) and $t = 0.5$ s (d).

without numerical friction due to the conservation of free slip along a straight boundary (Section 6.2). In the principal Mach stem, the discontinuities are slightly more oscillatory than in the aligned case. This can be identified as a post-shock oscil-

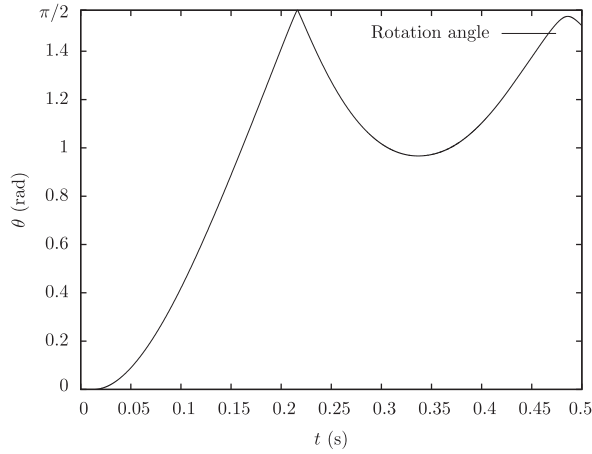


Fig. 17. Time evolution of the rotation of a door.

lation phenomenon to which Roe's scheme is especially prone (see, for instance, [28,4]), and is not related to the coupling method. Nevertheless, the perturbations stay localized in the vicinity of discontinuities.

7.3. Lift-off of a cylinder

This moving body test case was first proposed in [14], using a conservative method. A rigid cylinder of density 7.6 kg m^{-3} and diameter 0.1 m, initially resting on the lower wall of a $1 \text{ m} \times 0.2 \text{ m}$ two-dimensional channel filled with air at standard conditions ($\rho = 1 \text{ kg m}^{-3}$, $p = 1 \text{ Pa}$), is driven and lifted upwards by a Mach 3 shock wave. Gravity is not taken into account. The problem was simulated in [20,3,25,46]. In Fig. 11, we present our results on a uniform 1600×320 grid at times 0.14 s and 0.255 s. The cylinder was approximated by a polygon with 1240 faces.

Our results agree well on the position of the solid and of the shocks with Arienti et al. [3] and Hu et al. [25]. However, some differences should be noted. First of all, some reflected shock waves in our results seem to lag slightly behind their position in previous results. This difference might be caused by small differences in the final position of the solid. Hu et al. [25] also discuss the presence of a strong vortex under the cylinder in the results of Forrer and Berger [20]. They dismiss it as an effect of the space-time splitting scheme employed which affects the numerical dissipation. We also obtain this vortex, which does not disappear as we refine the mesh. We rather believe that this vortex is associated with a Kelvin–Helmholtz instability of the contact discontinuity present under the cylinder (Fig. 12).

In Figs. 13 and 14 we present convergence results on the final position of the center of mass of the cylinder, compared to those of Hu et al. [25]. We observe that our results exhibit a fast convergence process, which is not the case in [25]. Let us note that no exact solution exists for the final position of the cylinder. The final position we found is however in the same range as in [25]. The results also compare well with Arienti et al. [3]. The improvement lies in the combination of the conservative interface method [25] with a conservative coupling and a second-order time-scheme for the rigid body motion. For this difficult case, the maximal conservation relative errors due to coupling were bounded by 4×10^{-6} over the whole simulation time, and no drift was observed.

In Fig. 15 we present the relative computational cost of the coupling. The relative cost is defined as the ratio of the computational times dedicated to the coupling method and to the fluid and solid methods. In the rigid body case, the cost of the solid method is very low compared to that of the fluid method. As the coupling method is explicit and local, the computational cost is located on a manifold one dimension lower than the dimension of the whole space. In the two-dimensional case, the coupling is on a one-dimensional manifold. Indeed, we observe in Fig. 15 that the relative cost of the coupling decreases as the grid is refined, with a slope of 0.5, and that the coupling cost remains lower than the fluid and solid costs, amounting to approximately 10–20% for the grids yielding sufficient accuracy.

7.4. Flapping doors

We propose this new fluid–structure interaction case as a demonstration of the robustness of our approach and as a first step towards fracture and impact simulations. The flapping doors case involves separating or closing solid boundaries, with cells including several moving boundaries. The algorithm is shown to be able to deal with such difficulties. Two doors initially close a canal and are impacted from the left by a Mach 3 shock. The canal consists of two fixed rigid walls, 2 m long and 0.5 m apart. Each door consists of a 0.2-m long and 0.05 m-wide rectangle, completed at both ends by a half-circle of diameter 0.05 m. The doors are respectively fixed on points (0.5, 0.025) and (0.5, 0.475) at the center of the half-circles. They can rotate freely around these points. The Mach 3 shock is initially located at $x = 0.43 \text{ m}$. The density of the solid is 0.1 kg m^{-3} and the pre- and post-shock state of the fluid are $(\rho, u, v, p) = (1, 0, 0, 1)$ and $(\rho, u, v, p) = (3.857, 2.6929, 0, 10.333)$. In Fig. 16 we

show the density field obtained using a 1600×400 grid, at times 0.125 s, 0.25 s, 0.375 s and 0.5 s. After the incident shock hits the doors, it reflects to the left and the doors open due to the high rise in pressure. The opening of the doors produces a jet preceded by a shock wave propagating to the right. Then complex interactions of waves occur, due to door movements and interaction with the walls. Kelvin–Helmholtz instabilities of contact lines can be observed at $t = 0.5$ s. It is worth noting that symmetry of the flow about the centerline of the canal axis is remarkably well preserved by the coupling method.

As the doors remain tangent to the canal walls during their rotation, the fluid cannot pass between the wall and a door at its hinge. When the doors approach the walls at maximum rotation, the fluid is compressed, and eventually pushes them back. This is observed at time $t = 0.2162$ s and $t = 0.486$ s in Fig. 17, which presents the time evolution of the doors rotation angle. In the first case, the distance between each door's straight boundary and the wall is less than 0.002 m, while the size of a fluid cell is $\Delta x = 0.00125$ m. The method is able to deal with the fact that most cells along the wall are cut by the moving boundary and contain several moving boundaries. Treating this test case with an ALE method would require several remeshings in the course of the simulation, especially in the initial separation of the tangent door tips, and when the doors approach the walls.

8. Conclusion

We have presented a new coupling algorithm between a compressible fluid flows and a rigid body using an Embedded Boundary method. This explicit algorithm has the advantage of preserving the usual CFL stability condition: the time-step can be taken as the minimum of the full cell size fluid and solid time-steps. The combination of the Embedded Boundary method for the fictitious fluid domain and of the coupling strategy ensures the conservation of fluid mass and the balance of momentum and energy between fluid and solid. In addition, the exact conservation of the two constant states described in Section 6 gives good insight on the consistency of the method: we prove the conservation of a constant flow in which a solid moves at the same velocity and the fact that the treatment at the boundary introduces no spurious roughness or boundary layers. The numerical examples suggest the second-order convergence of the solid position and the super-linear convergence of the fluid state in L^1 norm, while our results on two-dimensional benchmarks agree very well with body-fitted methods and improve Immersed Boundary results. We are also capable of dealing with solid boundaries moving close to each other, which is promising for impact simulations. The method is computationally efficient, as the coupling adds an integration on a space one dimension smaller than the fluid and solid computation spaces. The present method is therefore perfectly liable to be extended to a deformable solid, and was designed to extend naturally in three space dimensions. The remaining difficulty is the ability to define and track the solid boundary surrounding a Discrete Element assembly.

References

- [1] R. Abgrall, How to prevent pressure oscillations in multicomponent flow calculations: a quasi conservative approach, *J. Comput. Phys.* 125 (1996) 150–160.
- [2] N. Aquelet, M. Souli, L. Olovsson, Euler–Lagrange coupling with damping effects: application to slamming problems, *Comput. Methods Appl. Mech. Eng.* 195 (1–3) (2006) 110–132.
- [3] R. Arrienti, P. Hung, E. Morano, J.E. Shepherd, A level set approach to Eulerian–Lagrangian coupling, *J. Comput. Phys.* 185 (2003) 213–251.
- [4] M. Arora, P.L. Roe, On postshock oscillations due to shock capturing schemes in unsteady flows, *J. Comput. Phys.* 130 (1997) 25–40.
- [5] O. Boiron, G. Chiavassa, R. Donat, A high-resolution penalization method for large mach number flows in the presence of obstacles, *J. Comput. Fluid* 38 (3) (2009) 703–714.
- [6] J.-I. Choi, R.C. Oberoi, J.R. Edwards, J.A. Rosati, An immersed boundary method for complex incompressible flows, *J. Comput. Phys.* 224 (2) (2007) 757–784.
- [7] P. Colella, D.T. Graves, B.J. Keen, D. Modiano, A Cartesian grid embedded boundary method for hyperbolic conservation laws, *J. Comput. Phys.* 211 (2006) 347–366.
- [8] V. Daru, C. Tenaud, High order one-step monotonicity-preserving schemes for unsteady compressible flow calculations, *J. Comput. Phys.* 193 (2) (2004) 563–594.
- [9] V. Daru, C. Tenaud, Numerical simulation of the viscous shock tube problem by using a high resolution monotonicity-preserving scheme, *Comput. Fluids* 38 (3) (2009) 664–676.
- [10] M. de Tullio, G. Iaccarino, Immersed Boundary Technique for Compressible Flow Simulations on Semi-structured Meshes, CTR Annual Research Briefs, Center for Turbulence Research, NASA Ames/Stanford Univ., 2005.
- [11] J. Donea, S. Giuliani, J.P. Halleux, An arbitrary Lagrangian Eulerian finite element method for transient dynamic fluid–structure interactions, *Comput. Methods Appl. Mech. Eng.* 33 (1982) 689–723.
- [12] Z. Dragomilovic, F. Najmabadi, M. Day, An embedded boundary method for viscous, conducting compressible flow, *J. Comput. Phys.* 216 (1) (2006) 37–51.
- [13] E.A. Fadlun, R. Verzicco, P. Orlandi, J. Mohd-Yusof, Combined immersed-boundary finite-difference methods for three-dimensional complex flow simulations, *J. Comput. Phys.* 161 (1) (2000) 35–60.
- [14] J. Falcovitz, G. Alfandary, G. Hanoch, A two-dimensional conservation laws scheme for compressible flows with moving boundaries, *J. Comput. Phys.* 138 (1997) 83–102.
- [15] C. Farhat, K.G. van der Zee, P. Geuzaine, Provably second-order time-accurate loosely-coupled solution algorithms for transient nonlinear computational aeroelasticity, *Comput. Methods Appl. Mech. Eng.* 195 (2006) 1973–2001.
- [16] N. Favrie, S.L. Gavrilyuk, R. Saurel, Solid–fluid diffuse interface model in cases of extreme deformation, *J. Comput. Phys.* 228 (2009) 6037–6077.
- [17] R.P. Fedkiw, Coupling an Eulerian fluid calculation to a Lagrangian solid calculation with the Ghost Fluid method, *J. Comput. Phys.* 175 (2002) 200–224.
- [18] R.P. Fedkiw, T. Aslam, B. Merriman, S. Osher, A non-oscillatory Eulerian approach to interfaces in multimaterial flows (the Ghost Fluid method), *J. Comput. Phys.* 152 (1999) 457–492.
- [19] M.A. Fernández, J.-F. Gerbeau, C. Grandmont, A projection semi-implicit scheme for the coupling of an elastic structure with an incompressible fluid, *Int. J. Numer. Methods Eng.* 69 (2007) 794–821.
- [20] H. Forrer, M. Berger, Flow Simulation on Cartesian Grids involving Complex Moving Geometries Flows, vol. 129, Springer, 1998.
- [21] H. Forrer, R. Jeltsch, A high-order boundary treatment for Cartesian-grid methods, *J. Comput. Phys.* 140 (1998) 259–277.

- [22] J. Glimm, X. Li, Y. Liu, Z. Xu, N. Zhao, Conservative front tracking with improved accuracy, SIAM J. Numer. Anal. 39 (2003) 179–200.
- [23] E. Hairer, C. Lubich, G. Wanner, Geometric Numerical Integration: Structure-Preserving Algorithms for Ordinary Differential Equations, Springer Series in Comput. Mathematics, second ed., vol. 31, Springer-Verlag, 2006.
- [24] C. Helzel, M.J. Berger, R.J. Leveque, A high-resolution rotated grid method for conservation laws with embedded geometries, SIAM J. Sci. Comput. 26 (2005) 785–809.
- [25] X.Y. Hu, B.C. Khoo, N.A. Adams, F.L. Huang, A conservative interface method for compressible flows, J. Comput. Phys. 219 (2) (2006) 553–578.
- [26] S.R. Idelsohn, J. Martí, A. Limache, E. Onate, Unified Lagrangian formulation for elastic solids and incompressible fluids: application to fluid–structure interaction problems via the PFEM, Comput. Methods Appl. Mech. Eng. 197 (19–20) (2008) 1762–1776.
- [27] G.-S. Jiang, C.-W. Shu, Efficient implementation of Weighted ENO schemes, J. Comput. Phys. 126 (1996) 202–228.
- [28] Shi Jin, Jian-Guo Liu, The effects of numerical viscosities: I. Slowly moving shocks, J. Comput. Phys. 126 (1996) 373–389.
- [29] G. Kalitzin, G. Iaccarino, Turbulence Modeling in an Immersed-boundary RANS Method, CTR Annual Research Briefs, Center for Turbulence Research, NASA Ames/Stanford Univ., 2002.
- [30] G. Kalitzin, G. Iaccarino, Towards Immersed Boundary Simulation of High Reynolds Number Flows, CTR Annual Research Briefs, Center for Turbulence Research, NASA Ames/Stanford Univ., 2003.
- [31] B. Keen, S. Karni, A second order kinetic scheme for gas dynamics on arbitrary grids, J. Comput. Phys. 205 (2005) 108–130.
- [32] Michel Lesoinne, Charbel Farhat, Geometric conservation laws for flow problems with moving boundaries and deformable meshes, and their impact on aeroelastic computations, Comput. Methods Appl. Mech. Eng. 134 (1996) 71–90.
- [33] R.J. Leveque, Z. Li, The immersed interface method for elliptic equations with discontinuous coefficients and singular sources, SIAM J. Numer. Anal. 31 (4) (1994) 1019–1044.
- [34] R.J. LeVeque, Z. Li, Immersed interface methods for Stokes flow with elastic boundaries or surface tension, SIAM J. Sci. Comput. 18 (3) (1997) 709–735.
- [35] C. Mariotti, Lamb's problem with the lattice model Mka3D, Geophys. J. Int. 171 (2007) 857–864.
- [36] G.H. Miller, P. Colella, A conservative three-dimensional Eulerian method for coupled solid–fluid shock capturing, J. Comput. Phys. 183 (1) (2002) 26–82.
- [37] J. Mohd-Yusof, Combined Immersed-boundary/b-spline Methods for Simulation of Flow in Complex Geometries, CTR Annual Research Briefs, Center for Turbulence Research, NASA Ames/Stanford Univ., 1997.
- [38] L. Monasse, C. Mariotti, An energy-preserving Discrete Element Method for elastodynamics, M2AN, submitted for publication.
- [39] W.F. Noh, Fundamental Methods of Hydrodynamics, Methods of Computational Physics, vol. 3, Academic Press, New York/London, 1964. pp. 117–179.
- [40] L. Olovsson, On the Arbitrary Lagrangian–Eulerian Finite Element Method, Ph.D. Thesis, Linköping University, 2000.
- [41] A. Paccou, G. Chiavassa, J. Liandrat, K. Schneider, A penalization method applied to the wave equation, CR Mécanique 333 (1) (2005) 79–85.
- [42] P. De Palma, M.D. de Tullio, G. Pascazio, M. Napolitano, An immersed-boundary method for compressible viscous flows, Comput. Fluid 35 (7) (2006) 693–702.
- [43] R.B. Pember, J.B. Bell, P. Colella, W.Y. Crutchfield, M.L. Welcome, An adaptive Cartesian grid method for unsteady compressible flow in irregular regions, J. Comput. Phys. 120 (1995) 278–304.
- [44] C.S. Peskin, Flow Patterns Around Heart Valves: A Digital Computer Method for Solving the Equations of Motion, Ph.D. Thesis, Albert Einstein College of Medicine, 1972.
- [45] C.S. Peskin, The immersed boundary method, Acta Numer. 11 (2002) 1–39.
- [46] S.K. Sambasivan, H.S. UdayKumar, Ghost Fluid method for strong shock interactions Part 2: Immersed solid boundaries, AIAA J. 47 (12) (2009) 2923–2937.
- [47] G. Strang, On construction and comparison of difference schemes, SIAM J. Numer. Anal. 5 (1968) 506–516.
- [48] P. Woodward, P. Colella, The numerical simulation of two-dimensional fluid flow with strong shocks, J. Comput. Phys. 54 (1984) 115–173.
- [49] S. Xu, Z. Jane Wang, An immersed interface method for simulating the interaction of a fluid with moving boundaries, J. Comput. Phys. 216 (2) (2006) 454–493.

I. Reyt, H. Bailliet, D. Baltean-Carlès, V. Daru, S. Moreau, J.-C. Valière, C. Weisman
"Fast acoustic streaming in standing waves : Generation of an additional outer streaming cell ".
Journal of the Acoustical Society of America, 134 (3), p. 1791–1801 (2013).

Fast acoustic streaming in standing waves: Generation of an additional outer streaming cell

Ida Rey

LIMSI-CNRS UPR 3251, Bât. 508 rue John Von Neumann, Campus Univ. Paris Sud, 91403 Orsay, France

Virginie Daru^{a)}

Arts et Métiers ParisTech Lab. DynFluid, 151 bd de l'hôpital, 75013 Paris, France

Hélène Bailliet, Solène Moreau,^{b)} and Jean-Christophe Valière

Institut Pprime, CNRS - Université de Poitiers-ENSMA, Département Fluides-Thermique-Combustion, ENSIP, 6 rue Marcel Doré Bât. B17-BP 633, 86022 Poitiers Cedex, France

Diana Baltean-Carlès^{a)} and Catherine Weisman^{a),c)}

UPMC Paris06 UFR 919, 4 Place Jussieu, 75252 Paris Cedex 05, France

(Received 18 April 2013; revised 11 July 2013; accepted 22 July 2013)

Rayleigh streaming in a cylindrical acoustic standing waveguide is studied both experimentally and numerically for nonlinear Reynolds numbers from 1 to 30 [$\text{Re}_{NL} = (U_0/c_0)^2(R/\delta_v)^2$, with U_0 the acoustic velocity amplitude at the velocity antinode, c_0 the speed of sound, R the tube radius, and δ_v the acoustic boundary layer thickness]. Streaming velocity is measured by means of laser Doppler velocimetry in a cylindrical resonator filled with air at atmospheric pressure at high intensity sound levels. The compressible Navier-Stokes equations are solved numerically with high resolution finite difference schemes. The resonator is excited by shaking it along the axis at imposed frequency. Results of measurements and of numerical calculation are compared with results given in the literature and with each other. As expected, the axial streaming velocity measured and calculated agrees reasonably well with the slow streaming theory for small Re_{NL} but deviates significantly from such predictions for fast streaming ($\text{Re}_{NL} > 1$). Both experimental and numerical results show that when Re_{NL} is increased, the center of the outer streaming cells are pushed toward the acoustic velocity nodes until counter-rotating additional vortices are generated near the acoustic velocity antinodes. © 2013 Acoustical Society of America. [http://dx.doi.org/10.1121/1.4817888]

PACS number(s): 43.25.Nm, 43.25.Gf [TB]

Pages: 1791–1801

I. INTRODUCTION

Rayleigh streaming refers to the second order mean velocity that is generated by effects related with the interaction of a solid surface and an acoustic wave in a fluid. In thermoacoustic devices, acoustic streaming results in convected heat flow that can reduce the efficiency of the devices. Because the power density of a thermoacoustic device is roughly proportional to the square of the acoustic pressure amplitude, the study of high acoustic amplitude phenomena is important to the field of thermoacoustics. A better understanding and characterization of the corresponding so-called “fast” Rayleigh streaming is therefore useful to assess its impact on the efficiency of thermoacoustic devices.

The reference solution derived by Rayleigh¹ concerns streaming generated by a standing wave between two infinite, widely separated plates. Together with further studies by Nyborg² and Westervelt³, this work yielded the so-called Rayleigh-Nyborg-Westervelt (RNW) streaming theory. For a better application to thermoacoustics, this theoretical

description has evolved in order to refine thermal effect description and to remove the restrictions to wide channels and to slow streaming. Concerning the first two points, during the last decades, thermoacoustic applications have motivated several theoretical works to take into account thermal effects^{4,5} and/or to remove the restriction to large channels.^{6,7} However, all these theoretical developments were restricted to slow streaming where fluid inertia is neglected. The dimensionless number characterizing the inertial effects with respect to viscous effects is the nonlinear Reynolds number Re_{NL} defined by Menguy and Gilbert.⁸ For slow streaming the nonlinear Reynolds number is such that $\text{Re}_{NL} \ll 1$. The influence of fluid inertia was studied only by Menguy and Gilbert and for Re_{NL} up to only about two; using a perturbation method with asymptotic expansions followed by time-averaging, they developed boundary layer streaming equations, matched with nonlinear streaming equations in the main acoustic field, thus demonstrating a noticeable distortion of the streaming velocity field.

Previous simulations of acoustic streaming in the linear regime were conducted by solving the flow dynamics between two plates inside a thermoacoustic refrigerator.⁹ More recently, Aktas and Farouk¹⁰ performed numerical simulations in the linear and nonlinear streaming regimes, solving the full compressible Navier-Stokes equations in the plane case with a flux corrected transport scheme. The

^{a)}Also at: LIMSI-CNRS UPR 3251, 91403 Orsay, France.

^{b)}Current address: Laboratoire Roberval CNRS 6253, Université de Technologie de Compiègne BP 20529, 60205 Compiègne Cedex, France.

^{c)}Author to whom correspondence should be addressed. Electronic mail: weisman@limsi.fr

acoustic excitation was provided by a moving wall. Their results show a distortion of the streaming field and the existence of multiple streaming cells for small values of Re_{NL} , even for values less than one. In their analysis, the authors correlate the existence of the nonlinear streaming regime with the values of the aspect ratio of the waveguide and with a different streaming Reynolds number [$Re_s = U_0^2/(\nu\omega)$, ω being the angular frequency]. When their results are analyzed as a function of Re_{NL} , the tendencies depicted are in contradiction with experiments.^{11,12} One of the goals of the present paper is to present direct numerical simulations of the Navier-Stokes equations in the cylindrical case using a recently developed high resolution numerical scheme¹³ tested successfully in several cases (including acoustics and streaming^{14,15}). In the present simulations, the acoustic wave is excited by shaking the entire resonator and there are no restrictions on the value of the Re_{NL} .

With respect to experimental studies, thanks to improving techniques in fluid dynamics, measurements of the streaming in a standing wave guide have been performed recently.^{11,16–19} Experimental works by Sharpe, Greated, and collaborators¹⁶ and by Thompson and Atchley¹⁹ first allowed quantitative study of streaming velocity in the core region on the basis of particle image velocimetry (PIV) or laser Doppler velocimetry (LDV) measurements. Moreau *et al.*¹¹ first performed LDV measurements of streaming in both the core and the near wall region to characterize inner streaming vortices. Their measurements were performed for Re_{NL} up to 140 but they mainly focused on inner streaming cells evolution. In their experimental study, Thompson and Atchley¹⁹ considered streaming for Re_{NL} up to 20 and found that the streaming fields is distorted for high nonlinear Reynolds number in correlation with the increasing temperature gradient along a streaming cell. Nabavi *et al.*¹² analyzed streaming in a square channel on the basis of PIV measurements; they found that for Re_{NL} up to 25, streaming cells are regular and correspond to “classical” streaming flow, whereas when Re_{NL} exceeds 25, streaming deforms to irregular and complex shaped patterns. Another goal of the present work is to present results of measurements of the streaming velocity field generated by an acoustic standing wave in a cylindrical resonator by means of LDV from low to high acoustic amplitudes (up to Re_{NL} greater than 25).

In the present study, numerical and experimental results are successfully compared with available theoretical expectations in the linear regime. For this purpose, a slow streaming analytical model that has been developed previously⁶ for the calculation of Rayleigh streaming in a cylindrical waveguide is used. Then the analysis of the nonlinear regime is conducted for the first time with a coupled numerical/experimental approach on a cylindrical geometry, and the results are confronted. Both simulations and experiments show that streaming at high Re_{NL} is associated with additional outer streaming cells appearing at a critical value of this number of about $Re_{NL} = 30$.

Section II presents the different methods for the calculation of streaming that are used or referred to in this paper (direct numerical method, work by Bailliet *et al.*,⁶ and work by Menguy and Gilbert⁸). The dimensionless numbers used

to describe the problem of Rayleigh streaming in a standing wave guide are presented as it is necessary to consider the respective values of these numbers in order to validate the comparison between numerical and experimental results. In Sec. III, experimental setup and procedure are presented. Section IV presents the numerical method used to calculate streaming velocity. Finally in Sec. V, these numerical and experimental results are compared with each other and with the available literature.

II. FUNDAMENTAL EQUATIONS AND NONDIMENSIONAL ANALYSIS

All the methods used to calculate the streaming flow in this paper are based on the fundamental equations that describe an acoustic wave propagation in the laminar regime along the z axis, in a cylindrical tube of radius R filled with air at atmospheric pressure. The ratio of the wavelength to the transverse dimension is supposed to be large so that the wave is plane. Air is considered as a Newtonian compressible fluid and there is no mean flow apart from acoustic streaming. Gravity is neglected. Neglecting the bulk viscosity in comparison with the shear viscosity, these fundamental equations (Navier-Stokes equations) that describe the fluid motion are written as

$$\begin{cases} \frac{\partial \rho}{\partial t} + \nabla \cdot (\rho \mathbf{u}) = 0 \\ \frac{\partial(\rho \mathbf{u})}{\partial t} + \nabla \cdot (\rho \mathbf{u} \otimes \mathbf{u}) + \nabla p = \nabla \cdot (\bar{\tau}) \\ \frac{\partial(\rho E)}{\partial t} + \nabla \cdot (\rho E \mathbf{u} + p \mathbf{u}) = \nabla \cdot (k \nabla T) + \nabla \cdot (\bar{\tau} \mathbf{u}), \end{cases} \quad (1)$$

where ρ is the density, p is the pressure, \mathbf{u} is the flow velocity vector, $E = e + (1/2)\mathbf{u} \cdot \mathbf{u}$ is the total energy, with $e = p/(\gamma - 1)\rho$ the internal energy, γ the specific heat ratio, $\bar{\tau} = -(2/3)\mu(\nabla \cdot \mathbf{u})\bar{I} + 2\mu\bar{D}$ the viscous stress tensor, with \bar{I} the identity tensor, $\bar{D} = (1/2)(\nabla \mathbf{u} + \nabla \mathbf{u}^T)$ the strain rate tensor, μ the dynamic viscosity, k the thermal conductivity. The gas is considered as a perfect gas obeying the state law $p = r_g \rho T$, where T is the temperature and r_g is the constant of the perfect gas (air in the present case).

A. Nondimensional analysis

In the previous equations, there are 6 unknown physical variables, ρ , \mathbf{u} (three components), p and T [the internal energy e can be replaced by $(c_p/\gamma)T$, c_p being the specific heat capacity at constant pressure] and six equations. The problem is written in a dimensionless form, using standard fluid mechanics scalings

$$\begin{aligned} \hat{\nabla} &= \frac{\nabla}{L_0}, & \hat{t} &= \frac{t}{t_0}, & \hat{\mathbf{u}} &= \frac{\mathbf{u}}{U_0}, & \hat{p} &= \frac{p}{p_0}, & \hat{\rho} &= \frac{\rho}{\rho_0}, \\ \hat{T} &= \frac{T}{T_0}, & \hat{\mu} &= \frac{\mu}{\mu_0}, & \hat{k} &= \frac{k}{k_0}, \end{aligned} \quad (2)$$

where L_0 , t_0 , U_0 are reference scales for length, time and velocity (based on the acoustic propagation), and p_0 , ρ_0 , T_0 , μ_0 ,

k_0 are scales for pressure, density, temperature, dynamic viscosity and conductivity (based on fluid properties at rest). In the context of acoustics, the adiabatic speed of sound is defined as $c_0 = \sqrt{(\partial p / \partial \rho)_{s,0}}$, also written as $c_0 = \sqrt{\gamma(p_0 / \rho_0)}$ using the first-order Taylor expansion of pressure. The characteristic acoustic time and length scales are given by $t_0 = 1/\omega$, $L_0 = c_0/\omega$, where ω is the fundamental acoustic angular frequency. U_0 is a reference

value of the acoustic velocity, for example the maximum amplitude of the fundamental component of the wave. With these reference scales, three independent dimensionless numbers are defined by rewriting the set of Eq. (1): the acoustic Mach number $M = U_0/c_0$, the acoustic Reynolds number $Re = \rho_0 c_0^2 / \mu_0 \omega$, and the Prandtl number $Pr = \mu_0 c_p / k_0$.

Equation (1) in dimensionless form is indeed

$$\left\{ \begin{array}{l} \frac{\partial \hat{\rho}}{\partial \hat{t}} + M \hat{\nabla} \cdot (\hat{\rho} \hat{\mathbf{u}}) = 0 \\ \frac{\partial(\hat{\rho} \hat{\mathbf{u}})}{\partial \hat{t}} + M \hat{\nabla} \cdot (\hat{\rho} \hat{\mathbf{u}} \otimes \hat{\mathbf{u}}) + \frac{1}{\gamma M} \hat{\nabla} \hat{p} = \frac{1}{Re} \hat{\nabla} \cdot (\hat{\bar{\tau}}) \\ \frac{1}{\gamma} \frac{\partial(\hat{\rho} \hat{T})}{\partial \hat{t}} + M^2(\gamma - 1) \frac{\partial \left(\hat{\rho} \frac{1}{2} |\hat{\mathbf{u}}|^2 \right)}{\partial \hat{t}} + \frac{M}{\gamma} \hat{\nabla} \cdot (\hat{\rho} \hat{T} \hat{\mathbf{u}}) + M^3(\gamma - 1) \hat{\nabla} \cdot \left(\hat{\rho} \hat{\mathbf{u}} \frac{1}{2} |\hat{\mathbf{u}}|^2 \right) + \frac{\gamma - 1}{\gamma} M \hat{\nabla} \cdot (\hat{\rho} \hat{\mathbf{u}}) \\ = \frac{1}{Re Pr} \hat{\nabla} \cdot (\hat{k} \hat{\nabla} \hat{T}) + \frac{1}{Re} M^2(\gamma - 1) \hat{\nabla} \cdot (\hat{\bar{\tau}} \hat{\mathbf{u}}). \end{array} \right. \quad (3)$$

The working fluid being air, the Prandtl number is fixed, of order 1. This leaves out two nondimensional numbers to monitor wave propagation in the tube (M and Re). In order to characterize the streaming flow associated with a standing wave, the ∇ operator should be separated into an axial and a radial part, that is, a separate reference length scale for the radial direction has to be introduced, inducing that a supplementary nondimensional number is needed. Menguy and Gilbert⁸ showed that this additional required number is the Shear number, defined as $Sh = \delta_\nu / R$, $\delta_\nu = \sqrt{2\nu/\omega}$ being the acoustic boundary layer thickness in the near wall region (with $\nu = \mu/\rho_0$ the kinematic viscosity).

Here, the acoustic wave amplitude ranges from linear ($M \ll 1$) to weakly nonlinear. The Reynolds number compares inertial effects and viscous effects over the wavelength and is large with respect to 1 for the present range of audible frequencies. Then, the third dimensionless number compares the boundary layer thickness to the tube radius. The hypothesis $Sh \ll 1$ corresponds to large tubes, which is the case in all the studies we deal with in this paper. Finally when working with air, the same flow behavior is expected for studies where $M \ll 1$, $Re \gg 1$ and $Sh \ll 1$. This asymptotic similarity will be considered as valid for the numerical and experimental flows under study in the following. In order to be able to compare our experimental and numerical results to a reference, in the following section, two available models for streaming flow are briefly presented: a linear model developed by Bailliet *et al.*⁶ (used for quantitative comparison with direct numerical simulations and experiments in the slow streaming regime) and a nonlinear model developed by Menguy and Gilbert⁸ (used for the description of the evolution of the streaming flow for moderate streaming regime). The latter shows that when dealing with streaming flow, an

additional dimensionless number has to be considered, as discussed in the following.

B. Slow streaming

In the literature, there are several analytical models for slow streaming.^{2,3,7} In this paper, the model developed by Bailliet *et al.*⁶ is used. This model is based on the fundamental equations presented above. Additional assumptions allow us to obtain an expression of the second order time averaged axial velocity as function of the first order acoustic quantities. The streaming is supposed to be slow so that the effect of inertia on the streaming motion is neglected by comparison with viscous effects. The solid is supposed to have an infinite heat capacity. Under these assumptions, the method of successive approximation is applied, the first order quantities having a $e^{-i\omega t}$ dependence. Through time averaging a combination of the continuity equation and of the axial component of the Navier-Stokes equations written to the second order, the following equation is obtained:

$$\frac{1}{R^2} \mu_0 \nabla_\eta^2 \langle u_2 \rangle = \partial_z p_2 + \partial_z (\rho_0 \langle u_{1z}^2 \rangle) + \frac{1}{R} \nabla_\eta (\rho_0 \langle u_{1z} u_{1\eta} \rangle) - \frac{1}{R^2} \nabla_\eta (\langle \mu_1 \nabla_\eta u_{1z} \rangle), \quad (4)$$

where $\langle - \rangle$ denotes the time average and $\eta = r/R$, with r the radial coordinate. An expression for the second order pressure gradient $\partial_z p_2$ is obtained by writing that, in a closed resonator, there is no net mass flow across the section, i.e., the second order time average mass flow rate across the cross section must be zero. Successive integration of the expression obtained yields the second order pressure gradient as a function of the first order acoustic quantities. In turn,

successive integration of Eq. (4) yields the axial streaming velocity [see formula (16) from Bailliet *et al.*⁶]. In the case of widely spaced parallel plates, this velocity is equal to the one obtained by the RNW theory, but the calculation is valid also for narrow guides (that is in the near wall region of any guide) and it takes into account the dependence of viscosity on temperature. This calculation is also valid in the presence of a temperature gradient (not set in the present study). This analytical study will be used as a reference for our experimental and numerical results. However, high acoustic amplitudes will be considered here and therefore the slow streaming assumption is expected to be restrictive, and the effect of streaming inertia should be analyzed.

C. Effect of inertia on streaming

The only available theoretical study that is not restricted to slow streaming is the one by Menguy and Gilbert.⁸ By writing the fundamental equations up to the third order in the main acoustic field followed by time averaging over the acoustic period, Menguy and Gilbert derived the governing equations for the streaming field in the boundary layer and in the main central part of the tube. Under the above presented assumptions ($M \ll 1$, $Re \gg 1$, $Sh \ll 1$), an asymptotic analysis can be performed, allowing to derive the fluid behavior at the first and second order. A time averaging over the acoustic period yields equations for streaming flow both inside and outside the acoustic viscous/thermal boundary layer. Under the previous hypotheses on M , Re , and Sh numbers, streaming equations inside the boundary layer are always linear. Outside the boundary layer, streaming equations can be linear or nonlinear depending on the ratio between inertia and viscous terms. Menguy and Gilbert⁸ showed that in the central part of the tube, the equation that governs the streaming velocity \hat{u}_s has a unique nonlinear term

$$\frac{Sh^2}{M^2} \frac{1}{\hat{r}} \frac{\partial}{\partial \hat{r}} \left(\hat{r} \frac{\partial \hat{u}_s}{\partial \hat{r}} \right).$$

This clearly shows that the outer streaming nonlinearity depends only upon one dimensionless number

$$Re_{NL} = \frac{M^2}{Sh^2}$$

called the nonlinear Reynolds number, which compares inertia and viscosity. For $Re_{NL} = O(1)$ the classical streaming models are no longer valid and the nonlinear effects of inertia must be taken into account. The latter cause distortion of the streaming velocity field in the tube and Menguy and Gilbert⁸ discuss the distortion of the toroidal vortex patterns. When $Re_{NL} \ll 1$, inertia terms are negligible with respect to viscous terms and the streaming equation reduces to the linear model of streaming (see Sec. II B).

Finally, four dimensionless numbers are to be considered when dealing with Rayleigh streaming. At fixed Pr , for asymptotic similarity when $M \ll 1$, $Sh \ll 1$ and $Re \gg 1$, the nonlinear Reynolds number is expected to be the driving

parameter for acoustic streaming. The behavior of the streaming flow will then be analyzed and discussed upon the values of the nonlinear Reynolds number.

III. EXPERIMENTAL APPARATUS AND PROCEDURE

The setup used to observe the phenomenon of acoustic streaming is shown in Fig. 1 and consists in a cylindrical tube connected at each end to a loudspeaker via connecting tubes designed to avoid separation effect related to the singularities in change of section. The cylindrical part of the waveguide has inner radius $R = 19.5$ mm and the waveguide is filled with atmospheric air. The total length of the waveguide is $L_{exp} = 2.13$ m and the system is tuned on two distinct frequencies corresponding to two different resonant modes: the first mode corresponding to $L_{exp} = \lambda/2$ and the third mode corresponding to $L_{exp} = 3\lambda/2$, λ being the wavelength of the fundamental mode.

In the following, results will be presented for acoustic streaming across one or two cells and whatever the working frequency, the position along the guide axis will be given by the axial coordinate z , with $z = \pm\lambda/4$ corresponding to two adjacent streaming cells.

The acoustic wave is generated by two loudspeakers driven by a wave generator whose frequency and amplitude are controlled. Wood smoke is used as seeding particles in order to perform LDV measurements. The single component LDV system is a Dantec Dynamic model 2580, the probe is mounted on a three-axis positioning system. The argon krypton laser has an optical wavelength of 514.5 μ m and a power of 25 W. The parameters of LDV system are adjusted for sound measurements²⁰ and the axial streaming velocity is measured following the work of Valière *et al.*²¹ along the centerline of the guide. The LDV measurements yield the Eulerian particle velocity. In agreement with Moreau *et al.*,¹¹ measurements were performed more than 26 min after the acoustic field is switched on and are stable after this time. Also, following this latter reference, in order to reach convergence in the measured streaming velocity, we choose to acquire either 70 000 points or to stop acquisition after 10s. This gives a good compromise between a sufficient number of measured tracer particles per point for a precise

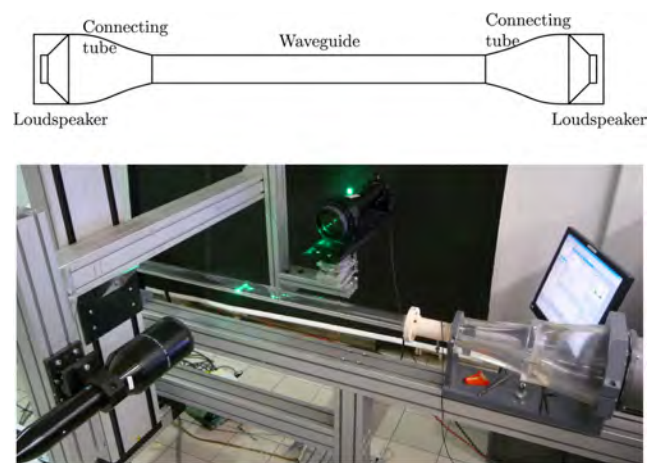


FIG. 1. (Color online) Photo and diagram of the experimental apparatus.

streaming velocity measurement and a small measuring time resulting from a correct seeding.

In order to get as close as possible to the isothermal boundary conditions used in the numerical calculation and because it was found in the literature that temperature gradients along the guide walls greatly influence Rayleigh streaming,¹⁹ the resonator wall is forced to correspond to an isothermal boundary condition with the help of fans used to insure that the wall temperature is equal to the room temperature. The temperature is measured along one streaming cell using seven thermocouples with a resolution of about 0.05°C. These thermocouples are placed at the outer wall of the resonator and are insulated from the external environment by a polystyrene covering. Using fans to force heat transfer from the guide to the environment yields a residual temperature difference of 0.3°C between the acoustic velocity node and antinode at $Re_{NL} = 31.8$. This temperature difference would be equal to 3.1°C if no fans were used.

IV. NUMERICAL APPROACH

A. Numerical method

In order to initiate an acoustic standing wave in the cylindrical tube of length L , it is shaken in the longitudinal direction z , so that an harmonic velocity law is imposed, $\vec{V}(t) = (0, V(t))^T$, with $V(t) = z_p \omega \cos(\omega t)$, z_p being the amplitude of the tube displacement. The flow can be modeled by the compressible Navier-Stokes Eq. (1), expressed in the moving frame attached to the tube, so that a forcing source term h^s is added to the system of Eq. (1). The model can be written in vector form

$$\frac{\partial w}{\partial t} + \frac{1}{r} \frac{\partial}{\partial r} [r(f - f^v)] + \frac{\partial}{\partial z} (g - g^v) = h + h^s, \quad (5)$$

where w is the vector of conservative variables $(\rho, \rho u, \rho v, \rho E)^T$, f and g are the inviscid fluxes $f = (\rho u, \rho u^2 + p, \rho uv, \rho Eu + pu)^T$ and $g = (\rho v, \rho uv, \rho v^2 + p, \rho Ev + pv)^T$, f^v , and g^v being the viscous fluxes $f^v = [0, \tau_{rr}, \tau_{rz}, k(\partial T / \partial r) + u\tau_{rr} + v\tau_{rz}]^T$, $g^v = [0, \tau_{rz}, \tau_{zz}, k(\partial T / \partial z) + u\tau_{rz} + v\tau_{zz}]^T$. The source terms read $h = [0, -(\tau_{\theta\theta}/r) + (p/r), 0, 0]^T$, $h^s = [0, 0, -\rho(dV/dt), -\rho u(dV/dt)]^T$.

The model is numerically solved by using high order finite difference schemes, developed by Daru and Tenaud.¹³ An upwind scheme, third order accurate in time and space, is used for convective terms, and a centered scheme, second order, is used for diffusion terms. Traveling shock waves are present in the flow for high acoustic levels, which generate numerical oscillations. However they are of weak intensity and produce very small oscillations that do not spoil the solution. Thus it was not necessary to add a costly shock capturing procedure.

The numerical procedure is briefly described thereafter. Denoting by $w_{i,j}^n$ the numerical solution at time $t = n\delta t$ and grid point $(r, z) = (i\delta r, j\delta z)$, with δt and δr , δz the time and space discretization steps respectively, the following Strang splitting procedure is used to obtain a second order accuracy every two time steps:

$$w_{i,j}^{n+2} = L_{\delta r} L_{\delta z} L_{\delta z} L_{\delta r} w_{ij}^n, \quad (6)$$

where $L_{\delta r}$ (resp. $L_{\delta z}$) is a discrete approximation of $L_r(w) = w + \delta t[-(1/r)(rf)_r + (1/r)(rf^v)_r + h + h^s]$ [resp. $L_z(w) = w + \delta t(-g_z + g_z^v)$]. The 1D operators being similar in both directions, only the r operator is described. The scheme is implemented as a correction to the second order MacCormack scheme. It consists of three steps, as follows:

$$\begin{aligned} w_{i,j}^* &= w_{i,j}^n - \frac{\delta t}{r_{i,j}\delta r} [r_{i+(1/2),j}(f_{i+1,j} - f_{i+(1/2),j}^v) - r_{i-(1/2),j}(f_{i,j} - f_{i-(1/2),j}^v)]^n + \delta t(h + h^s)_{i,j}^n \\ w_{i,j}^{**} &= w_{i,j}^* - \frac{\delta t}{r_{i,j}\delta r} [r_{i+(1/2),j}(f_{i,j} - f_{i+(1/2),j}^v) - r_{i-(1/2),j}(f_{i-1,j} - f_{i-(1/2),j}^v)]^* \\ w_{i,j}^{n+1} &= \frac{1}{2}(w_{i,j}^n + w_{i,j}^{**}) + \frac{1}{r_{i,j}}(r_{i+(1/2),j}C_{i+(1/2),j}^r - r_{i-(1/2),j}C_{i-(1/2),j}^r). \end{aligned} \quad (7)$$

In (7), the subscripts $(i \pm 1/2, j)$ denote a value at the interface between cells (i, j) and $(i \pm 1, j)$. The viscous fluxes are discretized at each interface using centered second order finite differences. The corrective terms $C_{i \pm (1/2),j}^r$ provide the third order accuracy and upwinding for the inviscid terms. Details on the model can be found in Daru *et al.*^{14,15,22}

The physical boundary conditions employed in the moving frame are: no slip on the wall, symmetry at the ends of the tube, and isothermal walls.

The acoustic streaming is generated by the interaction of the imposed plane standing wave and the tube wall. Resonant conditions are imposed, for which $L = \lambda/2$,

being the wavelength calculated for a dissipative gas. The boundary layer δ_ν is of small thickness and must be correctly resolved by the discretization mesh. After several trials, it was found that a value of five points per boundary layer thickness is sufficient for reasonable accuracy of the simulations. All results presented below are thus obtained using a Cartesian mesh of rectangular cells of constant size δr and δz , composed of 500 points in the axial direction z , and of $5 \times R/\delta_\nu$ points in the radial direction.

The flow being assumed to be axisymmetric (at least in the range of parameters treated), only the region $0 \leq r \leq R$ and $0 \leq z \leq L$ was considered. Also, the scheme being fully

explicit, the time step δt is fixed such as to satisfy the stability condition of the scheme. In all cases considered here, the time step limitation is acoustic, it reads $\delta t \leq \frac{1}{2} \delta r / c_0$. Taking $\delta t = \frac{1}{2} \delta r / c_0$ and $\delta r = \delta_\nu / 5$, this results in a number of time steps N_T per period of oscillation proportional to \sqrt{L} , $N_T = 1/(f\delta t) = 10\sqrt{(2\pi c_0)/\nu}\sqrt{L}$.

Because the LDV measurements yield the Eulerian particle velocity, the numerical results are based on the Eulerian time-average of fluid velocity. The numerical streaming velocity is obtained by calculating a simple mean value of the particle velocity over the discretized acoustic period, thus a time average made with respect to the fixed measuring position, for each mesh point.

B. Simulation parameters

A cylindrical tube is considered, initially filled with air at standard thermodynamic conditions, $p_0 = 101\,325$ Pa, $\rho_0 = 1.2$ kgm $^{-3}$, $T_0 = 294.15$ K. The thermo-physical properties of air are $\mu_0 = 1.795 \times 10^{-5}$ kgm $^{-1}$ s $^{-1}$ and $k_0 = 0.025$ Wm $^{-1}$ K $^{-1}$. Viscosity is expressed as a power law of temperature, $\mu(T) = \mu_0(T/T_0)^{0.77}$. Also for air, $\gamma = 1.4$ and $r_g = 287.06$ Jkg $^{-1}$ K $^{-1}$. The Prandtl number Pr is equal to 0.726. This results in an initial speed of sound $c_0 = 343.82$ ms $^{-1}$.

In the experimental case presented in Sec. III, the half-wavelength is about 0.7 m long, which would yield a limiting time step corresponding to $N_T \approx 25\,000\sqrt{L}$, that is 21 000 iterations per period. Since transients of several hundreds of periods may be needed in order to reach stabilized streaming flow, several millions of iterations are necessary for each simulation. Considering these numerical constraints, a high-frequency wave is chosen for numerical calculations, with $f = 20\,000$ Hz. Taking into account the viscous dissipation, this corresponds to a shorter wave guide with $L = 8.396$ mm. The resulting boundary layer thickness is $\delta_\nu = 1.54 \times 10^{-5}$ m. For computational ease, the Shear number was fixed in the numerical simulations to be 1/40.

The time step $\delta t = 8 \times 10^{-9}$ s is chosen in order to satisfy the numerical stability condition, corresponding to 6250

time iterations per period. The acoustic velocity produced in the wave guide depends on the imposed amplitude of the horizontal displacement z_p . It varies approximately linearly with z_p , for a given ratio R/δ_ν . Therefore it is possible via the only choice of z_p to approximately set the value of the desired nonlinear Reynolds number Re_{NL} , so that to approximately fit the ones obtained in experimental configurations.

V. RESULTS AND DISCUSSION

As seen in Secs. III and IV, several differences exist between experimental and simulated configurations. As discussed in Sec. II these differences should not be associated with different behaviors of acoustic streaming if the nonlinear Reynolds number Re_{NL} is the same, and if the other relevant dimensionless numbers Sh, Re, and M are of the same order of magnitude. The acoustic amplitude of the fundamental mode at the velocity antinode $z = 0$ is chosen as the velocity reference U_0 .

Table I summarizes then the values of these dimensionless parameters for both the experimental and numerical configurations together with the ones for several studies of the literature^{8,10,12,19} that are used for comparison with the present study.

As shown by Table I and as stated in the previous Sec. IV, all numerical calculations were performed for a given frequency in air at atmospheric pressure, corresponding to one acoustic Reynolds number Re . Because the experimental setup could be tuned at two different resonant modes, two different Re numbers could be achieved. Whatever the frequency condition is in numerical and experimental configurations, the acoustic Reynolds number is always much larger than one. Therefore, we can expect similarity to hold between the different configurations studied here in terms of Re .

When working on the $\lambda/2$ experimental mode, the Sh number is $1.2 \cdot 10^{-2}$ (the corresponding experimental configurations are labeled E_1 and E_2), whereas when working on the $3\lambda/2$ experimental mode, the Sh number is $7.2 \cdot 10^{-3}$

TABLE I. Nondimensional numbers used for the present study together with those of several studies in the literature.

Reference	Name	Re_{NL}	M	Sh	Re
Experiments (present study)	E_1	0.47	$8.2 \cdot 10^{-3}$	$1.2 \cdot 10^{-2}$	$1.4 \cdot 10^7$
	E_2	4.8	$2.6 \cdot 10^{-2}$		
	E_3	7.7	$2 \cdot 10^{-2}$	$7.2 \cdot 10^{-3}$	$5.2 \cdot 10^6$
	E_4	14.6	$2.7 \cdot 10^{-2}$		
	E_5	31.8	$4 \cdot 10^{-2}$		
Numerical (present study)	N_1	0.25	$1.2 \cdot 10^{-2}$	$2.5 \cdot 10^{-2}$	$6.3 \cdot 10^4$
	N_2	4.91	$5.5 \cdot 10^{-2}$		
	N_3	7.93	$7.0 \cdot 10^{-2}$		
	N_4	15.2	$9.7 \cdot 10^{-2}$		
	N_5	38.6	$15 \cdot 10^{-2}$		
Menguy and Gilbert ⁸	[0.5 – 2]		$\ll 1$	$\ll 1$	$\gg 1$
Thompson <i>et al.</i> ¹⁹	[2.1 – 22]		$[8 - 25] \cdot 10^{-3}$	$5.3 \cdot 10^{-3}$	$4.1 \cdot 10^6$
Nabavi <i>et al.</i> ¹²	[6.6 – 78]		$[7.7 - 34] \cdot 10^{-3}$	$[3 - 4] \cdot 10^{-3}$	$[1 - 1.9] \cdot 10^6$
Aktas and Farouk ¹⁰	[0.035 – 16.4]		$[3.7 - 79] \cdot 10^{-3}$	$[2 - 10] \cdot 10^{-2}$	$6.6 \cdot 10^4$

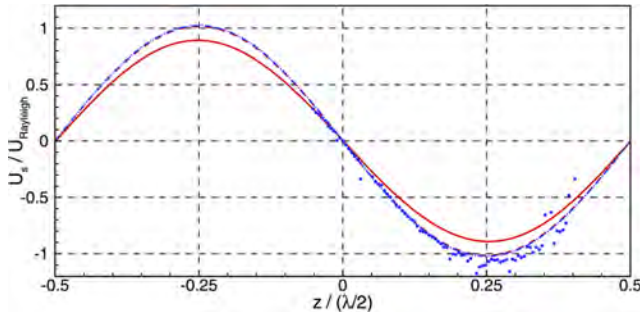


FIG. 2. (Color online) Variation of the axial streaming velocity component along the central axis of the guide normalized by $U_{\text{Rayleigh}} = (-3/8)(U_0^2/c_0)$. (—) N_1 numerical simulation at $\text{Re}_{NL} = 0.25$; (---) analytical results using the conditions of the simulation; (•) E_1 , experimental measurements $\text{Re}_{NL} = 0.47$; (···) analytical results using the conditions of the experiment.

(labeled E_3 to E_5). In the numerical simulations the Sh number is $2.5 \cdot 10^{-2}$. As will be shown in the following section, such differences in Sh numbers do not yield any significant difference in the acoustic streaming regime.

Finally, by changing the acoustic amplitude, the M and Re_{NL} numbers are modified. Since the Re_{NL} number is the relevant parameter to study nonlinear acoustic streaming, numerical and experimental configurations were chosen such that the Re_{NL} numbers are as close as possible for comparisons. The corresponding acoustic Mach number ranges from $8.2 \cdot 10^{-3}$ to $4 \cdot 10^{-2}$ for experiments and from $1.2 \cdot 10^{-2}$ to $1.5 \cdot 10^{-1}$ for numerical simulations, and therefore attention should be paid to the possible effects of such different dynamic ranges.

In the following Secs. V A–V C, results for experiments and numerical simulations are presented for different ranges of Re_{NL} , then in Sec. V D the effect of other dimensionless numbers are considered and discussed.

A. Streaming velocity at low nonlinear Reynolds number

The results presented in this section refer to situations where the nonlinear Reynolds number Re_{NL} is smaller than one. The experimental case selected for this comparison at low nonlinear Reynolds number corresponds to $\text{Re}_{NL} = 0.47$ (E_1), and the numerical simulation case corresponds to $\text{Re}_{NL} = 0.25$ (N_1).

Figure 2 displays results from measurements and from numerical simulations for the axial streaming velocity component u_s along the scaled central axis $z / (\lambda/2)$ together with two different results from the analytical analysis presented in

Sec. II corresponding to the numerical and experimental cases respectively. In all figures, the velocities are normalized by $U_{\text{Rayleigh}} = (3/8)(U_0^2/c_0)$ that corresponds to the amplitude of the streaming velocity in Rayleigh's theory. The nonlinear effects being negligible for these values of Re_{NL} , the axial streaming velocity should follow Rayleigh's law for linear streaming, which is $u_{\text{Rayleigh}} = (-3/8)(U_0^2/c_0) \sin(4\pi z/\lambda)$ in the present coordinate system. Figure 2 shows that it is indeed the case for all results presented in the figure, except for a slight difference between numerical and both analytical and experimental results. The source of this difference is unclear. The acoustic wave is created in a different manner in the three studies (analytical, numerical, and experimental). This can create discrepancies between the results. Moreover, it is important to recall that the numerical simulations are long and the streaming flow is of the second order. These are difficult conditions, especially for small values of the nonlinear Reynolds number. Therefore this difference in streaming velocity between numerical and analytical results is very satisfying.

The streamlines of the streaming flow are plotted in Fig. 3. Two outer streaming cells and two inner cells can be observed, corresponding to the classical Rayleigh streaming pattern. The streaming vortices are present either sides of the central axis and spaced at interval of $\lambda/4$. For outer streaming, the flow along the central axis is directed toward the acoustic velocity antinodes and returns in the vicinity of the wall to complete a closed loop. In the near wall region, the inner streaming vortices have directions of rotation opposite to those of the outer cells. In the cylindrical resonator, those vortices form toroidal flows around the central axis.

Figure 4 shows the variation of the axial streaming velocity component along the radial axis on a cross-section positioned at $z = -\lambda/8$, for the same cases as in Fig. 2. There is good agreement between all results in the core flow, away from the walls. Small discrepancies between numerical and experimental results can be observed near the walls, when $0.8R < r < R$ that can be attributed to the difference between the Shear numbers in the experimental and numerical configurations. To cope with this effect of different Shear numbers, the evolution of the streaming radial dependency $u_s(r)$ will no further be discussed, but only the evolution of the axial dependency $u_s(z)$ along the axis with Re_{NL} .

Also, given the similarity between the two analytical curves along the center line, it is chosen in the following to plot only the analytical result corresponding to the experimental configuration.

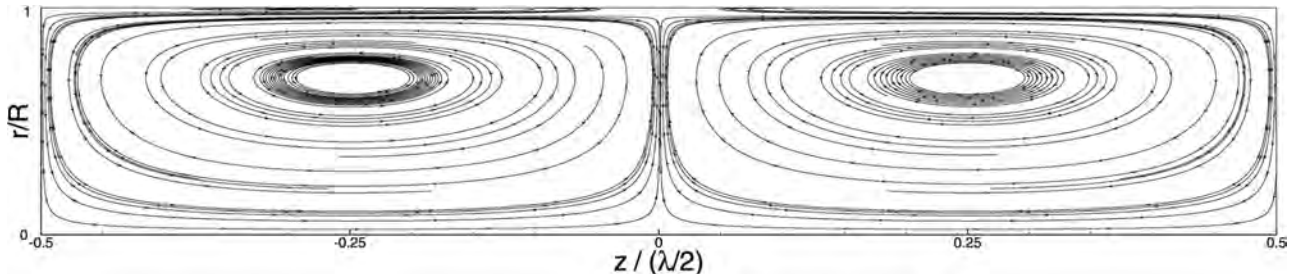


FIG. 3. Streamlines of the streaming flow, from numerical simulation at $\text{Re}_{NL} = 0.25$.

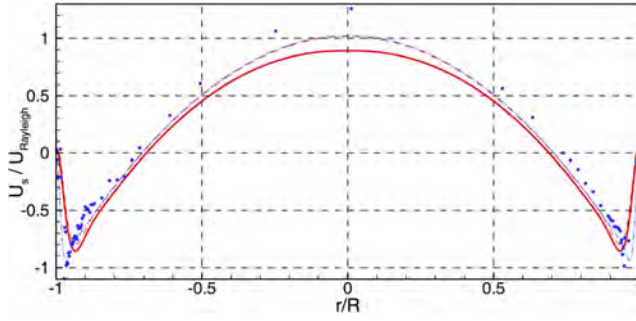


FIG. 4. (Color online) Variation of the normalized axial streaming velocity component along the radial axis, at $z = -\lambda/8$. (—) N_1 , numerical simulation at $Re_{NL} = 0.11$; (---) analytical results using the conditions of the simulation; (•) E_1 , experimental measurements at $Re_{NL} = 0.47$; (···) analytical results using the conditions of the experiment.

B. Streaming velocity at moderate nonlinear Reynolds number

Figures 5–7 display results of measurements and calculations for the centerline streaming velocity along the axis for increasing values of Re_{NL} , up to $Re_{NL} \approx 15$. They show that as Re_{NL} increases, the streaming velocity departs from the linear theoretical expectation, especially at streaming antinodes [i.e., $z/(\lambda/2) = \pm 0.25$ in the considered figures] where it gets significantly lower than Rayleigh expectation. As shown in Fig. 6, the streaming structure keeps its symmetry with respect to the $z = 0$ position, both in numerical simulations and in experimental measurements. It was checked that this symmetry is kept even for higher amplitude, and therefore, in the rest of the figures, measurements are presented along one cell only [from about $z = 0$ to $z/(\lambda/2) = 0.5$].

The figures clearly show a continuous decrease of the maximum value of the streaming velocity as Re_{NL} increases both in the experimental results and the numerical simulations even so the decrease is not as pronounced in the numerical simulations as in experiments (see Fig. 7). Potential sources of this discrepancy will be discussed in Sec. V D.

C. Streaming velocity at high nonlinear Reynolds number

As the Reynolds number is further increased, as shown in Fig. 8, the difference between measured and calculated

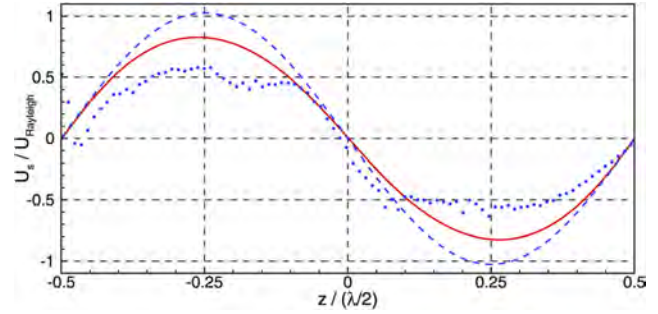


FIG. 6. (Color online) Variation of the normalized axial streaming velocity component along the central axis of the guide. (---) Analytical results using the conditions of the experiment; (•) E_3 , experimental measurements at $Re_{NL} = 7.7$; (—) N_3 , numerical simulation at $Re_{NL} = 7.93$.

streaming on one hand, and linear theory on the other hand is even more pronounced.

In Fig. 8, experimental results are very different from the linear theory along the axis except near the streaming velocity nodes [$z = 0$ and $z/(\lambda/2) = 0.5$ positions]. In the $z = 0$ region, the curve for the measured streaming velocity along the central axis has successive changes of slope. The maximum measured streaming velocity keeps on decreasing when Re_{NL} is increased until it crosses the zero-velocity axis for $Re_{NL} > 30$, corresponding to the apparition of a new streaming cell.

The numerical simulation shows an overall similar behavior, although the new cells appearing around the central axis are smaller in the z extent. Near the ends of the guide small additional cells appear in the numerical simulations. The streamlines obtained numerically are shown on Fig. 9 enabling the visualization of the new streaming cells. Even if the experimental and numerical results do not superimpose perfectly, it is remarkable that the same qualitative and overall quantitative behaviors are observed for close values of the Re_{NL} number. Figure 10 shows the numerical results for the modification of the streaming field as Re_{NL} increases, clearly exhibiting the emergence of new streaming cells for Re_{NL} greater than 30.

D. Discussion

As seen in the previous sections, numerical, experimental and analytical results all agree for small values of Re_{NL} .

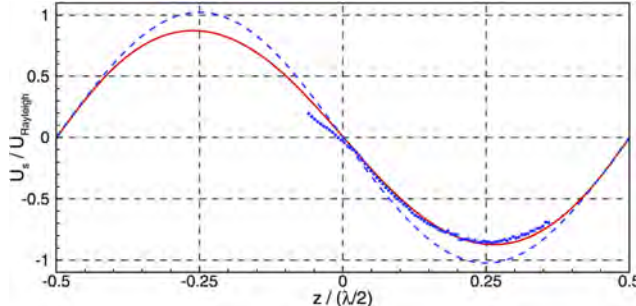


FIG. 5. (Color online) Variation of the normalized axial streaming velocity component along the central axis of the guide. (---) Analytical results using the conditions of the experiment; (•) E_2 , experimental measurements at $Re_{NL} = 4.8$; (—) N_2 , numerical simulation $Re_{NL} = 4.91$.

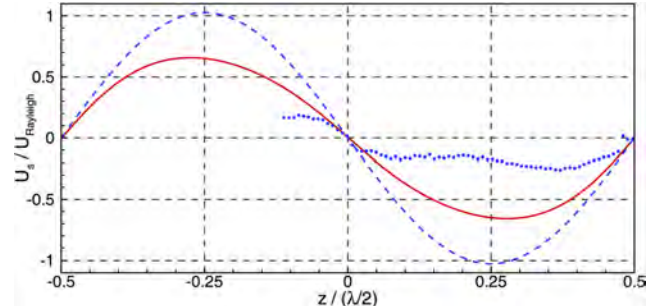


FIG. 7. (Color online) Variation of the normalized axial streaming velocity component along the central axis of the guide. (---) Analytical results using the conditions of the experiment; (•) E_4 , experimental measurements at $Re_{NL} = 14.6$; (—) N_4 , numerical simulation at $Re_{NL} = 15.2$.

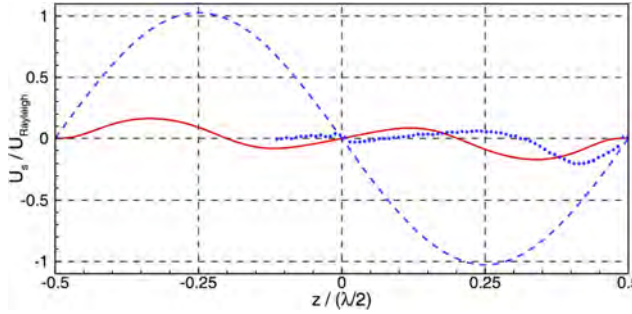


FIG. 8. (Color online) Variation of the normalized axial streaming velocity component along the central axis of the guide. (—) Analytical results using the conditions of the experiment; (•) E_5 , experimental measurements at $Re_{NL} = 31.8$; (—) N_5 , numerical simulation at $Re_{NL} = 38.6$.

As Re_{NL} increases, the tendencies are similar for numerical simulations and experiments: the levels of dimensionless streaming decrease and new streaming cells appear at a critical value $Re_{NL} \approx 30$. In order to identify a physical source for this evolution of streaming with Re_{NL} , several hypotheses are discussed in the following sections on the basis of the present literature review.

1. Thermal effects

Following Thompson *et al.*,¹⁹ the influence of thermal effects can be questioned. They performed measurements in a standing wave guide for nonlinear Reynolds numbers up to 22, the three other dimensionless numbers (M , Re , and Sh) respecting the above mentioned asymptotic conditions of our study, see Table I. They explored the evolution of the streaming for three different thermal conditions: isothermal, uncontrolled and insulated and for different nonlinear Reynolds numbers. They observed that when the magnitude of the temperature gradient was increased by changing the thermal condition for a given high nonlinear Reynolds number, the magnitude of the streaming decreased and the shape of the streaming cell became increasingly distorted. They found that the thermoacoustically induced axial temperature gradient strongly influences the axial component of the acoustic streaming velocity and concluded that the deviation from the theories of Rott (characterizing slow streaming with an axial temperature gradient) is due to the influence of thermal effect more than fluid inertia.

In our numerical simulations, isothermal boundary conditions are imposed and thermal effects are accounted for. Nevertheless, the axial streaming velocity profile is deformed

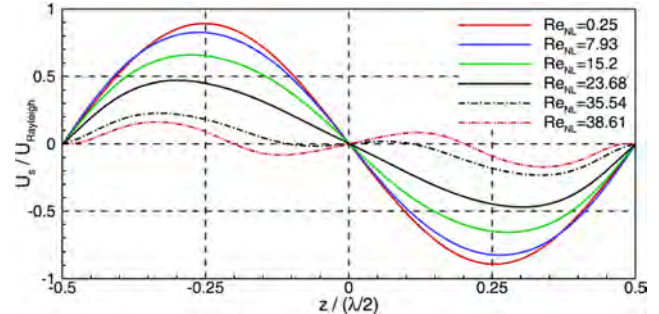


FIG. 10. (Color online) Numerical simulations: variation of the normalized axial streaming velocity component along the central axis of the guide for several values of Re_{NL} .

with increasing Re_{NL} . The same tendency is observed in the experimental results presented in Figs. 5–8, even if the thermal condition maintained for our set up is only *quasi*-isothermal (as a 0.3°C temperature difference between acoustic velocity node and acoustic velocity antinode is measured). For $Re_{NL} = 31.8$ the streaming flow already presents additional vortices compared to Rayleigh expectation, as shown by the change of sign of the axial streaming velocity in Fig. 8.

Therefore, if we agree that thermal effects are very important in understanding acoustic streaming (the difference between experimental and numerical thermal conditions could be at the origin of the difference in results) it appears from our study that the presence of a temperature gradient is not the cause of the divergence from slow streaming expectation at high Re_{NL} observed both numerically and experimentally.

2. Irregular streaming

Another possible cause of streaming distortion at high amplitudes exposed in the numerical and experimental literature is the change of regime from “regular” (or classical) to “irregular” streaming. In the literature the term “regular” is used when streaming flow exhibits the well-known patterns (toroidal outer and inner cells), while the term “irregular” is used to characterize any streaming flow that deviates from these patterns.

Aktas and Farouk¹⁰ studied acoustic streaming in a 2D rectangular channel numerically. They found that there is a limit in the value of the enclosure height to wavelength ratio above which the streaming flow structures are always irregular and complex. Since their working frequency is constant, it is equivalent to consider a limit value of the inverse of the Shear number. Based on their numerical results, they

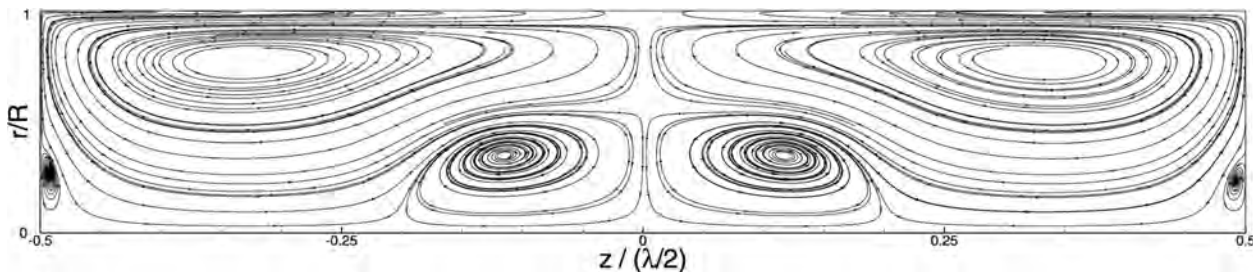


FIG. 9. Streamlines of the streaming flow, from numerical simulation at $Re_{NL} = 38.6$.

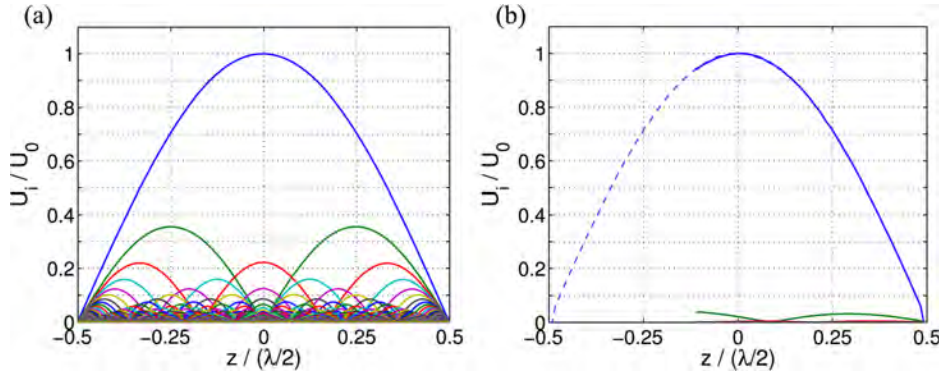


FIG. 11. (Color online) Distribution of the harmonics along the guide. (a) Numerical simulation N_5 ; (b) experimental study E_5 .

estimate this limit value of $1/\text{Sh}$ between 30 and 40. In the present paper, results for values greater or equal to 40 are shown, and we do observe regular streaming for low values of Re_{NL} (cases E_1 and N_1). The results presented by Aktas and Farouk¹⁰ do not exhibit any clear correlation between the regularity of the streaming and the value of Re_{NL} . For example, for two nonlinear Reynolds numbers corresponding to slow streaming cases $\text{Re}_{NL} = 0.10$ (called $C-3$ in their paper) and $\text{Re}_{NL} = 0.08$ ($D-2$), they observe two different streaming structures, respectively classical and irregular. The case with irregular streaming structure has a value of $1/\text{Sh}$ of 40. This last case is almost similar to our simulation N_1 where $\text{Re}_{NL} = 0.25$, shown in Fig. 3. In this figure, the streaming velocity field is clearly regular. Although our results are obtained for axisymmetrical configurations, whereas those of Aktas and Farouk¹⁰ concern a rectangular enclosure, previous work¹⁴ showed similar behavior in planar geometry compared to the present observations in the axisymmetrical case. This is indeed coherent with the asymptotic approach.

In the experimental literature, Nabavi *et al.*¹² mentioned irregular Rayleigh streaming for nonlinear Reynolds number above 20. Their experiments were performed in the case of isothermal boundary conditions. They found that for nonlinear Reynolds number above 25, the classical streaming deforms to an irregular and complex flow structure. The deformation they observe is similar to what we observe for some of their irregular cases, however the pattern of the irregular streaming is not always consistent among the experiments and with the value of Re_{NL} . In the above presented results, the streaming flow remains stable, consistent and show a continuous evolution from low to high amplitudes. Measurements have been repeated several times, they were always performed for steady flow and the results obtained are very reproducible.

Finally, we choose not to use the terms “regular” or “irregular” to describe the streaming flow regimes observed both numerically and experimentally. Instead, we would rather describe them as “regular” streaming flow regimes with either two ($\text{Re}_{NL} < 30$) or three ($\text{Re}_{NL} > 30$) toroidal structures, with a smooth transition as Re_{NL} increases.

3. Nonlinear propagation

Our analysis has been done under the assumption of low Mach number. But as the nonlinear Reynolds number

increases, so does the Mach number, creating situations where nonlinear acoustic propagation should be of importance, thus the generation of higher harmonics has to be considered. This brings up the question of higher harmonics influence on the streaming in competition with inertial effects associated with high values of nonlinear Reynolds number.

Figure 11 shows the harmonic distribution of the acoustic field, obtained by projecting the total velocity signals on a sine basis, in both numerical [Fig. 11(a)] and experimental [Fig. 11(b)] results for $\text{Re}_{NL} \approx 30$. It shows that the nonlinear propagation induces the existence of shockwaves in the simulations whereas the magnitude of higher harmonics never reaches more than 4% of the magnitude of the fundamental in the experiments, due to the difference in geometrical configurations between experimental and numerical studies. Now for a first approach a superposition principle is applied in order to identify the acoustic streaming due to multiple frequency components. But this crude assumption cannot cope with nonlinear effects. So, as stated in Sec. II C, because the boundary layer can be considered as a region where the streaming is linear, we choose to superimpose the streaming fields resulting from higher harmonics in the vicinity of this region. We choose the particular radial position corresponding to the limit between inner and outer streaming cell, which is at $(R - r) \approx 3\delta_\nu$, at which the streaming is expected to be close to linear streaming. Figure 12 shows the streaming velocity obtained from the numerical simulation at $\text{Re}_{NL} = 38.6$ (N_5), the analytical calculation resulting from the fundamental component of the numerical signal,

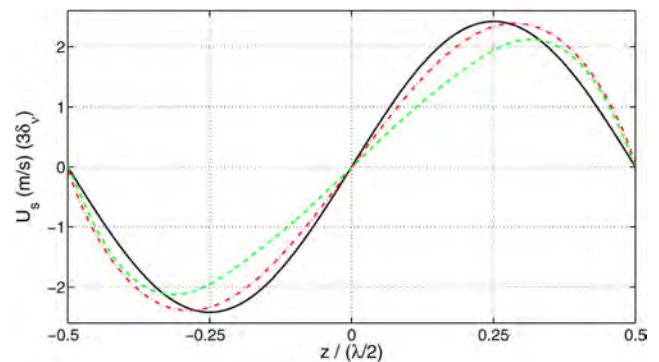


FIG. 12. (Color online) Streaming velocity profile along the axis of the guide at $(R - r) \approx 3\delta_\nu$, for $\text{Re}_{NL} = 38.6$. (—) Analytical solution; (---) Streaming velocity from analytical superposition of frequency components of the numerically calculated acoustic velocity; (- - -) Numerical simulation.

and the analytical calculation resulting from the linear superposition of all the harmonic components of the numerical signal. First, the distortion of the streaming close to the boundary layer (Fig. 12) is found to be much weaker than in the core of the resonator (Figs. 8 and 10). The effect of the harmonics superposition at $(R - r) \approx 3\delta_v$ results in a shift of the streaming velocity maxima toward the acoustic velocity nodes associated with a small change in the velocity magnitude. The same type of distortion can be observed on the numerical profile (Fig. 12), but with a stronger change in the velocity magnitude (the maximum value and the slope of the curve at $z = 0$ are much smaller). Moreover, as the distortion in acoustic streaming is qualitatively the same in both experimental and numerical study along the centerline of the guide, we conclude that while the harmonic content of experimental and numerical signals are very different, the influence of higher harmonics is not the main cause of the divergence of the streaming field from Rayleigh's expectation.

Finally we are left with only one hypothesis to explain this divergence: the inertial effects cannot be neglected anymore when the streaming is fast.

VI. CONCLUSION

In this paper a coupled experimental and numerical study of Rayleigh streaming from low to high acoustic amplitudes was conducted. As expected, slow streaming (both numerically and experimentally obtained) agrees with analytical slow streaming expectations for small Re_{NL} . The divergence from these analytical results that occurs when the Re_{NL} is increased is very similar for numerical and experimental results. As Re_{NL} increases, the cell centers are pushed towards the acoustic velocity nodes and the maximum axial streaming velocity decreases with respect to the analytical Rayleigh reference amplitude. It was also shown that for Re_{NL} larger than about 30, additional outer cells are formed through a smooth transition between coherent streaming flow patterns. This is why the streaming flow regimes can be called "regular" throughout the transition between two ($Re_{NL} < 30$) and three ($Re_{NL} > 30$) toroidal structures. After having considered all potential sources for the observed divergence from slow streaming flow, we have concluded that inertial effects on acoustic streaming are the main source. Logically the Re_{NL} is the driving parameter for the acoustic streaming in the regime considered here.

ACKNOWLEDGMENTS

All the experiments were conducted at the Pprime Institute. The authors wish to acknowledge the technical support of Pascal Biais, Laurent Philippon, and Philippe Szeger. The authors wish to thank the GDR 3058 Thermoacoustique

(thermoacoustics research group) to have given them the impetus for this collaboration.

- ¹L. Rayleigh, "On the circulation of air observed in Kundt's tubes, and on some allied acoustical problems," *Philos. Trans. R. Soc. London* **175**, 1–21 (1884).
- ²W. L. Nyborg, *Acoustic Streaming* (Academic, New York, 1965), Vol. 2B(11).
- ³P. J. Westervelt, "The theory of steady rotational flow generated by a sound field," *J. Acoust. Soc. Am.* **25**, 60–67 (1953).
- ⁴J. Olson and G. Swift, "Acoustic streaming in pulse tube refrigerators: tapered pulse tubes," *Cryogenics* **37**, 769–776 (1997).
- ⁵M. F. Hamilton, Y. A. Ilinskii, and E. A. Zabolotskaya, "Thermal effects on acoustic streaming in standing waves," *J. Acoust. Soc. Am.* **114**, 3092–3101 (2003).
- ⁶H. Bailliet, V. Gusev, R. Raspet, and R. A. Hiller, "Acoustic streaming in closed thermoacoustic devices," *J. Acoust. Soc. Am.* **110**, 1808–1821 (2001).
- ⁷M. F. Hamilton, Y. A. Ilinskii, and E. A. Zabolotskaya, "Acoustic streaming generated by standing waves in two-dimensional channels of arbitrary width," *J. Acoust. Soc. Am.* **113**, 153–160 (2003).
- ⁸L. Menguy and J. Gilbert, "Nonlinear effect of the inertia of the fluid on acoustic streaming in cylindrical guides," *J. Acoust. Soc. Am.* **105**, 958 (1999).
- ⁹D. Marx and P. Blanc-Benon, "Computation of the mean velocity field above a stack plate in a thermoacoustic refrigerator," *C. R. Méc.* **332**, 867–874 (2004).
- ¹⁰M. K. Aktas and B. Farouk, "Numerical simulation of acoustic streaming generated by finite-amplitude resonant oscillations in an enclosure," *J. Acoust. Soc. Am.* **116**, 2822–2831 (2004).
- ¹¹S. Moreau, H. Bailliet, and J.-C. Valière, "Measurements of inner and outer streaming vortices in a standing waveguide using laser Doppler velocimetry," *J. Acoust. Soc. Am.* **123**, 640–647 (2008).
- ¹²M. Nabavi, K. Siddiqui, and J. Dargahi, "Analysis of regular and irregular acoustic streaming patterns in a rectangular enclosure," *Wave Motion* **46**, 312–322 (2009).
- ¹³V. Daru and C. Tenaud, "High order one-step monotonicity-preserving schemes for unsteady compressible flow calculations," *J. Comput. Phys.* **193**, 563–594 (2004).
- ¹⁴V. Daru, D. Baltean-Carlès, C. Weisman, P. Debesse, and G. Gandikota, "Two-dimensional numerical simulations of nonlinear acoustic streaming in standing waves," *Wave Motion* **50**, 955–963 (2013).
- ¹⁵V. Daru and X. Glaefelt, "Aeroacoustic computations using a high order shock-capturing scheme," *AIAA J.* **45**, 2474–2486 (2007).
- ¹⁶J. Sharpe, C. Created, C. Gray, and D. M. Campbell, "The measurements of acoustic streaming using particle image velocimetry," *Acustica* **68**, 168–172 (1989).
- ¹⁷M. Campbell, J. Cosgrove, C. Created, S. Jack, and D. Rockliff, "Review of LDA and PIV applied to the measurement of sound and acoustic streaming," *Opt. Laser Technol.* **32**, 629–639 (2000).
- ¹⁸M. Thompson and A. Atchley, "Simultaneous measurement of acoustic and streaming velocities in a standing wave using laser Doppler anemometry," *J. Acoust. Soc. Am.* **117**, 1828–1838 (2005).
- ¹⁹M. Thompson, A. Atchley, and M. Maccarone, "Influences of a temperature gradient and fluid inertia on acoustic streaming in a standing wave," *J. Acoust. Soc. Am.* **117**, 1839–1849 (2005).
- ²⁰S. Moreau, H. Bailliet, J.-C. Valière, R. Boucheron, and G. Poignard, "Development of laser techniques for acoustic boundary layer measurements. Part II: Comparison of LDV and PIV measurements to analytical calculation," *Acta Acust. Acust.* **95**, 805–813 (2009).
- ²¹J.-C. Valière, S. Moreau, and H. Bailliet, "Development of laser techniques for acoustic boundary layer measurements. Part I: LDV signal processing for high acoustic displacements," *Acta Acust. Acust.* **95**, 585–594 (2009).
- ²²V. Daru and C. Tenaud, "Evaluation of TVD high resolution schemes for unsteady viscous shocked flows," *Comput. Fluids* **30**, 89–113 (2001).

V. Daru, I. Reyt, H. Bailliet, C. Weisman, D. Baltean-Carlès

" Acoustic and streaming velocity components in a resonant waveguide at high acoustic
levels "

Journal of the Acoustical Society of America, 141 (1), pp. 563-574, (2017).

Acoustic and streaming velocity components in a resonant waveguide at high acoustic levels

Virginie Daru and Ida ReyHélène BaillietCatherine Weisman and Diana Baltean-Carlès

Citation: *J. Acoust. Soc. Am.* **141**, 563 (2017); doi: 10.1121/1.4974058

View online: <http://dx.doi.org/10.1121/1.4974058>

View Table of Contents: <http://asa.scitation.org/toc/jas/141/1>

Published by the *Acoustical Society of America*

Articles you may be interested in

Porosity predicted from ultrasound backscatter using multivariate analysis can improve accuracy of cortical bone thickness assessment

J. Acoust. Soc. Am. **141**, (2017); 10.1121/1.4973572

Acoustic and streaming velocity components in a resonant waveguide at high acoustic levels

Virginie Daru^{a)} and Ida Rey

Arts et Métiers ParisTech - Lab. DynFluid - 151 bd de l'Hôpital 75013 Paris, LIMSI, CNRS, F-91405 Orsay, France

Hélène Bailliet

Institut Pprime, CNRS - Université de Poitiers - ENSMA, ENSIP, 6 rue Marcel Doré, Bâtiment B17 - BP 633, 86022 Poitiers Cedex, France

Catherine Weisman and Diana Baltean-Carlès

Sorbonne Universités, UPMC Univ Paris 06, UFR d'Ingénierie, 4 Place Jussieu, 75252 Paris Cedex 05, LIMSI, CNRS, F-91405 Orsay, France

(Received 24 August 2016; revised 14 December 2016; accepted 2 January 2017; published online 26 January 2017)

Rayleigh streaming is a steady flow generated by the interaction between an acoustic wave and a solid wall, generally assumed to be second order in a Mach number expansion. Acoustic streaming is well known in the case of a stationary plane wave at low amplitude: it has a half-wavelength spatial periodicity and the maximum axial streaming velocity is a quadratic function of the acoustic velocity amplitude at antinode. For higher acoustic levels, additional streaming cells have been observed. Results of laser Doppler velocimetry measurements are here compared to direct numerical simulations. The evolution of axial and radial velocity components for both acoustic and streaming velocities is studied from low to high acoustic amplitudes. Two streaming flow regimes are pointed out, the axial streaming dependency on acoustics going from quadratic to linear. The evolution of streaming flow is different for outer cells and for inner cells. Also, the hypothesis of radial streaming velocity being of second order in a Mach number expansion, is not valid at high amplitudes. The change of regime occurs when the radial streaming velocity amplitude becomes larger than the radial acoustic velocity amplitude, high levels being therefore characterized by nonlinear interaction of the different velocity components. © 2017 Acoustical Society of America.

[<http://dx.doi.org/10.1121/1.4974058>]

[MFH]

Pages: 563–574

I. INTRODUCTION

Acoustic streaming is a mean flow generated by Reynolds stresses in a fluid that supports an acoustic wave, either due to absorption in the main body of an irrotational sound beam (for Eckart streaming or Quartz wind), or associated to Stokes boundary layer adjacent to a solid boundary. This second type of streaming is usually referred to as Rayleigh streaming because Lord Rayleigh developed a solution that describes the steady vortices generated in the core of the fluid (also called outer cells) in a wide channel.¹ Rayleigh's analysis applied to the case of a large cylindrical guide yields

$$u_{2,\text{Rayleigh}} = -\frac{3U_{\text{ac}}^2}{8c} \sin(2kx)[1 - 2\eta^2], \quad (1)$$

$$v_{2,\text{Rayleigh}} = \frac{3U_{\text{ac}}^2}{8c} kR \cos(2kx)[\eta - \eta^3], \quad (2)$$

with $u_{2,\text{Rayleigh}}$ (respectively, $v_{2,\text{Rayleigh}}$) the axial (respectively, radial) component of streaming velocity, U_{ac} the

acoustic velocity amplitude at its antinode, c the speed of sound, R the channel radius, x the axial coordinate, k the complex wave number, $\eta = r/R$ the radial coordinate with r the distance from guide axis. In order to obtain these equations, terms in $e^{-R(1-\eta)/\delta_v}$ were neglected in the complete equations of Rayleigh solution, which is valid far enough from the boundary layer (with $\delta_v = \sqrt{2\nu/\omega}$ the acoustic boundary layer thickness, ω being the angular frequency). These equations clearly show the main characteristics of Rayleigh streaming: Streaming velocities are of second order in powers of acoustic Mach number, with vortices that span $\lambda/4$; axial and radial streaming components have quite different axial and radial dependencies. Subsequently, Schlichting² first described the inner streaming vortices confined to the boundary layer and rotating in the opposite direction than that of the Rayleigh outer cells, under the hypothesis of incompressible flow. Later, Qi³ included the fluid compressibility and temperature effects to improve the description of inner streaming. Rott⁴ improved the description of the outer streaming by taking into account thermal effects. Experimental studies were started later than theoretical ones, using second order time average pressure measurements⁵ or making profit of the development of laser velocimetry techniques (e.g., Ref. 6).

^{a)}Electronic mail: daru@limsi.fr

The above-described characteristics of Rayleigh streaming are modified when the acoustics are increased to high levels. Available studies focused on the description of high level axial component of the streaming velocity. Thompson and Atchley⁷ first observed that the variation of the axial component of streaming velocity, with respect to the transverse coordinate, departs from a parabola and that its axial dependence departs from a pure sinusoidal function at high acoustic amplitudes. Moreau *et al.*⁸ further described these distortions; they characterized the change of regime of the axial component of the streaming velocity from parabolic Rayleigh theory and found that for $Re_{NL} > 20$ axial streaming velocity is not in agreement with any available theory [see Eq. (3) for the definition of Re_{NL}]. Then it was found both experimentally⁹ and numerically¹⁰ that when the acoustic level is further increased, the previously described distortion of centerline axial streaming velocity towards acoustic velocity nodes leads to the generation of counter-rotating additional vortices near the acoustic velocity antinodes. This kind of behaviour was found to be followed by outer streaming cells only; results in the near wall region show that inner streaming vortices are only slightly modified.

The investigation of the origins of the mutation of streaming at high amplitudes has already been considered in the literature. The effect of inertia on streaming was the first phenomenon suspected to lead to high level deformation of streaming. Menguy and Gilbert¹¹ introduced the nonlinear Reynolds number,

$$Re_{NL} = \left(\frac{U_{ac}}{c} \right)^2 \left(\frac{R}{\delta_\nu} \right)^2 \quad (3)$$

that compares inertia of streaming and viscosity and determines the degree to which nonlinear effects of fluid inertia become dominant. This nonlinear Reynolds number has then been commonly used as criteria to range the conformity of streaming to Rayleigh pattern, the case $Re_{NL} \ll 1$ being referred to as “slow streaming” and the case $Re_{NL} \geq 1$ as “nonlinear streaming” or “fast streaming.” All available analytical models are restricted to slow streaming (e.g., Ref. 12). The effect of inertia on streaming was further analyzed by Daru *et al.*,¹³ thanks to the development of an averaged model simulation that permitted to isolate inertia from other high level effects. This model showed that the distortion associated with inertia of streaming flow is opposite to the one observed both experimentally [by laser Doppler velocimetry (LDV)] and numerically [with direct numerical simulations (DNS)] for streaming at high level: Inertia is associated with a distortion of streaming towards the acoustic velocity antinodes, making impossible the emergence of new streaming cells. This allowed us to identify the effect of inertia in the establishment of acoustic streaming and to assert that it is not the leading phenomena in the evolution of Rayleigh cells at high amplitudes.

Other effects have been considered as possibly responsible for the mutation of streaming at high amplitudes:¹⁰ Nonlinear propagation and thermal effects associated with acoustically induced heat transfer in a standing waveguide.

However, it was also shown that even if these phenomena do influence the streaming pattern at high levels, neither can be considered as being at the origin of the change of regime for Rayleigh vortices. Therefore, it was necessary to go further into the investigation of the origins of this mutation. In the present paper, we decided to investigate the possible nonlinear interaction between streaming and acoustics. The method of successive approximations is usually applied in acoustics and in particular, when approaching acoustic streaming. It implies that the different order components (including the acoustic first order and the streaming second order components) do not interact with each other. The aim of this paper is to evaluate the validity of this hypothesis when the acoustic amplitude is increased. To this effect, numerical and experimental results are gathered in order to further describe the modifications of streaming and acoustics at high acoustic amplitudes. A description of the usually considered axial velocity components for streaming and acoustics from low to high level regimes is proposed together with a description of the less considered radial velocity components, again for streaming and acoustics. The evolution of the outer streaming velocity amplitude U_s with the acoustic amplitude U_{ac} is further described. An important change is noticed: U_s is found to go from a quadratic to a linear dependence on U_{ac} . Attention is paid to both outer and inner streaming and it is shown that the variation of streaming velocity amplitude with acoustic velocity amplitude does not occur similarly for the two kinds of streaming. It is shown that the hypothesis of streaming velocity being much smaller than acoustic velocity is restrictive at high amplitudes for the radial velocities.

The paper is organized as follows. Section II presents the experimental setup and the numerical method and procedure. In Sec. III, the evolution of axial components of acoustic and streaming velocities are described from low to high amplitudes. The change of regime from quadratic to linear dependence of the axial streaming velocity on the acoustic amplitude is analyzed. In Sec. IV, the evolution of radial components of acoustic and streaming velocities is discussed from low to high amplitudes and the nonlinear interaction of radial acoustic and streaming velocities is investigated.

II. METHODS AND CONFIGURATIONS

As stated above, both experimental and numerical studies are used in this paper to obtain a thorough description of the evolution of streaming from low to high acoustic levels. In both these approaches, a cylindrical tube of length L and radius R is considered. The tube is filled with air at atmospheric pressure, in which a high level standing wave is generated by exciting a resonant mode.

Because we want to focus on one among other high level phenomena that can be responsible for the evolution of Rayleigh streaming, it is necessary to separate the contribution of the different phenomena encountered at high level, or at least to scale them. Thompson *et al.*¹⁴ first showed that temperature gradients influence Rayleigh streaming. In the experimental setup, the thermal condition corresponded to the “uncontrolled” condition as defined by Ref. 14, that is, the resonator was exchanging heat with the surrounding air

and a small temperature gradient was created. In the numerical simulations isentropic acoustic oscillations are considered so that thermal variations are not taken into account and the energy equation is not considered.

Shock wave formation can also influence Rayleigh streaming. In the experimental setup, a cylindrical guide is connected to loudspeakers via convergents; the resulting coupled resonant system offers the advantage that its modes are not in a harmonic series, preventing the cascade of energy from ω (the angular frequency of the acoustic wave) to its harmonics by nonlinear propagation. This is not the case of the configuration studied numerically, where shock waves can develop (as shown in Ref. 10), but we have checked that they are of small intensity and do not have drastic influence on streaming cells, during the physical time corresponding to numerical simulations (≈ 200 periods).

In the following, the experimental setup and procedure is first described and then the numerical calculation is presented. Finally the experimental and numerical data set selected for analysis are given.

A. Experimental setup

The setup used to observe the acoustic streaming phenomenon is shown in Fig. 1. The cylindrical tube, with $R = 19.5$ mm, is connected at each end to a loudspeaker via connecting tubes, designed to avoid separation effects related to the singularities in change of section. Either the first mode corresponding to $L_{\text{exp}} = \lambda/2$ or the third mode corresponding to $L_{\text{exp}} = 3\lambda/2$ is excited. The total length of the waveguide is $L_{\text{exp}} = 2.13$ m so that the two distinct resonance frequencies are 88 and 240 Hz.

Wood smoke is used as seeding particles in order to perform particle velocity measurements by Laser. LDV allows us to access the axial particle velocity and particle image velocimetry (PIV) allows us to access the streaming velocity field in a (x, r) plane.

The single component LDV system is a Dantec Dynamic model 2580; the probe is mounted on a three-axis positioning system. The argon krypton laser has an optical wavelength of 514.5 nm and a power of 25 W. The parameters of LDV system are adjusted for axial particle velocity measurements and the axial streaming velocity is deduced from these measurements. Moreau *et al.*⁸ showed that in such a setup it is necessary to wait for 26 min after the acoustic field is switched on to ensure that the streaming field is fully established. Also they found that a good compromise between a sufficient number of measured tracer particles per measuring point for a precise streaming velocity estimate and a short enough measuring time that insures a correct seeding during a whole scan is obtained when choosing to acquire either 70 000 points or to stop acquisition after 10 s.

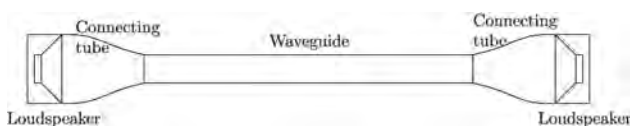


FIG. 1. Diagram of the experimental apparatus.

The results presented in the following were obtained with these settings.

On the other hand, PIV measurements were performed by generating a laser sheet of 1 mm thickness with a pulsed laser (Quantel Mini-Yag) having a 532 nm wavelength, issuing a pulsed energy of 30 mJ and synchronized with a maximum frequency of 20 Hz. To insure convergence of the streaming velocity field calculation, 500 pairs of pictures were recorded by a JAI RM-4200CL camera (maximum of 15 pictures/s, 2048×2048 pixels) and the 500 phase locked velocity fields obtained were averaged. This installation allows the discretization of the velocity field with resolution along the guide axis/radius $\Delta x = \Delta r = 0.52$ mm. For more information on the evaluation of the streaming velocity see the work of Reyt *et al.*⁹

B. Numerical method

The configuration numerically studied consists in a fluid oscillating as the result of an acoustic standing wave initiated by shaking a resonator along its axial direction at ω . Resonant conditions are imposed and the $L = \lambda/2$ mode is excited. The flow is modeled with the compressible Navier-Stokes equations expressed in the moving frame attached to the tube, so that a forcing source term is added. Because the wave propagation is considered as isentropic (in order to approach the experimental “uncontrolled” thermal condition), the energy equation is decoupled from the other equations and we only solve the mass and momentum equations. The equations are numerically solved with an axisymmetric formulation using high order finite difference schemes.^{10,15}

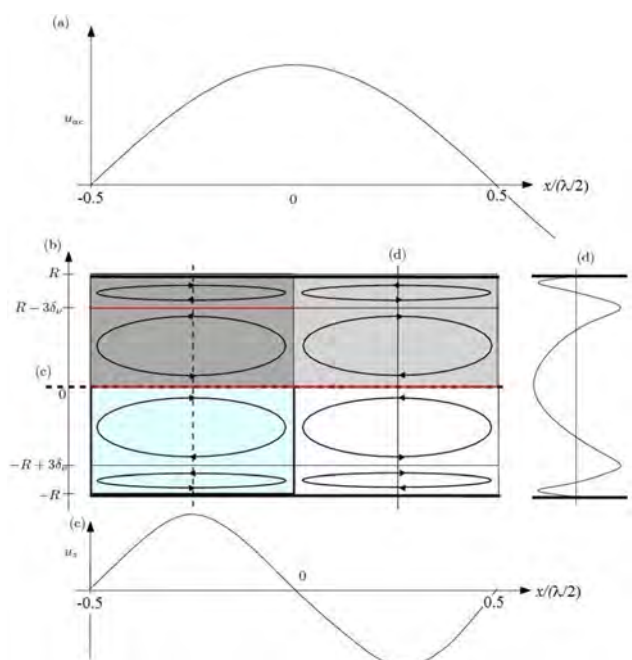


FIG. 2. (Color online) (a) Acoustic wave pattern. (b) Schematic representation of the corresponding slow streaming velocity field. Grey and dark grey zone: simulation domain. Blue and dark grey zone: PIV measurements. Red lines: LDV measurements. (c) Variation of axial streaming velocity with respect to the axial coordinate at $r = 0$. (d) Variation of axial streaming velocity with respect to the radial coordinate at $x = \lambda/8$.

TABLE I. Parameters of the different presented cases.

Name	f (Hz)	R/δ_ν	R/λ	U_{ac} (m/s)	U_s (m/s)	Re_{NL}
N_1	20 000	20	2×10^{-3}	[0.2 – 60]	$[0.4 \times 10^{-4} – 2.4]$	$[1.3 \times 10^{-4} – 12.18]$
N_2	20 000	40	3.7×10^{-2}	[0.4 – 80]	$[1.6 \times 10^{-4} – 4.9]$	$[2 \times 10^{-3} – 86.62]$
N_3	20 000	50	4.5×10^{-2}	[0.5 – 73]	$[2.6 \times 10^{-4} – 4.2]$	$[5.3 \times 10^{-3} – 112.7]$
N_4	5000	50	2.25×10^{-2}	[0.5 – 62]	$[2.6 \times 10^{-4} – 3.3]$	$[5.3 \times 10^{-3} – 81.3]$
E_1	88	84	5×10^{-3}	[2.7 – 45]	$[90 \times 10^{-4} – 1.5]$	$[0.43 – 120.87]$
E_2	240	138	1.4×10^{-2}	[2.7 – 30]	$[80 \times 10^{-4} – 0.4]$	$[1.17 – 145]$

The physical boundary conditions in the moving frame are: no slip on the boundary walls parallel to horizontal symmetry axis, and symmetry conditions on the vertical boundaries. The instantaneous flow is calculated with a DNS approach and the mean flow is obtained by time averaging over an acoustic period. All results presented below are obtained using a regular mesh of rectangular cells composed of 500 points along the axis, and of $5 \times R/\delta_\nu$ points in the radial direction. The time step δt is fixed in order to insure stability of the numerical scheme ($\delta t = 8 \times 10^{-9}$ s for N_1 , N_2 , N_3 , $\delta t = 1.6 \times 10^{-8}$ s for N_4 , the different numerical configurations being defined in Sec. II C).

C. Studied configurations

A schematic representation of streaming expected in the acoustic resonators under study is given in Fig. 2. The domain considered for numerical simulations is shown in grey. LDV scans correspond to the horizontal red lines (along the resonator axis and in the near wall region) and the PIV measurement domain is depicted by the light blue/dark grey zone. Figure 2 recalls that in the outer cells (located in the resonator core) the flow is circulating from the acoustic velocity nodes towards the acoustic velocity antinodes along the central axis and returns in the vicinity of the wall to complete a closed loop. The location $r = R - 3\delta_\nu$ corresponds to the limit between the two streaming cells (inner cell and outer cell), so that the amplitude of the axial streaming velocity has a local maximum [Fig. 2(d)] which will be referred to as the inner streaming amplitude in the following.

In this study we compare results from two experimental (noted E_1 and E_2) and four numerical (N_1 to N_4) configurations. The corresponding parameters are summarized in Table I. Note that for the chosen configurations, $20 \leq R/\delta_\nu < 140$, and thus the inner vortices fill a much smaller portion of the guide than in Fig. 2(b) where the represented guide is narrow (R/δ_ν is about 4). For the large guides under study, Eqs. (1) and (2) provide a good description of outer streaming cells at low acoustic amplitudes. The range of variation of U_{ac} which is the amplitude of the axial acoustic velocity at antinode, shown in Table I, is chosen to encompass a variety of streaming flows in order to exhibit the different flow regimes (there are between 6 and 19 data points covering the range of U_{ac} values). Because the size of the numerical system is very different from the size of the experimental system (to reduce computational time), working frequencies are very different. Nondimensional analysis,¹⁰ however, shows that the same flow behaviour is expected if $M \ll 1$, $Re \gg 1$ and $Sh \ll 1$, where $M = U_{ac}/c$, $Re = 1/2 (\lambda/\pi\delta_\nu)^2$, $Sh = \delta_\nu/R$. These

conditions are fulfilled by all experimental and numerical configurations under study.

In this paper we want to check if the oscillation part and the mean part (of different order of magnitude) of the particle velocity can be considered as independent from each other. For this purpose we consider the two particle velocity components: axial and radial and we consider the evolution of the contribution of acoustics and streaming to these components as the acoustic level is increased. Several strategic positions are chosen for discussing these evolutions, summarized in Table II.

III. AXIAL ACOUSTIC AND STREAMING VELOCITIES FROM LOW TO HIGH LEVELS

A. Mutation of streaming at high level

The characteristics of Rayleigh streaming described by Fig. 2 and Eq. (1) are also observed on Fig. 3, top-left, that shows contours of the axial streaming velocity resulting from the averaged PIV measurements for the experimental data set E_2 at relatively low level. The limit between two streaming cells is shown by thick vertical dotted lines. Due to the fact that the guide is much larger than in Fig. 2(b), only the Rayleigh outer cells are visible. Similarly, Fig. 3, top-right, representing the contours of the axial streaming velocity together with velocity vectors of the streaming flow calculated from N_3 numerical simulations, show results in agreement with the above description of slow streaming. In Fig. 3 top, one can see that the shape of the outer cells is not perfectly elliptic as it is the case in the schematic representation given by Fig. 2; the center of a cell is located approximately at $r/R = 0.7$, in agreement with Eq. (1).

TABLE II. Spatial evolution of the velocity components considered.

Component	Axial evolution	Radial evolution	Section
Axial acoustics	$u_{ac}(x, r = 0)$	$u_{ac}(x = \lambda/8, r)$	III B
	$u_{ac}(x, r = R - 2\delta_\nu)$		III B
Axial streaming	$u_s(x, r = 0)$	$u_s(x = \lambda/8, r)$	III B
	$u_s(x, r = R - 2\delta_\nu)$		III B
Radial acoustics		$v_{ac}(x = -\lambda/4 + 3\lambda/100, r)$	IV A
		$v_{ac}(x = -\lambda/4 + 7\lambda/100, r)$	IV A
		$v_{ac}(x = -\lambda/4 + 11\lambda/100, r)$	IV A
		$v_{ac}(x = -\lambda/4 + 15\lambda/100, r)$	IV A
		$v_{ac}(x = -\lambda/4 + 19\lambda/100, r)$	IV A
		$v_{ac}(x = -\lambda/4 + 23\lambda/100, r)$	IV A
Radial streaming	$v_s(x, r = 0.564R)$	$v_s(x = 0, r)$	IV A
		$v_s(x = \lambda/2, r)$	IV A

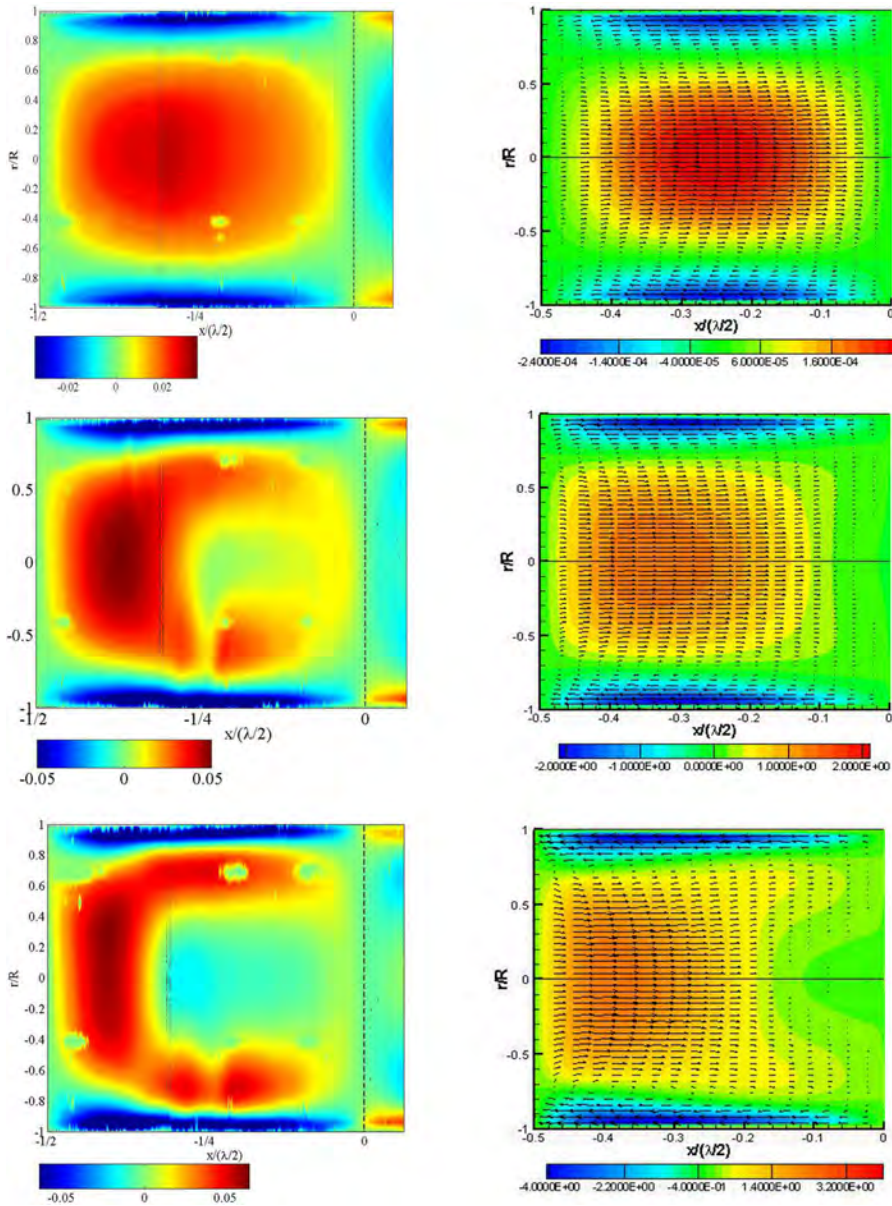


FIG. 3. (Color online) Contours of axial streaming velocity colored by its value (in m/s) and velocity vectors. Left: PIV results from E_2 for $Re_{NL} = 6, 14, 30$, respectively, from top to bottom. Right: numerical results from N_3 for $Re_{NL} = 0.006, 51, 111$, respectively, from top to bottom.

Figure 3 middle and bottom show the evolution of streaming when the acoustic level is increased. As found previously, the cell centers are first pushed towards the acoustic velocity nodes and then a counter-rotating cell appears along the resonator axis.^{9,10} PIV data are altered by light reflections on the tube glass but still display the C-shape formed by the area of positive velocity (the yellow/red area). The change in the streaming pattern is not significant in the near-wall region. The position of the streaming velocity maximum in the near-wall region only shifts toward the acoustic velocity node as the acoustic level increases.

This presentation of the mutation of streaming at high levels is the one found in the literature. We need to consider it from another point of view in order to find its origin. In the following, in order to investigate the possible nonlinear interaction between streaming and acoustics and the associated validity of the method of successive approximations, we extract from the studied configurations presented in Table II a comparison of acoustic and streaming contribution

to the different components of particle velocity at several strategic positions. In this section axial velocities are considered, Sec. IV being devoted to the investigation of radial velocities.

B. Evolution of axial velocities

Figure 4 shows acoustic and streaming axial velocities along the axis of the guide on a half wavelength span for two different acoustic levels extracted from E_2 set. An electric circuit equivalent to the electro-acoustic system has been developed that allows us to calculate the acoustic pressure and particle velocity along the resonator at any working frequency. Theoretical expectations obtained from this electro-acoustic model are given for acoustic velocity and theoretical expectations for streaming from Rayleigh law [Eq. (1)] are also given. This figure makes it apparent that although the streaming is highly distorted at high amplitudes, the axial acoustic velocity keeps the same axial evolution.

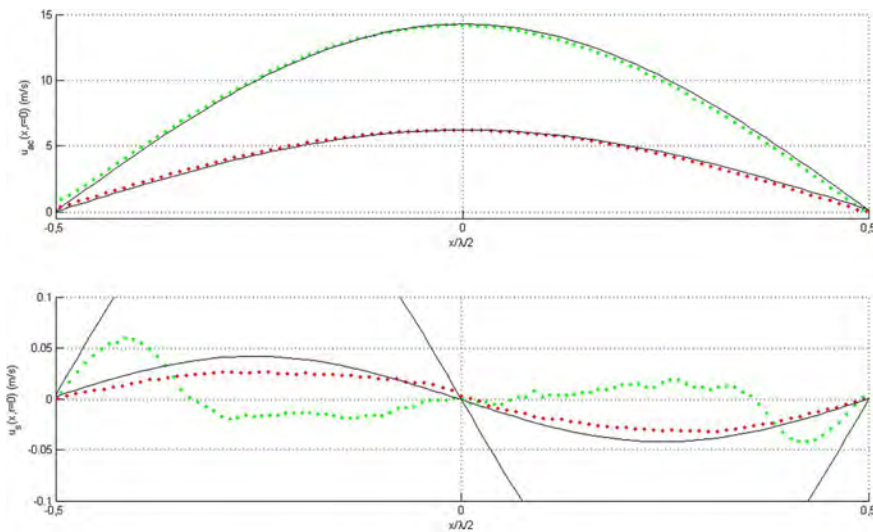


FIG. 4. (Color online) Top: axial acoustic velocity wave pattern: $u_{ac}(x, r = 0)$ in m/s and bottom: axial streaming velocity along the guide axis: $u_s(x, r = 0)$ in m/s for low (red) and high (green) acoustic levels. Dots: experimental results from E_2 . Lines: theoretical results from an electrodynamic model of the system (top) and from Eq. (1) (bottom).

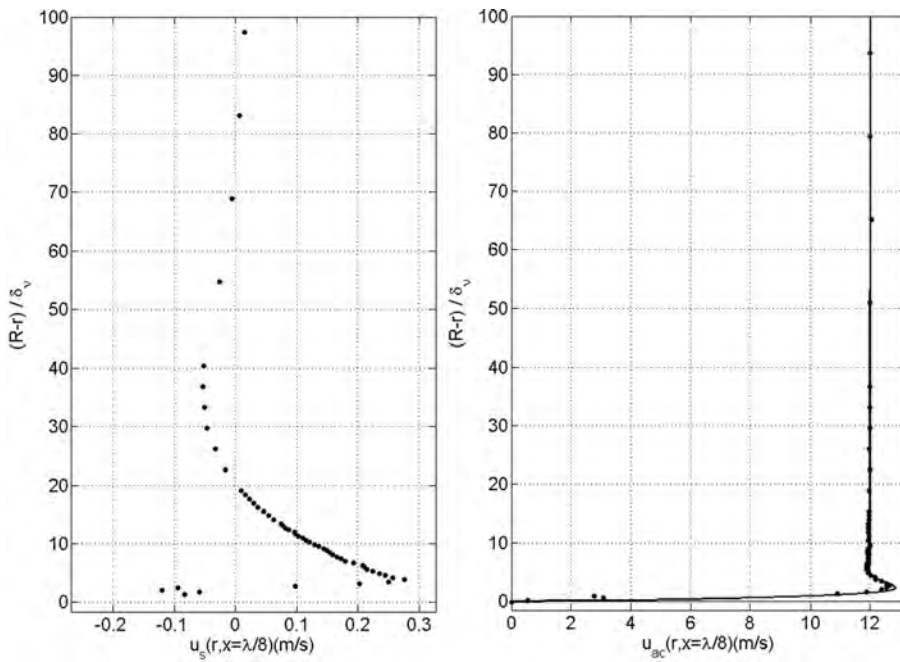


FIG. 5. Left: radial dependence of axial acoustic streaming velocity: $u_s(x = \lambda/8, r)$ in m/s. Right: radial dependence of axial acoustic velocity: $u_{ac}(x = \lambda/8, r)$ in m/s for high acoustic level. Dots: LDV experimental results from E_2 . Lines: theoretical expectation from Eq. (4).

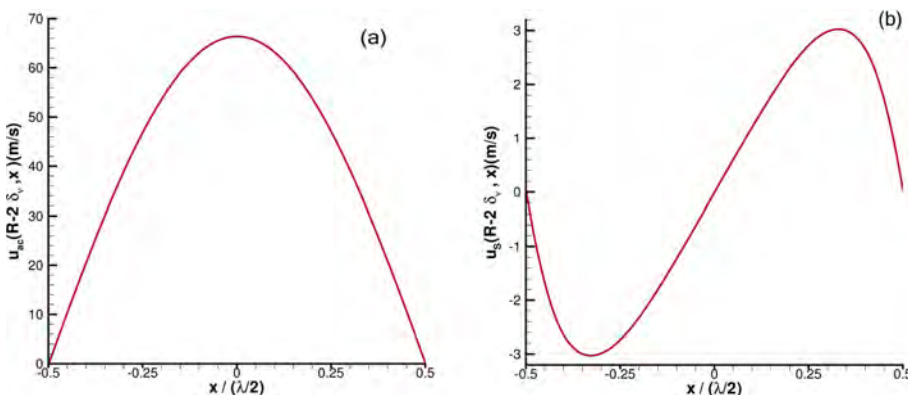
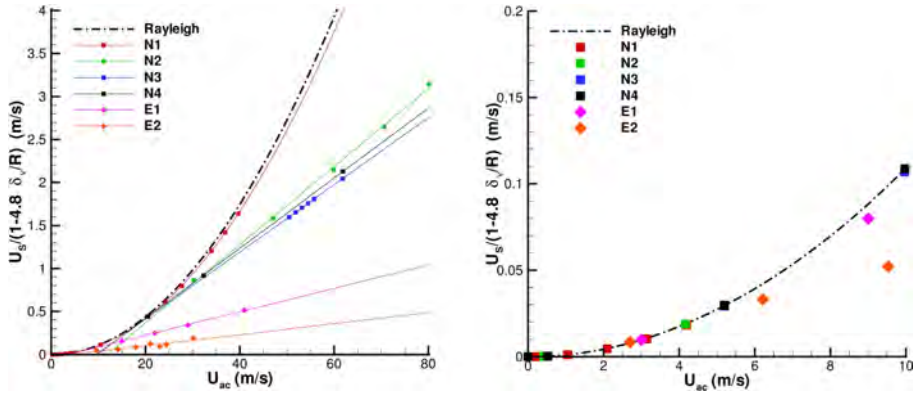


FIG. 6. (Color online) (a) Axial acoustic velocity wave pattern: $u_{ac}(x, r = R - 2\delta_\nu)$ in m/s and (b) Axial streaming velocity: $u_s(x, r = R - 2\delta_\nu)$ in m/s for high acoustic levels ($Re_{NL} = 81$). Numerical results from N_3 .



Similarly Fig. 5 shows acoustic and streaming axial velocities along the radial coordinates for an high acoustic level extracted from E_2 set. Theoretical expectation for axial acoustic velocity is also given. The latter is obtained from the integration of the first order axial component of Navier-Stokes equations, giving

$$u_{ac}(x, r) = \frac{1}{i\omega\rho_0} \frac{\partial p_{ac}}{\partial x} \left(1 - \frac{J_0(br/R)}{J_0(b)} \right), \quad (4)$$

with $b = (1 + i)R/\delta_\nu$, ρ_0 the mean density of the fluid, p_{ac} the acoustic pressure and J_0 is the Bessel function of the first kind of order 0. Again this figure shows that although the axial streaming velocity has a radial dependence very different from a parabola as described in Eq. (1), the axial acoustic velocity keeps the same radial evolution even in the very near wall region where streaming could be expected to alter acoustics velocity due to severe velocity gradients encountered.

Numerical results confirm this evolution as shown by Fig. 6 where axial acoustic and streaming velocities are represented along a streaming cell in the near wall region: $u_{ac}(x, r = R - 2\delta_\nu)$ and $u_s(x, r = R - 2\delta_\nu)$, for high acoustic level. As already observed, the streaming pattern in this condition is distorted; however, the acoustic velocity is not modified.

C. Relationship between streaming and acoustic velocities

1. Outer streaming

In this section we further investigate the validity of Eq. (1) and particularly the dependence of the axial streaming velocity on the acoustic velocity for different configurations. Figure 7 is the result of a search of a relationship between the axial outer streaming velocity amplitude U_s and the acoustic velocity amplitude U_{ac} . At low amplitude, the best fit with numerical and experimental results is found when representing the variation of $U_s \times \{1/[1 - 4.8(\delta_\nu/R)]\}$ against U_{ac} . Therefore, a dependence upon the aspect ratio R/δ_ν should be included in Eq. (1) for slow streaming:

$$U_s \propto U_{ac}^2 \left(1 - 4.8 \frac{\delta_\nu}{R} \right). \quad (5)$$

Figure 7 also shows that in each configuration the quadratic dependence given by Rayleigh's law Eq. (1) is only true up to

FIG. 7. (Color online) Axial streaming velocity amplitude $U_s \times [1/1 - 4.8(\delta_\nu/R)]$ against acoustic velocity amplitude U_{ac} . Right: zoom on the low level region.

a certain value of U_{ac} . The dependence then becomes linear and this dependence is different for each configuration (different slopes of straight lines departing from the quadratic curve).

Figure 8 presents the same results as Fig. 7 but normalized with $U_{Rayleigh} = 3U_{ac}^2/8c$ and in a log-log scale. The ordinate is $U_s/U_{Rayleigh} \times \{1/[1 - 4.8(\delta_\nu/R)]\}$ so that at low regime all curves start from 1. It confirms that at low amplitudes the quadratic dependence is satisfied: All points fall on the horizontal line. The corresponding flow regime is thereafter called the first regime (Regime 1). Then a second regime (Regime 2) can be identified, for which all curves are of slope -1 on a log-log scale.

There exist configurations in Regime 2 where the emergence of the extra cell has not been observed yet (N_4). Therefore, there is no simple and direct correlation between the transition to the second regime and the appearance of a new cell.

2. Inner streaming

As for outer streaming, a relationship between the axial inner streaming velocity maximum U_s and the acoustic velocity amplitude U_{ac} is searched. The best fit results in a parabolic variation of $U_s(x_m, r = R - 3\delta_\nu)/[1 - 6.8(\delta_\nu/R)]$ against U_{ac} as shown in Fig. 9. The coefficient 6.8 is different from the coefficient obtained for outer streaming because

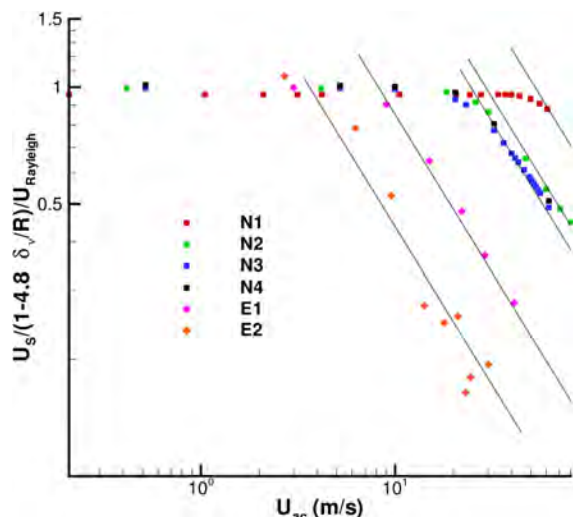


FIG. 8. (Color online) $(U_s/U_{Rayleigh}) \times [1/1 - 4.8(\delta_\nu/R)]$ against U_{ac} on a log-log scale.

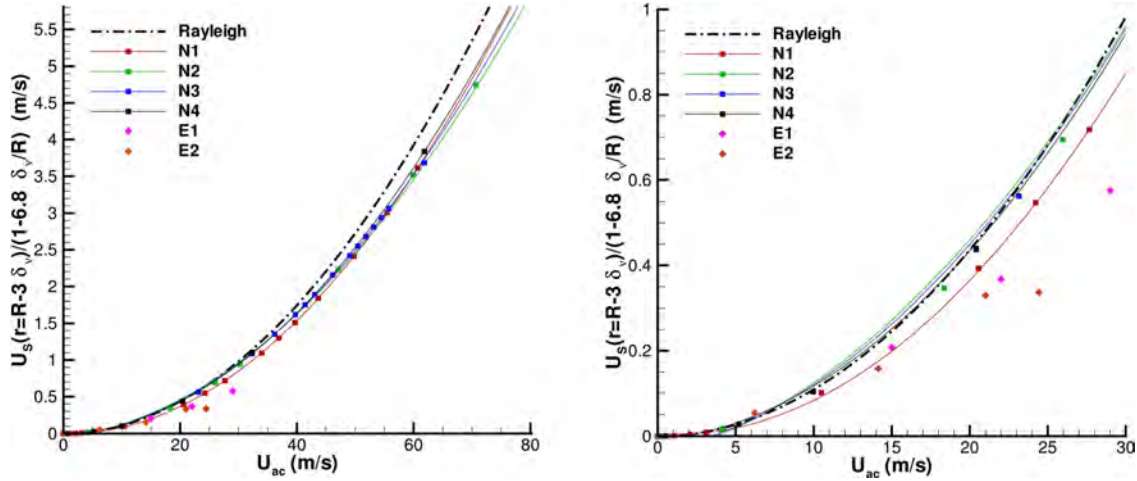


FIG. 9. (Color online) $U_s/[1 - 6.8(\delta_\nu/R)]$ against U_{ac} within the near-wall region. Right: zoom for low levels.

the two streaming velocities are at two different radial positions, $r = R - 3\delta_\nu$ for inner streaming and $r = 0$ for outer streaming. In the simulation, x_m corresponds to the axial position of streaming velocity maximum at $r = R - 3\delta_\nu$ which is the place of inner streaming amplitude. All simulation points follow the same curve. Experimental data are taken in the near-wall region but it could not be precisely set at the same relevant position so the fit of experimental data is not obvious. However, in all cases it can be concluded that the quadratic dependence of inner streaming on acoustics still holds even at high amplitudes.

IV. RADIAL ACOUSTIC AND STREAMING VELOCITIES FROM LOW TO HIGH LEVELS

Finally in this section the mutation of axial streaming velocity was further investigated and it was shown that there is no need to reconsider the application of the perturbation method for axial components of particle velocity. In Sec. IV A, the case of radial velocities is considered.

A. Evolution of radial velocities

The radial component of acoustic particle velocity can be obtained from the radial integration of the first order continuity equation (e.g., Ref. 16)

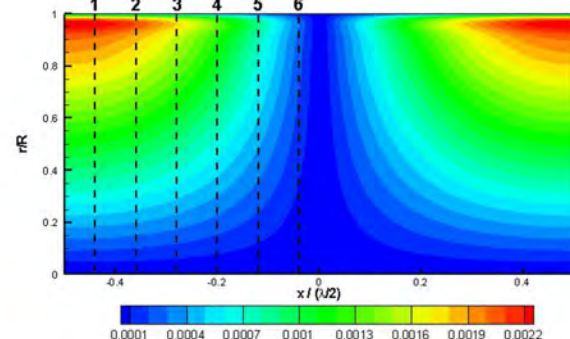
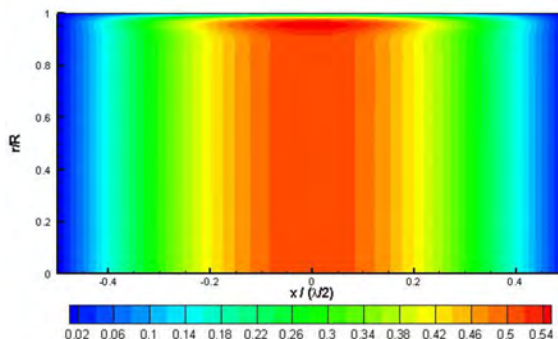


FIG. 10. (Color online) Contours of the axial acoustic velocity u_{ac} (m/s) (left) and the radial acoustic velocity v_{ac} (m/s) (right) colored by its value obtained with the DNS simulation (N_3), $Re_{NL} = 0.006$.

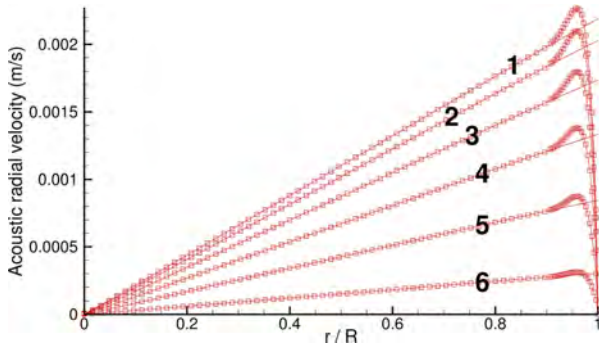


FIG. 11. (Color online) Radial dependence of radial acoustic velocity obtained from the DNS calculation at different axial locations: $v_{ac}(-\lambda/4 + m, r)$ with $m = 3, 7, 11, 15, 19$, and $23 \times \lambda/100$ for curves labeled, respectively, from 1 to 6 (Fig. 10, right) in m/s for low acoustic level $Re_{NL} = 0.006$. Squares: numerical results from N_3 ; Plain lines: linear fit.

In the region $x=0$, the radial streaming velocity v_s is higher than the radial acoustic velocity v_{ac} .

The following figures show that the above listed low amplitude features of radial velocities are modified for both the acoustic and the streaming radial velocities as the acoustic amplitude is increased. Figure 13, left (similar to Fig. 10, right but for higher amplitude: $Re_{NL} = 22$) shows that when the acoustic amplitude is increased, the radial acoustic velocity encounters significant changes. Figure 13, right shows the radial variation of the radial acoustic velocity $v_{ac}(r)$ obtained at different axial positions (labeled from 1 to 6, highlighted on Fig. 13, left). In the region around $x=0$ (curve labeled 6), the profile is no longer linear in r , but is a polynomial of the 3rd order, as found by a polynomial fit in the core region. Therefore, it appears that even if the axial acoustic velocity u_{ac} is not modified [neither in its axial variation $u_{ac}(x)$ nor in its radial variation $u_{ac}(r)$] when the acoustic amplitude is increased, the radial acoustic velocity v_{ac} is modified.

Figure 14 shows the corresponding evolution of radial streaming velocity. $v_s(x, r = 0.564R)$ is no longer sinusoidal [see Fig. 14(c)] and the symmetry between $v_s(x = 0, r)$ and $v_s(x = \lambda/2, r)$ is no longer observed, with the radial streaming velocity around $x = 0$ globally decreasing [see Fig. 14(b)]. In this region, however, v_s is still higher than v_{ac} .

Let us now consider the case N_3 , $Re_{NL} = 81$, which corresponds to a case in Regime 2 with an extra counter-rotating cell. Figure 15 displays the radial acoustic velocity obtained from the DNS calculation. The profiles in the core are very distorted and correctly fitted by a polynomial of 6th order. Only in the $x = \pm \lambda/4$ regions does the radial acoustic velocity keep a linear radial variation. In addition, as shown by Fig. 16, when the acoustic level is increased, the radial streaming velocity in the $x = 0$ region continues to decrease until tending to zero and then changing sign, in association with the generation of the additional outer streaming cell.

Finally, both the radial acoustic velocity and the radial streaming velocity are subject to important changes as the acoustic level is increased. Due to the fact that the modification of the radial acoustic velocity first occurs in the region where the radial streaming velocity is large, it can be hypothesized that streaming alters acoustics. This possibility is investigated in Sec. IV B.

B. Nonlinear interaction of radial acoustic and streaming velocities

In order to assess the interaction between acoustic and streaming flows, a DNS calculation is conducted where at the end of each period, the averaged flow over the preceding period is subtracted from the total instantaneous velocity field, before starting a new time step. By doing so, we intend to artificially remove the influence of the streaming flow on the acoustic field. Figure 17 shows the radial variation of the resulting radial acoustic velocity component $v_{ac}(r)$ for the case discussed in Sec. IV A (N_3 , $Re_{NL} = 81$, see Fig. 15). In the core region, the profile remains linear whereas the acoustic field extracted from the full DNS calculation had a radial component with a 6th order polynomial variation in the radial direction (see Fig. 15, right). This observation proves that streaming flow influences the acoustic field through the radial component.

This is confirmed when looking back at the radial variation of the axial streaming velocity $u_s(r)$ and comparing results for the full DNS calculation with those obtained after having removed the influence of streaming on acoustics. The left part of Fig. 18 shows the radial variation of the axial streaming velocity calculated with full DNS. The profiles in the core are correctly fitted by a polynomial of 5th order. On

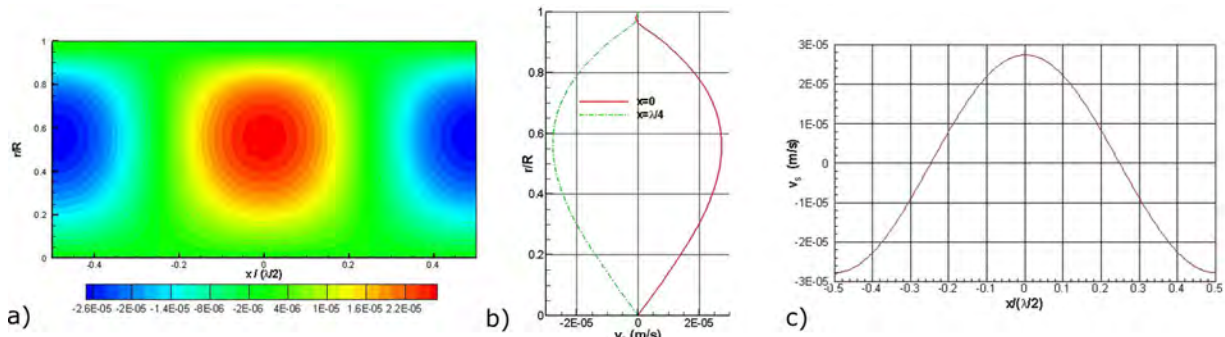


FIG. 12. (Color online) (a) Contours of the radial streaming velocity v_s colored by its value obtained with the DNS simulation. (b) Radial dependence of radial streaming velocity: $v_s(x = 0, r)$ and $v_s(x = \lambda/4, r)$ in m/s. (c) Axial dependence of radial streaming velocity: $v_s(x, r = 0.564R)$ in m/s. Numerical results from N_3 , $Re_{NL} = 0.006$.

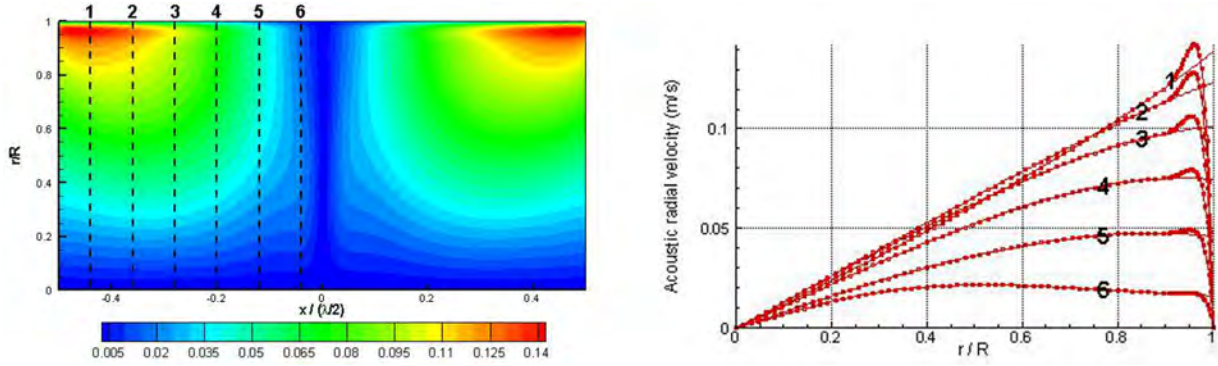


FIG. 13. (Color online) Left: contours of the radial acoustic velocity v_{ac} amplitude colored by its value. Right: radial variation of the radial acoustic velocity obtained from the full DNS calculation at different axial locations $v_{ac}(-\lambda/4 + m, r)$ with $m = 3, 7, 11, 15, 19$, and $23 \times \lambda/100$ for curves labeled, respectively, from 1 to 6 (see left figure), in m/s, $N_3 = 22$. Solid lines: polynomial fit in the core region.

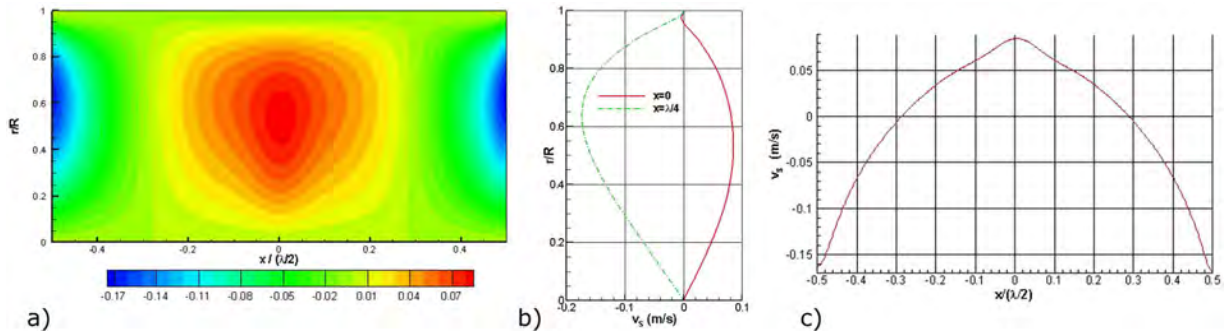


FIG. 14. (Color online) (a) Contours of the radial streaming velocity v_s colored by its value obtained with the DNS simulation. (b) Radial dependence of radial streaming velocity: $v_s(x = 0, r)$ and $v_s(x = \lambda/4, r)$ in m/s. (c) Axial dependence of radial streaming velocity: $v_s(x, r = 0.564R)$ in m/s. Numerical results from $N_3, Re_{NL} = 22$.

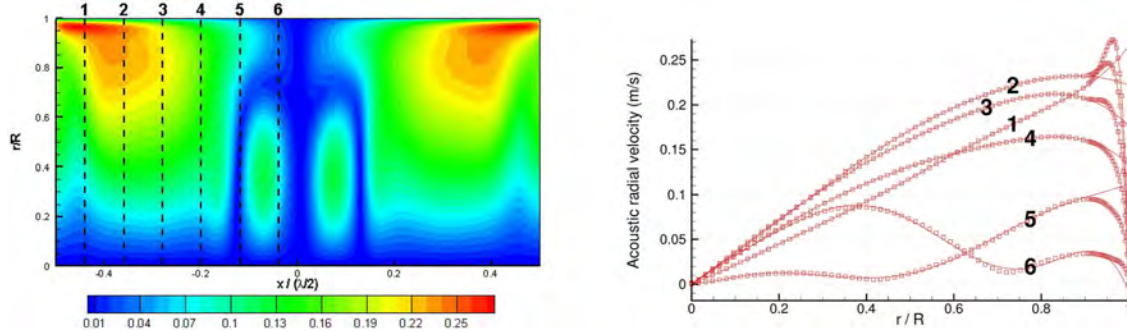


FIG. 15. (Color online) Left: contours of the radial acoustic velocity v_{ac} amplitude colored by its value. Right: radial variation of the radial acoustic velocity obtained from the full DNS calculation at different axial locations $v_{ac}(-\lambda/4 + m, r)$ with $m = 3, 7, 11, 15, 19$, and $23 \times \lambda/100$ for curves labelled, respectively, from 1 to 6 (see left figure) in m/s, $N_3, Re_{NL} = 81$. Solid lines: polynomial fit in the core region.

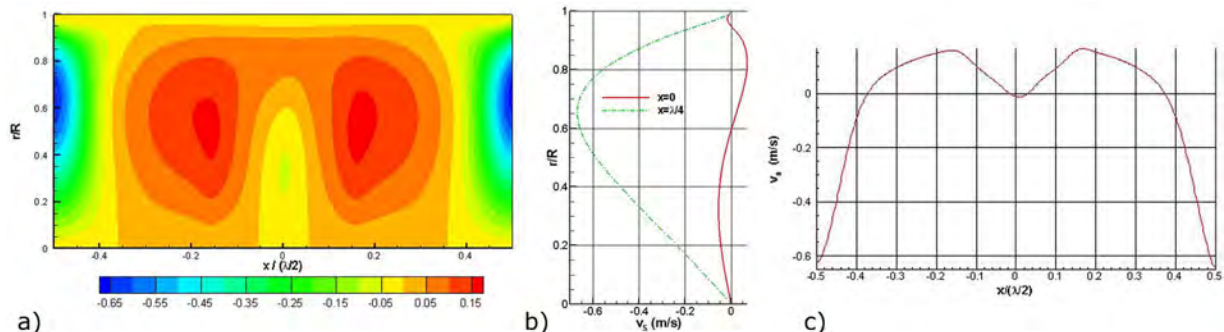


FIG. 16. (Color online) (a) Contours of the radial streaming velocity v_s colored by its value obtained with the DNS simulation. (b) Radial dependence of radial streaming velocity: $v_s(x = 0, r)$ and $v_s(x = \lambda/4, r)$ in m/s. (c) Axial dependence of radial streaming velocity: $v_s(x, r = 0.564R)$ in m/s. Numerical results from $N_3, Re_{NL} = 81$.

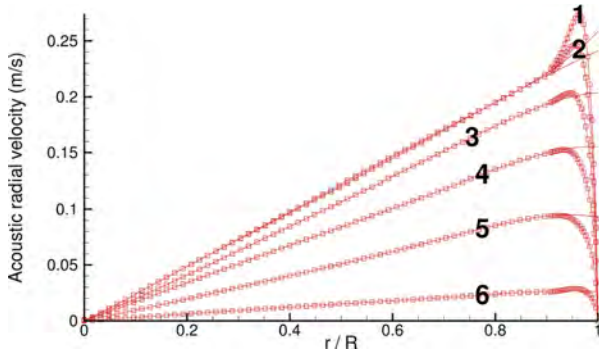


FIG. 17. (Color online) Radial variation of the radial acoustic velocity at different axial locations $v_{ac}(-\lambda/4 + m, r)$ with $m = 3, 7, 11, 15, 19$, and $23 \times \lambda/100$ for curves labeled, respectively, from 1 to 6, in m/s when removing the influence of the streaming flow on the acoustic flow, N_3 , $Re_{NL} = 81$. Solid lines: linear fit in the core region.

one of the profiles we can see negative values of the axial streaming velocity in the core, assessing the presence of the extra counter-rotating outer streaming cell. Now if the interaction between streaming and acoustics is removed, the right part of Fig. 18 shows the profiles are parabolic as shown by a polynomial fit and no extra cell is observed since the velocities are all positive in the core. The associated streaming pattern has a similar structure as a Regime 1 streaming flow pattern although created by a high intensity acoustic wave. This shows the major role played by the coupling between the streaming flow and the acoustic field. This coupling works as a two-way interaction through the radial components.

Let us now explore the relative amplitude of the radial acoustic and streaming velocity components. The left part of Fig. 19 shows the maximum absolute value of radial streaming velocity (empty symbols) and radial acoustic velocity (full symbols) as functions of the axial acoustic velocity amplitude U_{ac} for the sets N_1 to N_3 . One can observe that the radial acoustic velocity amplitude V_{ac} depends linearly on U_{ac} and is independent of R/δ_ν , in agreement with Eq. (6). The radial streaming velocity amplitude V_s is a quadratic function of U_{ac} , in agreement with Eq. (2). The amplitude of V_s increases with R/δ_ν . After the intersection of the two sets of curves, V_s becomes greater than V_{ac} , which occurs for sets

N_2 and N_3 but not for N_1 . This is consistent with the transition from the first to the second regime of streaming described previously: The value of U_{ac} corresponding to V_s becoming greater than V_{ac} in Fig. 19 is the same as the value of U_{ac} corresponding to the change of regime (from quadratic to linear) in Fig. 8. The right part of Fig. 19 shows similar results for the experimental configuration $E2$. Here the amplitude of streaming velocity was estimated from PIV measurements and the dependency of radial acoustic velocity on axial acoustic velocity was obtained by using Eq. (6). As was the case for numerical results (left part of Fig. 19), the value of U_{ac} corresponding to V_s becoming greater than V_{ac} is close to the value in Fig. 8 corresponding to the change of regime (from quadratic to linear). The quadratic dependency of V_s on U_{ac} is verified experimentally. As was the case for U_s (see Fig. 7), V_s is close to Rayleigh's law Eq. (2) only for low acoustic levels. However, we do not observe here any change of regime for V_s as was discussed for U_s : Even if V_s diverges from Eq. (2), it still depends quadratically on U_{ac} .

Finally these results confirm that the strong nonlinear relation between the different velocity components for acoustics and streaming is responsible for the mutation of streaming patterns at high amplitude.

V. CONCLUSION

A study including numerical and experimental results was presented in order to analyse the different streaming flow regimes in a cylindrical waveguide. Two different regimes were identified. The first regime, Regime 1, corresponds to low acoustic amplitudes for which the axial streaming velocity amplitude is a quadratic function of the acoustic amplitude. In the second (high amplitudes) regime, Regime 2, streaming velocity becomes a linear function of the acoustic amplitude. A nonlinear interaction between the radial component of acoustic streaming and the radial component of acoustic velocity is responsible for this change of regime that occurs when the radial streaming velocity becomes larger than the radial acoustic velocity. This interaction then yields the generation of additional outer streaming cells. The axial and radial variations of the axial acoustic velocity remain the same when the acoustic level is

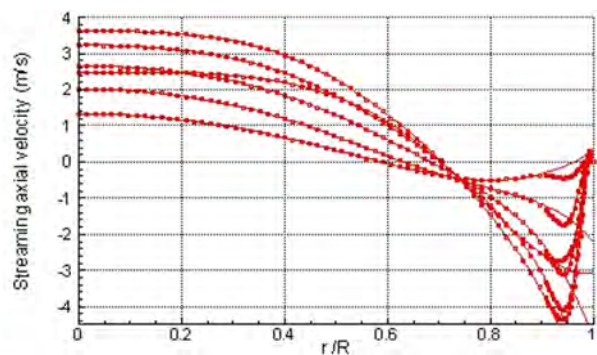
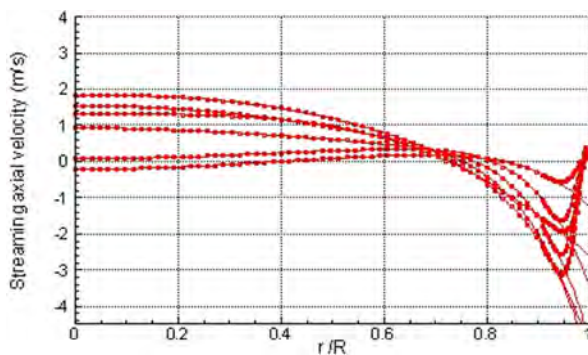


FIG. 18. (Color online) Radial variation of the axial streaming velocity induced by the acoustic flow shown in Fig. 15 (left: full DNS simulation) and 17 (right: when removing the influence of streaming on acoustics), $u_{ac}(x = 3, 7, 11, 15, 19, \text{ and } 23 \times \lambda/100, r)$, N_3 , $Re_{NL} = 81$. Solid lines: polynomial fit in the core region.

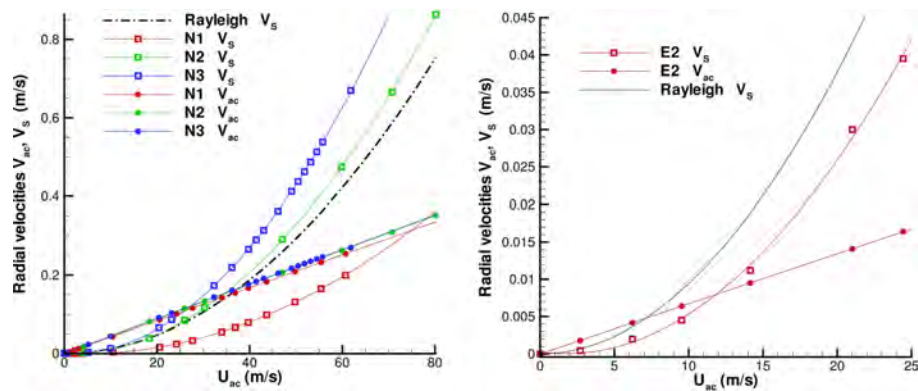


FIG. 19. (Color online) Maximum radial streaming (empty symbols) and acoustic (full symbols) velocities versus U_{ac} (maximum axial acoustic amplitude). Left: numerical results. Right: experimental results [using Eq. (6) for an estimate of V_{ac}].

increased. On the contrary, the radial acoustic velocity and both the axial and radial streaming velocities are very different from low level velocities.

- ¹L. Rayleigh, "On the circulation of air observed in Kundt's tubes, and on some allied acoustical problems," *Philos. Trans. R. Soc. London* **175**, 1–21 (1884).
- ²H. Schlichting, "Berechnung ebener periodischer grenzschichtströmungen (Calculation of plane periodic boundary layer streaming)," *Phys. Z.* **33**(8), 327–335 (1932).
- ³Q. Qi, "The effect of compressibility on acoustic streaming near a rigid boundary for a plane traveling wave," *J. Acoust. Soc. Am.* **94**, 1090–1098 (1993).
- ⁴N. Rott, "The influence of heat conduction on acoustic streaming," *Z. Angew. Math. Phys. (ZAMP)* **25**, 417–421 (1974).
- ⁵R. L. Smith and G. W. Swift, "Measuring second-order time-average pressure," *J. Acoust. Soc. Am.* **110**(2), 717–723 (2001).
- ⁶J. Sharpe, C. Greated, C. Gray, and D. M. Campbell, "The measurements of acoustic streaming using particle image velocimetry," *Acta Acust united Ac* **68**(2), 168–172 (1989).
- ⁷M. Thompson and A. Atchley, "Simultaneous measurement of acoustic and streaming velocities in a standing wave using laser Doppler anemometry," *J. Acoust. Soc. Am.* **117**, 1828–1838 (2005).
- ⁸S. Moreau, H. Bailliet, and J.-C. Valière, "Measurements of inner and outer streaming vortices in a standing waveguide using laser Doppler velocimetry," *J. Acoust. Soc. Am.* **123**, 640–647 (2008).
- ⁹I. Reyt, H. Bailliet, and J.-C. Valière, "Experimental investigation of acoustic streaming in a cylindrical waveguide up to high streaming Reynolds numbers," *J. Acoust. Soc. Am.* **135**, 27–37 (2014).
- ¹⁰I. Reyt, V. Daru, H. Bailliet, S. Moreau, J.-C. Valière, D. Baltean-Carlès, and C. Weisman, "Fast acoustic streaming in standing waves: Generation of an additional outer streaming cell," *J. Acoust. Soc. Am.* **134**, 1791–1801 (2013).
- ¹¹L. Menguy and J. Gilbert, "Non-linear acoustic streaming accompanying a plane stationary wave in a guide," *Acta Acust united Ac* **86**(2), 249–259 (2000).
- ¹²S. Boluriaan and P. J. Morris, "Numerical simulation of acoustic streaming in high amplitude standing wave," *9th AAIA/CEAS Aeroacoustics Conference*, Hilton Head, SC, AIAA Paper N° 2003-3152 (12–14 May 2003).
- ¹³V. Daru, D. Baltean-Carlès, and C. Weisman, "Inertial effects on non-linear acoustic streaming," *AIP Conf. Proc.* **1685**, 030003 (2015).
- ¹⁴M. Thompson, A. Atchley, and M. Maccarone, "Influences of a temperature gradient and fluid inertia on acoustic streaming in a standing wave," *J. Acoust. Soc. Am.* **117**, 1839–1849 (2005).
- ¹⁵V. Daru, D. Baltean-Carlès, C. Weisman, P. Debesse, and G. Gandikota, "Two-dimensional numerical simulations of nonlinear acoustic streaming in standing waves," *Wave Motion* **50**, 955–963 (2013).
- ¹⁶H. Bailliet, V. Gusev, R. Raspet, and R. A. Hiller, "Acoustic streaming in closed thermoacoustic devices," *J. Acoust. Soc. Am.* **110**, 1808–1821 (2001).
- ¹⁷N. Sugimoto, "Nonlinear theory for thermoacoustic waves in a narrow channel and pore subject to a temperature gradient," *J. Fluid Mech.* **797**, 765–801 (2016).

D. Baltean-Carlès, V. Daru, C. Weisman, S. Tabakova, H. Bailliet
" An unexpected balance between outer Rayleigh streaming sources ".
Journal of Fluid Mechanics 867, p. 985-1011 (2019).

An unexpected balance between outer Rayleigh streaming sources

D. Baltean-Carlès^{1,3}, V. Daru^{2,3}, C. Weisman^{1,3,†}, S. Tabakova⁴ and H. Bailliet⁵

¹Sorbonne-Université, Faculté des Sciences et Ingénierie, UFR d’Ingénierie, 4 Place Jussieu, 75005 Paris, France

²DynFluid Lab., ENSAM, 151 boulevard de l’hôpital, 75013, Paris, France

³LIMSI, CNRS, Université Paris-Saclay, Bât. 508, Rue John Von Neumann, Campus Universitaire, F-91405 Orsay CEDEX, France

⁴Institute of Mechanics, BAS, 4 acad. G. Bontchev, 1113 Sofia, Bulgaria

⁵Institut Pprime, CNRS - Université de Poitiers - ISAE-ENSMA, ENSIP, 6 Rue Marcel Doré, Bâtiment B17 - BP 633, 86022 Poitiers CEDEX, France

(Received 25 July 2018; revised 20 December 2018; accepted 4 February 2019)

Acoustic streaming generated by a plane standing wave between two infinite plates or inside a cylindrical tube is considered, under the isentropic flow assumption. A two-dimensional analysis is performed in the linear case of slow streaming motion, based on analytical formal solutions of separate problems, each associated with a specific source term (Reynolds stress term). In order to obtain these analytical solutions, a necessary geometrical hypothesis is that $(R/L)^2 \ll 1$, where R and L are the guide half-width (or radius) and length. The effect of the two source terms classically taken into account is quantified in order to derive the dependence of the maximum axial streaming velocity on the axis as a function of the ratio R/δ_v , where δ_v is the acoustic boundary layer thickness. The effect of two other source terms that are usually neglected, is then analysed. It is found that one of these terms can generate a counter-rotating streaming flow. While negligible for very narrow guides, this term can become important for some values of the aspect ratio L/R .

Key words: acoustics, boundary layers, low-Reynolds-number flows

1. Introduction

Rayleigh streaming generated by a plane standing wave between two infinite plates or inside a cylindrical tube is considered in the present paper. This acoustic wind is a mean flow generated by Reynolds stresses in the Stokes boundary layer formed along the solid walls of an acoustic guide (with no other mean flow and a no-slip boundary condition on the guide walls). It is usually referred to as Rayleigh streaming because Lord Rayleigh (1884) was the first to develop an analytical solution that describes the steady vortices generated in the core of the fluid in a wide channel formed by two

† Email address for correspondence: catherine.weisman@limsi.fr

infinite parallel adiabatic plates. These vortices, also called outer cells, are the main object of the present study.

Rayleigh–Nyborg–Westervelt (RNW) classical approach. Consider a standing plane acoustic wave of wavelength λ and angular frequency ω propagating in a wide channel formed by two infinite parallel plates. Assuming that the viscous penetration depth is small compared to the channel width and that they are both small compared to the wavelength, Rayleigh (1884) established the equations that govern the second-order velocity (responsible for the streaming motion), based on successive approximations. These second-order equations were obtained in the case of slow streaming motion (associated with low acoustic amplitudes) and therefore they are linear. The source terms that create the streaming motion are provided by the solution of the first-order problem (linear acoustics). In Rayleigh's solution the first-order motion is assumed to be divergence free in the viscous boundary layer. The resulting reference solution for the second-order velocity, far away from the guide wall is

$$\bar{u}_{Rayleigh} = -\frac{3U_{ac}^2}{16c_0} \sin(2kx) \left[1 - 3 \left(\frac{y}{R} \right)^2 \right], \quad (1.1)$$

$$\bar{v}_{Rayleigh} = -\frac{3U_{ac}^2}{8c_0} kR \cos(2kx) \left[\frac{y}{R} - \left(\frac{y}{R} \right)^3 \right], \quad (1.2)$$

with $\bar{u}_{Rayleigh}$ (respectively $\bar{v}_{Rayleigh}$) the axial (respectively vertical) component of the streaming velocity i.e. the time average over an acoustic period of the velocity component, U_{ac} the acoustic velocity amplitude at its antinode, c_0 the speed of sound, R the channel half-width, x the axial coordinate, k the complex wavenumber and y the distance from the guide axis. Rayleigh's analysis was applied to the case of a large cylindrical guide by Schuster & Matz (1940) yielding the following second-order velocity components:

$$\bar{u}_{Rayleigh} = -\frac{3U_{ac}^2}{8c_0} \sin(2kx) \left[1 - 2 \left(\frac{y}{R} \right)^2 \right], \quad (1.3)$$

$$\bar{v}_{Rayleigh} = -\frac{3U_{ac}^2}{8c_0} kR \cos(2kx) \left[\frac{y}{R} - \left(\frac{y}{R} \right)^3 \right], \quad (1.4)$$

where here R is the cylinder radius. In order to obtain these solutions, terms in $e^{-(R-y)/\delta_v}$ were neglected in the complete Rayleigh solution, with $\delta_v = \sqrt{2\nu/\omega}$ the acoustic viscous boundary layer thickness. Here ν is the gas kinematic viscosity, related to the gas dynamic viscosity μ by the classical relation $\nu = \mu/\rho_0$, where ρ_0 is the reference gas density. This is valid far enough from the wall. These expressions show the main characteristics of Rayleigh streaming: velocities are of second order in powers of acoustic Mach number $M = U_{ac}/c_0$, with counter-rotating vortices that span $\lambda/4$ in the axial direction. The transverse streaming velocity is much smaller and has a $\lambda/4$ spatial phase shift with the axial streaming velocity.

Later Westervelt (1953) and Nyborg (1953) improved this analytical model by proposing a complete solution to the problem considered by Rayleigh. This solution is based on a vorticity equation and there is no assumption on the divergence of the acoustic velocity. The theoretical description issued from the works of Rayleigh, Westervelt and Nyborg is usually associated with the so-called RNW streaming theory Lighthill (1978).

Sources of streaming. The analytical studies mentioned above (and most of the subsequent ones) are based on the same process of derivation of the streaming velocity: write fundamental laws of fluid motion, use a perturbation method with asymptotic expansions and then time average. As discussed by Lighthill (1978), this process leads to an equation of the form

$$\mu \nabla^2 \bar{u} = -\bar{F} + \nabla \bar{p}, \quad (1.5)$$

where \bar{p} is the second-order pressure and \bar{F} is a product of first-order quantities and their derivatives. The source terms composing \bar{F} are based on acoustic quantities. They are also referred to as Reynolds stresses.

In all studies mentioned above, the source terms that appear in the transverse momentum equation are neglected, as discussed by Lighthill (1978). The averaged acoustic velocity source term \bar{F} (Reynolds stresses) is approximated as the sum of the two largest source terms, that are associated with the axial momentum equation. The variation of these two source terms with the radius was analysed analytically in annular resonators, in the case of a pure travelling wave by Amari, Gusev & Joly (2003). An investigation of the streaming flow generation through the analysis of the contribution of each source term was conducted recently by Paridaens, Koudri & Jebali Jerbi (2013), in the case of a thermoacoustic system. Again, only the two dominant Reynolds stress terms were considered.

One of the goals of the present study is to show that one of the terms that compose \bar{F} and that is classically neglected in the analysis of Rayleigh streaming can be responsible for drastic change of acoustic streaming patterns within a given range of guide geometry. It will be shown that it can be the case even in the linear regime. A modified analytical expression for the streaming velocity is proposed, that takes into account the other two acoustic source terms associated with the transverse component of the momentum equation. This represents an improved approximation for the Rayleigh problem. This enriched solution exhibits an unexpected balance between outer Rayleigh streaming sources.

Beyond RNW streaming. As stated above, RNW analysis concerns streaming in wide channels outside the viscous boundary layers that results in large counter-rotating vortices usually referred to as outer vortices. These vortices are actually generated by a driving mean flow taking place inside the viscous boundary layers, associated with slender counter-rotating vortices usually referred to as inner streaming vortices. A sketch of inner and outer streaming cells, as well as transverse and axial profiles of the axial streaming velocity are shown in figure 1, in the case of a $\lambda/2$ resonator. Schlichting (1932) first described the inner streaming vortices, under the hypothesis of incompressible flow. Reviews of theoretical investigations for inner and outer streaming were proposed by Nyborg (1965) and Zaremba (1971). As shown by figure 1, the limit between inner and outer streaming cells is generally considered to be equal to $3\delta_v$ from the wall. In the present study the evolution of this limit with the dimensions of the channel will be briefly addressed.

Rott (1974) improved the description of outer streaming by taking into account thermal effects and Qi (1993) included the fluid compressibility and temperature effects to improve the description of inner streaming. Investigations of streaming in channels of arbitrary width with a mean temperature gradient were performed by Waxler (2001) and Bailliet *et al.* (2001) in the context of thermoacoustic applications where heat transport associated with the streaming flow is an important mechanism that may limit the efficiency of the systems. Sugimoto (2016) obtained a nonlinear

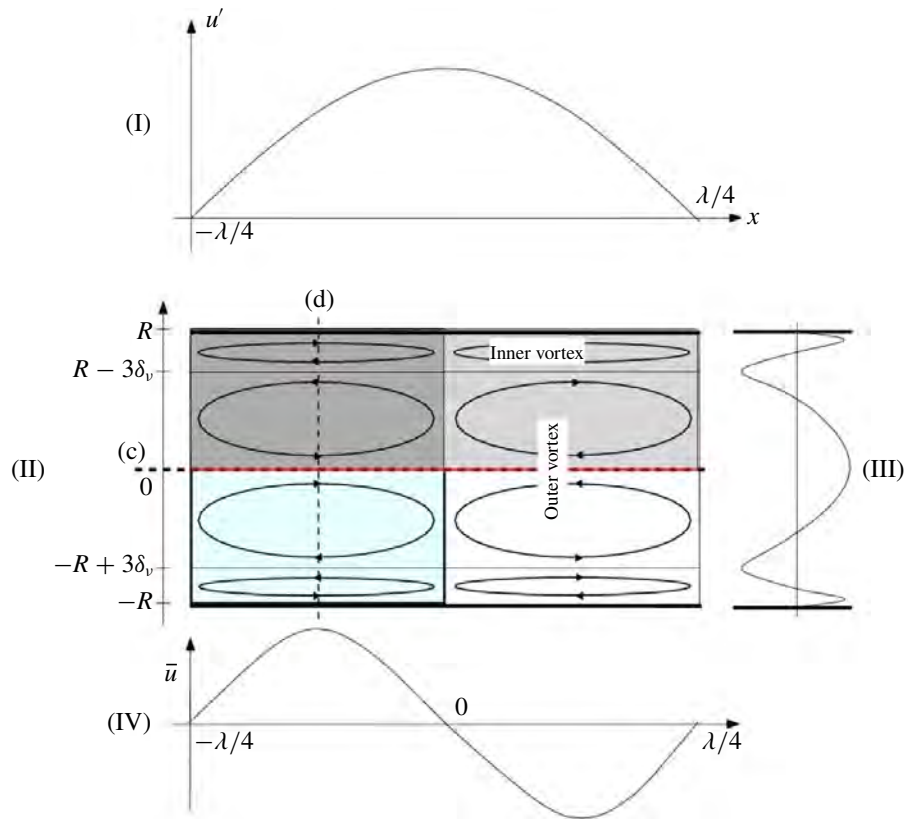


FIGURE 1. (Colour online) RNW theory. (II) sketch of inner and outer streaming cells in the case of two infinite parallel plates, showing lines (c) and (d). (I) axial acoustic velocity u' profile along line (c). (III) axial streaming velocity \bar{u} profile along line (d). (IV) axial streaming velocity \bar{u} profile along line (c).

thermoacoustic wave equation inside narrow channels and the associated streaming flow results can be applied to pore modelling in thermoacoustic engines.

Also in thermoacoustics the overall mass transport velocity is usually considered instead of the time-averaged velocity:

$$\bar{\mathbf{u}}^M = \frac{\rho \bar{\mathbf{u}}}{\bar{\rho}}. \quad (1.6)$$

Here the previously considered \bar{u} velocity is called Eulerian streaming velocity. Hamilton, Ilinskii & Zabolotskaya (2003a), Olson & Swift (1997) adopted a Lagrangian approach, considering the density weighted average velocity $\bar{\mathbf{u}}^M$, also referred to as the Favre average (Favre 1965), because it is responsible for effective mass and heat transport. Hamilton *et al.* (2003a), Hamilton, Ilinskii & Zabolotskaya (2003b) proposed an analytical solution for the average mass transport velocity with or without temperature effects. They studied the influence of the channel width on the relative size of the inner and outer streaming vortices. Most of the present study is conducted following an Eulerian approach but the consequences of the results presented thereafter will also be briefly discussed following a Lagrangian approach.

Thermoacoustic applications which require large amplitude acoustic waves also led the authors to reconsider the hypothesis of slow streaming that is one of the bases of RNW streaming, as discussed in the extensive review proposed by Boluriaan & Morris (2003). In the last decades experimental studies (Thompson, Atchley & Maccarone

2004; Moreau, Bailliet & Valière 2008) and numerical studies (Menguy & Gilbert 2000a; Daru *et al.* 2013; Reyt *et al.* 2013) on acoustic streaming from slow to fast regimes were performed (the fast regime is associated with high amplitude acoustics). These studies exhibited streaming behaviour departing from the RNW theory: in the fast regime the dependence of the streaming velocity on the acoustic velocity is no longer parabolic and new streaming cells can emerge near the guide axis. In the slow regime, it was found that the axial streaming velocity along the axis, when normalized by Rayleigh's solution, is a linear function of the ratio δ_v/R (Daru *et al.* 2017a). Another goal of the present study is to quantify further this linear function, and also to show a dependency on the aspect ratio (length over width or length over radius) of the wave guide.

The hypotheses are listed in § 2, along with a description of the geometries under study. Section 3 then focuses on the rectangular case. The classical Rayleigh solution of the (first order) acoustic problem is described (§ 3.1) and the source terms for the streaming flow are deduced (§ 3.2). An analysis of the influence of each of the source terms is conducted and their effect on streaming flow patterns is highlighted (§§ 3.2.1–3.2.6). The effect of both Reynolds stress source terms, classically considered, is shown first, and then the effects of the third and fourth source terms, classically neglected, are also discussed.

The influence of the aspect ratio of the channel geometry on the streaming velocity is quantified. The results show that for specific values of the aspect ratio new streaming counter-rotating cells appear next to the guide axis. Then other characteristics of the streaming flow are examined in §§ 3.2.7–3.2.9: slip velocity, mass transport velocity, transverse component of streaming velocity. The axisymmetric case is briefly addressed in § 4.

2. Position of the problem

In the present approach, the discussed geometry is valid for both a cylindrical acoustic guide and acoustic flow between two infinite parallel plates. We consider a rectangular (or cylindrical) channel, of length L , and half-width (or radius) R , filled with a perfect gas of density ρ_0 and pressure p_0 . The sound velocity in the ideal gas is $c_0 = \sqrt{\gamma p_0 / \rho_0}$, γ being the specific heat ratio ($\gamma = 1.4$ for air). We use a coordinate system (x, y) (or (x, r)) with the origin located at the centre of the channel, that is $-L/2 \leq x \leq L/2$, $-R \leq y \leq R$ (or $0 \leq r \leq R$).

By exploiting the symmetry of the problem, only the upper half-channel $0 \leq y \leq R$ is considered in the plane case. The symbolic computational software Mathematica (Wolfram 2018) is used to solve the equations throughout this study.

Throughout this work, the angular frequency is always considered to be equal to ω_0 , the angular frequency corresponding to the acoustic standing wave resonating at its first mode along x (so-called $\lambda/2$ mode), in the case of a non-viscous gas ($\omega_0 = \pi c_0 / L$).

It is assumed that an acoustic wave propagates laminarly along the x axis of the guide. There is no mean flow apart from acoustic streaming. A main hypothesis is that the wave is plane. More precisely the condition that only plane modes propagate is that the working frequency is lower than the first mode cutoff frequency. In cylindrical guides the cutoff frequency is $f_{c(1,0)} = 1.84c_0/2\pi R$ (e.g. Pierce 1989) and the condition of a plane wave is equivalent to $\lambda > 2\pi/1.84R$. In the case of a half-wavelength guide, the plane wave condition becomes $L/R > 1.7$. For rectangular channels the cutoff frequency is $c_0/2R$ or equivalently $L/R > 1$.

Another important hypothesis is that the effect of viscosity is assumed to be concentrated in the near wall region, that is, volume viscosity is neglected because the real part of the wavenumber associated with volume viscosity is negligible compared to the one associated with the viscous boundary layer. This hypothesis is valid if $1/(ReSh) \ll 1$, where $Re = \rho_0 c_0^2 / (\mu \omega)$ is the acoustic Reynolds number and $Sh = \delta_v / R$ is the Shear number (Menguy & Gilbert 2000b).

We also make the assumption of an isentropic flow, in order to exclude thermal effects on streaming that are not within the scope of this work. Under these hypotheses, acoustic pressure is independent of y , and, as a consequence of isentropy, so is acoustic density.

Finally, several hypotheses on streaming flow are imposed. Only channels with moderate to large width values ($R/\delta_v \gtrsim 6$) are considered here in which outer streaming vortices do exist (Bailliet *et al.* 2001; Hamilton *et al.* 2003a). Another hypothesis is that $(R/L)^2 \ll 1$ which means that momentum diffusion in the axial direction is negligible with respect to momentum diffusion in the transverse direction. Moreover the present study concerns the slow streaming regime, in which the streaming flow equations are linear. This hypothesis is valid if inertial effects are negligible, which is usually related to small values of the nonlinear Reynolds number $Re_{NL} = (M/Sh)^2 \ll 1$ (Menguy & Gilbert 2000b).

3. Flow between two parallel plates

3.1. Acoustics

Let us note u' and v' the axial and vertical components of the acoustic velocity, and $\rho' = \rho - \rho_0$, $p' = p - p_0$ the associated density and pressure fluctuations. Using the hypothesis $\partial^2 u'/\partial x^2 \ll \partial^2 u'/\partial y^2$, the linearized equations governing acoustics are

$$\frac{\partial \rho'}{\partial t} + \rho_0 \left(\frac{\partial u'}{\partial x} + \frac{\partial v'}{\partial y} \right) = 0 \quad (3.1a)$$

$$\rho_0 \frac{\partial u'}{\partial t} + \frac{\partial p'}{\partial x} = \mu \frac{\partial^2 u'}{\partial y^2} \quad (3.1b)$$

$$\frac{\partial p'}{\partial y} = 0. \quad (3.1c)$$

Using the assumption of isentropic flow, we have $p' = c_0^2 \rho'$.

The following change of variables is introduced

$$\hat{y} = y/\delta_v, \quad \hat{x} = x/L, \quad \hat{t} = t/T, \quad \hat{R} = R/\delta_v, \quad \hat{L} = L/\delta_v, \quad (3.2a-e)$$

T being the acoustic time period so that $L/T = (1/2)c_0$. The half-channel is then described by $-1/2 \leq \hat{x} \leq 1/2$, $0 \leq \hat{y} \leq \hat{R}$ and the dependency on \hat{x} is of $e^{i\pi\hat{x}}$ form. Let us note that this is only a convenient change of variables that allows us to work with non-dimensional parameters \hat{R} and \hat{L} instead of dimensional values of R and L . Velocity, pressure and density are left in dimensional units.

The boundary and symmetry conditions for u' and v' with respect to \hat{y} are

$$u' = 0 \quad \text{at } \hat{y} = \hat{R}; \quad \frac{\partial u'}{\partial \hat{y}} = 0 \quad \text{at } \hat{y} = 0, \quad (3.3a,b)$$

$$v' = 0 \quad \text{at } \hat{y} = 0 \text{ and } \hat{y} = \hat{R}. \quad (3.3c)$$

Following Rayleigh (1884), the axial acoustic velocity is expressed as

$$u'(\hat{x}, \hat{y}, \hat{t}) = U_{ac} \cos(\pi\hat{x}) [(-1 + e^{\hat{y}-\hat{R}} \cos(\hat{R} - \hat{y})) \cos(2\pi\hat{t}) + e^{\hat{y}-\hat{R}} \sin(\hat{R} - \hat{y}) \sin(2\pi\hat{t})], \quad (3.4)$$

where U_{ac} is the acoustic amplitude at the velocity antinode.

Using the hypothesis that ρ' depends on \hat{x} and \hat{t} only, together with the boundary conditions, equation (3.1a) is integrated with respect to \hat{y} to obtain the vertical acoustic velocity component

$$v'(\hat{x}, \hat{y}, \hat{t}) = -\frac{\pi U_{ac}}{2\hat{R}} \frac{1}{\hat{L}} \sin(\pi\hat{x}) [\hat{y}(\cos(2\pi\hat{t}) + \sin(2\pi\hat{t})) + \hat{R}e^{\hat{y}-\hat{R}} (\sin(\hat{R} - \hat{y} - 2\pi\hat{t}) - \cos(\hat{R} - \hat{y} - 2\pi\hat{t})) + e^{-\hat{R}}(\hat{R} - \hat{y})(\cos(\hat{R} - 2\pi\hat{t}) - \sin(\hat{R} - 2\pi\hat{t}))]. \quad (3.5)$$

Finally the density fluctuation ρ' is obtained by integrating (3.1a) with respect to time

$$\rho'(\hat{x}, \hat{t}) = \frac{\rho_0 U_{ac}}{2c_0 \hat{R}} \sin(\pi\hat{x}) [(1 - 2\hat{R}) \sin(2\pi\hat{t}) - \cos(2\pi\hat{t}) + e^{-\hat{R}}(\cos(\hat{R} - 2\pi\hat{t}) + \sin(\hat{R} - 2\pi\hat{t}))]. \quad (3.6)$$

3.2. Streaming flow

The averaged equations are derived from the Navier–Stokes equations with each variable f divided into a fluctuating, periodic, component f' , and a steady component \bar{f} (corresponding to the streaming flow) according to

$$f = \bar{f} + f'. \quad (3.7)$$

where the overline denotes the average operator in time over one period. For any two variables f and g

$$\overline{fg} = \bar{f}\bar{g} + \overline{f'g'}. \quad (3.8)$$

Using the hypotheses that $\partial^2/\partial x^2 \ll \partial^2/\partial y^2$ and $Re_{NL} = (M/Sh)^2 \ll 1$, the Navier–Stokes equations are averaged in time over one period, linearized and simplified as

$$\begin{cases} \rho_0 \left(\frac{\partial \bar{u}}{\partial x} + \frac{\partial \bar{v}}{\partial y} \right) = -\frac{\partial}{\partial x}(\overline{\rho' u'}) - \frac{\partial}{\partial y}(\overline{\rho' v'}) \\ \mu \frac{\partial^2 \bar{u}}{\partial y^2} = \frac{\partial \bar{p}}{\partial x} + \rho_0 \frac{\partial}{\partial x}(\overline{u' u'}) + \rho_0 \frac{\partial}{\partial y}(\overline{u' v'}) \\ \mu \frac{\partial^2 \bar{v}}{\partial y^2} = \frac{\partial \bar{p}}{\partial y} + \rho_0 \frac{\partial}{\partial x}(\overline{u' v'}) + \rho_0 \frac{\partial}{\partial y}(\overline{v' v'}). \end{cases} \quad (3.9)$$

where \bar{u} , \bar{v} and \bar{p} are the averaged velocity components and pressure.

Making the same change of variables as in § 3.1, equations (3.9) above are rewritten as

$$\begin{cases} \rho_0 \left(\frac{\partial \bar{u}}{\partial \hat{x}} + \hat{L} \frac{\partial \bar{v}}{\partial \hat{y}} \right) = -\frac{\partial}{\partial \hat{x}}(\overline{\rho' u'}) - \hat{L} \frac{\partial}{\partial \hat{y}}(\overline{\rho' v'}) \\ \rho_0 \frac{\pi}{2} c_0 \frac{\partial^2 \bar{u}}{\partial \hat{y}^2} = \frac{\partial \bar{p}}{\partial \hat{x}} + \rho_0 \frac{\partial}{\partial \hat{x}}(\overline{u' u'}) + \rho_0 \hat{L} \frac{\partial}{\partial \hat{y}}(\overline{u' v'}). \\ \rho_0 \frac{\pi}{2} c_0 \frac{\partial^2 \bar{v}}{\partial \hat{y}^2} = \hat{L} \frac{\partial \bar{p}}{\partial \hat{y}} + \rho_0 \frac{\partial}{\partial \hat{x}}(\overline{u' v'}) + \rho_0 \hat{L} \frac{\partial}{\partial \hat{y}}(\overline{v' v'}). \end{cases} \quad (3.10)$$

The boundary conditions for \bar{u} and \bar{v} are

$$\bar{u} = 0 \quad \text{at } \hat{y} = \hat{R}; \quad \frac{\partial \bar{u}}{\partial \hat{y}} = 0 \quad \text{at } \hat{y} = 0, \quad (3.11a,b)$$

$$\bar{v} = 0 \quad \text{at } \hat{y} = 0 \text{ and } \hat{y} = \hat{R}, \quad (3.11c)$$

$$\int_0^{\hat{R}} \bar{u} d\hat{y} = 0. \quad (3.11d)$$

The third condition in (3.11) is obtained by integrating the continuity equation in (3.10) over the half-width of the channel.

The expression of the five averaged products (Reynolds stresses) on the right-hand side of (3.10) are obtained from (3.4), (3.5) and (3.6):

$$\begin{aligned} \overline{\rho' u'} &= \frac{\rho_0 U_{ac}^2}{8c_0 \hat{R}} \sin(2\pi\hat{x}) \{1 - e^{\hat{y}-\hat{R}}(\cos(\hat{R}-\hat{y}) + (2\hat{R}-1)\sin(\hat{R}-\hat{y})) \\ &\quad + e^{\hat{y}-2\hat{R}}(\cos \hat{y} + \sin(\hat{y})) - e^{-\hat{R}}(\cos(\hat{R}) + \sin(\hat{R}))\}, \end{aligned} \quad (3.12)$$

$$\begin{aligned} \overline{\rho' v'} &= \frac{\pi \rho_0 U_{ac}^2}{4c_0 \hat{R}} \frac{1}{\hat{L}} \sin^2(\pi\hat{x}) \{\hat{y} + e^{\hat{y}-\hat{R}}(-\hat{R}\cos(\hat{R}-\hat{y}) + \sin(\hat{R}-\hat{y})(1-\hat{R})) \\ &\quad + e^{\hat{y}-2\hat{R}} \sin \hat{y} + e^{-\hat{R}}((\hat{R}-\hat{y})\cos \hat{R} + (\hat{R}-\hat{y}-1)\sin \hat{R})\}, \end{aligned} \quad (3.13)$$

$$\overline{u' u'} = \frac{1}{2} U_{ac}^2 \cos^2(\pi\hat{x}) (1 + e^{2(\hat{y}-\hat{R})} - 2e^{\hat{y}-\hat{R}} \cos(\hat{R}-\hat{y})), \quad (3.14)$$

$$\begin{aligned} \overline{u' v'} &= \frac{\pi U_{ac}^2}{8\hat{R}\hat{L}} \sin(2\pi\hat{x}) \{\hat{y} + e^{\hat{y}-\hat{R}}(-(\hat{R}+\hat{y})\cos(\hat{R}-\hat{y}) + (\hat{R}-\hat{y})\sin(\hat{R}-\hat{y})) \\ &\quad + \hat{R}e^{2(\hat{y}-\hat{R})} + e^{\hat{y}-2\hat{R}}((\hat{y}-\hat{R})\cos \hat{y} + (\hat{R}-\hat{y})\sin \hat{y}) \\ &\quad + e^{-\hat{R}}((\hat{R}-\hat{y})\cos \hat{R} - (\hat{R}-\hat{y})\sin \hat{R})\}, \end{aligned} \quad (3.15)$$

$$\begin{aligned} \overline{v' v'} &= \frac{\pi U_{ac}^2}{\hat{L}^2} \frac{1}{4\hat{R}^2} \sin^2(\pi\hat{x}) \{\hat{y}^2 - 2e^{\hat{y}-\hat{R}}\hat{y}\hat{R}\cos(\hat{R}-\hat{y}) + e^{2(\hat{y}-\hat{R})}\hat{R}^2 \\ &\quad + 2\hat{R}e^{\hat{y}-2\hat{R}}(\hat{y}-\hat{R})\cos \hat{y} + 2e^{-\hat{R}}\hat{y}(\hat{y}+\hat{R})\cos \hat{R} + e^{-2\hat{R}}(\hat{R}-\hat{y})^2\}. \end{aligned} \quad (3.16)$$

Under the hypothesis $\hat{R} \gtrsim 6$, terms of the same magnitude as $e^{-\hat{R}}$ or smaller can be neglected in the previous expressions of the averaged products. Nevertheless, all symbolic calculations were performed using the full expressions.

Following Westervelt (1953), we take the curl of the momentum equations, which eliminates pressure, and use the assumption $\partial \bar{v}/L \partial \hat{x} \ll \partial \bar{u}/\delta_v \partial \hat{y}$, to obtain

$$-\frac{\pi}{2} c_0 \hat{L} \frac{\partial^3 \bar{u}}{\partial \hat{y}^3} = -\hat{L} \frac{\partial^2(\bar{u}' \bar{u}')}{\partial \hat{x} \partial \hat{y}} - \hat{L}^2 \frac{\partial^2(\bar{u}' \bar{v}')}{\partial \hat{y}^2} + \frac{\partial^2(\bar{u}' \bar{v}')}{\partial \hat{x}^2} + \hat{L} \frac{\partial^2(\bar{v}' \bar{v}')}{\partial \hat{x} \partial \hat{y}}. \quad (3.17)$$

Classical studies (e.g. Rayleigh 1884, Westervelt 1953, Bailliet *et al.* 2001, Hamilton *et al.* 2003a) always consider an added approximation in which the last two source terms on the right-hand side of (3.17) are negligible. Neglecting these two terms was justified by an analysis of the orders of magnitude, based on the variations in the

viscous boundary layer. The usual assumptions are $\partial/\partial x \propto 1/\lambda \propto 1/L$ and $\partial/\partial y \propto 1/\delta_v$, so that $\partial/\partial \hat{x} \propto 1$ and $\partial/\partial \hat{y} \propto 1$. Therefore equations (3.14), (3.15), (3.16) yield

$$\hat{L} \frac{\partial^2(\bar{u}'\bar{u}')}{\partial \hat{x}\partial \hat{y}} \propto \hat{L}U_{ac}^2, \quad \hat{L}^2 \frac{\partial^2(\bar{u}'\bar{v}')}{\partial \hat{y}^2} \propto \hat{L}U_{ac}^2, \quad \frac{\partial^2(\bar{u}'\bar{v}')}{\partial \hat{x}^2} \propto \frac{U_{ac}^2}{\hat{L}}, \quad \hat{L} \frac{\partial^2(\bar{v}'\bar{v}')}{\partial \hat{x}\partial \hat{y}} \propto \frac{U_{ac}^2}{\hat{L}}. \quad (3.18a-d)$$

It follows that the third and fourth terms are respectively $1/\hat{L}^2$ smaller than the first two terms.

In his analysis, Lighthill (1978) states that making a decision to keep or neglect a term should be based on an order of magnitude analysis and not a perturbation expansion alone. In the present work it will be shown that even an order of magnitude analysis on the acoustic source terms is not sufficient to neglect a term. This is because the different terms in (3.17) do not have the same \hat{y} dependence; some are proportional to \hat{y} , others to \hat{y}^2 and others do not have any \hat{y} dependence so that the successive integrations over \hat{y} needed to obtain \bar{u} from (3.17) together with the boundary conditions will change the balance between the effects of these different source terms. Even though they do not have the same order of magnitude, the source terms can have effects of the same order on the streaming velocity. Therefore, they will all be considered. (The change in balance between the source terms can take place independently of the fact that $\partial \bar{v}/L\partial \hat{x} \ll \partial \bar{u}/\delta_v \partial \hat{y}$, which is given by the fundamental equations for streaming (3.9). Thus the process of keeping all the terms on the right-hand side of (3.17) is consistent with neglecting the \bar{v} term on its left-hand side.)

In order to analyse in detail the effect of each of the source terms, we will consider separately the four problems linked to each source term. We will normalize the solutions with Rayleigh's solution on the axis $\bar{u}_R = -(3/16)U_{ac}^2/c_0 \sin(2\pi\hat{x})$. The solution of problem i , associated with the i th source term, will be denoted by \bar{u}_i , $i = 1, 2, 3, 4$. In the following, for the sake of simplicity, the expressions for each solution \bar{u}_i will be presented in an approximated form, in which terms of the same magnitude as $e^{-\hat{R}}$ or smaller will be neglected with respect to terms of order $1/\hat{R}^n$, for $n \in \mathbb{N}$. However the symbolic computations are still performed using the full expressions.

3.2.1. Problem 1: first source term

When reducing equation (3.17) by taking into account the first source term only, the equation to be solved is

$$\frac{\pi}{2} c_0 \frac{\partial^3 \bar{u}_1}{\partial \hat{y}^3} = \frac{\partial^2(\bar{u}'\bar{u}')}{\partial \hat{x}\partial \hat{y}}, \quad (3.19)$$

with boundary conditions (3.11a,b)–(3.11d), for \bar{u}_1 . Integrating equation (3.19) and using the boundary conditions yields the following simplified solution:

$$\begin{aligned} \bar{u}_1(\hat{x}, \hat{y}) = & -\frac{U_{ac}^2}{16c_0} \sin(2\pi\hat{x}) \left\{ 15\frac{\hat{y}^2}{\hat{R}^3} - \frac{15}{\hat{R}} - 6\frac{\hat{y}^2}{\hat{R}^2} \right. \\ & \left. + 2(1 + 2e^{2(\hat{y}-\hat{R})} + 8e^{\hat{y}-\hat{R}} \sin(\hat{R} - \hat{y})) \right\}. \end{aligned} \quad (3.20)$$

Along the axis, by normalizing with Rayleigh's solution and neglecting smaller terms, we obtain at $O(1/\hat{R})$:

$$\frac{\bar{u}_1(\hat{x}, 0)}{\bar{u}_R} = \frac{2}{3} - \frac{5}{\hat{R}}. \quad (3.21)$$

The second-order pressure gradient can also be obtained, and as expected is independent of \hat{y} . It is given by

$$\frac{d\bar{p}_1}{d\hat{x}} = \frac{\rho_0 \pi U_{ac}^2}{16} \sin(2\pi\hat{x}) \left(8 + \frac{6}{\hat{R}^2} - \frac{15}{\hat{R}^3} \right). \quad (3.22)$$

3.2.2. Problem 2: second source term

The equation to be solved for the acoustic streaming issued from the second source term in equation (3.17) is

$$\frac{\pi}{2} c_0 \frac{\partial^3 \bar{u}_2}{\partial \hat{y}^3} = \hat{L} \frac{\partial^2 (\bar{u}' v')}{\partial \hat{y}^2}, \quad (3.23)$$

with boundary conditions (3.11a,b)–(3.11d) for \bar{u}_2 . Integrating (3.23) gives the following simplified expression for \bar{u}_2

$$\begin{aligned} \bar{u}_2(\hat{x}, \hat{y}) = & -\frac{U_{ac}^2}{32c_0} \sin(2\pi\hat{x}) \left\{ \frac{1}{\hat{R}} + 3\frac{\hat{y}^2}{\hat{R}^3} (1 - 2\hat{R}) + 2(1 - 2e^{2(\hat{y}-\hat{R})}) \right. \\ & \left. + \frac{4}{\hat{R}} e^{\hat{y}-\hat{R}} [(-1 + 2\hat{y}) \cos(\hat{R} - \hat{y}) + (1 - 2\hat{R}) \sin(\hat{R} - \hat{y})] \right\}. \end{aligned} \quad (3.24)$$

Along the axis, we obtain at the order $O(1/\hat{R})$:

$$\frac{\bar{u}_2(\hat{x}, 0)}{\bar{u}_R} = \frac{1}{3} + \frac{1}{6\hat{R}}, \quad (3.25)$$

and the corresponding pressure gradient is

$$\frac{d\bar{p}_2}{d\hat{x}} = -\frac{\rho_0 \pi U_{ac}^2}{32} \sin(2\pi\hat{x}) \left(\frac{4}{\hat{R}} - \frac{6}{\hat{R}^2} + \frac{3}{\hat{R}^3} \right). \quad (3.26)$$

3.2.3. Analysis of the effect of the first two source terms

It is interesting to analyse the right-hand side of the axial component of the momentum equation in (3.10). For the first problem, the right-hand side is $RHS_1 = \partial \bar{p}_1 / \partial \hat{x} + \rho_0 (\partial / \partial \hat{x})(\bar{u}' \bar{u}')$. For the second problem, the right hand side is $RHS_2 = \partial \bar{p}_2 / \partial \hat{x} + \rho_0 \hat{L} (\partial / \partial \hat{y})(\bar{u}' \bar{v}')$.

The right-hand sides are therefore composed of two terms, a pressure gradient term and a Reynolds stress term. Figure 2 shows, for $\hat{R} = 20$, at $\hat{x} = -1/4$, the transverse profile of both terms composing RHS_1 figures 2(a) and RHS_2 2(b), normalized by $\rho_0 U_{ac}^2$. Comparing figure 2(a,b) shows that the terms in RHS_2 are much smaller than in RHS_1 , and also that the pressure gradient and Reynolds stress terms almost compensate each other in the core of the guide, for both problems 1 and 2. The pressure gradients of problems 1 and 2 have opposite signs, and also $d\bar{p}_2/d\hat{x}$ is much

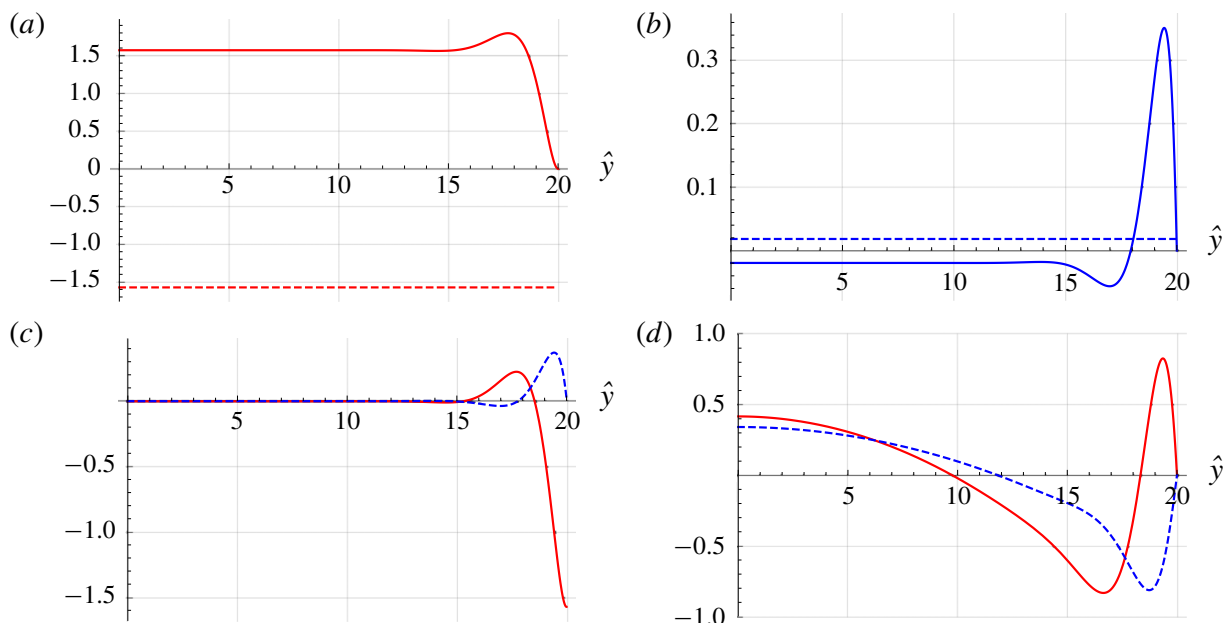


FIGURE 2. (Colour online) Variation with \hat{y} , for $\hat{x} = -1/4$ and $\hat{R} = 20$ of (a) Reynolds stresses term (red solid line) and normalized pressure gradient term (red dashed line) in RHS_1 , (b) Reynolds stresses term (blue solid line) and normalized pressure gradient term (blue dashed line) in RHS_2 , (c) total normalized RHS_1 (red solid line) and RHS_2 (blue dashed line), (d) normalized axial streaming velocity \bar{u}_1/\bar{u}_R (red solid line) and \bar{u}_2/\bar{u}_R (blue dashed line).

smaller than $d\bar{p}_1/d\hat{x}$, with $d\bar{p}_2/d\hat{x} \rightarrow 0$ when \hat{R} becomes large (refer to equations (3.22) and (3.26)).

Figure 2(c) shows the transverse profile of the complete right-hand sides RHS_1 and RHS_2 , normalized by $\rho_0 U_{ac}^2$, again for $\hat{R} = 20$, at $\hat{x} = -1/4$. This figure shows that the two complete right-hand sides are of the same order, with significant values only near the wall. This stresses the fact that streaming is generated only by viscous boundary layer effects. The outer streaming is created from momentum diffusion of the velocity created near the guide wall, and not from pressure gradient effects. As stated by Menguy & Gilbert (2000a) (p. 253): pressure is created directly by the acoustic wave, and not by the mean flow. Outer streaming flow can thus be considered as a driven flow, similar to a Couette flow (see the driven cavity analogy developed in Daru *et al.* (2017b)).

The resulting normalized axial streaming velocity transverse profiles are plotted on figure 2(d). The following observation can be made: the first problem is responsible for the inner streaming (Schlichting streaming), while the second problem only contributes to the outer streaming (Rayleigh streaming), as also noticed in Paridaens *et al.* (2013). This is related to the fact that RHS_2 vanishes for $\hat{y} = \hat{R}$, while RHS_1 does not, as can be seen in figure 2(c).

Let us now consider the superposition of problems 1 and 2 considered above, which is usually assumed in the literature to give the total axial streaming velocity $\bar{u}_{1+2} = \bar{u}_1 + \bar{u}_2$. Figure 3 shows the normalized axial streaming velocity transverse profiles \bar{u}_1 , \bar{u}_2 and \bar{u}_{1+2} . This figure also illustrates that the first problem is responsible for the inner streaming, while the second problem only contributes to the outer streaming: only \bar{u}_1 takes a positive value near the wall, while \bar{u}_2 remains negative.

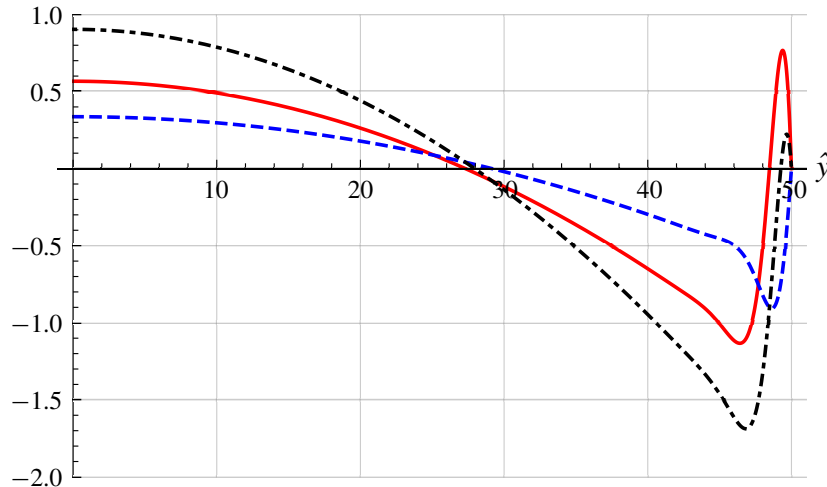


FIGURE 3. (Colour online) Axial streaming velocities $\bar{u}_1(-1/4, \hat{y})/\bar{u}_R$ (red solid line), $\bar{u}_2(-1/4, \hat{y})/\bar{u}_R$ (blue dashed line) and $\bar{u}_{1+2}(-1/4, \hat{y})/\bar{u}_R$ (black dot-dashed line). $\hat{R} = 50$.

The expression for \bar{u}_{1+2} obtained on the axis is approximated as:

$$\frac{\bar{u}_{1+2}(\hat{x}, 0)}{\bar{u}_R} = 1 - \frac{29}{6} \frac{1}{\hat{R}}. \quad (3.27)$$

For large guides ($\hat{R} \gg 1$, but still $(\hat{R}/\hat{L})^2 \ll 1$), we thus recover Rayleigh's solution. As noticed by Lighthill (1978) and as shown by equations (3.21) and (3.25), the contributions of the first and second source terms in Rayleigh's solution are respectively $2/3$ and $1/3$. Equation (3.27) also shows a linear variation with $1/\hat{R}$, which is not negligible for moderate values of \hat{R} . The first source term is the main contributor to this dependency: -5 in (3.21) versus $1/6$ in (3.25).

The total axial pressure gradient is

$$\frac{d\bar{p}_{1+2}}{d\hat{x}} = \frac{\rho_0 \pi U_{ac}^2}{2} \sin(2\pi\hat{x}) \left(1 - \frac{1}{8\hat{R}} + \frac{3}{16\hat{R}^2} - \frac{27}{32\hat{R}^3} \right). \quad (3.28)$$

It follows that, for large values of \hat{R}

$$\frac{d\bar{p}_{1+2}}{d\hat{x}} \simeq \frac{d\bar{p}_1}{d\hat{x}} = \frac{\rho_0 \pi U_{ac}^2}{2} \sin(2\pi\hat{x}). \quad (3.29)$$

Integrating equation (3.29) with respect to \hat{x} yields

$$\bar{p}_{1+2} \simeq \bar{p}_1 = p_0 - \frac{\rho_0 U_{ac}^2}{4} \cos(2\pi\hat{x}). \quad (3.30)$$

When scaling $\bar{p}_{1+2} - p_0$ by $(\gamma/4)p_0(U_{ac}/c_0)^2$, we recover the theoretical result for the dimensionless hydrodynamic streaming pressure known in the literature $P_{2s} = -\cos(2\pi\hat{x})$ (e.g. Menguy & Gilbert 2000a).

3.2.4. Problem 3: third source term

We now consider the third source term, yielding the following equation

$$\frac{\pi}{2} c_0 \hat{L} \frac{\partial^3 \bar{u}_3}{\partial \hat{y}^3} = -\frac{\partial^2 (\bar{u}' \bar{v}')}{\partial \hat{x}^2}, \quad (3.31)$$

with boundary conditions (3.11a,b)–(3.11d) for \bar{u}_3 . Integrating (3.31) gives the simplified solution

$$\begin{aligned} \bar{u}_3(\hat{x}, \hat{y}) = & \frac{\pi^2 U_{ac}^2}{480 c_0 \hat{L}^2} \frac{1}{\hat{R}^2} \sin(2\pi \hat{x}) \left\{ 4\hat{R}^3 + 150 - \frac{585}{\hat{R}} + \frac{720}{\hat{R}^2} \right. \\ & - 3\hat{y}^2 \left(\frac{240}{\hat{R}^4} - \frac{315}{\hat{R}^3} + \frac{150}{\hat{R}^2} + 8\hat{R} \right) + 60e^{2(\hat{y}-\hat{R})} + 20\frac{\hat{y}^4}{\hat{R}} \\ & \left. + 20e^{\hat{y}-\hat{R}} \left(\left(12 - \frac{18}{\hat{R}} \right) \cos(\hat{R} - \hat{y}) - \frac{18}{\hat{R}} \sin(\hat{R} - \hat{y}) + 12\frac{\hat{y}}{\hat{R}} \sin(\hat{R} - \hat{y}) \right) \right\}. \end{aligned} \quad (3.32)$$

Along the axis we obtain, neglecting terms of order $O(e^{-\hat{R}})$ and smaller

$$\frac{\bar{u}_3(\hat{x}, 0)}{\bar{u}_R} = -\frac{2\pi^2}{45} \left(\frac{\hat{R}}{\hat{L}} \right)^2 \left[\hat{R} + \frac{75}{2} - \frac{585}{4\hat{R}} + \frac{180}{\hat{R}^2} \right]. \quad (3.33)$$

Since the term in brackets is always positive, velocity \bar{u}_3 is of the opposite sign to Rayleigh's solution. Thus the associated vortices are reversed.

Note that in this equation the dominant term $\hat{R}(\hat{R}/\hat{L})^2$ could increase significantly for large values of \hat{R} . However, our working hypotheses are that the linear regime of streaming is respected, that is $Re_{NL} = (M\hat{R})^2 \ll 1$, and also that $(\hat{R}/\hat{L})^2 \ll 1$. These relations imply that the product $\hat{R}(\hat{R}/\hat{L})^2$ and consequently the velocity component \bar{u}_3 will both remain bounded for large values of \hat{R} .

The second-order pressure gradient in the x direction can be calculated from

$$\frac{\partial \bar{p}_3}{\partial \hat{x}} = \rho_0 \frac{\pi}{2} c_0 \frac{\partial^2 \bar{u}_3}{\partial \hat{y}^2}, \quad (3.34)$$

yielding

$$\begin{aligned} \frac{\partial \bar{p}_3}{\partial \hat{x}} = & -\frac{\rho_0 \pi^3 U_{ac}^2}{2\hat{L}^2} \sin(2\pi \hat{x}) \left\{ \frac{3}{\hat{R}^4} - \frac{63}{16\hat{R}^3} + \frac{15}{8\hat{R}^2} + \frac{\hat{R}}{10} - \frac{\hat{y}^2}{2\hat{R}} - \frac{1}{20} e^{2(\hat{y}-\hat{R})} \right. \\ & \left. + \frac{1}{2} e^{\hat{y}-\hat{R}} \left(\frac{-1+2\hat{y}}{\hat{R}} \cos(\hat{R} - \hat{y}) + \left(\frac{1}{\hat{R}} - 2 \right) \sin(\hat{R} - \hat{y}) \right) \right\}. \end{aligned} \quad (3.35)$$

For this source term the axial pressure gradient (which is very small) does depend on \hat{y} .

3.2.5. Problem 4: fourth source term

Considering the fourth source term yields

$$\frac{\pi}{2} c_0 \hat{L} \frac{\partial^3 \bar{u}_4}{\partial \hat{y}^3} = -\hat{L} \frac{\partial^2 (\bar{v}' \bar{v}')}{\partial \hat{x} \partial \hat{y}}, \quad (3.36)$$

with boundary conditions (3.11a,b)–(3.11d) for \bar{u}_4 . Integrating equation (3.36) and using the boundary conditions, the following simplified solution is found:

$$\bar{u}_4(\hat{x}, \hat{y}) = \frac{\pi^2 U_{ac}^2}{120 c_0} \sin(2\pi \hat{x}) \left(\frac{\hat{R}}{\hat{L}} \right)^2 \left[1 - 6 \left(\frac{\hat{y}}{\hat{R}} \right)^2 + 5 \left(\frac{\hat{y}}{\hat{R}} \right)^4 \right]. \quad (3.37)$$

Along the axis we obtain the following expression for the normalized axial streaming velocity

$$\frac{\bar{u}_4(\hat{x}, 0)}{\bar{u}_R} = \frac{2\pi^2}{45} \left(\frac{\hat{R}}{\hat{L}} \right)^2. \quad (3.38)$$

Comparing equations (3.38) and (3.33) shows that $\bar{u}_4(\hat{x}, 0)/\bar{u}_R$ is equal to $-1/\hat{R}$ times the first term of $\bar{u}_3(\hat{x}, 0)/\bar{u}_R$. The contribution of the fourth source term is thus negligible for large enough guides.

3.2.6. Superposition of solutions

Gathering together the four components \bar{u}_1 , \bar{u}_2 , \bar{u}_3 and \bar{u}_4 , and neglecting the lower-order terms, the total streaming velocity along the axis is given by

$$\frac{\bar{u}(\hat{x}, 0)}{\bar{u}_R} = \frac{\sum_{i=1}^4 \bar{u}_i(\hat{x}, 0)}{\bar{u}_R} = 1 - \frac{29}{6} \frac{1}{\hat{R}} - \frac{2\pi^2}{45} \frac{\hat{R}^3}{\hat{L}^2} \left[1 + \frac{73}{2\hat{R}} - \frac{585}{4\hat{R}^2} + \frac{180}{\hat{R}^3} \right]. \quad (3.39)$$

This expression shows that, under certain circumstances, the streaming flow can be reversed on the axis ($\bar{u}(\hat{x}, 0)/\bar{u}_R < 0$). This occurs when

$$\hat{L} < \hat{L}_{limit} = \pi \sqrt{\frac{2}{45}} \left(\frac{\hat{R}^3 \left(1 + \frac{73}{2\hat{R}} - \frac{585}{4\hat{R}^2} + \frac{180}{\hat{R}^3} \right)}{1 - \frac{29}{6} \frac{1}{\hat{R}}} \right)^{1/2}. \quad (3.40)$$

Figure 4 shows the variation with \hat{R} of the limit value \hat{L}_{limit}/\hat{R} . For geometries that fall under the curve, there exists a reversed flow on the axis. Minimum values are $\hat{R} = 13.52$, $\hat{L}/\hat{R} = L/R = 5.24$. These values are compatible with the hypothesis $(\hat{R}/\hat{L})^2 \ll 1$. For example, for $\hat{R} = 100$, reversed outer streaming velocity occurs if $\hat{L} < 789$, or $L/R < 7.89$.

In order to characterize the possible applications, let us consider a practical case of reverse flow along the guide axis. Let \hat{L} and \hat{R} be fixed. For resonance conditions, $\lambda = 2L$ and $\omega = \pi c_0/L$. Using $\delta_v^2 = 2\nu/\omega$ and $\hat{L} = L/\delta_v$, the following equations are obtained

$$L = \frac{2\nu}{\pi c_0} \hat{L}^2, \quad R = L \frac{\hat{R}}{\hat{L}}. \quad (3.41a,b)$$

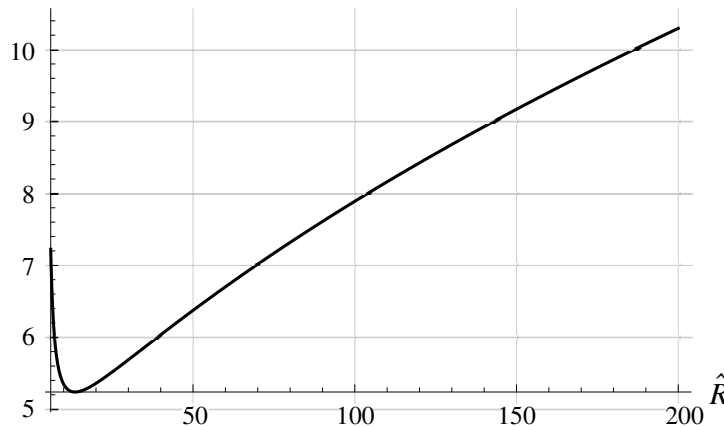


FIGURE 4. Limit value $\hat{L}_{\text{limit}}(\hat{R})/\hat{R}$ under which the flow is reversed on the axis.
Minimum values: $\hat{R} = 13.52$, $\hat{L}_{\text{limit}}/\hat{R} = 5.24$.

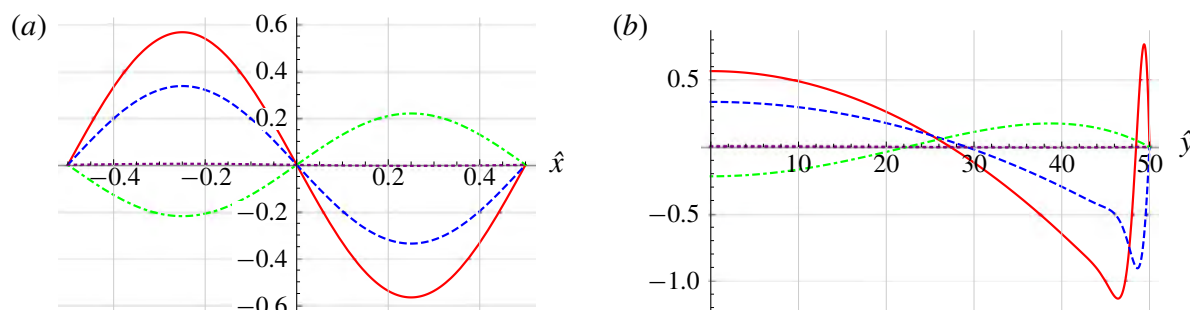


FIGURE 5. (Colour online) Axial streaming velocities $\bar{u}_1(\hat{x}, \hat{y})/\bar{u}_R$ (red solid line), $\bar{u}_2(\hat{x}, \hat{y})/\bar{u}_R$ (blue dashed line), $\bar{u}_3(\hat{x}, \hat{y})/\bar{u}_R$ (green dotdashed line) and $\bar{u}_4(\hat{x}, \hat{y})/\bar{u}_R$ (purple dotted line). $\hat{R} = 50$, $\hat{L} = 500$. (a) $\hat{y} = 0$; (b) $\hat{x} = -1/4$.

Let $\hat{L} = 789$ and $\hat{R} = 100$, as previously. Taking standard values corresponding to air, $\nu = 1.496 \times 10^{-5} \text{ m}^2 \text{ s}^{-1}$ and $c_0 = 343.82 \text{ m s}^{-1}$, we obtain $L = 17.2 \text{ mm}$, $R = 2.15 \text{ mm}$ and the resonance frequency $f = 10 \text{ kHz}$. These dimensions are small and could concern microfluidics systems, where Rayleigh streaming is used, for example within the field of acoustic particle trapping and manipulation or efficient fluid mixing. It is interesting to remark that some experiments in microfluidics have shown Rayleigh streaming vortices rotating in the opposite direction to that expected. Our results could give an explanation to this phenomenon that is a subject of debate (Wiklund, Green & Ohlin 2012).

Figure 5 shows the four components \bar{u}_1/\bar{u}_R , \bar{u}_2/\bar{u}_R , \bar{u}_3/\bar{u}_R and \bar{u}_4/\bar{u}_R along the axis (a) and along \hat{y} for $\hat{x} = -1/4$ (b). Here we have $\hat{R} = 50$ and $\hat{L} = 500$. We notice that the fourth contribution is negligible, and that the third contribution is of the same order of magnitude as the second one. Figure 6 shows the total axial velocity \bar{u} profile for $\hat{R} = 100$ and two values of \hat{L} : $\hat{L} = 600$ and $\hat{L} = 8000$. The difference between the two profiles is important in the core of the guide, whereas in the very near wall region, both profiles are very close.

This feature was also observed (even though the acoustic regime and the geometric configuration were different) in experiments as well as numerical simulations, that revealed situations where the outer streaming flow was greatly modified (up to occurrence of reverse flow), while the inner streaming flow was nearly unmodified (Reyt *et al.* 2013; Reyt, Bailliet & Valière 2014).

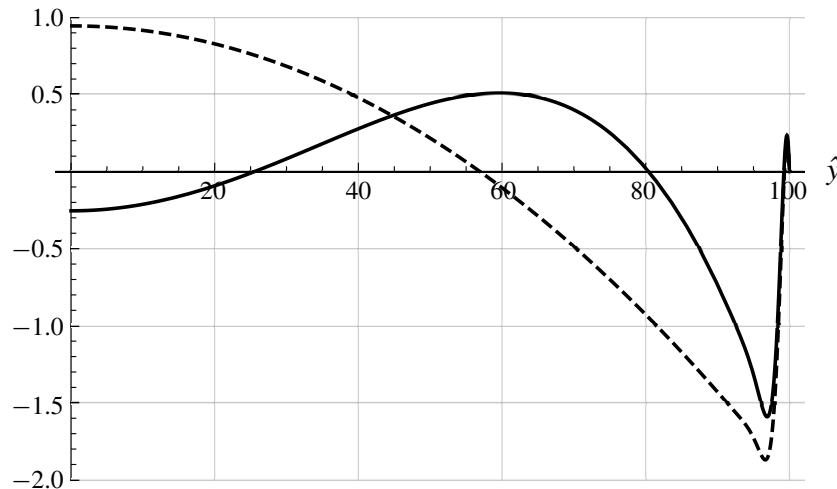


FIGURE 6. Total normalized axial streaming velocity transverse profile $u(-1/4, \hat{y})/\bar{u}_R$ for $\hat{R} = 100$ and $\hat{L} = 600$ (solid line), $\hat{L} = 8000$ (dashed line).

At this stage we have shown that the usually neglected third source term of outer streaming is responsible for drastic change of behaviour of acoustic streaming for certain (\hat{L}, \hat{R}) conditions. The ratio R/δ_v is usually considered as the criterion to differentiate between different streaming regimes, from narrow guides with only inner cells to large guides with mostly outer cells. The present study implies that not only R/δ_v but also R/L ratios should be considered in order to examine the organization of the streaming flow.

In the following sections we consider the impact of this finding on other characteristics of streaming flow: slip velocity, mass transport velocity, vertical component of streaming velocity.

3.2.7. Slip velocity

The viscous boundary layer vortex thickness (inner streaming) was estimated to be approximatively equal to $1.9\delta_v$ by Schlichting (1932), who did not consider streaming outside the boundary layer. As shown by experiments (Moreau *et al.* 2008), the limit for large guides between inner and outer streaming cells is $3\delta_v$ from the wall, as illustrated in figure 1. At $3\delta_v$ from the guide wall, the axial streaming velocity was indeed found to reach its maximum. The flow in the core of the guide is initiated by transverse diffusion of momentum from there. This position is the limit between inner and outer streaming cells and the value of the axial streaming velocity at non-dimensional $\hat{y} = \hat{y}^l = \hat{R} - 3$ is thus generally considered as a slip velocity when inner streaming is not described. Rayleigh's solution for the slip velocity is given by $\bar{u}_R^{sv} = (3/8)U_{ac}^2/c_0 \sin(2\pi\hat{x})$.

The actual non-dimensional transverse location \hat{y}^{sv} of the maximum of the axial streaming velocity can however deviate from this standard value, depending on values of \hat{R} and \hat{L} . Figure 7 shows the difference (or offset) $\hat{y}^{sv} - \hat{y}^l$ between the actual and standard location of the slip velocity as a function of \hat{R} (for $6 < \hat{R} < 200$), for two values of \hat{L} . For the largest value of \hat{L} , we note that the actual location shifts slightly away from the wall as \hat{R} increases (it is placed at the standard value for $\hat{R} = 28$). This is in agreement with previous results showing the evolution of the axial streaming velocity transverse profile with the ratio R/δ_v (e.g. figure 4 of Bailliet *et al.* (2001) and figure 4 of Hamilton *et al.* (2003a)).

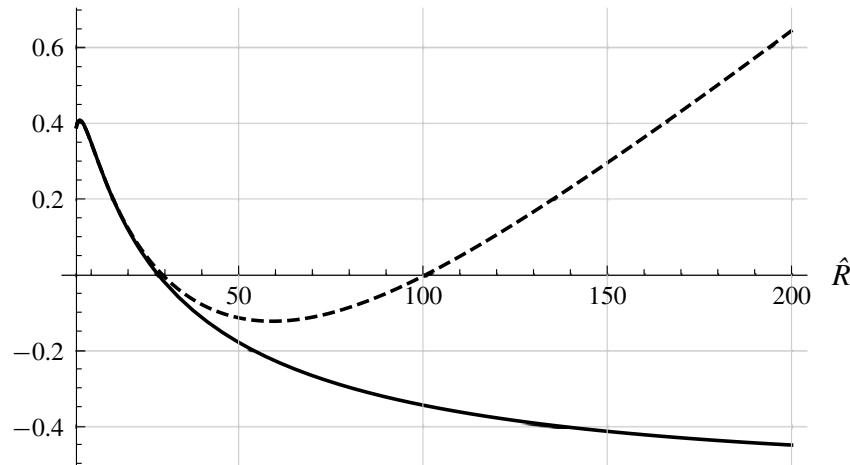


FIGURE 7. Difference (or offset) between the actual location \hat{y}^{SV} and the standard location $\hat{R} - 3$ of the slip velocity, as a function of \hat{R} . Solid line: $\hat{L} = 8000$, dashed line: $\hat{L} = 500$.

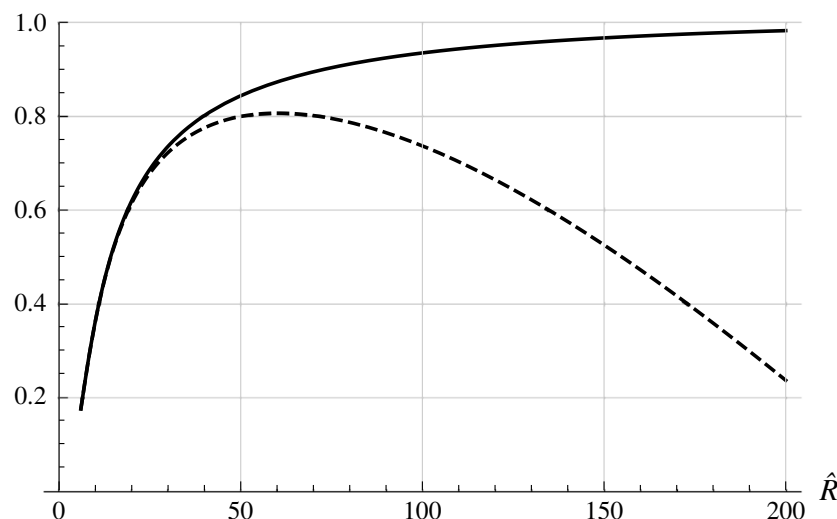


FIGURE 8. Normalized axial slip velocity at position $\hat{y} = \hat{y}^{SV}$, as a function of \hat{R} . Solid line: $\hat{L} = 8000$, dashed line: $\hat{L} = 500$.

For the smallest value of \hat{L} , the actual location of the slip velocity shifts closer to the wall as \hat{R} increases. This can be related to the fact that the \bar{u}_3 contribution becomes large (see figure 5).

Figure 8 shows the axial slip velocity \bar{u} , normalized by \bar{u}_R^{SV} , at the actual position $\hat{y} = \hat{y}^{SV}$ (corresponding to figure 7). It can be noted that the normalized value goes naturally to almost 1 as \hat{R} becomes large for the largest value of \hat{L} . However this is not the case for the smallest value of \hat{L} and the normalized value is reduced significantly for $\hat{R} > 50$.

Here again we explore the limit of validity of the classical approach by showing that both the position and the value of the slip velocity are dependent not only on \hat{R} but also on \hat{L} . This is stressed also by results shown in figure 9 that gives a comparison of the slip velocity and the maximum normalized axial velocity on the guide axis, for $\hat{L} = 8000$ and $\hat{L} = 500$. We can see that the axial slip velocity departs from Rayleigh's solution more than that on the axis for small values of \hat{R} (the solid curve is below

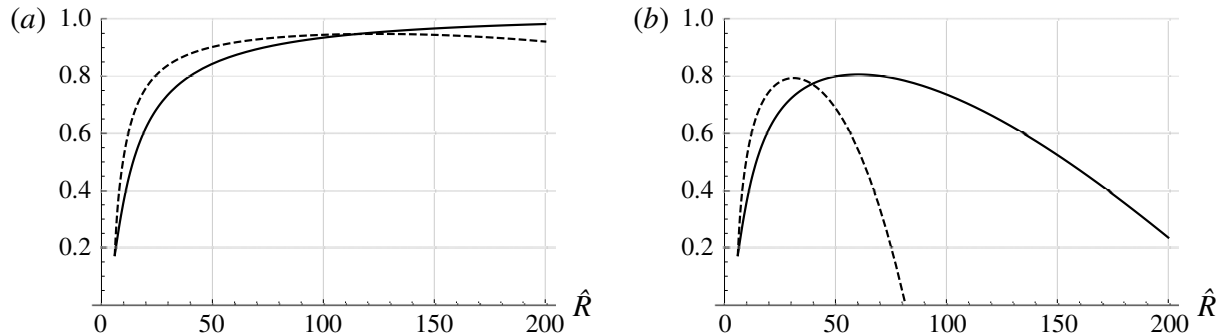


FIGURE 9. Normalized axial slip velocity versus \hat{R} (solid line), and maximum normalized axial streaming velocity on the axis (dashed line). (a) $\hat{L} = 8000$, (b) $\hat{L} = 500$.

the dashed curve). For large values of \hat{R} , the opposite is true: the slip velocity departs from Rayleigh's solution less than the axial streaming velocity on the guide axis. Comparing figure 9 (a,b) shows that this tendency is emphasized for smaller values of \hat{L} , due to increased importance of \bar{u}_3 .

3.2.8. Average mass transport velocity

The streaming velocity considered up to now in this study, is often referred to as 'Eulerian' time-average velocity. The 'average mass transport' velocity, associated with streaming mass transport, is often considered, especially for thermoacoustic applications where heat transport due to streaming is the relevant quantity of interest. The axial component of the average mass transport velocity \bar{u}^M , at the first order of approximation, is given by

$$\bar{u}^M(\hat{x}, \hat{y}) = \bar{u} + \frac{\overline{\rho' u'}}{\rho_0}. \quad (3.42)$$

Along the axis, using (3.12) and neglecting terms of order $O(e^{-\hat{R}})$ and lower, it follows that

$$\frac{\bar{u}^M(\hat{x}, 0)}{\bar{u}_R} = 1 - \frac{11}{2} \frac{1}{\hat{R}} - \frac{2\pi^2}{45} \frac{\hat{R}^2}{\hat{L}^2} \left[\hat{R} - 1 + \frac{30}{\hat{R}^2} - \frac{60}{\hat{R}^3} + \frac{45}{\hat{R}^4} \right]. \quad (3.43)$$

Figure 10 shows the transverse profiles of axial streaming velocities \bar{u} and \bar{u}^M , for three values of \hat{R} (6, 50 and 90), and two values of \hat{L} (8000 and 500). The difference between \bar{u} and \bar{u}^M is most significant in the viscous boundary layer, as usually considered. For small values of \hat{R} , differences are significant everywhere, including on the axis. These differences between \bar{u} and \bar{u}^M are obviously associated with the additional term $\overline{\rho' u'}$. As shown by expressions (3.4) and (3.6) this term is nearly zero since it is the product of two terms nearly in quadrature apart from viscous boundary layers effects. Indeed on the axis the acoustic velocity oscillates as $\cos(2\pi\hat{t})$ (see dominant terms in equation (3.4)) and the acoustic density oscillates as $\sin(2\pi\hat{t})$ (see dominant terms in equation (3.6)). This feature is associated with the standing wave

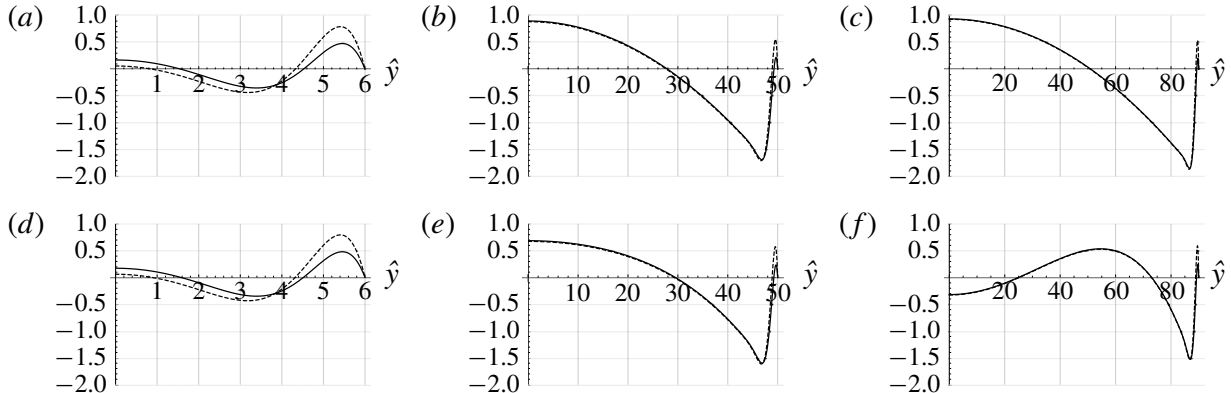


FIGURE 10. Axial velocities $\bar{u}^M(-1/4, \hat{y})/\bar{u}_R$ (dashed line), $\bar{u}(-1/4, \hat{y})/\bar{u}_R$ (solid line). (a) $\hat{R} = 6$, $\hat{L} = 8000$, (b) $\hat{R} = 50$, $\hat{L} = 8000$, (c) $\hat{R} = 90$, $\hat{L} = 8000$, (d) $\hat{R} = 6$, $\hat{L} = 500$, (e) $\hat{R} = 50$, $\hat{L} = 500$, (f) $\hat{R} = 90$, $\hat{L} = 500$.

character of the oscillation in the guide under study that is closed at both ends and excited at its resonance frequency. In such resonators acoustic pressure (and thus density oscillations) are in quadrature with acoustic velocity due to boundary layers effects. Therefore for large guides (see figure 10b,c,e,f) the difference between \bar{u} and \bar{u}^M is only significant close to the wall. For narrow guides, the inner streaming takes up most of the guide, thus \bar{u} and \bar{u}^M are different through the whole guide section (see figure 10a,d).

Also in the case $\hat{R} = 90$ and $\hat{L} = 500$ (figure 10f), the change of sign of \bar{u} at $\hat{y} \approx 25$ indicates the appearance of a new vortex with reverse flow near the axis.

3.2.9. Vertical streaming velocity

It can also be useful to consider the vertical component of streaming velocity, especially to detect the appearance of new cells. Let us define the average mass transport vertical velocity variable given by, in the first order of approximation

$$\bar{v}^M(\hat{x}, \hat{y}) = \bar{v} + \frac{\overline{\rho' v'}}{\rho_0}. \quad (3.44)$$

The continuity equation (first equation in (3.10)) becomes

$$\frac{\partial \bar{u}^M}{\partial \hat{x}} + \hat{L} \frac{\partial \bar{v}^M}{\partial \hat{y}} = 0. \quad (3.45)$$

Integrating equation (3.45) and using the boundary conditions (3.11c) yields the simplified expression

$$\begin{aligned} \bar{v}^M(\hat{x}, \hat{y}) = & \frac{\pi U_{ac}^2}{16c_0 \hat{L}} \cos(2\pi \hat{x}) \left\{ \frac{\hat{y}}{\hat{R}} \left(-33 + 6\hat{R} - 4\pi^2 \frac{\hat{R}^4}{\hat{L}^2} \right) + \frac{\hat{y}^3}{\hat{R}^3} \left(11 - 6\hat{R} + \frac{8\pi^2}{15} \frac{\hat{R}^4}{\hat{L}^2} \right) \right. \\ & - \frac{4\pi^2}{15} \frac{\hat{R}^4}{\hat{L}^2} \frac{\hat{y}^5}{\hat{R}^5} + e^{\hat{y}-\hat{R}} \left[\cos(\hat{R} - \hat{y}) \left(16 + 4\frac{\hat{y}}{\hat{R}} \right) + \sin(\hat{R} - \hat{y}) \left(16 - 4\frac{\hat{y}}{\hat{R}} \right) \right] \\ & \left. + 2e^{2(\hat{y}-\hat{R})} \right\}. \end{aligned} \quad (3.46)$$

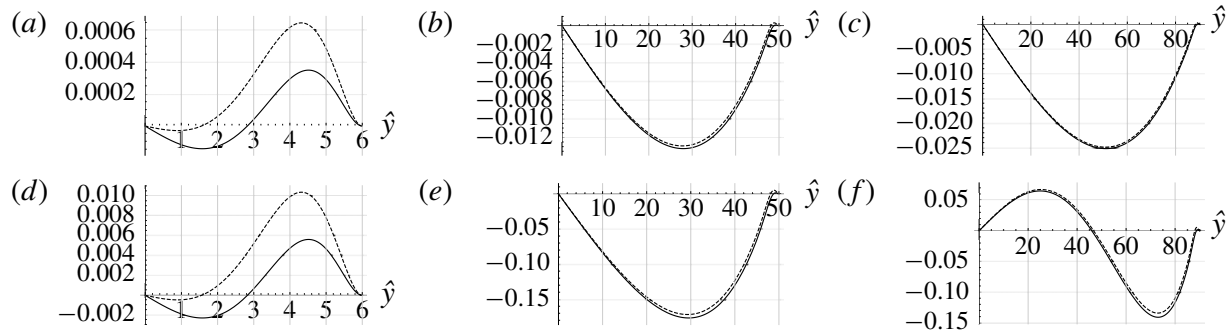


FIGURE 11. Vertical average mass transport velocities $\bar{v}^M(-1/2, \hat{y})/\bar{u}_R$ (dashed line), $\bar{v}(-1/2, \hat{y})/\bar{u}_R$ (solid line). (a) $\hat{R}=6$, $\hat{L}=8000$, (b) $\hat{R}=50$, $\hat{L}=8000$, (c) $\hat{R}=90$, $\hat{L}=8000$, (d) $\hat{R}=6$, $\hat{L}=500$, (e) $\hat{R}=50$, $\hat{L}=500$, (f) $\hat{R}=90$, $\hat{L}=500$.

The Eulerian velocity \bar{v} can be obtained using (3.44) and (3.13). Figure 11 shows the vertical velocities \bar{v} and \bar{v}^M for several values of \hat{R} and two values of \hat{L} . For small values of \hat{R} (figure 11a,d), \bar{v} and \bar{v}^M are very different. Also in the case $\hat{R}=90$ and $\hat{L}=500$ (figure 11f), the change of sign of \bar{v} and \bar{v}^M at $\hat{y} \approx 46$ indicates the appearance of a new vortex with reverse flow near the axis.

Finally, as a summary, figure 12 shows the streamlines of the streaming flow plotted using (3.42) and (3.46), for $\hat{R}=90$ and $\hat{L}=500$ and 8000. For such large values of \hat{R} , the inner streaming is restrained in a very small region near the wall. For $\hat{L}=8000$, Rayleigh streaming is composed of two counter-rotating vortices as usual, while for $\hat{L}=500$ it is composed of four vortices, the flow along the axis being reversed.

4. The axisymmetric case

Streaming flow in cylindrical guides shows common features with the one between plates. It is composed of toroidal vortices that span $\lambda/4$ in the axial direction and inner and outer vortices coexist. Figure 1 corresponds to the streaming patterns observed in an axial section. However the value of the axial streaming velocity on the axis, and the position of the centre of the outer streaming vortex, are quite different from the case of parallel plates. We have performed an analysis similar to that presented above for the case of a cylindrical guide. One goal is to deduce the condition for L/R such that additional counter-rotating streaming cells appear, associated with the third source term.

4.1. Acoustics

With the same change of variables as in the plane case ($\hat{r}=r/\delta_v$, where r is the radial coordinate), the linearized equations governing acoustics in the axisymmetric case are

$$\frac{1}{2} c_0 \frac{\partial \rho'}{\partial \hat{t}} + \rho_0 \left(\frac{\partial u'}{\partial \hat{x}} + \hat{L} \frac{1}{\hat{r}} \frac{\partial}{\partial \hat{r}} (\hat{r} v') \right) = 0 \quad (4.1a)$$

$$\rho_0 \frac{c_0}{2} \frac{\partial u'}{\partial \hat{t}} + c_0^2 \frac{\partial \rho'}{\partial \hat{x}} = \rho_0 \frac{\pi}{2} c_0 \frac{1}{\hat{r}} \frac{\partial}{\partial \hat{r}} \left(\hat{r} \frac{\partial u'}{\partial \hat{r}} \right) \quad (4.1b)$$

$$\frac{\partial \rho'}{\partial \hat{r}} = 0, \quad (4.1c)$$

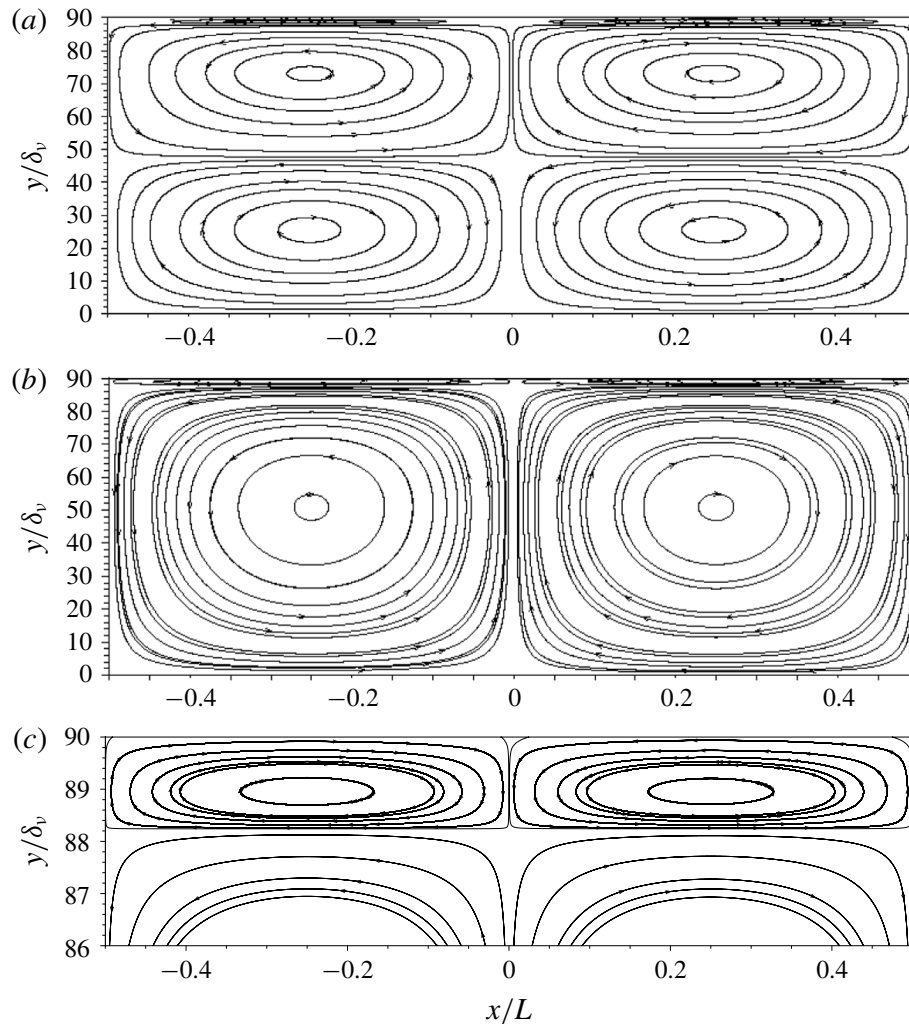


FIGURE 12. Streamlines of the mass transport velocity for $\hat{R} = 90$; $\hat{L} = 500$ (a), $\hat{L} = 8000$ (b). (c) Zoom on the inner region of top figure.

where u' and v' are the axial and radial components of the acoustic velocity. The boundary conditions for u' and v' remain given by (3.3), replacing \hat{y} by \hat{r} .

We start again with a given axial velocity solution of (4.1), approximated following Schuster & Matz (1940) for moderate and large channels ($\hat{R} \geq 6$)

$$u'(\hat{x}, \hat{r}, \hat{t}) = U_{ac} \cos(\pi\hat{x}) \left[\left(-1 + \frac{1}{2} \frac{I_0((1-i)\hat{r})}{I_0((1-i)\hat{R})} + \frac{1}{2} \frac{I_0((1+i)\hat{r})}{I_0((1+i)\hat{R})} \right) \cos(\omega\hat{t}) - \left(\frac{1}{2i} \frac{I_0((1-i)\hat{r})}{I_0((1-i)\hat{R})} - \frac{1}{2i} \frac{I_0((1+i)\hat{r})}{I_0((1+i)\hat{R})} \right) \sin(\omega\hat{t}) \right], \quad (4.2)$$

where I_0 is the modified Bessel function of the first kind.

Using the hypothesis that ρ' depends on \hat{x} and \hat{t} only, together with the boundary conditions, equation (4.1a) is integrated with respect to \hat{r} to obtain the radial acoustic

velocity component

$$v'(\hat{x}, \hat{r}, \hat{t}) = \frac{\pi}{4} U_{ac} \frac{\hat{r}}{\hat{L}} \sin(\pi \hat{x}) \left[\frac{{}_0\tilde{F}_1 \left(; 2, \frac{i\hat{r}^2}{2} \right) - {}_0\tilde{F}_1 \left(; 2, \frac{i\hat{R}^2}{2} \right)}{I_0((1+i)\hat{R})} (\cos(\omega\hat{t}) - i \sin(\omega\hat{t})) + \frac{{}_0\tilde{F}_1 \left(; 2, \frac{-i\hat{r}^2}{2} \right) - {}_0\tilde{F}_1 \left(; 2, \frac{-i\hat{R}^2}{2} \right)}{I_0((1-i)\hat{R})} (\cos(\omega\hat{t}) + i \sin(\omega\hat{t})) \right], \quad (4.3)$$

where ${}_0\tilde{F}_1(; b, z)$ is the regularized confluent hypergeometric function.

4.2. Streaming flow equations

Using the same change of variables as in the plane case, the equations to be solved are

$$\begin{cases} \rho_0 \left(\frac{\partial \bar{u}}{\partial \hat{x}} + \hat{L} \frac{1}{\hat{r}} \frac{\partial}{\partial \hat{r}} (\hat{r} \bar{v}) \right) = -\frac{\partial}{\partial \hat{x}} (\bar{\rho}' u') - \hat{L} \frac{1}{\hat{r}} \frac{\partial}{\partial \hat{r}} (\hat{r} \bar{\rho}' v') \\ \rho_0 \frac{\pi}{2} c_0 \frac{1}{\hat{r}} \frac{\partial}{\partial \hat{r}} \left(\hat{r} \frac{\partial \bar{u}}{\partial \hat{r}} \right) = \frac{\partial \bar{p}}{\partial \hat{x}} + \rho_0 \frac{\partial}{\partial \hat{x}} (\bar{u}' u') + \rho_0 \hat{L} \frac{1}{\hat{r}} \frac{\partial}{\partial \hat{r}} (\hat{r} \bar{u}' v') \\ \rho_0 \frac{\pi}{2} c_0 \frac{1}{\hat{r}} \frac{\partial}{\partial \hat{r}} \left(\hat{r} \frac{\partial \bar{v}}{\partial \hat{r}} \right) = \hat{L} \frac{\partial \bar{p}}{\partial \hat{r}} + \rho_0 \frac{\partial}{\partial \hat{x}} (\bar{u}' v') + \rho_0 \hat{L} \frac{1}{\hat{r}} \frac{\partial}{\partial \hat{r}} (\hat{r} \bar{v}' v') \end{cases} \quad (4.4)$$

and the boundary conditions for \bar{u} and \bar{v} are now

$$\bar{u} = 0 \quad \text{at } \hat{r} = \hat{R}; \quad \frac{\partial \bar{u}}{\partial \hat{r}} = 0 \quad \text{at } \hat{r} = 0, \quad (4.5a,b)$$

$$\bar{v} = 0 \quad \text{at } \hat{r} = 0 \text{ and } \hat{r} = \hat{R}, \quad (4.5c)$$

$$\int_0^{\hat{R}} \hat{r} \bar{u} d\hat{r} = 0. \quad (4.5d)$$

The average products of fluctuations are calculated with the expressions of u' and v' from equations (4.2) and (4.3). Since the complete expressions are complicated, we only give here $\bar{u}' u'$ and $\bar{u}' v'$:

$$\bar{u}' u'(\hat{x}, \hat{r}) = \frac{U_{ac}^2}{2} \cos^2(\pi \hat{x}) \frac{(I_0((1+i)\hat{r}) - I_0((1+i)\hat{R}))(I_0((1-i)\hat{r}) - I_0((1-i)\hat{R}))}{I_0((1-i)\hat{R})I_0((1+i)\hat{R})} \quad (4.6)$$

$$\begin{aligned} \bar{u}' v'(\hat{x}, \hat{r}) = & \frac{1}{16}(1-i) \frac{\pi U_{ac}^2}{\hat{R}} \frac{1}{\hat{L}} \frac{\sin(2\pi \hat{x})}{I_0((1-i)\hat{R})I_0((1+i)\hat{R})} [(I_0((1-i)\hat{r}) \\ & - I_0((1-i)\hat{R})) \left(\hat{R}J_1((1+i)\hat{r}) - \hat{r}I_1((1+i)\hat{R}) \right) \\ & + (I_0((1+i)\hat{r}) - I_0((1+i)\hat{R}))(\hat{R}J_1((1+i)\hat{r}) - \hat{r}J_1((1+i)\hat{R}))], \end{aligned} \quad (4.7)$$

where J_1 is the Bessel function of the first kind.

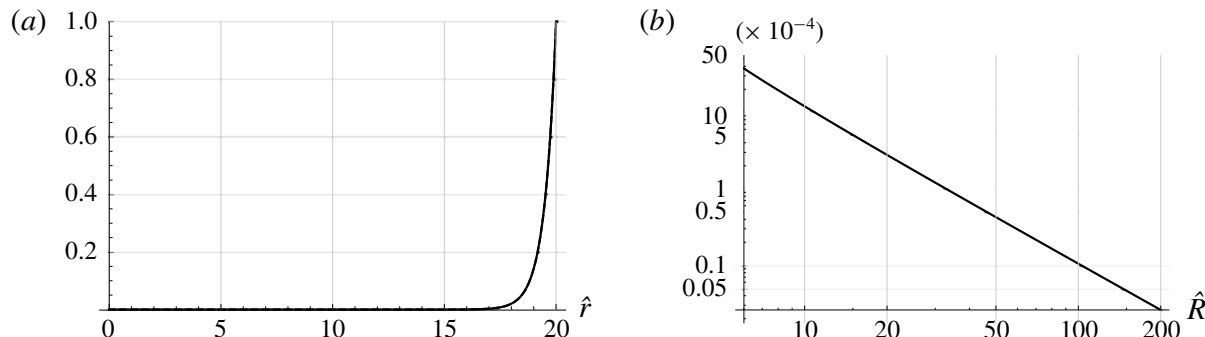


FIGURE 13. (a) $T(\hat{r}, 20)$ (solid line), approximated function (dashed line). (b) Maximum relative error as a function of \hat{R} (log–log plot).

Taking the curl of the momentum equations results in

$$\begin{aligned} -\frac{\pi}{2}c_0\hat{L}\frac{\partial}{\partial\hat{r}}\left(\frac{1}{\hat{r}}\frac{\partial}{\partial\hat{r}}\left(\hat{r}\frac{\partial\bar{u}}{\partial\hat{r}}\right)\right) &= -\hat{L}\frac{\partial^2(\bar{u}'\bar{u}')}{\partial\hat{r}\partial\hat{x}} \\ &\quad -\hat{L}^2\frac{\partial}{\partial\hat{r}}\left(\frac{1}{\hat{r}}\frac{\partial(\hat{r}\bar{u}'\bar{v}')}{\partial\hat{r}}\right) + \frac{\partial^2(\bar{u}'\bar{v}')}{\partial\hat{x}^2} + \hat{L}\frac{1}{\hat{r}}\frac{\partial^2(\hat{r}\bar{v}'\bar{v}')}{\partial\hat{x}\partial\hat{r}}. \end{aligned} \quad (4.8)$$

4.3. Results

In the same way as in the plane case, we consider separately the four problems associated with each source term in equation (4.8).

However, there is no symbolic form for the integral of terms of the form $T(\hat{r}, \hat{R}) = \text{Re}[(1+i)I_0((1+i)\hat{r})/I_0((1+i)\hat{R}) \cdot I_1((1-i)\hat{r})/I_0((1-i)\hat{R})]$ that appear in the successive integrations. Nevertheless these terms can be approximated with good accuracy using an exponential function that can be integrated symbolically. Figure 13 (a) shows $T(\hat{r}, 20)$ together with the approximated function (a purely exponential function based on a two-point interpolation) that is used instead in the successive integrations. The curves are nearly superimposed and indistinguishable. The maximum relative error between the two functions is represented in a log–log plot in figure 13 (b) for values of \hat{R} between 6 and 200, showing excellent accuracy and a variation in $1/\hat{R}^2$. The full expressions for the streaming velocity components are not developed below, since the formulae are very lengthy. Instead, the following fitted formula is obtained for the axial streaming velocity along the axis, normalized by Rayleigh's solution, which is now $\bar{u}_R = -(3/8)U_{ac}^2/c_0 \sin(2\pi\hat{x})$

$$\frac{\bar{u}}{\bar{u}_R} = 1 - 5.676\frac{1}{\hat{R}^{0.98}} - 0.296\frac{\hat{R}^{2.98}}{\hat{L}^2}. \quad (4.9)$$

This expression shows a similar but slightly different dependence on \hat{R} compared to that obtained in the plane case (3.39). It also shows that an extra cell of reversed flow may still appear near the axis in circumstances where the ratio $\hat{R}^{2.98}/\hat{L}^2$ in the third term is not negligible. More precisely, the condition for this is

$$\hat{L} \leq \hat{L}_{limit}(\hat{R}) = \left(\frac{0.296\hat{R}^{2.98}}{1 - \frac{5.676}{\hat{R}^{0.98}}} \right)^{1/2}. \quad (4.10)$$

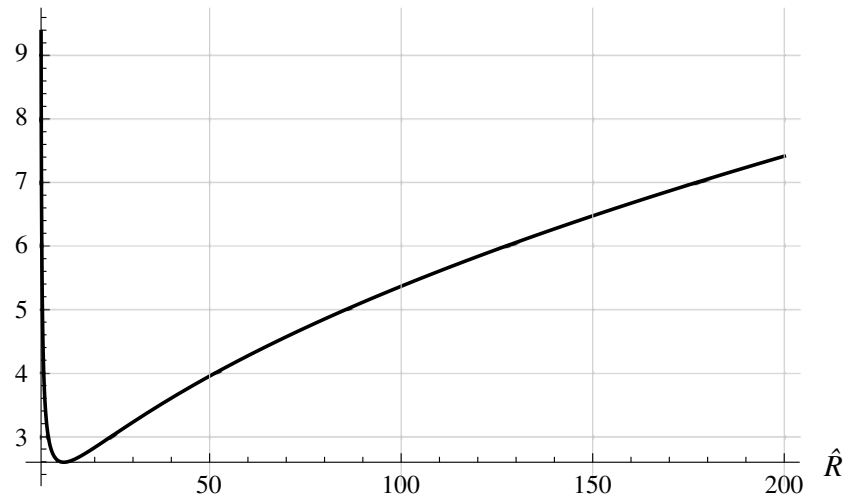


FIGURE 14. Limit value $\hat{L}_{\text{limit}}(\hat{R})/\hat{R}$ under which the flow is reversed on the axis.
Minimum values: $\hat{R} = 11.93$, $\hat{L}/\hat{R} = 2.6$.

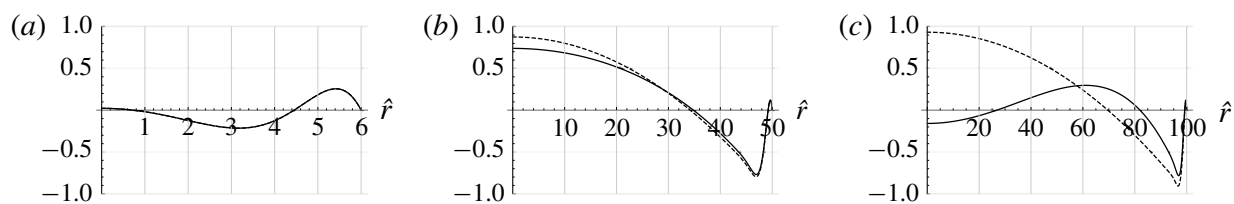


FIGURE 15. Axial velocities $\bar{u}(-1/4, \hat{y})/\bar{u}_R$, $\hat{L} = 500$ (solid line), $\hat{L} = 8000$ (dashed line).
(a) $\hat{R} = 6$, (b) $\hat{R} = 50$, (c) $\hat{R} = 100$.

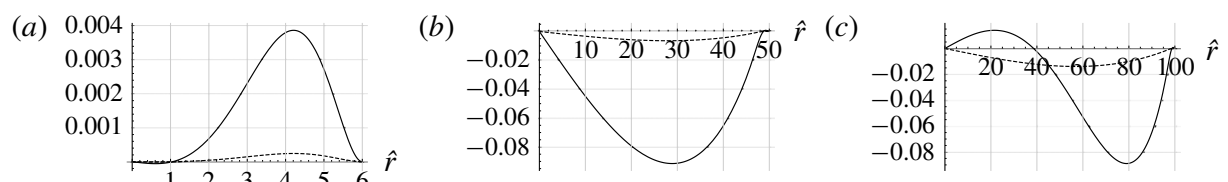


FIGURE 16. Radial velocities $\bar{v}(-1/2, \hat{y})/\bar{u}_R$, $\hat{L} = 500$ (solid line), $\hat{L} = 8000$ (dashed line). (a) $\hat{R} = 6$, (b) $\hat{R} = 50$, (c) $\hat{R} = 100$.

Figure 14 shows, for the axisymmetric case, the variation with \hat{R} of $\hat{L}_{\text{limit}}/\hat{R}$ for the appearance of reverse flow on the axis. For example, for $\hat{R} = 100$, the extra cell will appear for $\hat{L} < 536$ in the axisymmetric case, that is for a shorter guide than in the plane case. Note that for small values on the vertical axis of figure 14 the limit of validity of the hypothesis $(R/L)^2 \ll 1$ is reached.

This has to be kept in mind when assessing geometries compatible with the existence of the extra cell.

Figures 15 and 16 show the radial profiles of axial and radial streaming velocities \bar{u} , \bar{v} , for three values of \hat{R} (6, 50 and 100), and two values of \hat{L} (500 and 8000). The behaviour of the streaming flow is similar to that in the plane case. The inner

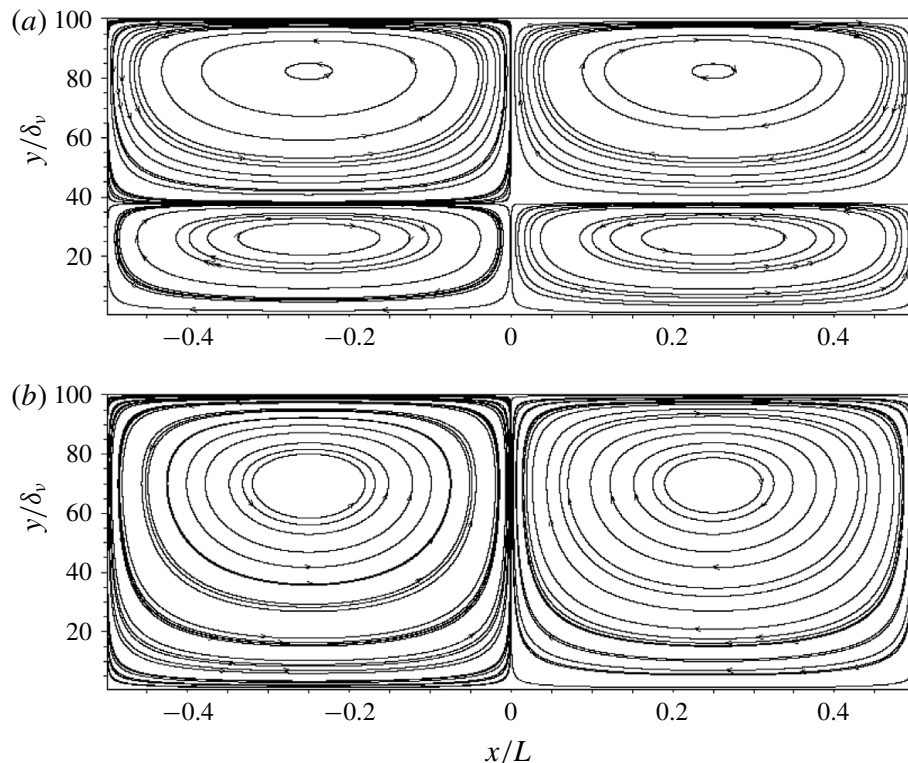


FIGURE 17. Streamlines of the mass transport velocity in an axial plane section for $\hat{R} = 100$; $\hat{L} = 500$ (a), $\hat{L} = 8000$ (b).

streaming is of lower amplitude than in the plane case. It is also seen that the centre of the outer vortex is closer to the wall than in the plane case, as expected (Rayleigh 1884). The influence of the third source term is visible in the case $\hat{R} = 50$, $\hat{L} = 500$. An extra vortex appears and the flow is reversed on the axis for $\hat{R} = 100$, $\hat{L} = 500$. Figure 17 shows the corresponding streamlines of the mass transport velocity in an axial plane section. The inner vortex is very narrow in this case and not visible on this figure.

5. Conclusion

Rayleigh's outer streaming flow in standing wave guides (infinite parallel plates or cylindrical tubes) was revisited, by solving the full linear streaming equations for moderate to large guides, using symbolic computations. The effect of each Reynolds stress source term was analysed separately and several features that were not previously reported were exhibited: analysis of the effect of the two classically dominant Reynolds stress source terms highlighted the commonly accepted fact that the streaming flow is generated only by viscous boundary layer effects. The outer streaming is created from momentum diffusion of the velocity created near the guide wall, and not from pressure gradient effects. The dependency with the guide's length and the radius of the axial streaming velocity normalized by Rayleigh's solution along the axis was quantified. It was shown that the effect of the third Reynolds stress source term which is usually neglected can become important for some geometrical parameters that were identified. In these situations, a vortex with reverse flow is created along the guide axis. Several characteristics of the streaming flow were analysed, such as slip velocity, mass transport velocity and transverse

component of streaming flow, in connection with the effect of the third source term. For all these characteristics it was shown that not only the ratio of wave guide width (or radius) to viscous boundary layer thickness, but also the ratio of guide width (or radius) to guide length, are driving criteria for the organization of streaming.

REFERENCES

- AMARI, M., GUSEV, V. & JOLY, N. 2003 Temporal dynamics of the sound wind in acoustitron. *Acta Acust. united with Acustica* **89**, 1008–1024.
- BAILLIET, H., GUSEV, V., RASPET, R. & HILLER, R. A. 2001 Acoustic streaming in closed thermoacoustic devices. *J. Acoust. Soc. Am.* **110**, 1808–1821.
- BOLURIAAN, S. & MORRIS, P. J. 2003 Acoustic streaming: from Rayleigh to today. *Intl J. Aeroacoust.* **2** (3–4), 255–292.
- DARU, V., BALTEAN-CARLÈS, D., WEISMAN, C., DEBESSE, P. & GANDIKOTA, G. 2013 Two-dimensional numerical simulations of nonlinear acoustic streaming in standing waves. *Wave Motion* **50**, 955–963.
- DARU, V., REYT, I., BAILLIET, H., WEISMAN, C. & BALTEAN-CARLÈS, D. 2017a Acoustic and streaming velocity components in a resonant wave guide at high acoustic levels. *J. Acoust. Soc. Am.* **141** (1), 563–574.
- DARU, V., WEISMAN, C., BALTEAN-CARLÈS, D., REYT, I. & BAILLIET, H. 2017b Inertial effects on acoustic Rayleigh streaming flow: transient and established regimes. *Wave Motion* **74**, 1–17.
- FAVRE, A. 1965 Équations des gaz turbulents compressibles ii.-méthode des vitesses moyennes; méthode des vitesses macroscopiques pondérées par la masse volumique. *J. Méch.* **87**, 391–421.
- HAMILTON, M. F., ILINSKII, Y. A. & ZABOLOTSKAYA, E. A. 2003a Acoustic streaming generated by standing waves in two-dimensional channels of arbitrary width. *J. Acoust. Soc. Am.* **113** (1), 153–160.
- HAMILTON, M. F., ILINSKII, Y. A. & ZABOLOTSKAYA, E. A. 2003b Thermal effects on acoustic streaming in standing waves. *J. Acoust. Soc. Am.* **114** (6), 3092–3101.
- LIGHTHILL, J. 1978 Acoustic streaming. *J. Sound Vib.* **61**, 391–418.
- MENGUY, L. & GILBERT, J. 2000a Non-linear acoustic streaming accompanying a plane stationary wave in a guide. *Acta Acust. united with Acustica* **86**, 249–259.
- MENGUY, L. & GILBERT, J. 2000b Weakly nonlinear gas oscillations in air-filled tubes; solutions and experiments. *Acta Acust. united with Acustica* **86** (5), 798–810.
- MOREAU, S., BAILLIET, H. & VALIÈRE, J.-C. 2008 Measurements of inner and outer streaming vortices in a standing waveguide using laser doppler velocimetry. *J. Acoust. Soc. Am.* **123** (2), 640–647.
- NYBORG, W. L. 1953 Acoustic streaming due to attenuated plane waves. *J. Acoust. Soc. Am.* **25**, 68–75.
- NYBORG, W. L. 1965 Acoustic streaming. In *Physical Acoustics* (ed. W. P. Mason), vol. 2B, pp. 265–331. Academic Press.
- OLSON, J. R. & SWIFT, G. W. 1997 Acoustic streaming in pulse tube refrigerators: tapered pulse tubes. *Cryogenics* **37**, 769–776.
- PARIDAENS, R., KOUIDRI, S. & JEBALI JERBI, F. 2013 Investigation on the generation mechanisms of acoustic streaming in a thermoacoustic prime mover. *Cryogenics* **58**, 78–84.
- PIERCE, A. D. 1989 *Acoustics: An Introduction to its Physical Principles and Applications*. ASA.
- QI, Q. 1993 The effect of compressibility on acoustic streaming near a rigid boundary for a plane traveling wave. *J. Acoust. Soc. Am.* **94**, 1090–1098.
- RAYLEIGH, LORD 1884 On the circulation of air observed in Kundt tubes, and on some allied acoustical problems. *Phil. Trans. R. Soc. Lond.* **175**, 1–21.
- REYT, I., DARU, V., BAILLIET, H., MOREAU, S., VALIÈRE, J.-C., BALTEAN-CARLÈS, D. & WEISMAN, C. 2013 Fast acoustic streaming in standing waves: generation of an additional outer streaming cell. *J. Acoust. Soc. Am.* **134**, 1791–1801.

- REYT, I., BAILLIET, H. & VALIÈRE, J.-C. 2014 Experimental investigation of acoustic streaming in a cylindrical wave guide up to high streaming Reynolds numbers. *J. Acoust. Soc. Am.* **135** (1), 27–37.
- ROTT, N. 1974 The influence of heat conduction on acoustic streaming. *Z. Angew. Math. Phys.* **25**, 417–421.
- SCHLICHTING, H. 1932 Berechnung ebener periodischer Grenzschicht- strommungen [calculation of plane periodic boundary layer streaming]. *Phys. Zcit.* **33**, 327–335.
- SCHUSTER, V. K. & MATZ, W. 1940 Über stationare Strömungen im Kundtschen Rohr (on stationary streaming in Kundt tubes). *Akust. Zh.* **5**, 349–352.
- SUGIMOTO, N. 2016 Nonlinear theory for thermoacoustic waves in a narrow channel and pore subject to a temperature gradient. *J. Fluid Mech.* **797**, 765–801.
- THOMPSON, M. W., ATCHLEY, A. A. & MACCARONE, M. J. 2004 Influences of a temperature gradient and fluid inertia on acoustic streaming in a standing wave. *J. Acoust. Soc. Am.* **117** (4), 1839–1849.
- WAXLER, R. 2001 Stationary velocity and pressure gradients in a thermoacoustic stack. *J. Acoust. Soc. Am.* **109** (6), 2739–2750.
- WESTERVELT, P. J. 1953 The theory of steady rotational flow generated by a sound field. *J. Acoust. Soc. Am.* **25**, 60–67.
- WIKLUND, M. G., GREEN, R. & OHLIN, M. 2012 Acoustofluidics 14: applications of acoustic streaming in microfluidic devices. *Lab on a Chip* **12**, 2438–2451.
- WOLFRAM RESEARCH INC. 2018 Mathematica, Version 11.3, Champaign, IL.
- ZAREMBO, L. K. 1971 Acoustic streaming. In *High-Intensity Ultrasonic Fields* (ed. L. D. Rozenberg), vol. 175, pp. 135–199. Plenum Press.

V. Daru, C. Weisman, D. Baltean-Carlès, H. Bailliet

" Thermal effects on fast acoustic streaming inside a resonator".

Soumis au Journal of Fluid Mechanics, février 2020.

Thermal effects on fast acoustic streaming inside a resonator

Virginie Daru^{1,3†}, Catherine Weisman^{2,3}, Diana Baltean-Carlès^{2,3},
Hélène Bailliet⁴

¹DynFluid Lab., ENSAM, 151 boulevard de l'hôpital, 75013, Paris, France

²Sorbonne-Université, Faculté des Sciences et Ingénierie, UFR d'Ingénierie, 4 Place Jussieu,
75005 Paris, France

³LIMSI, CNRS, Université Paris-Saclay, Bât. 508, Rue John Von Neumann, Campus
Universitaire, F-91405 Orsay Cedex, France

⁴Institut Pprime, CNRS - Université de Poitiers - ENSMA, ENSIP, 6 rue Marcel Doré, Bât.
B17 - BP 633, 86022 Poitiers Cedex, France

(Received xx; revised xx; accepted xx)

The effect of a transversely stratified mean temperature distribution on the acoustic streaming flow generated by a standing wave between two parallel plates is considered. Analytical expressions for acoustic first-order quantities are developed. These first-order quantities are used to express the sources of linear streaming. The influence of a transverse temperature variation on the streaming velocity is clearly identified through a term proportional to the temperature difference and to the square of the half-width of the guide. This term modifies the Rayleigh streaming patterns and may generate an additional vortex. At high acoustic levels, when heat is convected by the streaming flow, the transverse temperature difference to be expected in the waveguide is estimated, assuming that it is proportional to the longitudinal temperature difference. The latter is calculated as a cumulated effect of thermoacoustic heat transport in the fluid, heat conduction in the wall and heat convection of the air outside the resonator. Combining these expressions brings out a new criterium parameter for the non linear Reynolds number characterizing the transition in streaming patterns at high acoustic levels. This parameter depends on the wall thickness, on the thermophysical properties of the fluid and the solid wall, on the wave frequency and on the heat transfer coefficient with the outside air. This result explains previous experimental and numerical observations of the streaming flow dynamics in the fast regime, under different temperature boundary conditions, and can provide a powerful prediction tool for streaming pattern transitions.

Key words:

1. Introduction

Acoustic streaming is a steady flow generated by Reynolds stresses in an acoustically oscillating fluid, either due to absorption in the main body of an irrotational sound beam (for Eckart streaming or Quartz wind) or associated to the Stokes boundary layer adjacent to a solid boundary (Rayleigh streaming Rayleigh (1884)). Quartz wind is generally observed in systems where the length scale is much longer than the wavelength whereas

† Email address for correspondence: Virginie.Daru@ensam.eu

Rayleigh streaming is associated with a length scale of the same order of magnitude as the wavelength. It is well established that in the case of a plane standing wave at low amplitude, Rayleigh streaming is composed of toroidal so-called inner and outer vortices that have a half-wavelength spatial periodicity, the maximum axial streaming velocity being a quadratic function of the acoustic velocity amplitude at antinode. For higher acoustic levels, Menguy & Gilbert (2000) showed that the influence of inertial effects on the streaming flow is characterized by a reference nonlinear Reynolds number $Re_{NL} = (M \times R/\delta_v)^2$, where M is the acoustic Mach number, $M = U_{ac}/c_0$, with U_{ac} the maximum acoustic velocity on the channel axis and c_0 the initial speed of sound, R being the half width of the channel and δ_v the viscous boundary layer thickness. They found that the outer vortices are distorted by inertia, while the inner vortices are not affected. However their study was limited to low values of Re_{NL} (up to $Re_{NL} = 6$) and they used the assumption of isentropic flow. Later it was found, both experimentally by Thompson *et al.* (2005); Moreau *et al.* (2008); Reyt *et al.* (2013, 2014) and numerically by Boluriaan & Morris (2003); Reyt *et al.* (2013); Daru *et al.* (2013, 2017a), that the longitudinal streaming velocity component along the axis, which is a sinusoidal function of the axial coordinate at low acoustic level, becomes distorted as the acoustic level is increased. For high acoustic amplitudes, this distortion leads to the generation of counter-rotating additional vortices in the center of the guide near the acoustic velocity antinodes, while in the near wall region inner streaming vortices are only slightly modified.

In order to disentangle the physical phenomena responsible for the mutation of streaming at high acoustic levels, the isentropic case was analysed in Daru *et al.* (2017b). A similar mutation of streaming pattern was observed, although for higher values of Re_{NL} than in experiments. It was shown numerically that inertial effects cannot be considered as the leading phenomenon to explain this mutation, which was rather attributed to nonlinear interactions between acoustic and streaming flows (Daru *et al.* (2017a)). The mutation was shown to occur when the radial streaming velocity becomes larger than the radial acoustic velocity.

Thermal effects on acoustic streaming flow were investigated analytically at low acoustic levels by Hamilton *et al.* (2003) in channels/cylindrical guides of arbitrary width where the base state (including temperature) is spatially uniform. They included variation of thermophysical gas properties with temperature (for several gases corresponding to several Prandtl numbers) and showed that thermal effects have a limited influence on the streaming flow.

The influence of an imposed longitudinal temperature gradient on acoustic streaming was considered theoretically by Rott (1974); Olson & Swift (1997); Bailliet *et al.* (2001) in the context of thermoacoustic devices, where parts of the resonator are maintained under large temperature gradients using heat exchangers. Thompson *et al.* (2005) showed experimentally the strong effect of a small thermoacoustically induced longitudinal temperature gradient on the acoustic streaming flow for high values of the nonlinear Reynolds number Re_{NL} . The temperature gradient measured on the outside wall was small (up to 8 K/m, corresponding to a temperature difference across the streaming cell of 2.3 K). These streaming velocity measurements were not explained by theoretical studies in previously cited references.

The influence of an imposed transverse temperature gradient on Rayleigh streaming flow has been far less studied. Lin & Farouk (2008); Aktas & Ozgumus (2010) conducted some 2D-numerical simulations with the two longitudinal walls maintained at different temperatures. They found that the outer symmetric vortices are distorted and merge to one vortex pattern for high values of the temperature difference (up to 60 K). Note that gravity is neglected in these studies. Nabavi *et al.* (2008) studied experimentally the

influence of differentially heated horizontal walls on acoustic streaming in a parallelepipedic channel of square cross-section. They applied a vertical bottom-top temperature difference (bottom wall hotter than the top wall) ranging from 0.8 K to 3 K and found that streaming patterns are greatly modified, both in shape and in value; the streaming velocity amplitude was increased when the temperature difference was increased. In their experiment the channel width is very large, of about $400\delta_r$. However, in their study it is difficult to distinguish between buoyancy and inhomogeneity of temperature effects on the acoustic streaming flow. More recently Chini *et al.* (2014); Michel & Chini (2019) conducted theoretical studies of the acoustic streaming flow produced in a fluid with inhomogeneous background temperature and density, based on a multiple scale analysis. They called this streaming flow "baroclinic acoustic streaming", and showed that it is of the order of magnitude of the acoustic velocity, which is one order of magnitude larger than classical Rayleigh streaming flow. The motivation was the study of high-intensity discharge lamps, where large temperature differences exist and a strong two-way coupling between the acoustic field and the streaming flow is to be expected.

Cervenka *et al.* (2017) numerically studied in 2D-channels the evolution of streaming patterns with inhomogeneous background temperature, the inhomogeneity being introduced via varying prescribed temperature distribution along the resonator walls. They found that the resulting temperature heterogeneity in the direction perpendicular to the resonator axis has a great influence on the streaming field if the ratio of the channel width to the viscous boundary layer thickness is large enough. Depending on the conditions they showed that Rayleigh streaming can be enhanced (for the axis colder than the wall) or decreased (for the axis hotter than the wall), and that the streaming patterns can be considerably distorted even if the transverse temperature difference is small. In Cervenka *et al.* (2018), the authors studied the added effect of convective heat transport on the streaming field in a cylindrical geometry. Their study was however limited to weak convective effects (and thus low values of Re_{NL}), because their model was not numerically stable for values of the Reynolds number of the streaming flow, $Re_{NL} > 4$. They explained that when a longitudinal temperature gradient is established in the tube due to the thermoacoustic effect, the streaming flow convects heat along the axis from the acoustic velocity node towards the antinode, causing the appearance of a transverse temperature gradient responsible for the modification of streaming patterns at high acoustic levels. Even though the mechanism for the distortion of streaming due to temperature effects was qualitatively identified, the effects need to be further quantified.

The present study proposes to focus on the coupling between inhomogeneity of temperature and Rayleigh streaming flow in a half wavelength resonating waveguide. Our final aim is to exhibit the scaling parameters that predict the modification of streaming observed experimentally and numerically at high acoustic levels by Thompson *et al.* (2005); Reyt *et al.* (2013); Daru *et al.* (2017a). Following Cervenka *et al.* (2018), we postulate that a major effect on the streaming flow patterns is to be attributed to the change of the temperature field distribution due to heat transport by convective effect.

In order to illustrate the phenomenology of the mechanism under study, Figure 1 shows schematically the evolution of the mean temperature field as acoustic level is increased. The section shown is a longitudinal half-section between the axis (bottom) and the resonator wall (top) of length $\lambda/2$ (where λ is the wavelength). Figure 1(a) shows the mean temperature distribution obtained by thermoacoustic effect in the waveguide at low acoustic levels. There is longitudinal temperature stratification, with hot values near the acoustic nodes and cold values near the antinode. Figure 1(b) shows the temperature distribution in the waveguide at higher acoustic levels. The thermoacoustic effect develops in the near wall region (a linear/slow streaming region) and therefore there

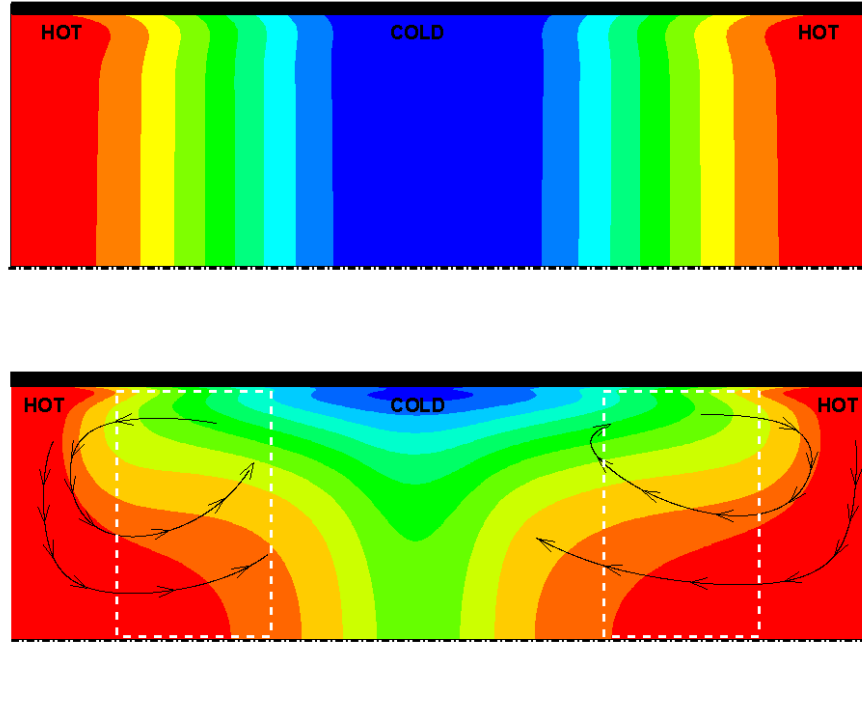


FIGURE 1. Schematics of isothermal lines obtained in the waveguide at (a) low acoustic levels and (b) high acoustic levels. The white dashed-line rectangles indicate the transversely stratified temperature regions.

is a longitudinal temperature difference in the boundary layer Merkli & Thomann (1975); Gopinath *et al.* (1998). Due to convective transport by the streaming flow towards the acoustic velocity antinode near the waveguide axis and towards the acoustic velocity node near the wall, a large zone of transverse temperature stratification appears in the central part of the streaming cells (similar temperature distributions were observed in early numerical simulations by Gopinath *et al.* (1994)). In the case of Figure 1(b), the streaming pattern is modified primarily as a consequence of the temperature reorganisation and far less as a consequence of inertial effects. Following this analysis we thus expect that the streaming flow at high acoustic levels (so-called non linear/fast streaming) can be adequately studied theoretically by solving linear equations for both acoustic and streaming flows with an imposed background transversely stratified temperature distribution. The transverse temperature difference observed in Figure 1(b) is proportional to the longitudinal temperature difference observed in the boundary layer. The latter could be well approximated by the longitudinal temperature difference calculated on the inside boundary of the wall. Since the longitudinal temperature gradient due to thermoacoustic effect is expected to be small, the transverse variations of temperature under study here are supposed to be small. This is quite different from the configurations analyzed in Chini *et al.* (2014); Michel & Chini (2019).

Following the ideas presented above, the present study is divided in five sections. In section 2 the effect of a transversely stratified temperature distribution on the streaming flow is analysed in the plane case of low acoustic amplitude. The analytical model developed in Baltean-Carlès *et al.* (2019) for isentropic flow is extended here to the case of variable mean temperature for a perfect gas. As in Baltean-Carlès *et al.* (2019), the symbolic computational software Mathematica (Wolfram (2018)) is used to solve the equations throughout this study. The plane case is addressed because analytical expressions are simpler and also we expect a behaviour very similar to the axisymmetric

case (a cylindrical geometry would involve integration of products of Bessel function that do not have any known analytic expression). The relevant similarity parameters are identified and quantified.

In section 3 the wall temperature distribution is calculated from the combined thermoacoustic effect in the fluid, heat conduction in the wall and convection from the outside air. The maximum transverse temperature difference to be expected due to convective transport can then be estimated, since it is proportional to the maximum longitudinal temperature difference (Figure 1(b)).

These results are then combined in Section 4 to exhibit a new criterium characterizing the transition in streaming pattern.

This criterium is shown in Section 5 to be in good agreement with the experimental results in the literature reported by Thompson *et al.* (2005); Reyt *et al.* (2014).

2. Analytical solution for streaming flow under a transverse gradient of temperature

In this section the effect of a transverse gradient of temperature on acoustic streaming is investigated. As stated in the introduction, previous studies by Chini *et al.* (2014); Cervenka *et al.* (2017, 2018); Michel & Chini (2019) have already shown that transverse variations of the fluid temperature lead to drastic changes in the streaming flow structure. Our goal here is to quantify these changes with respect to the geometrical parameters of the guide, thermophysical characteristics of the gas and transverse temperature difference.

The configuration under study consists in a wave guide filled with a perfect gas initially at rest. A plane standing acoustic wave of angular frequency ω is installed inside the channel. The channel has a length L and a half-width R . The reference state corresponds to uniform temperature T_0 , density ρ_0 , pressure p_0 . The corresponding sound velocity is $c_0 = \sqrt{\gamma p_0 / \rho_0}$, with γ the ratio of specific heats. The angular frequency is equal to ω_0 corresponding to the acoustic standing wave resonating at its first mode along x (so-called $\lambda/2$ mode), in the case of a non-viscous gas ($\omega_0 = \frac{\pi c_0}{L}$). The channel length is large compared to its width, $L \gg R$. The effects of gravity are not included in this study.

In the following, coordinates x , y and velocity components u , v correspond respectively to the axial and transverse directions. The origin is at the center of the channel. Pressure, density and temperature are denoted respectively p , ρ , and T . The following non-dimensional quantities are used:

$$\hat{y} = y/\delta_\nu, \quad \hat{x} = x/L, \quad \hat{R} = R/\delta_\nu, \quad \hat{L} = L/\delta_\nu$$

where $\delta_\nu = \sqrt{\frac{2\mu}{\rho_0 \omega_0}}$ is the oscillating viscous boundary layer thickness, μ being the dynamic viscosity of the gas. For symmetry reasons only a half channel is considered, that is the velocity and temperature fields are calculated and shown for $-1/2 \leq \hat{x} \leq 1/2$ and $0 \leq \hat{y} \leq \hat{R}$ only. The propagation of a low amplitude plane acoustic wave is associated with a perturbation of the initial state (defined by p_0 , ρ_m and T_m) for the fluid yielding

$$p = p_0 + p', \quad u = u', \quad v = v', \quad T = T_m + T', \quad \rho = \rho_m + \rho'. \quad (2.1)$$

We introduce the complex acoustic amplitudes \tilde{p} , $\tilde{\rho}$, \tilde{u} , \tilde{v} , \tilde{T} such that $p' = \text{Re}(\tilde{p} \exp(i2\pi\hat{t}))$, $\rho' = \text{Re}(\tilde{\rho} \exp(i2\pi\hat{t}))$, etc., where $\hat{t} = \frac{\omega_0}{2\pi}t$ is the non dimensional time.

Using Reynolds decomposition, any fluid variable ϕ is separated into a fluctuating,

periodic, component ϕ' , and a steady component $\bar{\phi}$ according to

$$\phi = \bar{\phi} + \phi' \quad (2.2)$$

where the over-line denotes the average over an acoustic period. It should be noted that the averaged product of variables ϕ and ψ writes

$$\overline{\phi\psi} = \bar{\phi}\bar{\psi} + \overline{\phi'\psi'}. \quad (2.3)$$

It is assumed that the transport properties of the gas such as specific heats c_p and c_v , heat conductivity k and viscosity μ are constant, since the effect of their variation with temperature is expected to be very small for the range of temperature variations under study. Only gases with Prandtl number $Pr < 1$ are considered here (where $Pr = \frac{\mu c_p}{k}$).

The wall temperature is constant and equal to the reference temperature T_0 . The temperature difference in the fluid between the wall and the resonator axis is noted ΔT . As stated before, for our application, ΔT is supposed to be small, that is $\Theta = \frac{\Delta T}{T_0} \ll 1$. Axial symmetry for temperature induces $\frac{\partial T}{\partial \hat{y}}|_{\hat{y}=0} = 0$.

The initial temperature distribution is taken as the simplest function $T_m(\hat{y})$ satisfying both boundary and symmetry conditions:

$$\frac{T_m}{T_0} = 1 + \Theta(1 - \frac{\hat{y}^2}{\hat{R}^2}) = f(\hat{y}). \quad (2.4)$$

This temperature distribution induces a density distribution in order to satisfy the equation of state $p_0 = r\rho_m T_m$ (where $r = c_p - c_v$), and the average density $\rho_m(\hat{y})$ takes the form

$$\frac{\rho_m}{\rho_0} = \frac{1}{f(\hat{y})}. \quad (2.5)$$

The imposed temperature distribution also induces a modification of the acoustic quantities. The following paragraph is devoted to establish the modified expression of the acoustic field.

2.1. Acoustics

For the configuration under study $\frac{\partial u'}{\partial x}/\frac{\partial u'}{\partial y}$ scales as $\delta_\nu/\lambda \ll 1$, therefore $\frac{\partial^2 u'}{\partial x^2} \ll \frac{\partial^2 u'}{\partial y^2}$ and the first order equations governing acoustics are

$$\left\{ \begin{array}{l} \frac{c_0}{2} \frac{\partial \rho'}{\partial \hat{t}} + \rho_m \frac{\partial u'}{\partial \hat{x}} + \hat{L} \frac{\partial}{\partial \hat{y}} (\rho_m v') = 0 \\ \rho_m \frac{c_0}{2} \frac{\partial u'}{\partial \hat{t}} + \frac{\partial p'}{\partial \hat{x}} = \rho_0 \frac{\pi}{2} c_0 \frac{\partial^2 u'}{\partial \hat{y}^2} \\ \frac{\partial p'}{\partial \hat{y}} = 0 \\ \rho_m \frac{\partial T'}{\partial \hat{t}} = \rho_0 \frac{\pi}{Pr} \frac{\partial^2 T'}{\partial \hat{y}^2} + \frac{1}{c_p} \frac{\partial p'}{\partial \hat{t}} \end{array} \right. \quad \begin{array}{l} a) \\ b) \\ c) \\ d) \end{array} \quad (2.6)$$

The first order equation of state for density is

$$\frac{\rho'}{\rho_m} = \frac{p'}{p_0} - \frac{T'}{T_m} \quad (2.7)$$

The boundary and symmetry conditions for u' , v' and T' with respect to \hat{y} give

$$\left\{ \begin{array}{ll} u' = 0 & \text{at } \hat{y} = \hat{R}; \quad \frac{\partial u'}{\partial \hat{y}} = 0 & \text{at } \hat{y} = 0, \\ v' = 0 & \text{at } \hat{y} = \hat{R} \text{ and at } \hat{y} = 0, \\ T' = 0 & \text{at } \hat{y} = \hat{R}; \quad \frac{\partial T'}{\partial \hat{y}} = 0 & \text{at } \hat{y} = 0. \end{array} \right. \quad \begin{array}{l} a) \\ b) \\ c) \end{array} \quad (2.8)$$

The acoustic pressure amplitude \tilde{p} is real and written as

$$\tilde{p} = \rho_0 c_0 U_{ac} \sin(\pi \hat{x}). \quad (2.9)$$

Here the maximum value of the pressure amplitude $\rho_0 c_0 U_{ac}$ has been expressed in terms of the velocity amplitude U_{ac} at velocity antinode and the gas characteristic impedance $\rho_0 c_0$. The complex acoustic velocity amplitude \tilde{u} should verify the following equation

$$i\tilde{u} - \frac{1}{2} f(\hat{y}) \frac{\partial^2 \tilde{u}}{\partial \hat{y}^2} = -\frac{1}{\rho_0 \pi c_0} f(\hat{y}) \frac{d\tilde{p}}{d\hat{x}} . \quad (2.10)$$

Because we were not able to find an exact formal solution for Eq. (2.10), the following approximate solution is proposed $\tilde{u} = \tilde{u}_1 f(\hat{y})$, where \tilde{u}_1 is the solution of

$$i\tilde{u}_1 - \frac{1}{2} \frac{\partial^2 \tilde{u}_1}{\partial \hat{y}^2} = -\frac{1}{\rho_0 \pi c_0} \frac{d\tilde{p}}{d\hat{x}}, \quad (2.11)$$

that is the usual equation written when temperature is homogeneous. The corresponding solution for \tilde{u}_1 is:

$$\tilde{u}_1 = \frac{i}{\rho_0 \pi c_0} \left(1 - e^{(1+i)(\hat{y}-\hat{R})} \right) \frac{d\tilde{p}}{d\hat{x}} . \quad (2.12)$$

Therefore \tilde{u} is equal to:

$$\tilde{u} = i U_{ac} f(\hat{y}) \left(1 - e^{(1+i)(\hat{y}-\hat{R})} \right) \cos(\pi \hat{x}) . \quad (2.13)$$

In order to test the validity of this approximation, \tilde{u} is replaced in equation (2.10), resulting in

$$i\tilde{u} - \frac{1}{2} f(\hat{y}) \frac{\partial^2 \tilde{u}}{\partial \hat{y}^2} = -\frac{1}{\rho_0 \pi c_0} f(\hat{y}) \frac{d\tilde{p}}{d\hat{x}} \left[1 + \delta(\Theta, \hat{y}, \hat{R}) \right] \quad (2.14)$$

with $\delta(\Theta, \hat{y}, \hat{R}) = \frac{\Theta}{\hat{R}^2} \left(-i + e^{(1+i)(\hat{y}-\hat{R})} (i + \hat{R}^2 - 2(1-i)\hat{y} - \hat{y}^2) \right)$.

The error function δ (shown in Figure 2) has maximum modulus values for $\hat{y} = \hat{R}$, where $|\delta(\Theta, \hat{R}, \hat{R})| = 2\sqrt{2}\frac{\Theta}{\hat{R}}$. Therefore $|\delta(\Theta, \hat{R}, \hat{R})|$ remains less than 8×10^{-3} for $0 \leq \Theta \leq 5/T_0$ ($T_0 = 294$ K) and $6 \leq \hat{R} \leq 200$. The applications under study in the present paper correspond to small enough transverse temperature gradient and large enough guides to validate the approximation of the solution of Eq. (2.10) by Eq. (2.13).

The oscillating temperature amplitude \tilde{T} verifies an equation similar to (2.10)

$$i\tilde{T} - \frac{1}{2Pr} f(\hat{y}) \frac{\partial^2 \tilde{T}}{\partial \hat{y}^2} = i \frac{1}{\rho_0 c_p} f(\hat{y}) \tilde{p} . \quad (2.15)$$

Following the same approach as for the velocity amplitude, the solution is approximated as

$$\tilde{T} = \frac{1}{\rho_0 C_p} f(\hat{y}) \left(1 - e^{(1+i)\sqrt{Pr}(\hat{y}-\hat{R})} \right) \tilde{p} \quad (2.16)$$

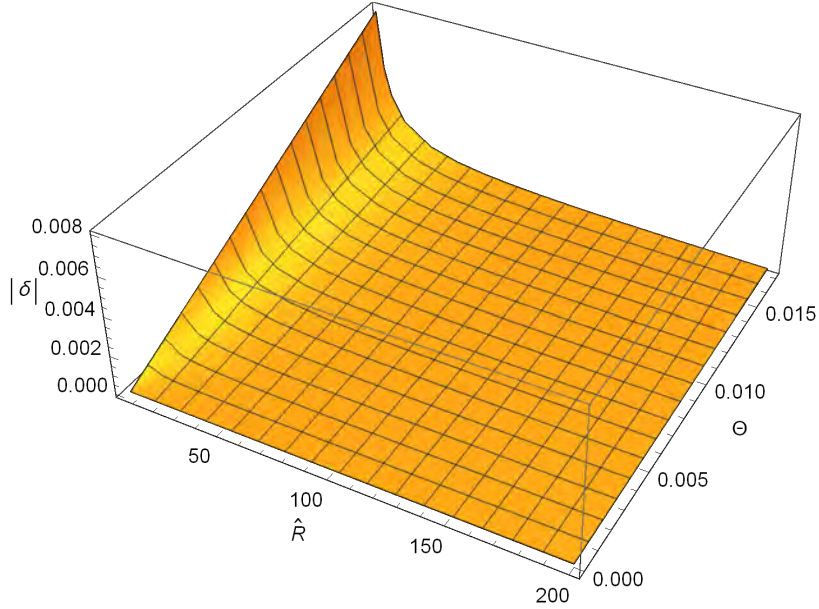


FIGURE 2. Values of $|\delta(\Theta, \hat{R}, \hat{R})|$. Θ varies between 0 and $5/294$, \hat{R} between 6 and 200.

Finally the transverse acoustic velocity amplitude \tilde{v} is calculated by integrating the continuity equation. The density amplitude $\tilde{\rho}$ is obtained from the equation of state:

$$\frac{\tilde{\rho}}{\rho_m} = \frac{\tilde{p}}{p_0} - \frac{\tilde{T}}{T_m} . \quad (2.17)$$

Reporting (2.17) in (2.6 a) gives the equation for \tilde{v}

$$i\pi c_0 \left(\frac{\tilde{p}}{p_0} - \frac{1}{f(\hat{y}) T_0} \right) + \frac{\partial \tilde{u}}{\partial \hat{x}} + \hat{L} f(\hat{y}) \frac{\partial}{\partial \hat{y}} \left(\frac{1}{f(\hat{y})} \tilde{v} \right) = 0 . \quad (2.18)$$

Developing (2.18) and neglecting terms in Θ^2 results in the following differential equation for \tilde{v}

$$\hat{L} \left(\frac{\partial \tilde{v}}{\partial \hat{y}} + 2\Theta \frac{\hat{y}}{\hat{R}^2} \tilde{v} \right) = -i\pi c_0 \left(\frac{\tilde{p}}{p_0} - \frac{1}{f(\hat{y}) T_0} \right) - \frac{\partial \tilde{u}}{\partial \hat{x}} . \quad (2.19)$$

The resulting expression for \tilde{v} provided by formal integration is very lengthy and will not be given here. Instead, Figure 3 shows the transverse profiles of \tilde{u} and \tilde{v} for $\Delta T = 0$ and 5 K. This figure shows that the two velocity component profiles are not modified inside the boundary layer. Outside the boundary layer, the axial velocity amplitude is barely modified (maximum variation of $5/294 = 1.7\%$) while the transverse velocity amplitude varies by a maximum of about 15%. We have previously shown in Daru *et al.* (2017a) that such variations on the transverse velocity amplitude can lead to significant modifications of the streaming flow. In that previous study, the modification of the transverse velocity was identified as coming from the nonlinear interaction between streaming and acoustic flows. The present development shows that another source of modification of transverse acoustic velocity and thus of acoustic streaming is the presence of a transverse temperature gradient.

As can be seen in Figure 3, the influence of the inhomogeneity of temperature is less apparent on the axial acoustic velocity than on the radial one. However, as shown in the next section, both components have comparable resulting influence on the streaming velocity.

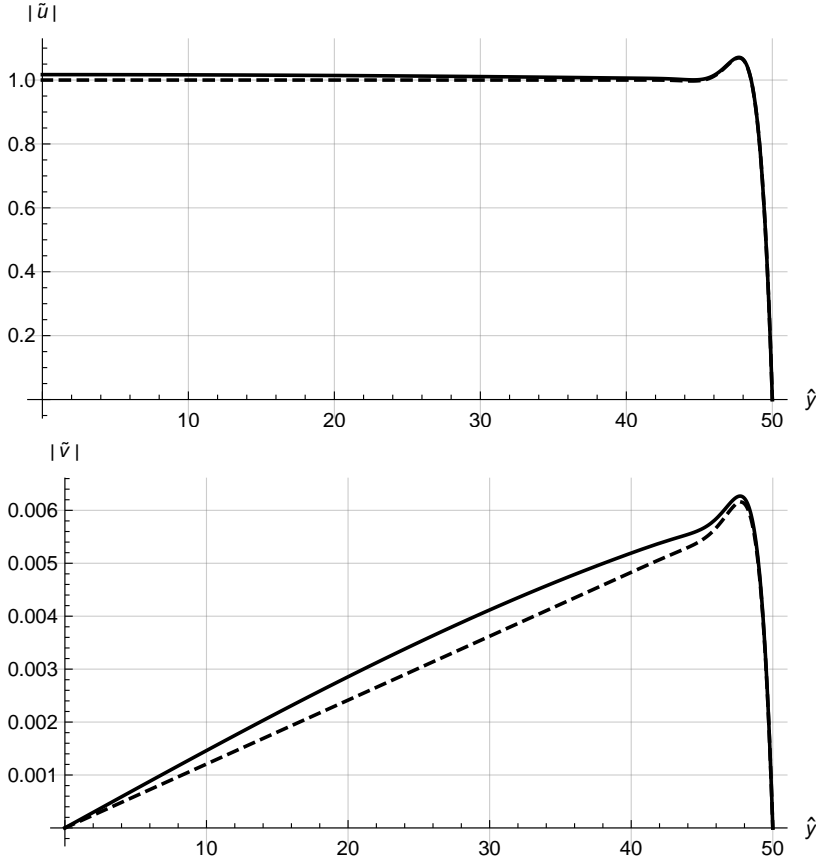


FIGURE 3. Transverse profiles of axial ($\hat{x} = 0$, top) and transverse ($\hat{x} = -1/2$, bottom) acoustic velocities (m/s), $\hat{R} = 50$. $\Delta T = 5$ K (solid), $\Delta T = 0$ K (dashed). $U_{ac} = 1$ m/s, air.

2.2. Streaming flow

In this section, the effect of a small transverse temperature gradient on acoustic streaming is investigated using the acoustic quantities calculated in the previous section.

Using the hypothesis that $\frac{\partial^2 \bar{u}}{\partial \hat{x}^2} \ll \frac{\partial^2 \bar{u}}{\partial \hat{y}^2}$, Navier-Stokes equations are averaged in time over one acoustic period, linearized and simplified as

$$\left\{ \begin{array}{l} \frac{\partial}{\partial \hat{x}}(\rho_m \bar{u}) + \hat{L} \frac{\partial}{\partial \hat{y}}(\rho_m \bar{v}) = -\frac{\partial}{\partial \hat{x}}(\bar{p}') - \hat{L} \frac{\partial}{\partial \hat{y}}(\bar{v}') \\ \rho_0 \frac{\pi}{2} c_0 \frac{\partial^2 \bar{u}}{\partial \hat{y}^2} = \frac{\partial \bar{p}}{\partial \hat{x}} + \frac{\partial}{\partial \hat{x}}(\rho_m \bar{u}' \bar{u}') + \hat{L} \frac{\partial}{\partial \hat{y}}(\rho_m \bar{u}' \bar{v}') \\ \frac{\partial \bar{p}}{\partial \hat{y}} = 0 \end{array} \right. , \quad (2.20)$$

where \bar{u} , \bar{v} and \bar{p} are the averaged velocity components and pressure, and the fluid mean density ρ_m is given by Eq. (2.5). The averaged terms on the right hand side of system (2.20) are the averaged products (Reynolds stresses) of acoustic quantities. They are the sources of streaming. In the present study, two of the three sources of streaming that were investigated in Baltean-Carlès *et al.* (2019) are taken into consideration. This is because the third source is negligible for the configuration presently studied.

The boundary conditions for \bar{u} and \bar{v} are

$$\begin{cases} \bar{u} = 0 \text{ at } \hat{y} = \hat{R}; \frac{\partial \bar{u}}{\partial \hat{y}} = 0 \text{ at } \hat{y} = 0, & a) \\ \bar{v} = 0 \text{ at } \hat{y} = 0 \text{ and } \hat{y} = \hat{R}, & b) \\ \int_0^{\hat{R}} \rho_m \bar{u} d\hat{y} = 0. & c) \end{cases} \quad (2.21)$$

The third condition in (2.21) is obtained by integrating the continuity equation in (2.20) over the half width of the channel.

Following Westervelt (1953), we take the curl of the momentum equations, which eliminates pressure, and use the assumption $\frac{\partial \bar{v}}{L \partial \hat{x}} \ll \frac{\partial \bar{u}}{\delta_\nu \partial \hat{y}}$, to obtain

$$\frac{\pi}{2} c_0 \frac{\partial^3 \bar{u}_1}{\partial \hat{y}^3} = \frac{\partial}{\partial \hat{y}} \left(\frac{1}{f(\hat{y})} \frac{\partial(\bar{u}' u')}{\partial \hat{x}} \right) + \hat{L} \frac{\partial^2}{\partial \hat{y}^2} \left(\frac{1}{f(\hat{y})} \bar{u}' v' \right). \quad (2.22)$$

Since the formulae are very lengthy, formal integration is simplified for large guides and small transverse temperature gradient by neglecting terms proportional to $e^{-\hat{R}}$ and smaller as well as terms quadratic in Θ and smaller.

The solution of the problem given by (2.22) is the superposition of solutions associated with each source term. Therefore in the following the two problems associated with the two source terms in equation (2.22) are solved successively.

2.2.1. First problem

The equation to be solved for the axial streaming velocity corresponding to the first source term is

$$\frac{\pi}{2} c_0 \frac{\partial^3 \bar{u}_1}{\partial \hat{y}^3} = \frac{\partial}{\partial \hat{y}} \left(\frac{1}{f(\hat{y})} \frac{\partial(\bar{u}' u')}{\partial \hat{x}} \right). \quad (2.23)$$

The solution results in a lengthy expression not developed here. However along the axis when smaller terms can be neglected the solution can be simplified into

$$\frac{\bar{u}_1(\hat{x}, 0)}{\bar{u}_R} = \frac{2}{3} - \frac{5}{\hat{R}} - \frac{4}{45} \Theta \hat{R}^2, \quad (2.24)$$

where the reference Rayleigh solution has been used for normalization

$$\bar{u}_R = -\frac{3}{16} \frac{U_{ac}^2}{c_0} \sin(2\pi \hat{x}). \quad (2.25)$$

2.2.2. Second problem

The equation to be solved for the axial streaming velocity corresponding to the second source term writes

$$\frac{\pi}{2} c_0 \frac{\partial^3 \bar{u}_2}{\partial \hat{y}^3} = \hat{L} \frac{\partial^2}{\partial \hat{y}^2} \left(\frac{1}{f(\hat{y})} \bar{u}' v' \right). \quad (2.26)$$

Again only the streaming velocity along the axis is given here, neglecting smaller terms and normalizing with Rayleigh's solution; it writes

$$\begin{aligned} \frac{\bar{u}_2(\hat{x}, 0)}{\bar{u}_R} = & \frac{1}{3} + \frac{2}{3} \frac{(\gamma - 1)\sqrt{Pr}}{1 + Pr} + \\ & \frac{1}{6\hat{R}} \left[1 + \frac{2(\gamma - 1)}{Pr^{3/2}(1 + Pr)^2} \left(3 + 5Pr + 6Pr^{3/2} - 8Pr^2 - 4Pr^3 \right) \right] + \frac{2}{45} \Theta \hat{R}^2 \end{aligned} \quad (2.27)$$

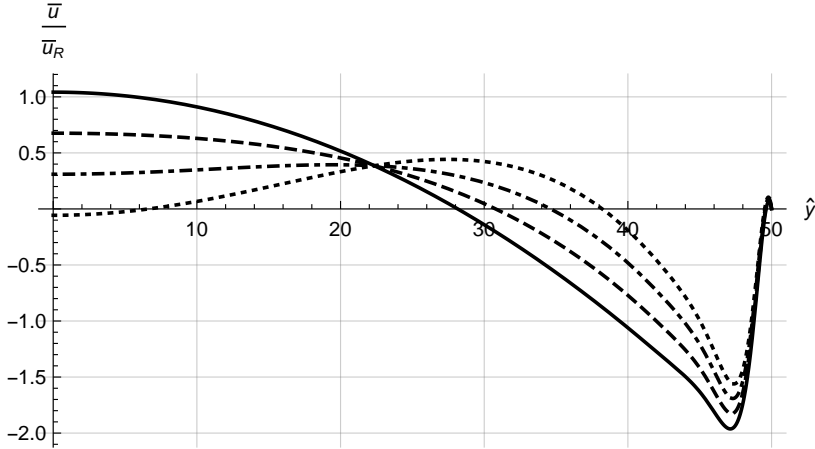


FIGURE 4. Transverse profiles of axial streaming velocity normalised by Rayleigh streaming for different transverse temperature gradients. $\hat{R} = 50$, $\hat{x} = -1/4$, Θ varies between 0 (solid line) and $3/T_0$ (dotted line).

Note that the second term in the r.h.s. of (2.27) is the same as in Rott (1974). The additional term in Θ is of sign opposite to the one in the first problem.

2.2.3. Total axial streaming velocity

The total axial streaming velocity is given by $\bar{u} = \bar{u}_1 + \bar{u}_2$, resulting along the axis in

$$\frac{\bar{u}(\hat{x}, 0)}{\bar{u}_R} = 1 + \frac{2}{3} \frac{(\gamma - 1)\sqrt{Pr}}{1 + Pr} - \frac{29}{6} \frac{1}{\hat{R}} - \frac{2}{45} \Theta \hat{R}^2 + \frac{1}{6\hat{R}} \left[\frac{2(\gamma - 1)}{Pr^{3/2}(1 + Pr)^2} \left(3 + 5Pr + 6Pr^{3/2} - 8Pr^2 - 4Pr^3 \right) \right] . \quad (2.28)$$

This expression depicts the huge effect of transverse temperature variation on the streaming velocity field, that is due to the term that varies in \hat{R}^2 . This term, proportional to $\Theta \hat{R}^2$ may be at the origin of the generation of an additional vortex. Expression (2.28) shows that this additional vortex rotates in the same direction as Rayleigh outer cell if Θ is negative (corresponding to the fluid near the axis being colder than the fluid near the wall), increasing the global amplitude of the outer streaming flow. In the opposite case where $\Theta \geq 0$ (fluid near the axis hotter than near the wall), the additional cell rotates in the opposite direction, thus decreasing the outer streaming flow. This phenomenon can eventually result in streaming flowing reversely with respect to the usual Rayleigh streaming flow. This is consistent with findings by Chini *et al.* (2014); Michel & Chini (2019), Cervenka *et al.* (2017, 2018). The interest of the present work is to provide simple expressions that quantify this phenomenon in cases of small temperature gradients.

Let us consider the condition for reversing streaming flow for two guide widths. Figure 4 shows the axial streaming velocity amplitude normalized with the reference Rayleigh solution \bar{u}_R as a function of \hat{y} for $\hat{R} = 50$ and for four values of Θ ($\Theta \times T_0 = 0, 1, 2, 3$ K). In this case, a temperature gradient of a few degrees changes drastically the velocity which becomes negative on the axis. Figure 5 shows analogous curves for a wider guide, corresponding to $\hat{R} = 150$ and for four values of Θ ($\Theta \times T_0 = 0, 0.1, 0.2, 0.3$ K). Here the effect of temperature is even more important: only a few tenths of degrees are necessary to reverse the velocity on the axis. Comparing these two figures illustrates the fact that as \hat{R} increases, the ΔT needed to reverse the streaming flow on the axis decreases since it is inversely proportional to \hat{R}^2 .

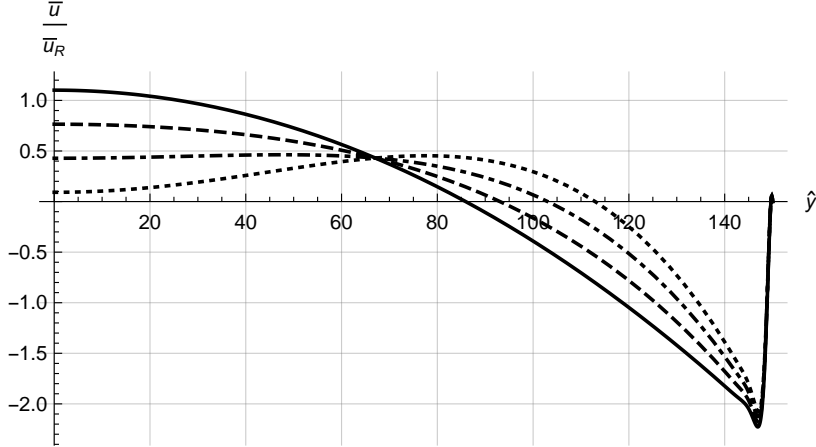


FIGURE 5. Transverse profiles of axial streaming velocity normalised by Rayleigh streaming for different transverse temperature gradients. $\hat{R} = 150$, $\hat{x} = -1/4$, Θ varies between 0 (solid line) and $0.3/T_0$ (dotted line).

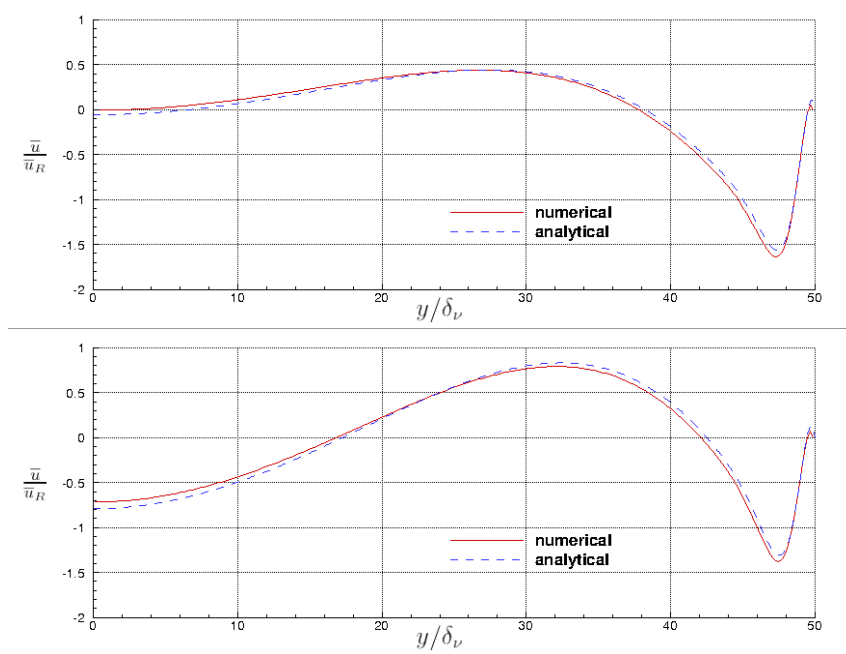


FIGURE 6. Comparison between numerical simulation and analytical solution. Top: $\Theta = 3/T_0$,
Bottom: $\Theta = 5/T_0$.

2.2.4. Comparison with direct numerical simulation.

To validate the simplifications made in our analytical study, we run a numerical simulation using the code described in Daru *et al.* (2013), that solves the complete compressible Navier-Stokes equations. In the code, the acoustic wave is created by shaking the tube periodically in the axial direction. The displacement amplitude is small in order to remain in the monofrequency acoustic regime. An initial temperature profile (2.4) is imposed, and maintained by adding the corresponding source term in the energy equation. The configuration used in this case corresponds to an acoustic wave frequency of 20000Hz in a channel of width $\hat{R} = 50$, filled with air at standard conditions. The results are shown in Figure 6, showing the normalised axial streaming velocity along the transverse direction, in the middle of the cell $\hat{x} = -\frac{1}{4}$. A very good agreement between numerical and analytical solutions is observed, showing that our analytical approach gives a very good approximation of the complete problem.

3. Temperature distribution along the resonator wall

In order to describe the interaction between acoustic streaming and thermal effects in a standing wave guide, as stated in the introduction, we now focus on the resonator mean wall temperature and its longitudinal variation. The wall temperature distribution is a result of the combination of thermoacoustic effect in the fluid, heat conduction in the wall and possible convection by the outside air.

The channel walls are assumed of thickness w and made with a material of thermal conductivity k_s , density ρ_s and specific heat c_s . The initial temperature field is supposed to be uniform in the fluid, in the wall and outside the wave guide, that is $T = T_0$ everywhere. Three different thermal boundary conditions on the resonator wall are encountered in experimental studies: isothermal, uncontrolled and insulated. In the following, the temperature distribution along the wall is set first for the so-called "isothermal" condition, where the outer side of the wall is maintained at temperature T_0 . Secondly the influence of convection outside the guide is taken into account by using a heat transfer coefficient. This second case should mimic the so-called "uncontrolled" boundary conditions in experimental studies. The third boundary condition encountered in experimental studies is the insulated condition. If the walls were perfectly insulated, there would not be any thermoacoustic effect. However, in experiments, there always remains a very small heat exchange with the outside air. Therefore, this condition is equivalent to an uncontrolled boundary condition with a much smaller effective wall conductivity.

3.1. Isothermal condition

In the isothermal case, the temperature of the fluid outside the guide is supposed constant and equal to T_0 . The equation governing heat transfer by the fluid inside the wave guide is written by averaging over an acoustic period and neglecting terms smaller than second-order in M (Swift (1988)):

$$\frac{T_0}{\rho_0} \frac{\partial}{\partial \hat{x}} (\rho_0 \bar{u} + \overline{\rho' u'}) + \frac{\partial}{\partial \hat{x}} \overline{u' T'} + \frac{T_0}{\rho_0} \hat{L} \frac{\partial}{\partial \hat{y}} (\rho_0 \bar{v} + \overline{\rho' v'}) + \hat{L} \frac{\partial}{\partial \hat{y}} \overline{v' T'} = \frac{1}{2} \pi c_0 \frac{1}{Pr} \frac{\partial^2 \bar{T}}{\partial \hat{y}^2}. \quad (3.1)$$

Integrating (3.1) from 0 to \hat{R} and taking into account that the second order mass flux over the channel section is zero yields

$$\int_0^{\hat{R}} \frac{\partial}{\partial \hat{x}} \overline{u' T'} dy = \frac{1}{2} \pi c_0 \frac{1}{Pr} \frac{\partial \bar{T}}{\partial \hat{y}} \Big|_{\hat{y}=\hat{R}}. \quad (3.2)$$

It is assumed that the steady state is established within the wall so that the temperature profile is linear across the wall, that is between $\hat{y} = \hat{R}$ and $\hat{y} = \hat{R} + \hat{w}$, with $\hat{w} = w/\delta_\nu$. Let us denote $\bar{T}_{w,in}$ the mean temperature on the inner side of the wall. The boundary condition for the heat flux at the wall is

$$k \frac{\partial \bar{T}}{\partial \hat{y}} \Big|_{\hat{y}=\hat{R}} = k_s \frac{T_0 - \bar{T}_{w,in}}{\hat{w}}. \quad (3.3)$$

Combining (3.2) and (3.3) gives an expression for the temperature of the inner side of the wall

$$\bar{T}_{w,in} = T_0 - \frac{2Pr}{\pi c_0} \frac{k}{k_s} \hat{w} \int_0^{\hat{R}} \frac{\partial}{\partial \hat{x}} \overline{u' T'} dy. \quad (3.4)$$

In order to calculate the integral in (3.4), we use the classical acoustic velocity u' given

by (2.13) with $f(\hat{y}) = 1$:

$$u' = \operatorname{Re} \left[iU_{ac} \left(1 - e^{(1+i)(\hat{y}-\hat{R})} \right) \cos(\pi\hat{x}) \exp(i2\pi\hat{t}) \right] \quad (3.5)$$

and the fluctuating temperature for conducting walls given by Swift (1988) and simplified for large enough guides ($\hat{R} \gtrsim 6$):

$$T' = \operatorname{Re} \left[\frac{1}{\rho_0 c_p} p' \left(1 - \frac{1}{1 + \varepsilon_0} \exp \left((1+i)\sqrt{Pr}(\hat{y} - \hat{R}) \right) \right) \right]. \quad (3.6)$$

In this expression $p' = \tilde{p} \exp(i2\pi\hat{t})$, with \tilde{p} given by Equation (2.9) and $\varepsilon_0 = \sqrt{\frac{\rho_0}{\rho_s} \frac{k}{k_s} \frac{c_p}{c_s}}$. Also, the convective term depending on the average temperature gradient in the x direction has not been included, as opposed to Swift (1988). This is because in Swift (1988), the axial temperature gradient was supposed to be of order $O(1)$, which is not the case in our study, where the initial temperature is uniform.

Replacing the expressions for the first order quantities, the simplified solution (neglecting terms smaller than $e^{-\hat{R}}$) for $\bar{T}_{w,in}$ is obtained after time and space integration in (3.4) as:

$$\bar{T}_{w,in} = T_0 + \hat{w} \frac{k}{k_s} \frac{U_{ac}^2}{2c_p} \sqrt{Pr} \left[\frac{-1 + Pr^{3/2} + \varepsilon_0 \sqrt{Pr}(1 + Pr)}{(1 + \varepsilon_0)(1 + Pr)} \right] \cos(2\pi\hat{x}) . \quad (3.7)$$

It is apparent from (3.7) that the inner wall temperature depends neither on the length of the channel nor on its width. It only depends on the thickness of the wall, the fluid to solid conductivity ratio, the acoustic velocity amplitude, the Prandtl number and the fluid specific heat c_p . The parameter ε_0 being generally very small has a very small effect on the wall temperature. Note that a similar dependence on the Prandtl number was reported by Gopinath *et al.* (1998) in the expression of the mean driving temperature gradient at the inner fluid-solid interface in a resonant channel.

3.2. Uncontrolled condition

In the "uncontrolled" condition, the air surrounding the guide is heated and not maintained at the reference temperature T_0 . In this case, convection occurs and the outside boundary condition is modified following Newton's law of cooling. Taking into account heat conduction within the wall results in

$$k \frac{\partial \bar{T}}{\partial y}|_R = k_s \frac{\bar{T}_{w,out} - \bar{T}_{w,in}}{w} = h(T_0 - \bar{T}_{w,out}) \quad (3.8)$$

where $\bar{T}_{w,out}$ is the outside wall temperature and h the heat transfer coefficient. Now T_0 is the temperature outside of the heated layer of air surrounding the guide. For convection in calm air, h takes values between 2 and 25 (e.g. Incropera *et al.* (2013)). The resulting expression for the inner wall temperature becomes

$$\bar{T}_{w,in} = T_0 + \left(\frac{k}{k_s} \hat{w} + \frac{k}{h\delta_\nu} \right) \frac{U_{ac}^2}{2c_p} \sqrt{Pr} \left[\frac{-1 + Pr^{3/2} + \varepsilon_0 \sqrt{Pr}(1 + Pr)}{(1 + \varepsilon_0)(1 + Pr)} \right] \cos(2\pi\hat{x}) . \quad (3.9)$$

Equation (3.9) shows that the surrounding air layer has a very strong influence on the wall temperature, since $\frac{k}{k_s}$ is generally small, implying that the dominant term in the coefficient $(\frac{k}{k_s} \hat{w} + \frac{k}{h\delta_\nu})$ is $\frac{k}{h\delta_\nu}$. The outside wall temperature takes the form

$$\bar{T}_{w,out} = T_0 + \frac{k_s}{k_s + h\hat{w}\delta_\nu} (\bar{T}_{w,in} - T_0) . \quad (3.10)$$

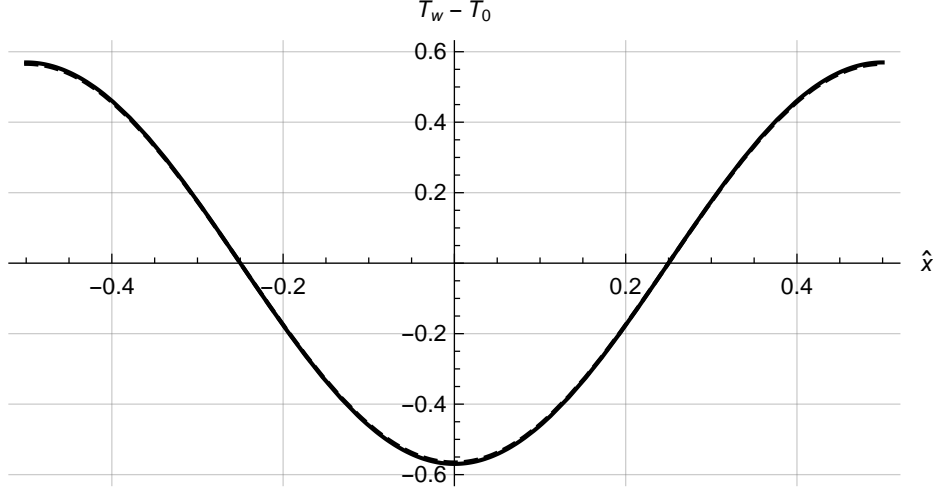


FIGURE 7. Temperature difference, in Kelvin, $T_{w,in} - T_0$ (solid) and $T_{w,out} - T_0$ (dashed). $\hat{R} = 150$, air at standard conditions, $k_s = 1.2 \text{ W}/(\text{m K})$, $\hat{w} = 20$, $h = 3 \text{ W}/(\text{m}^2 \text{ K})$, $U_{ac} = 10 \text{ m/s}$, $\delta_\nu = 1.4 \times 10^{-4} \text{ m}$.

As an example, Figure 7 shows both temperature differences $\bar{T}_{w,in} - T_0$ and $\bar{T}_{w,out} - T_0$ as a function of \hat{x} , in a case representative of experiments, corresponding to $\hat{R} = 150$, air at standard conditions, $k_s = 1.2 \text{ W}/(\text{m K})$, $\hat{w} = 20$, $h = 3 \text{ W}/(\text{m}^2 \text{ K})$, $U_{ac} = 10 \text{ m/s}$, $\delta_\nu = 1.4 \times 10^{-4} \text{ m}$. As expected, the wall is cooled in the middle of the channel, and heated at the edges (Merkli & Thomann (1975)). The temperature difference between the inner and outer wall is very small. Indeed, if the heat transfer coefficient h is varied between 2 and 25 $\text{W}/(\text{m}^2 \text{ K})$, the ratio $(\bar{T}_{w,out} - T_0)/(\bar{T}_{w,in} - T_0)$ varies from 0.997 to 0.96. It is thus adequate to consider that the mean wall temperature \bar{T}_w is the same inside and outside the wall $\bar{T}_w \simeq \bar{T}_{w,in} \simeq \bar{T}_{w,out}$.

Therefore, using Eq (3.9), the longitudinal wall temperature difference ΔT_{long} between acoustic velocity node ($\hat{x} = -1/2$) and antinode ($\hat{x} = 0$) can be written as

$$\Delta T_{long} = \left(\frac{k}{k_s} \hat{w} + \frac{k}{h \delta_\nu} \right) \frac{1}{c_p} \sqrt{Pr} \left[\frac{-1 + Pr^{3/2} + \varepsilon_0 \sqrt{Pr}(1 + Pr)}{(1 + \varepsilon_0)(1 + Pr)} \right] U_{ac}^2 , \quad (3.11)$$

which shows that ΔT_{long} is proportional to the square of the acoustic velocity amplitude, U_{ac}^2 . This was verified experimentally, and will allow us to estimate the heat transfer coefficient h (see Section 5).

4. Transition criterium

The transition in streaming pattern occurs when the streaming velocity vanishes on the guide axis in between the acoustic node and antinode. Equation (2.28) shows that the streaming velocity on the axis can vanish or become negative for $\Theta \geq 0$, when neglecting terms in $1/\hat{R}$ as a first approximation, if:

$$\frac{\Delta T}{T_0} \geq \frac{45}{2} \frac{1}{\hat{R}^2} \left(1 + \frac{2}{3} \frac{(\gamma - 1)\sqrt{Pr}}{1 + Pr} \right) . \quad (4.1)$$

where ΔT is the transverse temperature difference. As previously stated, ΔT is proportional to the longitudinal temperature difference between cold and hot regions generated by thermoacoustic effect. We choose to estimate the average value of ΔT at the middle of the cell, corresponding to $\hat{x} = -1/4$. For this longitudinal position, the wall temperature

is T_0 and the temperature on the axis is equal to $\bar{T}_{w,in}(\hat{x} = -1/2)$ because of convective heat transport (see Figure 1 b)). Neglecting small terms in ε_0 in (3.9), this results in:

$$\Delta T = \bar{T}_{w,in}(\hat{x} = -1/2) - T_0 = \left(\frac{k}{k_s} \hat{w} + \frac{k}{h\delta_\nu} \right) \frac{U_{ac}^2}{2c_p} \sqrt{Pr} \left[\frac{1 - Pr^{3/2}}{(1 + Pr)} \right] , \quad (4.2)$$

which, using the relation $c_p T_0 = \frac{c_0^2}{\gamma - 1}$, can equivalently be written as:

$$\frac{\Delta T}{T_0} = \frac{1}{2} \left(\frac{k}{k_s} \hat{w} + \frac{k}{h\delta_\nu} \right) (\gamma - 1) M^2 \sqrt{Pr} \frac{1 - Pr^{3/2}}{1 + Pr} \quad (4.3)$$

where M is the Mach number.

Replacing (4.3) in (4.1) results in:

$$\frac{1}{2} \left(\frac{k}{k_s} \hat{w} + \frac{k}{h\delta_\nu} \right) (\gamma - 1) M^2 \sqrt{Pr} \frac{1 - Pr^{3/2}}{1 + Pr} \geq \frac{45}{2} \frac{1}{\hat{R}^2} \left(1 + \frac{2}{3} \frac{(\gamma - 1)\sqrt{Pr}}{1 + Pr} \right) \quad (4.4)$$

or equivalently, since $Re_{NL} = M^2 \hat{R}^2$:

$$Re_{NL} \geq K_C \quad (4.5)$$

where

$$K_C = 30 \frac{k_s/k}{\hat{w} + k_s/(h\delta_\nu)} \left(1 + \frac{3}{2} \frac{1 + Pr}{(\gamma - 1)\sqrt{Pr}} \right) \frac{1}{(1 - Pr^{3/2})}. \quad (4.6)$$

This shows that the parameter Re_{NL} is indeed adequate for the study of streaming at high acoustic levels, and K_C given by (4.6) is a new parameter characterizing the transition of streaming pattern. The value of K_C depends on the thermo-physical characteristics of the fluid and the wall, as well as on the wave frequency and on the heat transfer coefficient. In the case of isothermal wall conditions (no air convection effects), the term $k_s/(h\delta_\nu)$ in (4.6) should be set to zero. Therefore the value of K_C depends strongly on the wall temperature boundary conditions.

5. Comparison with experimental results

In order to compare results from the previous sections with experimental data available in the literature, we have selected experiments by Thompson *et al.* (2005); Reyt *et al.* (2014) that include temperature and Rayleigh streaming velocity measurements for low and high acoustics and several thermal boundary conditions. Note that these experiments were conducted in cylindrical waveguides and therefore some discrepancy with our theoretical results (obtained for a plane geometry) is to be expected. Geometrical and thermal parameters related to both experiments are detailed in Table 1, with $T_{w,max}$ the highest value of T_w reported.

In both cases, air at standard conditions was used as the working fluid, so that $\rho_0 = 1.2 \text{ kg/m}^3$, $\mu = 1.795 \cdot 10^{-5} \text{ kg m}^{-1}\text{s}^{-1}$, $k = 0.026 \text{ W m}^{-1}\text{K}^{-1}$, $c_p = 1004.5 \text{ J/kg/K}$ resulting in $Pr = 0.726$. The tube wall was constituted of borosilicate glass (Thompson *et al.* (2005)) or pyrex (Reyt *et al.* (2014)) of similar thermophysical properties, $\rho_s = 2230 \text{ kg/m}^3$, $k_s = 1.2 \text{ W m}^{-1}\text{K}^{-1}$, $c_s = 830 \text{ J/kg/K}$.

In the experiments reported in Thompson *et al.* (2005), (uncontrolled boundary condition), the inner temperature was found to be less than 0.1 K higher than the outer temperature. This confirms that it is adequate to consider that the wall temperature is the same inside and outside the wall. Thompson *et al.* (2005) also verified experimentally that the longitudinal wall temperature difference between acoustic velocity node and

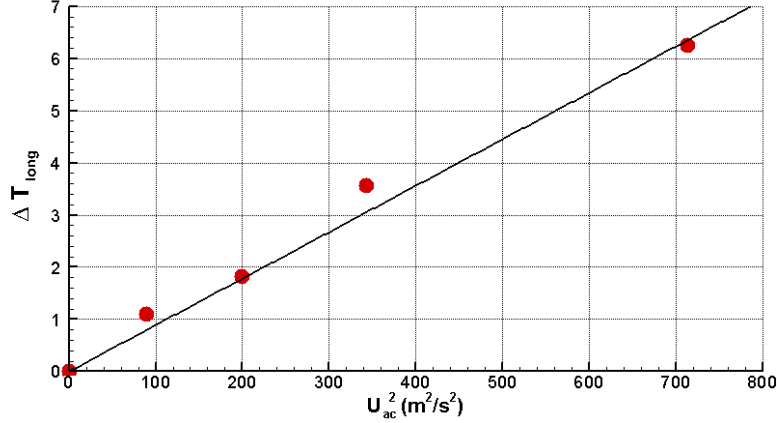


FIGURE 8. Longitudinal wall temperature difference between acoustic node and antinode ΔT_{long} as a function of U_{ac}^2 . Data corresponding to experiments in Reyt *et al.* (2014).

TABLE 1. Geometrical and thermal parameters of experiments reported in Thompson *et al.* (2005); Reyt *et al.* (2014)

Experiment	R cm	w mm	$\lambda/2$ m	δ_ν mm	T_0 K	$T_{w,max}$ K
Thompson <i>et al.</i> (2005)	2.325	2	0.56	0.124	296	297.1
Reyt <i>et al.</i> (2014)	1.96	2.5	0.712	0.139	291	297.25

antinode (ΔT_{long}) is proportional to the square of the acoustic velocity amplitude, even for high acoustic amplitudes, in agreement with Equation (3.11).

In Figure 8 are shown the longitudinal temperature differences across a streaming cell measured in the experimental setup described in Reyt *et al.* (2014), in the case of uncontrolled thermal conditions for several acoustic velocity amplitudes. Here also values of ΔT_{long} are proportional to U_{ac}^2 (with a slope equal to 0.0089). We assume also that the wall temperature is the same inside and outside the wall. Using (3.11) gives an estimate of the heat transfer coefficient h . Corresponding values of h are reported in Table 2 for both reference experiments.

For a horizontal cylinder of radius R with outside wall temperature T_w , placed in air at temperature T_0 , the average heat transfer coefficient \bar{h} can be calculated using the following correlation giving the global Nusselt coefficient \overline{Nu}_D (Churchill *et al.* (1975)), valid for $Ra_D \lesssim 10^{12}$:

$$\overline{Nu}_D = \frac{\bar{h}D}{k} = \left(0.6 + \frac{0.387 Ra_D^{1/6}}{\left(1 + \left(\frac{0.559}{Pr} \right)^{9/16} \right)^{8/27}} \right)^2 \quad (5.1)$$

with $Ra_D = \frac{2g\rho_0 c_p}{\mu k} \frac{T_w - T_0}{T_w + T_0} D^3$ the Rayleigh number based on the tube diameter $D = 2R$ and g the gravitational acceleration. The Rayleigh number Ra_D is calculated based on $T_{w,max}$.

Corresponding values of Ra_D , \overline{Nu}_D and \bar{h} are reported in Table 2 for both reference experiments. The values of h and \bar{h} are very comparable and therefore reliable.

In the case of experiment by Thompson *et al.* (2005), using the value found for h

TABLE 2. Values of the parameters.

Ref. experiment	h W m ⁻² K ⁻¹	Ra_D	\overline{Nu}_D	\bar{h} W m ⁻² K ⁻¹
Thompson <i>et al.</i> (2005)	2.35	10862	4.47	2.5
Reyt <i>et al.</i> (2014)	3.19	38909	6.12	4.1

($h = 2.35$) in Eq. 4.6 yields $K_C = 7.57$. In Thompson *et al.* (2005) the axial streaming velocity was shown to almost vanish on the axis for $Re_{NL} = 10$ and to reach zero on the axis for $Re_{NL} = 20$ in the case of uncontrolled thermal boundary conditions. Therefore we expect K_C to fall in between these two values. The agreement is pretty good keeping in mind that the theoretical approach was conducted in the plane case. In cylindrical tubes at low acoustic amplitudes, the maximum axial streaming velocity on the axis is twice that of the plane case. This could explain that K_C slightly underestimates the transition in streaming pattern.

The situation is very similar in Reyt *et al.* (2014). Using the value found for h ($h = 3.19$) in Eq. 4.6 yields $K_C = 11$. In these experiments, the axial streaming velocity was shown to almost vanish on the axis for $Re_{NL} = 14$ and to reach zero on the axis for $Re_{NL} = 30$ in the uncontrolled case. Here again K_C slightly underestimates the transition. However, our prediction of the Re_{NL} value corresponding to the transition is higher for experiments in Reyt *et al.* (2014) than for those of Thompson *et al.* (2005), in the same ratio as the measured values of Re_{NL} .

Conditions corresponding to the change in streaming flow patterns are very different in the case of isothermal walls. In this case, for values of parameters corresponding to Thompson *et al.* (2005), we obtain $K_C = 931$. This shows that in these experiments, the Mach number should be larger than 0.16 in order to satisfy the inequality (4.5), implying $U_{ac} \geq 56$ m/s. In Thompson *et al.* (2005) the largest acoustic amplitude, equal to 8.6 m/s (corresponding to $Re_{NL} = 20$), is much smaller than this limit velocity. This is why the streaming flow measured by Thompson *et al.* (2005) in the isothermal case is almost unchanged compared to the low amplitude case.

6. Conclusion

Coupling between inhomogeneity of temperature and Rayleigh streaming flow in a half wavelength resonating waveguide at high acoustic levels was analysed by following a combined formal and phenomenological approach. In such a wave-guide, a longitudinal temperature difference in the boundary layer near the wall (which is a linear/slow streaming region) is first created by thermoacoustic effect. Due to convective transport by the streaming flow towards the acoustic velocity antinode near the waveguide axis and towards the acoustic velocity node near the wall, a large zone of transverse temperature stratification appears in the central part of the streaming cells.

We thus started by solving equations for both acoustic and streaming flows with an imposed background transversely stratified temperature distribution. For this, we solved the linear equations of streaming flow, by considering the effect of dominant Reynolds stress source terms. It was shown that when the fluid near the axis is hotter than close to the wall, the total axial streaming velocity can vanish on the guide axis in

between the acoustic node and antinode. This eventually results in streaming flowing reversely with respect to the usual Rayleigh streaming flow hence a modification of the streaming pattern. The temperature reorganisation therefore has a large impact on streaming patterns. In fact, the streaming pattern is modified primarily as a consequence of the temperature reorganisation and far less as a consequence of inertial effects. We concluded that by solving linear equations for both acoustic and streaming flows with an imposed background transversely stratified temperature distribution, we could reproduce the mechanism of the modification of the streaming flow pattern at high acoustic levels (so-called non linear/fast streaming).

In order to estimate the transverse temperature difference to be expected at high acoustic levels, we started by estimating the wall temperature. Inner and outer wall temperature distribution were calculated from the combined thermoacoustic effect in the fluid, heat conduction in the wall and convection from the outside air. It was shown that for all considered applications, the temperature difference between the inner and outer wall remains very small.

At high acoustic levels, since heat is transported by the streaming flow towards the acoustic velocity antinode near the waveguide axis, the maximum transverse temperature difference was expected to be proportional to the longitudinal temperature difference between cold and hot regions generated by thermoacoustic effect. The results were then combined to exhibit a new criterium characterizing the transition in streaming pattern: the transition occurs when the classical nonlinear Reynolds parameter Re_{NL} becomes greater than a transition parameter we called K_C . The value of K_C depends on the thermophysical characteristics of the fluid and the solid constituting the tube wall, as well as on the wave frequency. This new criterium allows to explain the role of thermal boundary conditions on dynamics of streaming flow at high acoustic levels. In particular it can explain the different behaviours observed under uncontrolled or isothermal boundary conditions that had not been understood previously. In the case of isothermal wall conditions, the transition value becomes so large that it is not usually attained so that streaming Rayleigh flow patterns are almost unmodified. For "uncontrolled" thermal boundary conditions, the new criterium gives a lower bound for the transition in streaming pattern.

To conclude, we highlighted in this paper the two-way coupling interaction between the mean temperature distribution and the streaming flow. This coupling is somehow similar, but with a much stronger effect, to the non linear interaction between acoustic and streaming flows exhibited numerically in Daru *et al.* (2017a) in the isentropic case. A complete numerical simulation in a configuration similar to existing experiments is under study and will be addressed in a follow-up paper.

Declaration of Interests. The authors report no conflict of interest.

REFERENCES

- AKTAS, M. K. & OZGUMUS, T. 2010 The effects of acoustic streaming on thermal convection in an enclosure with differentially heated horizontal walls. *Int. J. Heat and Mass Transfer* **53** (23-24), 5289-5297.
- BAILLIET, H., GUSEV, V., RASPET, R. & HILLER, R. A. 2001 Acoustic streaming in closed thermoacoustic devices. *J. Acoust. Soc. Am.* **110**, 1808–1821.
- BALTEAN-CARLÈS, D., DARU, V., WEISMAN, C., TABAKOVA, S. & BAILLIET, H. 2019 An unexpected balance between outer Rayleigh streaming sources. *J. Fluid Mech.* **867**, 985–1011.
- BOLURIAAN, S. & MORRIS, P. J. 2003 Numerical simulation of acoustic streaming in high

- amplitude standing wave. *9th AIAA/CEAS Aeroacoustics Conference and Exhibit 12-14 May 2003, Hilton Head, South Carolina* AIAA 2003-3152
- CERVENKA, M. & BEDNARRIK, M. 2017 Effect of inhomogeneous temperature fields on acoustic streaming structures in resonators. *J. Acoust. Soc. Am.* **141**, 4418–4426.
- CERVENKA, M. & BEDNARRIK, M. 2018 Numerical study of the influence of the convective heat transport on acoustic streaming in a standing wave. *J. Acoust. Soc. Am.* **143**, 727.
- CHINI, G. P., MALECHA, Z. & DREEBEN, T. B. 2014 Large-amplitude acoustic streaming. *J. Fluid Mech.* **744**, 329–351.
- CHURCHILL, S. W. & CHU, H. H. S. 1975 Correlating equations for laminar and turbulent free convection from a horizontal cylinder. *Int. J. Heat Mass Transfer* **18**(9), 1323–1329.
- DARU, V., BALTEAN-CARLÈS, D., WEISMAN, C., DEBESSE, P. & GANDIKOTA, G. 2013 Two-dimensional numerical simulations of nonlinear acoustic streaming in standing waves. *Wave Motion* **50**, 955–96
- DARU, V., REYT, I., BAILLIET, H., WEISMAN, C. & BALTEAN-CARLÈS, D. 2017a Acoustic and streaming velocity components in a resonant wave guide at high acoustic levels. *J. Acoust. Soc. Am.* **141** (1), 563–574
- DARU, V., WEISMAN, C., BALTEAN-CARLÈS, D., REYT, I. & BAILLIET, H. 2017b Inertial effects on acoustic Rayleigh streaming flow: Transient and established regimes. *Wave Motion* **74**, 1–17.
- GOPINATH, A. & MILLS, A. F. 1994 Convective heat transfer due to acoustic streaming across the ends of a Kundt tube, *J. Heat Transfer* **102**(3) 47–53
- GOPINATH, A., TAIT, N. L. & GARRETT, S. L. 1998 Thermoacoustic streaming in a resonant channel: The time averaged temperature distribution. *J. Acoust. Soc. Am.* **102**(3), 1388–1405.
- GUBAIDULLIN, A. A. & YAKOVENKO, A. V. 2015 Effects of heat exchange and nonlinearity on acoustic streaming in a vibrating cylindrical cavity. *J. Acoust. Soc. Am.* **137**, 3281–3287.
- GUBAIDULLIN, A. A. & PYATKOVA, A. V. 2016 Acoustic streaming with allowance for heat transfer. *Acoustical Physics* **62** (3), 300–305.
- HAMILTON, M. F., ILINSKII, Y. A. & ZABOLOTSKAYA, E. A. 2003 Thermal effects on acoustic streaming in standing waves. *J. Acoust. Soc. Am.* **114**(6), 3092–3101.
- INCROPERA, F. P., DEWIT, D. P., BERGMAN, T. L. & LAVINE, A. S. 2013 Principles of heat and mass transfer. Seventh Edition. *John Wiley & Sons*.
- LIN, Y. & FAROUK, B. 2008 Heat transfer in a rectangular chamber with differentially heated horizontal walls: Effects of a vibrating sidewall. *Int. J. Heat Mass Transfer* **51**, 3179–3189.
- MENGUY, L. & GILBERT, J. 2000 Non-linear Acoustic Streaming Accompanying a Plane Stationary Wave in a Guide. *Acta Acustica united with Acustica* **86**, 249–259.
- MERKLI, P. & THOMANN, H. 1975 Thermoacoustic effects in a resonance tube. *J. Fluid Mech.* **70**, 161–177.
- MICHEL, G. & CHINI, G. P. 2019 Strong wave-mean-flow coupling in baroclinic acoustic streaming. *J. Fluid Mech.* **858**, 536–564.
- MOREAU, S., BAILLIET, H. & VALIÈRE, J.-C. 2008 Measurements of inner and outer streaming vortices in a standing waveguide using laser doppler velocimetry. *J. Acoust. Soc. Am.* **123**(2), 640–647.
- NABAVI, M., SIDDIQUI, K. & DARGAHI, J. 2008 Influence of differentially heated horizontal walls on the streaming shape and velocity in a standing wave resonator. *International Communications in Heat and Mass Transfer* **35**, 106–1064.
- OLSON, J. R. & SWIFT, G. W. 1997 Acoustic streaming in pulse tube refrigerators: Tapered pulse tubes *Cryogenics* **37**, 769–776.
- LORD RAYLEIGH 1884 On the circulation of air observed in Kundt tubes, and on some allied acoustical problems. *Philos. Trans. R. Soc. London* **175**, 1–21
- REYT, I., DARU, V., BAILLIET, H., MOREAU, S., VALIÈRE, J.-C., BALTEAN-CARLÈS, D. & WEISMAN, C. 2013 Fast acoustic streaming in standing waves: Generation of an additional outer streaming cell. *J. Acoust. Soc. Am.* **134**, 1791–1801.
- REYT, I., BAILLIET, H. & VALIÈRE, J.-C. 2014 Experimental investigation of acoustic streaming in a cylindrical wave guide up to high streaming Reynolds numbers. *J. Acoust. Soc. Am.* **135** (1), 27–37.

- ROTT, N. 1974 The influence of heat conduction on acoustic streaming. *Zeitschrift für Angewandte Mathematik und Physik (ZAMP)* **25**, 417–421.
- SWIFT, G. W. 1988 Thermoacoustic engines. *J. Acoust. Soc. Am.* **84**, 1145–1180.
- THOMPSON, M. W., ATCHLEY, A. A. & MACCARONE, M. J. 2005 Influences of a temperature gradient and fluid inertia on acoustic streaming in a standing wave. *J. Acoust. Soc. Am.* **117**(4) 1839–1849.
- WESTERVELT, P. J. 1953 The Theory of Steady Rotational Flow Generated by a Sound Field. *J. Acoust. Soc. Am.* **25**, 60–67.
- WOLFRAM RESEARCH, INC. 2018 Mathematica, Version 11.3, Champaign, IL.